UNIVERSITÉ DU QUÉBEC À TROIS-RIVIÈRES

CONCEPTION, MODÉLISATION ET CARACTÉRISATION D'UN DISPOSITIF DE RÉCUPÉRATION D'ÉNERGIE PIÉZOÉLECTRIQUE DE TYPE MEMS FABRIQUÉ PAR IMPRESSION 4D

THÈSE PRÉSENTÉE
COMME EXIGENCE PARTIELLE DU DOCTORAT
EN INGÉNIERIE (CONC. GÉNIE MÉCANIQUE)

PAR
AMAL MEGDICH

MAI 2025

Université du Québec à Trois-Rivières

Service de la bibliothèque

Avertissement

L'auteur de ce mémoire ou de cette thèse a autorisé l'Université du Québec à Trois-Rivières à diffuser, à des fins non lucratives, une copie de son mémoire ou de sa thèse.

Cette diffusion n'entraîne pas une renonciation de la part de l'auteur à ses droits de propriété intellectuelle, incluant le droit d'auteur, sur ce mémoire ou cette thèse. Notamment, la reproduction ou la publication de la totalité ou d'une partie importante de ce mémoire ou de cette thèse requiert son autorisation.

UNIVERSITÉ DU QUÉBEC À TROIS-RIVIÈRES

DOCTORAT (PH.D.)

Direction de recherche :

Prof. Luc Laperrière
Prénom Nom — Directeur de recherche

Prof. Mohamed Habibi
Prénom Nom — Codirecteur de recherche

Jury d'évaluation

Prof. Éric Loranger, UQTR
Prénom Nom, Nom établissement — Président

Prof. Sasan Sattarpanah Karganroudi, UQTR
Prénom Nom, Nom établissement — Évaluateur interne

Prof. Yasmine Abdin, UBC
Prénom Nom, Nom établissement — Évaluateur externe

Prof. Luc Laperrière, UQTR
Prénom Nom, Nom établissement — Directeur de recherche

Prof. Mohamed Habibi, UQTR
Prénom Nom, Nom établissement — Codirecteur de recherche

REMERCIEMENTS

À l'issue de cette thèse, je tiens à exprimer ma profonde gratitude à toutes les personnes qui ont contribué, de près ou de loin, à la réalisation de ce travail.

Tout d'abord, mes remerciements les plus sincères vont à mon directeur de recherche, Professeur Luc Laperrière, pour sa confiance, son encadrement bienveillant et ses conseils avisés tout au long de cette aventure scientifique. Son expertise et sa rigueur m'ont guidée dans l'élaboration de cette recherche et ont contribué à l'enrichissement de mes connaissances.

Je tiens également à remercier mon codirecteur, Professeur Mohamed Habibi, pour son accompagnement précieux, sa disponibilité et ses encouragements constants. Son approche méthodique et ses suggestions pertinentes ont été essentielles pour mener à bien ce travail.

Je remercie chaleureusement les membres du jury qui ont accepté d'évaluer cette thèse. Votre temps, votre regard critique et vos recommandations sont une source d'enrichissement et de valorisation de mes recherches.

Un immense merci à mes collègues et amis de laboratoire, Abdelhamid, Karima et Mounib, avec qui j'ai partagé des échanges scientifiques stimulants, des moments de collaboration enrichissants et des instants de convivialité qui ont rendu cette expérience encore plus précieuse.

Je tiens à exprimer ma gratitude infinie à ma famille, qui a toujours été mon pilier. Merci à mes parents pour leur amour inconditionnel, leur soutien indéfectible et leurs encouragements constants, qui m'ont donné la force de persévérer dans cette aventure exigeante. Merci à mon frère qui a toujours cru en moi et m'a apporté un soutien sans faille.

Enfin, je remercie tous mes amis, qui, par leur présence, leur écoute et leurs encouragements, ont contribué à faire de ce parcours une expérience humaine inoubliable.

À vous tous, merci du fond du cœur.

RÉSUMÉ

Dans un contexte où l'optimisation énergétique et l'autonomie des systèmes électroniques sont devenues des enjeux majeurs, cette thèse explore une approche innovante combinant des systèmes micro-électromécaniques piézoélectriques (MEMS) et l'impression 4D afin de développer des dispositifs intelligents et adaptatifs capables de capter efficacement l'énergie mécanique ambiante.

Nous avons d'abord étudié en profondeur les MEMS piézoélectriques, en nous concentrant sur l'optimisation de matériaux nanocomposites à base de PVDF, enrichis d'additifs tels que le titanate de baryum et les nanotubes de carbone, afin d'améliorer leurs performances piézoélectriques et mécaniques. De plus, une technique de polarisation avancée basée sur l'intelligence artificielle a été adaptée pour améliorer les performances piézoélectriques et diélectriques des nanocomposites. La conception des structures a été optimisée grâce à une modélisation numérique avancée, maximisant leur efficacité. De plus, l'impression 3D a été explorée comme méthode de fabrication alternative, assurant une précision accrue et une flexibilité structurelle optimale pour ces dispositifs. Enfin, un modèle analytique a été développé pour prédire le comportement électromécanique des MEMS.

En parallèle, des travaux ont été menés sur l'impression 4D, une technologie émergente permettant la fabrication de structures dynamiques capables de changer de forme sous l'effet de stimuli externes. Nous avons étudié des polymères à mémoire de forme électroactifs et thermosensibles, afin de comprendre leur comportement et d'optimiser leur intégration dans des dispositifs intelligents. Des simulations numériques et des expériences ont été réalisées pour modéliser la capacité de conversion courant-chaleur et l'adaptabilité structurelle des nanocomposites développés.

L'une des principales nouveautés et contributions de cette recherche a été l'intégration de ces deux technologies. En combinant les capacités de récupération d'énergie des MEMS piézoélectriques avec la flexibilité adaptative offerte par l'impression 4D, nous avons développé des MEMS imprimés en 4D, capables de modifier dynamiquement leurs caractéristiques structurelles pour optimiser leur efficacité énergétique. Cette innovation ouvre de nouvelles perspectives pour la conception de dispositifs autonomes dans divers domaines, notamment l'électronique portable, la biomédecine et les systèmes intelligents.

En conclusion, cette thèse propose une approche innovante pour le développement de MEMS adaptatifs et intelligents, basée sur les avancées récentes de l'impression 4D et des matériaux

nanocomposites. Ces travaux contribuent à l'évolution des systèmes de récupération d'énergie et ouvrent la voie à une nouvelle génération de systèmes autonomes, durables et efficaces.

Mots-clés : MEMS piézoélectriques, impression 4D, nanocomposites, récupération d'énergie, fabrication additive, systèmes autonomes.

TABLE DES MATIÈRES

REMERCIEMENTS ii

RÉSUMÉ iii

TABLE DES MATIÈRES v

LISTE DES TABLEAUX xi

LISTE DES FIGURES xiii

LISTE DES ABRÉVIATION xviii

Chapitre 1: Introduction 20

1.1 Contexte général 20
1.2 Problématique 21
1.3 Objectifs de la thèse 23
1.4 Structure de la thèse 24

Partie I : Modélisation, caractérisation, optimisation, et fabrication par impression 3D des MEMS piézoélectriques 27

Chapitre 2: Revue de littérature sur les MEMS piézoélectriques 28

2.1 Abstract 30
2.2 Introduction 30
2.3 Materials used for piezoelectric energy harvesting 35
2.3.1 Piezoelectric materials properties 35
2.3.2 Lead-based piezoelectric materials 36
2.3.3 Inorganic materials 36
2.3.4 Organic lead-free piezoelectric materials 37
2.4 3DP of PEHs 55
2.4.1 Comparison between additive manufacturing and traditional fabrication methods 56
2.4.2 3DP technologies for PEH 58
2.4.3 Multi-Material 3DP Processes 62
2.5 Applications 63
2.5.1 Wearable products 63
2.5.2 Automotive industry applications 65
2.5.3 Healthcare applications 68
2.6 Conclusions 74
2.7 Futur direction 75
2.8 Achnowlegdment 77
2.9 References 77

Chapitre 3: Modélisation et optimisation des paramètres de polarisation basées sur l'intelligence artificielle 98

3.1 Abstract 100
3.2 Introduction 100
3.3 Process parameter selection 102
3.4 Experimental section 103
3.4.1 Materials 103
3.4.2 Design of experiment 104
3.4.3 Sample preparation 105
3.4.4 Poling 105
3.4.5 Characterization 106
3.5 Results and discussions 107
3.5.1 Statistical analysis 107
3.5.2 Neural network prediction 112
3.5.3 Model analysis 113
3.5.4 Optimization of process parameters 115
3.6 Conclusion 116
3.7 Acknowledgments 117
3.8 References 117

Chapitre 4: Caractérisation, conception, et fabrication de PEH à base de nanocomposites PVDF/BT 121

4.1 Abstract 123
4.2 Introduction 123
4.3 Experimental section 126
4.3.1 Materials 126
4.3.2 Preparation of PVDF-Based Nanocomposite Filament 126
4.3.3 Poling method 127
4.3.4 Characterization 128
4.4 Results and discussion 130
4.5 Conclusion 141
4.6 Acknowledgements 142
4.7 References 142

Chapitre 5: Caractérisation, conception, et fabrication de PEH à base de nanocomposites PVDF/MWCNTs 145

5.1 Abstract 147
5.2 Introduction 148
5.3 Experimental section 150

5.3.1 Materials 150
5.3.2 Preparation of PVDF-Based Nanocomposite Filament 151
5.3.3 Poling method 152
5.3.4 Characterization 152
5.4 Results and discussion 154
5.4.1 Characterization results 154
5.4.2 Effective design and parametric study 160
5.4.3 Fabrication, Piezoelectric tests, and application 163
5.5 Conclusion 167
5.6 Acknowledgements 168
5.7 References 168
Chapitre 6: Modélisation électromécanique des systèmes de récupération d'énergie piézoélectrique 172
6.1 Abstract 174
6.2 Introduction 174
6.3 Analytical modeling 178
6.3.1 Model description 178
6.3.2 Equations of motion and boundary conditions 182
6.3.3 Electromechanical coupling harmonic response analysis 183
6.4 Structural natural frequencies and mode shapes 184
6.4.1 Analytical mode shapes and natural frequencies 185
6.4.2 Numerical mode shapes and natural frequencies 185
6.5 Reduced order model and analytical solutions 187
6.5.1 Reduced order model of H_1 188
6.5.2 Reduced order model of H_2 189
6.5.3 Reduced order model of H_3 190
6.5.4 Analytical solutions of H_1 190
6.5.5 Analytical solutions of H_2 191
6.5.6 Analytical solutions of H_3 191
6.6 Results and discussions 192
6.6.1 Analytical and numerical validations 192
6.6.2 Experimental validations 193
6.6.3 Performances of H_1 and H_3 197
6.6.4 Effective design and comparative study 200
6.7 Conclusions 203
6.8 Acknowledgment 204
6.9 References 208

Partie II : Conception, optimisation et impression 4D de polymères et nanocomposites à mémoire de forme électroactifs pour dispositifs intelligents 212

Chapitre 7: Revue de littérature sur l'impression 4D 213

7.1 Abstract 215
7.2 Introduction 215
7.3 Applied stimulus 217
7.4 AM methods for 4DP applications 218
7.5 Conclusion 220
7.6 Acknowledgment 220
7.7 References 220

Chapitre 8: Caractérisation, conception, et impression 4D de nanocomposites électroactifs à mémoire de forme 222

8.1 Abstract 224
8.2 Introduction 224
8.3 Materials and methods 227
8.3.1 Materials 227
8.3.2 Materials processing 227
8.3.3 Experimental Characterization 230
8.4 Results and discussion 231
8.4.1 Scanning Electron Microscopy (SEM) 231
8.4.2 Differential Scanning Calorimetry (DSC) 234
8.4.3 X-ray Diffraction (XRD) 234
8.4.4 Fourier Transform Infrared Spectroscopy (FTIR) 236
8.4.5 Mechanical properties 237
8.4.6 Thermal and electrothermal performance of PLA/MWCNT nanocomposites 239
8.4.7 Evaluation of Electroresponsive SMP Structure Design 242
8.4.8 Finite Element Electrothermal and Thermomechanical Simulation 244
8.4.9 3D printing of bio-inspired multi-material structures using PLA/PVDF SMP blends and PLA/MWCNTs nanocomposites 246
8.4.10 3D printing of robotic hand with human-inspired joints using PLA/PVDF SMP blends and PLA/MWCNTs nanocomposites 248
8.5 Conclusion 248
8.6 Acknowledgment 252
8.7 References 252

Partie III : Intégration de l'impression 4D et des technologies MEMS piézoélectriques – Vers des dispositifs autonomes et adaptatifs 255

Chapitre 9: Revue de littérature sur l'impression 4D des MEMS piézoélectriques 256

9.1 Abstract 258
9.2 Introduction 258
9.3 AM processes 260
9.3.1 Fused Deposition Modeling (FDM) 262
9.3.2 Stereolithography (SLA) 268
9.3.3 Direct Light Printing (DLP) 273
9.3.4 Direct Ink Writing (DIW) 277
9.4 Applied stimuli 281
9.4.1 Applied stimuli in piezoelectric energy harvesting 281
9.4.2 Applied stimuli in 4d printing 288
9.5 Smart materials 297
9.5.1 Smart Polymers 297
9.5.2 Smart Ceramics 306
9.5.3 Smart Composites 311
9.6 4DP of Piezoelectric energy harvesters 317
9.7 Outlook and perspective 319
9.8 Future Research and Development Priorities 320
9.9 Conclusion 321
9.10 Acknowledgment 322
9.11 References 322
Chapitre 10: Impression 4D d'un système de récupération d'énergie piézoélectrique adaptatif à fréquences naturelles variables 340
10.1 Abstract 342
10.2 Introduction 342
10.3 Analytical modeling 345
10.3.1 Models description 345
10.3.2 Constitutive equations 346
10.3.3 Hamilton's principle 347
10.3.4 Equations of motion and boundary conditions 349
10.3.5 Electrical equations 350
10.3.6 Structural natural frequencies and mode shapes 351
10.3.7 Reduced-order model and analytical solution 353
10.4 Experimental section 356
10.4.1 Materials 356
10.4.2 Materials synthesis 356
10.4.3 Characterization 358
10.5 Results and discussion 359

10.5.1 Analytical modeling results 359
10.5.2 Morphological and crystalline structure 360
10.5.3 Piezoelectric and dielectric behavior 366
10.5.4 Heat transfer and shape memory performances 367
10.5.5 Fabrication, test, and experimental validations 371
10.6 Conclusion 373
10.7 Acknowledgment 374
10.8 References 374
Chapitre 11: Conclusions et Perspectives 377
11.1 Conclusions 377
LISTE DE RÉFÉRENCES GLOBALE DES 9 ARTICLES 381
ANNEXE 1 427
ANNEXE 2 432
ANNEXE 3 441
ANNEXE 4 453
ANNEXE 5 463

LISTE DES TABLEAUX

Table 1: Stretching process parameters and their effect on β-phase content in PVDF. 41
Table 2: Poling process parameters and their effects on PVDF piezoelectricity 47
Table 3: Fillers used with PVDF matrix and their effects on PEHs performances. 54
Table 4: Comparison of fractures and surfaces appearance, and mechanical and thermal properties of molded and 3D printed parts. 57
Table 5: Materials, advantages, and disadvantages of the most commonly used 3DP technologies to fabricate PEHs. 59
Table 6: Most used 3DP technologies to fabricate PEHs. 61
Table 7: Electric power and electric energy density generated by different piezoelectric materials used in this work [280]. 67
Table 8: Factors and their levels. 104
Table 9: Coded levels for the BBD design. 105
Table 10: ANOVA table based upon the SN values of the d33 coefficient. 108
Table 11: Ranking of input parameters for d33 coefficient. 108
Table 12: ANOVA table based on the SN values of the permittivity. 108
Table 13: Ranking of input parameters for the permittivity. 109
Table 14: Ranking of input parameters for f F(β). 110
Table 15: ANOVA table based upon the SN values of F(β). 110
Table 16: ANOVA predictions and experimental validations for the optimized outputs. 111
Table 17: Printing parameters. 126
Table 18: PVDF-based nanocomposites with varying compositions. 127
Table 19: Poling parameters for PVDF/BT samples 128
Table 20: Thermal properties of PVDF and PVDF/ BT nanocomposites determined by DSC test and F(β) values measured with FT-IR data. 133
Table 21: Printing parameters. 151
Table 22: Thermal properties of PVDF and PVDF/ MWCNTs nanocomposites determined by DSC test and F(β) values measured with FT-IR data. 158
Table 23: Physical and geometric properties of the structure of H_1 180
Table 24: Expressions of the parameters in the equation of motion and boundary conditions for each system. 183
Table 25: First three resonance frequencies of H_1, H_2, and H_3 obtained analytically and numerically under open circuit conditions. 186
Table 26: Quantitative comparisons of theoretical and experimental results of the first two resonance frequencies and output voltages with bending motions. 195

Table 27: Quantitative comparisons of theoretical and experimental results on the first resonance frequencies and output voltages with torsional motion. 197
Table 28: Quantitative comparisons of the power output of H_1 with bending motion and with both bending and torsional motions on the first three resonance frequencies. 200
Table 29: Quantitative comparison of the three PEHs' performances. 203
Table 30: Materials, advantages and disadvantages of the most used 3DP technologies in 4DP. 219
Table 31: Printing parameters. 229
Table 32: PLA/PVDF SMP blends and PLA/MWCNTs nanocomposites with varying compositions. 229
Table 33: Thermal properties of PVDF, PLA and PLA/PVDF SMP blends determined by DSC test. 236
Table 34: Materials, Performances, advantages, and limitations of the most used 3DP technologies for both 4D printing and PEHs fabrication. 261
Table 35: Overview of Shape Memory Polymers in 3D Printing: Stimuli Response, Performances, and Applications. 304
Table 36: First two resonance frequencies of the different configurations obtained analytically and numerically under open circuit conditions. 353
Table 37: Printing parameters. 357
Table 38: PLA/MWCNTs and PVDF/BT nanocomposites with varying compositions. 357
Table 39: Thermal properties of PLA and PLA/MWCNTs SMC determined by DSC test. 363
Table 40: Quantitative comparisons of theoretical and experimental results of the first resonance frequencies and output voltages of each configuration with bending motions. 372

LISTE DES FIGURES

Figure 1: (a) Structure générale de la thèse par articles ; (b) Schéma illustrant les liens logiques et complémentaires entre les trois grandes parties de la thèse. 26
Figure 2: (a) poling process and (b) Stretching process. 32
Figure 3: Most used piezoelectric materials and 3DP technologies to fabricate piezoelectric energy harvesting devices and recent application industries. 34
Figure 4: (a) α-PVDF, (b) β-PVDF, (c) γ-PVDF. 38
Figure 5: Influence of stretching conditions and additives on β-phase content in PVDF. 40
Figure 6: Comparison of the poling effect with other post-printing processes (heating and annealing) effects [189]. 43
Figure 7: Effect of poling on β-phase content of the nanocomposite PVDF/BT with different BT fractions [192]. 45
Figure 8: Influence of stretching conditions and additives on β-phase content in PVDF. 46
Figure 9: Impact of BT filler content on β-phase and crystallinity of PVDF 48
Figure 10: Stress–strain curve for PVDF/BT composite at 5 mm/min strain rate with different BT fractions (Reproduced with permission [204]). 49
Figure 11: Generalized S–N curve for PVDF/BT composite with different BT fractions Reproduced with permission [204]. 49
Figure 12: Effect of adding $BiFeO_3$ with different volume fractions on the PVDF (a) piezoelectric charge constant and (b) piezoelectric voltage constant (Reproduced with permission [215]). 50
Figure 13: Effects of various additives on β-phase formation in PVDF. 51
Figure 14: : Effect of adding GO with different weight fractions on the PVDF (a) tensile modulus and (b) tensile strength (Reproduced with permission [223]). 53
Figure 15: Effect of adding $Ba_{0.7}Sr_{0.3}TiO_3$ with different volume fractions on the PVDF (a) ultimate stress and (b) Young's modulus [224]. 53
Figure 16: Comparison between molded part and SLS part properties ((a) crystallinity, (b) β-phase relative fraction) (Reproduced with permission [205]). 58
Figure 17: Microstructure and SAXS analysis of PVDF/BT composites fabricated by casting and FDM 63
Figure 18: Performance of smart footwear integrating PEH nanocomposites under different user conditions 64
Figure 19: Schematics and tests of an intelligent wheel-integrated piezoelectric harvester 66
Figure 20: Some PEH applications in the healthcare sector 68
Figure 21: In vivo testing of piezoelectric energy harvesters in animals. 70

Figure 22: Working principle of ultrasonic wireless energy harvesting system. Reproduced with permission [285]. 71
Figure 23: (a) Ex-vivo and (b) In-vivo tests of the transmuscular piezoelectric ultrasonic energy harvester in a porcine muscle and an anesthetized mouse, respectively (Reproduced with permission [289]). 72
Figure 24: Some PEH applications in robotics. 73
Figure 25: Prospects for future developments of 3D-printed piezoelectric materials for microrobotics applications. 76
Figure 26: Schematic diagram of the experimental steps and the poling setup. 105
Figure 27: SN Ratio diagram for the dielectric constant of PVDF as a function of (a) “T”, (b) “t”, (c) “V”, and (d) “BT”. 109
Figure 28: SN Ratio diagram for the β-phase relative fraction of PVDF as a function of (a) “T”, (b) “t”, (c) “V”, and (d) “BT” 110
Figure 29: (a) Neural network topology, (b) Neural network performance. 112
Figure 30: Comparison of ANN-predicted and experimental values of piezoelectric and dielectric properties 113
Figure 31: Surface plot of d33 coefficient for BT=30 wt% according to ANN. 114
Figure 32: Surface plot of permittivity for T=150°C according to ANN. 114
Figure 33: Surface plot of F(β) for BT=30 wt% according to ANN. 114
Figure 34: Optimal output values (red spheres) using ANN and genetic algorithm. 115
Figure 35: (a) Errors between predicted values and experimental results for the optimal output values, (b) comparison of piezoelectric and dielectric properties of the PVDF/BT nanocomposite under study with other results reported in the literature (Purple: [331], Blue: [332], Yellow: [333], Brown: [334], Green: [335], Black: [336], Gray: [337], Pink: [338], Orange: [339]). 115
Figure 36: Schematic diagram of the manufacture of PVDF/BT PEH. 127
Figure 37: SEM images and particles detection of (a) BT-20, (b) BT-30, and (c) BT-40. 130
Figure 38: Spectroscopic and thermal analysis of PVDF/BT nanocomposites before and after poling 132
Figure 39: Dielectric and piezoelectric performance of PVDF/BT nanocomposites 134
Figure 40: Bioinspired design and optimization of 3D PEH structures 135
Figure 41: Influence of structural porosity on the performance of compact and porous PEHs : Influence of structural porosity on the performance of compact and porous PEHs 136
Figure 42: Fabrication and performance testing of 3D-printed PEHs with various compositions 139
Figure 43: Durability and practical application of bioinspired PEHs under cyclic loading 140
Figure 44: Operational principle of PEH with auxetic structure polarized in 3-direction in both d31 and d32 modes under a single excitation force. 149
Figure 45: Schematic diagram of PVDF/MWCNTs PEH fabrication process. 151

Figure 46: SEM images of as received (a) PVDF, and (b) MWCNTs; (c) high magnification TEM images of as received MWCNTs; and (d) X-ray diffraction patterns of as received MWCNTs. 154
Figure 47: Morphology analysis of PVDF/MWCNTs composites and the effect of printing temperature 156
Figure 48: FTIR, XRD, and DSC characterization of PVDF/MWCNTs composites..... 157
Figure 49: Dielectric and piezoelectric properties of PVDF/MWCNTs composites..... 159
Figure 50: FEM-based structural optimization of various auxetic and conventional PEH geometries 161
Figure 51: Optimization using three different sets of dimensional parameters of the reentrant shape structure using the FEM simulation results of the mechanical and electrical performances. 162
Figure 52: Fabrication and output signals of 3D-printed PVDF/MWCNTs PEHs..... 164
Figure 53: Evaluation of auxetic PEH structures in terms of performance, durability, and real-time application..... 166
Figure 54: Schematic of the L-shaped bimorph PEHs (a) H_1, (b) H_2, and (c) H_3 with four PZT layers, two steel layers, and two lumped mass blocks. 178
Figure 55: Schematic Illustration of the deformation patterns in PEHs (A) H_1 (B), H_2, and (C) H_3, undergoing bending and torsional motions, defined by the transverse displacement of the main and auxiliary beams ($v_1(x,t)$ and $v_2(x,t)$) and the torsional angle $\theta(x,t)$ of the main beam. 179
Figure 56: Layer positions of the composite cross-section in the beam's local coordinate system (x, y, z). 180
Figure 57: Comparison of the analytical and numerical results of the first three bending mode shapes of H_2. 187
Figure 58: (a) Analytical and (b) numerical validations of the power output of H_2 with bending and torsional modes versus different excitation frequencies (20 Hz–200 Hz) under harmonic excitations abz = abx = 0.5 m/s^2 and load resistance R = 17 kΩ. 193
Figure 59: Voltage output comparison under bending mode and varying resistive loads 194
Figure 60: Voltage output comparison under torsional mode and varying resistive loads 196
Figure 61: Power output analysis of PEHs H1 and H3 under dynamic excitation. 198
Figure 62: Comparison of PEH performance before and after activating d36 mode..... 199
Figure 63: Power output improvements following effective PEH design 200
Figure 64: Comparative analysis of beam contributions to PEH power output under various excitation. 202
Figure 65: 4DP smart material structures..... 216
Figure 66: Schematic illustration of the shape-shifting mechanisms in 4DP..... 217
Figure 67: Publications for 4DP with different AM technologies in the past 5 years (from 2018 to September 2022)..... 220

Figure 68: Preparation and multi-material 3d printing process for electroresponsive SMPs using PLA/PVDF blends and PLA/MWCNT nanocomposite joints.....228
Figure 69: SEM images of as received (a) PLA, (b) PVDF, and (c) MWCNTs; high and low magnification SEM of (d) P7F3, (e) P5F5, (f) P3F7, and the extruded filaments of (g) C-7,5, and (h) C-10. 233
Figure 70: Thermal and structural characterization of PLA/PVDF and PLA/MWCNTs samples 235
Figure 71: Mechanical performance of different PLA/PVDF blend ratios.....238
Figure 72: Electrothermal performance of PLA/MWCNTs nanocomposites under electrical stimulus. 240
Figure 73: Evaluation of electroactive SMPs 243
Figure 74: Electrothermal simulations and experimental validation of shape memory behavior.....245
Figure 75: Demonstration of bioinspired shape morphing using electroactive SMPs 247
Figure 76: Shape fixity test of a 3D-printed PLA/PVDF-based robotic hand with PLA/MWCNTs joints using 0.14A electric current. 250
Figure 77: Shape recovery test of a 3D-printed PLA/PVDF-based robotic hand with PLA/MWCNTs joints using 0.14A electric current. 251
Figure 78: Advanced multi-material 3D printing techniques for piezoelectric device fabrication.....264
Figure 79: Innovative FDM-based 4D printing methods for shape memory networks and actuators.. 267
Figure 80: SLA and PuSL techniques for fabricating miniature piezoelectric transducers 269
Figure 81: Design and performance of thermoresponsive hydrogels and photolithography-based processes 271
Figure 82: DLP-based fabrication of complex bio-inspired piezoelectric structure 274
Figure 83: Advanced DLP printing strategies for multifunctional 4D printed materials.....276
Figure 84: Direct Ink Writing and freeze-drying-assisted multi-material 3D printing for piezo-composites.....278
Figure 85: DIW-printed bio-inspired composites and microfluidics-enabled 4D printing systems ...280
Figure 86: DIW-printed bio-inspired composites and microfluidics-enabled 4D printing systems....282
Figure 87: 4D-printed composites for soft robotics and bioinspired sensor applications. 284
Figure 88: Adaptive multi-material systems for intelligent actuators and wearable sensors. 286
Figure 89: Structural optimization of 4D-printed lattice networks using DLP and direct writing. ...289
Figure 90: SLA-printed piezoelectric structures and self-morphing mechanisms in smart ceramics. 291
Figure 91: Electrothermal responses and actuation mechanisms in 4D printed smart structure.....293
Figure 92: Magnetic actuation and shape recovery behavior of smart printed composites 295
Figure 93: Structural and electrical characterization of PVDF-based piezoelectric devices 299
Figure 94: Fabrication and design strategies for high-resolution shape memory and photothermal polymers.....303

Figure 95: Architectured piezoceramics and immunomodulatory scaffolds for bio-applications. 308
Figure 96: Architectured piezoceramics and immunomodulatory scaffolds for bio-applications]. 310
Figure 97: Printed nanocomposites with induced polarization, mechanical flexibility, and hybrid structures 314
Figure 98: Bioinspired 3D-printed composites with off-center and layered architectures 316
Figure 99: Bioinspired 3D-printed composites with off-center and layered architecture 345
Figure 100: Preparation process and multi-material 3D printing of PVDF/BT-based PEH combined with multi-responsive SMC using PLA/MWCNTs nanocomposites. 357
Figure 101: (a) Output voltage of the MSMC-PEH in its various shapes. (b) Comparison of the output voltages between a simple 3D-printed cantilever beam and a 4D-printed one. 359
Figure 102: SEM and image-based analysis of component morphology and dispersion in PVDF/BT and PLA/MWCNTs 360
Figure 103: FTIR, XRD, and DSC characterization of 3D-printed nanocomposites before and after electrical poling. 362
Figure 104: Dielectric and piezoelectric performance comparison of 3D-printed PVDF-based composites. 367
Figure 105: Current to heat conversion performances of PLA/MWCNTs nanocomposites 368
Figure 106: Shape memory behavior of PLA/MWCNTs composites under thermal and electric activation 370
Figure 107: Fabrication and performance evaluation of MSMC-PEH in multiple configurations 372

LISTE DES ABRÉVIATION

AC : Alternative Current (Courant alternatif)

AI : Artificial Intelligence (Intelligence artificielle)

ANN : Artificial Neural Network (Réseau de neurones artificiel)

ANSYS : Simulation Software (Logiciel de simulation)

BNT : Bismuth Sodium Titanate (Titanate de sodium et de bismuth)

BT : Barium Titanate (Titanate de baryum)

CNF : Carbon Nanofibers (Nanofibres de carbone)

DC : Direct Current (Courant continu)

DIW : Direct Ink Writing (Impression directe à l'encre)

DLP : Digital Light Processing (Traitement numérique de la lumière)

DMF : N,N-Dimethylformamide (Diméthylformamide)

DMA : Dynamic Mechanical Analysis (Analyse mécanique dynamique)

DSC : Differential Scanning Calorimetry (Calorimétrie différentielle à balayage)

FDM : Fused Deposition Modeling (Modélisation par dépôt de fil fondu)

FEM : Finite Element Method (Méthode des éléments finis)

FTIR : Fourier Transform Infrared Spectroscopy (Spectroscopie infrarouge à transformée de Fourier)

GA : Genetic Algorithm (Algorithme génétique)

GNP : Graphene Nanoplatelets (Nanoplaquettes de graphène)

GO : Graphene Oxide (Oxyde de graphène)

HV : High Voltage (Haute tension)

LCE : Liquid Crystal Elastomer (Élastomère à cristaux liquides)

LP : Low Power (Basse puissance)

MEMS : Micro-Electro-Mechanical Systems (Systèmes micro-électromécaniques)

MOF : Metal-Organic Framework (Structure organométallique)

MWCNTs : Multi-Walled Carbon Nanotubes (Nanotubes de carbone multi-parois)

NIR : Near Infrared (Proche infrarouge)

PAN : Polyacrylonitrile

PDMS : Polydimethylsiloxane

PE : Polyethylene (Polyéthylène)

PEH : Piezoelectric Energy Harvester (Récupérateur d’énergie piézoélectrique)

PEG : Polyethylene Glycol (Polyéthylène glycol)

PET : Polyethylene Terephthalate (Polyéthylène téréphtalate)

PLA : Polylactic Acid (Acide polylactique)

PMMA : Polymethyl Methacrylate (Polyméthacrylate de méthyle)

PP : Polypropylene (Polypropylène)

PS : Polystyrene (Polystyrène)

PVDF : Polyvinylidene Fluoride (Polyfluorure de vinylidène)

PVA : Polyvinyl Alcohol (Alcool polyvinylique)

PZT : Lead Zirconate Titanate (Titanate de zirconate de plomb)

RMS : Root Mean Square (Valeur quadratique moyenne)

ROM : Reduced-Order Model (Modèle d'ordre réduit)

SEM : Scanning Electron Microscopy (Microscopie électronique à balayage)

SLA : Stereolithography (Stéréolithographie)

SLS : Selective Laser Sintering (Frittage sélectif par laser)

SMP : Shape Memory Polymer (Polymère à mémoire de forme)

TEM : Transmission Electron Microscopy (Microscopie électronique en transmission)

TGA : Thermogravimetric Analysis (Analyse thermogravimétrique)

TPU : Thermoplastic Polyurethane (Polyuréthane thermoplastique)

UV : Ultraviolet

XRD : X-Ray Diffraction (Diffraction des rayons X)

Chapitre 1: Introduction

1.1 Contexte général

Dans un monde en quête permanente d'efficacité énergétique et d'innovation technologique, deux avancées majeures se démarquent : les systèmes micro-électromécaniques (MEMS) et l'impression 4D. Les MEMS, dispositifs miniaturisés capables de combiner électronique et mécanique, permettent de réaliser des fonctions complexes comme la récupération d'énergie mécanique à partir des vibrations ambiantes. De son côté, l'impression 4D, évolution de l'impression 3D, introduit une dimension temporelle en utilisant des matériaux intelligents capables de changer de forme ou de propriétés en réponse à des stimuli externes. La combinaison de ces deux technologies promet une nouvelle génération de dispositifs adaptatifs, dynamiques et performants, ouvrant la voie à de nouvelles applications dans des domaines tels que l'énergie, la biomédecine et les systèmes intelligents.

(a) Les MEMS : Une révolution dans la récupération d'énergie

Les défis de l'épuisement des énergies fossiles et de la transition énergétique mondiale ont placé les technologies de récupération d'énergie au cœur des stratégies de développement durable. Dans ce contexte, les systèmes micro-électromécaniques piézoélectriques (MEMS) se positionnent comme une solution innovante et prometteuse pour exploiter l'énergie mécanique ambiante. Ces dispositifs miniaturisés, qui combinent microélectronique et matériaux piézoélectriques, convertissent les vibrations, mouvements ou forces mécaniques provenant de diverses sources – telles que les machines, les infrastructures ou les activités humaines – en énergie électrique exploitable. En plus de réduire la dépendance aux sources d'énergie conventionnelles, cette technologie ouvre la voie à des dispositifs autonomes et à faible impact, alignés avec les ambitions mondiales pour une économie verte et résiliente.

(b) L'impression 4D : Une technologie de fabrication adaptative et innovante

L'impression 4D, évolution de l'impression 3D, intègre des matériaux capables de modifier leur structure ou leurs propriétés en réponse à des stimuli environnementaux tels que la température, l'humidité, les champs magnétiques ou électriques. En ajoutant la dimension temporelle à la fabrication additive, cette technologie ouvre de nouvelles perspectives dans des domaines variés comme la biomédecine, la robotique, l'aérospatiale et les dispositifs électroniques intelligents.

Le concept repose principalement sur l'utilisation de matériaux dits « intelligents », tels que les polymères à mémoire de forme ou les composites actifs, qui permettent aux structures imprimées d'adopter des formes ou des fonctions dynamiques. Ces matériaux multifonctionnels offrent des possibilités révolutionnaires, notamment pour les dispositifs nécessitant une adaptabilité aux conditions changeantes ou un ajustement précis de leurs propriétés. Par exemple, un dispositif imprimé en 4D peut ajuster sa fréquence de résonance ou sa géométrie en fonction des stimuli externes, améliorant ainsi ses performances et sa polyvalence.

(c) Intégration des MEMS et de l'impression 4D : Vers une nouvelle génération de dispositifs énergétiques

La combinaison des MEMS piézoélectriques et de l'impression 4D constitue une opportunité unique pour concevoir des dispositifs intelligents capables de répondre aux défis énergétiques actuels. En intégrant des matériaux à mémoire de forme dans les MEMS, il devient possible de développer des systèmes dynamiques dont la géométrie ou les propriétés changent en fonction de stimuli externes. Ces structures adaptatives permettront, par exemple, de moduler les fréquences naturelles des MEMS pour mieux s'adapter aux vibrations ambiantes, améliorant ainsi leur efficacité énergétique. Cette intégration ouvre également des perspectives inédites pour surmonter les limitations des MEMS traditionnels. D'une part, l'impression 4D offre une flexibilité de conception et une capacité à fabriquer des architectures complexes qui seraient impossibles à réaliser avec les méthodes traditionnelles. D'autre part, les dispositifs MEMS imprimés en 4D peuvent être conçus pour fonctionner dans des environnements variables, en modifiant leurs propriétés physiques ou leur comportement en temps réel.

Ainsi, l'intégration des MEMS piézoélectriques et de l'impression 4D ne se limite pas à une simple technique avancée. Elle marque une étape décisive vers la création de dispositifs énergétiques autonomes, durables et polyvalents, capables de répondre aux besoins des systèmes électroniques modernes, notamment dans des domaines tels que la santé, la robotique et les infrastructures intelligentes.

1.2 Problématique

(a) Défis des MEMS piézoélectriques

Les MEMS piézoélectriques présentent une technologie clé pour la récupération d'énergie mécanique à petite échelle. Cependant, leur efficacité reste limitée par plusieurs facteurs.

Premièrement, le choix des matériaux piézoélectriques reste crucial. Les céramiques offrent des propriétés piézoélectriques exceptionnelles, mais leur fragilité limite leur durabilité. À l'inverse, les polymères comme le polyfluorure de vinylidène (PVDF) sont flexibles et légers, mais leurs performances piézoélectriques ont nécessité des améliorations pour répondre aux exigences pratiques. Deuxièmement, les structures MEMS sont souvent limitées par le décalage entre leurs fréquences naturelles et les vibrations ambiantes, ce qui limite leur efficacité de récupération d'énergie. Enfin, les méthodes de fabrication traditionnelles peinent à répondre aux besoins croissants de miniaturisation et de complexité architecturale, freinant ainsi l'optimisation des performances de ces systèmes.

(b) Limites actuelles de l'impression 4D

L'impression 4D, grâce à l'utilisation de matériaux intelligents capables de réagir à des stimuli externes, promet de révolutionner la conception de dispositifs adaptatifs et dynamiques. Elle représente une technologie émergente et sous-exploitée dans de nombreux domaines. Les défis actuels incluent l'optimisation des matériaux utilisés, la maîtrise des processus de fabrication, ainsi que l'intégration efficace des stimuli pour des applications pratiques. Parmi les défis majeurs figurent également la conception de matériaux multi-réactifs capables de répondre simultanément à plusieurs types de stimuli (température, champ électrique ou magnétique, etc.), ainsi que le contrôle précis des transformations pour assurer une adaptabilité optimale. L'intégration de l'impression 4D dans des dispositifs réels, tout en conservant robustesse mécanique et performances énergétiques, représente un problème complexe et peu exploré.

(c) Intégration des MEMS et de l'impression 4D : une opportunité inexploitée

Bien que les MEMS et l'impression 4D soient des technologies complémentaires, leur intégration reste largement inexplorée. Combiner les propriétés dynamiques et adaptatives de l'impression 4D avec les MEMS pourrait permettre de concevoir des dispositifs capables de moduler leur géométrie ou leurs fréquences de fonctionnement en fonction des vibrations ambiantes, surmontant ainsi les limitations des MEMS traditionnels. Cependant, de nombreuses questions demeurent : comment intégrer efficacement des matériaux à mémoire de forme dans les MEMS tout en conservant leurs propriétés piézoélectriques ? Comment optimiser les structures MEMS imprimées en 4D pour répondre à des conditions environnementales complexes et variables ?

Face à ces défis, cette recherche vise à répondre à une question fondamentale : comment concevoir et intégrer des MEMS piézoélectriques et des structures imprimées en 4D pour dépasser les limites des technologies actuelles et développer des dispositifs adaptatifs, performants et durables ?

1.3 Objectifs de la thèse

L'objectif principal de cette thèse est de concevoir, modéliser et fabriquer des dispositifs micro-électromécaniques (MEMS) piézoélectriques avancés en exploitant les potentialités de l'impression 4D pour créer des structures intelligentes et adaptatives. L'association de ces deux technologies vise à améliorer la récupération d'énergie mécanique à micro-échelle, tout en introduisant des fonctionnalités dynamiques qui permettent aux MEMS d'optimiser leur rendement en fonction de leur environnement.

Trois objectifs spécifiques distincts mais interdépendants émergent de cette poursuite déterminée de notre objectif global, tel que présenté ci-dessous.

- **Optimisation et fabrication des MEMS piézoélectriques pour la récupération d'énergie**

- Développer et caractériser des nanocomposites piézoélectriques à base de PVDF optimisés par l'incorporation d'additifs (tels que le titanate de baryum et les nanotubes de carbone) afin d'améliorer leurs propriétés piézoélectriques, mécaniques et diélectriques.
- Mettre en place des techniques avancées de polarisation basées sur l'intelligence artificielle (réseaux de neurones, algorithmes génétiques) pour maximiser la conversion d'énergie des dispositifs fabriqués.
- Modéliser et simuler numériquement des structures MEMS innovantes afin d'optimiser leur géométrie et leurs paramètres de fonctionnement pour une récupération d'énergie maximale.
- Fabriquer des MEMS par impression 3D en optimisant les paramètres de fabrication pour assurer une haute précision, une excellente adhérence entre les couches et une durabilité mécanique optimale.
- Exploiter la grande capacité de récupération d'énergie des MEMS développés pour des applications innovantes dans les domaines de l'électronique et de la domotique.

- **Développement et caractérisation de matériaux à mémoire de forme pour l'impression 4D**

- Concevoir et développer des matériaux à mémoire de forme multi-réactifs (thermosensibles, électrosensibles) adaptés à l'impression 4D pour permettre des transformations structurelles précises et réversibles.
- Caractériser les propriétés mécaniques, thermiques et électromécaniques de ces matériaux afin de comprendre leur comportement en réponse aux stimuli externes et d'optimiser leur intégration dans des dispositifs MEMS.
- Simuler numériquement la capacité de conversion courant-chaleur et le comportement électro-réactif des nanocomposites développés.
- Expérimenter et modéliser les effets des transformations structurelles induites par l'impression 4D sur les performances mécaniques et énergétiques des structures fabriquées.
- Exploiter les matériaux à mémoire de forme de haute performance, pour développer des applications dans le domaine de la robotique.

- **Intégration de l'impression 4D dans les MEMS pour des dispositifs adaptatifs et intelligents**

- Concevoir des MEMS imprimés en 4D capables de modifier leur géométrie en fonction des variations environnementales, permettant ainsi d'ajuster leurs fréquences de résonance aux vibrations ambiantes et d'améliorer leur rendement énergétique.
- Mettre en place des méthodes de fabrication et d'assemblage permettant d'intégrer de manière optimale les nanocomposites piézoélectriques dans des structures MEMS imprimées en 4D tout en conservant leurs propriétés fonctionnelles.
- Développer un modèle analytique pour prédire les réponses dynamiques et piézoélectriques des MEMS fabriqués par impression 4D et valider les résultats du modèle numériquement et expérimentalement.
- Évaluer expérimentalement les performances des dispositifs MEMS-4D en termes de récupération d'énergie, de stabilité structurelle et de capacité d'adaptation aux stimuli externes.

1.4 Structure de la thèse

Cette thèse est structurée en trois parties principales, chacune répondant à un des trois objectifs spécifiques ci-dessus,

- La première partie est consacrée aux MEMS piézoélectriques et se concentre sur la modélisation, la caractérisation, l'optimisation et la fabrication par impression 3D de ces

dispositifs. Elle commence par une revue de la littérature sur les récupérateurs d'énergie piézoélectriques imprimés en 3D, suivie d'une étude sur l'optimisation des paramètres de polarisation des nanocomposites PVDF/BT à l'aide de l'intelligence artificielle. Cette section explore ensuite la conception et la fabrication de PEH à base de nanocomposites, intégrant des structures bio-inspirées et auxétiques imprimées en 3D, avant de conclure par une modélisation électromécanique avancée des systèmes de récupération d'énergie.

- La deuxième partie se concentre sur les matériaux électroactifs à mémoire de forme et leur fabrication par impression 4D. Elle commence par une revue détaillée des technologies d'impression 4D, des matériaux utilisés et des stimuli d'activation. Elle se concentre ensuite sur la conception et la fabrication de nanocomposites électroactifs optimisés pour une activation rapide et efficace sous champ électrique. Une attention particulière est portée à l'impression 4D multi-matériaux, combinant un nanocomposite PLA/MWCNTs dédié à la conversion électrothermique et un mélange de polymères à mémoire de forme assurant une récupération de forme programmée.

- La troisième partie marque l'aboutissement de cette thèse en intégrant les deux technologies explorées précédemment : l'impression 4D et les MEMS piézoélectriques. Une revue de la littérature est d'abord réalisée sur les récupérateurs d'énergie piézoélectriques et l'impression 4D de matériaux à mémoire de forme, mettant en avant les procédés d'impression, les stimuli d'activation et les matériaux utilisés dans les deux domaines. Enfin, cette section se conclut par la conception et la fabrication d'un système de récupération d'énergie piézoélectrique adaptatif, intégrant une structure imprimée en 4D capable de modifier ses fréquences naturelles pour optimiser la conversion d'énergie dans des environnements dynamiques.

Le lien entre les trois parties de cette thèse s'établit de manière progressive et complémentaire. La première partie se consacre à la conception, la modélisation et la fabrication de dispositifs MEMS piézoélectriques, tandis que la deuxième explore indépendamment l'optimisation et l'impression 4D de structures intelligentes à mémoire de forme. Ces deux axes sont développés séparément afin de maximiser leur potentiel technique respectif. La troisième partie vient ensuite les fusionner dans une approche intégrée, combinant les capacités de récupération d'énergie des MEMS avec les propriétés de transformation dynamique des matériaux 4D. Cette intégration permet le développement de dispositifs adaptatifs et autonomes, illustrant ainsi l'apport conjoint de ces technologies et donnant une cohérence d'ensemble à la démarche scientifique suivie.

Ainsi, cette thèse suit une progression logique depuis la conception et l'optimisation de matériaux fonctionnels jusqu'à leur intégration dans des dispositifs hybrides avancés, avec pour objectif final de développer des systèmes autonomes et intelligents pour la récupération d'énergie et les applications de capteurs adaptatifs. La Figure 1 présente l'architecture générale de cette thèse par articles, articulée en trois grandes parties, et met en évidence la cohérence et la complémentarité entre ces blocs thématiques.

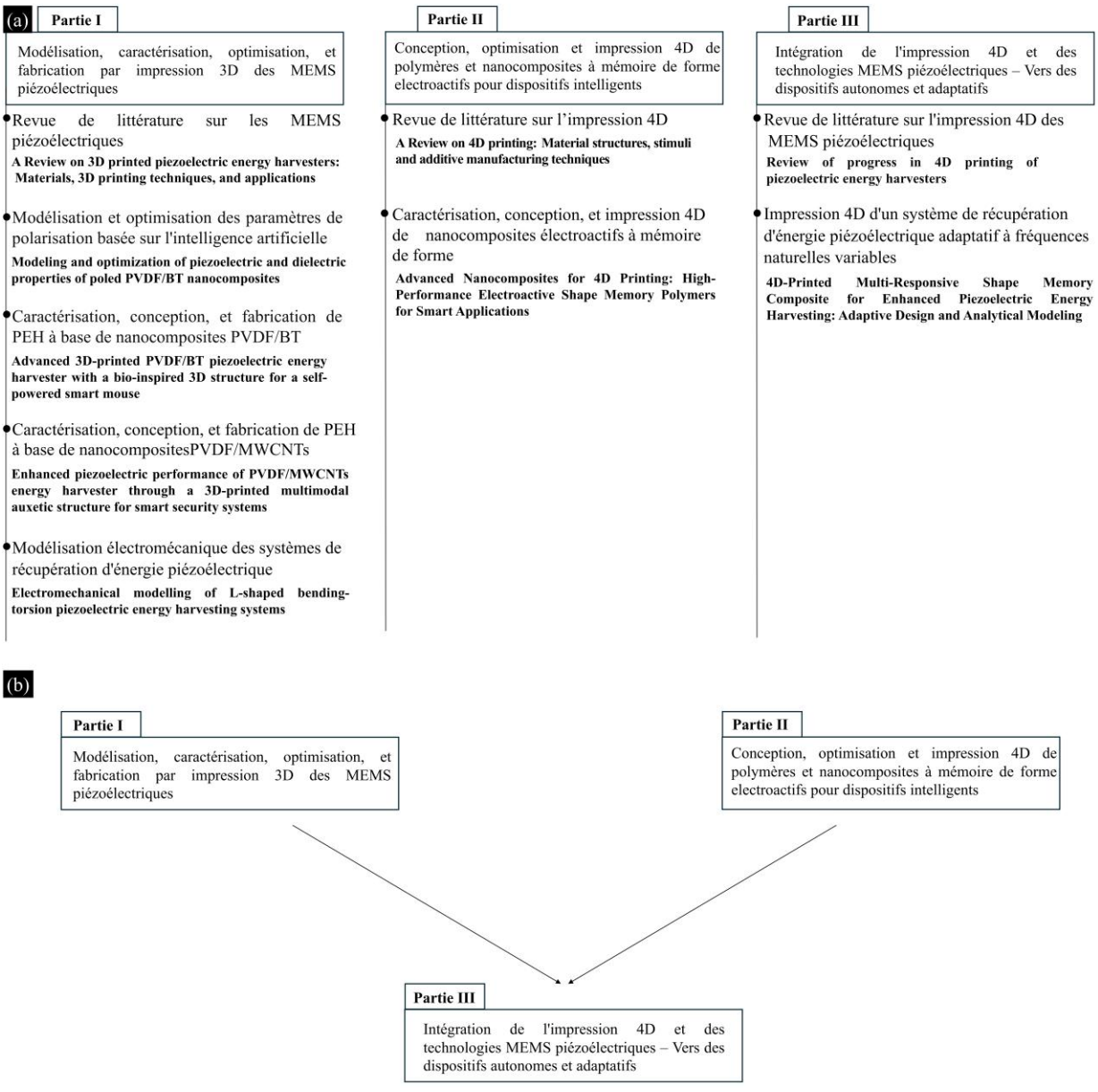

Figure 1: (a) Structure générale de la thèse par articles ; (b) Schéma illustrant les liens logiques et complémentaires entre les trois grandes parties de la thèse.

Partie I : Modélisation, caractérisation, optimisation, et fabrication par impression 3D des MEMS piézoélectriques

Chapitre 2: Revue de littérature sur les MEMS piézoélectriques

Ce chapitre a fait l'objet d'une publication :
MEGDICH, Amal, HABIBI, Mohamed, and LAPERRIÈRE, Luc.
A review on 3D printed piezoelectric energy harvesters: materials, 3D printing techniques, and applications *Materials Today Communications*, 2023, vol. 35, p. 105541.
Il peut être consulté en ligne à l'adresse suivante :
https://doi.org/10.1016/j.mtcomm.2023.105541

Cet article propose une analyse approfondie des avancées récentes dans le domaine de la récupération d'énergie piézoélectrique en mettant l'accent sur l'impression 3D comme technologie clé pour la fabrication de ces dispositifs.
L'objectif principal de cette étude est de fournir une synthèse des connaissances sur les matériaux piézoélectriques et les procédés de fabrication qui influencent les performances des systèmes de récupération d'énergie. Plus précisément, l'article passe en revue les propriétés des matériaux piézoélectriques les plus couramment utilisés, notamment les céramiques et les polymères tels que le PVDF, en comparant leurs avantages et leurs limites. Une attention particulière est accordée aux stratégies d'amélioration des propriétés piézoélectriques des polymères par des traitements mécaniques (étirement uniaxial et biaxiale), thermiques (recuit) et électriques (polarisation à champ élevé), ainsi que par l'incorporation de charges fonctionnelles telles que le titanate de baryum (BT), les nanotubes de carbone (CNT) et l'oxyde de zinc (ZnO). L'article explore également les techniques d'impression 3D appliquées aux récupérateurs d'énergie piézoélectriques, soulignant les avantages de cette approche par rapport aux méthodes de fabrication conventionnelles. La modélisation par dépôt de fil fondu (FDM), la stéréolithographie (SLA) et l'impression à jet d'encre (DIW) sont examinées en termes de précision, de compatibilité avec les matériaux piézoélectriques et de capacité à produire des architectures complexes qui favorisent l'optimisation des performances électromécaniques. L'étude met en évidence les défis de l'impression de polymères piézoélectriques, notamment en ce qui concerne le contrôle de la cristallisation des phases β et γ du PVDF et la nécessité d'adapter les paramètres d'impression pour maximiser la réponse piézoélectrique des dispositifs fabriqués.
Enfin, l'étude aborde les applications émergentes des récupérateurs d'énergie piézoélectriques imprimés en 3D dans divers domaines, notamment l'électronique embarquée, les capteurs

autonomes, et la robotique. L'intégration de ces dispositifs dans des systèmes intelligents et auto-alimentés représente une étape majeure vers des solutions énergétiques durables et autonomes, réduisant la dépendance aux batteries traditionnelles et ouvrant la voie à une nouvelle génération de capteurs capables d'exploiter l'énergie ambiante provenant des vibrations, des mouvements humains ou des structures en fonctionnement.

L'article fournit une vision globale des opportunités et des défis liés à l'impression 3D de dispositifs piézoélectriques pour la récupération d'énergie. Il met en évidence les perspectives de recherche et les améliorations nécessaires pour optimiser l'intégration de ces technologies dans des systèmes énergétiques autonomes et efficaces.

A Review on 3D printed piezoelectric energy harvesters: Materials, 3D printing techniques, and applications

Amal Megdich[a], Mohamed Habibi[a,*], Luc Laperrière[a]

[a]*Department of mechanical engineering, Université du Québec à Trois Rivières, 3351 Bd des Forges, G8Z 4M3, Trois-Rivières, Canada*

2.1 Abstract

The worldwide energy and environmental pollution crisis is caused partly by the rising usage of non-renewable energy sources. Researchers try to find alternative energy systems capable of harvesting energies present in the ambient environment. For more than two decades, piezoelectric energy harvesting devices have been investigated since they represent a viable alternative to traditional power sources for small and low-power electronic devices. The properties of piezoelectric materials and their manufacturing technique significantly impact the performance of a piezoelectric energy harvesting device. Lead zirconate titanate (PZT) is known as the most effective piezoelectric material. However, its rigidity and toxic lead component are major concerns. Due to its high flexibility and excellent piezoelectric capabilities, Poly(vinylidene fluoride) (PVDF), a lead-free piezoelectric material, was proposed as an alternative solution. In addition, in recent years, three-dimensional printing (3DP) techniques, particularly FDM, have received a lot of interest in the piezoelectric energy harvesting field. Moreover, research studies have shown that piezoelectric energy harvesting can be used for many applications, including robotics. This paper aims to provide an overview of current piezoelectric materials and 3DP technology used in the fabrication of piezoelectric energy harvesters (PEHs) and their novel applications.

Keywords: Piezoelectric energy harvesting, piezoelectric materials properties, PVDF, 3DP, applications

2.2 Introduction

The rapid advancement of mobile electronic technologies and artificial intelligence necessitates the ongoing increase of battery energy density. On the other hand, traditional batteries have limited energy storage capacity [1], short life cycles [2-4], and low efficiency. However, the emergence of renewable clean energy and its storage may provide a solution to the energy challenges in the future years. Thus, scientists have created different energy conversion systems to harvest energy from universal energy sources, including wind energy [5-7], solar

energy from the sun [8-11], geothermal energy from the heat inside the earth [12-15], hydropower from flowing water [16-19], biomass from plants [20-23] and mechanical vibration [24-28].

Though existing green energy sources can efficiently power electronic devices, they are challenging to apply to microelectronic devices with power on the scale of mW or μW due to their demanding usage conditions and significant power production [29]. As a result of these factors, mechanical vibration energy has become a preferred energy source for microelectronic systems. Furthermore, mechanical energy sources are diverse: mechanical impacts [30-32], vibration waves [33-35], water flow or rain drop [36-38], vehicle transportation [39-42], body movements [43-46], blood circulation [47, 48], heartbeat [49-51], breathing and respiration movement [52-54], etc. The mechanical energy gathered might be utilized immediately or stored in a battery for later use.

There are three methods for converting mechanical energy created by vibration or motion into the electrical energy needed by electronic devices [55]: electromagnetic [56-60], electrostatic [61-65], and piezoelectric effects [66-69]. Piezoelectric materials outperform electromagnetic and electrostatic methods due to their high energy conversion performance and high piezoelectric sensitivity [70]. PEHs are robust and consistent and are not impacted by external conditions such as humidity [71]. When a piezoelectric material is subjected to mechanical stress, electrical charges emerge between its two opposing electrodes. The mechanical strain will be generated if an electrical field is applied to this material. These are the direct and reverse piezoelectric effects, respectively [72]. The type of piezoelectric material used in a power harvesting application can have a significant impact on the harvester's effectiveness. A variety of piezoelectric materials have been produced to date. PZT, a piezoelectric ceramic, is the most prevalent form of piezoelectric employed in power harvesting applications [73]. Although PZT is commonly used as a power harvesting material, its exceedingly fragile nature limits the amount of strain it can safely withstand without being harmed [74]. To overcome the limitations of piezoelectric ceramic materials, researchers have designed and evaluated new, more flexible piezoelectric materials, called polymer piezoelectric materials, that can be employed in energy harvesting applications [75]. PVDF is one of the most often utilised piezoelectric polymers in the energy harvesting literature. Because of its high relative permittivity, low weight, simplicity of production, and its long-term stability under high electric fields [76]. Compared to PZT, PVDF is a piezoelectric polymer with a high degree of flexibility [77]. Because of their capacity to harvest great amounts of strain, flexible

piezoelectric materials, like PVDF, are appealing for power harvesting applications. Greater deformation makes more mechanical energy accessible for conversion into electrical energy. PVDF is a semi-crystalline polymer that comes in five polymorphic forms: α-phase, β-phase, γ-phase, δ-phase and ϵ-phase [78]. PVDF is typically seen in non-polar crystalline with α-phase. β-phase is often the most useful phase due to its piezoelectric and ferroelectric capabilities, which may be obtained from the α-phase by poling, mechanical stretching, annealing [79], or adding fillers [80-83]. Poling is an essential step after piezoelectric device fabrication. It involves aligning the molecular dipoles in a single global direction within a structure by applying a high electric field (Figure 2). Poling is mainly performed in two ways: Corona and thermal poling. In addition, the so-called stretching or drawing is one of the most useful techniques for generating polarity in piezoelectric polymer materials. These polymers must be uniaxially or biaxially stretched to convert non-polar phases into polar ones (2(b)). Moreover, Numerous studies recently have discussed the incorporation of fillers such as ceramics, carbon, metal oxides, and graphene into the polymer matrix. This significantly improves the piezoresponse of the PVDF, depending on the filler added and its proportion. Most of the published studies focused on the addition of BT [84, 85], Carbon nanotube (CNT) [86, 87], and ZnO nanoparticles [88, 89] to the polymer matrix.

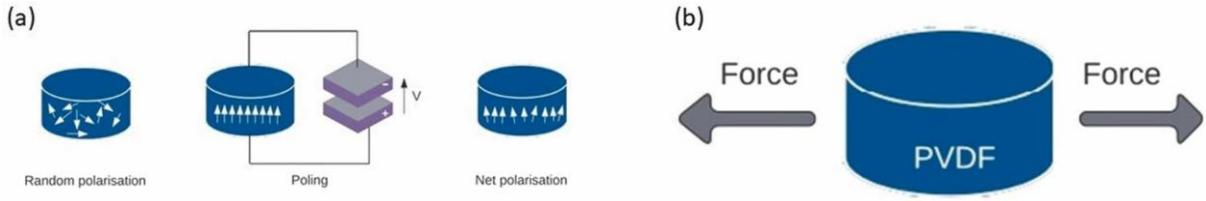

Figure 2: (a) poling process and (b) Stretching process.

Manufacturing of PEHs has progressed from mechanization to automation and subsequently to computerization during the last three decades. Additive manufacturing (AM), one of the most advanced manufacturing technologies, has been extensively used to design and manufacture various parts from piezoelectric materials with complex shapes. Compared to conventional technologies, AM has many advantages:

-Low-cost manufacturing technology: Since moulds are not required, many variants can be produced without additional cost, and complex shapes can be produced without additional steps in the manufacturing process. In addition, AM can reduce waste, lead times and costs.

-Multi-material parts: Several studies have suggested that multi-material piezoelectric energy harvesting devices may have better electromechanical performance. Fortunately, the FDM process is the most widely used additive manufacturing technology, making it easy to produce high-precision multi-material parts simultaneously.

-Electromechanical response: The electromechanical response may be controlled directly from the 3D design. This shift is due to the synergistic augmentation of approachable strain and coupling between the in-plane and out-of-plane piezoelectric coefficients, which increases the device's voltage output and sensitivity while enhancing electromechanical conversion efficiency. This 3D electronic integration technology successfully boosts electromechanical responsivity, which is crucial in enhancing the sensing effectiveness of piezoelectric sensors, the frequency of focussed ultrasonic devices, and the energy harvester collecting efficiency.

-Piezoelectric constant: Traditional piezoelectric materials have a charge motion governed by the internal crystal, and the crystal orientation is somewhat random, hindering material performance. The additive manufacturing method can manipulate and design arbitrary piezoelectric constants, allowing users to specify and program voltage responses via 3D active topologies, enabling free combinations of arbitrary piezoelectric constants in the material and amplifying, reversing, or suppressing them in any direction. When applied to piezoelectric sensors, it may improve their flexibility and responsiveness and correctly determine the location, size, and direction of the impact at any place by responding to mechanical pressure, impact force, and vibration via an electrical signal.

-Size and shape: Traditional methods such as etching and cutting technology have been used to control the size and shape of the device, which generate mechanical stress that can lead to grain loss, strength degradation, and near-surface-area depolarization, resulting in a significant reduction in the performance of the piezoelectric element. It is difficult to form a piezoelectric array with a complicated geometry using these methods because fragile ceramics cannot be molded into a higher-order 3D structure. High-resolution additive manufacturing technology can fabricate complex forms and exact structures, removing the need for additional production stages. It may increase the precision of piezoelectric devices and significantly improve their performance, such as mechanical properties, sensitivity, and sensing effectiveness.

Along with the rapid production of low-integrated circuits and high-efficiency energy storage options, piezoelectric energy harvesting technologies are expected to usher in an era of self-powered autonomous operation in a variety of fields, including aeronautics [90-93], healthcare

[94-97], wireless data transmission [98-101], civil engineering [102-104], automotive industry [105-107], environmental monitoring [108-110], and robotics [111-113].

Although the piezoelectric effect is a great way to power electronic devices and additive manufacturing is the manufacturing trend of the future, no review article covers the most commonly used piezoelectric materials, identifies the most commonly used methods to improve their piezoelectricity and outlines the reasons for choosing 3DP as the manufacturing process for piezoelectric energy harvesting devices. Moreover, despite the numerous applications of piezoelectric energy harvesting devices in various fields, most review articles to date have focused only on healthcare [114-117], and wearable products [118-120] applications. With this background as motivation, in this article, the authors provide an overview of various topics related to energy harvesting with piezoelectric materials, including material selection, techniques for improving material properties, fabrication methods, and applications in the automotive, wearable products, healthcare, and robotics sectors, as illustrates Figure 3. Such a review article is of great significance to relevant research and can provide researchers with new ideas.

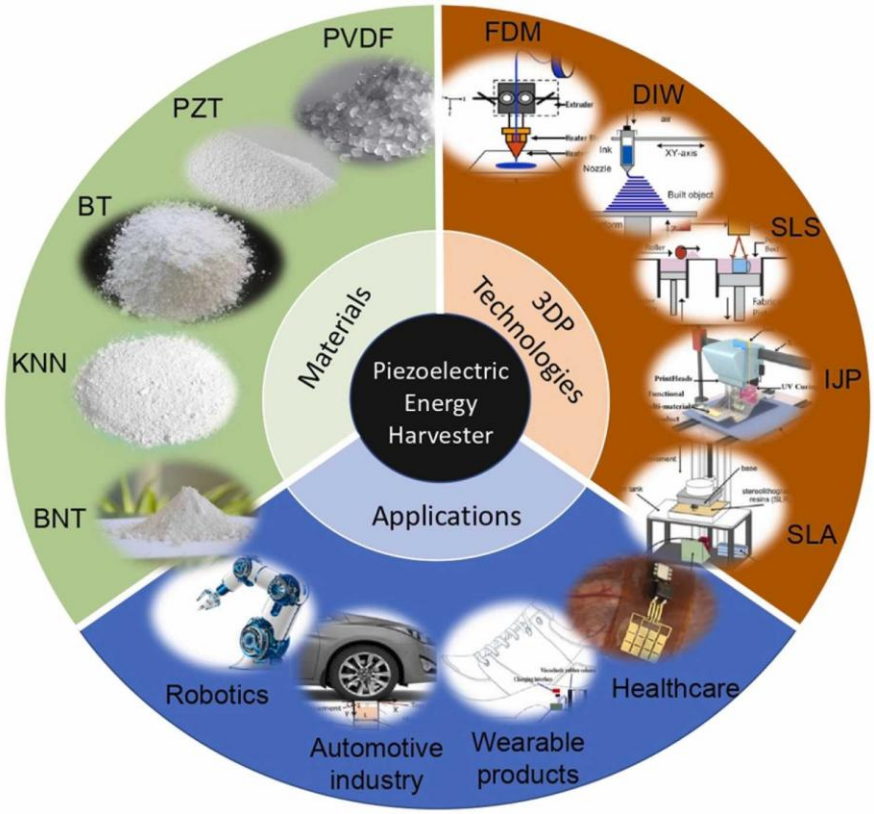

Figure 3: Most used piezoelectric materials and 3DP technologies to fabricate piezoelectric energy harvesting devices and recent application industries.

The remainder of this paper is organized as follows. Section 2 provides a detailed review of the piezoelectric materials used in the literature and their properties, the benefits of using PVDF to create PEHs, and the existing research progress of the existing PVDF piezoelectric and mechanical properties improvement techniques. Section 3 compares 3DP to traditional manufacturing methods such as molding to emphasize the relevance of 3DP technology, particularly FDM owing to its ability to fabricate multi-material products. Section 4 describes recent applications of piezoelectric materials in various areas (wearable products, automotive industry, healthcare, and robotics), followed by a conclusion in Section 5 and future directions in section 6.

2.3 Materials used for piezoelectric energy harvesting

Lead-based piezoelectric materials, particularly PZT, are widely recognized for their exceptional piezoelectric characteristics. However, given the toxicity of lead and its derivatives, there is widespread support for creating environmentally beneficial lead-free products, as indicated by the European Union regulations [121]. Piezoelectric lead-free materials include both organic (mainly polymers) and inorganic materials. Piezoelectricity occurs in inorganic piezoelectric crystals due to the arrangement of ions in the dielectric material's non-inverse symmetric structure. The material's internal polarization varies linearly with applied stress, forming an electrical field across the material border. While in organic piezoelectric materials, the polymer's molecular structure and orientation produce the piezoelectric effect [122].

2.3.1 Piezoelectric materials properties

For more than two decades, researchers have investigated piezoelectric energy harvesting systems as an alternative to traditional power sources (e.g., batteries) [123, 124] for small-sized and low-power electronic devices. The operating concept of piezoelectric materials is that when an external force is applied, a potential difference is formed, known as a positive piezoelectric effect [125]. When an electric field is supplied to a piezoelectric material, it produces mechanical stress, which is known as an inverse piezoelectric effect [126]. To evaluate the performance of piezoelectric materials, numerous characteristics must be considered.

The first is the piezoelectric coefficient, which represents the coupling connection between piezoelectric structures' mechanical and dielectric properties. The piezoelectric coefficient [127] is commonly defined as d_{xy}, where x and y indicate the electric field direction and the stress or strain direction, respectively and it's expressed in m/V or C/N [128]. The

electromechanical coupling coefficient (k) [129], representing the degree of energy transformation, is the second parameter. There are as well many other factors to consider, such as the planar electromechanical coupling factor (k_p) [130], the transverse and longitudinal electromechanical coupling factors (k_{31} and k_{33} respectively), the dielectric constant (also known as relative permittivity) (ϵ_r) [131], the depolarization temperature (T_d) [132-134], the curie temperature (Tc) [135, 136], the remanent polarization (P_r) [137], the dielectric loss (tan δ) [138, 139], and the resistance (R) [140]. Effective piezoelectric material is always characterized by high d33, k, ϵ_r, T_d, Tc, and P_r, and reduced tan δ and R.

2.3.2 Lead-based piezoelectric materials

The first lead-based piezoelectric material explored was PZT [141-143], which was followed by lead metaniobate [144], lead titanate [145], lithium niobate [146], and modified lead titanate [147]. Due to its favourable dielectric, piezoelectric, pyroelectric, ferroelectric, and optical characteristics, PZT has become the mainstream of lead based piezoelectric materials. Unfortunately, PZT is known by its weak mechanical properties. Moreover, the lead component of these lead based piezoelectric material is harmful to humans and ecosystems [148]. Hence lead-free piezoelectric materials have gained popularity in recent years. Lead-free piezoelectric materials have previously been investigated in both inorganic (such as piezoelectric ceramics and ZnO nanostructures) and organic (such as piezoelectric polymers or certain polymer nanocomposites) [149]. Compared to PZT, these lead-free materials demonstrated equivalent or even greater piezoelectric characteristics. Furthermore, they are eco-friendly and biocompatible, and they are predicted to replace their lead-based counterparts in the future. Lead-free materials are divided into two categories, organic and inorganic piezoelectric materials.

2.3.3 Inorganic materials

The barium titanate (BT) based ceramic material is the first inorganic lead-free piezoelectric material to be disclosed. The BT-based ceramic system possesses stable electrical characteristics, high electromechanical coupling, and low dielectric loss at room temperature, but it is restricted by low curie temperature T_c and piezoelectric coefficient d33 [150]. The sodium-potassium niobate (KNN) based ceramic system is another piezoelectric ceramic material that has been regarded as one of the most promising lead-free piezoelectric materials because of its good overall properties, such as high T_c, high P_r, and large k_p [151]. KNN-based ceramic system is often created using a solid-state technique, which is well-known for its ease

of use. Yet, it necessitates a very high temperature (1000-1500 °C); however, the purity and performance of the result are insufficient.

The sodium bismuth titanate (BNT) based ceramic system is widely recognized for its large Pr and high T_c [132]. As a result, the BNT-based piezoelectric system has gotten a lot of interest in the field of piezoelectricity. The most promising system has been identified as the BT-modified $(1-x)(Na_{0.5}Bi_{0.5})TiO_3-xBaTiO_3$ system (NBBT). Unfortunately, the NBBT monocrystal remains restricted for many applications because of its high leakage current, significant tan δ, and low T_d. The bismuth layer-structured ferroelectrics (BLSFs), also, are lead-free piezoelectric material with high Tc [152], small tan δ, but weak ϵ_r and d33.

2.3.4 Organic lead-free piezoelectric materials

PVDF and other organic piezoelectric materials such as epoxy [153-155], nylon [156-158], and silicone [159, 160] are examples of lead-free piezoelectric materials, often known as piezoelectric polymers.

2.3.4.1 PVDF properties

PVDF is a semi-crystalline polymer commercially available as powder, pellets, or semi-transparent films. It has a melting temperature (T_m) of 170 °C and a melt viscosity acceptable for melt processing. It contains five polymorphs: the α, β, γ, δ and ϵ phases. The arrangement of carbon, hydrogen, and fluorine atoms in a three-dimensional molecule determines the presence of these phases. Figure 4 illustrates the difference between the atomic configurations of α-PVDF, β-PVDF and γ-PVDF.

The α-phase is the most thermodynamically stable and easily generated when the polymer crystallizes from the melt because of its higher crystallization rate at elevated temperatures (110-150°C) [161]. However, the α-phase has a semi-helical TGTG' [162] (trans-gauche-trans-gauche) configuration making it non-polar due to the anti-parallel packing of the dipoles within the unit cell. Another important piezoelectric phase is the polar β-phase (all trans-TTT chain configurations), which can transform mechanical stress into electrical energy because the fluorine (-) and hydrogen (+) atoms that generate the dipole moments are on opposite sides). When loaded in the chain direction, the hydrogen atoms respond with a positive potential and the fluorine atoms respond with a negative potential, resulting in a potential difference. The γ-phase (T3GT3G' configurations) also has strong piezoelectric properties, allowing it to convert mechanical stresses into electrical fields. However, research has shown that the piezoelectric

effect of γ phase is lower than that of the β-phase, due to the presence of a gauche bond in every fourth repetition unit [163].

PVDF has attracted the interest of researchers in recent years due to its low density, high flexibility [164], low resistance, and pretty large piezoelectric constant. PVDF also has a high degree of polarity, excellent piezoelectric and mechanical capabilities, and stable chemical properties. Because of these advantages, they are currently commonly employed in manufacturing energy harvesters.

Some significant strategies are employed to increase the piezoelectric effect of the PVDF. Stretching, poling, and the addition of fillers to the polymer matrix are the most commonly used processes [165].

2.3.4.2 Effect of stretching on the PVDF piezoelectricity

Stretching is a crystalline transition that induces piezoelectricity in semicrystalline polymers such as PVDF by applying mechanical stress. For example, it is possible to make β-PVDF from α-PVDF by applying mechanical stresses. Under stretching temperatures around 100 °C and drawing ratios of more than 3, the relative proportion of β-phases in the material can reach 80%.

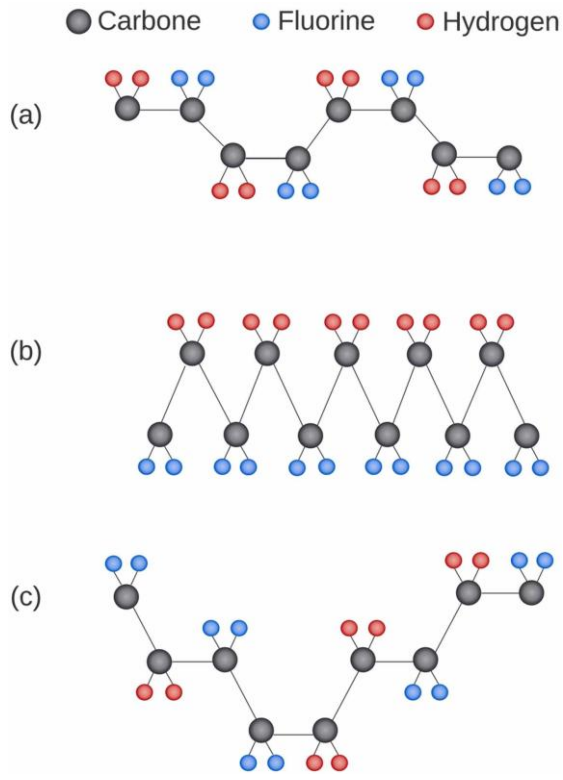

Figure 4: (a) α-PVDF, (b) β-PVDF, (c) γ-PVDF.

Li et al. [166] studied the stretching effect on the PVDF piezoelectricity by adjusting stretching temperature (T_s= 80 C, 90 C, 100 C, 110 C, 120 C, 130 C, 140 C, 150 C), tensile speed (S=1 μm/s, 50 μm/s, 100 μm/s, 200 μm/s, 1000 μm/s), and stretching ratio (λ= 1, 1.5, 2, 3, 4, 5). According to the findings, stretching should be performed with T_s around 100°C, S about 50 mm/s, and λ above 3 to get the maximum β-phase fraction. A similar experiment was conducted by Wang et al. [167]. Results revealed that when increasing the stretching ratio from 2 to 3, the β-phase relative fraction increases from 69% to 75%. Moreover, Ting et al. [168] demonstrated that the β-phase content improves when the stretching ratio increases and the temperature decreases. The authors also proved that uniaxially stretched samples with a high stretching ratio have a higher β-phase content than biaxially stretched samples. Uniaxial stretching with a stretch ratio of λ=5 results in an excellent transition of α to β-phase, particularly at T=80 °C (Figure 5(a)). Biaxial stretching with a stretch ratio of λ=4×4 is the second best at the same temperature, with a little greater value than 3×3. In order to show the impact of mechanical stretching, Men et al. [169] performed both stretching and annealing treatments to enhance the PVDF piezoelectric properties. After applying the two processes, the authors confirmed that the β-phase content in PVDF cast films rose dramatically by 49.4% when stretching was used, compared to 27%-39% using annealing.

Moreover, several recent studies proposed adding filler to the PVDF matrix to further increase the effect of stretching on the α to β-phase conversion.

Jahan et al. [170] demonstrated that during stretching, in the presence of nanoclay, $CaCO_3$ could lead to increasing local stress in the PVDF compared to the critical stress. In this instance, the $CaCO_3$ fillers are expected to transmit the excess stress to the matrix, and an efficient transition from α to β-phase at the interfacial area between the fillers (nanoclay and $CaCO_3$) and PVDF is possible. Because the interfacial area rises with the proportion of CaCO3 and clay, as shown in Figure 5(b), the composite with a greater $CaCO_3$ and clay contents has a larger F(β) value. Zhou et al. [171] also showed the effect of adding different fractions of poly(methyl methacrylate) (PMMA) filler (15 wt%, 20 wt%, 25 wt%, and 30 wt%) to the PVDF matrix while applying biaxial stretching under three distinct stretching ratios (2×2, 2.5×2.5, and 3×3). The results revealed that the effect of stretching rises as the percentage of PMMA in PVDF increases (Figure 5(c)). This is due to increased contact between oxygen atoms of C=O groups in PMMA and hydrogen atoms of CH2 groups in PVDF, which causes crystals to form [172]. In addition, Mishra et al. [173] proved that when GO is added to the

PVDF matrix, the optimal F(β) that can be achieved is 86% and 84% with 0.5 wt% and 0.1 wt% of GO content, respectively, under the stretch ratio of 2, as shown in Figure 5(d). Moreover, Khan et al. [174] demonstrated that stretching of pure PVDF films results primarily in α to β-phase conversion, whereas stretching of BT/PVDF films leads largely to γ to β-phase conversion. There are two possible explanations for this: The first reason is that pure PVDF films contain a greater percentage of alpha phase in their pre-stretched state than BT/PVDF; probable the composite films' low α-phase content does not successfully transition to β-phase with stretching. Another theory is that organic-inorganic contacts between the BT filler and the PVDF matrix reduce polymer chain mobility [175, 176], requiring larger elongation ratios for α to β-phase transformation in BT/PVDF composites.

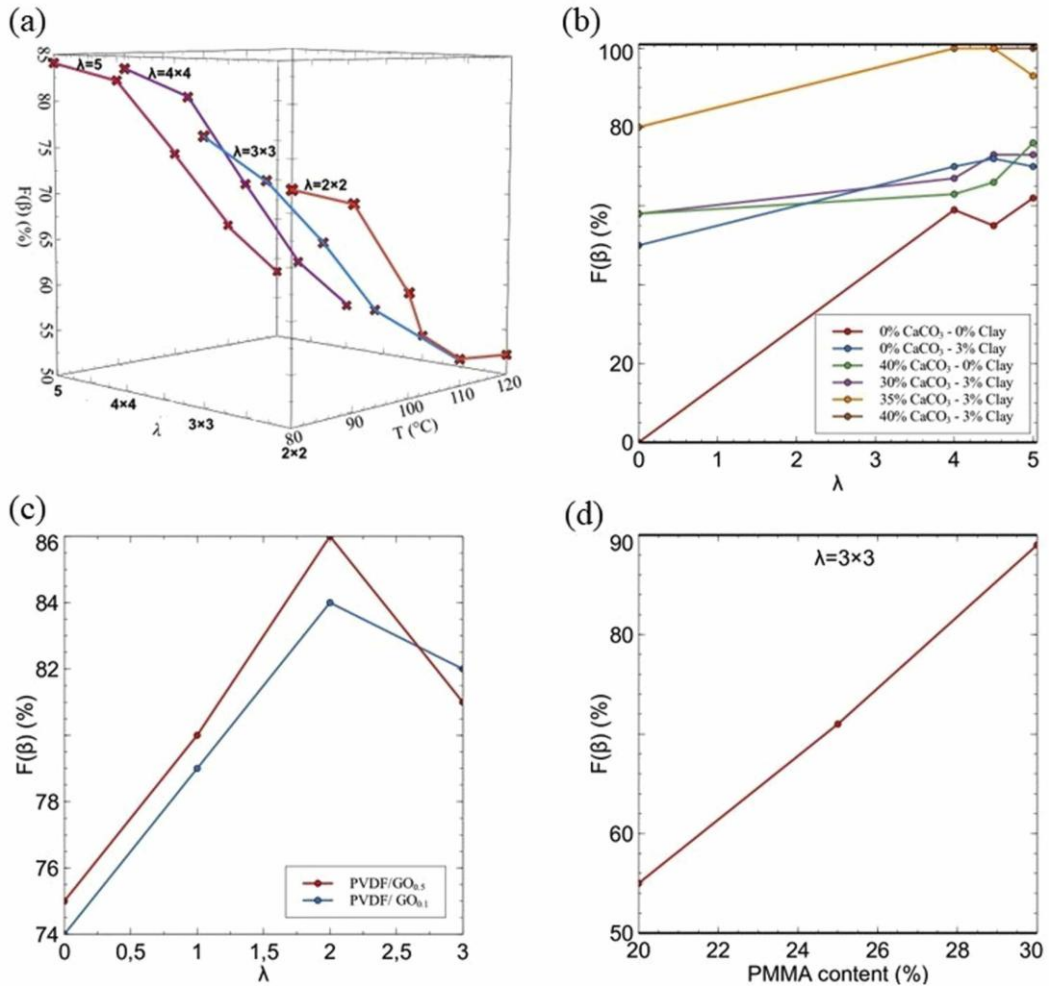

Figure 5: Influence of stretching conditions and additives on β-phase content in PVDF : Effect of (a) stretching temperature [168], (b) adding CaCO3 and clay [170], (c) adding PMMA [171], and (d) adding GO [173] with different quantities to the PVDF material on the β-phase content when applying mechanical stretching with different stretching ratio λ.

Furthermore, Martin et al. [177] have shown that simple compression under pressures of up to 20 kN cm^{-2} applied for 5 min and temperatures between 140 °C and 150 °C are sufficient to transform non-polar α-PVDF into a piezoelectric γ phase having a piezoelectric coefficient d33 of 36 pm V^{-1}, higher than that of β-PVDF (31 ± pm V^{-1}); and this is significantly greater than previously reported values for electroformed γ-PVDF (15 pm V^{-1}). The stretching parameters used in the works described above as well as the β-phase relative fraction of the PVDF resulting from the stretching effect are summarized in Table 1.

Table 1: Stretching process parameters and their effect on β-phase content in PVDF.

Ts (°C)	S (μm/s)	Λ	F(β) (%)	Ref
100	50	3	80	[166]
110	80	3	75	[167]
120	33.33	1.5	77.79	[169]
90	41.66	5	93	[170]
140	3600	2×2 (biaxial)	93	[171]
80	11.11	5	84.1	
		2×2 (biaxial)	72.2	[168]
		3×3 (biaxial)	76.8	
		4×4(biaxial)	83.4	
80	-	1.5	79.8	[174]
80	6.66	2	86	[173]

2.3.4.3 Effect of poling on the PVDF piezoelectricity

Poling is another technique for increasing the piezoelectricity of polymers by applying a high electric field at a high temperature to reorient the crystallites (molecular dipoles) [178]. Direct-contact thermal poling [179-181] and non-contact corona poling [182-184] are two common poling methods. Thermal poling involves directly connecting a sample with attached electrodes on both sides to a high DC voltage on both sides. To avoid the breakdown of the surrounding air, the entire sample is usually immersed in a silicon oil bath at a high temperature. Corona poling is accomplished by suspending a high-voltage metal needle above the sample, with only the bottom electrode necessary and grounded. Ionization of the air near the needle tip produces charge ions, concentrating on the polymer surface and forming a poling electrical field. Before

poling, the directions of polarization of individual crystallites are randomly distributed. After poling, the polymer's molecular dipoles are sustained and permanently orientated in the electric field direction [185]. Apart from the α to β-phase transition, by poling at a strong electric field, the δ-phase also may be transformed into β-phase [186].

Pariy et al. [187] recently conducted a study to assess the influence of poling on the piezoelectric properties of PVDF. After applying a 0.25 MV/m electric field for 2 hours, the β-phase content rose from 22% (immediately after printing) to 42%. The enhancement of the β-phase content can be explained by the fact that the distribution of the polarized domains is random before the polarization of the samples. As a result of polarization, the orientation of the domains becomes in the direction of the applied electric field. In addition, results show that the crystallinity of the polymer increases from 12% to 22.7% after poling the PVDF samples.

Moreover, the impact of poling appears mainly in the reference [188], when samples before and after poling were compared. In this work, four experiences were prepared, where no post-printing process was applied in the first one. The sample was only stretched in the second. In the third experience, the harvester was subjected to a stretching and poling voltage of 5 KV/cm, and in the last experience, the sample was stretched and poled at 10 KV/cm. Before processing, pure PVDF generated a low output voltage of about 0.7 V. The device with stretched PVDF produced a pretty high voltage output (almost 2 V), whereas the same sample, after poling at 10 KV/cm, produced a very high voltage output of approximately 7.5 V. Furthermore, studies revealed that the piezoelectric coefficients display powerful poling voltage dependency, which can be seen by a greater d33 value of 30 pC/N at poling voltages of 10 KV/cm vs. the significantly lower value of 12 pC/N at poling voltages of 5 KV/cm. To further emphasis the importance of poling process compared with some other methods for increasing PVDF piezoelectric properties, Tu et al. [189] conducted 14 experiments: E1: PVDF cast in solvent from a DMF solution, E2: PVDF printed from a DMF solution (parallel filling), E3: PVDF printed from a DMF solution (alternating filling), E4: PVDF printed from a DMSO solution (parallel filling), E5: PVDF printed from a DMSO solution (alternating filling), E6: PVDF printed from a DMF solution then heated to 80°C, E7: PVDF printed from a DMF solution then heated to 130°C, E8: PVDF printed from a DMF solution then heated to 180°C, E9: PVDF printed from a DMSO solution then heated to 80° C, E10: PVDF printed from DMSO solution then heated to 130°C, E11: PVDF printed from DMSO solution then heated to 180°C, E12: PVDF printed from DMF solution then annealed to 80°C, E13: PVDF printed from a DMF solution then hot pressed at 80°C and E14: PVDF printed from a DMF solution then polarized

by electric field. In the first 13 studies, no poling was performed on the samples. Figure 6 shows that the greatest β-phase content achieved in the first 13 experiments was 73% (E12). In experiment E14, a 750 KV/cm voltage was applied and the proportion of β-phase reached 78%. Furthermore, when applied to β-PVDF, the poling can also improve the material's mechanical strength, particularly in the direction parallel to the polymeric chains, and causes changes at the molecular level that persist after the material has melted. Costa et al. [190] demonstrated that the material's Young modulus along the polymeric chains increased from 0.9 GPa to 1.3 GPa after poling.

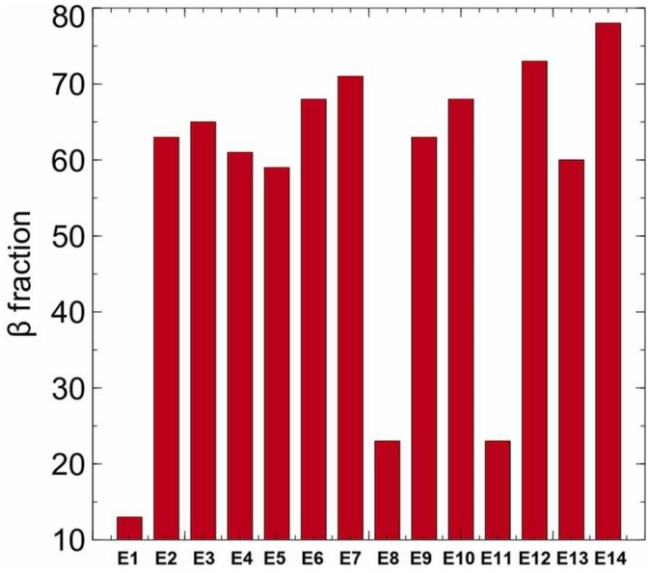

Figure 6: Comparison of the poling effect with other post-printing processes (heating and annealing) effects [189].

Moreover, most recent publications recommended adding fillers to the piezoelectric polymer to boost the poling impact on the PVDF piezoelectric, dielectric, and mechanical properties. Pariy et al. [191] investigated the effect of poling and the addition of rGO to PVDF on its piezoelectric properties. The piezoelectric coefficient of the initial simple, which was only printed, was 64 pm/V. The β- phase content in this sample was 16%. After adding 0.1 wt% rGO and applying a poling voltage of 3.5 MV/m at 90°C for 1 hour, the piezoelectric coefficient increased to 75 pm/V and the fraction of β-phase was raised to 20%. Then, after adding 0.4 wt% rGO to PVDF and poling it, d33 reached 79 pm/V and the β-phase content hit 23%. Similarly, Su et al. [192] produced three PVDF/BT composite samples with varying amounts of BT to demonstrate the influence of the poling procedure on the PVDF piezoelectric characteristics. Figure 7(a) indicates that after applying an electric field to each sample, the β-phase fraction rose considerably. In particular, the sample with 0.1 wt% BT exhibited an increase in β-phase fraction from 49.5% to 52.5%. For the same sample, the piezoelectric

coefficient increased by 0.57 pm/V, as shown in Figure 7 (b). In addition, Ahn et al. [193] studied the impact of changing multi-walled carbon nanotube (MWCNT) content and the application of stretching and poling processes on the piezoelectric properties of PVDF. The results revealed that by only adding 10% wt of MWCNT, the relative proportion of β-phase rose from about 32% to 47%. At the same time, the β-phase relative fraction can reach 90% in samples subjected to poling and stretching with the same quantity of MWCNT. Also, Kumar et al. [194] demonstrated the effect of poling and the addition of fillers on the PVDF piezoelectric properties and its performances as a PEH. The filler used in this study is CNT, which was introduced in various amounts (0.25 wt%, 0.5 wt% , 0.75 wt%, and 1 wt%). The prepared CNT/PVDF nanofibers with the greatest piezoelectric characteristics were 0.5-CNF/PVDF. The produced nanofibers were electrically interrogated for 6 hours at 30°C by contact at 300 KV/cm. As a result of this process, the β-phase relative content of the sample with the optimal composition increased from 13% to 85%, and the voltage output generated by the same sample improved from 4.2 V to 5.8 V. Kim et al. [195] performed the same study with varying quantities of CNT (0, 0.1, 0.2, 0.3, 0.5, 1 wt%). The results reveal that when 0.2 wt% CNT is added to the PVDF material, the β-phase relative fraction can approach 96% after drawing and poling operations. The great β-phase fraction emphasizes the significance of post-printing operations on the performance of PVDF material.

Furthermore, an efficient in situ poling technique was proposed by Song et al. [196]. This method was compared with the traditional ex-situ poling approach. Figure 8 (a) depicts the increase in d33 of polyvinylidenefluoride-co-hexafluoropropylene (PVDF-HFP) samples during in situ poling at various poling electric fields (from 0.3 to 1 KV). The d33 value observed in samples under a low poling electric field was modest, but it grew dramatically as the poling electric field increased, reaching approximately 42 pC/N when 1 KV was applied. For the same poling voltage (1 KV), ex-situ poling experiments with varied time duration at room temperature were done. PVDF-HFP samples without in situ poling achieved d33 values equivalent to their in situ poling counterparts after a very long period of electrical poling treatment (10 h), as shown in Figure 8 (b). Thus, as compared to the standard ex-situ poling method, this methodology can save ten times the overall time needed to achieve the same piezoelectric properties. Apart from direct field poling, another poling procedure known as corona poling has been studied. Over the typical electrode poling approach, this poling process offers several advantages, including large-scale poling, greater poling fields, the ability to pole despite flaws, and poling without deposited electrodes.

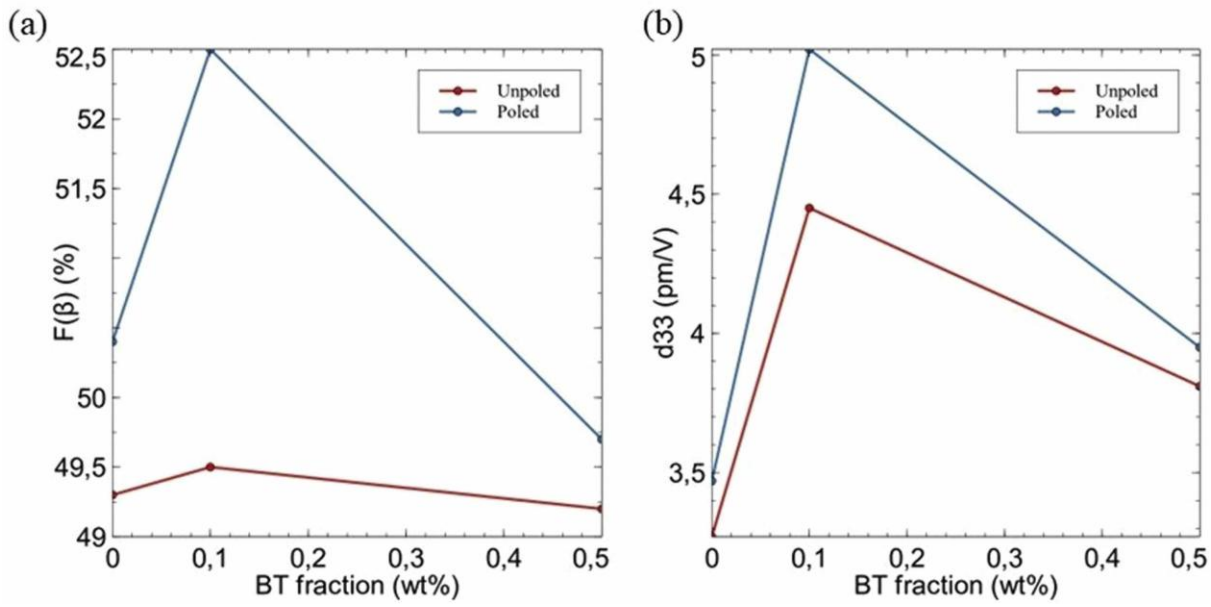

Figure 7: Effect of poling on β-phase content of the nanocomposite PVDF/BT with different BT fractions [192].

To identify the optimal corona poling parameters, Liu et al. [197] conducted several experiments to investigate the effects of poling voltages (Figure 8(c)), poling temperatures (Figure 8 (d)), and poling duration (Figure 8 (e)) on the piezoelectric constant (d33). Results showed that the optimal corona poling parameter combination is (10.5 KV/cm, 60°C, 90 min). Li et al. [198] also conducted several experiments to determine the ideal set of corona poling inputs (voltage, time) to optimize the piezoelectric characteristics of the PVDF material. First, the poling voltage was altered as follows: 15 KV, 20 KV, 25 KV, 30 KV, 35 KV, and 40 KV, with a poling period of 10 cycles. The temperature of the poling was set to room temperature. The piezoelectricity of poled PVDF-TrFE coatings improves gradually with increasing poling voltage, as seen in Figure 8(f). When the poling voltage was raised over 35 KV, there was no discernible improvement in piezoelectricity, and many electric arc strikes occurred throughout the poling process. This is because the coatings were harmed and deteriorated. Thus, the optimal d33 can be reached when a voltage poling of 35 KV is applied. Consequently, the second step applied a 35 KV voltage field for various periods. The results indicated that when a 35 KV voltage is applied for 5 cycles, the d33 coefficient reaches its maximum (almost 20 pV/m), as shown in Figure 8 (g).

In situ contact poling and ex-situ corona poling were compared by Ikei et al. [199] in 2021. Four samples were printed and poled at a constant temperature at four different electric voltages (2 KV, 4KV, 6KV, and 8KV).

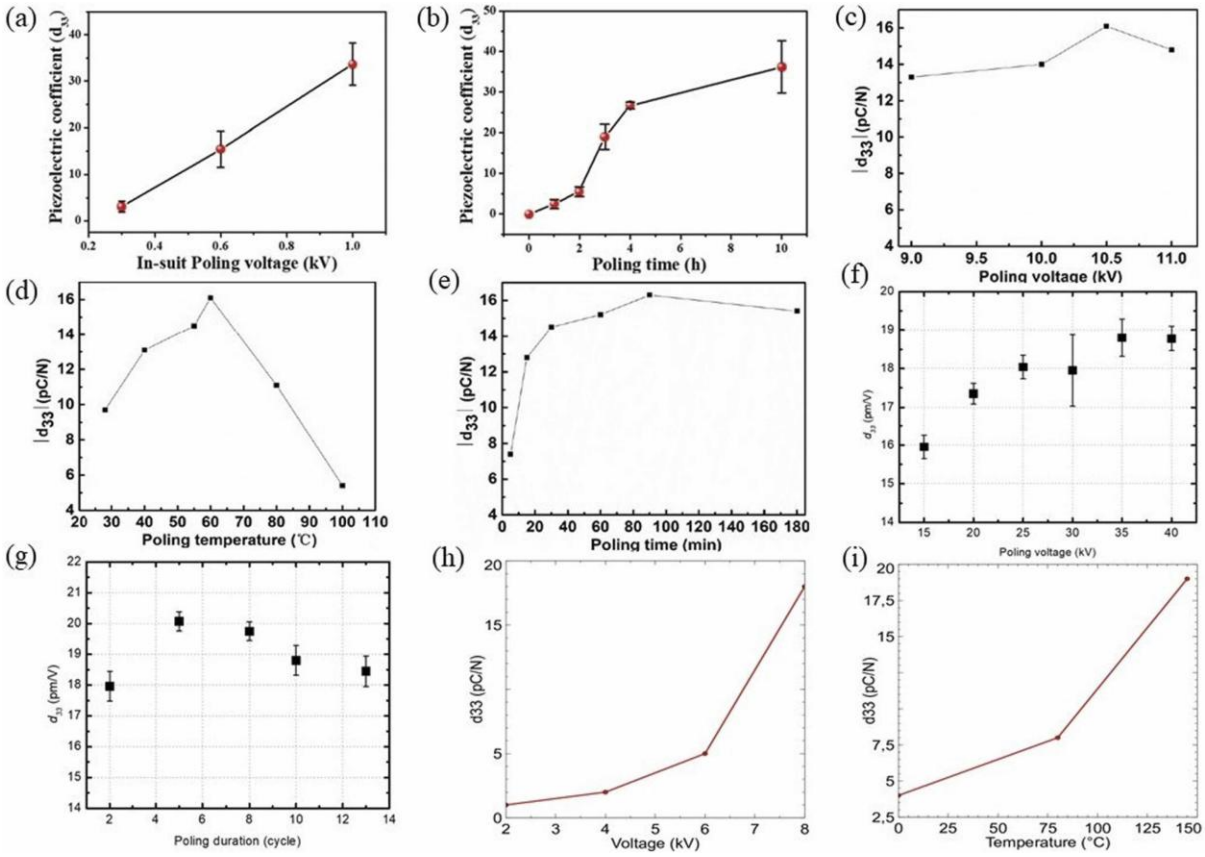

Figure 8: Influence of stretching conditions and additives on β-phase content in PVDF : The effects of poling voltage (Subfigure; (a) from [196], (c) from [197], (f) from [198], (h) from [199]), poling temperature (Subfigure; (d) from [197], (i) from [199]) and poling duration (Subfigure; (b) from [196], (e) from [197], (g) from [198]) on d33 coefficient (Reproduced with permission [196], [185], [198]).

Figure 8 (h) illustrates that as the voltage supplied to the sample grew, so performed. Ex-situ corona poling was carried out in a fixed high electric field. The sample was brought down from the poling temperature to room temperature, ranging from 0 (unheated sample) to 145 °C. Figure 8 (i) demonstrated that when the temperature applied during poling increased, so did the d33 coefficient, which was most likely owing to increasing dipole mobility. Because corona poling requires a very high electric field and poling temperature to obtain strong piezoelectric performances, the authors confirmed that the in-situ poling technique is more practical. Table 2 summarizes the materials used in the works mentioned above, as well as the applied poling voltage, poling temperature, and duration. In addition, the outcomes of each study are presented in terms of β-phase relative fraction or d33 after employing the poling technique.

Table 2: Poling process parameters and their effects on PVDF piezoelectricity

Materials	Voutput	Temperature	Time	F(β) (%) d33 (pC/N)	Ref
PVDF	0.25 MV/m	130 °C	2h	42 %	[187]
PVDF/CNF 0.5 wt%	300 KV/cm	30 °C	6h	85 %	[194]
PVDF/MWCNT	500 KV/cm	120 °C	20 min	>90 %	[193]
PVDF	750 KV/cm	80 °C	2h	78 %	[189]
PVDF	10 KV/cm	-	-	75%	[188]
PVDF/TiO_2 0.5 wt%	10.5 KV/cm	60 °C	90 min	83.8%	[197]
PVDF/rGO 0.4 wt%	3.5 MV/m	90 °C	1h	23%	[191]
PVDF	10 KV/cm	30 °C	10 min	75%	[200]
PVDF/MWCNT 0.2 wt%	1.5 MV/cm	100 °C	30 min	96%	[195]
BT/Norland 40 wt%	15 KV/cm	100 °C	90 min	26 pC/N	[201]
PVDF/BT 66 wt%	100 KV/cm	100 °C	2h	3-4 pC/N	[202]

2.3.4.4 Effect of adding fillers on the PVDF piezoelectricity

Another method for enhancing the creation of a more stable β-phase in PVDF is adding fillers to the polymer matrix. This results in a considerable improvement in polymer piezoresponse depending on the fraction and processing of the polymer.

The BT is the most used filler in 3D printed PVDF samples [203-208] for various reasons: First, BT works as a nucleating agent, increasing the β-phase content. Because the nucleation of the β- phase of the PVDF is proportional to the specific area of the filler during thermal operations such as filament extrusion and 3DP, it is expected that the addition of BT filler had the most significant impact on β-phase growth [204]. Figure 9 shows the influence of adding BT filler on the dielectric properties of the PVDF matrix. The addition of BT and the electrospinning processes in these present studies [203-206] result in eradicating the nonpolar phase, which leads to the high content development of the polar phase in the BT/PVDF

nanocomposite. However, as shown in Figure 8(c), 9(d) and 9(e), with a high amount of BT, the dielectric characteristics of the composites are reduced due to a large number of structural flaws [205].

Thus, these results show that a suitable quantity of BT causes the development of a substantial fraction of the β-phase; moreover, it signifies that greater availability of dipoles may be orientated. The second reason is that the addition of BT has been shown to improve the degree of crystallinity of the BT/PVDF nanocomposite membrane. Jiang et al. [206] demonstrated that the crystallinity of a BT/PVDF nanocomposite membrane rises from 37.4 to 42.3% when 10% BT is added.

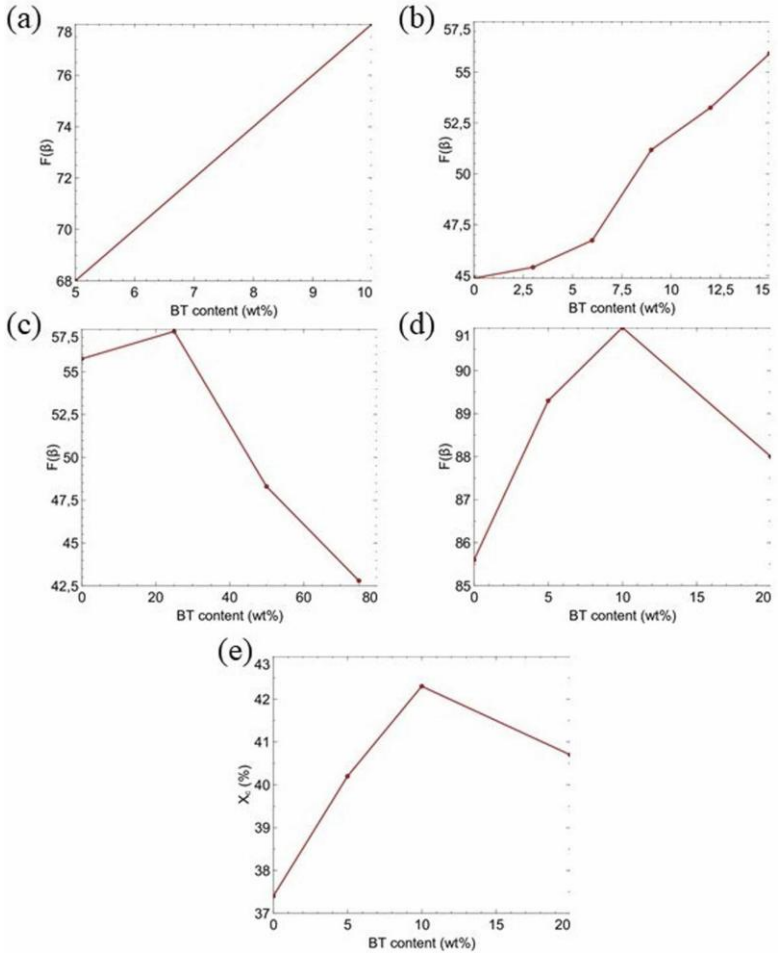

Figure 9: Impact of BT filler content on β-phase and crystallinity of PVDF : Effect of adding BT filler to the PVDF with different fractions on the PVDF β-phase content. Subfigure; (a) from [203], (b) from [204], (c) from [205], (d) from [206], and (e) Effect of adding BT on the crystallinity rate of PDVF [209].

Finally, Kim et al. [204] revealed that the 3D printed 3 wt% BT/PVDF film had higher ultimate tensile strength and fatigue strength (Figure 10) than PVDF. Furthermore, the BT filler enhanced the strain, and samples containing 15% wt BT were stretched up to 500% (Figure

11). It is thought that greater filler helped limit fracture development, and hence increased BT filler enhanced toughness. Because of the high flexibility of BT/PVDF nanocomposite membranes, harvesters may be employed in various applications, including artificial intelligence, health monitoring, and motion detection [206].

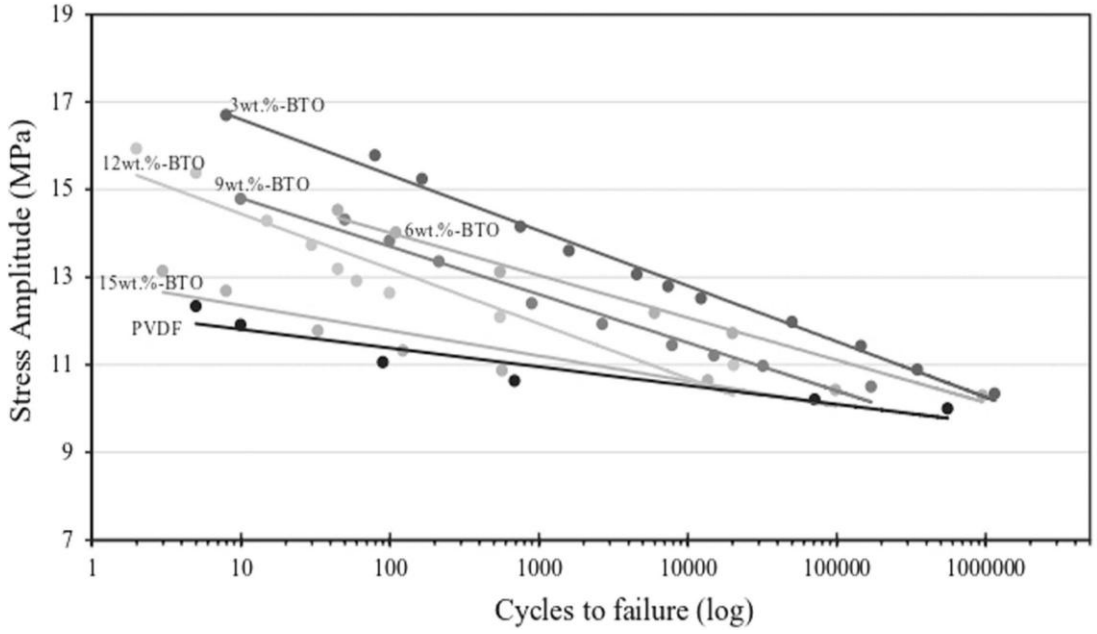

Figure 10: Stress–strain curve for PVDF/BT composite at 5 mm/min strain rate with different BT fractions (Reproduced with permission [204]).

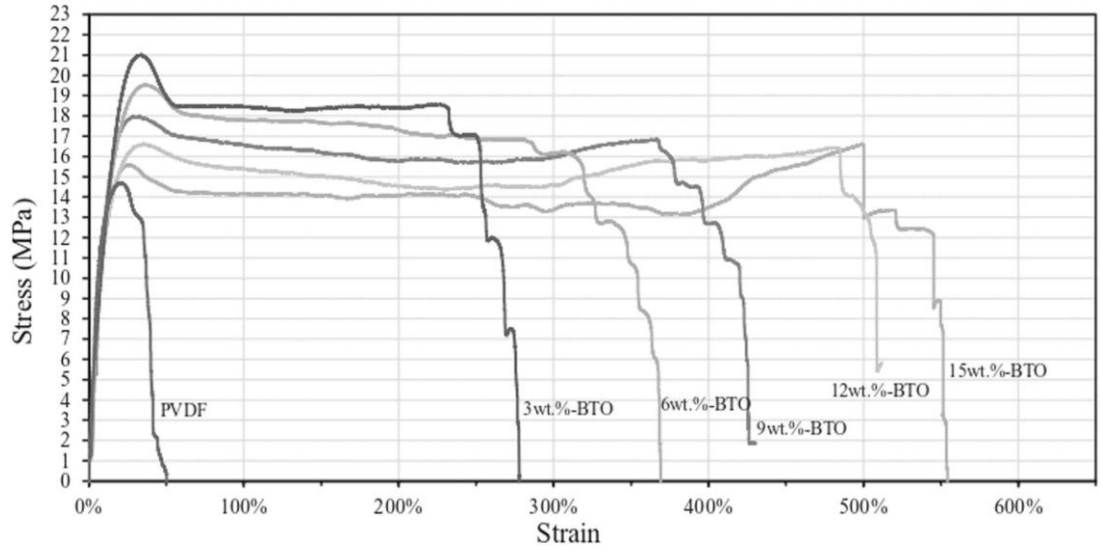

Figure 11: Generalized S–N curve for PVDF/BT composite with different BT fractions Reproduced with permission [204].

Several research have recently been published on the effect of adding nanoclay to α-PVDF, which has been shown to considerably improve the synthesis of β-PVDF [210-212]. The

nanoclay's incorporated and exfoliated structures helped in the development of β-phase in PVDF. It was proposed that matching the clay's crystal structure with that of β-phase PVDF is most likely responsible for the development and stabilization of β-phase in PVDF. It has also been discovered that adding nanoclay to PVDF improves its mechanical characteristics and toughness. In addition, Kim et al. [213] were the first to create a PEH by using methylammonium lead iodide ($MAPbI_3$) perovskite thin films as an active piezoelectric layer, sandwiched between two electrodes of FTO/glass and Au/Ti/PET. The results showed an output voltage of 2.7 V and a current density of 140 nA/cm^{-2}. Based on this finding, in 2018, Jella et al. [214] used a composite film made of $MAPbI_3$ perovskite as a fiber and PVDF as a flexible polymer matrix to achieve excellent performance, flexibility, and cost-effectiveness. The results revealed that by utilizing composite films with a 25% volume fraction of $MAPbI_3$, the PEH generates an output voltage of 45.6 V and a current density of 4.7 μ A cm−2. In 2021, Tuluk et al. [215] produced 5 PEHs with varied Bismuth Ferrite ($BiFeO_3$) volume fractions ranging from 20% to 60% to demonstrate the effect of adding $BiFeO_3$ filler to the polymer matrix (PVDF). Figure 12(a) indicates that as the volume percentage of $BiFeO_3$ increased, so did the piezoelectric constant. The sample with 60% BiFeO3 achieved the highest value of d33 of 31 pC/N.

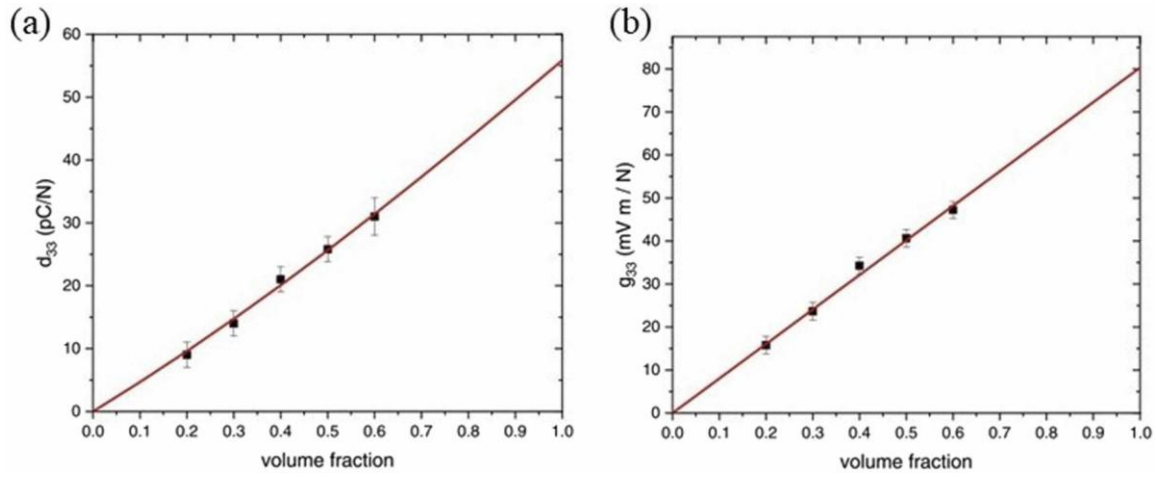

Figure 12: Effect of adding $BiFeO_3$ with different volume fractions on the PVDF (a) piezoelectric charge constant and (b) piezoelectric voltage constant (Reproduced with permission [215]).

The piezoelectric constant should climb practically linearly with increasing ceramic volume fraction because the PVDF dielectric constant (approximately 61 at room temperature) is quite comparable to that of $BiFeO_3$ (almost 85), as a result, the field distribution in the composite should be uniform. As the piezoelectric voltage constant (g33) is proportional to the piezoelectric constant (d33), the two coefficients should have the same variation function of

$BiFeO_3$ volume fraction (see Figure 12 (b)). Thus, the maximum value of g33 (47 mV m/N) was reached when adding 60% of $BiFeO_3$ to the PVDF material. Moreover, Li et al. [216] demonstrated that adding $(1 - x)Pb(Mg_{1/3}Nb_{2/3})O_3 - xPbTiO_3$ (PMN-PT) to the PVDF matrix improves its mechanical and dielectric properties. Four samples were performed with different PMN-PT fractions (0 wt%, 10 wt%, 20 wt%, 25 wt%). The tensile strength, yield strength, and Young's nanocomposites' modulus were found to be higher than those of pure PVDF. The samples with the highest Young's modulus of 1.71 GPa contain 20 wt% wt of PMN-PT. In an open circuit, the pure PVDF device also yields voltages ranging from 0.6 to 0.8 V. The highest output voltage of 10.3 V was also recorded in samples containing 20 wt% wt PMN-PT. However, the voltage output dropped to 6.3–6.7 V when PMN-PT content raised to 25 wt% because of the bad contact at the PMN-PT/PVDF interface.

In addition, Ca-Al with varying weight fractions was added by Shamitha et al. [217] in order to improve the PVDF performances and dielectric properties. The β-phase relative fraction of pure PVDF material was 45.45%. After adding 5% of Ca-Al, β-phase relative content reached 82.79%, as shown in Figure 13(a). Compared to Ca-Al, the addition of TPU does not greatly affect the PVDF piezoelectric properties. According to Shehata et al. [209], the β-phase relative content of pure PVDF was 79.06%. The β-phase relative fraction dropped when 5%, 10%, and 12.5% were added, as seen in Figure 13(b). With 15% of TPU, the β-phase content of the composite may exceed the β-phase content of pure PVDF by only 0.94%. Furthermore, when 17.5% of this filler was added, the β-phase content was reduced to 70.10%.

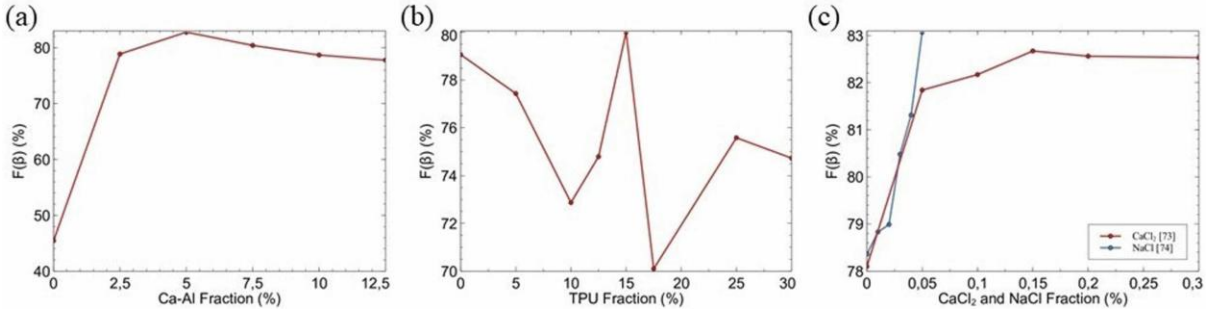

Figure 13: Effects of various additives on β-phase formation in PVDF : (a) Effect of adding Ca-Al with different weight fractions on the PVDF β-phase relative fraction [217], (b) Effect of adding TPU with different weight fractions on the PVDF β-phase relative fraction [220], and (c) Effect of adding $CaCl_2$ [218] and NaCl [219] with different weight fractions on the PVDF β-phase relative fraction.

Furthermore, Wang et al. [218] demonstrated that adding 0.05 wt% $CaCl_2$ to the PVDF and N-Methyl pyrrolidone (NMP) solvent raised the β-phase relative content from 78.10% to 81.84%. Figure 13(c) shows that adding 0.15 wt% $CaCl_2$ boosted the β-phase content to 82.67%. The

ion Ca^{2+} of the $CaCl_2$ filler in the (NMP) polar solvent contains two units of positive charge, which will attract two negatively charged F− in the PVDF segment. The ion-dipole interaction produced by the NMP polar solvent leads F atoms in the carbon chain to be deflected to the same side, resulting in an all-anti structure for the PVDF chain. While the addition of only 0.05 wt% NaCl raises the β-phase fraction from 78.36% to 83.07% [219], as seen in Figure 13(c). The reason for this is that the positive conductivity created by sodium chloride is attracted to the negatively charged F atom in the molecular chain. When it is positively induced in the direction of sodium chloride, F creates an ion-dipole interaction with Na+. This interaction shifts the F atom to one side, enabling PVDF's transition from the all-trans beta-phase. In 2019 Li et al. [221] proved that after adding 5% ZnO, the generator produces an open circuit voltage of around 85 V, which is approximately four times the voltage output of the pure PVDF generator. This is because when pure PVDF is exposed to mechanical stress via bending movements, only the piezoelectric β-phase of PVDF generates piezoelectric charges. When an external mechanical force is applied to the sample containing ZnO filler, however, additional piezoelectric charges are created because ZnO fillers function as nucleating agents, resulting in a more polar β-phase development in PVDF. Second, subjected to bending, ZnO may produce piezoelectric charges. Also, Liu et al. [197] used TiO_2 filler to enhance the piezoelectric generator performances. The results showed that after adding 0.5 wt% of TiO_2, the voltage output generated by the simple raised from 2.1 V to 3.5 V, and the current density increased by 160 nA/cm². Moreover, Ponnamma et al. [222] compared the effects of TiO_2, ZnO, and both TiO_2 and ZnO fillers. The sample made of pure PVDF material produced a voltage output of 1.9 V, according to the results. When TiO2 is added, the sample produces a voltage output of roughly 2 V; when ZnO is introduced, the voltage output reaches 5 volts. However, when both TiO_2 and ZnO are present, the piezoelectric generator produces an electric voltage of 14 V. The PVDF/CNT device also shows a higher piezoelectric output voltage than the pure PVDF film. The CNT inserted in the PVDF induces a local electric field resulting in spontaneous polarization in PVDF, which increases the piezoelectric characteristics of the device (d33=9.4 C/N) and leads to greater produced voltage output (12 V). Furthermore, Abzan et al. [223] demonstrated that GO may enhance the piezoelectricity of the PVDF polymer and its mechanical properties. When 0.5 wt% GO was added, the β-phase fraction rose from 64.5% to 77.4%. Increased GO concentration up to 3 wt% improved PVDF tensile modulus and strength from, respectively, 8.1±1.4 and 0.8±0.2 MPa to 17.0±3.7 and 1.4±0.4 MPa, as shown in Figure 14. To improve the mechanical characteristics of the PVDF material, varying percentages of Ba0.7St0.3TiO3 (BST) (25%, 30%, 35%, 40%, 45%, 50%) were added by Pan

et al. [224] to the PVDF matrix. The results revealed that the more BST ceramic powder used, the greater the fiber tensile strength and Young's modulus. As shown in Figure 15, PVDF material with 50% of BST filler had a maximum tensile strength of 74.92 MPa and a Young's coefficient of 3.74 GPa. Thus, the tensile strength and Young's modulus of PVDF fibers may be successfully increased by increasing the quantity of BST ceramic powder.

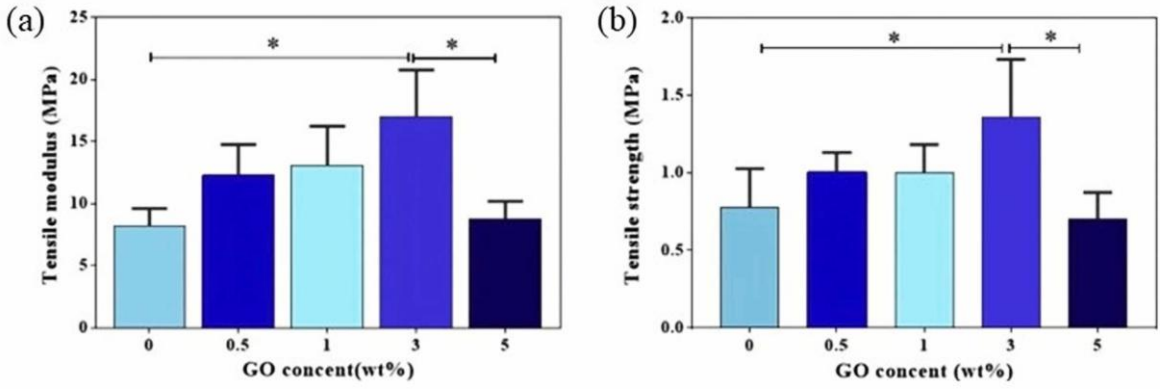

Figure 14: : Effect of adding GO with different weight fractions on the PVDF (a) tensile modulus and (b) tensile strength (Reproduced with permission [223]).

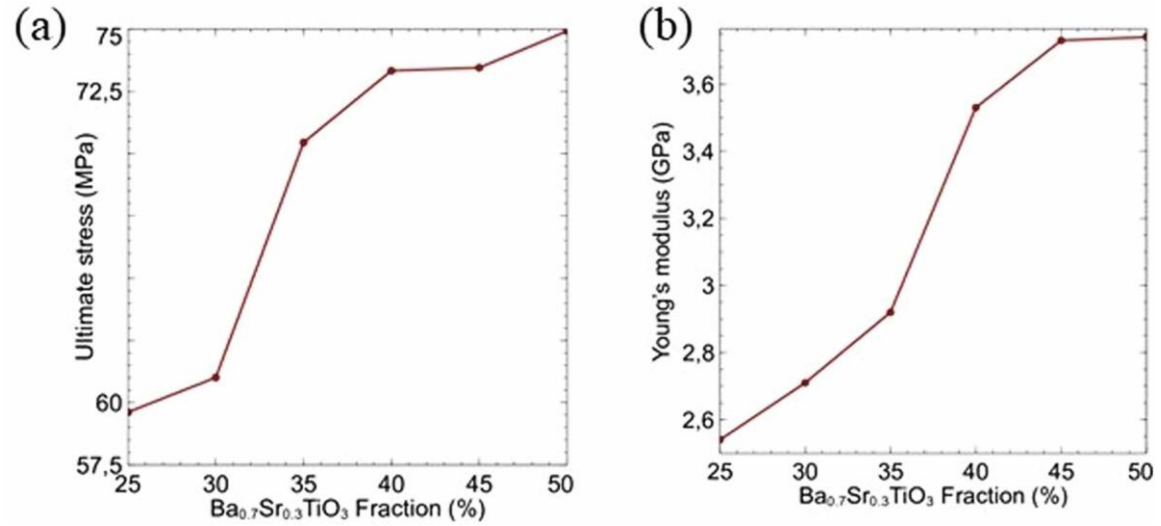

Figure 15: Effect of adding $Ba_{0.7}Sr_{0.3}TiO_3$ with different volume fractions on the PVDF (a) ultimate stress and (b) Young's modulus [224].

Table 3 summarizes the fillers employed in these studies, the ideal proportion added to the PVDF according to the authors, the dimensions of the samples and the findings in terms of voltage and current output, as well as d33 and g33 coefficients. Another way to develop highly efficient piezoelectric materials is to incorporate PVDF or its copolymer as a fiber into a piezoelectric ceramic material. In this way, the high flexibility of the polymer fibers and the excellent piezoelectric coefficient of the ceramic matrix can be explored in the same structure.

In this context, Hong et al. [225] fabricated a flexible, air-permeable, and high-performance PZT/P(VDF-TrFE) composite based on a template-assisted sol-gel method. The composite exhibited excellent piezoelectric properties (d33 of 190 pm V^{-1}), high output voltage (120 V), and high flexibility (Young's modulus of 0.35 GPa).

Table 3: Fillers used with PVDF matrix and their effects on PEHs performances.

Fillers	Fraction	Harvester dimensions (cm)	Results	Ref
Nanoclay	5 wt%	Length ≃ 2.8	Voutput =2.76 V	[211]
$MAPI_3$	25 v%	3.5 cm×3.5cm	Voutput =45.6 V	[214]
$Ba_{0.7}Sr_{0.3}TiO_3$	50 v%	2.2 cm×2.2cm	Voutput =1025 mV d_{33}=31 pC/N	[224]
$BiFeO_3$	60 v%	-	g33=47 mV m/N	[215]
PMN-PT	20 wt%	1.5 cm×1.5cm	Voutput = 10.3 V	[216]
BT	10 wt%	-	d_{33}=-6 pC/N	[207]
Ca-Al (LDH)	5 wt%	4.6 cm²	Voutput= 4.1 V	[217]
ZnO	5 wt%	3.5 cm×1.5cm	Voutput= 85 V d_{33}=9.4 pC/N	[221] [220]
CNT	20 wt%	-	Voutput=12 V	
TPU	15 v%	6 cm²	Voutput=3.7 V	[209]
BT	10 wt%	1 cm×1cm	Voutput=50 V	[206]
IL	10% wt	1 cm×1cm	d_{33}=27 pC/N	[226]
TiO_2 and ZnO	-	Diameter = 2	Voutput= 14 V	[222]
IL	10 wt%	Diameter= 2.4 Thickness=0.05	Voutput = 13 V	[227]
BNNS	<1.5 wt%	4 cm×1cm	Voutput between -0.9V and 0.7 V	[228]

Table 3: Fillers used with PVDF matrix and their effects on PEHs performances (suite).

Fillers	Fraction	Harvester dimensions (cm)	Results	Ref
TiO_2	0.5 wt%	1 cm²	d_{33}=16.4 pC/N Voutput= 3.5 V	[197]
BNNS	2 wt%	2 cm×1cm	d_{33}= 40 pC/N	[229]
GO	0.5 wt%	2 cm×1cm	Voutput = 1.78 V	[223]
BT	20 wt%	2.5 cm×2.5cm	Voutput = 11.69 V	[208]
BT	10 wt%	2.5 cm×0.5cm × 0.01cm	d_{31}=18 pC/N	[203]
BT	15 wt%	-	Voutput= 2.8 V d_{33}=0.101 pC/N	[204]
$CaCl_2$	0.15 wt%	2 cm×2cm	Ioutput = 0.0422 nA F(β)=82.67%	[218]
NaCl	0.05 wt%	2 cm ×2cm	d_{33}=-8.5 pC/N F(β)=83.07%	[219]
BT	50 wt%	4.2 cm×4.2cm × 0.8cm	Voutput= 20 V Ioutput = 1.1 μ A	[230]

2.4 3DP of PEHs

Using 3DP with multitudinous piezoelectric materials is a significant component of modern product development efforts in many industries, including automotive, biomedical, and robotic industries. The development of various 3DP processes has enabled product research teams to create effective PEHs directly from Computer-Aided Design (CAD) data, eliminating the need for expensive tools and fixtures. Fused deposition modelling (FDM) is the most often used 3DP method due to its low cost, multimaterial part creation capacity, and a wide variety of molding materials.

Below is a comparison between 3DP and traditional manufacturing methods, and a quick overview of 3DP procedures.

2.4.1 Comparison between additive manufacturing and traditional fabrication methods

Compared to traditional methods such as molding, additive manufacturing provides several advantages. The smooth transition from 3D CAD to additive manufacturing speeds up development. Because no molds are required, multiple versions may be made at no additional expense, and complicated forms can be manufactured without additional process steps. Furthermore, 3DP can reduce waste, lead time, and costs. When using soluble support material and adequate space between the parts, assembled parts with relative motion can be printed together. 3DP may also print multi-materials products [231] and also smart materials [232]. Multiple studies have compared the mechanical, piezoelectric, and thermal performances of parts created using these two manufacturing technologies. Kaynak and Varsavas [233] examined the performance of polylactide (PLA), its thermoplastic polyurethane elastomer (TPU), and its E-glass fiber (GF) reinforced composites when using traditional injection molding process versus 3DP. Photographic images and scanning electron microscope (SEM) were used to compare the fracture and surface morphologies. To compare the strength and elastic modulus values, tension tests and three-point bending flexural tests were performed. Differential scanning calorimetry (DSC) was used to compare the thermal behaviors. The results of this study are resumed in table 4.

Song et al. [205] created PVDF/BT composite samples with different BT fractions using both fabrication methods to compare the SLS and molding processes. Results showed that different processing methods resulted in varying K_b. SLS items have a substantially higher K_b than molded parts. The SLS treatment, which induces a partial melting of the powder, was indeed favourable to PVDF crystallization. As a result, SLS components might keep the powder crystal structure to a great extent. In contrast, the powder was totally melted during the molding process, destroying the crystal structure. Figure 16(a) shows that when 25 wt% BT was added to the PVDF, the molded pieces attained a maximum crystallinity of roughly 50 %. The crystallinity of the SLS portion was about 55% with the identical composite composition. Furthermore, because of the increased β-phase content, SLS parts' piezoelectric properties were greater than those of molded parts. As demonstrated in Figure 16 (b), all SLS parts with varied BT fractions had higher β-phase relative fractions than molded parts. This demonstrates the tremendous capabilities of SLS processing in preparing harvesters with high piezoelectric properties.

Table 4: Comparison of fractures and surfaces appearance, and mechanical and thermal properties of molded and 3D printed parts.

Materials	Surface morphology			Mechanical properties		Thermal properties	
	3DP	Molding	Interpretation	3DP & Molding	Interpretation	3DP & Molding	Interpretation
PLA PLA/TPU	Opaque	Transparent	3D printed PLA has much higher crystallinity than the molded one.	Same strength values. Elastic modulus of the 3DP parts is higher. Both fracture toughness values (K_{IC} and G_{IC}) of 3D printed samples are more beneficial.	A stiffening action and additional toughening mechanism of 'crack deflection' of the textured structure was formed during ± 45 raster angle orientation.	Same transition temperatures (Glass transition (T_g), T_c and T_m). Differences in the enthalpies ΔHm and ΔHc, led to higher crystallinity for the 3D printed samples.	Cooling rate over 3DP is rather lower than the cooling rate during molding, so there is more time for macromolecular PLA chains to crystallize during 3DP.
PLA/GF PLA/TPU /GF	GF reinforcements oriented to the fracture plane with +45° and -45°.	GF reinforcements perpendicular to the fracture plan.	During 3D printing, the equipment scans the specimen with ±45°. During injection, molding pressure is applied parallel to the longitudinal direction of the test specimens.				

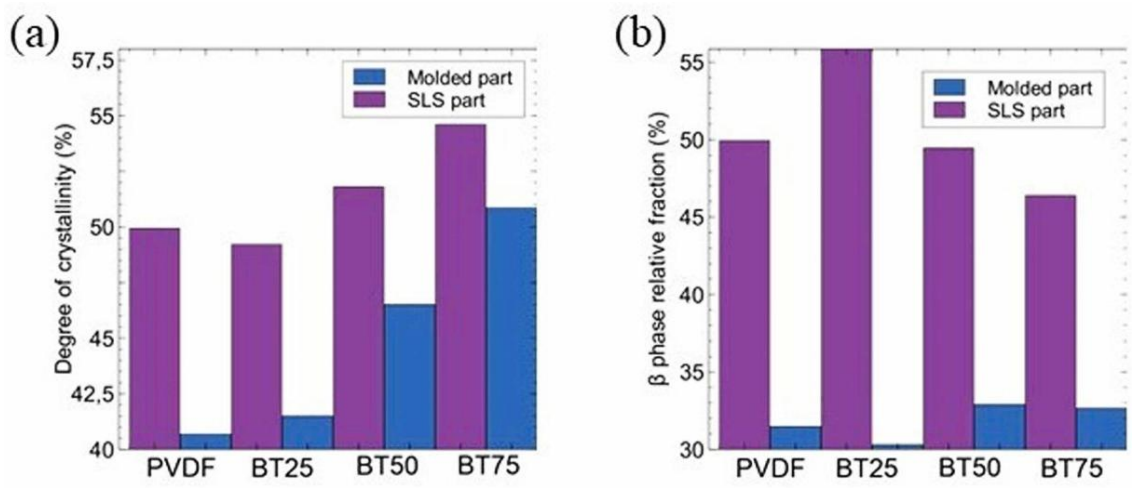

Figure 16: Comparison between molded part and SLS part properties ((a) crystallinity, (b) β-phase relative fraction) (Reproduced with permission [205]).

2.4.2 3DP technologies for PEH

3DP techniques are classified into seven categories: material extrusion (direct writing (DIW) and fused deposition modelling (FDM)); vat photopolymerization (stereolithography (SLA)); powder bed fusion (selective laser sintering (SLS) and direct metal laser sintering); material jetting (inkjet printing (IJP)); sheet lamination (laminated object manufacturing (LOM)); directed energy deposition and binder jetting.

The most common 3DP methods used to fabricate PEHs are: Inkjet printing (IJP) [234, 235], which has mostly been used for printing electronics because of its ability to print complex patterns with high resolution and a wide range of materials. Polymer jetting and binder jetting are two key processes of IJP. In the former, the inkjet print head deposits photosensitive polymer onto the substrate, which is then cured by a light source. In the instance of binder jetting, the binder is selectively ejected onto a powder bed to produce a cross-section of the item.

Direct ink writing (DIW) [236-238] uses direct material deposition and works by extruding a paste-like ink with a shear-thinning characteristic. The inks must have a high enough yield stress and storage modulus to allow for form preservation of extruded lines and distortion-free bridging of spanning filaments. This method enables the computer-aided construction of successive layers.

Selective laser sintering (SLS) is also often used [239-243]; It includes the use of a high-power laser to fuse small particles of plastic powders into a mass with a desired three-dimensional

form. The laser selectively fuses powdered material on the surface of a powder bed by scanning cross-sections created from a 3-D digital description of the component (for example, from a CAD file or scan data). After scanning each cross-section, the powder bed is lowered by one layer thickness, a second layer of material is put on top, and the selective laser sintering process is repeated until the item is done.

Stereolithography (SLA), also used for manufacturing PEHs [244-247], is a 3DP technique that uses light to solidify photocurable resin. The original SLA technique involves scanning a tiny laser spot over a photocurable resin with a focussed beam or light, which causes photopolymerization and, consequently, solidification. The SLA technology may make incredibly tiny structures by enhancing the focus of the laser source. Last but not least,

Fused deposition modeling (FDM) [248-256], is a 3DP process that deposits filament-shaped thermoplastic materials that have been heated to their glass transit state to build 3D objects layer by layer. When the material is extruded from a brass nozzle and rests on the platform, it solidifies to form a cross-section of the items formed. The advantages and disadvantages of techniques and the material utilized for each are described in Table 5. Table 6 summarizes current research in which 3DP technologies were applied to create PEHs from various materials. The findings shown in the table show excellent piezoelectric material properties and excellent nanogenerator performances, particularly when the device is manufactured using the FDM process. This is owing to the FDM's shearing force, which aids the directed arrangement of the dipoles, resulting in a printed PVDF device with self-polarization properties even without poling

Table 5: Materials, advantages, and disadvantages of the most commonly used 3DP technologies to fabricate PEHs.

3DP	Material	Advantages	Disadvantages	Ref
FDM	Thermoplastic (acrylonitrile butadiene, styrene (ABS), polylactic acid (PLA) polycarbonate (PC) polyamide (PA)) glass; metal	Multi-material structures, low-cost materials, and equipment (for thermoplastic material), high porosity, variable mechanical strength.	high cost for glass and metal materials, narrow printable materials range	[257-260]

Table 5: Materials, advantages, and disadvantages of the most commonly used 3DP technologies to fabricate PEHs (suite).

3DP	Material	Advantages	Disadvantages	Ref
SLA	Photosensitive resin	High precision, simple sand rapid fabrication, ability of producing complicated structures with great features details, wide variety of applications.	Single material limited cationic photopolymerization resins, high-cost technology, support materials should be removed.	[257, 260, 261]
SLS	Thermoplastic, metal	No need for support material, strong and precise parts, self-sustaining process, lower cost materials if used in large volume.	Limited mechanical properties, high cost, messy powders, Inhalation risk, rough surface and required elaborate post-processing (for metals)	[257-259]
IJP	Gel, ceramics, composites, papers, plastic substrates conductive polymers, carbon-based nanoparticle, metals, protein materials.	High-resolution structure, wide range of materials.	low areal capacity, lack structural diversities, specific requirements for the printable ink.	[260, 262, 263]
DIW	Plastic, ceramics, Living cells, composites, gels, polymers, metals, nanomaterials (graphene 2D MXene, perovskite, organic frameworks…).	Versatility, low cost, strong design ability, easy operation, wide range of materials, diversity structures, high printing resolution, complex multi-scale architectures.	Require post processing, necessity of preparing printing inks with high rheological qualities to make printing work smoothly.	[257, 260, 262, 263]

Table 6: Most used 3DP technologies to fabricate PEHs.

Material	Fillers	3DP technology	F(β) (%)	d_{33}/d_{31} (PC/N)	Voutput	Ioutput	Ref
PVDF	IL (15 wt%)	FDM	98.3	-	4.2 V	17.5 nA/cm²	[248]
PVDF	BT (10 wt%)	DIW	78	-	4 V	-	[203]
PVDF	GR (0.03 wt%)	DIW	61.52	d_{33}=-8.7	0.35 V	-	[236]
PVDF	TrFE (30 wt%)	DIW	75-80	-	298.3 mV	-	[237]
PLZT	Epoxy	DIW	-	d_{33}= 347 d_{31}=-123	-	-	[238]
PVDF	BT (10 wt%) /CNT (0.3%)	SLS+ Sc-CO_2	79.5	d_{33}= 2.6	19.3 V	415 nA	[264]
PVDF	GP (1.5 wt%)	SLS	-	-	16.97 V	274 nA	[240]
PVDF	BT/Ag	SLS	-	-	10 V	142 nA	[241]
PVDF	BT /carbon	SLS	92.2	-	5.7 V	79.8 nA	[242]
PVDF	IL (15 wt%)	FDM	93.3	-	8.69 V	90.8 nA	[249]
PVDF	BT_2 (10 wt%) /IL	FDM	95.9	-	10.9 V	126.9 nA	[250]
PVDF	BT (30 wt%)	FDM	84.9	d_{33}=4.2	11.5 V	220 nA	[251]
PVDF	IL (10 wt%)	FDM	86.72	-	13 V	0.27 μA/cm²	[227]
PVDF	BT (20 wt%)	SLS + Sc-CO_2	80.6	-	20.9 V	0.371 μA/cm²	[243]
PVDF	IL (15 %wt)	FDM	97.4	-	8.2 V	300 nA	[252]
PVDF	No fillers	FDM	56.83	d_{31}=0.048	-	0.106 nA	[253]
PVDF	IL (2 wt%)	FDM	90	-	6 V	83 nA	[254]
PVDF	TPPC (5 wt%)	FDM	83.8	d_{33}=-1.85	6.62 V	108.15 nA/cm²	[255]
BT	PVDF (9 wt%)	FDM	68.1	d_{33}=0.021	-	0.15 nA	[256]

2.4.3 Multi-Material 3DP Processes

The majority of 3D printed PEHs are made up of a variety of materials. Multi-material 3DP allows for the simultaneous application of many functions to 3D structures with complex features, appearances, and characteristics (mechanical [265], electrical [266], chemical [267], and thermal [268]) at a single build station. When compared to traditional manufacturing procedures, the construction of 3D printed structures employing multi-material offers various benefits. This method can reduce manufacturing time without increasing the expense of morphological complexity. Although there are many commercially accessible 3D printers today, only a few of them can produce 3D products created of heterogeneous materials. FDM is a good example of a multi-material 3D printer since it can employ several materials [269]. Moreover, FDM fabricates multi-material PEHs with excellent piezoelectric properties. Taking the example of the PVDF/BT2 nanocomposite proposed by Liu et al. [250]; FDM ensures the horizontal arrangement of the BT2 nanorods in the PVDF matrix enabling the harvester to generate the maximum of electrical energy due to the unidirectional piezoelectricity of BT2. Figure 17 (a) depicts a scanning electron microscope (SEM) image of the surface of PVDF/BT2 composites made without FDM fabrication method. The BT2 nanorods are visibly disordered organised, and there is a partial aggregation phenomenon in the PVDF matrix. The small-angle X-ray scattering analysis (SAXS) was carried out to examine further the properties of BT2 nanorods in the casted PVDF/BT2 composite. The SEM images of the surface and cross-section of the sample after FDM printing, as shown in Figure 17(b) and Figure 17(c), respectively, visibly reveal that the BT2 particles are organized horizontally in the PVDF matrix without agglomeration. Furthermore, BT2 nanorods and PVDF interface are completely bound, with no gaps or tiny holes. As illustrated in Figure 17(d), the sample has a typical isotropic diffuse ring comparable to pure PVDF (Figure 17(f)), showing that BT2 nanorods are randomly scattered in PVDF. Furthermore, in contrast to the casted film, the SAXS analysis result (Figure 17(e)) shows that the FDM-printed PVDF/BT2 sample has two obvious sharp peaks at 170° and 350° on the I-Φ graph, indicating that the BT2 nanorods are arranged in an organized orientation along the printing direction, which approves well with the SEM results. Thus, the shearing and stretching forces produced by the FDM printing technique successfully align BT2 nanorods in the PVDF matrix along the extrusion direction, which enhances the piezoelectric properties and the performances of the multi-material harvester. FDM-based process is very popular due to easy and low-cost maintenance and a wide range of customizable materials. Furthermore, instead of solid filaments, liquid/paste materials, polymer melts, and

molten materials have been employed with a pressured syringe in a variety of applications. One advantage of these low-cost machines is that they allow the use of bespoke materials with desired attributes, such as electrical conductivity and mechanical strength.

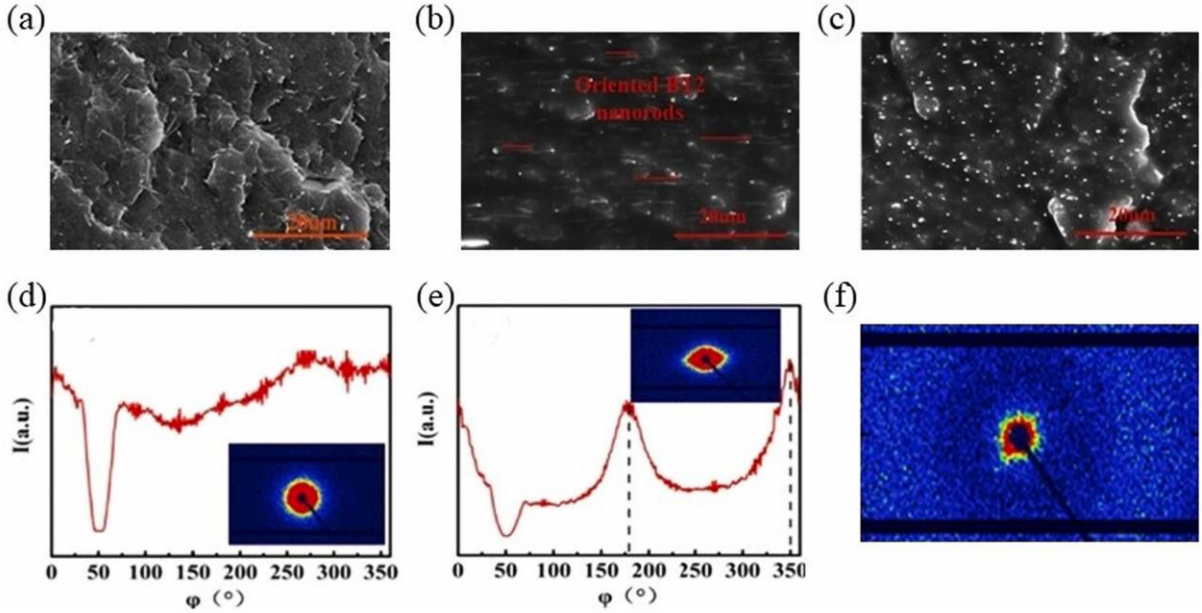

Figure 17: Microstructure and SAXS analysis of PVDF/BT composites fabricated by casting and FDM : (a) SEM image of the surface of the casted PVDF/BT2 composite, SEM image of (b) the surface and (c) the section of the FDM printed PVDF/BT2; (d) SAXS analysis of the casted PVDF/BT2 composite, (e) SAXS results of the FDM printed PVDF/BT2 composite, and (f) SAXS analysis of the pure PVDF (Reproduced with permission [250].

2.5 Applications

Recent improvements in energy harvesting have been accelerated due to the rising demand for portable or wireless devices and systems with long life spans for a wide range of possible applications. Piezoelectric energy harvesting devices have been carefully developed to gather ambient energy and support the sensor as an independent module or in conjunction with the electronics to increase its lifetime. This section shows some preliminary experiments and applications for PEHs, such as harvesting energy from human activities to power wearable devices, harvesting vibration energy from automobiles to power self-powered wireless sensors, harvesting vibration energy from muscle vibration to power health monitoring devices, and harvesting vibration energy from human motion to power robots' actuators.

2.5.1 Wearable products

Because battery life is often short for improved performance of electronic devices, with the fast de- velopment of low-power portable electronics and wearable sensors, batteries cannot qualify

as an effective power source. As a result, energy harvesting is promoted as an alternative to traditional batteries. Previous studies have identified it as a viable method of harvesting energy from the human body motion [270-272] , particularly the foot, which may provide significant mechanical energy. In this context, a PEH based on a polydopamine (PAD)@ BT /PVDF nanocomposite was fabricated by Yang et al. [273] and inserted into a smart shoe. The PEH generates output voltages of 1 V, 6.5 V, and 3.8 V during walking (Figure 18(a)), jumping (Figure 18(b)) and running (Figure 18(c)), respectively. Moreover, under an impact force of 12 N, the peak-to-peak voltages reached 9.3 V for 17 wt% PDA@BTO/PVDF with a fast response time of 61 ms.

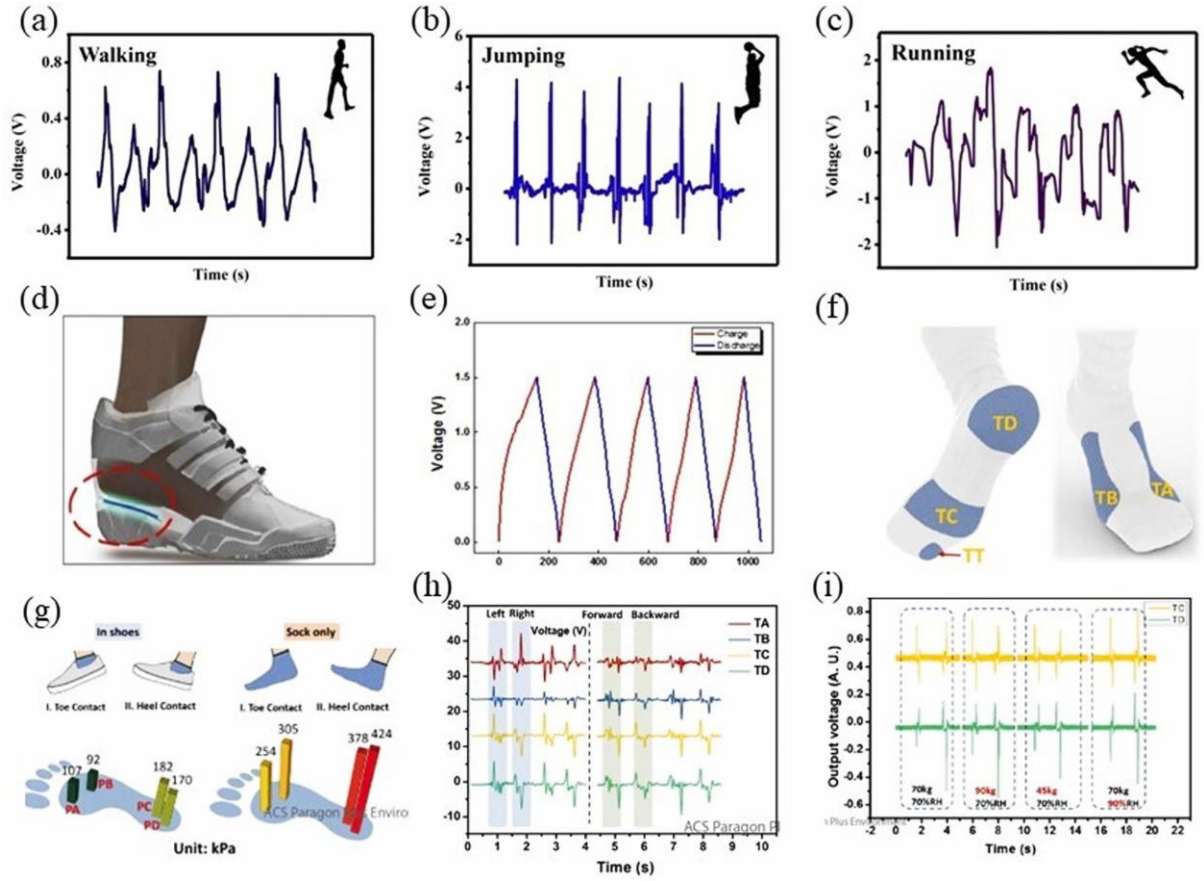

Figure 18: Performance of smart footwear integrating PEH nanocomposites under different user conditions : (a) Power generated by the PEH with 17 wt% PAD@ BT /PVDF PEH nanocomposite from walking, (b) jumping, (c) running (Reproduced with permission [273]), (d) schematic representation of the smart shoes, (e) Cyclic charging/discharging sequence of the capacitor used during human walking for the PEH with the 15 wt% BT-P(VDF-TrFE) nanocomposite; placed inside the shoe under the heel (Reproduced with permission [274]), (f) Schematic representation of the coating areas of the sock, (g) Pressure deduced from the voltage output with and without shoes at toe and heel contact, (h) Voltage output from four coated areas under walking in different directions, and (i) Test of the smart sock under different user weight (45 kg, 70 kg, and 90 kg) and humidity (70% RH and 90% RH) (Reproduced with permission [275]).

Additionally, Siddiqui et al. [274] introduce a PEH made of P(VDF- TrFE) and piezoelectric BT nanoparticles. The PEH, which is inserted inside a shoe under the heel during walking, as shown in Figure 18(d), generates an output voltage of 25 V at a walking frequency of 0.6 Hz with high mechanical resistance under high loads (600 N). The output voltage was rectified and stored in a capacitor. The time required by the PEH for one charging cycle was 120 seconds, as shown in Figure 18(e); this corresponds to walking 72 steps. Moreover, the same device can charge the capacitor several times. To create a self-powered and self-functional sock that can perform a variety of functions, including energy harvesting and sensing diverse physiological signals, Zhu et al. [275] integrated PZT and poly(3, 4-ethylenedioxythiophene) polystyrene sulfonate (PEDOT:PSS) in different areas of a sock called TA, TB, TC, TD and TT (Figure 18(f)). The sock was tested in a variety of situations, including with or without shoes, toe or heel contact (Figure 18(g)), during jumping or walking, in different walking directions (left, right, forward, backward) (Figure 18(h)), with different load resistances, in different humidity conditions and user's weight (Figure 18(i)). During light jumping at 2 Hz and a load resistance of 59.7 M, the smart sock showed an output power of 1.71 mW.

2.5.2 Automotive industry applications

Monitoring devices, such as wheel pressure sensors, are becoming required for automobiles to improve road user safety. Vibration energy harvesters, which transform mechanical energy in the environment into electrical power, are a viable alternative to electrochemical batteries for powering vehicle monitoring systems [276-278]. These harvesters avoid the possible replacement expenses associated with batteries.

Rui et al. [279] created a PEH, which converts the mechanical energy of the wheel rotation into electric energy to power low-power electronics (Temperature sensor, pressure sensor, deformation sensor, torque sensor...) in intelligent vehicle wheels to develop a wireless self-powered system, as shown in Figure 19(a). The harvester is inserted in the spokes and is known as the intelligent wheel-spoke PEH (IWSPEH). The IWSPEH serves as a technical foundation for creating smart wheels, giving continuous power to sensors on the wheels. Sensors may be placed into the wheels without the use of wires, thanks to energy harvesting technology. This smart wheel can achieve a range of motion parameters to assure vehicle safety, particularly for self-driving vehicles in the future.

IWSPEH consists of a piezoelectric beam collector, which is placed into the spokes of the intelligent wheel. When the car is moving, the cantilever beam spins synchronously around the

wheel's axis, and the free end moves up and down due to gravity, as explained in Figure 19(b). The cantilever beam's resonant frequency may be modified with vehicle speed thanks to the centrifugal force design, resulting in a wide-band harvester. To validate this study, a prototype was tested on a real road, as depicted in Figure 19(c), and the findings revealed that the effective power could reach 0.61–6.28 mW in the 40–120 kph range. The study's findings have several significant implications for the future practice of intelligent vehicle wheels.

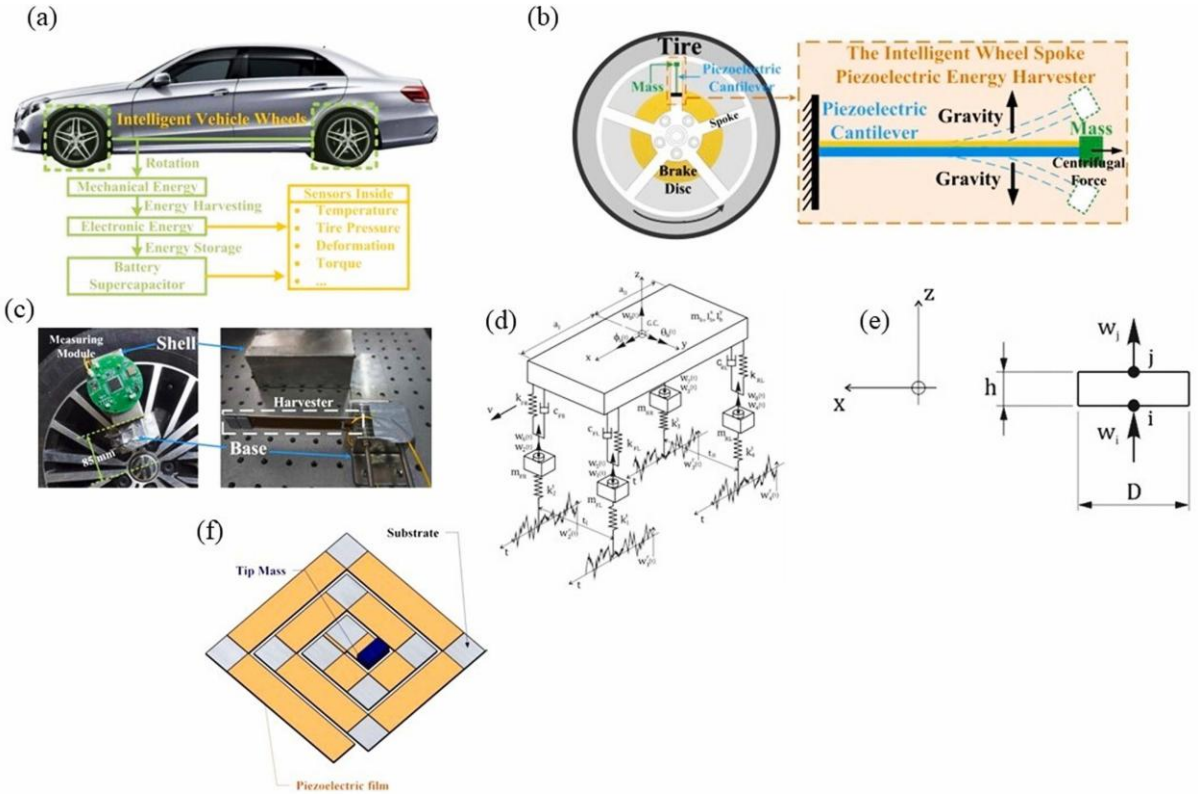

Figure 19: Schematics and tests of an intelligent wheel-integrated piezoelectric harvester : (a) Schematic diagram of the operation and concept of the intelligent wheel, (b) Schematic diagram of the proposed IWSPEH, (c) Experiments on the road to measure harvester output in motion (Reproduced with permission [279]), (d) The 19-DOF car and piezoelectric model for estimating the energy harvesting, (e) The finite element model of the PEH (Reproduced with permission [280]), and (f) schematic of the Oso (Reproduced with permission [281]).

In addition, Morangueira and Pereira [280] created a linear finite element of a piezoelectric disc incorporated into the spring damper assembly of a 19-degree-of-freedom car dynamic model to power on-board electronic devices such as sensors by recovering mechanical energy wasted.

Using five different piezoelectric materials (BaTiO3, PbTiO3, PbZrTiO3, PZT-5A, and PZT-5H), the elec- tromechanical performance of the car-PEH system was evaluated applying mathematical models and nu- merical simulations. Figure 19(d) depicts a schematic illustration

of this mathematical model, which includes a stiff body supported by a suspension system with four wheels, to each one a piezoelectric material is attached. As shown in Figure 19(e), the PEH finite element model is represented as a disc of diameter D and thickness h. There is a mechanical load and an electrical load on each node, which are connected to mechanical and electrical displacements, respectively. The results achieved with this coupled car and piezoelectric model in terms of electric power and energy density are shown in Table 7. Results show that PZT is the piezoelectric material with the greatest potential for automotive applications in embedded electronic systems.

Table 7: Electric power and electric energy density generated by different piezoelectric materials used in this work [280].

	$BaTiO_3$	$PbTiO_3$	Pb $(ZrTi)O_3$	PZT-5A	PZT-5H
RMS electric power [mW]	1.3	2.1	7.2	9.8	11.3
Peak electric power [mW]	3.95	6.29	25.64	44.72	32.99
RMS electric energy density [mJ/cm^3]	0.1279	0.2235	1.0116	1.5986	1.7382
Peak electric energy density [mJ/cm^3]	0.476	0.810	4.497	8.888	6.291

Thus, this work presents a robust procedure to estimate the energy recovery from unnecessary vibrations of vehicle suspensions by using piezoelectric materials.

Moreover, PEHs are also used to improve freight train operating security [282-284]. Lopes et al. [281] employed Vibrational Energy Harvesting (VEH) Orthogonal Spiral (OSo) Piezoelectric Multibeam to power sensors that measure forces in large freight-loaded and unloaded trains, particularly in carriages positioned far away from the main locomotive, to help the driver in identifying potential malfunctions, to avoid accidents and derailments.

An optimization method targeted at optimizing output power as well as safety factors has been developed in this study. This optimization algorithm is based on four solutions: the $\max(f_1(X))$ and $\max(f_2(X))$ solutions, which correspond to the maximum generated power for the loaded and unloaded stages, respectively, the $\max(f_3(X))$ solution, which represents the configuration with the highest safety coefficient, and the $\max(Ft(X))$ solution, which is the best trade-off among the optimization criteria, based on their fitness function. This optimization approach revealed the safety parameters for the aluminum structures and the PZT's fragile ceramic, with

a tip mass, guaranteeing that they do not shatter when subjected to high amplitude vibrations over time. The suggested OSo structure with the aluminum substrate, the PZT, and the tip mass is depicted in Figure 19(f). An analytical study conducted in this work revealed that the best configuration for an aluminum structure and a PZT ceramic results in an overall safety factor of 1.51 and generates up to 2,73 mW (charged) and 16 mW (discharged), which would be sufficient to supply many low power sensors.

2.5.3 Healthcare applications

Implantable medical devices are a type of electronic technology that has a growing influence on improving quality of life by monitoring or replacing sensory functions. The concept of employing an implanted medical device to help patients dates back to the 1950s, when the introduction of transistors enabled the development of entirely implantable pacemakers. As a result, numerous technologies such as the retinal electric stimulation system, deep brain stimulation system, and hearing aid system have been created (Figure 20).

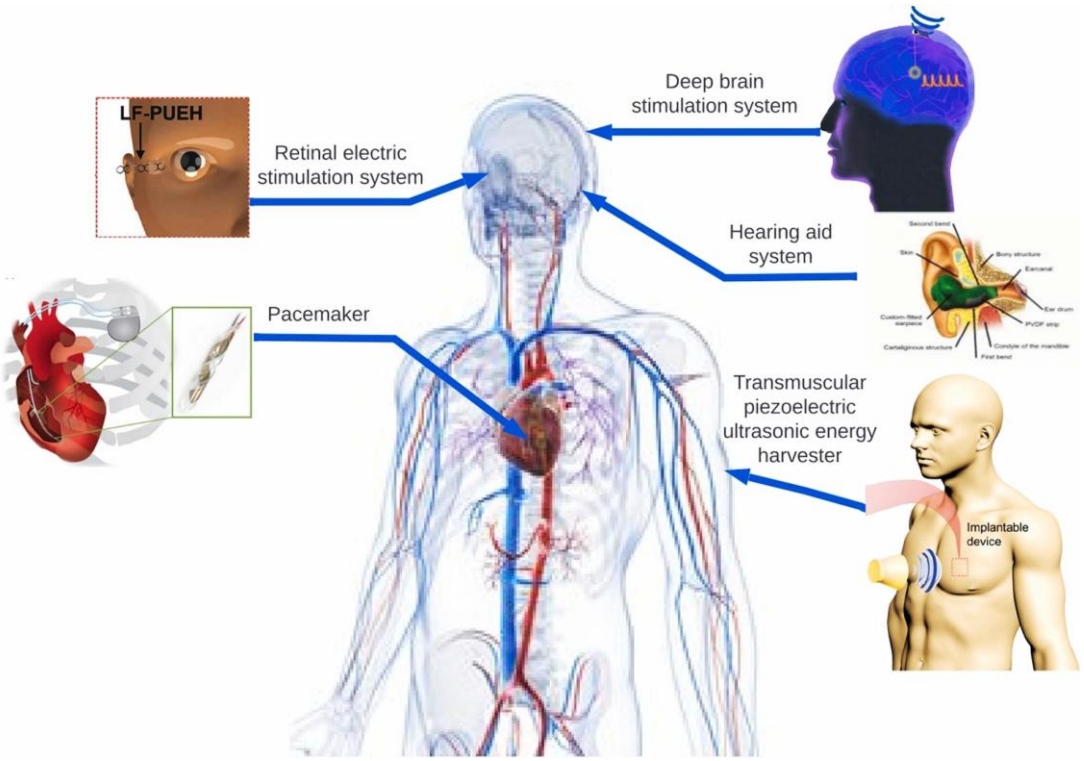

Figure 20: Some PEH applications in the healthcare sector (Retinal electric stimulation [285], pacemaker [286], deep brain stimulation [287], hearing aids [288], and transmuscular piezoelectric ultrasonic energy harvester [289]).

Because of its short lifespan, cost and impact on the environment, battery is unsuitable for implanted devices. Furthermore, batteries necessitate a new surgical procedure for replacement

or must be recharged via a wireless device. The concept of recovering energy from the environment using piezoelectric materials has been introduced to address these difficulties.

2.5.3.1 Pacemaker

Heart disorders continue to be the primary cause of mortality worldwide; despite continual advancements in treatment options, invasive operations generate challenges for patients both during surgery and recovery. Recognizing the difficulties that cardiovascular patients face, as well as the present techniques and technologies for treatment, it is evident that one of the most significant restrictions is the limited battery life of pacemakers.

Traditional pacemakers use a fully charged, nonrechargeable battery to deliver electric signals to the heart. Researchers have developed a new pacemaker called Flex-Pacer to overcome this problem. FlexPacer is a revolutionary device that employs a piezoelectric crystal that is triggered by the heart's muscular action [290]. As seen in Figure 21(a), heart's mechanical energy can be transformed into electrical energy and stored in the capacitor within the microprocessor, avoiding re-surgeries due to battery replacement.

To optimize the voltage output provided by the piezoelectric material to power the pacemaker, Anand and Kundu [291] suggested a PEH with a spiral structure. The proposed PEH structure yields 3.2 V peak output open circuit voltage at 45.8 Hz resonant frequency and 1g excitation acceleration. At the same time, Xu et al. [292] suggested incorporating ZnO and multiwall carbon nanotubes into microporous P(VDF-TrFE) films to boost energy production. The combining ratios of 30% ZnO and 0.1% MWCNTs produced a voltage of 3.22±0.24 V. Moreover, Azimi et al. [293] demonstrated that by adding only 0.1 wt% of ZnO/rGO (90/10) to PVDF nanofibers, the harvester could collect mechanical energy from local impacts and create open circuit voltage and short circuit current of 1.39±0.31 V and 0.90±0.15 A, respectively, with each heartbeat. To evaluate the performances of the PEH, in-vivo experiments were performed by Dong et al. [294] in female Sprague Dawley (SD) rats weighing between 170 and 180 g and aged 6 to 7 weeks (Figure 21(b)). In addition, Xie et al. [286] used standard pacemaker lead insertion procedures to introduce the device through a vascular sheath and progress it into the right ventricle of a porcine heart under fluoroscopic supervision (Figure 21 (c)).

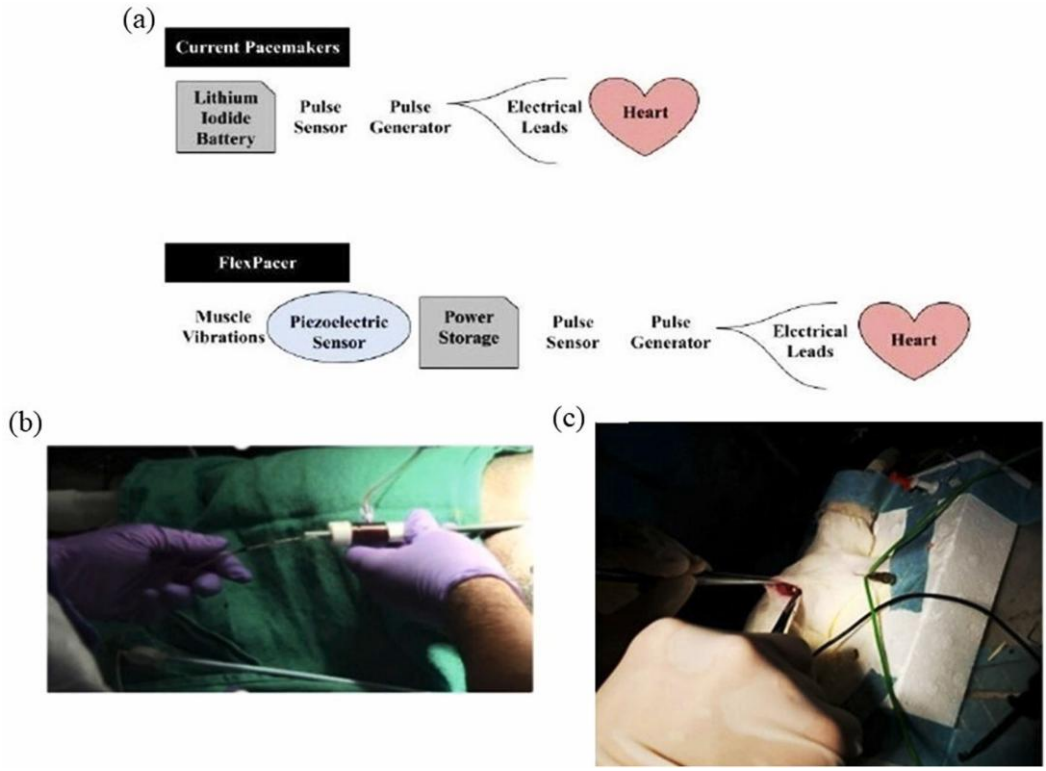

Figure 21: In vivo testing of piezoelectric energy harvesters in animals : (a) Working principle of current pacemakers vs. FlexPacer (Reproduced with permission [290]), (b) In vivo test of the piezoelectric vibration energy harvester in female SD rats (Reproduced with permission [294]), and (c) In vivo test of the piezoelectric vibration energy harvester in porcine (Reproduced with permission [286]).

2.5.3.2 Retinal electrical stimulation system

Humans' eyes are undoubtedly their most essential sense organ. Retinal degenerative illnesses, such as neurodegenerative disorders and age-related macular degeneration, would result in photoreceptor loss and substantial vision losses for those affected [295]. A novel retinal electrical stimulation approach for persons with neurodegenerative disorders was also developed using piezoelectric materials. This stimulation has proved to be effective for direct neuron activation to restore eyesight. To accomplish this, Jiang et al. [285] developed ultrasonic-driven wireless energy harvesting technology to transform acoustic energy into electricity using the piezoelectric effect. The piezoelectric ultrasonic energy collector can be implanted in the eyeballs to detect and convert ultrasonic impulses delivered from a few centimetres distant. Figure 22 shows the working principle of the ultrasonic wireless energy harvesting system.

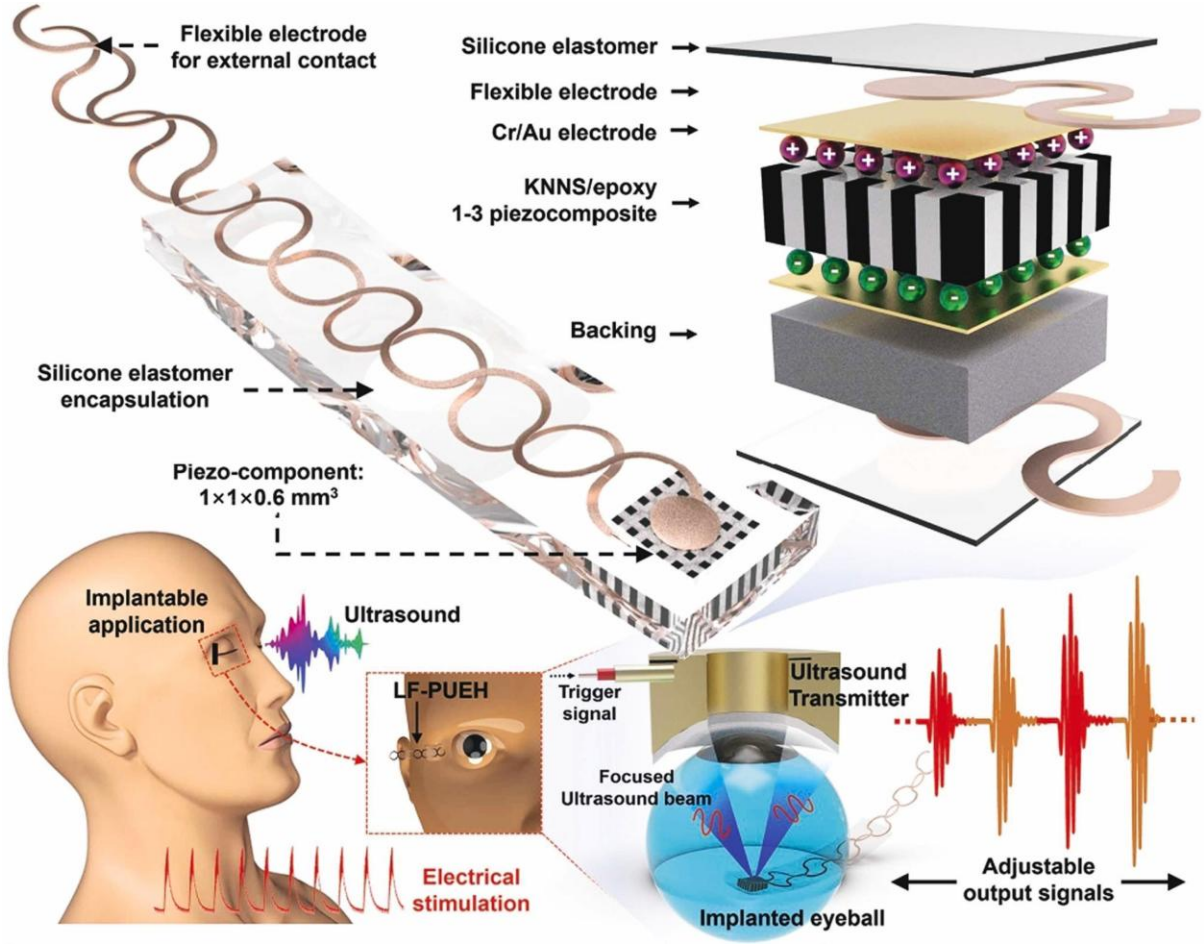

Figure 22: Working principle of ultrasonic wireless energy harvesting system. Reproduced with permission [285].

2.5.3.3 Deep brain-stimulation system

Deep brain stimulation is a neurosurgery operation that uses electric pulses to stimulate a specific brain region. It is a useful therapy for various neurologic and psychiatric problems [296]. However, because of its high operation power, the implanted brain stimulator requires repeated procedures to replace the battery every 3 to 5 years, resulting in a very limited lifespan. Invasive medical treatments for battery replacement provide a risk of inflammation as well as a cost burden to patients. A potential solution to this energy problem is to include a self-powered piezoelectric energy source based on ultrasonic energy harvesting into an implanted deep brain stimulation device to deliver electric energy forever.

Wireless power supply is a complex technological challenge that is critical for implanted biomedical devices. Zhang et al. [287] developed a novel implanted piezoelectric ultrasonic energy harvesting device that is especially relevant for deep brain stimulation in order to cure disorders such as Parkinson's disease, essential tremor, dystonia, pain, and so on. The piezoelectric energy device may be implanted into the head and convert ultrasonic energy into

electrical energy, that is transmitted to the brain, activating the periaqueductal grey brain region instantaneously.

2.5.3.4 Hearing aid system

According to the World Health Organization, hundreds of millions of people suffer from various forms of hearing impairment, with tens of millions of hearing aids in use today [297]. Hearing aids and other in-ear gadgets, such as digital earplugs, smart hearing protectors, and Bluetooth communication earpieces, often use little power and have stringent size constraints. They have been significantly updated in recent years and are becoming less energy use. Energy harvesting technologies are gaining popularity as an alternative to batteries for in-ear gadgets since they are often suited for low-power portable devices. Mangaiyarkarasi et al. [288] designed PEH able to power the Ear-Canal Bending sensor when excited by the ear canal deformation caused by temporomandibular joint (jaw joint) activity, also known as "ear canal dynamic motion" [298]. After performing parameter optimization, the harvester produced voltage, current and power of about 480V, 0.24mA and 6mW, respectively, Which is sufficient to supply the Ear canal bending sensor.

2.5.3.5 Transmuscular piezoelectric ultrasonic energy harvester

Inspired by natural wood structures, Hong et al. [289] have fabricated a transmuscular wood-templated piezoelectric ultrasonic energy harvester (W-PUEH) from ceramic-polymer composites to power implantable medical devices.

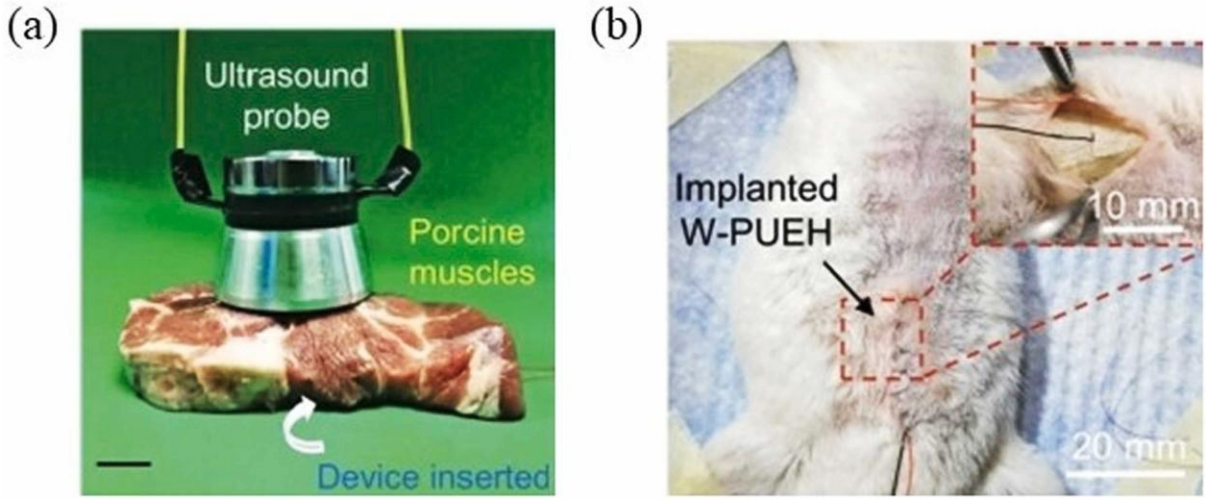

Figure 23: (a) Ex-vivo and (b) In-vivo tests of the transmuscular piezoelectric ultrasonic energy harvester in a porcine muscle and an anesthetized mouse, respectively (Reproduced with permission [289]).

Ex-vivo and in-vivo tests were conducted to evaluate the performance of the W-PUEH. In ex vivo characterization, the W-PUEH was inserted into a porcine muscle at various depths from 5 to 18.5 mm and excited with ultrasound probes (Figure 23). The power generated at 10 mm depth was 81.8 µW. In in vivo characterization, when the W-PUEH was implanted under an anesthetized mouse's skin (1 mm), the electrical power generated was 100 µW. These results indicate that the W-PUEH can provide sufficient energy to power implantable medical devices. (E.g., 1-10 µW for pacemakers).

4.3 Robotic applications

Almost every facet of developing a microrobot that works in a blood artery presents significant obstacles. It is essential to construct an effective small device to gather energy from the environment or to receive energy sent wirelessly, especially when the microrobot is operating in vivo. Liu et al. [299] created a PEH to power a microrobot in a human artery.

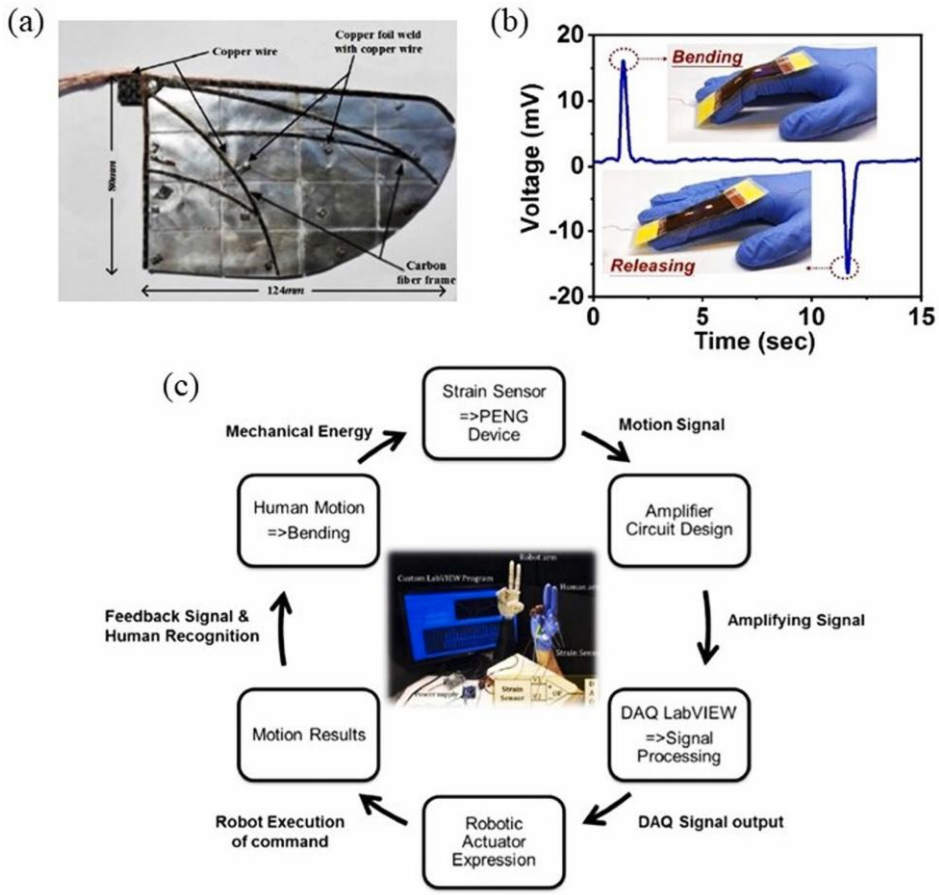

Figure 24: Some PEH applications in robotics : (a) Piezoelectric wing composed of PVDF and carbon fiber frame (Reproduced with permission [300]), (b) Piezoelectric energy harvesting device attached to a human finger to detect the mechanical energy caused by the finger's movement (Reproduced with permission [301]) and (c) Experimental setup and system design (Reproduced with permission [301]).

The energy harvesting system in this study employs a PVDF cantilever framework to capture kinetic energy delivered wirelessly from outside the human body, such as an ultrasonic wave. Piezoelectric materials may also be used to create new piezoelectric wings that can power microelectronic devices like LED lights for flapping wing micro aircraft. This wing might create electric energy as a result of its deformation. Flapping wings were conceived and built by Liu et al. [300] using the vein network and membrane form of fruit flies. Aside from being light and sturdy, the wing airfoil should be able to tolerate high flapping frequency without breaking.

As a result, the wings in this study were made of carbon fiber frame vein and PVDF membrane, as indicated in Figure 24(a). Furthermore, Yang et al. [301] demonstrated that PEH devices may also be employed as a synchronous human-robot interface driving unit for a sophisticated smart sign language system. The flexible PEH, attached to Human fingers, creates signals when fingers bend and stretch as seen in Figure 24(b). The output signals created by the PEH, may be used to drive a robotic hand through a succession of signal creation, processing, and recognition steps simultaneously (Figure 24(c)). These studies will soon pave the way for developing sensing technologies and human-machine interfaces.

2.6 Conclusions

In this work, recent advances in 3D-printed PEH technology were investigated. A comparison was made between piezoelectric materials based on their mechanical, dielectric, and piezoelectric properties. Various methods to improve the piezoelectric properties of PVDF were reported (stretching, poling, addition of fillers), allowing effective mechanical-electrical energy conversion. The stretching and poling parameters, as well as the amount of added fillers, can have a significant impact on the PEH's performance. Numerous research papers have investigated the effects of poling and stretching with different parameters on the piezoelectric and mechanical properties of PVDF. Two types of poling processes have been reported in the literature: Contact poling and corona poling. In addition, two stretching strategies have been used in previous works: uniaxial stretching and biaxial stretching. The 3DP technologies, which enable piezoelectric energy harvesting devices' fast and easy production, have effectively displaced traditional manufacturing methods. To demonstrate the advantages of 3D printing, some previous studies have compared the piezoelectric, mechanical, morphological, and thermal properties of 3D printed parts and molded parts. PEHs are manufactured using five 3DP processes (IJP, DIW, SLS, SLA, and FDM). FDM may be the best option for 3D-printed

multi-material structures, especially for PVDF-based nanocomposite structures. The shear effect of the FDM nozzle promotes the formation of β crystals in PVDF. In addition, the 3D printed PVDF-based nanocomposite parts using FDM technology exhibit an ordered distribution of nanorods in the PVDF matrix compared to those produced by conventional methods, resulting in excellent dielectric properties of the nanocomposite. Although its applications target various fields, including wearable products, health, robotics, and automotive, piezoelectric energy harvesting devices in micro-robotics are still limited. Moreover, most of the applications reported in the literature have been performed with piezoelectric energy harvesting devices produced by conventional manufacturing processes.

2.7 Futur direction

Up to now, there are few practical applications for 3D-printed vibration-based energy harvesting systems in micro-robotics. Most reports have only used models for guidance. Three factors limit the applications of vibration-based PEHs in this field:

First, PEHs must have excellent mechanical properties to avoid breaking under vibration. Therefore, the development of flexible and robust piezoelectric materials is required. However, rigid materials such as piezoelectric ceramics made up most piezoelectric materials. On the other hand, PVDF and its copolymers have received much attention and have become a research focus due to their excellent flexibility. However, although 3DP technologies, especially FDM, can improve the piezoelectric properties of PVDF due to the shear force that supports the directional arrangement of dipoles, the mechanical properties of 3D-printed PEHs remain modest (i.e., high Young's modulus). Therefore, solutions need to be sought to improve the mechanical properties of 3D printed piezoelectric materials, e.g., by developing an algorithm to optimise the input parameters of the printer.

Second, the performance of piezoelectric energy harvesting devices must be improved to be sufficient for micro-robot operation. This requires the development of new piezoelectric materials with a high piezoelectric coefficient. As mentioned earlier, the piezoelectric coefficient of PVDF is somewhat weak. Therefore, developing new piezoelectric materials by combining PVDF with other fillers will usher in a new era of PEHs. If the additional fillers are properly selected, they can improve the mechanical and piezoelectric properties of PVDF. Other methods to enhance PVDF performance include poling and stretching with optimized input settings. However, most previous experiments provided modest output voltages using

stretched and poled PVDF-based piezoelectric energy harvesting devices. Therefore, new techniques are needed to improve the piezoelectric properties of PVDF.

Third, microrobots usually require complex structures with fine features. Therefore, conventional manufacturing methods cannot meet the demand. On the other hand, 3DP technology enables the fabrication of structures with complex shapes without requiring additional steps in the manufacturing process. Although the evolution from conventional manufacturing technologies to 3DP is a trend nowadays, only a few articles compare the two manufacturing methods in PEH fabrication. Therefore, for future work, it is recommended that comparisons be made between 3D printed and traditionally manufactured piezoelectric devices with different piezoelectric materials, fillers, and printing conditions (temperature, speed, etc.).

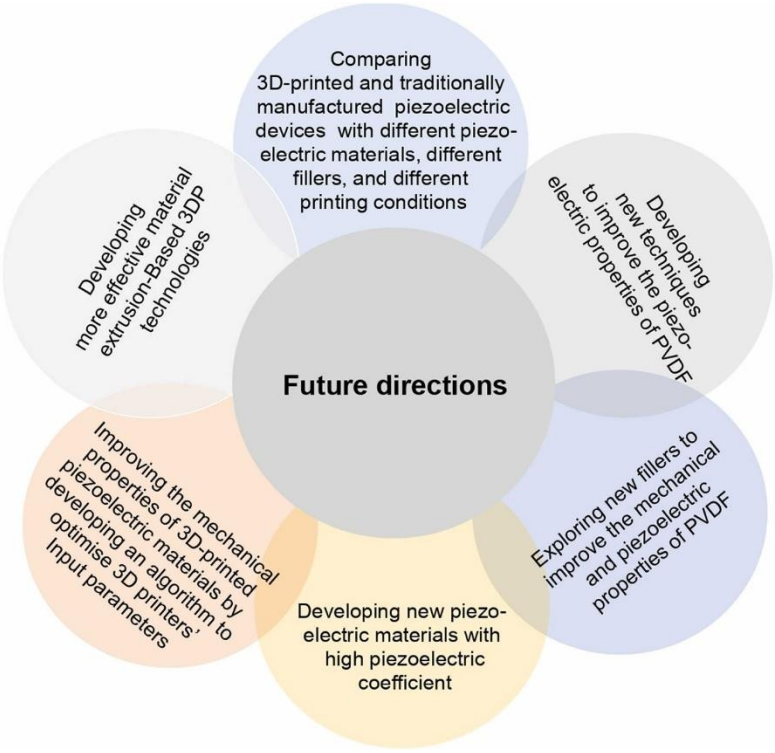

Figure 25: Prospects for future developments of 3D-printed piezoelectric materials for microrobotics applications.

In addition, few 3DP technologies can print PVDF-based materials. FDM is the best choice for such applications, although it is sometimes difficult to print such materials when a high percentage of fillers is used or when the filament section is not smooth and uniform. Therefore, the development of more effective material extrusion-based 3DP technologies is needed. In order to direct the development of these techniques toward the goal of advanced microrobots,

it is crucial to consider all of the issues discussed and find ways to overcome the challenges, as described in Figure 25.

2.8 Achnowlegdment

The authors acknowledge the funding provided by the Natural Sciences and Engineering Research Council (NSERC) of Canada in the form of Discovery Grants (grant number: CRSNG – RGPIN -2021-02846) and various equipment grants.

2.9 References

[1] S. Chalasani, J.M. Conrad, A survey of energy harvesting sources for embedded systems, IEEE SoutheastCon 2008, IEEE, 2008, pp. 442-447.

[2] M. Guan, W. Liao, On the efficiencies of piezoelectric energy harvesting circuits towards storage device voltages, Smart Materials and Structures 16(2) (2007) 498.

[3] H.A. Sodano, G. Park, D. Inman, Estimation of electric charge output for piezoelectric energy harvesting, Strain 40(2) (2004) 49-58.

[4] H.A. Sodano, D.J. Inman, G. Park, A review of power harvesting from vibration using piezoelectric materials, Shock and Vibration Digest 36(3) (2004) 197-206.

[5] S. Li, J. Yuan, H. Lipson, Ambient wind energy harvesting using cross-flow fluttering, Journal of applied physics 109(2) (2011).

[6] M.A. Weimer, T.S. Paing, R.A. Zane, Remote area wind energy harvesting for low-power autonomous sensors, 2006 37th IEEE Power Electronics Specialists Conference, IEEE, 2006, pp. 1-5.

[7] S. Li, H. Lipson, Vertical-stalk flapping-leaf generator for wind energy harvesting, Smart materials, adaptive structures and intelligent systems, 2009, pp. 611-619.

[8] Z. Abdin, M.A. Alim, R. Saidur, M.R. Islam, W. Rashmi, S. Mekhilef, A. Wadi, Solar energy harvesting with the application of nanotechnology, Renewable and sustainable energy reviews 26 (2013) 837-852.

[9] V. Raghunathan, A. Kansal, J. Hsu, J. Friedman, M. Srivastava, Design considerations for solar energy harvesting wireless embedded systems, IPSN 2005. Fourth International Symposium on Information Processing in Sensor Networks, 2005., IEEE, 2005, pp. 457-462.

[10] E.-J. Yoon, C.-G. Yu, Power management circuits for self-powered systems based on micro-scale solar energy harvesting, International Journal of Electronics 103(3) (2016) 516-529.

[11] D. Dondi, A. Bertacchini, L. Larcher, P. Pavan, D. Brunelli, L. Benini, A solar energy harvesting circuit for low power applications, 2008 IEEE International Conference on Sustainable Energy Technologies, IEEE, 2008, pp. 945-949.

[12] E.H.H. Al-Qadami, Z. Mustaffa, M.E. Al-Atroush, Evaluation of the pavement geothermal energy harvesting technologies towards sustainability and renewable energy, Energies 15(3) (2022) 1201.

[13] P.A. Østergaard, H. Lund, A renewable energy system in Frederikshavn using low-temperature geothermal energy for district heating, Applied Energy 88(2) (2011) 479-487.

[14] W.E. Glassley, Geothermal energy: renewable energy and the environment, CRC press2014.

[15] K. Wang, B. Yuan, G. Ji, X. Wu, A comprehensive review of geothermal energy extraction and utilization in oilfields, Journal of Petroleum Science and Engineering 168 (2018) 465-477.

[16] D. Jiang, M. Xu, M. Dong, F. Guo, X. Liu, G. Chen, Z.L. Wang, Water-solid triboelectric nanogenerators: An alternative means for harvesting hydropower, Renewable and Sustainable Energy Reviews 115 (2019) 109366.

[17] D.L. Vu, C.D. Le, K.K. Ahn, Functionalized graphene oxide/polyvinylidene fluoride composite membrane acting as a triboelectric layer for hydropower energy harvesting, International Journal of Energy Research 46(7) (2022) 9549-9559.

[18] J. Maas, C. Graf, Dielectric elastomers for hydro power harvesting, Smart Materials and Structures 21(6) (2012) 064006.

[19] S. Pobering, N. Schwesinger, A novel hydropower harvesting device, 2004 International Conference on MEMS, NANO and Smart Systems (ICMENS'04), IEEE, 2004, pp. 480-485.

[20] D. Abbas, D. Current, M. Phillips, R. Rossman, H. Hoganson, K.N. Brooks, Guidelines for harvesting forest biomass for energy: A synthesis of environmental considerations, Biomass and Bioenergy 35(11) (2011) 4538-4546.

[21] R. Singh, A.D. Setiawan, Biomass energy policies and strategies: Harvesting potential in India and Indonesia, Renewable and Sustainable Energy Reviews 22 (2013) 332-345.

[22] C.-H. Ko, S. Chaiprapat, L.-H. Kim, P. Hadi, S.-C. Hsu, S.-Y. Leu, Carbon sequestration potential via energy harvesting from agricultural biomass residues in Mekong River basin, Southeast Asia, Renewable and Sustainable Energy Reviews 68 (2017) 1051-1062.

[23] C.B. Field, J.E. Campbell, D.B. Lobell, Biomass energy: the scale of the potential resource, Trends in ecology & evolution 23(2) (2008) 65-72.

[24] A. Erturk, J. Hoffmann, D.J. Inman, A piezomagnetoelastic structure for broadband vibration energy harvesting, Applied Physics Letters 94(25) (2009).

[25] S.P. Beeby, R.N. Torah, M.J. Tudor, P. Glynne-Jones, T. O'Donnell, C.R. Saha, S. Roy, A micro electromagnetic generator for vibration energy harvesting, Journal of Micromechanics and microengineering 17(7) (2007) 1257.

[26] L. Zuo, X. Tang, Large-scale vibration energy harvesting, Journal of intelligent material systems and structures 24(11) (2013) 1405-1430.

[27] L. Gammaitoni, I. Neri, H. Vocca, Nonlinear oscillators for vibration energy harvesting, Applied Physics Letters 94(16) (2009).

[28] V.R. Challa, M.G. Prasad, Y. Shi, F.T. Fisher, A vibration energy harvesting device with bidirectional resonance frequency tunability, Smart Materials and Structures 17(1) (2008) 015035.

[29] L. Mateu, F. Moll, Review of energy harvesting techniques and applications for microelectronics, VLSI Circuits and Systems II, SPIE, 2005, pp. 359-373.

[30] P. Basset, D. Galayko, F. Cottone, R. Guillemet, E. Blokhina, F. Marty, T. Bourouina, Electrostatic vibration energy harvester with combined effect of electrical nonlinearities and mechanical impact, Journal of Micromechanics and Microengineering 24(3) (2014) 035001.

[31] P. Podder, A. Amann, S. Roy, Combined effect of bistability and mechanical impact on the performance of a nonlinear electromagnetic vibration energy harvester, IEEE/ASME Transactions On Mechatronics 21(2) (2015) 727-739.

[32] D. Cao, W. Xia, W. Hu, Low-frequency and broadband vibration energy harvester driven by mechanical impact based on layer-separated piezoelectric beam, Applied Mathematics and Mechanics 40(12) (2019) 1777-1790.

[33] G. Shi, D. Tong, Y. Xia, S. Jia, J. Chang, Q. Li, X. Wang, H. Xia, Y. Ye, A piezoelectric vibration energy harvester for multi-directional and ultra-low frequency waves with magnetic coupling driven by rotating balls, Applied Energy 310 (2022) 118511.

[34] Y. Hu, J. Yang, Q. Jing, S. Niu, W. Wu, Z.L. Wang, Triboelectric nanogenerator built on suspended 3D spiral structure as vibration and positioning sensor and wave energy harvester, ACS nano 7(11) (2013) 10424-10432.

[35] N.V. Viet, X. Xie, K.M. Liew, N. Banthia, Q. Wang, Energy harvesting from ocean waves by a floating energy harvester, Energy 112 (2016) 1219-1226.

[36] C.H. Wong, Z. Dahari, Development of vibration-based piezoelectric raindrop energy harvesting system, Journal of Electronic Materials 46 (2017) 1869-1882.

[37] L.E. Helseth, Harvesting electrical energy from water drops falling on a vibrating cantilever, Smart Materials and Structures 31(3) (2022) 035031.

[38] R. Guigon, J.-J. Chaillout, T. Jager, G. Despesse, Harvesting raindrop energy: experimental study, Smart Materials and Structures 17(1) (2008) 015039.

[39] X. Jiang, Y. Li, J. Li, J. Wang, J. Yao, Piezoelectric energy harvesting from traffic-induced pavement vibrations, Journal of Renewable and Sustainable Energy 6(4) (2014).

[40] D.B. Ashebo, C.A. Tan, J. Wang, G. Li, Feasibility of energy harvesting for powering wireless sensors in transportation infrastructure applications, Nondestructive Characterization for Composite Materials, Aerospace Engineering, Civil Infrastructure, and Homeland Security 2008, SPIE, 2008, pp. 265-272.

[41] Y. Pan, T. Lin, F. Qian, C. Liu, J. Yu, J. Zuo, L. Zuo, Modeling and field-test of a compact electromagnetic energy harvester for railroad transportation, Applied Energy 247 (2019) 309-321.

[42] X. Xie, Q. Wang, Energy harvesting from a vehicle suspension system, Energy 86 (2015) 385-392.

[43] C. Saha, T. O'donnell, N. Wang, P. McCloskey, Electromagnetic generator for harvesting energy from human motion, Sensors and Actuators A: Physical 147(1) (2008) 248-253.

[44] I. Izadgoshasb, Y.Y. Lim, N. Lake, L. Tang, R.V. Padilla, T. Kashiwao, Optimizing orientation of piezoelectric cantilever beam for harvesting energy from human walking, Energy conversion and management 161 (2018) 66-73.

[45] M. Renaud, P. Fiorini, R. van Schaijk, C. Van Hoof, Harvesting energy from the motion of human limbs: the design and analysis of an impact-based piezoelectric generator, Smart Materials and Structures 18(3) (2009) 035001.

[46] K. Xia, Z. Zhu, H. Zhang, C. Du, Z. Xu, R. Wang, Painting a high-output triboelectric nanogenerator on paper for harvesting energy from human body motion, Nano Energy 50 (2018) 571-580.

[47] M.V. Tholl, A. Haeberlin, B. Meier, S. Shaheen, L. Bereuter, B. Becsek, H. Tanner, T. Niederhauser, A. Zurbuchen, An intracardiac flow based electromagnetic energy harvesting mechanism for cardiac pacing, IEEE transactions on biomedical engineering 66(2) (2018) 530-538.

[48] A. Nanda, M.A. Karami, Energy harvesting from arterial blood pressure for embedded brain sensing, International Design Engineering Technical Conferences and Computers and Information in Engineering Conference, American Society of Mechanical Engineers, 2016, p. V003T11A015.

[49] H. Ouyang, Z. Liu, N. Li, B. Shi, Y. Zou, F. Xie, Y. Ma, Z. Li, H. Li, Q. Zheng, Symbiotic cardiac pacemaker, Nature communications 10(1) (2019) 1821.

[50] M. Ansari, M.A. Karami, Modeling and experimental verification of a fan-folded vibration energy harvester for leadless pacemakers, Journal of Applied Physics 119(9) (2016).

[51] M. Amin Karami, D.J. Inman, Powering pacemakers from heartbeat vibrations using linear and nonlinear energy harvesters, Applied Physics Letters 100(4) (2012).

[52] Q. Zheng, B. Shi, F. Fan, X. Wang, L. Yan, W. Yuan, S. Wang, H. Liu, Z. Li, Z.L. Wang, In vivo powering of pacemaker by breathing-driven implanted triboelectric nanogenerator, Advanced materials 26(33) (2014) 5851-5856.

[53] S. Wang, Y. Jiang, H. Tai, B. Liu, Z. Duan, Z. Yuan, H. Pan, G. Xie, X. Du, Y. Su, An integrated flexible self-powered wearable respiration sensor, Nano Energy 63 (2019) 103829.

[54] A. Panahi, A. Hassanzadeh, A. Moulavi, Design of a low cost, double triangle, piezoelectric sensor for respiratory monitoring applications, Sensing and Bio-Sensing Research 30 (2020) 100378.

[55] M.P. Mahmud, S.R. Bazaz, S. Dabiri, A.A. Mehrizi, M. Asadnia, M.E. Warkiani, Z.L. Wang, Advances in mems and microfluidics-based energy harvesting technologies, Advanced Materials Technologies 7(7) (2022) 2101347.

[56] S.P. Beeby, T. O'Donnell, Electromagnetic energy harvesting, Energy Harvesting Technologies (2009) 129-161.

[57] W. Shen, S. Zhu, Harvesting energy via electromagnetic damper: Application to bridge stay cables, Journal of Intelligent Material Systems and Structures 26(1) (2015) 3-19.

[58] Y.-J. Wang, C.-D. Chen, C.-K. Sung, System design of a weighted-pendulum-type electromagnetic generator for harvesting energy from a rotating wheel, IEEE/ASME Transactions on Mechatronics 18(2) (2012) 754-763.

[59] X. Zhao, J. Cai, Y. Guo, C. Li, J. Wang, H. Zheng, Modeling and experimental investigation of an AA-sized electromagnetic generator for harvesting energy from human motion, Smart Materials and Structures 27(8) (2018) 085008.

[60] H. Liu, Y. Qian, C. Lee, A multi-frequency vibration-based MEMS electromagnetic energy harvesting device, Sensors and Actuators A: Physical 204 (2013) 37-43.

[61] Y. Zhang, T. Wang, A. Luo, Y. Hu, X. Li, F. Wang, Micro electrostatic energy harvester with both broad bandwidth and high normalized power density, Applied energy 212 (2018) 362-371.

[62] X. Guo, Y. Zhang, K. Fan, C. Lee, F. Wang, A comprehensive study of non-linear air damping and "pull-in" effects on the electrostatic energy harvesters, Energy conversion and management 203 (2020) 112264.

[63] D. Liu, X. Yin, H. Guo, L. Zhou, X. Li, C. Zhang, J. Wang, Z.L. Wang, A constant current triboelectric nanogenerator arising from electrostatic breakdown, Science advances 5(4) (2019) eaav6437.

[64] Y. Naito, K. Uenishi, Electrostatic MEMS vibration energy harvesters inside of tire treads, Sensors 19(4) (2019) 890.

[65] B. Vysotskyi, D. Aubry, P. Gaucher, X. Le Roux, F. Parrain, E. Lefeuvre, Nonlinear electrostatic energy harvester using compensational springs in gravity field, Journal of Micromechanics and Microengineering 28(7) (2018) 074004.

[66] B. Shi, Z. Li, Y. Fan, Implantable energy-harvesting devices, Advanced Materials 30(44) (2018) 1801511.

[67] H. Liang, G. Hao, O.Z. Olszewski, A review on vibration-based piezoelectric energy harvesting from the aspect of compliant mechanisms, Sensors and Actuators A: Physical 331 (2021) 112743.

[68] H. Shao, G. Chen, H. He, Elastic wave localization and energy harvesting defined by piezoelectric patches on phononic crystal waveguide, Physics Letters A 403 (2021) 127366.

[69] Z. Liu, L. Wang, X. Yu, J. Zhang, R. Yang, X. Zhang, Y. Ji, M. Wu, L. Deng, L. Li, Piezoelectric-effect-enhanced full-spectrum photoelectrocatalysis in p–n heterojunction, Advanced Functional Materials 29(41) (2019) 1807279.

[70] A. Rahman, O. Farrok, M.R. Islam, W. Xu, Recent progress in electrical generators for oceanic wave energy conversion, IEEE Access 8 (2020) 138595-138615.

[71] D.K. Khatua, S.-J. Kim, Perspective on the development of high performance flexible piezoelectric energy harvesters, Journal of Materials Chemistry C 10(8) (2022) 2905-2924.

[72] K. Kapat, Q.T. Shubhra, M. Zhou, S. Leeuwenburgh, Piezoelectric nano-biomaterials for biomedicine and tissue regeneration, Advanced Functional Materials 30(44) (2020) 1909045.

[73] K.K. Sappati, S. Bhadra, Flexible piezoelectric 0–3 PZT-PDMS thin film for tactile sensing, IEEE Sensors Journal 20(9) (2020) 4610-4617.

[74] T.P. Comyn, P.I. Cowin, T. Stevenson, High strength piezoelectric materials for extreme environments, 2021 IEEE Sensors, IEEE, 2021, pp. 1-4.

[75] A. Anand, D. Meena, M. Bhatnagar, Synthesis and characterization of flexible PVDF/Bi2Al4O9/RGO based piezoelectric materials for nanogenerator application, Journal of Alloys and Compounds 843 (2020) 156019.

[76] T. Vijayakanth, D.J. Liptrot, E. Gazit, R. Boomishankar, C.R. Bowen, Recent advances in organic and organic–inorganic hybrid materials for piezoelectric mechanical energy harvesting, Advanced Functional Materials 32(17) (2022) 2109492.

[77] C. Zhang, W. Fan, S. Wang, Q. Wang, Y. Zhang, K. Dong, Recent progress of wearable piezoelectric nanogenerators, ACS Applied Electronic Materials 3(6) (2021) 2449-2467.

[78] Z. Yin, B. Tian, Q. Zhu, C. Duan, Characterization and application of PVDF and its copolymer films prepared by spin-coating and Langmuir–Blodgett method, Polymers 11(12) (2019) 2033.

[79] Z. He, F. Rault, M. Lewandowski, E. Mohsenzadeh, F. Salaün, Electrospun PVDF nanofibers for piezoelectric applications: A review of the influence of electrospinning parameters on the β phase and crystallinity enhancement, Polymers 13(2) (2021) 174.

[80] M.S.A. Salem, A.H. El-Shazly, M.R. El-Marghany, M.N. Sabry, N. Nady, Effect of adding functionalized graphene on the performance of PVDF membrane in direct contact membrane distillation, Key Engineering Materials 801 (2019) 337-342.

[81] A. Ahmad, U. Farooqui, N. Hamid, Effect of graphene oxide (GO) on Poly (vinylidene fluoride-hexafluoropropylene)(PVDF-HFP) polymer electrolyte membrane, Polymer 142 (2018) 330-336.

[82] F. Ram, P. Kaviraj, R. Pramanik, A. Krishnan, K. Shanmuganathan, A. Arockiarajan, PVDF/BaTiO3 films with nanocellulose impregnation: Investigation of structural, morphological and mechanical properties, Journal of Alloys and Compounds 823 (2020) 153701.

[83] J. Zhou, W. Zhou, D. Cao, C. Zhang, W. Peng, T. Yao, J. Zuo, J. Cai, Y. Li, PVDF reinforced with core–shell structured Mo@ MoO3 fillers: effects of semi-conductor MoO3 interlayer on dielectric properties of composites, Journal of Polymer Research 29(3) (2022) 72.

[84] S. Kalani, R. Kohandani, R. Bagherzadeh, Flexible electrospun PVDF–BaTiO 3 hybrid structure pressure sensor with enhanced efficiency, RSC advances 10(58) (2020) 35090-35098.

[85] S. Mirjalali, A. Mahdavi Varposhti, S. Abrishami, R. Bagherzadeh, M. Asadnia, S. Huang, S. Peng, C.H. Wang, S. Wu, A review on wearable electrospun polymeric piezoelectric sensors and energy harvesters, Macromolecular Materials and Engineering 308(1) (2023) 2200442.

[86] A.S.M.I. Uddin, D. Lee, C. Cho, B. Kim, Impact of multi-walled CNT incorporation on dielectric properties of PVDF-BaTiO3 nanocomposites and their energy harvesting possibilities, Coatings 12(1) (2022) 77.

[87] L. Wu, Z. Jin, Y. Liu, H. Ning, X. Liu, Alamusi, N. Hu, Recent advances in the preparation of PVDF-based piezoelectric materials, Nanotechnology Reviews 11(1) (2022) 1386-1407.

[88] P. Fakhri, B. Amini, R. Bagherzadeh, M. Kashfi, M. Latifi, N. Yavari, S.A. Kani, L. Kong, Flexible hybrid structure piezoelectric nanogenerator based on ZnO nanorod/PVDF nanofibers with improved output, RSC advances 9(18) (2019) 10117-10123.

[89] W. Feng, Y. Chen, W. Wang, D. Yu, A waterproof and breathable textile pressure sensor with high sensitivity based on PVDF/ZnO hierarchical structure, Colloids and Surfaces A: Physicochemical and Engineering Aspects 633 (2022) 127890.

[90] H. Elahi, K. Munir, M. Eugeni, M. Abrar, A. Khan, A. Arshad, P. Gaudenzi, A review on applications of piezoelectric materials in aerospace industry, Integrated Ferroelectrics 211(1) (2020) 25-44.

[91] F.C. Bolat, S. Basaran, S. Sivrioglu, Piezoelectric and electromagnetic hybrid energy harvesting with low-frequency vibrations of an aerodynamic profile under the air effect, Mechanical Systems and Signal Processing 133 (2019) 106246.

[92] H. Elahi, The investigation on structural health monitoring of aerospace structures via piezoelectric aeroelastic energy harvesting, Microsystem Technologies 27(7) (2021) 2605-2613.

[93] M. Akbar, A.R. Firdaus, S. Wibowo, N. Wirawan, Piezoelectric energy harvesting from a fixed-wing unmanned aerial vehicle, 2019 2nd International Conference on Applied Engineering (ICAE), IEEE, 2019, pp. 1-4.

[94] J. Wang, T. He, C. Lee, Development of neural interfaces and energy harvesters towards self-powered implantable systems for healthcare monitoring and rehabilitation purposes, Nano Energy 65 (2019) 104039.

[95] M. Wu, K. Yao, D. Li, X. Huang, Y. Liu, L. Wang, E. Song, J. Yu, X. Yu, Self-powered skin electronics for energy harvesting and healthcare monitoring, Materials Today Energy 21 (2021) 100786.

[96] Y. Huang, P. Yang, Z. Zhang, An ecg acquisition system with piezoelectric energy harvesting for low power healthcare devices, 2021 IEEE 14th International Conference on ASIC (ASICON), IEEE, 2021, pp. 1-4.

[97] W. Deng, Y. Zhou, A. Libanori, G. Chen, W. Yang, J. Chen, Piezoelectric nanogenerators for personalized healthcare, Chemical Society Reviews 51(9) (2022) 3380-3435.

[98] R. Esmaeeli, H. Aliniagerdroudbari, S.R. Hashemi, A. Nazari, M. Alhadri, W. Zakri, A.H. Mohammed, C. Batur, S. Farhad, A rainbow piezoelectric energy harvesting system for intelligent tire monitoring applications, Journal of Energy Resources Technology 141(6) (2019) 062007.

[99] S. Du, Y. Jia, E. Arroyo, S. Fernandez, S.T. Riches, A.A. Seshia, MEMS piezoelectric energy harvester powered wireless sensor module driven by noisy base excitation, 2019 20th International Conference on Solid-State Sensors, Actuators and Microsystems & Eurosensors XXXIII (TRANSDUCERS & EUROSENSORS XXXIII), IEEE, 2019, pp. 350-353.

[100] S. Kassan, J. Gaber, P. Lorenz, Autonomous energy management system achieving piezoelectric energy harvesting in wireless sensors, Mobile Networks and Applications 25(2) (2020) 794-805.

[101] Z.J. Chew, T. Ruan, M. Zhu, Power management circuit for wireless sensor nodes powered by energy harvesting: On the synergy of harvester and load, IEEE Transactions on Power Electronics 34(9) (2018) 8671-8681.

[102] P. Cahill, A. Mathewson, V. Pakrashi, Experimental validation of piezoelectric energy-harvesting device for built infrastructure applications, Journal of Bridge Engineering 23(8) (2018) 04018056.

[103] Z. Zhang, H. Xiang, Z. Shi, J. Zhan, Experimental investigation on piezoelectric energy harvesting from vehicle-bridge coupling vibration, Energy Conversion and Management 163 (2018) 169-179.

[104] P. Cahill, B. Hazra, R. Karoumi, A. Mathewson, V. Pakrashi, Vibration energy harvesting based monitoring of an operational bridge undergoing forced vibration and train passage, Mechanical Systems and Signal Processing 106 (2018) 265-283.

[105] Z. Zhao, T. Wang, J. Shi, B. Zhang, R. Zhang, M. Li, Y. Wen, Analysis and application of the piezoelectric energy harvester on light electric logistics vehicle suspension systems, Energy Science & Engineering 7(6) (2019) 2741-2755.

[106] D.H. Jeon, J.Y. Cho, J.P. Jhun, J.H. Ahn, S. Jeong, S.Y. Jeong, A. Kumar, C.H. Ryu, W. Hwang, H. Park, A lever-type piezoelectric energy harvester with deformation-guiding mechanism for electric vehicle charging station on smart road, Energy 218 (2021) 119540.

[107] W. Tian, Y. Shi, H. Cui, J. Shi, Research on piezoelectric energy harvester based on coupled oscillator model for vehicle vibration utilizing a L-shaped cantilever beam, Smart Materials and Structures 29(7) (2020) 075014.

[108] B. Bao, Q. Wang, A rain energy harvester using a self-release tank, Mechanical Systems and Signal Processing 147 (2021) 107099.

[109] M. Shi, E.M. Yeatman, A.S. Holmes, Energy harvesting piezoelectric wind speed sensor, Journal of Physics: Conference Series, IOP Publishing, 2019, p. 012044.

[110] S. Bhuvaneswari, K. Maheswari, K. Chandraprakash, S. Deepak, Piezo electric rainfall energy harvester with proactive protection mechanism with Integrated IOT device, IOP Conference Series: Materials Science and Engineering, IOP Publishing, 2021, p. 012105.

[111] X. Cao, Y. Xiong, J. Sun, X. Zhu, Q. Sun, Z.L. Wang, Piezoelectric nanogenerators derived self-powered sensors for multifunctional applications and artificial intelligence, Advanced Functional Materials 31(33) (2021) 2102983.

[112] Y.-C. Wang, E. Kohtanen, A. Erturk, Characterization of a multifunctional bioinspired piezoelectric swimmer and energy harvester, Smart Materials, Adaptive Structures and Intelligent Systems, American Society of Mechanical Engineers, 2020, p. V001T06A012.

[113] E. Kar, N. Bose, B. Dutta, N. Mukherjee, S. Mukherjee, Ultraviolet-and microwave-protecting, self-cleaning e-skin for efficient energy harvesting and tactile mechanosensing, ACS applied materials & interfaces 11(19) (2019) 17501-17512.

[114] S. Panda, S. Hajra, K. Mistewicz, P. In-na, M. Sahu, P.M. Rajaitha, H.J. Kim, Piezoelectric energy harvesting systems for biomedical applications, Nano Energy 100 (2022) 107514.

[115] F. Ali, W. Raza, X. Li, H. Gul, K.-H. Kim, Piezoelectric energy harvesters for biomedical applications, Nano Energy 57 (2019) 879-902.

[116] A. Ballo, M. Bottaro, A.D. Grasso, A review of power management integrated circuits for ultrasound-based energy harvesting in implantable medical devices, Applied Sciences 11(6) (2021) 2487.

[117] P. Gljušćić, S. Zelenika, D. Blažević, E. Kamenar, Kinetic energy harvesting for wearable medical sensors, Sensors 19(22) (2019) 4922.

[118] H.-T. Deng, Y.-L. Wang, D.-L. Wen, X.-R. Zhang, P. Huang, X.-S. Zhang, Progress of biomechanical energy harvesters for wearable electronic applications, Journal of Micromechanics and Microengineering 32(8) (2022) 083001.

[119] X. Mo, H. Zhou, W. Li, Z. Xu, J. Duan, L. Huang, B. Hu, J. Zhou, Piezoelectrets for wearable energy harvesters and sensors, Nano Energy 65 (2019) 104033.

[120] Y.-W. Chong, W. Ismail, K. Ko, C.-Y. Lee, Energy harvesting for wearable devices: A review, IEEE Sensors Journal 19(20) (2019) 9047-9062.

[121] P. Panda, Environmental friendly lead-free piezoelectric materials, Journal of materials science 44(19) (2009) 5049-5062.

[122] M.T. Chorsi, E.J. Curry, H.T. Chorsi, R. Das, J. Baroody, P.K. Purohit, H. Ilies, T.D. Nguyen, Piezoelectric biomaterials for sensors and actuators, Advanced Materials 31(1) (2019) 1802084.

[123] H.A. Sodano, D.J. Inman, G. Park, Comparison of piezoelectric energy harvesting devices for recharging batteries, Journal of intelligent material systems and structures 16(10) (2005) 799-807.

[124] A. Nechibvute, A. Chawanda, P. Luhanga, Piezoelectric energy harvesting devices: an alternative energy source for wireless sensors, Smart Materials Research 2012(1) (2012) 853481.

[125] R. Li, Y. Yu, B. Zhou, Q. Guo, M. Li, J. Pei, Harvesting energy from pavement based on piezoelectric effects: Fabrication and electric properties of piezoelectric vibrator, Journal of Renewable and Sustainable Energy 10(5) (2018).

[126] C.N. Kumar, Energy collection via Piezoelectricity, Journal of Physics: Conference Series, IOP Publishing, 2015, p. 012031.

[127] N. Sezer, M. Koç, A comprehensive review on the state-of-the-art of piezoelectric energy harvesting, Nano energy 80 (2021) 105567.

[128] H.S. Kim, J.-H. Kim, J. Kim, A review of piezoelectric energy harvesting based on vibration, International journal of precision engineering and manufacturing 12 (2011) 1129-1141.

[129] Y. Shu, I. Lien, Analysis of power output for piezoelectric energy harvesting systems, Smart materials and structures 15(6) (2006) 1499.

[130] I. Coondoo, N. Panwar, H. Maiwa, A.L. Kholkin, Improved piezoelectric and energy harvesting characteristics in lead-free Fe 2 O 3 modified KNN ceramics, Journal of Electroceramics 34 (2015) 255-261.

[131] B.A. Seddik, G. Despesse, E. Defay, Wideband mechanical energy harvester based on piezoelectric longitudinal mode, 10th IEEE International NEWCAS Conference, IEEE, 2012, pp. 453-456.

[132] S. Manotham, P. Jaita, P. Butnoi, N. Lertcumfu, G. Rujijanagul, Improvements of depolarization temperature, piezoelectric and energy harvesting properties of BNT-based ceramics by doping an interstitial dopant, Journal of Alloys and Compounds 897 (2022) 163021.

[133] S. Manotham, P. Butnoi, P. Jaita, D. Tantraviwat, N. Boothrawong, G. Rujijanagul, Role of ZnO nanoparticle doping on depolarization temperature, piezoelectric and energy harvesting properties of lead-free Bi0. 5 (Na0. 84K0. 16) 0.5 TiO3 ceramics, Materials Research Bulletin 128 (2020) 110859.

[134] X. Yang, F. Zhuo, C. Wang, Y. Liu, Z. Wang, C. He, X. Long, Tunable pyroelectricity, depolarization temperature and energy harvesting density in Pb (Lu0. 5Nb0. 5) O3-xPbTiO3 ceramics, Acta Materialia 186 (2020) 523-532.

[135] H.-T. Kim, J.-H. Ji, B.S. Kim, J.-H. Koh, Strain related curie temperature and improved piezoelectric properties of lead-free (1-x) Ba (Sn, Ti) O3-x (Ba, Ca) TiO3 ceramics, Ceramics International 46(16) (2020) 25050-25057.

[136] T.P. Pham Thi, Z. Yan, G. Nick, K. Hamideh, H.D. Nguyen Phuc, Z. Xuefan, Z. Dou, Z. Kechao, D. Steve, B. Chris, Demonstration of enhanced piezo-catalysis for hydrogen generation and water treatment at the ferroelectric curie temperature, Iscience 23(5) (2020).

[137] H.-C. Song, P. Kumar, D. Maurya, M.-G. Kang, W.T. Reynolds, D.-Y. Jeong, C.-Y. Kang, S. Priya, Ultra-low resonant piezoelectric MEMS energy harvester with high power density, Journal of Microelectromechanical Systems 26(6) (2017) 1226-1234.

[138] A. Morel, G. Pillonnet, Y. Wanderoild, A. Badel, Dielectric losses considerations for piezoelectric energy harvesting, Journal of Low Power Electronics 14(2) (2018) 244-254.

[139] J. Liang, H.S.-H. Chung, W.-H. Liao, Dielectric loss against piezoelectric power harvesting, Smart materials and structures 23(9) (2014) 092001.

[140] W. Wang, J. Cao, C.R. Bowen, S. Zhou, J. Lin, Optimum resistance analysis and experimental verification of nonlinear piezoelectric energy harvesting from human motions, Energy 118 (2017) 221-230.

[141] M.-G. Kang, W.-S. Jung, C.-Y. Kang, S.-J. Yoon, Recent progress on PZT based piezoelectric energy harvesting technologies, Actuators, MDPI, 2016, p. 5.

[142] D.-J. Shin, S.-J. Jeong, C.-E. Seo, K.-H. Cho, J.-H. Koh, Multi-layered piezoelectric energy harvesters based on PZT ceramic actuators, Ceramics international 41 (2015) S686-S690.

[143] K. Morimoto, I. Kanno, K. Wasa, H. Kotera, High-efficiency piezoelectric energy harvesters of c-axis-oriented epitaxial PZT films transferred onto stainless steel cantilevers, Sensors and Actuators A: Physical 163(1) (2010) 428-432.

[144] A.K. Batra, S. Bhattacharjee, A.K. Chilvery, M.D. Aggarwal, M.E. Edwards, A. Bhalla, Simulation of energy harvesting from roads via pyroelectricity, Journal of Photonics for Energy 1(1) (2011) 014001-014001-12.

[145] R. Tu, B. Zhang, H.A. Sodano, Lead titanate nanowires/polyamide-imide piezoelectric nanocomposites for high-temperature energy harvesting, Nano Energy 97 (2022) 107175.

[146] K. Kim, J. Yoo, H.G. Lim, M. Lee, S.-M. Park, H.H. Kim, Lead-free piezoelectric composite with lithium niobate and barium titanate fabricated by interdigital pair bonding technique, IEEE Access 9 (2021) 85894-85902.

[147] B.B. Bohara, A.K. Batra, C. Bowen, Lanthanum-modified lead zirconate titanate based paint for sensor and energy harvesting applications, Journal of Materials Science: Materials in Electronics 29 (2018) 20931-20941.

[148] J. Sun, H. Guo, J. Ribera, C. Wu, K. Tu, M. Binelli, G. Panzarasa, F.W. Schwarze, Z.L. Wang, I. Burgert, Sustainable and biodegradable wood sponge piezoelectric nanogenerator for sensing and energy harvesting applications, ACS nano 14(11) (2020) 14665-14674.

[149] S. Banerjee, S. Bairagi, S.W. Ali, A critical review on lead-free hybrid materials for next generation piezoelectric energy harvesting and conversion, Ceramics International 47(12) (2021) 16402-16421.

[150] Z. Butt, S.U. Rahman, R.A. Pasha, S. Mehmood, S. Abbas, H. Elahi, Characterizing barium titanate piezoelectric material using the finite element method, Transactions on Electrical and Electronic materials 18(3) (2017) 163-168.

[151] J. Lin, Y. Cao, K. Zhu, F. Yan, C. Shi, H. Bai, G. Ge, J. Yang, W. Yang, G. Li, Ultrahigh energy harvesting properties in temperature-insensitive eco-friendly high-performance KNN-based textured ceramics, Journal of Materials Chemistry A 10(14) (2022) 7978-7988.

[152] Z. Chen, Y. Zhang, P. Huang, X. Li, J. Du, W. Bai, L. Li, F. Wen, P. Zheng, W. Wu, Enhanced piezoelectric properties and thermal stability in Mo/Cr co-doped CaBi2Nb2O9 high-temperature piezoelectric ceramics, Journal of Physics and Chemistry of Solids 136 (2020) 109195.

[153] Q. Lu, L. Liu, X. Lan, Y. Liu, J. Leng, Dynamic responses of SMA-epoxy composites and application for piezoelectric energy harvesting, Composite Structures 153 (2016) 843-850.

[154] B. Toroń, P. Szperlich, M. Kozioł, SbSI composites based on epoxy resin and cellulose for energy harvesting and sensors—The influence of SBSI nanowires conglomeration on piezoelectric properties, Materials 13(4) (2020) 902.

[155] Z. Zeng, L. Gai, A. Petitpas, Y. Li, H. Luo, D. Wang, X. Zhao, A flexible, sandwich structure piezoelectric energy harvester using PIN-PMN-PT/epoxy 2-2 composite flake for wearable application, Sensors and Actuators A: Physical 265 (2017) 62-69.

[156] S. Anwar, M. Hassanpour Amiri, S. Jiang, M.M. Abolhasani, P.R. Rocha, K. Asadi, Piezoelectric nylon-11 fibers for electronic textiles, energy harvesting and sensing, Advanced Functional Materials 31(4) (2021) 2004326.

[157] A. Datta, Y.S. Choi, E. Chalmers, C. Ou, S. Kar-Narayan, Piezoelectric nylon-11 nanowire arrays grown by template wetting for vibrational energy harvesting applications, Advanced Functional Materials 27(2) (2017) 1604262.

[158] F. Ram, S. Radhakrishnan, T. Ambone, K. Shanmuganathan, Highly flexible mechanical energy harvester based on nylon 11 ferroelectric nanocomposites, ACS Applied Polymer Materials 1(8) (2019) 1998-2005.

[159] D. Zabek, R. Pullins, M. Pearson, A. Grzebielec, T. Skoczkowski, Piezoelectric-silicone structure for vibration energy harvesting: Experimental testing and modelling, Smart Materials and Structures 30(3) (2021) 035002.

[160] T. Ali, F.U. Khan, A silicone based piezoelectric and electromagnetic hybrid vibration energy harvester, Journal of Micromechanics and Microengineering 31(5) (2021) 055003.

[161] M. Tascan, Optimization of process parameters of wet-spun solid PVDF fibers for maximizing the tensile strength and applied force at break and minimizing the elongation at break using the Taguchi method, Journal of Engineered Fibers and Fabrics 9(1) (2014) 155892501400900119.

[162] S. Mohammadpourfazeli, S. Arash, A. Ansari, S. Yang, K. Mallick, R. Bagherzadeh, Future prospects and recent developments of polyvinylidene fluoride (PVDF) piezoelectric polymer; fabrication methods, structure, and electro-mechanical properties, RSC advances 13(1) (2023) 370-387.

[163] B. Jaleh, A. Jabbari, Evaluation of reduced graphene oxide/ZnO effect on properties of PVDF nanocomposite films, Applied Surface Science 320 (2014) 339-347.

[164] F. Mokhtari, M. Shamshirsaz, M. Latifi, J. Foroughi, Nanofibers-based piezoelectric energy harvester for self-powered wearable technologies, Polymers 12(11) (2020) 2697.

[165] S. Sukumaran, S. Chatbouri, D. Rouxel, E. Tisserand, F. Thiebaud, T. Ben Zineb, Recent advances in flexible PVDF based piezoelectric polymer devices for energy harvesting applications, Journal of Intelligent Material Systems and Structures 32(7) (2021) 746-780.

[166] L. Li, M. Zhang, M. Rong, W. Ruan, Studies on the transformation process of PVDF from α to β phase by stretching, Rsc Advances 4(8) (2014) 3938-3943.

[167] H. Wang, Q. Chen, W. Xia, X. Qiu, Q. Cheng, G. Zhu, Electroactive PVDF thin films fabricated via cooperative stretching process, Journal of Applied Polymer Science 135(22) (2018) 46324.

[168] Y. Ting, Suprapto, C.W. Chiu, H. Gunawan, Characteristic analysis of biaxially stretched PVDF thin films, Journal of Applied Polymer Science 135(36) (2018) 46677.

[169] S. Men, Z. Gao, R. Wen, J. Tang, J.M. Zhang, Effects of annealing time on physical and mechanical properties of PVDF microporous membranes by a melt extrusion-stretching process, Polymers for Advanced Technologies 32(6) (2021) 2397-2408.

[170] N. Jahan, F. Mighri, D. Rodrigue, A. Ajji, Enhanced electroactive β phase in three phase PVDF/CaCO3/nanoclay composites: effect of micro-CaCO3 and uniaxial stretching, Journal of Applied Polymer Science 134(24) (2017).

[171] Y. Zhou, W. Liu, B. Tan, C. Zhu, Y. Ni, L. Fang, C. Lu, Z. Xu, Crystallinity and β phase fraction of PVDF in biaxially stretched PVDF/PMMA films, Polymers 13(7) (2021) 998.

[172] C. Mi, Z. Ren, H. Li, S. Yan, X. Sun, Synergistic effect of hydrogen bonds and diffusion on the β-crystallization of poly (vinylidene fluoride) on poly (methyl methacrylate) interface, Industrial & Engineering Chemistry Research 58(17) (2019) 7389-7396.

[173] S. Mishra, R. Sahoo, L. Unnikrishnan, A. Ramadoss, S. Mohanty, S.K. Nayak, Investigation of the electroactive phase content and dielectric behaviour of mechanically stretched PVDF-GO and PVDF-rGO composites, Materials Research Bulletin 124 (2020) 110732.

[174] F. Khan, T. Kowalchik, S. Roundy, R. Warren, Stretching-induced phase transitions in barium titanate-poly (vinylidene fluoride) flexible composite piezoelectric films, Scripta Materialia 193 (2021) 64-70.

[175] Y. Bormashenko, R. Pogreb, O. Stanevsky, E. Bormashenko, Vibrational spectrum of PVDF and its interpretation, Polymer testing 23(7) (2004) 791-796.

[176] R. Gregorio, M. Cestari, F. Bernardino, Dielectric behaviour of thin films of β-PVDF/PZT and β-PVDF/BaTiO 3 composites, Journal of Materials Science 31 (1996) 2925-2930.

[177] J. Martín, D. Zhao, T. Lenz, I. Katsouras, D.M. de Leeuw, N. Stingelin, Solid-state-processing of δ-PVDF, Materials Horizons 4(3) (2017) 408-414.

[178] C.K. McGinn, K.A. Kam, M.-M. Laurila, K. Lozano Montero, M. Mäntysalo, D. Lupo, I. Kymissis, Formulation, printing, and poling method for piezoelectric films based on PVDF–TrFE, Journal of Applied Physics 128(22) (2020).

[179] C. Lee, J.A. Tarbutton, Polyvinylidene fluoride (PVDF) direct printing for sensors and actuators, The International Journal of Advanced Manufacturing Technology 104(5) (2019) 3155-3162.

[180] J. Fan, D. Gonzalez, J. Garcia, B. Newell, R.A. Nawrocki, The effects of additive manufacturing and electric poling techniques on PVdF thin films: Towards 3D printed functional materials, Smart Materials, Adaptive Structures and Intelligent Systems, American Society of Mechanical Engineers, 2020, p. V001T04A010.

[181] J. Fan, B. Newell, J. Garcia, R.M. Voyles, R.A. Nawrocki, Contact-poling enhanced, fully 3d printed pvdf pressure sensors: towards 3d printed functional materials, Smart Materials, Adaptive Structures and Intelligent Systems, American Society of Mechanical Engineers, 2021, p. V001T02A007.

[182] A. Sasmal, S. Sen, P.S. Devi, Frequency dependent energy storage and dielectric performance of Ba–Zr Co-doped BiFeO3 loaded PVDF based mechanical energy harvesters: Effect of corona poling, Soft Matter 16(36) (2020) 8492-8505.

[183] S.K. Mahadeva, J. Berring, K. Walus, B. Stoeber, Effect of poling time and grid voltage on phase transition and piezoelectricity of poly (vinyledene fluoride) thin films using corona poling, Journal of physics D: applied physics 46(28) (2013) 285305.

[184] V. Sencadas, S. Lanceros-Mendez, D. Chinaglia, A. Pouzada, Influence of the processing conditions and corona poling on the morphology of/spl beta/-pvdf, 2005 12th International Symposium on Electrets, IEEE, 2005, pp. 161-164.

[185] G. Rui, Y. Huang, X. Chen, R. Li, D. Wang, T. Miyoshi, L. Zhu, Giant spontaneous polarization for enhanced ferroelectric properties of biaxially oriented poly (vinylidene fluoride) by mobile oriented amorphous fractions, Journal of Materials Chemistry C 9(3) (2021) 894-907.

[186] L. Ruan, X. Yao, Y. Chang, L. Zhou, G. Qin, X. Zhang, Properties and applications of the β phase poly (vinylidene fluoride), Polymers 10(3) (2018) 228.

[187] I. Pariy, A. Ivanova, V. Shvartsman, D. Lupascu, G. Sukhorukov, M. Surmeneva, R. Surmenev, Poling and annealing of piezoelectric Poly (Vinylidene fluoride) micropillar arrays, Materials Chemistry and Physics 239 (2020) 122035.

[188] A. Gaur, C. Kumar, S. Tiwari, P. Maiti, Efficient energy harvesting using processed poly (vinylidene fluoride) nanogenerator, ACS Applied Energy Materials 1(7) (2018) 3019-3024.

[189] R. Tu, E. Sprague, H.A. Sodano, Precipitation-printed high-β phase poly (vinylidene fluoride) for energy harvesting, ACS Applied Materials & Interfaces 12(52) (2020) 58072-58081.

[190] C.M. Costa, V. Sencadas, J.F. Mano, S. Lanceros-Méndez, Effect of poling on the mechanical properties of β-poly (vinylidene fluoride), Materials science forum, Trans Tech Publ, 2006, pp. 951-955.

[191] I.O. Pariy, A.A. Ivanova, V.V. Shvartsman, D.C. Lupascu, G.B. Sukhorukov, T. Ludwig, A. Bartasyte, S. Mathur, M.A. Surmeneva, R.A. Surmenev, Piezoelectric response in hybrid

micropillar arrays of poly (vinylidene fluoride) and reduced graphene oxide, Polymers 11(6) (2019) 1065.

[192] Y.P. Su, L.N. Sim, H.G. Coster, T.H. Chong, Incorporation of barium titanate nanoparticles in piezoelectric PVDF membrane, Journal of Membrane Science 640 (2021) 119861.

[193] Y. Ahn, J.Y. Lim, S.M. Hong, J. Lee, J. Ha, H.J. Choi, Y. Seo, Enhanced piezoelectric properties of electrospun poly (vinylidene fluoride)/multiwalled carbon nanotube composites due to high β-phase formation in poly (vinylidene fluoride), The Journal of Physical Chemistry C 117(22) (2013) 11791-11799.

[194] R.S. Kumar, T. Sarathi, K. Venkataraman, A. Bhattacharyya, Enhanced piezoelectric properties of polyvinylidene fluoride nanofibers using carbon nanofiber and electrical poling, Materials Letters 255 (2019) 126515.

[195] G.H. Kim, S.M. Hong, Y. Seo, Piezoelectric properties of poly (vinylidene fluoride) and carbon nanotube blends: β-phase development, Physical chemistry chemical physics 11(44) (2009) 10506-10512.

[196] H. Song, H. Li, S. Lim, Fast 3D digital light process printing of PVDF-HFP composite with electric in situ poling system for piezoelectric applications, Macromolecular Materials and Engineering 306(10) (2021) 2100266.

[197] R. Liu, Q. Liu, D. He, G. Sun, Z. Li, Y. Zhu, Enhancement of the piezoelectric property of polyvinylidene fluoride through electroactive phase enrichment and the application in piezoelectric generators, ACS Applied Electronic Materials 3(4) (2021) 1804-1812.

[198] Y. Li, W. Feng, L. Meng, K.M. Tse, Z. Li, L. Huang, Z. Su, S. Guo, Investigation on in-situ sprayed, annealed and corona poled PVDF-TrFE coatings for guided wave-based structural health monitoring: From crystallization to piezoelectricity, Materials & Design 199 (2021) 109415.

[199] A. Ikei, J. Wissman, K. Sampath, G. Yesner, S.N. Qadri, Tunable in situ 3d-printed pvdf-trfe piezoelectric arrays, Sensors 21(15) (2021) 5032.

[200] G. Xue, Y. Zhang, T. Xie, Z. Zhang, Q. Liu, X. Li, X. Gou, Cell adhesion-mediated piezoelectric self-stimulation on polydopamine-modified poly (vinylidene fluoride) membranes, ACS Applied Materials & Interfaces 13(15) (2021) 17361-17371.

[201] R. Mansour, O. Omoniyi, R. O'Leary, J.F. Windmill, Fabrication of ultraviolet-curable piezoelectric composite for sensor and actuator applications, 2018 IEEE SENSORS, IEEE, 2018, pp. 1-4.

[202] B. Tiller, A. Reid, B. Zhu, J. Guerreiro, R. Domingo-Roca, J.C. Jackson, J. Windmill, Piezoelectric microphone via a digital light processing 3D printing process, Materials & Design 165 (2019) 107593.

[203] S. Bodkhe, G. Turcot, F.P. Gosselin, D. Therriault, One-step solvent evaporation-assisted 3D printing of piezoelectric PVDF nanocomposite structures, ACS applied materials & interfaces 9(24) (2017) 20833-20842.

[204] H. Kim, F. Torres, D. Villagran, C. Stewart, Y. Lin, T.L.B. Tseng, 3D printing of BaTiO3/PVDF composites with electric in situ poling for pressure sensor applications, Macromolecular Materials and Engineering 302(11) (2017) 1700229.

[205] S. Song, Y. Li, Q. Wang, C. Zhang, Facile preparation of high loading filled PVDF/BaTiO 3 piezoelectric composites for selective laser sintering 3D printing, RSC advances 11(60) (2021) 37923-37931.

[206] J. Jiang, S. Tu, R. Fu, J. Li, F. Hu, B. Yan, Y. Gu, S. Chen, Flexible piezoelectric pressure tactile sensor based on electrospun BaTiO3/poly (vinylidene fluoride) nanocomposite membrane, ACS applied materials & interfaces 12(30) (2020) 33989-33998.

[207] A. Ferri, S. Barrau, R. Bourez, A. Da Costa, M.-H. Chambrier, A. Marin, J. Defebvin, J.-M. Lefebvre, R. Desfeux, Probing the local piezoelectric behavior in stretched barium titanate/poly (vinylidene fluoride) nanocomposites, Composites Science and Technology 186 (2020) 107914.

[208] S.H. Lee, Y.C. Choi, M.S. Kim, K.M. Ryu, Y.G. Jeong, Fabrication and characterization of piezoelectric composite nanofibers based on poly (vinylidene fluoride-co-hexafluoropropylene) and barium titanate nanoparticle, Fibers and Polymers 21 (2020) 473-479.

[209] N. Shehata, R. Nair, R. Boualayan, I. Kandas, A. Masrani, E. Elnabawy, N. Omran, M. Gamal, A.H. Hassanin, Stretchable nanofibers of polyvinylidenefluoride (PVDF)/thermoplastic polyurethane (TPU) nanocomposite to support piezoelectric response via mechanical elasticity, Scientific Reports 12(1) (2022) 8335.

[210] M.M. Abolhasani, M. Naebe, A. Jalali-Arani, Q. Guo, Crystalline structures and α→ β and γ polymorphs transformation induced by nanoclay in PVDF-based nanocomposite, Nano 9(06) (2014) 1450065.

[211] Y. Xin, X. Qi, H. Tian, C. Guo, X. Li, J. Lin, C. Wang, Full-fiber piezoelectric sensor by straight PVDF/nanoclay nanofibers, Materials Letters 164 (2016) 136-139.

[212] S. Tiwari, A. Gaur, C. Kumar, P. Maiti, Enhanced piezoelectric response in nanoclay induced electrospun PVDF nanofibers for energy harvesting, Energy 171 (2019) 485-492.

[213] Y.-J. Kim, T.-V. Dang, H.-J. Choi, B.-J. Park, J.-H. Eom, H.-A. Song, D. Seol, Y. Kim, S.-H. Shin, J. Nah, Piezoelectric properties of CH 3 NH 3 PbI 3 perovskite thin films and their applications in piezoelectric generators, Journal of Materials Chemistry A 4(3) (2016) 756-763.

[214] V. Jella, S. Ippili, J.-H. Eom, J. Choi, S.-G. Yoon, Enhanced output performance of a flexible piezoelectric energy harvester based on stable MAPbI3-PVDF composite films, Nano Energy 53 (2018) 46-56.

[215] A. Tuluk, T. Mahon, S. van der Zwaag, P. Groen, Estimating the true piezoelectric properties of BiFeO3 from measurements on BiFeO3-PVDF terpolymer composites, Journal of Alloys and Compounds 868 (2021) 159186.

[216] C. Li, W. Luo, X. Liu, D. Xu, K. He, PMN-PT/PVDF nanocomposite for high output nanogenerator applications, Nanomaterials 6(4) (2016) 67.

[217] C. Shamitha, A. Mahendran, S. Anandhan, Effect of polarization switching on piezoelectric and dielectric performance of electrospun nanofabrics of poly (vinylidene fluoride)/Ca–Al LDH nanocomposite, Journal of Applied Polymer Science 137(20) (2020) 48697.

[218] A. Wang, J. Liu, C. Shao, Y. Zhang, C. Chen, Electro-assisted 3d printing multi-layer PVDF/CaCl2 composite films and sensors, Coatings 12(6) (2022) 820.

[219] A. Wang, C. Chen, J. Qian, F. Yang, L. Wang, M. Zhang, Enhanced electrical properties of PVDF thin film by addition of NaCl by near-electric-field 3D printing, Journal of Electronic Materials 50(8) (2021) 4781-4786.

[220] S. Badatya, D.K. Bharti, N. Sathish, A.K. Srivastava, M.K. Gupta, Humidity sustainable hydrophobic poly (vinylidene fluoride)-carbon nanotubes foam based piezoelectric nanogenerator, ACS Applied Materials & Interfaces 13(23) (2021) 27245-27254.

[221] J. Li, S. Chen, W. Liu, R. Fu, S. Tu, Y. Zhao, L. Dong, B. Yan, Y. Gu, High performance piezoelectric nanogenerators based on electrospun ZnO nanorods/poly (vinylidene fluoride) composite membranes, The Journal of Physical Chemistry C 123(18) (2019) 11378-11387.

[222] D. Ponnamma, M.M. Chamakh, A.M. Alahzm, N. Salim, N. Hameed, M.A.A. AlMaadeed, Core-shell nanofibers of polyvinylidene fluoride-based nanocomposites as piezoelectric nanogenerators, Polymers 12(10) (2020) 2344.

[223] N. Abzan, M. Kharaziha, S. Labbaf, Development of three-dimensional piezoelectric polyvinylidene fluoride-graphene oxide scaffold by non-solvent induced phase separation method for nerve tissue engineering, Materials & Design 167 (2019) 107636.

[224] C.-T. Pan, S.-Y. Wang, C.-K. Yen, A. Kumar, S.-W. Kuo, J.-L. Zheng, Z.-H. Wen, R. Singh, S.P. Singh, M.T. Khan, Polyvinylidene fluoride-added ceramic powder composite near-field electrospinned piezoelectric fiber-based low-frequency dynamic sensors, ACS omega 5(28) (2020) 17090-17101.

[225] Y. Hong, B. Wang, Z. Long, Z. Zhang, Q. Pan, S. Liu, X. Luo, Z. Yang, Hierarchically interconnected piezoceramic textile with a balanced performance in piezoelectricity, flexibility, toughness, and air permeability, Advanced Functional Materials 31(42) (2021) 2104737.

[226] A. Lopes, J. Gutiérrez, J. Barandiarán, Direct fabrication of a 3D-shape film of polyvinylidene fluoride (PVDF) in the piezoelectric β-phase for sensor and actuator applications, European Polymer Journal 99 (2018) 111-116.

[227] L. Song, R. Dai, Y. Li, Q. Wang, C. Zhang, Polyvinylidene fluoride energy harvester with boosting piezoelectric performance through 3D printed biomimetic bone structures, ACS Sustainable Chemistry & Engineering 9(22) (2021) 7561-7568.

[228] J. Zhang, D. Liu, Q. Han, L. Jiang, H. Shao, B. Tang, W. Lei, T. Lin, C.H. Wang, Mechanically stretchable piezoelectric polyvinylidene fluoride (PVDF)/Boron nitride nanosheets (BNNSs) polymer nanocomposites, Composites Part B: Engineering 175 (2019) 107157.

[229] J. Zhang, H. Wang, P. Blanloeuil, G. Li, Z. Sha, D. Wang, W. Lei, C. Boyer, Y. Yu, R. Tian, Enhancing the triboelectricity of stretchable electrospun piezoelectric polyvinylidene fluoride/boron nitride nanosheets composite nanofibers, Composites Communications 22 (2020) 100535.

[230] S. Song, Y. Li, Q. Wang, C. Zhang, Facile preparation of high loading filled PVDF/$BaTiO_3$ piezoelectric composites for selective laser sintering 3D printing, (2021).

[231] P.K. Mishra, P. Senthil, Prediction of in-plane stiffness of multi-material 3D printed laminate parts fabricated by FDM process using CLT and its mechanical behaviour under tensile load, Materials Today Communications 23 (2020) 100955.

[232] A. Ahmed, A. Azam, Y. Wang, Z. Zhang, N. Li, C. Jia, R.T. Mushtaq, M. Rehman, T. Gueye, M.B. Shahid, Additively manufactured nano-mechanical energy harvesting systems: advancements, potential applications, challenges and future perspectives, Nano convergence 8 (2021) 1-42.

[233] C. Kaynak, S.D. Varsavas, Performance comparison of the 3D-printed and injection-molded PLA and its elastomer blend and fiber composites, Journal of Thermoplastic Composite Materials 32(4) (2019) 501-520.

[234] O. Machida, A. Shimofuku, R. Tashiro, A. Takeuchi, Y. Akiyama, E. Ohta, Fabrication of lead zirconate titanate films by inkjet printing, Japanese Journal of Applied Physics 51(9S1) (2012) 09LA11.

[235] B. Andò, S. Baglio, A.R. Bulsara, T. Emery, V. Marletta, A. Pistorio, Low-cost inkjet printing technology for the rapid prototyping of transducers, Sensors 17(4) (2017) 748.

[236] C. Chen, F. Cai, Y. Zhu, L. Liao, J. Qian, F.-G. Yuan, N. Zhang, 3D printing of electroactive PVDF thin films with high β-phase content, Smart Materials and Structures 28(6) (2019) 065017.

[237] N.A. Shepelin, V.C. Lussini, P.J. Fox, G.W. Dicinoski, A.M. Glushenkov, J.G. Shapter, A.V. Ellis, 3D printing of poly (vinylidene fluoride-trifluoroethylene): a poling-free technique to manufacture flexible and transparent piezoelectric generators, MRS Communications 9(1) (2019) 159-164.

[238] Y.-Y. Li, L.-T. Li, B. Li, Direct ink writing of 3–3 piezoelectric composite, Journal of Alloys and Compounds 620 (2015) 125-128.

[239] C. Yang, S. Song, F. Chen, N. Chen, Fabrication of PVDF/BaTiO3/CNT piezoelectric energy harvesters with bionic balsa wood structures through 3D printing and supercritical carbon dioxide foaming, ACS Applied Materials & Interfaces 13(35) (2021) 41723-41734.

[240] S. Song, Y. Li, Q. Wang, C. Zhang, Boosting piezoelectric performance with a new selective laser sintering 3D printable PVDF/graphene nanocomposite, Composites Part A: Applied Science and Manufacturing 147 (2021) 106452.

[241] C. Shuai, G. Liu, Y. Yang, F. Qi, S. Peng, W. Yang, C. He, G. Wang, G. Qian, A strawberry-like Ag-decorated barium titanate enhances piezoelectric and antibacterial activities of polymer scaffold, Nano Energy 74 (2020) 104825.

[242] F. Qi, Z. Zeng, J. Yao, W. Cai, Z. Zhao, S. Peng, C. Shuai, Constructing core-shell structured BaTiO3@ carbon boosts piezoelectric activity and cell response of polymer scaffolds, Materials Science and Engineering: C 126 (2021) 112129.

[243] C. Yang, F. Chen, J. Sun, N. Chen, Boosted mechanical piezoelectric energy harvesting of polyvinylidene fluoride/barium titanate composite porous foam based on three-dimensional printing and foaming technology, ACS omega 6(45) (2021) 30769-30778.

[244] M.-L. Seol, R. Ivaškevičiūtė, M.A. Ciappesoni, F.V. Thompson, D.-I. Moon, S.J. Kim, S.J. Kim, J.-W. Han, M. Meyyappan, All 3D printed energy harvester for autonomous and sustainable resource utilization, Nano Energy 52 (2018) 271-278.

[245] U.J. Yang, J.W. Lee, J.P. Lee, J.M. Baik, Remarkable output power enhancement of sliding-mode triboelectric nanogenerator through direct metal-to-metal contact with the ground, Nano Energy 57 (2019) 293-299.

[246] Z. Chen, X. Song, L. Lei, X. Chen, C. Fei, C.T. Chiu, X. Qian, T. Ma, Y. Yang, K. Shung, 3D printing of piezoelectric element for energy focusing and ultrasonic sensing, Nano Energy 27 (2016) 78-86.

[247] Y. Chen, X. Bao, C.-M. Wong, J. Cheng, H. Wu, H. Song, X. Ji, S. Wu, PZT ceramics fabricated based on stereolithography for an ultrasound transducer array application, Ceramics International 44(18) (2018) 22725-22730.

[248] X. Liu, Y. Shang, J. Zhang, C. Zhang, Ionic liquid-assisted 3D printing of self-polarized β-PVDF for flexible piezoelectric energy harvesting, ACS Applied Materials & Interfaces 13(12) (2021) 14334-14341.

[249] J. Liu, Y. Shang, Z. Shao, X. Liu, C. Zhang, Three-Dimensional Printing to Translate Simulation to Architecting for Three-Dimensional High Performance Piezoelectric Energy Harvester, Industrial & Engineering Chemistry Research 61(1) (2021) 433-440.

[250] X. Liu, Y. Shang, J. Liu, Z. Shao, C. Zhang, 3D printing-enabled in-situ orientation of BaTi2O5 nanorods in β-PVDF for high-efficiency piezoelectric energy harvesters, ACS Applied Materials & Interfaces 14(11) (2022) 13361-13368.

[251] H. Pei, S. Shi, Y. Chen, Y. Xiong, Q. Lv, Combining solid-state shear milling and FFF 3D-printing strategy to fabricate high-performance biomimetic wearable fish-scale PVDF-based piezoelectric energy harvesters, ACS Applied Materials & Interfaces 14(13) (2022) 15346-15359.

[252] X. Liu, J. Liu, L. He, Y. Shang, C. Zhang, 3D printed piezoelectric-regulable cells with customized electromechanical response distribution for intelligent sensing, Advanced Functional Materials 32(26) (2022) 2201274.

[253] H. Kim, F. Torres, Y. Wu, D. Villagran, Y. Lin, T.-L.B. Tseng, Integrated 3D printing and corona poling process of PVDF piezoelectric films for pressure sensor application, Smart Materials and Structures 26(8) (2017) 085027.

[254] L. He, J. Lu, C. Han, X. Liu, J. Liu, C. Zhang, Electrohydrodynamic pulling consolidated high-efficiency 3D printing to architect unusual self-polarized β-PVDF arrays for advanced piezoelectric sensing, Small 18(15) (2022) 2200114.

[255] H. Pei, Y. Xie, Y. Xiong, Q. Lv, Y. Chen, A novel polarization-free 3D printing strategy for fabrication of poly (Vinylidene fluoride) based nanocomposite piezoelectric energy harvester, Composites Part B: Engineering 225 (2021) 109312.

[256] H. Kim, T. Fernando, M. Li, Y. Lin, T.-L.B. Tseng, Fabrication and characterization of 3D printed BaTiO3/PVDF nanocomposites, Journal of Composite Materials 52(2) (2018) 197-206.

[257] A. Ambrosi, M. Pumera, 3D-printing technologies for electrochemical applications, Chemical society reviews 45(10) (2016) 2740-2755.

[258] J.U. Pucci, B.R. Christophe, J.A. Sisti, E.S. Connolly Jr, Three-dimensional printing: technologies, applications, and limitations in neurosurgery, Biotechnology advances 35(5) (2017) 521-529.

[259] Q. Yan, H. Dong, J. Su, J. Han, B. Song, Q. Wei, Y. Shi, A review of 3D printing technology for medical applications, Engineering 4(5) (2018) 729-742.

[260] Z. Lyu, G.J. Lim, J.J. Koh, Y. Li, Y. Ma, J. Ding, J. Wang, Z. Hu, J. Wang, W. Chen, Design and manufacture of 3D-printed batteries, Joule 5(1) (2021) 89-114.

[261] H. Quan, T. Zhang, H. Xu, S. Luo, J. Nie, X. Zhu, Photo-curing 3D printing technique and its challenges, Bioactive materials 5(1) (2020) 110-115.

[262] F. Zhang, M. Wei, V.V. Viswanathan, B. Swart, Y. Shao, G. Wu, C. Zhou, 3D printing technologies for electrochemical energy storage, Nano Energy 40 (2017) 418-431.

[263] M. Pei, H. Shi, F. Yao, S. Liang, Z. Xu, X. Pei, S. Wang, Y. Hu, 3D printing of advanced lithium batteries: a designing strategy of electrode/electrolyte architectures, Journal of Materials Chemistry A 9(45) (2021) 25237-25257.

[264] C. Yang, S. Song, F. Chen, N. Chen, Fabrication of PVDF/$BaTiO_3$/CNT Piezoelectric Energy Harvesters with Bionic Balsa Wood Structures through 3D Printing and Supercritical Carbon Dioxide Foaming, (2021).

[265] H. Kim, E. Park, S. Kim, B. Park, N. Kim, S. Lee, Experimental study on mechanical properties of single-and dual-material 3D printed products, Procedia Manufacturing 10 (2017) 887-897.

[266] H.K. Sezer, O. Eren, FDM 3D printing of MWCNT re-inforced ABS nano-composite parts with enhanced mechanical and electrical properties, Journal of manufacturing processes 37 (2019) 339-347.

[267] R.F. Quero, B.M. de Castro Costa, J.A.F. da Silva, D.P. de Jesus, Using multi-material fused deposition modeling (FDM) for one-step 3D printing of microfluidic capillary electrophoresis with integrated electrodes for capacitively coupled contactless conductivity detection, Sensors and Actuators B: Chemical 365 (2022) 131959.

[268] D. Espalin Jr, Development of a multi-material, multi-technology FDM system for process improvement experimentation, The University of Texas at El Paso2012.

[269] D. Yadav, D. Chhabra, R.K. Garg, A. Ahlawat, A. Phogat, Optimization of FDM 3D printing process parameters for multi-material using artificial neural network, Materials Today: Proceedings 21 (2020) 1583-1591.

[270] S.H. Ji, Y.-S. Cho, J.S. Yun, Wearable core-shell piezoelectric nanofiber yarns for body movement energy harvesting, Nanomaterials 9(4) (2019) 555.

[271] Y. Liu, H. Khanbareh, M.A. Halim, A. Feeney, X. Zhang, H. Heidari, R. Ghannam, Piezoelectric energy harvesting for self-powered wearable upper limb applications, Nano Select 2(8) (2021) 1459-1479.

[272] D. Sarkar, N. Das, M.M. Saikh, P. Biswas, S. Das, S. Das, N.A. Hoque, R. Basu, Development of a sustainable and biodegradable sonchus asper cotton pappus based piezoelectric nanogenerator for instrument vibration and human body motion sensing with mechanical energy harvesting applications, ACS omega 6(43) (2021) 28710-28717.

[273] Y. Yang, H. Pan, G. Xie, Y. Jiang, C. Chen, Y. Su, Y. Wang, H. Tai, Flexible piezoelectric pressure sensor based on polydopamine-modified BaTiO3/PVDF composite film for human motion monitoring, Sensors and Actuators A: Physical 301 (2020) 111789.

[274] S. Siddiqui, D.-I. Kim, E. Roh, T.Q. Trung, M.T. Nguyen, N.-E. Lee, A durable and stable piezoelectric nanogenerator with nanocomposite nanofibers embedded in an elastomer under high loading for a self-powered sensor system, Nano Energy 30 (2016) 434-442.

[275] M. Zhu, Q. Shi, T. He, Z. Yi, Y. Ma, B. Yang, T. Chen, C. Lee, Self-powered and self-functional cotton sock using piezoelectric and triboelectric hybrid mechanism for healthcare and sports monitoring, ACS nano 13(2) (2019) 1940-1952.

[276] X. Rui, Y. Li, X. Zheng, Z. Sha, Z. Zeng, Design and experimental study of a piezoelectric energy harvester in automotive spokes, Journal of Physics D: Applied Physics 52(35) (2019) 355501.

[277] R. Esmaeeli, H. Aliniagerdroudbari, A. Nazari, S.R. Hashemi, M. Alhadri, W. Zakri, A.H. Mohammed, C. Batur, S. Farhad, Optimization of a rainbow piezoelectric energy harvesting system for tire monitoring applications, Energy Sustainability, American Society of Mechanical Engineers, 2018, p. V001T02A004.

[278] R. Esmaeeli, H. Aliniagerdroudbari, S.R. Hashemi, M. Alhadri, W. Zakri, C. Batur, S. Farhad, Design, modeling, and analysis of a high performance piezoelectric energy harvester for intelligent tires, International Journal of Energy Research 43(10) (2019) 5199-5212.

[279] X. Rui, Z. Zeng, Y. Zhang, Y. Li, H. Feng, X. Huang, Z. Sha, Design and experimental investigation of a self-tuning piezoelectric energy harvesting system for intelligent vehicle wheels, IEEE Transactions on Vehicular Technology 69(2) (2019) 1440-1451.

[280] Y.L. Morangueira, J.C.d.C. Pereira, Energy harvesting assessment with a coupled full car and piezoelectric model, Energy 210 (2020) 118668.

[281] M.V. Lopes, J.J. Eckert, T.S. Martins, A.A. dos Santos, Multi-objective optimization of piezoelectric vibrational energy harvester orthogonal spirals for ore freight cars, Journal of the Brazilian Society of Mechanical Sciences and Engineering 43(6) (2021) 295.

[282] Z. Wang, W. Wang, L. Tang, R. Tian, C. Wang, Q. Zhang, C. Liu, F. Gu, A.D. Ball, A piezoelectric energy harvester for freight train condition monitoring system with the hybrid nonlinear mechanism, Mechanical Systems and Signal Processing 180 (2022) 109403.

[283] B. Dziadak, M. Kucharek, J. Starzyński, Powering the WSN node for monitoring rail car parameters, using a piezoelectric energy harvester, Energies 15(5) (2022) 1641.

[284] F. Yang, M. Gao, P. Wang, J. Zuo, J. Dai, J. Cong, Efficient piezoelectric harvester for random broadband vibration of rail, Energy 218 (2021) 119559.

[285] L. Jiang, Y. Yang, R. Chen, G. Lu, R. Li, J. Xing, K.K. Shung, M.S. Humayun, J. Zhu, Y. Chen, Ultrasound-induced wireless energy harvesting for potential retinal electrical stimulation application, Advanced Functional Materials 29(33) (2019) 1902522.

[286] F. Xie, X. Qian, N. Li, D. Cui, H. Zhang, Z. Xu, An experimental study on a piezoelectric vibration energy harvester for self-powered cardiac pacemakers, Annals of translational medicine 9(10) (2021).

[287] T. Zhang, H. Liang, Z. Wang, C. Qiu, Y.B. Peng, X. Zhu, J. Li, X. Ge, J. Xu, X. Huang, Piezoelectric ultrasound energy–harvesting device for deep brain stimulation and analgesia applications, Science advances 8(15) (2022) eabk0159.

[288] P. Mangaiyarkarasi, P. Lakshmi, V. Sasrika, Grey wolf optimization based flexible piezoelectric energy harvester for hearing aid applications, 2019 IEEE International Systems Conference (SysCon), IEEE, 2019, pp. 1-8.

[289] Y. Hong, L. Jin, B. Wang, J. Liao, B. He, T. Yang, Z. Long, P. Li, Z. Zhang, S. Liu, A wood-templated unidirectional piezoceramic composite for transmuscular ultrasonic wireless power transfer, Energy & Environmental Science 14(12) (2021) 6574-6585.

[290] S. Gururaj, A. Applequist, S. Bhattarai, A.M. Appaji, P. Kadambi, Self-powered cardiac pacemaker: the viability of a piezoelectric energy harvester, 2020 International Conference on COMmunication Systems & NETworkS (COMSNETS), IEEE, 2020, pp. 70-75.

[291] A. Anand, S. Kundu, Design of mems based piezoelectric energy harvester for pacemaker, 2019 Devices for Integrated Circuit (DevIC), IEEE, 2019, pp. 465-469.

[292] Z. Xu, C. Jin, A. Cabe, D. Escobedo, N. Hao, I. Trase, A.B. Closson, L. Dong, Y. Nie, J. Elliott, Flexible energy harvester on a pacemaker lead using multibeam piezoelectric composite thin films, ACS applied materials & interfaces 12(30) (2020) 34170-34179.

[293] S. Azimi, A. Golabchi, A. Nekookar, S. Rabbani, M.H. Amiri, K. Asadi, M.M. Abolhasani, Self-powered cardiac pacemaker by piezoelectric polymer nanogenerator implant, Nano Energy 83 (2021) 105781.

[294] L. Dong, A.B. Closson, M. Oglesby, D. Escobedo, X. Han, Y. Nie, S. Huang, M.D. Feldman, Z. Chen, J.X. Zhang, In vivo cardiac power generation enabled by an integrated helical piezoelectric pacemaker lead, Nano Energy 66 (2019) 104085.

[295] L. Jiang, G. Lu, Y. Zeng, Y. Sun, H. Kang, J. Burford, C. Gong, M.S. Humayun, Y. Chen, Q. Zhou, Flexible ultrasound-induced retinal stimulating piezo-arrays for biomimetic visual prostheses, Nature communications 13(1) (2022) 3853.

[296] J.S. Perlmutter, J.W. Mink, Deep brain stimulation, Annu. Rev. Neurosci. 29(1) (2006) 229-257.

[297] A. Delnavaz, J. Voix, Energy harvesting for in-ear devices using ear canal dynamic motion, IEEE Transactions on Industrial Electronics 61(1) (2013) 583-590.

[298] A. Delnavaz, J. Voix, Ear canal dynamic motion as a source of power for in-ear devices, Journal of Applied Physics 113(6) (2013).

[299] W. Liu, X. Cheng, X. Fu, C. Stefanini, P. Dario, Preliminary study on development of PVDF nanofiber based energy harvesting device for an artery microrobot, Microelectronic engineering 88(8) (2011) 2251-2254.

[300] Q. Liu, Q. Li, Z. Fang, X. Zhou, R. Wang, C. Zuo, Piezoelectric energy harvesting for flapping wing micro air vehicle and flapping wing sensing based on flexible polyvinylidene fluoride, Applied Sciences 11(3) (2021) 1166.

[301] P.-K. Yang, S.-A. Chou, C.-H. Hsu, R.J. Mathew, K.-H. Chiang, J.-Y. Yang, Y.-T. Chen, Tin disulfide piezoelectric nanogenerators for biomechanical energy harvesting and intelligent human-robot interface applications, Nano Energy 75 (2020) 104879.

Chapitre 3: Modélisation et optimisation des paramètres de polarisation basées sur l'intelligence artificielle

Ce chapitre a fait l'objet d'une publication :

MEGDICH, Amal, HABIBI, Mohamed, and LAPERRIÈRE, Luc.

Modeling and optimization of piezoelectric and dielectric properties of poled PVDF/BT nano-composites *Polymer Bulletin*, 2024, vol. 81, no 10, p. 9181-9201.

Il peut être consulté en ligne à l'adresse suivante :

https://doi.org/10.1007/s00289-024-05157-5

Sur la base de la revue de la littérature présentée dans le chapitre précédent, il apparaît clairement que l'amélioration des performances piézoélectriques du PVDF repose sur deux stratégies principales : l'application d'un procédé de polarisation et l'ajout de charges fonctionnelles. Malgré ces avancées, l'optimisation des paramètres de polarisation reste un défi majeur, car leur influence sur les propriétés finales du PVDF est fortement non linéaire et dépend de plusieurs facteurs. Jusqu'à présent, la plupart des études se sont concentrées sur l'optimisation empirique de ces paramètres à travers un nombre limité de tests expérimentaux, sans approche systématique ni modélisation avancée. A ce jour, aucun travail n'a utilisé l'intelligence artificielle pour modéliser et optimiser les propriétés piézoélectriques du PVDF en fonction des paramètres de polarisation et du taux de charges céramiques. Cette lacune scientifique motive le présent travail qui vise à intégrer des approches de modélisation basées sur des réseaux de neurones artificiels (RNA) et des algorithmes d'optimisation évolutive (GA) pour étudier en profondeur les relations complexes entre paramètres de fabrication et performances électromécaniques des nanocomposites PVDF/BT.

L'objectif principal de cette étude est d'analyser l'influence des paramètres de polarisation et de la teneur en charge céramique sur les propriétés piézoélectriques et diélectriques du PVDF/BT. Quatre paramètres clés ont été étudiés dans ce travail : la température de polarisation, le temps de polarisation, la tension de polarisation et la fraction massique BT. Une méthodologie de conception expérimentale basée sur le Box-Behnken Design (BBD) a été utilisée pour modéliser et analyser systématiquement l'influence de ces facteurs sur les coefficients piézoélectriques, la permittivité et la fraction de phase β du PVDF.

L'étude intègre une approche qui combine des techniques expérimentales et des méthodes avancées de modélisation numérique. Un réseau neuronal artificiel (RNA) a été utilisé pour prédire les propriétés piézoélectriques et diélectriques des nanocomposites en fonction des paramètres de polarisation et du contenu en BT. Un algorithme génétique (GA) a ensuite été mis en œuvre pour optimiser ces paramètres et déterminer la meilleure configuration conduisant à une efficacité piézoélectrique maximale. L'optimisation a conduit à un coefficient d33 de 25,259 pC/N, une constante diélectrique de 24,282 et une fraction de phase β de 95,435 %. Ces résultats ont été validés expérimentalement avec des écarts de 9,789 %, 0,338 % et 0,305 %, respectivement, confirmant la robustesse des modèles de prédiction.

Les travaux soulignent l'intérêt croissant pour l'amélioration des matériaux polymères piézoélectriques et l'importance des approches numériques avancées pour améliorer les performances des dispositifs de récupération d'énergie. Cette étude apporte une contribution significative en proposant une méthodologie intégrée qui combine la conception expérimentale, la modélisation des réseaux neuronaux et l'optimisation génétique, ouvrant la voie à un meilleur contrôle des propriétés des nanocomposites piézoélectriques à base de PVDF/BT pour des applications innovantes dans la récupération d'énergie et les capteurs intelligents.

Note : des informations complémentaires (supporting information) ont également été publiées pour cet article. Ils se retrouvent en Annexe 1 de cette thèse et sont identifiées par les références « Figure Si » ou « Table Si » dans cet article.

Modeling and optimization of piezoelectric and dielectric properties of poled PVDF/BT nanocomposites

Amal Megdich[1], Mohamed Habibi[1,*], Luc Laperrière[1]

[1] Department of mechanical engineering, Université du Québec à Trois Rivières, 3351 Bd des Forges, G8Z 4M3, Trois-Rivières, Canada

3.1 Abstract

Poling parameters and barium titanate (BT) content significantly affect the piezoelectric and dielectric properties of poly(vinylidene fluoride) (PVDF). Selecting the best possible values for these process parameters is indeed a significant challenge. In this study, piezoelectric nanocomposites for high-energy conversion were prepared by mixing PVDF with BT. The dependence of piezoelectric and dielectric properties on process parameters was investigated. The input parameters, including poling temperature, time and voltage, and the mass fraction of BT, were considered as input variables. A Box-Behnken Design (BBD) was used to design and analyze the experiments. ANOVA was performed to study the significance of poling parameters and BT mass fraction. An Artificial Neural Network (ANN) was used to model PVDF-based nanocomposite properties as a function of the four process parameters. A genetic algorithm was applied to search for the optimal poling conditions and BT mass fraction. The optimal combination leads to a d33 coefficient of 25.259 pC/N, a dielectric constant of 24.282, and a β-phase fraction of 95.435%. These results were experimentally validated, and the errors were 9.789%, 0.338%, and 0.305%, respectively. Following the optimization, a PVDF-based nanocomposite with excellent piezoelectric and dielectric properties (d33= 28pC/N, permittivity=24.2, F(β)=95.7%) was fabricated for energy conversion applications.

Keywords: PVDF, BT, Poling, ANN, Genetic algorithm.

3.2 Introduction

The development of modern technologies is closely linked to the development of new functional materials. Advances in synthesizing new piezoelectric polymer materials have enabled the fabrication of highly efficient, lightweight, and flexible piezoelectric energy harvesters. The most important properties of piezoelectric polymers for practical purposes are piezoelectricity and dielectricity. Although the piezoelectric and dielectric coefficients of piezoelectric ceramics are generally more significant than those of piezoelectric polymers, lead-based

piezoelectric ceramics cause pollution and environmental problems due to the volatilization of lead oxide toxin during manufacture. They also exhibit higher fragility, brittleness, and rigidity [302]. PVDF is one of the most commonly used piezoelectric polymers in the energy harvesting literature due to its high relative dielectric constant, lightweight, ease of fabrication, and long-term stability under a high electric field [303]. PVDF is a semi-crystalline polymer that exists in four different phases (α-phase, β-phase, γ-phase, and δ-phase). The nonpolar α-phase is the most thermodynamically stable. The β-phase is the most useful phase due to its piezoelectric properties [304], which can be obtained by poling or adding fillers. Poling is very important and is the focus of this article. Several conventional research papers have investigated the poling of PVDF film [194, 305-307]. Several parameters in the poling process affect the piezoelectric and dielectric properties of the piezoelectric polymer material, including poling time, poling temperature, and poling voltage. The temperatures vary from room temperature [308] to 150°C [309]. The poling process at room temperature is called cold poling. However, the alignment of molecular dipoles in PVDF is a temperature-dependent process. At room temperature, the polymer chains' mobility is limited, making it difficult to achieve a high degree of dipole alignment. This limited mobility can lead to weaker net polarization and, thus, less efficient piezoelectric and dielectric properties. To overcome this problem, mineral oil [180, 181, 310], silicone oil [208, 311], or vacuum [312] have typically been used to keep the temperature stable during the poling process and eliminate oxygen between the film and the plate. The poling duration is one of the parameters that can affect the piezoelectric and dielectric properties of PVDF. H. Song et al. demonstrated that longer poling time can lead to a higher degree of molecular alignment, which can improve the piezoelectric properties of the material [196]. However, Y. Li et al. showed that the relationship between poling time and piezoelectric properties is not linear [198], and there is an optimum poling time that maximizes piezoelectric properties.

Previous works have shown that the optimum poling time can vary depending on the type of PVDF material and the processing condition. In general, a poling time between 30 min [195] and 120 min [187, 189] has been shown to be effective in improving the piezoelectric properties of PVDF materials. Poling times longer than 2 hours can reduce piezoelectric response due to the formation of electrical breakdown and defects.

The poling voltage is the most important factor affecting the piezoelectric properties of PVDF. Increasing the poling voltage can increase the degree of polarization of the polymer material, increasing the overall piezoelectric response [199]. However, a high applied voltage can damage or degrade the material [197]. The optimum poling voltage for PVDF depends on

several factors, such as the overall quality of the material. Generally, a moderate poling voltage of about 20 to 100 kV/cm [313-315] is used for most applications, as it provides a good balance between increasing the piezoelectric response and avoiding damage to the material.

Another method to improve the formation of a more stable β-phase in PVDF is the addition of fillers to the polymer matrix, which significantly improves the polymer's piezo-response. Numerous studies have recently investigated the incorporation of fillers such as BT [316, 317], Ionic liquid (IL) [318, 319], Graphene Oxide (GO) [320], ZnO nanoparticles [321-323], and Carbon Nanotubes (CNT) [324-326] into the polymer matrix. In this work, we have chosen to add BT nanoparticles in different proportions (20, 30, and 40 wt%) to PVDF to combine the advantages of ultra-high piezoelectric and dielectric coefficients (d33 and permittivity) of ceramics and the excellent flexibility of polymers.

Although many previous works have focused on the effect of poling parameters on the piezoelectric and dielectric properties of PVDF [180, 311, 315, 327, 328], the research in this field is still restricted, since all these works present results limited to experimental works. However, in the present work, a neural network algorithm was used to predict the variation of PVDF properties in a continuous range of the poling parameters (temperature, time, and voltage) and BT content in PVDF. A genetic algorithm was then used to find the optimal input set that yields the highest d33 coefficient, permittivity, and F(β).

3.3 Process parameter selection

Due to its excellent molecular properties and structure, polyvinylidene fluoride (PVDF) is an excellent piezoelectric material [329]. Its flexibility and light weight make it ideal for wearable electronics, robotics, and biomedical devices; it has a wide frequency range and excellent sensitivity, making it well suited for sensing applications such as pressure sensors, accelerometers, and vibration sensors [330]; and it is known for its high linearity, i.e., the proportionality of the output voltage to the applied excitation, making it particularly useful for accurate measurements.

PVDF is a durable and reliable material for long-term use, as it is highly resistant to harsh conditions such as high temperatures, humidity, and UV radiation. Moreover, PVDF is a low-cost and easy-to-process material suitable for the mass production of piezoelectric devices. PVDF's unique molecular structure and properties make it an excellent piezoelectric material for various applications where flexibility, sensitivity, durability, and cost-effectiveness are critical.

Poling is a critical step in the fabrication of a PVDF-based piezoelectric material. Before poling, PVDF exhibits a random polarization distribution. During poling, the PVDF is subjected to an electric field, which causes the material's internal structure to align, resulting in a net polarization of the material. The strength of the electric field, as well as the temperature and duration of the poling process, affect the final polarization of the material.

The desired piezoelectric and dielectric properties of the material can be achieved by optimizing the poling settings. For example, increasing the poling temperature can improve the piezoelectric response of the material, but too high a temperature can lead to depolarization. Similarly, increasing the voltage or duration of the poling can also improve the material's polarization; however, if the voltage or time is too high, the material may degrade. To ensure that the material has the appropriate piezoelectric properties and performs well in the intended application, the poling settings must be optimized.

Furthermore, the addition of fillers to PVDF can improve its performance. This is because the local mechanical stresses that nanoparticles can exert on the polymer chains can produce higher polarization. BT is one of the most used fillers in PVDF-based PEH. BT acts as a nucleating agent and increases the content of β-phases. The piezoelectric coefficient and dielectric constant of PVDF can also increase with the addition of BT nanoparticles.

To achieve the appropriate piezoelectric properties for a given application, the BT content in the PVDF/BT composite must be optimized. The concentration of BT nanoparticles in the PVDF matrix significantly impacts the composite's properties, including the piezoelectric coefficient and the dielectric constant. If the concentration of BT nanoparticles is too low, the generated local mechanical stresses in the PVDF matrix may not be sufficient to noticeably increase the degree of polarization, and the resulting piezoelectric response may not be suitable for the intended application. On the other hand, the BT nanoparticles may aggregate if the concentration is too high. In some of these agglomerates, the orientation of the polymer chain may be disturbed, which may affect the overall piezoelectric properties of the material.

3.4 Experimental section

3.4.1 Materials

PVDF (Mw ≈ 64.04 g/mol) powder, BT (Mw ≈ 233.24g/mol) powder, and N,N-dimethylformamide (DMF, 99.8+%) were purchased from commercial distributors.

3.4.2 Design of experiment

Following previous studies [196, 197, 205], four factors are considered with their respective values, as shown in Table 8. The other factors are left at the values shown in Table 9. The factors' levels were selected per a literature review and previous tests, as described in Figure S1. A Box-Behnken experimental design was chosen to determine the relationship between the response variables (d33, dielectric constant, and β-phase fraction) and the controlled variables, each with three levels (poling temperature, poling time, poling voltage, and added BT fraction).

Table 8: Factors and their levels.

					Controlled factors			
Factor	Value	Unit	Factor	Symbol	Level			Unit
					Low (-1)	Center (0)	High (1)	
Stirring temperature	60	°C	Poling temperature	T	50	100	150	°C
Stirring speed	1500	Rpm	Poling time	t	60	90	120	min
Stirring time	1	H	Poling voltage	V	30	65	100	KV/cm
DMF evaporation temperature	130	°C	BT fraction	BT	20	30	40	wt%
DMF evaporation time	24	H						

Box-Behnken design is a second-order rotatable design based on a three-level incomplete factorial design. The arrangement of the Box-Behnken design levels allows the number of design points to increase at the same rate as the number of polynomial coefficients. With 4 factors each with 3 levels, the experimental design is divided into three orthogonal blocks of 9 runs. Each factor's maximum and minimum values are coded into +1 and -1, respectively, using Equation (1), so that, all input factors are in the same range.

$$\xi_{ij} = \frac{x_{ij} - \bar{x_i}}{\Delta x_i} \times 2; \quad \bar{x_i} = \frac{\sum_{j=1}^{3} x_{ij}}{3} \quad \text{and,} \quad \Delta x_i = x_{i3} - x_{i1} \qquad (1)$$

where ξ_{ij} and x_{ij} are the coded and actual values, respectively, of the j^{th} level of the i^{th} factor. The details of the experimental design employed in this study featuring the use of the BBD with the coded levels are outlined in Table 9.

Table 9: Coded levels for the BBD design.

Factors			
T	t	V	BT
±1	±1	0	0
0	0	±1	±1
0	0	0	0
±1	0	0	±1
0	±1	±1	0
0	0	0	0
±1	0	±1	0
0	±1	0	±1
0	0	0	0
±1	±1	0	0
0	0	±1	±1
0	0	0	0

3.4.3 Sample preparation

First, 10 g of PVDF powder containing different amounts of BT (20, 30, and 40 wt%) were dissolved in DMF solvent and stirred at 60 °C and 1500 rpm for 1 hour until completely dissolved. The mixture was then dried at 130 °C for 24 hours until the DMF solvent was volatilized entirely. The resulting polymer composite samples were cooled to room temperature and cut into small pieces of about 10×10 $mm^{2,}$ as shown in Figure 26.

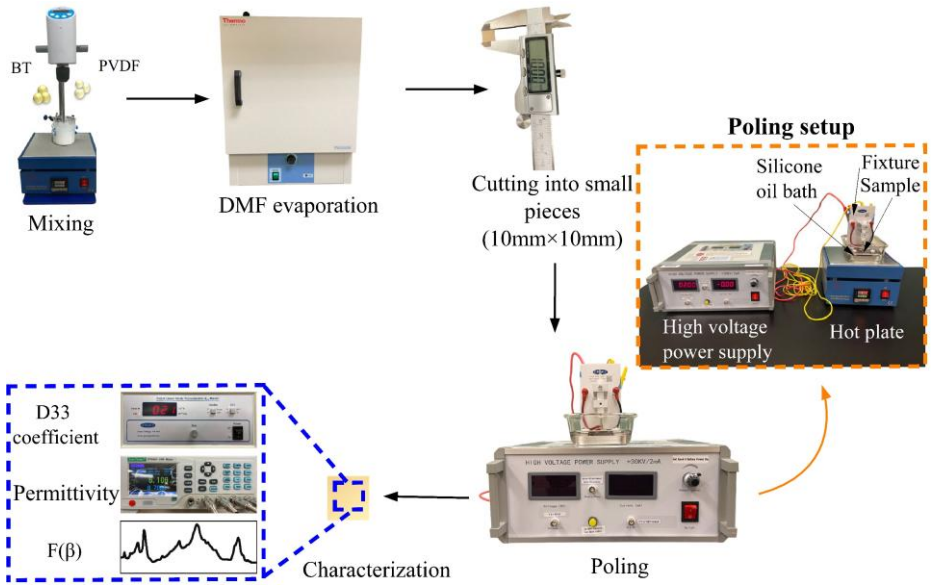

Figure 26: Schematic diagram of the experimental steps and the poling setup.

3.4.4 Poling

The poling setup consisted of three components: a fixture (Test Fixture for Piezoelectric Poling and High Voltage Ferroelectric Test, Polyk, USA.), a high voltage power supply (High Voltage Power Supply +30 kV, 2 mA, Polyk, USA.), and a heating plate. The fixture was made

of Teflon to provide electrical insulation. The samples were attached to both surfaces with conductive copper electrodes and immersed in silicone oil in a glass container to prevent an electrical breakdown during the poling process. To investigate the effects of the poling parameters on the piezoelectric and dielectric properties of the PVDF/BT nanocomposite, different voltages (30, 65, and 100 KV) were applied at different temperatures (50, 100, and 150 °C) and for different periods (60, 90, and 120 min). After poling, the samples were cooled to room temperature before the electric field was turned off to reduce the misalignment of the dipole moments [331].

3.4.5 Characterization

After poling, samples were air-cooled to room temperature. Then, the piezoelectric constant (d33) of the PVDF/BT nanocomposite was measured with a quasi-static d33 measuring instrument (Berlincourt Piezoelectric meter PKD3-2000, PolyK, USA).
Using the following equation:

$$\varepsilon = \frac{C_p \times d}{\varepsilon_0 \times A}, \qquad (2)$$

The permittivity was calculated from the electrical capacitance Cp measured by a multi-frequency LCR meter (electric Bridge Resistance Capacitance Tester Digital LCR Meter) at 100 Hz, where ε_0 is the permittivity of free space, A is the area, and d is the thickness of the material.

The phase transformation of PVDF was assessed by Fourier transform infrared (FT-IR) spectroscopy. The spectra were recorded in the range of wavenumbers from 600 to 1500 cm^{-1} with a resolution of 4 cm^{-1}. As the FT-IR spectra obey the Lambert-Beer law, the β-phase fraction within the PVDF/BT nanocomposite is calculated by the following equation:

$$F(\beta) = \frac{A_\beta}{\left(\frac{k_\beta}{k_\alpha}\right) \cdot A_\alpha + A_\beta}, \qquad (3)$$

where A_α and A_β are the structural absorbances at 766 and 840 cm^{-1}, respectively. K_β (6.1×10^4 cm^2/mol) and K_α (7.7×10^4 cm^2/mol) are the absorption coefficients at the corresponding wavenumber.

3.5 Results and discussions

3.5.1 Statistical analysis

After poling, samples were air-cooled to room temperature. Then, the piezoelectric constant (d33) of the PVDF/BT nanocomposite was measured with a quasi-static d33 measuring instrument (Berlincourt Piezoelectric meter PKD3-2000, PolyK, USA).

The data obtained from the BBD design (Table S1) were evaluated by signal-to-noise (S/N) ratio. Taguchi and Phadke classify factors into two types: control and noise factors. Control factors are determined by the designer, while the factors that can hardly be controlled or cannot be controlled at all are called noise factors, such as the humidity and the temperature of the environment. Therefore, in this work, the signal-to-noise ratio (S/N ratio) was used to make the process less sensitive to changes in the noise factors, which means a robust system is achieved. There are three types of S/N ratios based on the suitability of the result: smaller is better, nominal is better, bigger is better. In this work, the three outputs evaluated must have a significant value, so the equation 'bigger is the better" is used for the S/N ratio (Equation 4):

$$S / N = -10\, log\left(\frac{1}{n}\sum_{i=1}^{n}\frac{1}{Y_i^2}\right). \qquad (4)$$

In this work, n = 1 because the average of the two tests is taken to account for all outputs and runs. The results are presented in Table S2.

ANOVA was performed to evaluate the significance of the independent variables at 95% confidence in testing the null hypothesis. For the d33 coefficient (Table 10), all the 'parameters' probability values are less than 0.05. Thus, these parameters were considered significant at the 95% confidence level. Table 11 shows the ranking of process parameters for SN values of d33. As observed from Table 11, "V" has the most influence, which is to be expected since an increase in the poling voltage strengthens the alignment of the molecular dipoles, leading to a stronger piezoelectric effect. "T" also significantly affects the d33 coefficient of the PVDF samples. The material may become too rigid at low temperatures, making it difficult for the molecules to align and polarize properly, resulting in a lower d33 coefficient. At higher temperatures, the PVDF molecular mobility increases, making it easier for them to align in the direction of the poling electric field. This can lead to a higher d33 coefficient as more molecules are polarized and contribute to the overall piezoelectric effect. "BT" and "t" ranked third and fourth, respectively. BT is a piezoelectric ceramic with a high d33 constant. Thus, adding "BT" results in a nanocomposite PVDF/BT with a higher piezoelectric constant. In addition, the

nanoparticles of BT act as nucleation sites and promote the alignment of the dipoles of PVDF, resulting in a higher d33 coefficient. The main effect plot for SN ratios (Figure 27) shows that the sample poled with T=150 °C, t=90 min, V= 100 KV/cm poling conditions, and with 30 wt% of BT, has the highest d33 coefficient.

Table 10: ANOVA table based upon the SN values of the d33 coefficient.

Source	Sum Sq	Df	Mean Sq	F	Prob>F
T	1.253	2	0.627	2.352	0.12378
t	3.491	2	1.746	6.551	0.00728
V	8.305	2	4.152	15.585	0.00012
BT	5.809	2	2.904	10.901	0.00079
Error	4.796	18	0.266		
Total	23.27	26			

Table 11: Ranking of input parameters for d33 coefficient.

Levels	T	t	V	BT
1	16.636	19.402	16.018	18.048
2	20.785	20.988	19.744	21.524
3	22.086	18.811	25.306	19.63
Δ	5.45	2.177	9.287	3.477
Rank	2	4	1	3

For the permittivity, the probability values of "t", "V", and "BT" are less than 0.05 (Table 12), these three parameters were considered significant at the 95% confidence level. However, the parameter "T" is considered insignificant. Considering the data in Table 12 and Table 13, "V" has the most effective role. The poling voltage can affect the dielectric constant of PVDF by causing a change in the molecular orientation of the polymer that affects its electrical properties. Thus, higher poling voltage leads to stronger alignment, increasing the piezoelectric materials' permittivity. BT also has a significant effect on the permittivity of the PVDF samples. This is to be expected since "BT" is a ceramic material with a high dielectric constant. Thus, with increasing BT content, the dielectric constant of the formed PVDF/BT nanocomposite rises due to the high dielectric constant of "BT". The main effect plot for SN ratios (Figure 27) shows that the sample poled in T=150 °C, t=90 min, V= 100 KV/cm poling conditions, and with 40 wt% of BT, has the highest dielectric constant.

Table 12: ANOVA table based on the SN values of the permittivity.

Source	Sum Sq	Df	Mean Sq	F	Prob>F
T	1.253	2	0.627	2.352	0.12378
t	3.491	2	1.746	6.551	0.00728
V	8.305	2	4.152	15.585	0.00012
BT	5.809	2	2.904	10.901	0.00079
Error	4.796	18	0.266		
Total	23.27	26			

Table 13: Ranking of input parameters for the permittivity.

Levels	T	t	V	BT
1	26.113	26.246	25.436	25.475
2	26.118	26.504	26.263	26.384
3	26.756	25.659	27.072	26.728
Δ	0.644	0.845	1.636	1.252
Rank	4	3	1	2

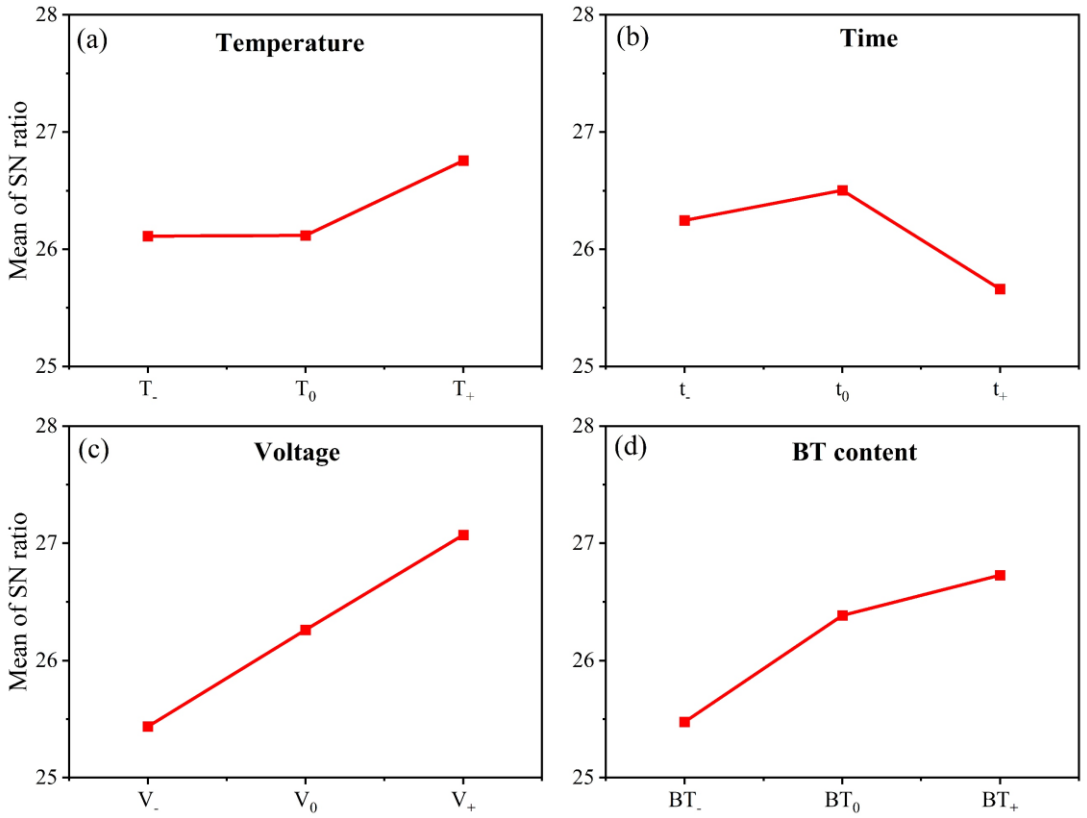

Figure 27: SN Ratio diagram for the dielectric constant of PVDF as a function of (a) “T”, (b) “t”, (c) “V”, and (d) “BT”.

For F(β), the probability values of "V", "T", and "BT" are less than 0.05 (Table 14). These parameters were considered significant at the 95% confidence level. Parameter "t" was not considered as significant. Based on Table 14 and Table 15, "V" plays the most influential role as it is ranked first, which is expected as an increase in the poling voltage enhances the alignment of molecular dipoles. "T" also significantly affects the PVDF samples' F(β) because as "T" increases, the PVDF material becomes more pliable and allows for greater molecular mobility, leading to more efficient alignment and polarization of the molecules during poling. The addition of BT also significantly affects the formation of the β-phase in PVDF, as it acts as a nucleating agent for the alignment of the PVDF chains. In this work, the significance of "t" is not recognized because the poling test was performed in short periods (max. 120 min). Previous works show that a significant increase in the poling time could affect the F(β) of

PVDF [303]. The main effect plot for SN ratios (Figure 29) shows that the sample poled in T=150 °C, t=90 min, V= 100 KV/cm poling conditions, and with 30 wt% of BT, has the highest d33 coefficient.

Table 14: Ranking of input parameters for f F(β).

Source	Sum Sq	Df	Mean Sq	F	Prob>F
T	1.999	2	0.999	6.745	0.00651
t	0.223	2	0.111	0.752	0.48584
V	3.516	2	1.758	11.865	0.00052
BT	1.239	2	0.619	4.181	0.03225
Error	2.667	18	0.148		
Total	9.612	26			

Table 15: ANOVA table based upon the SN values of F(β).

Levels	T	t	V	BT
1	38.359	38.707	38.317	38.441
2	38.748	38.795	38.669	38.934
3	39.16	38.694	39.399	38.614
Δ	0.802	0.101	1.082	0.493
Rank	2	4	1	3

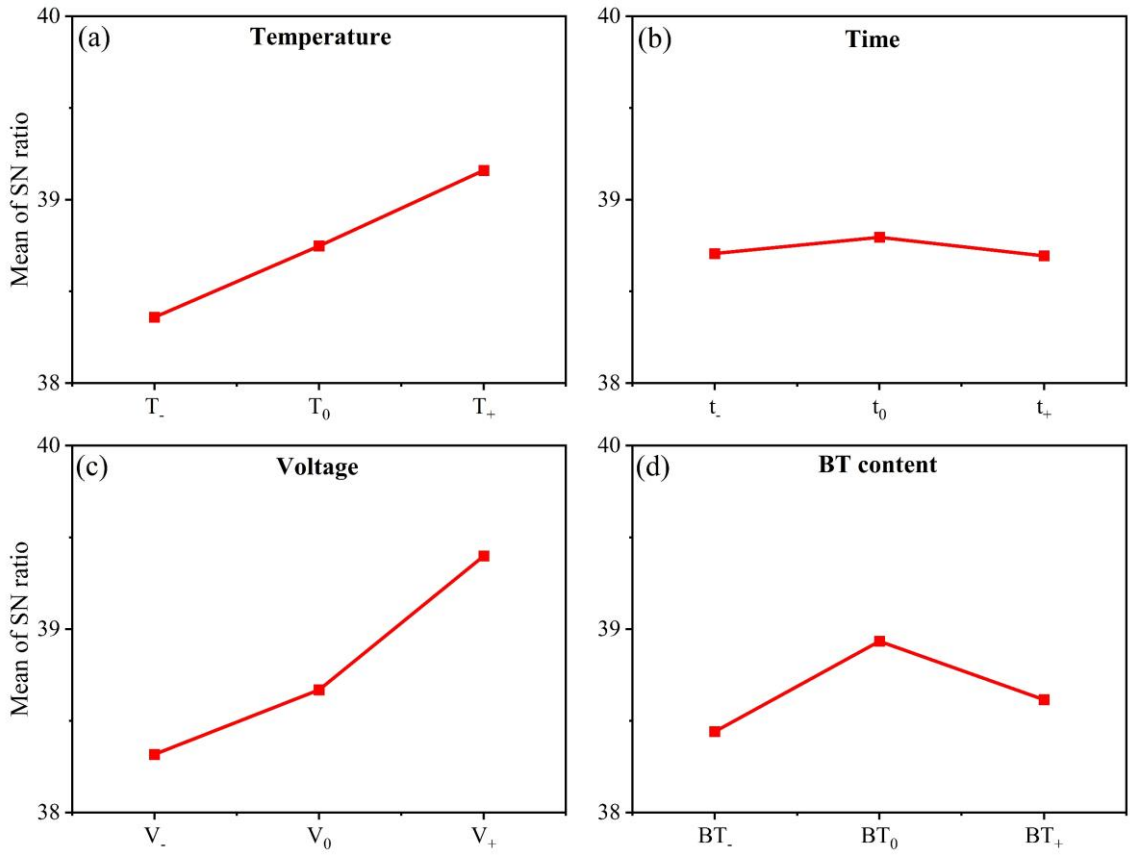

Figure 28: SN Ratio diagram for the β-phase relative fraction of PVDF as a function of (a) “T”, (b) “t”, (c) “V”, and (d) “BT”.

The obtained SN values (Tables 5, 7, and 9) can be used to predict the theoretical optimized outputs using the linear equation (5)

$$\eta_i = R_i + (R_{Ai-}R_i) + (R_{Bi-}R_i) + (R_{Ci-}R_i) + (R_{Di-}R_i); i = 1,2,3, \quad (5)$$

where

- For d33:

$$R_1 = 19.915, R_{A1} = 22.086, R_{B1} = 20.988, R_{C1} = 25.306, R_{D1} = 21.524\,. \quad (6)$$

- For permittivity:

$$R_2 = 26.229, R_{A2} = 26.756, R_{B1} = 26.659, R_{C1} = 27.072, R_{D1} = 26.728. \quad (7)$$

- For F(β):

$$R_3 = 38.737, R_{A3} = 39.160, R_{B3} = 38.795, R_{C3} = 39.399, R_{D3} = 38.934. \quad (8)$$

Inserting Equations (6), (7), and (8) in Equation (5), we obtain

$$\eta_1 = 30.160, \eta_2 = 28.371, \eta_3 = 39.997. \quad (9)$$

Finally, the optimized outputs can be written as follows:

$$d_{33opt} = 10^{\frac{\eta_1}{20}}, \text{Permittivity}_{opt} = 10^{\frac{\eta_2}{20}}, F(\beta)_{opt} = 10^{\frac{\eta_3}{20}}. \quad (10)$$

These results were used in the experimental validations shown in Table 16. It turns out that a large error is observed for the optimal value of d33 and that the values of input parameters that yield the optimum for d33 and F(β) are not the same for permittivity. ANN modeling and genetic algorithms were then used to fine tune the final optimization.

Table 16: ANOVA predictions and experimental validations for the optimized outputs.

Optimal values	Coded values (T, t, V, BT)	Experimental validations	Error (%)
$d33_{opt}$=32.210	(+1, 0, +1, 0)	$d33_{opt}$=24	25.488
$Permittivity_{opt}$=26.216	(+1, 0, +1, +1)	$Permittivity_{opt}$=24.693	6.038
$F(\beta)_{opt}$=99.965	(+1, 0, +1, 0)	$F(\beta)_{opt}$ =94.418	5.548

3.5.2 Neural network prediction

An ANN was used to model the poling process using MATLAB software. The four factors "T", "t", "V", and "BT" are used as input parameters. The database was then divided into three categories: Training data, which is used to train the ANN model by adjusting the weights and biases of the network; Validation data, which is used to evaluate the performance of ANN during training to avoid overfitting; and Test data, which is used to evaluate the final performance of the ANN model. Different ANN structures with different numbers of neurons in the hidden layer were tested. The topology 4-10-3 was selected (Figure 29(a)) based on the value of the correlation coefficient.

The transfer function in the hidden layer was a tan-sigmoidal transfer function, and the output layer neurons used a linear output transfer function (for denormalization back into engineering units). Figure 29(b) shows the regression analysis results between the network response and the corresponding target values. The predicted values and their related experimental results are presented in Table S3.

Figure 30(a), 31(b), and 31(c) compare the network response and experimental results for the three studied outputs.

Figure 30(d) shows that most errors between the predicted and target values are less than 5%.

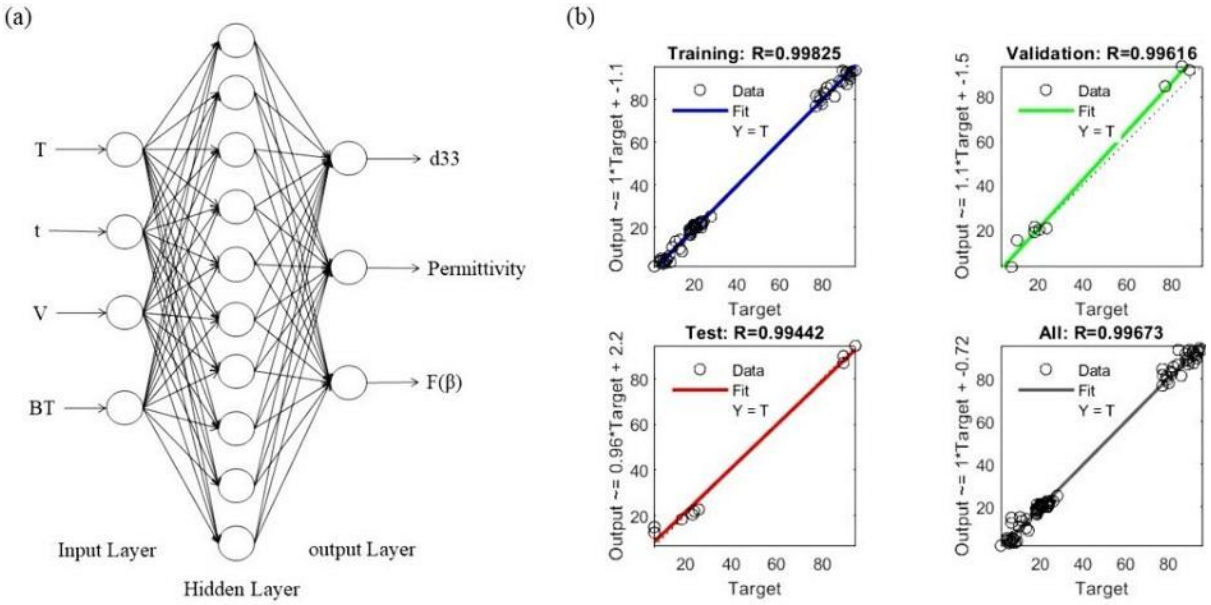

Figure 29: (a) Neural network topology, (b) Neural network performance.

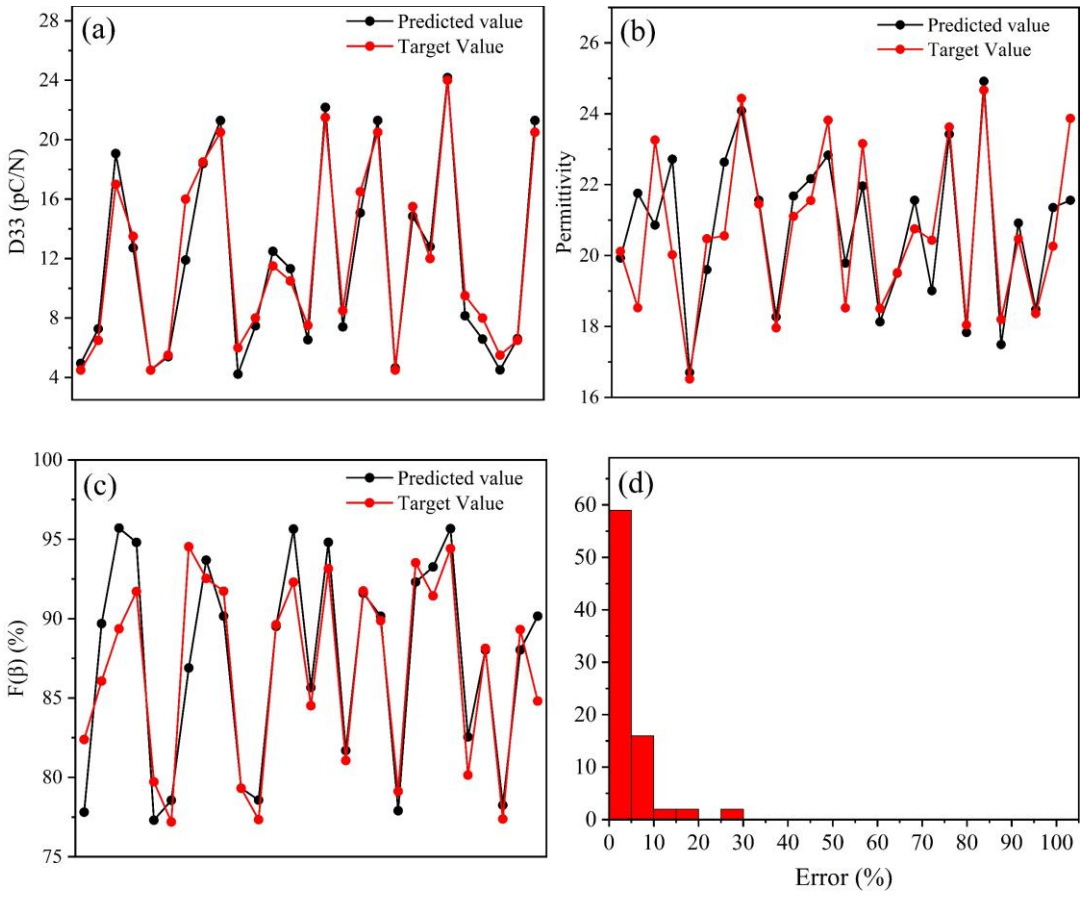

Figure 30: Comparison of ANN-predicted and experimental values of piezoelectric and dielectric properties : Comparison between ANN predicted values and experimental results for (a) d33 coefficient, (b) permittivity, and (c) F(β). (d) errors between predicted values and targets.

3.5.3 Model analysis

3D surface plots are used to understand the relationship between the model variables. According to Tables 5, 7, and 9, the input parameters "V" and "T" have the greatest effect on the d33 coefficient and F(β). The input parameters that have the greatest influence on the permittivity are "V" and "BT". These parameters are studied in detail in Figures 32-34 and Figures S2-S7. The red spheres in the plots, representing the experimental points, are very close to the predicted 3D surfaces, confirming an overall excellent performance of the ANN. Figure 31 shows that the coefficient d33 increases with increasing temperature and voltage, which is consistent with the results of ANOVA. Moreover, the input set (150, 90, 100, 30) yields the highest d33 (25.19 pC/N), confirming that the ANN and ANVOVA predictions are aligned. Figure 32 shows variations of the permittivity as a function of "V" and "BT". For T=150°C, the results of ANN show that for short poling durations, the dielectric constant increases with the increase of the applied poling voltage and the BT fraction. For longer poling durations (t=120 min), an

increase in the poling voltage or BT fraction can degrade the polymer material, decreasing the permittivity. As demonstrated by ANOVA, the maximum dielectric constant (23.96) is reached with the input set (150, 90, 100, 40). The predicted model of F(β) as a function of "V" and "T" at "BT" =30 wt% is shown in Figure 33. F(β) shows strong variations as a function of voltage, confirming that this parameter has the most significant influence on F(β). Substantial F(β) variations are also observed as a function of temperature. As the temperature increases, the energy available for the PVDF chains to align in a more ordered manner increases, resulting in a higher β-phase fraction. Finally, the ANN model shows that the input parameters (150, 90, 100, 30) gives the highest β-phase fraction (94%), confirming again the results of ANOVA.

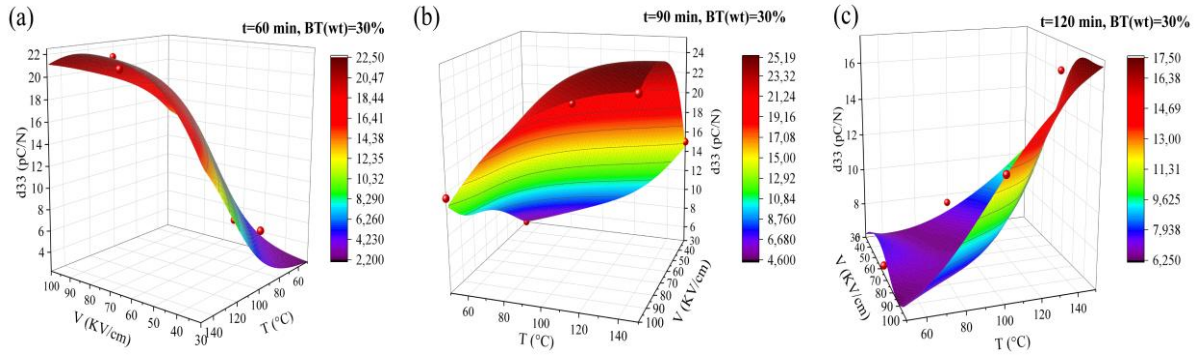

Figure 31: Surface plot of d33 coefficient for BT=30 wt% according to ANN.

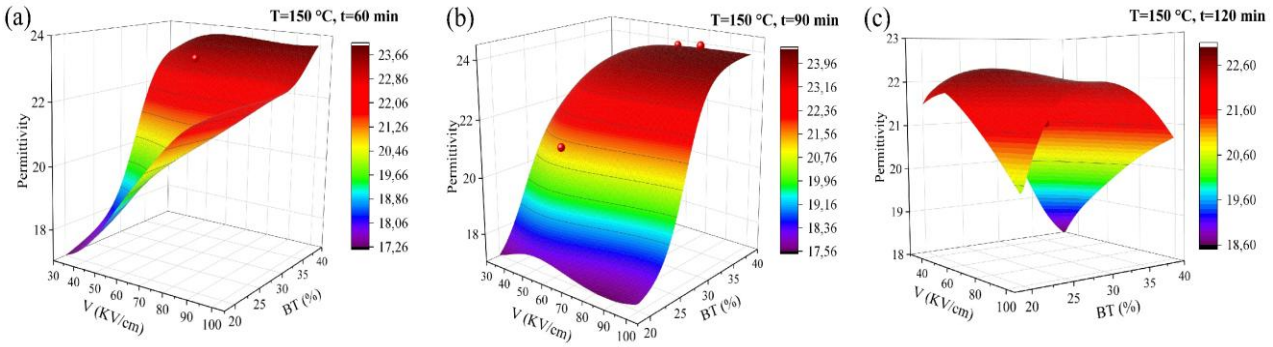

Figure 32: Surface plot of permittivity for T=150°C according to ANN.

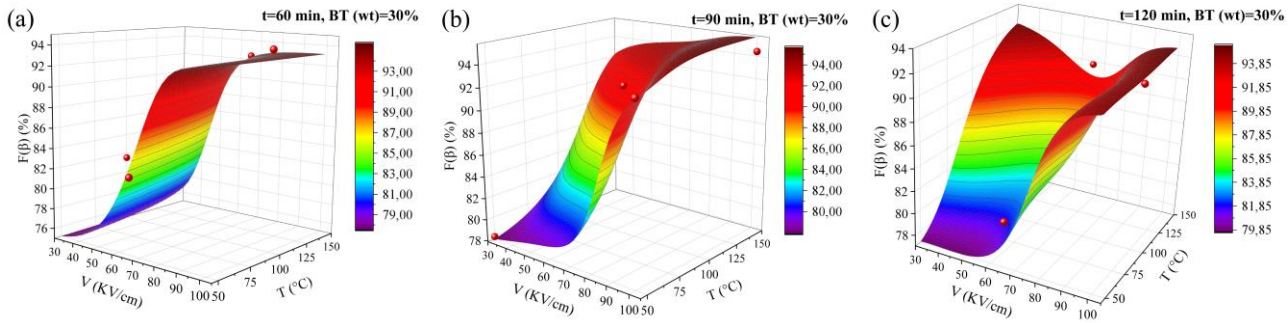

Figure 33: Surface plot of F(β) for BT=30 wt% according to ANN.

3.5.4 Optimization of process parameters

A genetic algorithm was used to find the best input variables that maximize the piezoelectric and dielectric properties of the PVDF/BT nanocomposite.

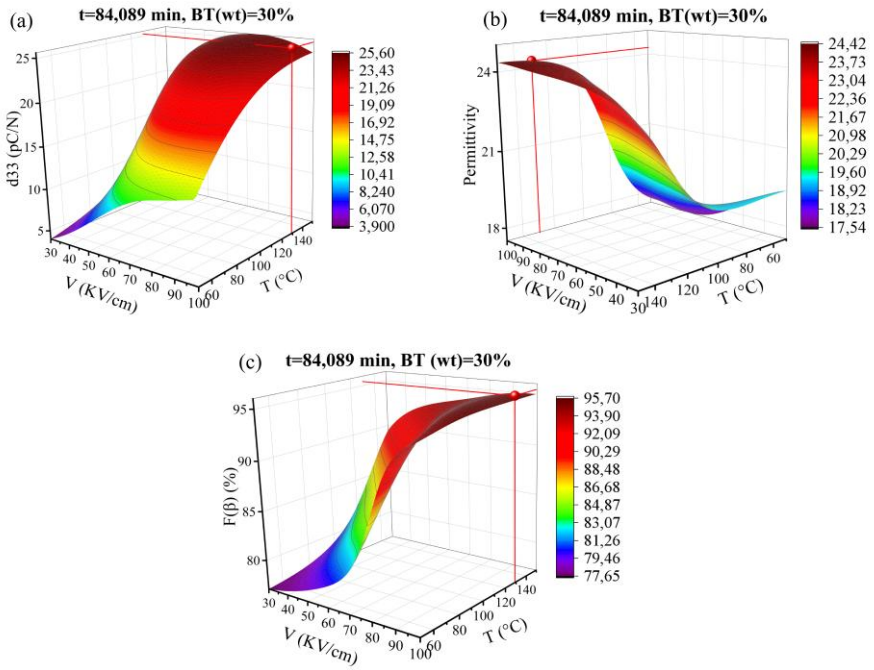

Figure 34: Optimal output values (red spheres) using ANN and genetic algorithm.

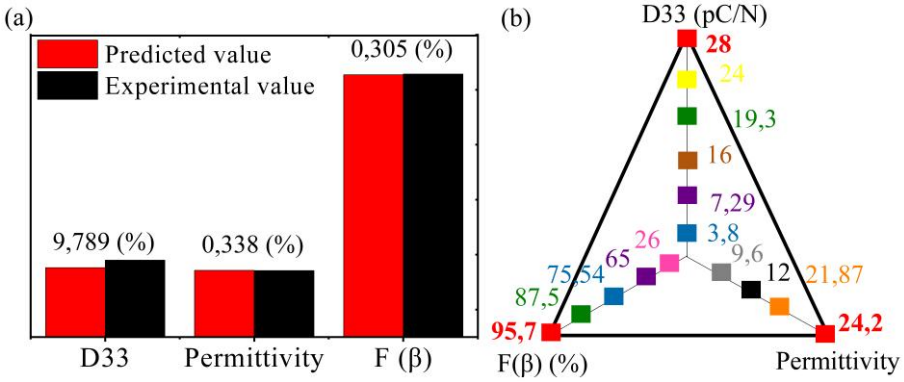

Figure 35: (a) Errors between predicted values and experimental results for the optimal output values, (b) comparison of piezoelectric and dielectric properties of the PVDF/BT nanocomposite under study with other results reported in the literature (Purple: [331], Blue: [332], Yellow: [333], Brown: [334], Green: [335], Black: [336], Gray: [337], Pink: [338], Orange: [339]).

The results show that the optimal input set is poling temperature of 129.989 °C, poling time of 83.089 minutes, poling voltage of 99.532 KV /cm, and a BT content of 30 wt%.

The optimum predicted output values corresponding to this input combination are a d33 coefficient of 25.259 pC/N, a permittivity of 24.282, and a β-phase fraction of 95.435%. Figure 35 clearly shows that the input set (129.989, 83.089, 99.532, 30) yields the optimal piezoelectric and dielectric properties.

The optimal solution found by the genetic algorithm was experimentally validated. Figure 35(a) shows the errors between the predicted and experimental values of the piezoelectric and dielectric properties of the PVDF/BT nanocomposite. The minor errors indicate that the predictions are in excellent agreement with the experiments.

The optimal experimental values for the d33 coefficient, dielectric constant, and F(β) are compared in Figure 35(b) with other values found in previous works.

3.6 Conclusion

In this work, the effect of poling and the addition of fillers on the piezoelectric performances of PVDF (d33 coefficient, dielectric constant, and β-phase fraction) was investigated experimentally and statistically using four process parameters: poling temperature, poling duration, poling voltage, and BT fraction. A Box-Benkhen design was used for experimentation and model building. The influence of the process parameters on the piezoelectric and dielectric properties of PVDF nanocomposites was investigated using ANOVA. An ANN was used to model the variations of piezoelectric and dielectric properties of PVDF/BT nanocomposite as a function of poling parameters and BT mass fraction. The curvatures in the 3D surface plots show a high degree of nonlinearity, indicating a complex relationship between the process parameters and output response.

The ANN model shows that the piezoelectric properties of PVDF increase with the increase of the poling voltage and the poling temperature, and the dielectric property increases with the addition of BT. This is expected because increasing the poling voltage increases the alignment of the molecular dipoles, resulting in a stronger piezoelectric effect. In addition, at higher temperatures, the PVDF material becomes more ductile and allows for greater molecular mobility, leading to more efficient alignment and polarization of the molecules during poling. The addition of BT leads to a high dielectric constant, as BT is a ceramic material with high permittivity.

A genetic algorithm was used to search the high dimensional ANN model and find the optimal poling settings and BT fraction (129.989°C, 83.089 min, 99.532 KV/cm, 30 wt%). With this combination, the coefficient d33, dielectric constant, and β-phase fraction of the PVDF-BT nanocomposite reached 25.259 pC/N, 24.282, and 95.435%, respectively. These optimal values were experimentally validated, and minor errors were found between the predicted and

experimental results. This modeling and optimization approach led to the development of a highly performant piezoelectric nanocomposite that will be used for energy conversion applications.

3.7 Acknowledgments

The authors acknowledge the funding provided by the Natural Sciences and Engineering Research Council (NSERC) of Canada (grant number: CRSNG – RGPIN -2021-02846).

3.8 References

1. Ibtehaj K, Jumali MHH, Al-Bati S. A novel facile preparation method of self-polarized Poly (vinylidene fluorides) nanofiber for high-performance piezoelectric nanogenerator. Polymer. 2020;208:122956.

2. Megdich A, Habibi M, Laperrière L. A Review on 3D printed piezoelectric energy harvesters: Materials, 3D printing techniques, and applications. Materials Today Communications. 2023:105541.

3. Brunengo E, Luciano G, Canu G, Canetti M, Conzatti L, Castellano M, et al. Double-step moulding: An effective method to induce the formation of β-phase in PVDF. Polymer. 2020;193:122345.

4. Kumar RS, Sarathi T, Venkataraman K, Bhattacharyya A. Enhanced piezoelectric properties of polyvinylidene fluoride nanofibers using carbon nanofiber and electrical poling. Materials Letters. 2019;255:126515.

5. Hu X, Ding Z, Fei L, Xiang Y, Lin Y. Wearable piezoelectric nanogenerators based on reduced graphene oxide and in situ polarization-enhanced PVDF-TrFE films. Journal of materials science. 2019;54:6401-9.

6. Yang J, Yao X, Meng Z. Investigation of molecular mechanisms of polyvinylidene fluoride under the effects of temperature, electric poling, and mechanical stretching using molecular dynamics simulations. Polymer. 2022;245:124691.

7. Darestani MT, Chilcott TC, Coster H. Effect of poling time on filtration properties of PVDF membranes treated in intense electric fields. Polymer bulletin. 2014;71:951-64.

8. Lei D, Hu N, Wu L, Ning H, Wang Y, Jin Z, et al. Improvement of the piezoelectricity of PVDF-HFP by CoFe2O4 nanoparticles. Nano Materials Science. 2023.

9. Gade H, Bokka S, Chase GG. Polarization treatments of electrospun PVDF fiber mats. Polymer. 2021;212:123152.

10. Fan J, Gonzalez D, Garcia J, Newell B, Nawrocki RA. The effects of additive manufacturing and electric poling techniques on pvdf thin films: Towards 3d printed functional materials. Smart Materials, Adaptive Structures and Intelligent Systems: American Society of Mechanical Engineers; 2020. p. V001T04A10.

11. Fan J, Newell B, Garcia J, Voyles RM, Nawrocki RA. Contact-poling enhanced, fully 3d printed pvdf pressure sensors: Towards 3d printed functional materials. Smart Materials,

Adaptive Structures and Intelligent Systems: American Society of Mechanical Engineers; 2021. p. V001T02A7.

12. Su YP, Sim LN, Li X, Coster HG, Chong TH. Anti-fouling piezoelectric PVDF membrane: Effect of morphology on dielectric and piezoelectric properties. Journal of Membrane Science. 2021;620:118818.

13. Peng B, Andriukaitis D, Ravikumar C, Valinevicius A, Markevicius V, Navikas D, et al. Quantitative Analysis of Parameters Dependence of PVDF Films Polarization. 2022 26th International Conference Electronics: IEEE; 2022. p. 1-6.

14. Lee SH, Choi YC, Kim MS, Ryu KM, Jeong YG. Fabrication and characterization of piezoelectric composite nanofibers based on poly (vinylidene fluoride-co-hexafluoropropylene) and barium titanate nanoparticle. Fibers and Polymers. 2020;21:473-9.

15. Thakur A, Dam S, Hussain S. Probing the effect of CdS loading on crystallinity and morphology of free standing thin films of CdS/PVDF. Materials Today: Proceedings. 2021;46:6156-60.

16. Song H, Li H, Lim S. Fast 3D digital light process printing of PVDF-HFP composite with electric in situ poling system for piezoelectric applications. Macromolecular Materials and Engineering. 2021;306(10):2100266.

17. Li Y, Feng W, Meng L, Tse KM, Li Z, Huang L, et al. Investigation on in-situ sprayed, annealed and corona poled PVDF-TrFE coatings for guided wave-based structural health monitoring: From crystallization to piezoelectricity. Materials & Design. 2021;199:109415.

18. Kim GH, Hong SM, Seo Y. Piezoelectric properties of poly (vinylidene fluoride) and carbon nanotube blends: β-phase development. Physical chemistry chemical physics. 2009;11(44):10506-12.

19. Pariy I, Ivanova A, Shvartsman V, Lupascu D, Sukhorukov G, Surmeneva M, et al. Poling and annealing of piezoelectric Poly (Vinylidene fluoride) micropillar arrays. Materials Chemistry and Physics. 2020;239:122035.

20. Tu R, Sprague E, Sodano HA. Precipitation-printed high-β phase poly (vinylidene fluoride) for energy harvesting. ACS Applied Materials & Interfaces. 2020;12(52):58072-81.

21. Ikei A, Wissman J, Sampath K, Yesner G, Qadri SN. Tunable in situ 3d-printed pvdf-trfe piezoelectric arrays. Sensors. 2021;21(15):5032.

22. Liu R, Liu Q, He D, Sun G, Li Z, Zhu Y. Enhancement of the piezoelectric property of polyvinylidene fluoride through electroactive phase enrichment and the application in piezoelectric generators. ACS Applied Electronic Materials. 2021;3(4):1804-12.

23. Ippili S, Jella V, Eom J-H, Kim J, Hong S, Choi J-S, et al. An eco-friendly flexible piezoelectric energy harvester that delivers high output performance is based on lead-free MASnI3 films and MASnI3-PVDF composite films. Nano Energy. 2019;57:911-23.

24. Panigrahi BK, Sitikantha D, Bhuyan A, Panda H, Mohanta K. Dielectric and ferroelectric properties of PVDF thin film for biomechanical energy harvesting. Materials Today: Proceedings. 2021;41:335-9.

25. Abdelaziem A, Mohamed AM, Yousry YM, Borayek R, Razeen AS, Zhang N, et al. Effect of poling on the dielectric properties of synthesized β-poly (vinylidene fluoride) foam. Journal of Applied Physics. 2023;133(12).

26. Tabhane GH, Giripunje SM. Robust flower-like ZnO assembled β-PVDF/BT hybrid nanocomposite: Excellent energy harvester. Polymer Testing. 2020;88:106564.

27. Athira B, George A, Vaishna Priya K, Hareesh U, Gowd EB, Surendran KP, et al. High-performance flexible piezoelectric nanogenerator based on electrospun PVDF-BaTiO3 nanofibers for self-powered vibration sensing applications. ACS Applied Materials & Interfaces. 2022;14(39):44239-50.

28. Hermenegildo B, Meira R, Díez A, Correia D, Ribeiro S, Serra J, et al. Ionic liquid modified electroactive polymer-based microenvironments for tissue engineering. Polymer. 2022;246:124731.

29. Mahdavi Varposhti A, Yousefzadeh M, Kowsari E, Latifi M. Enhancement of β-phase crystalline structure and piezoelectric properties of flexible PVDF/ionic liquid surfactant composite nanofibers for potential application in sensing and self-powering. Macromolecular Materials and Engineering. 2020;305(3):1900796.

30. Zeyrek Ongun M, Oguzlar S, Doluel EC, Kartal U, Yurddaskal M. Enhancement of piezoelectric energy-harvesting capacity of electrospun β-PVDF nanogenerators by adding GO and rGO. Journal of Materials Science: Materials in Electronics. 2020;31:1960-8.

31. Deng W, Yang T, Jin L, Yan C, Huang H, Chu X, et al. Cowpea-structured PVDF/ZnO nanofibers based flexible self-powered piezoelectric bending motion sensor towards remote control of gestures. Nano Energy. 2019;55:516-25.

32. Sabry RS, Hussein AD. PVDF: ZnO/BaTiO3 as high out-put piezoelectric nanogenerator. Polymer Testing. 2019;79:106001.

33. Dey R, Bhunia R, Hussain S, Chakraborty BR, Bhar R, Pal AK. Flexible and free-standing films containing cobalt-doped nanocrystalline zinc oxide dispersed in polyvinylidene fluoride matrix: synthesis and characterization. Polymer Bulletin. 2018;75:307-25.

34. Eun JH, Sung SM, Kim MS, Choi BK, Lee JS. Effect of MWCNT content on the mechanical and piezoelectric properties of PVDF nanofibers. Materials & Design. 2021;206:109785.

35. Sharafkhani S, Kokabi M. Ultrathin-shell PVDF/CNT nanocomposite aligned hollow fibers as a sensor/actuator single element. Composites Science and Technology. 2020;200:108425.

36. Kaeopisan A, Wattanasarn H. Piezoelectric PVDF/CNT Flexible Applied on Motorcycle. Integrated Ferroelectrics. 2021;214(1):166-72.

37. Jin Z, Lei D, Wang Y, Wu L, Hu N. Influences of poling temperature and elongation ratio on PVDF-HFP piezoelectric films. Nanotechnology Reviews. 2021;10(1):1009-17.

38. Nilsson E, Lund A, Jonasson C, Johansson C, Hagström B. Poling and characterization of piezoelectric polymer fibers for use in textile sensors. Sensors and Actuators A: Physical. 2013;201:477-86.

39. Lee HJ, Won JS, Lim SC, Lee SG. Preparation and characterization of the PVDF/LDPE thermoplastic composite having piezoelectric property. Polymer Bulletin. 2016;73:2639-47.

40. Elmezayyen AS, Zheng J, Xu C. Simply preparation of self-poled PVDF/nanoceria nanocomposite through one-step formation approach. Polymer Bulletin. 2021;78:5547-66.

41. Song S, Li Y, Wang Q, Zhang C. Facile preparation of high loading filled PVDF/BaTiO 3 piezoelectric composites for selective laser sintering 3D printing. RSC advances. 2021;11(60):37923-31.

42. Tao R, Shi J, Rafiee M, Akbarzadeh A, Therriault D. Fused filament fabrication of PVDF films for piezoelectric sensing and energy harvesting applications. Materials Advances. 2022;3(12):4851-60.

43. Zhang D, Zhang X, Li X, Wang H, Sang X, Zhu G, et al. Enhanced piezoelectric performance of PVDF/BiCl3/ZnO nanofiber-based piezoelectric nanogenerator. European Polymer Journal. 2022;166:110956.

44. Liu Z, Cai M, Zhang X, Yu X, Wang S, Wan X, et al. Cell-Traction-Triggered On-Demand Electrical Stimulation for Neuron-Like Differentiation. Advanced Materials. 2021;33(51):2106317.

45. Guo Y, Xu J, Wu W, Liu S, Zhao J, Pawlikowska E, et al. Ultralight graphene aerogel/PVDF composites for flexible piezoelectric nanogenerators. Composites Communications. 2020;22:100542.

46. Chen J-X, Li J-W, Cheng C-C, Chiu C-W. Piezoelectric property enhancement of PZT/Poly (vinylidenefluoride-co-trifluoroethylene) hybrid films for flexible piezoelectric energy harvesters. ACS omega. 2021;7(1):793-803.

47. Gheorghiu F, Stanculescu R, Curecheriu L, Brunengo E, Stagnaro P, Tiron V, et al. PVDF–ferrite composites with dual magneto-piezoelectric response for flexible electronics applications: synthesis and functional properties. Journal of Materials Science. 2020;55(9):3926-39.

48. Sasmal A, Sen S, Devi PS. Synthesis and characterization of SmFeO3 and its effect on the electrical and energy storage properties of PVDF. Materials Research Bulletin. 2020;130:110941.

49. Bairagi S, Ali SW. A unique piezoelectric nanogenerator composed of melt-spun PVDF/KNN nanorod-based nanocomposite fibre. European Polymer Journal. 2019;116:554-61.

50. Zazoum B. Investigation on Dielectric Permittivity of PVDF/BaTiO3 Nanocomposites Materials by Response Surface Methodology. ECS Journal of Solid State Science and Technology. 2022;11(7):073010.

Chapitre 4: Caractérisation, conception, et fabrication de PEH à base de nanocomposites PVDF/BT

Ce chapitre a fait l'objet d'une publication :
MEGDICH, Amal, HABIBI, Mohamed, LAPERRIÈRE, Luc, LI Zeshi, and ABDIN Yasmine. Advanced 3D-printed PVDF/BT piezoelectric energy harvester with a bio-inspired 3D structure for a self-powered smart mouse. *Nano Energy*, 2024, vol. 128, p. 109876.
Il peut être consulté en ligne à l'adresse suivante :
https://doi.org/10.1016/j.nanoen.2024.109876

Cet article est une continuation directe des travaux présentés dans l'étude précédente. En effet, après avoir sélectionné l'additif optimal à incorporer dans la matrice PVDF et identifié les paramètres de polarisation optimaux pour maximiser la fraction de phase β et le coefficient piézoélectrique d_{33}, il propose ici une approche innovante pour améliorer l'efficacité des nanocomposites PVDF/BT en optimisant non seulement leur composition et leur traitement, mais aussi leur structure géométrique. Bien que les études de l'article précédent aient démontré que l'ajout de charges céramiques et l'optimisation des paramètres de polarisation sont des leviers clés pour améliorer les performances piézoélectriques du PVDF, la structure physique du récupérateur d'énergie joue également un rôle fondamental dans l'amplification des contraintes mécaniques et donc dans la génération de charge électrique.

Dans ce travail, nous avons conçu une structure bio-inspirée, calquée sur les microarchitectures de la plante à fibres de cellulose, afin d'exploiter à la fois la flexibilité des structures 2D et la capacité des structures 3D à générer des contraintes accrues sous l'effet des vibrations mécaniques. Des simulations numériques ont été réalisées afin d'optimiser la conception de cette structure avant son impression 3D grâce à la technologie Fused Deposition Modeling (FDM). Une validation expérimentale a ensuite été menée, démontrant que cette architecture pouvait atteindre une tension en circuit ouvert de 30,8 V, permettant de charger un condensateur de 1 µF à 25 V en seulement 260 s.

Enfin, afin d'évaluer l'applicabilité de ce PEH dans des dispositifs électroniques autonomes, une démonstration a été réalisée à travers le développement d'une souris intelligente. Cette souris auto-alimentée intègre une couche piézoélectrique sous son bouton gauche, convertissant l'énergie mécanique générée par la pression de l'utilisateur en électricité. Cette

application illustre le potentiel des nanocomposites piézoélectriques imprimés en 3D pour remplacer les sources d'énergie traditionnelles dans les dispositifs électroniques et ouvrir la voie à des solutions durables et autonomes dans l'électronique portable.

Ainsi, les travaux de ce troisième article constituent une avancée majeure dans la conception et l'intégration de matériaux piézoélectriques optimisés, en combinant une approche multidisciplinaire allant de la formulation des matériaux à leur application dans des dispositifs concrets. Ils mettent en évidence l'impact de l'optimisation couplée des matériaux et de la conception structurelle, tout en exploitant la flexibilité offerte par la fabrication additive pour développer des solutions innovantes de récupération d'énergie.

Note : des informations complémentaires (supporting information) ont également été publiées pour cet article. Ils se retrouvent en Annexe 2 de cette thèse et sont identifiées par les références « Figure Si » ou « Table Si » dans cet article.

Advanced 3D-printed PVDF/BT piezoelectric energy harvester with a bio-inspired 3D structure for a self-powered smart mouse

Amal Megdich[1], Mohamed Habibi[1*], Luc Laperrière[1] , Zeshi Li[2] , and Yasmine Abdin[2]

[1]Department of mechanical engineering, Université du Québec à Trois-Rivières, Quebec, Canada.

[2]Department of Materials Engineering, The University of British Columbia, Vancouver, BC, Canada.

4.1 Abstract

Piezoelectric polymers such as poly(vinylidene fluoride) (PVDF) exhibit remarkable flexibility, lightweight, durability, and biocompatibility compared to their ceramic counterparts. This unique characteristic makes them highly suitable for harvesting mechanical vibrations. However, conventional manufacturing methods mainly result in two-dimensional (2D) piezoelectric energy harvester (PEHs) structures. This confines the internal stress and, as a result, limits their potential voltage output. This study introduces an innovative bio-inspired three-dimensional (3D) structure crafted through fused deposition modeling (FDM). Barium titanate (BT) nanoparticles were added as piezoelectric fillers to improve the performance of the PEH. The obtained nanocomposite was poled under optimal poling conditions, achieving a β-phase fraction of 95,72%, a piezoelectric charge coefficient (d33) of 28 pC/N, and a permittivity of 24.2 at 100 Hz. A parametric study was performed through numerical analysis, resulting in an effective and optimized structural configuration. The combined excellent piezoelectric properties of the nanocomposite with the optimized structure enabled the PEH to generate an open-circuit voltage of 30.8 V, enabling it to charge a commercial 1 μF capacitor to 25 V in just 260 s. The bioinspired PEH demonstrates its practical application by powering an innovative device known as the "smart mouse," showcasing its utility and potential in real-world applications.

Keywords: PVDF, bio-inspired 3D structure, FDM, BT, smart mouse.

4.2 Introduction

Piezoelectric energy harvesting is one of the most promising methods for harvesting mechanical energy from the environment [340]. This method holds immense potential, especially for the development of portable and wearable self-powered electronic devices [341-343].

The voltage generated by the piezoelectric energy harvester (PEH) is directly proportional to the piezoelectric coefficient, the Young's modulus, the strain, and the sample thickness [344]. Piezoelectric ceramics such as BT and PZT exhibit high piezoelectric coefficients and Young's moduli, enabling them to produce significant output voltages [345-347]. However, their brittleness restricts the amount of strain they can endure, making them unsuitable for flexible applications [348-350]. In response, researchers are turning to polymeric materials due to their flexibility [351, 352]. Flexible piezoelectric materials can absorb significant strain, which is crucial for energy harvesting applications. Among these polymers, polyvinylidene fluoride (PVDF) is characterized by its exceptional long-term stability, lightweight, and flexibility [162, 353, 354]. Nevertheless, piezoelectric polymers generally have lower piezoelectric coefficients than ceramics [355]. To take advantage of the high piezoelectric coefficients of ceramics and the flexibility of polymers, piezoelectric composites are being developed by incorporating ceramic fillers into the polymer matrix [356, 357]. This approach enhances strain generation under applied excitation forces and thus increases piezoelectric performance.

In addition, PVDF predominantly exists in its apolar α-phase, as it is thermodynamically the most stable [358]. However, the polar β-phase offers better piezoelectric properties. The transition of PVDF from the α-phase to the β-phase requires strategic processes like poling [304, 359, 360]. Although the high sensitivity of PVDF properties to poling process parameters such as poling time, temperature and field strength, the optimization of these parameters remains an area of ongoing research due to the complexity of the process.

Another approach to improve strain generation during excitation is to introduce controlled porosity into the structure [361, 362]. Increased porosity often leads to lower mechanical stiffness, resulting in higher deformation and consequently higher voltage output [363, 364]. Previous studies have shown a direct correlation between porosity and piezoelectric performance in foams. In addition, an increase in porosity enhances the hydrostatic strain coefficient ($d_h = d_{33}+2d_{31}$), leading to higher electrical charges [365].

Due to the remarkable correlation between the structure thickness and the output voltage, 3D PEHs have recently attracted a lot of attention owing to the advantageous geometrical stress confinement along the force axis [255, 366]. X. Liu et al. [252] have demonstrated that 3D architectures exhibit exceptional properties, including high piezoelectric output voltage, commendable flexibility, fast response time, excellent linearity over a wide pressure range, and increased structure-dependent sensitivity, properties previously unattainable with conventional 2D structures. However, the production of complex 3D structures using conventional manufacturing methods poses a major challenge. Therefore, the production of

PEHs has evolved over the last three decades from mechanization to automation and then computerization [367]. Additive manufacturing (AM), one of the most advanced manufacturing technologies, has emerged as a key tool for designing and manufacturing various parts from piezoelectric materials, especially those with intricate shapes. C. Yang et al. [243] have developed a porous piezoelectric 3D structure using selective laser sintering (SLS). This innovative approach leverages the 3D structure combined with the porous architecture to fully utilize the available space, amplify the stress-strain effect, and increase the piezoelectric performance. Similarly, H. Pei et al. [255] used fused deposition modeling (FDM) to fabricate PEHs with complex 3D structures and achieved the desired excellent piezoelectric properties [368-370].

However, 3D structures often exhibit a higher stiffness compared to their 2D counterparts. While stiffness is beneficial for maintaining structural integrity, it can compromise the deformability required for effective energy harvesting from mechanical vibrations.

In this work, we present an innovative approach to self-powered microelectronics through the development of a 3D-printed, bio-inspired PEH utilizing PVDF/ BT nanocomposites, with a focus on optimizing the BT concentration. First, BT nanoparticles were incorporated into the PVDF matrix to prepare piezoelectric nanocomposites with different BT weight fractions, aiming to harness the exceptional piezoelectric and dielectric properties of ceramics and the excellent flexibility of polymers. Subsequently, the optimal poling conditions for each PVDF/BT nanocomposite were selected and applied. In addition, a novel bio-inspired structure was introduced combining the advantageous flexibility of 2D structures with the increased stress generation capacity of 3D designs. This innovative approach was motivated by the structure's slender profile, which preserves flexibility while incorporating 3D features to improve compressive stress generation during excitation, thus enhancing voltage output. Numerical simulations were performed to refine the structural design of the PEH and evaluate its performance compared to conventional flat structures. In addition, a second strategy was applied to increase the applied strain in 3D structures by introducing porosity. Consequently, a highly porous structure was implemented, and numerical simulation tests were performed to optimize the element size of the structure. Both structures were 3D printed using FDM 3D printing technology and compared both numerically and experimentally.Finally, in this work, we introduce a novel electronic technology — the Smart Mouse. In this innovative application, the PEH is integrated under the mouse button converting the applied force from button presses into electrical energy. This generated energy has the potential to replace conventional batteries providing a sustainable and efficient power source for wireless mice.

4.3 Experimental section

4.3.1 Materials

The materials utilized in this study include PVDF powder (Mw ≈ 64.04 g/mol), BT powder (Mw ≈ 233.24 g/mol), and N, N-dimethylformamide (DMF) with a purity of 99.8%. All these materials were sourced from Thermo Fisher Scientific.

4.3.2 Preparation of PVDF-Based Nanocomposite Filament

First, PVDF powder was mixed with varying proportions of BT (0, 20, 30, and 40 wt%) and dissolved in DMF solvent. The mixture was stirred at 60 °C at a speed of 1500 rpm for 1 hour until completely dissolved. Following this, the mixture was dried at a temperature of 100°C for a duration of 24 hours to ensure complete evaporation of the DMF solvent. After drying, the obtained polymer composite was cooled to ambient temperature and subsequently cut into pellets. These nanocomposite pellets were then processed through a single-screw extruder operating at a speed of 22 rpm and heated to 190 °C, to produce the PVDF/BT nanocomposite filaments. The diameter of the filament was meticulously maintained at 2.85 ± 0.05 mm using a digital dial indicator for precise control. The final step involved 3D printing the PVDF-based nanocomposite filaments using the printing parameters detailed in Table 17. The synthesis process for preparing PVDF-BT composite is illustrated in Figure 36.

Table 17: Printing parameters.

Parameters	Conditions
Nozzle temperature (°C)	260
Build platform temperature (°C)	100
Layer thickness (mm)	0.4
Infill density (%)	100
Raster angle (deg)	0

The produced samples are labeled as BT-x, where 'x' denotes the weight percentage of BT in the composition.

Table 18 provides a detailed overview of the compositions of the sample.

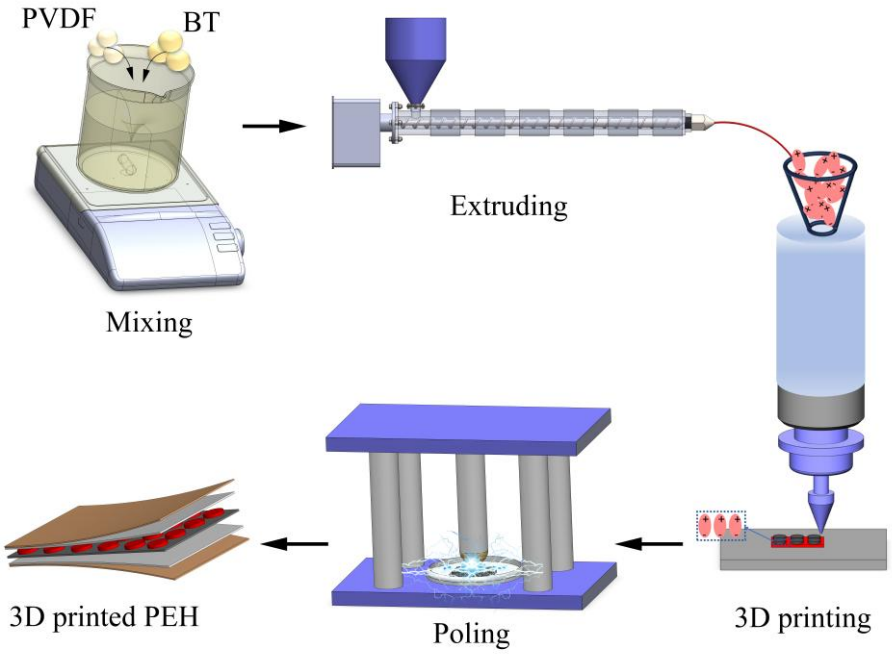

Figure 36: Schematic diagram of the manufacture of PVDF/BT PEH.

Table 18: PVDF-based nanocomposites with varying compositions.

Sample	PVDF	BT
Pure PVDF	100	0
BT-20	80	20
BT-30	70	30
BT-40	60	40

4.3.3 Poling method

The poling was carried out using a high-voltage supply unit (Polyk, USA), with the samples submerged in a silicone oil bath to ensure uniform temperature and prevent electrical discharge.

The samples were heated to the polarization temperature and an optimal electric field was applied and kept constant while the samples cooled down to room temperature.

The specific parameters used during the poling process, such as the magnitude of the electric field, duration of poling, and the temperature of the silicone oil bath, are detailed in Table 19. These parameters were meticulously chosen to optimize the piezoelectric and dielectric properties of the PVDF/BT nanocomposites (Figures S1-S3).

Table 19: Poling parameters for PVDF/BT samples.

Poling parameters	Samples		
	BT-20	BT-30	BT-40
Temperature (°C)	149.999	129.989	133.991
Duration (min)	83.446	83.089	88.672
Voltage (KV/cm)	99.932	99.532	99.999

4.3.4 Characterization

4.3.4.1 Morphological and crystalline structure

The investigation into the crystalline structure of PVDF was conducted using Fourier-transform infrared (FT-IR) spectroscopy. The FT-IR spectra were recorded with a resolution of 4 cm^{-1}, using the Attenuated Total Reflectance (ATR) mode. The ATR mode was used to analyze the representative bands across a wide spectral range of 4000-400 cm^{-1}. The presence and proportion of the β-phase, which is indicative of the piezoelectric properties within the PVDF/BT nanocomposite, were determined by analyzing specific absorption bands associated with this phase. Equation (11), derived from the Lambert-Beer law, was utilized to quantify the β-phase fraction within the nanocomposite based on the intensities of the characteristic absorption bands in the FT-IR spectra. This quantitative analysis provides a direct link between the molecular structure of the PVDF and its piezoelectric performance, enabling a deeper understanding of how the incorporation of BT nanoparticles influences the overall crystalline structure.

$$F(\beta) = \frac{A_\beta}{\left(\frac{k_\beta}{k_\alpha}\right)\cdot A_\alpha + A_\beta} \qquad (11)$$

Where A_α and A_β are the structural absorbances at 766 and 840 cm^{-1}, respectively. K_β (6.1×10^4 cm^2/mol) and K_α (7.7×10^4 cm^2/mol) are the absorption coefficients at the corresponding wavenumber.

Scanning electron microscopy (SEM) was used to examine the surface morphology of the samples and to assess the dispersion of BT nanoparticles within the PVDF matrix. X-ray Diffraction (XRD) analysis was performed to further elucidate the crystalline phases in PVDF and to analyze the overall crystalline structure of the nanocomposite. The XRD measurements were taken over an angle range of 5-80° with a scanning rate of 10°/min, allowing the identification of the crystalline phases within PVDF, with particular attention to the β-phase due to its significance in enhancing the piezoelectric performance of the material. Differential scanning calorimetry (DSC) was used to determine the thermal properties of the samples,

including the melting point (T_m) and the degree of crystallinity (X_c). The DSC scans were performed in the temperature range of 30-200 °C at a heating rate of 10°C/min under a nitrogen atmosphere to prevent oxidative degradation of the samples. The crystallinity was calculated using Equation (12).

$$Xc=\frac{\Delta H_m}{(1-\varphi)\Delta H_{100\%}}\times 100\% , \quad (12)$$

where ΔH_m is the melting enthalpy measured by DSC, $\Delta H_{100\%}$ (105 J/g) is the melting enthalpy of fully crystalline PVDF and φ is the mass fraction of BT.

4.3.4.2 Piezoelectric and dielectric behavior

To evaluate the piezoelectric properties of the PVDF/BT nanocomposite, the piezoelectric coefficient (d33) was measured using a quasi-static d33 meter. This instrument assesses the d33 value by applying a mechanical force to the sample and measuring the electrical charge generated, thus quantifying the material's ability to convert mechanical energy into electrical energy.

The dielectric behavior of the composites, which includes the dielectric constant (εr) and dielectric loss (tan δ), was characterized using an LCR meter. The dielectric constant was determined using equation (13).

$$\varepsilon r = \frac{C_p \times d}{\varepsilon_0 \times A} \quad (13)$$

Where ε_0 is the permittivity of free space, A is the area, and d is the thickness of the material.

4.3.4.3 Mechanical properties

The mechanical properties of the PVDF/BT nanocomposite, particularly the elastic modulus (E_{33}), were crucial not only for conducting accurate finite element analyses but also for understanding the behavior under mechanical stress, essential to design piezoelectric devices and other engineering applications.

To evaluate these properties, the mechanical behavior of the specific specimen, labeled BT-30 was examined through a tensile test. This test was conducted in accordance with ASTM D638 type IV standards. The dimensions of the tensile specimens and the specific parameters used during the 3D printing process are detailed in Figure S4. The outcomes of the tensile tests, which provide insights into the material's response to tensile stress, are illustrated in Figure S5 and summarized in Table S1. These results include the ultimate tensile stress (σ) and Young's modulus (E), calculated using Equation (14) and Equation (15), respectively.

$$\sigma = \frac{F}{S} \quad (14)$$

$$E = \frac{\sigma}{\varepsilon} \tag{15}$$

where F is the ultimate load, S is the sample cross-section, and ε is the tensile strain.

4.4 Results and discussion

Figure 37(a) presents SEM images of the BT-20 sample, which illustrate a uniform dispersion of BT nanoparticles throughout the PVDF matrix and excellent interfacial adhesion.

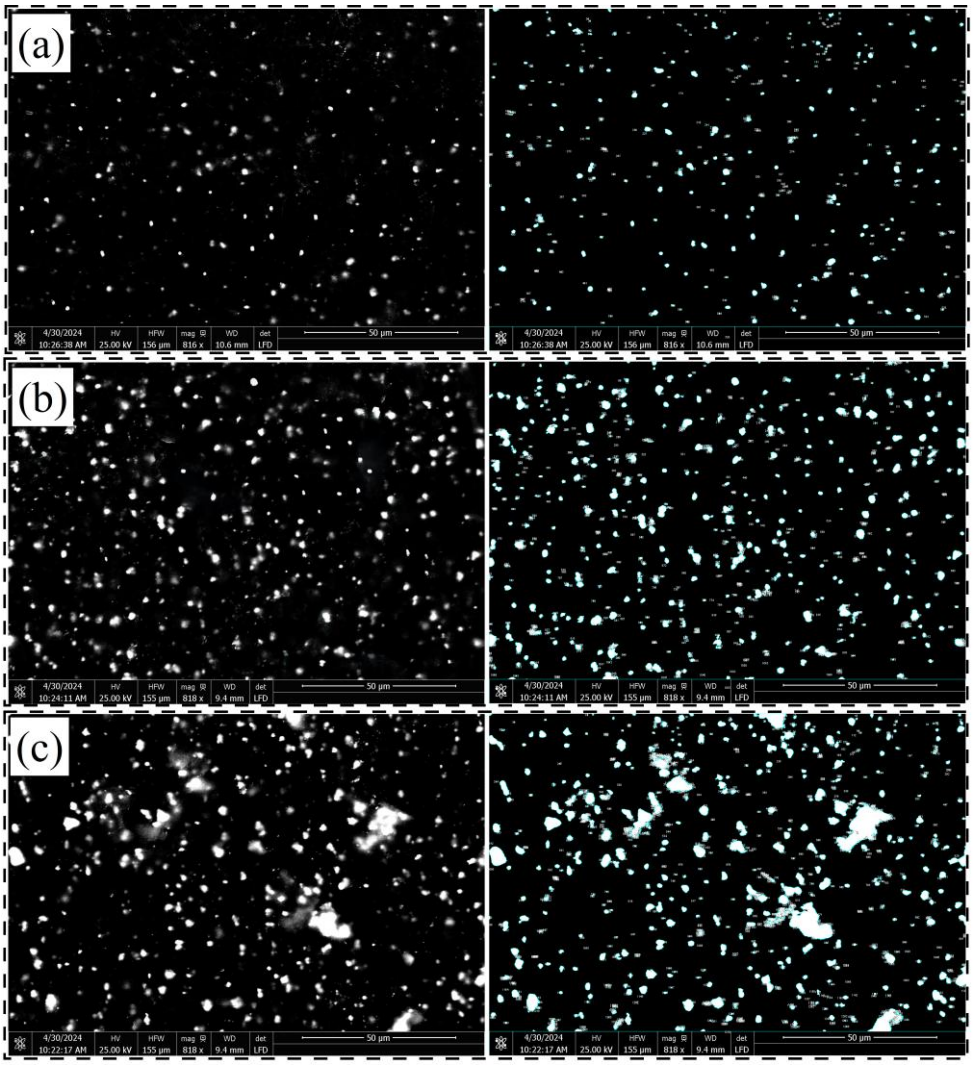

Figure 37: SEM images and particles detection of (a) BT-20, (b) BT-30, and (c) BT-40.

To further clarify the effective distribution of the particles in the matrix, a particle detection analysis was carried out. This homogeneous dispersion and strong interface bonding are attributed to the effective incorporation of the filler materials into the polymer matrix.

In contrast, Figure 37(b), showcasing the BT-30 sample, both the SEM image and the particle detection results depict a slight increase in nanoparticle agglomeration due to the higher loading of nanofillers content. Despite this, the overall dispersion remains relatively uniform,

indicating a controlled distribution of nanoparticles even at increased concentrations.

However, Figure 37(c), corresponding to the BT-40, reveals considerable defects and significant nanoparticle agglomeration. Such extensive agglomeration disrupts the uniformity of the nanocomposite structure, which could detrimentally impact its functional properties, particularly in terms of piezoelectric and mechanical properties.

The agglomeration suggests a threshold beyond which the addition of more nanoparticles leads to diminishing performances, highlighting the importance of optimizing filler content to maintain the balance between enhanced properties and structural integrity.

This absence is attributed to the limited infrared (IR) absorption of BT in FTIR spectra, mainly due to its ionic nature and crystal structure. The perovskite-type crystal structure of BT, characterized by ionic bonds between barium (Ba^{2+}) and titanium (Ti^{4+}) ions, tends to vibrate at frequencies outside the typical FTIR range. Consequently, the peaks detected in FTIR of PVDF/BT nanocomposites correspond primarily to PVDF phases. These results confirm the enhanced crystallization of the samples in the piezoelectrically favorable β-phase.

Using Equation 11, the β-phase crystallization fraction was calculated, with the outcomes, both pre- and post-poling, illustrated in Figure 38(b) and detailed in Table 20. Compared to the 41.357% β-phase in pure PVDF, the incorporation of 20 wt% BT, especially when combined with the poling process, significantly increases the β-phase proportion to 93.524%. This notable increase can be attributed to the role of BT nanoparticles as nucleating agents within the PVDF matrix, effectively promoting the alignment of PVDF molecules into the β-phase structure.

The highest β-phase content, reaching 95.727%, is attained with the incorporation of 30 wt% BT. This represents the optimal filler concentration for inducing the β-phase transition.

Figure 38(c) illustrates the XRD patterns of pure PVDF and its nanocomposites with varying concentrations of BT. In the pure PVDF sample, distinct reflection peaks are observed at 2θ of 17.6, 18.3, 19.9, and 26.5°. These peaks are characteristic of the (100), (020), (110), and (021) crystallographic planes, respectively, and are indicative of the α-phase of PVDF. With the introduction of BT nanoparticles into the PVDF matrix, there is a noticeable decrease in the intensity of these α-phase peaks, accompanied by the emergence and predominance of a new peak at 2θ = 20.6°. This peak is attributed to the β-phase of PVDF, aligning with the FT-IR analysis results. Moreover, the XRD patterns reveal diffraction peaks at 2θ angles of 23.1, 33.3, 39.2, and 44.09°, which correspond to the (100), (110), (200), and (210) reflections of the BT nanoparticles. Moreover, XRD analysis of the BT-30 composite revealed the appearance of new phases at a 2θ angle of 30.84 and 31.7°, attributed to electrostatic interactions between the

polar fluorine atoms of PVDF and the polarizable oxygen and barium ions of BT. This newfound phases at the PVDF-BT interface improve interfacial interaction facilitating stress transfer between the polymer matrix and the piezoelectric filler. This dynamic enables a more efficient conversion of mechanical energy into electrical energy. Thus, the 30% BT composition ensures an optimal balance, promoting favorable interactions between PVDF and BT, thus promoting nucleation and growth of the new phases.

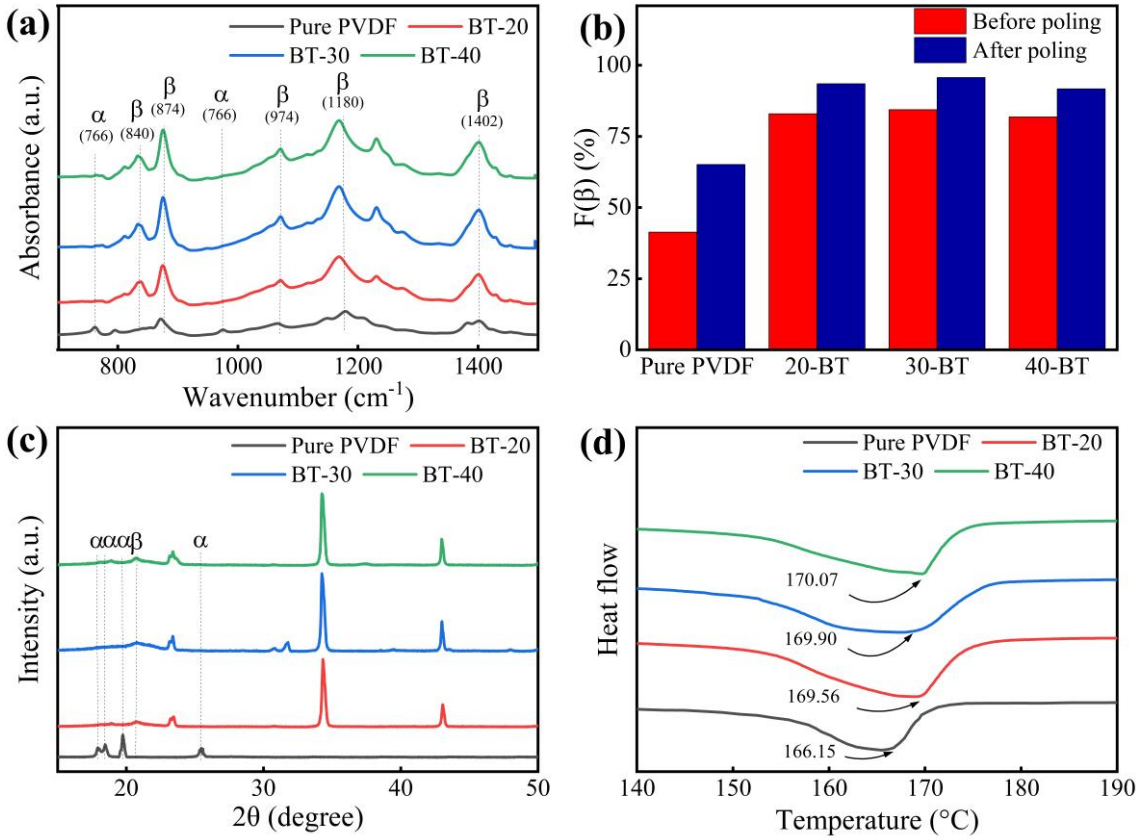

Figure 38: Spectroscopic and thermal analysis of PVDF/BT nanocomposites before and after poling : (a) FT-IR spectra of PVDF, BT, and PVDF/BT 3D printed samples (b) β-phase content of 3D-printed PVDF and PVDF/BT samples before and after poling (c) X-ray diffraction patterns of the FDM 3D-printed PVDF and PVDF/BT samples. (d) DSC curves of PVDF and PVDF/BT samples (heating curve).

Figure 38(d) presents the differential scanning calorimetry (DSC) analysis of the samples, offering insights into their melting behavior. The DSC curves and the parameters summarized in Table 20 show a shift in the melting temperature (Tm) peaks of the PVDF/BT nanocomposites towards higher temperatures with the addition of BT. This shift is indicative of the enhanced thermal stability conferred by the BT nanoparticles, which is expected due to their ceramic nature and inherently high melting point. Moreover, the interaction between BT

nanoparticles and PVDF molecules facilitate a higher degree of crystallinity within the PVDF matrix. This is evidenced by the highest crystallinity percentage of 62.32% observed in the BT-40 sample, suggesting that the presence of BT supports the formation of a more ordered and crystalline PVDF structure, further enhancing its piezoelectric properties.

Table 20: Thermal properties of PVDF and PVDF/ BT nanocomposites determined by DSC test and F(β) values measured with FT-IR data.

Sample	T_m (°C)	ΔH_m (J/g)	X_c (%)	F(β) (%)
Pure PVDF	166.15	57.667	54.920	41.357
BT-20	169.56	49.858	59.354	93.524
BT-30	169.90	45.273	61.595	95.727
BT-40	170.07	39.262	62.320	91.847

As shown in Figure 39(a), the investigation into the dielectric properties of PVDF/BT nanocomposites across a frequency range of $10^2 - 10^4$ Hz revealed a significant decline in the dielectric constant (εr) with an increase in frequency, particularly pronounced at lower frequencies. This behavior is likely due to the Maxwell-Wagner-Sillars (MWS) interfacial polarization at the interfaces between PVDF and BT nanoparticles.

In Figure 39(b), pure PVDF exhibits a moderate dielectric constant (ε = 9.50 at 100 Hz). The incorporation of BT nanoparticles leads to a progressive increase in the dielectric constant within the nanocomposites, reaching a peak of 24.8 for the BT-40 sample. The addition of BT also increases the dielectric loss, as illustrated in Figure 39(c), where the dielectric loss in the nanocomposites exceeds that of pure PVDF across the entire frequency spectrum, with a particular emphasis on low frequencies. Despite the rise in dielectric loss with increased BT content, the peak value remains relatively low (0.022 at 100 Hz), suggesting a minor detrimental effect on the material's practical applications. As shown in Figure 39(d), the BT-30 sample showcases the highest d33 value of 28 pC/N. However, increasing the BT content to 40 wt% results in a reduced d33 value of 22 pC/N. This decrease is attributable to the excessive BT incorporation, which introduces defects into the PVDF matrix, disrupting the proper alignment of PVDF chains and reducing the degree of polarization.

To improve the mechanical response of piezoelectric energy harvesters (PEHs) under applied mechanical simulations, the transition from 2D structures to 3D structures is essential to increase the normal stress during compression. Although 3D blocks offer higher mechanical stress, they are more difficult to deform during mechanical vibrations. Thus, this work proposes a novel approach to design 2D structures with 3D features inspired by the microarchitecture of

cellulose fiber plants (Figure 40(a)). These structures combine the flexibility of 2D structures with the greater width of 3D blocks, allowing easy deformation under mechanical vibrations while distributing the compressive forces over a larger area, resulting in higher mechanical stresses.

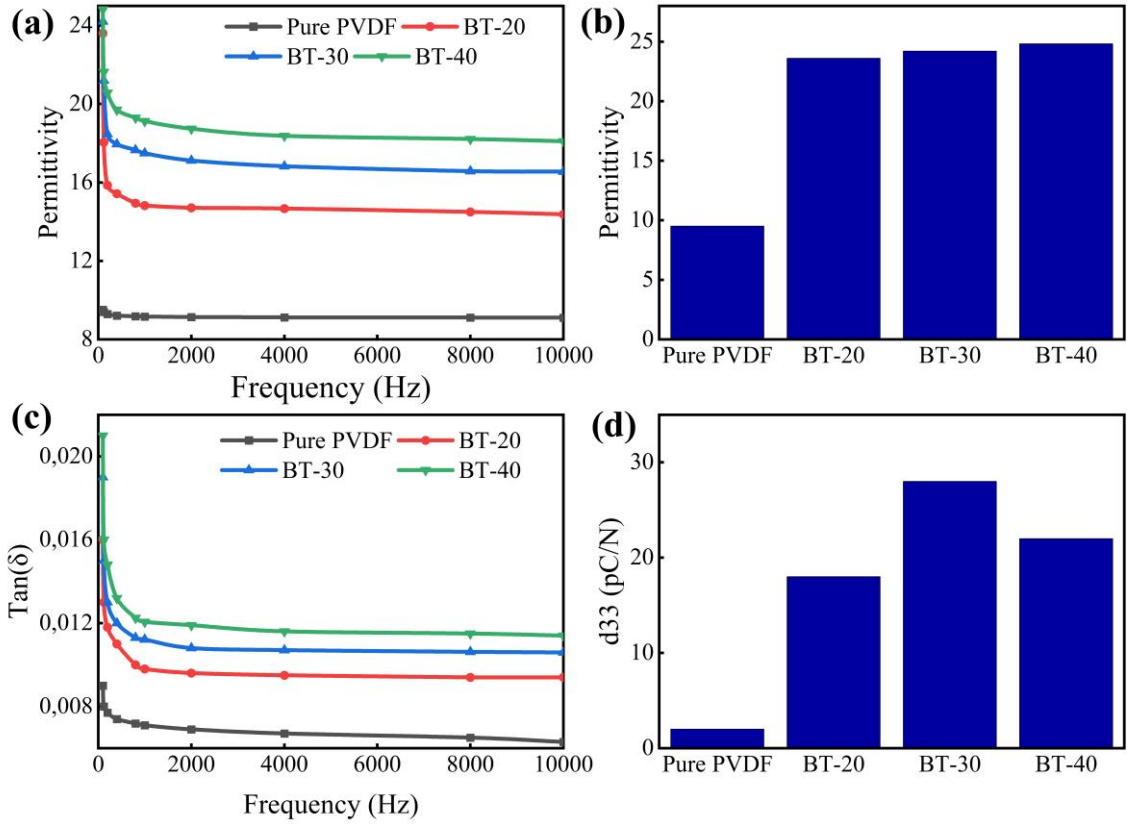

Figure 39: Dielectric and piezoelectric performance of PVDF/BT nanocomposites : (a) Frequency dependence of the dielectric constant (b) dielectric constant of the four prepared samples at 100 Hz (c) Frequency dependence of the dielectric loss (d) d33 coefficients of the piezoelectric nanocomposites.

FE simulations were performed using COMSOL software to compare the performance of this structure with three different cylinder dimensions and features to the 2D conventionnel structure (Figure 40). The dimensions and design details of the bio-inspired structures are shown in Figure S6, offering insights into the potential for leveraging natural microstructures to enhance the performance of piezoelectric devices.

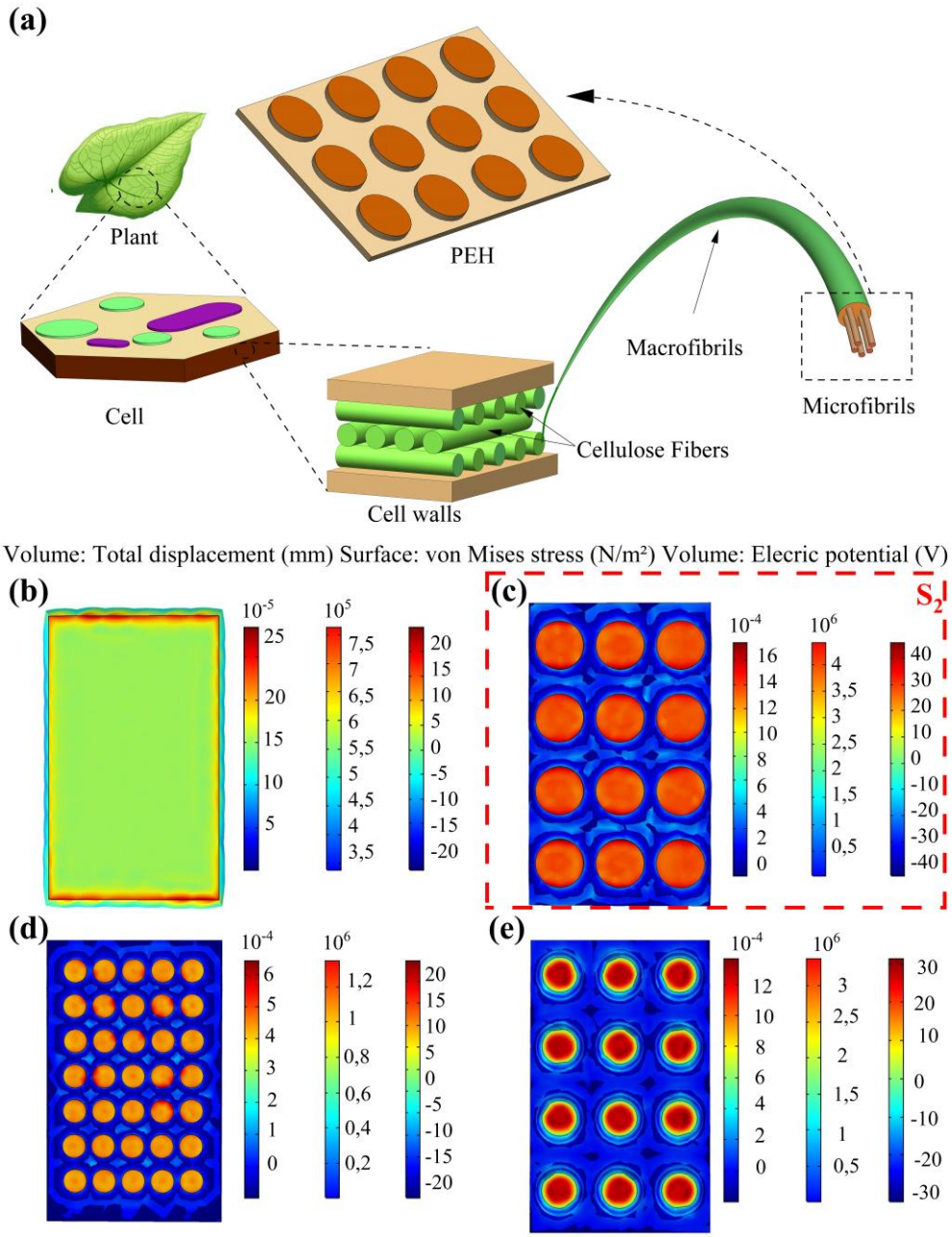

Figure 40: Bioinspired design and optimization of 3D PEH structures : (a) Bio-inspiration of the PEH structure from the micro-structure of the cellulose fiber plants; (b) optimization of the PEH structure design based on the FEM simulation results of the mechanical and electrical performances of the flat 2D structure, and (c) the bioinspired 3D structure consisting of 12 simple cylinders, (d) 35 simple cylinders, and (e) 12 cylinders with bevels.

In addition, introducing porosity into the structure can further increase its deformability. Porous structures exhibit lower stiffness and higher compliance compared to solid structures, allowing for easier deformation in response to applied forces. In this context, three lattice structures with different element sizes were proposed. As can be seen in Figure 41, Finite Element (FE) simulations have shown that these structures generate better compressive stresses and strains

compared to conventional flat plates.

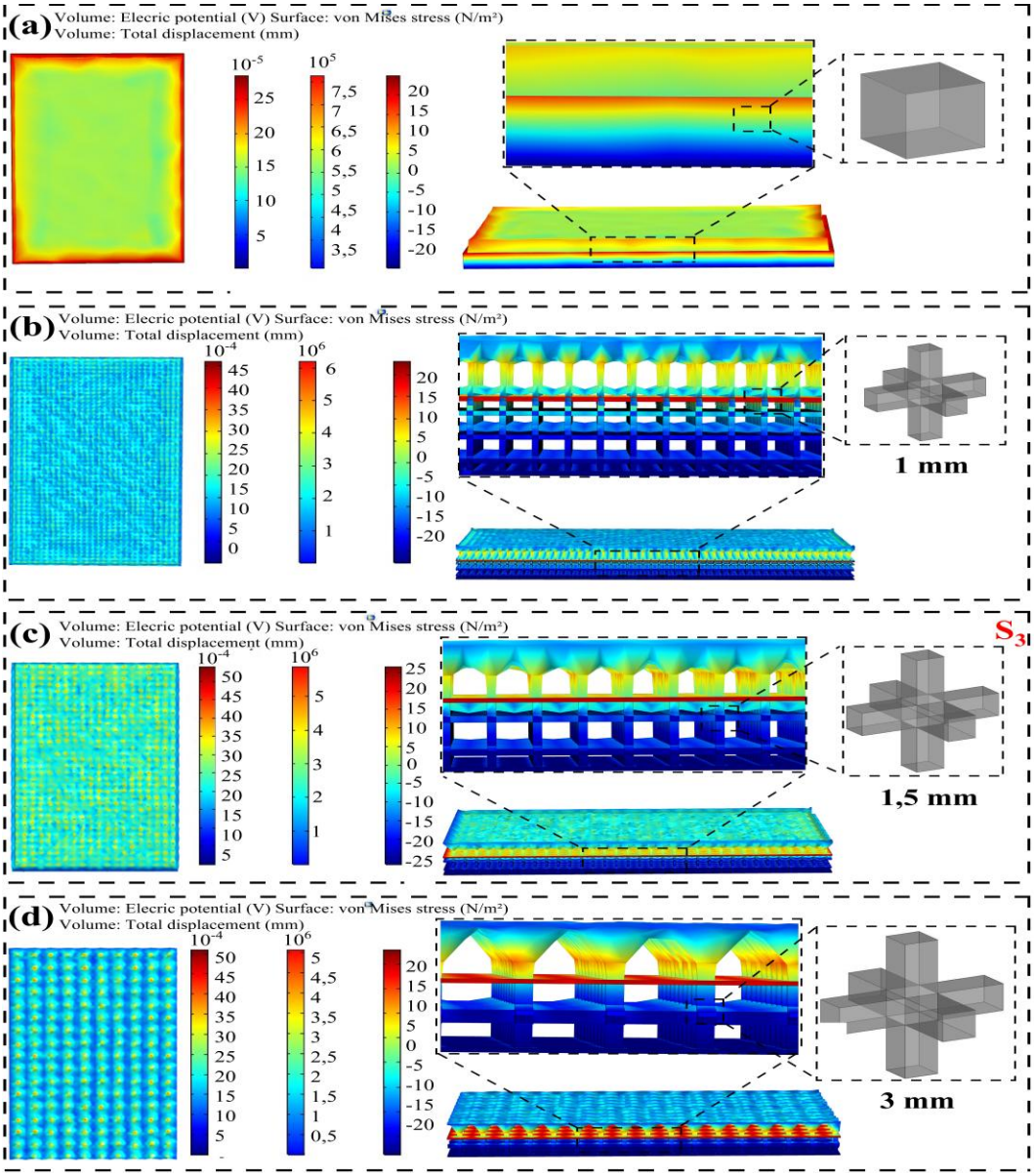

Figure 41: Influence of structural porosity on the performance of compact and porous PEHs： Influence of structural porosity on the performance of compact and porous PEHs ：Optimization of the PEH structure based on FEM simulation results of the mechanical and electrical performances of (a) the compact flat structure and the porous structures with different element sizes (b) 1 mm, (c) 1.5 mm, and (d) 3 mm.

Improved flexibility and compliance in porous grid structures improve power generation, making the harvester more sensitive and effective in low force environments. Moreover, the presence of pores in the structure means that less material is required, resulting in a lower overall weight. This weight reduction makes the PEH particularly suitable for weight-sensitive applications, such as small electronic devices.

Both configurations demonstrated superior compressive stresses and voltage outputs compared to the conventional flat plates. The performances of these designs, especially the optimal designs S2 and S3 (see Figure 40(c) and Figure 41(c), respectively), would then be experimentally tested and compared.

The fabrication of PVDF-based PEHs with varying concentrations of BT nanoparticles involved 3D printing the devices, as depicted in Figure 42(a). Post-printing, an annealing process was employed to mitigate the warping effects caused by internal stresses originating from the different thermal contraction behaviors of PVDF and BT during the cooling phase post-3D printing. Figure 42(b) highlights the excellent flexibility of the 3D-printed BT-30 sample (3×5cm), demonstrating its potential for applications requiring mechanical adaptability. The final assembly of the PEHs, illustrated in Figure 42(c), consist of a piezoelectric core layer between silver electrodes, all secured together with Kapton tape. The piezoelectric performance of these devices was assessed using a custom testing setup, as shown in Figure 42(d). This setup utilized computer-controlled excitation to apply oscillating pressure shocks to the PEHs. The resulting piezoelectric outputs were captured and analyzed with an oscilloscope. A detailed view of the actual testing apparatus is presented in Figure S7. The electrical outputs of the PEHs, specifically the short-circuit current (Isc) and open-circuit voltage (Voc), are presented in Figure 42(e) and 43(f), respectively. These figures reveal a significant enhancement in both Voc and Isc with increased BT content. This improvement can be attributed to two primary factors: firstly, the augmented concentration of BT nanoparticles elevates the density of electroactive fillers within the nanocomposites, directly enhancing their piezoelectric properties. Secondly, the BT particles induce stronger interfacial polarizations between the filler and the matrix, further boosting the piezoelectric output. At a BT concentration of 30 wt%, the Voc and Isc values peaked at 25.7 V and 3.78 μA, respectively, markedly surpassing the performance metrics of pure PVDF, which stood at 2.66 V for Voc and 0.42 μA for Isc. However, an upward adjustment of BT content to 40 wt% led to a decline in piezoelectric efficiency, likely due to the suboptimal dispersion of BT particles at higher concentrations. This phenomenon underscores the critical balance between filler content and material dispersion for optimizing the piezoelectric performance of nanocomposites. A video showcasing these results is available in Supplementary Video SV1, providing a visual demonstration of the PEHs' piezoelectric capabilities. To validate the numerical simulations and optimize the design of the PEH structure, we fabricated the four structures, including the traditional flat design and the three bio-inspired structures, using FDM 3D printing. Identical

boundary conditions in both experimental and numerical tests allowed a direct comparison of the results. Figure 42(g) shows a comparative analysis of voltage output with visual representations of the 3D printed and numerically tested structures. The observed errors were: 14.396% for the flat structure, 13.636% for the bio-inspired structure with 12 sample cylinders, 12.087% for the bio-inspired structure with 42 sample cylinders and 4.761% for the bio-inspired structure with 12 cylinders with bevels. The deviations are primarily due to the numerical simplifications, which cannot fully capture the complicated behavior of 3D-printed structures.

To assess the impact of various input parameters on the performance of PEHs, experiments were conducted with different excitation frequencies (1 Hz, 2.5 Hz, and 5 Hz) and sample compression ratios (0.3 mm, 0.4 mm, and 0.5 mm). The outcomes, elaborated in Figure S8, reveal significant insights. Figure 43(a) establishes a clear relationship between axial displacement and the output voltages of the PEHs. Figure 43(b) shows an increase in output voltage with rising excitation frequency, which can be attributed to the system's approach to its natural frequency, thereby optimizing its vibrational response. The comparative analysis of three different PEH structures—the conventional flat design (S1), the bio-inspired structure (S2), and the porous structure (S3)—highlighted the superior performance of the bio-inspired design (S2). S2 achieved the highest Voc of 30.8 V, surpassing the 25.7 V of S1 and 28.1 V of S3, as showcased in Figure 43(c). The inset of Figure 44 presents images of the three distinct 3D-printed structures coated with silver electrode paint. Given the intricate structural details of structure (S3), characterized by its high porosity, especially the voids within the layers plane which need to be filled to ensure the printability of subsequent layers (as highlighted in red in Figure 43(d)), we implemented a multi-material 3D printing approach. Polyvinyl alcohol (PVA) was used to fill these voids. PVA was chosen due to its high solubility in water, which ensures that the PVDF/BT nanocomposite remains intact during the dissolution process. The dissolution process took about 3 hours at 70°C and high stirring speed and resulted in the desired final structure. The entire printing process is shown in Figure 43(d), with the inset showing the real structure during and after printing. Furthermore, numerical simulation tests showed that during compression, the compressive stress was concentrated on the vertical features (Figure 43(e)). Consequently, the poling process of this structure focused mainly on these features. Despite the high flexibility and lightweight nature of this structure, the concentrated stress on the vertical features could lead to material fatigue and failure, which would affect the durability and longevity of the (PEH). Therefore, structure S2 is identified as

the more suitable design for the engineered PEH. The durability assessment conducted on the optimal S2 structure (Figure 43(f)) demonstrated its robustness, with the Voc value remaining consistent even after 1400 impacts, highlighting the structure's excellent durability and resilience. An energy storage experiment was performed where the alternating current generated by the PEH was converted to direct current via a bridge rectifier to charge a commercial capacitor.

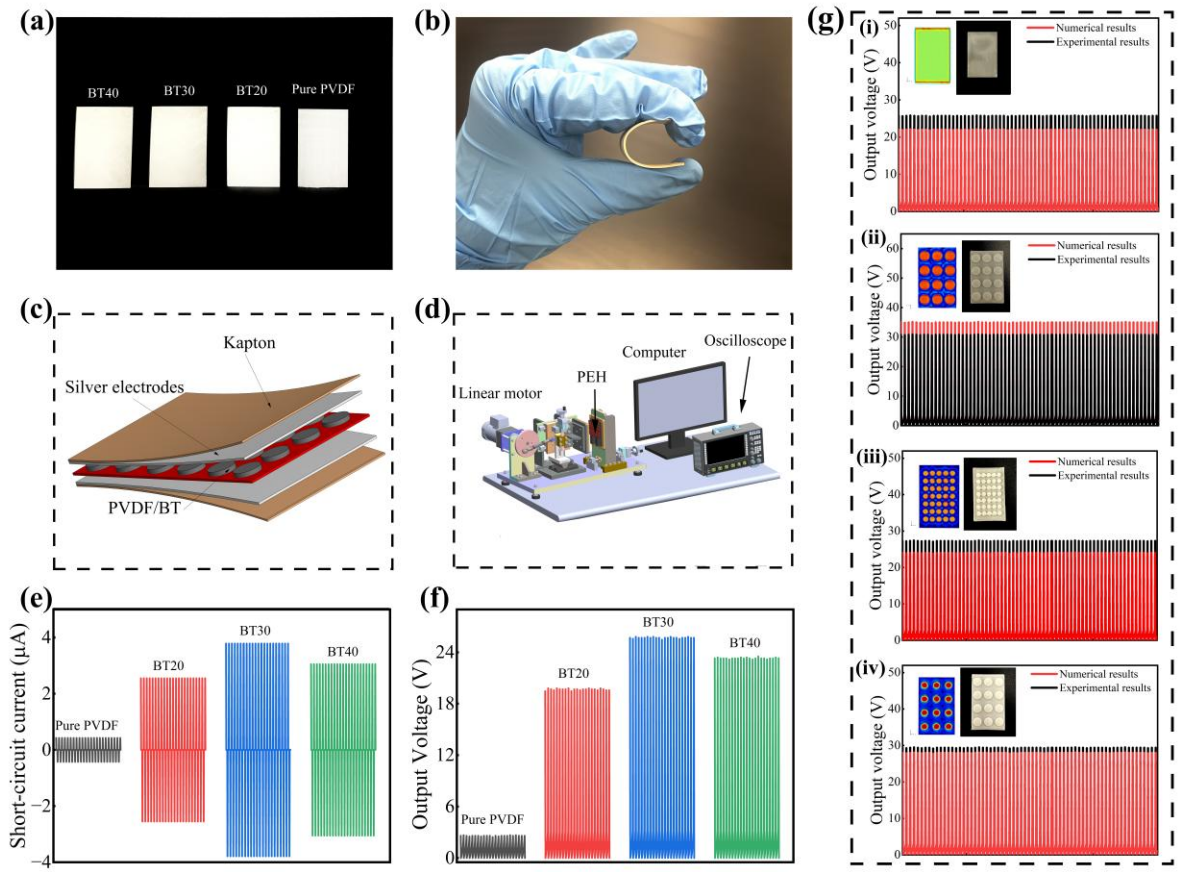

Figure 42: Fabrication and performance testing of 3D-printed PEHs with various compositions : (a) schematic diagram of the 3D printed PEHs with different compositions; (b) photo showing the high flexibility of the 3D printed BT-30 sample; (c) schematic diagram of the PEHs; (d) schematic diagram of the piezoelectric testing system;(e) short circuit current and (f) open-circuit voltage signals of the PEHS with the four tested compositions; (g) Numerical and experimental comparative analysis of the performances of (i) the flat structure, (ii) the bio-inspired structure with 12 sample cylinders, (iii) the bio-inspired structure with 42 simple cylinders, and (iv) the bio-inspired structure with 12 cylinders with bevels.

Remarkably, as depicted in Figure 43(g), the PEH was able to charge a 1 μF 50 V capacitor to 25 V within 260 seconds. The inset in Figure 43(g) displays the energy storage circuit utilized in this test. The PEH's potential to serve as an alternative power source for wireless devices,

such as a smart mouse, is further explored. The operating mechanism of the device is detailed in Figure S9. Numerical simulations, shown in Figure 43(h), demonstrated that the Voc generated by a single mouse button can reach nearly 4 V

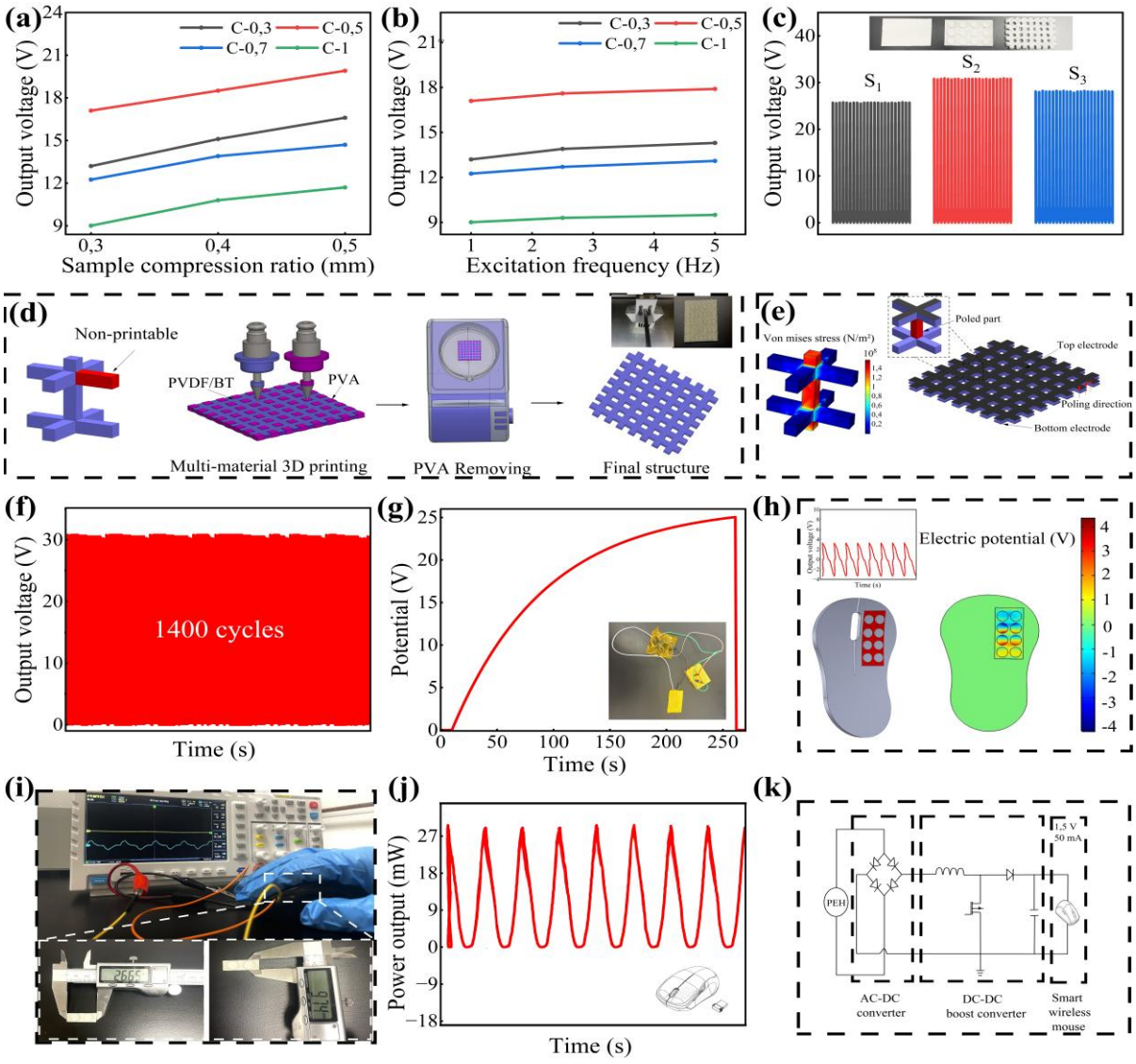

Figure 43: Durability and practical application of bioinspired PEHs under cyclic loading : (a) sample compression ratio and (b) frequency dependence of the open-circuit voltage signals; (c) comparison of the performances of the flat traditional structure (S1), the bio-inspired structure (S2), and the high porous structure (S3); (d) fabrication, and (e) poling processes of S3 (f) the output voltage of 1400 cycles illustrating the durability of S2; (g) curve of S2 charging the capacitor for 250 s; (h) numerical simulation and experimental validation of the application; (i) photo of the application during testing and the dimensions of the PEH; (j) simulated power signals of PEH when pressing the mouse button, (k) schematic of the application's circuit of S2 integrated into a self-powered system for charging a smart wireless mouse.

Experimental results, shown in the inset of Figure 44(h), confirm the PEH ability to generate a Voc of 3.28 V, confirming the numerical results. Figure 43(j) shows an experimental setup demonstrating the integration of the PEH into a smart wireless mouse, providing a real-world perspective on the device's size and implementation. Supplementary Video SV2 provides a dynamic visual representation of these results. Moreover, the PEH generated a voltage of 1.99 V across a 220ohm resistor, resulting in a current of 9 mA, as seen in supplementary video SV3. This means that the PEH can generate a power of approximately 29.651 mW by a finger press, as shown in Figure 43(j), further confirming its practical application. Figure 43(k) shows the complete circuit design, including AC-DC rectification and DC-DC conversion. The alternating current generated by the PEH must be converted to direct current using a bridge rectifier. The DC energy should then be stored in a capacitor. Once sufficient energy has been accumulated, a voltage regulator should be used to supply the mouse with a constant voltage of 1.5 V.

4.5 Conclusion

In this study, we introduced an innovative approach that leverages 3D printing technology and piezoelectric materials to develop PEHs using PVDF/BT nanocomposites. The incorporation of BT nanoparticles played a pivotal role in aligning the PVDF molecules into the highly desirable β-phase, significantly enhancing the piezoelectric properties of the composite. Among the various compositions tested, the BT-30 nanocomposite emerged as the most promising, demonstrating an impressive piezoelectric charge coefficient (d33) of 28 pC/N and a β-phase fraction of 95.727% post optimal poling. A key aspect of this work was the structural optimization of the PEHs through numerical simulations, which led to the development of bio-inspired 3D structures. These structures showed superior mechanical and electrical responses compared to traditional flat designs. Specifically, a flexible 3D-printed bio-inspired PEH, based on the BT-30 nanocomposite and featuring an optimized design, achieved an open-circuit voltage of 30.8 V and was capable of charging a 1 μF capacitor to 25 V within 260 seconds. A novel application for these PEHs, termed the "smart mouse," was also demonstrated, where the PEHs efficiently converted the mechanical energy generated from mouse button presses into electrical energy. Both experimental and simulation results confirmed that the PEHs could generate over 3 V per mouse button press, showcasing the potential of this technology in powering small electronic devices. This work represents a significant advancement in the field of smart electronics, highlighting the potential of 3D-printed, bio-inspired PEHs in various applications. The successful integration of optimized structural designs and piezoelectric

nanocomposites opens new avenues for the development of self-powered devices and sustainable energy solutions.

4.6 Acknowledgements

The authors acknowledge the funding provided by the Natural Sciences and Engineering Research Council (NSERC) of Canada in the form of Discovery Grants (Grant Number: CRSNG – RGPIN -2021-02846).

4.7 References

[1] C. Shao, Y. Zhao, L. Qu, Recent advances in highly integrated energy conversion and storage system, SusMat 2(2) (2022) 142-160.
[2] J. Lv, J. Chen, P.S. Lee, Sustainable wearable energy storage devices self-charged by human-body bioenergy, SusMat 1(2) (2021) 285-302.
[3] M. Wu, Y. Wang, S. Gao, R. Wang, C. Ma, Z. Tang, N. Bao, W. Wu, F. Fan, W. Wu, Solution-synthesized chiral piezoelectric selenium nanowires for wearable self-powered human-integrated monitoring, Nano energy 56 (2019) 693-699.
[4] J. Wang, H.Y. Man, C. Meng, P. Liu, S. Li, H.S. Kwok, Y. Zi, A fully self-powered, natural-light-enabled fiber-optic vibration sensing solution, SusMat 1(4) (2021) 593-602.
[5] H. Jiang, L. Song, Z.-X. Huang, M. Liu, Y. Zhao, S. Zhang, J. Guo, Y. Li, Q. Wang, J.-P. Qu, A novel concept of hierarchical porous structural design on enhancing output performance of piezoelectric nanogenerator, Nano Energy 104 (2022) 107921.
[6] M.C. Sekhar, E. Veena, N.S. Kumar, K.C.B. Naidu, A. Mallikarjuna, D.B. Basha, A review on piezoelectric materials and their applications, Crystal Research and Technology 58(2) (2023) 2200130.
[7] C. Chen, X. Wang, Y. Wang, D. Yang, F. Yao, W. Zhang, B. Wang, G.A. Sewvandi, D. Yang, D. Hu, Additive manufacturing of piezoelectric materials, Advanced Functional Materials 30(52) (2020) 2005141.
[8] X. Wang, Y. Huan, S. Ji, Y. Zhu, T. Wei, Z. Cheng, Ultra-high piezoelectric performance by rational tuning of heterovalent-ion doping in lead-free piezoelectric ceramics, Nano Energy 101 (2022) 107580.
[9] H. Kim, S. Yun, K. Kim, W. Kim, J. Ryu, H.G. Nam, S.M. Han, S. Jeon, S. Hong, Breaking the elastic limit of piezoelectric ceramics using nanostructures: A case study using ZnO, Nano Energy 78 (2020) 105259.
[10] J. Huang, M. Yao, X. Yao, A novel approach to improving the electromechanical properties of PZT-based piezoelectric ceramics via a grain coating modification strategy, Ceramics International 47(11) (2021) 16294-16302.
[11] T. Wittinanon, R. Rianyoi, A. Chaipanich, Effect of polyvinylidene fluoride on the fracture microstructure characteristics and piezoelectric and mechanical properties of 0-3 barium zirconate titanate ceramic-cement composites, Journal of the European Ceramic Society 40(14) (2020) 4886-4893.
[12] Y. Wu, Y. Ma, H. Zheng, S. Ramakrishna, Piezoelectric materials for flexible and wearable electronics: A review, Materials & Design 211 (2021) 110164.
[13] C. Zhang, Y. Li, W. Kang, X. Liu, Q. Wang, Current advances and future perspectives of additive manufacturing for functional polymeric materials and devices, SusMat 1(1) (2021) 127-147.

[14] S. Mohammadpourfazeli, S. Arash, A. Ansari, S. Yang, K. Mallick, R. Bagherzadeh, Future prospects and recent developments of polyvinylidene fluoride (PVDF) piezoelectric polymer; fabrication methods, structure, and electro-mechanical properties, RSC advances 13(1) (2023) 370-387.
[15] R. Dallaev, T. Pisarenko, D. Sobola, F. Orudzhev, S. Ramazanov, T. Trčka, Brief review of PVDF properties and applications potential, Polymers 14(22) (2022) 4793.
[16] L. Lu, W. Ding, J. Liu, B. Yang, Flexible PVDF based piezoelectric nanogenerators, Nano Energy 78 (2020) 105251.
[17] M. Smith, S. Kar-Narayan, Piezoelectric polymers: theory, challenges and opportunities, International Materials Reviews 67(1) (2022) 65-88.
[18] P. Eltouby, I. Shyha, C. Li, J. Khaliq, Factors affecting the piezoelectric performance of ceramic-polymer composites: A comprehensive review, Ceramics International 47(13) (2021) 17813-17825.
[19] S. Im, S.Y. Cho, J.-H. Cho, G.-T. Hwang, A.I. Kingon, S.D. Bu, W. Jo, S.-H. Kim, C.K. Jeong, Study on relaxor polymer interface matrix for piezoelectric nanocomposite generators, Applied Surface Science 613 (2023) 156031.
[20] A. Megdich, M. Habibi, L. Laperrière, A review on 3D printed piezoelectric energy harvesters: materials, 3D printing techniques, and applications, Materials Today Communications 35 (2023) 105541.
[21] A. De Neef, C. Samuel, H. Amorín, G. Stoclet, R. Jiménez, P. Dubois, J. Soulestin, J.-M. Raquez, Beta phase crystallization and ferro-and piezoelectric performances of melt-processed Poly (vinylidene difluoride) Blends with Poly (methyl methacrylate) copolymers containing ionizable moieties, ACS Applied Polymer Materials 2(9) (2020) 3766-3780.
[22] E. Brunengo, G. Luciano, G. Canu, M. Canetti, L. Conzatti, M. Castellano, P. Stagnaro, Double-step moulding: An effective method to induce the formation of β-phase in PVDF, Polymer 193 (2020) 122345.
[23] A.M. Chandran, S. Varun, P.K.S. Mural, Development of self-poled PVDF/MWNT flexible nanocomposites with a boosted electroactive β-phase, New Journal of Chemistry 44(34) (2020) 14578-14591.
[24] M. Yan, J. Zhong, S. Liu, Z. Xiao, X. Yuan, D. Zhai, K. Zhou, Z. Li, D. Zhang, C. Bowen, Flexible pillar-base structured piezocomposite with aligned porosity for piezoelectric energy harvesting, Nano Energy 88 (2021) 106278.
[25] M.M. Abolhasani, M. Naebe, M. Hassanpour Amiri, K. Shirvanimoghaddam, S. Anwar, J.J. Michels, K. Asadi, Hierarchically structured porous piezoelectric polymer nanofibers for energy harvesting, Advanced Science 7(13) (2020) 2000517.
[26] S. Song, Y. Han, Y. Li, Q. Wang, 3D printed piezoelectric porous structure with enhanced output performance and stress-electricity response for road energy harvesting, Additive Manufacturing 72 (2023) 103625.
[27] H. Pei, J. Jing, Y. Chen, J. Guo, N. Chen, 3D printing of PVDF-based piezoelectric nanogenerator from programmable metamaterial design: Promising strategy for flexible electronic skin, Nano Energy 109 (2023) 108303.
[28] R.W. Lewis, A.C. Dent, R. Stevens, C.R. Bowen, Microstructural modelling of the polarization and properties of porous ferroelectrics, Smart materials and structures 20(8) (2011) 085002.
[29] X. Yuan, X. Gao, J. Yang, X. Shen, Z. Li, S. You, Z. Wang, S. Dong, The large piezoelectricity and high power density of a 3D-printed multilayer copolymer in a rugby ball-structured mechanical energy harvester, Energy & Environmental Science 13(1) (2020) 152-161.

[30] H. Pei, Y. Xie, Y. Xiong, Q. Lv, Y. Chen, A novel polarization-free 3D printing strategy for fabrication of poly (Vinylidene fluoride) based nanocomposite piezoelectric energy harvester, Composites Part B: Engineering 225 (2021) 109312.
[31] X. Liu, J. Liu, L. He, Y. Shang, C. Zhang, 3D printed piezoelectric-regulable cells with customized electromechanical response distribution for intelligent sensing, Advanced Functional Materials 32(26) (2022) 2201274.
[32] Z. Abdelhamid, H. Mohamed, S. Kelouwani, The use of machine learning in process–structure–property modeling for material extrusion additive manufacturing: a state-of-the-art review, Journal of the Brazilian Society of Mechanical Sciences and Engineering 46(2) (2024) 70.
[33] C. Yang, F. Chen, J. Sun, N. Chen, Boosted mechanical piezoelectric energy harvesting of polyvinylidene fluoride/barium titanate composite porous foam based on three-dimensional printing and foaming technology, ACS omega 6(45) (2021) 30769-30778.
[34] A. Ziadia, M. Habibi, S. Kelouwani, Machine learning study of the effect of process parameters on tensile strength of FFF PLA and PLA-CF, Eng 4(4) (2023) 2741-2763.
[35] L. Koroglu, E. Ayas, N. Ay, 3D printing of polyvinylidene fluoride based piezoelectric nanocomposites: an overview, Macromolecular Materials and Engineering 306(10) (2021) 2100277.
[36] H. Zhang, F. Ke, J. Shao, C. Wang, H. Wang, Y. Chen, One-step fabrication of highly sensitive pressure sensor by all FDM printing, Composites Science and Technology 226 (2022) 109531.

Chapitre 5: Caractérisation, conception, et fabrication de PEH à base de nanocomposites PVDF/MWCNTs

Ce chapitre a fait l'objet d'une publication :
MEGDICH, Amal, HABIBI, Mohamed, LAPERRIÈRE, Luc, LI Zeshi, and ABDIN Yasmine. Enhanced piezoelectric performance of PVDF/MWCNTs energy harvester through a 3D-printed multimodal auxetic structure for smart security systems. *Materials Today Sustainability,* 2024, vol. 27, p. 100847.
Il peut être consulté en ligne à l'adresse suivante :
https://doi.org/10.1016/j.mtsust.2024.100847

Ce travail s'inscrit dans la continuité des recherches menées sur l'optimisation et l'intégration de nanocomposites piézoélectriques à base de PVDF. Après avoir identifié et optimisé l'incorporation de charges céramiques et examiné l'impact des paramètres de polarisation sur les propriétés piézoélectriques et diélectriques du PVDF, nous avons proposé une approche synergiquement liée à la modélisation et à la conception avancée de structures imprimées en 3D pour une efficacité maximale des PEHs. Les travaux précédents ont démontré l'impact des conceptions tridimensionnelles sur l'amélioration de la récupération d'énergie et ont abouti à la fabrication de dispositifs innovants intégrés dans des applications pratiques telles que la souris intelligente. Dans cette continuité, l'objectif est de proposer une nouvelle méthode d'amélioration de la récupération de l'énergie grâce à l'intégration de nanotubes de carbone multiparois (MWCNTs) dans la matrice en PVDF, en exploitant une structure auxétique imprimée en 3D. Les structures auxétiques se distinguent par un coefficient de Poisson négatif qui permet une génération de contraintes dans deux directions à la fois. Cela facilite l'activation simultanée des modes piézoélectriques d_{31}, d_{32} et d_{33}.

Dans ce travail, un nanocomposite PVDF/MWCNTs a été formulé avec différentes fractions massiques de MWCNTs et optimisé pour maximiser la fraction de phase β du PVDF. Le matériau a ensuite été utilisé pour fabriquer par impression 3D une structure auxétique réentrante soigneusement paramétrée par des simulations numériques. Des tests expérimentaux ont démontré que cette architecture pouvait générer une tension en circuit ouvert de 28,2 V en

mode d_{33} sous une force de compression et de 14,8 V en modes d_{31} et d_{32} sous une force de traction. Cette performance supérieure a également permis au dispositif de charger un condensateur de 1 µF à 22 V en seulement 260 secondes.

L'intégration de cette structure innovante dans un système de sécurité intelligent constitue une avancée majeure pour les applications industrielles et résidentielles. L'article propose une application dans laquelle des PEH PVDF/MWCNTs imprimés en 3D sont intégrés sous des dalles de sol pour convertir la pression des pas en signaux électriques, déclenchant ainsi un système d'alarme. Cette approche exploite la génération d'énergie piézoélectrique pour la détection d'intrusion dans des environnements de haute sécurité. L'efficacité du dispositif a été validée expérimentalement, démontrant une réponse rapide de 42 ms et une tension de sortie atteignant 19,8 V sous l'effet d'une personne de 60 kg.

Ces travaux marquent ainsi une avancée significative dans la conception de systèmes de récupération d'énergie piézoélectrique imprimés en 3D, combinant optimisation avancée des matériaux et architectures structurelles pour maximiser leur efficacité. Ils ouvrent également de nouvelles perspectives pour le développement de capteurs autonomes intégrés dans des infrastructures intelligentes, renforçant ainsi la synergie entre la fabrication additive, l'optimisation des nanocomposites et les applications pratiques en sécurité et surveillance.

Note : des informations complémentaires (supporting information) ont également été publiées pour cet article. Ils se retrouvent en Annexe 3 de cette thèse et sont identifiées par les références « Figure Si » ou « Table Si » dans cet article.

Enhanced piezoelectric performance of PVDF/MWCNTs energy harvester through a 3D-printed multimodal auxetic structure for smart security systems

Amal Megdich[1], Mohamed Habibi[1*], Luc Laperrière[1], Zeshi Li[2], and Yasmine Abdin[2]

[1]Department of mechanical engineering, Université du Québec à Trois-Rivières, Quebec, Canada.

[2]Department of Materials Engineering, The University of British Columbia, Vancouver, BC, Canada.

5.1 Abstract

Piezoelectric energy harvesters (PEHs) have attracted considerable attention over recent decades for their ability to convert mechanical energy into electrical energy. However, the current landscape is characterized by a lack of structural variety, which constrains the potential for notable performance improvements and the expansion of applications of these devices. To address these challenges, three distinct metamaterial structures are investigated through numerical simulations in this study. An auxetic, reentrant shape with carefully optimized dimensions was found as the best choice for the development of an efficient Polyvinylidene fluoride/multi-walled carbon nanotubes (PVDF/MWCNTs) PEH with optimized composition. This structure exhibits a remarkable capability to activate three different piezoelectric modes. Given it is polarization in the z-direction, the structure activates both d31 and d32 modes upon stretching in the x-direction, benefitting from the structure's negative Poisson's ratio and generating an open circuit voltage of 14.8 V. In contrast, compression in the z-direction activates the d33 mode, resulting in an open-circuit voltage of 28.2 V. This design allows the harvester to charge a 1 μF capacitor to 22 V within 260 seconds. The structure's feasibility is further evidenced by its fabrication using Fused Deposition Modeling (FDM) 3D printing technology. To further extend its practicality and real-world application, the PEH can be seamlessly integrated into large-scale commercial, industrial, and residential flooring, offering a novel approach to security systems. In this innovative approach, the PVDF/MWCNTs PEH converts the compressive force of footsteps into electrical signals. These signals serve as triggers for an integrated alarm system. Essentially, the electrical signal functions as a switch: its transmission acts like a closed switch that triggers the activation of the alarm system. Conversely, the absence of the signal is an open switch, indicating that no external force is acting on the tiles and a safe condition is maintained. Remarkably, the PEH can produce a voltage of 19.8 V when activated by the footsteps of a 60 kg person, demonstrating its practical utility.

Keywords: PVDF, MWCNTs, auxetic structure, FDM, security system.

5.2 Introduction

In an era of rapid technological advancement, the pursuit of efficient energy harvesting systems is of paramount importance. Piezoelectric materials have emerged as key players in this endeavor [371-373]. They have attracted considerable attention due to their remarkable ability to convert mechanical stress into electrical energy, offering a promising avenue for sensing devices [342, 374, 375]. Piezoelectric materials can be broadly categorized into polymers and ceramics. Ceramic materials, such as lead zirconate titanate (PZT), barium titanate (BaTiO3) and zinc oxide (ZnO), exhibit high piezoelectric coefficients[376-379]. However, these materials are brittle by nature and are difficult to shape into intricate 3D structures [348, 380]. In contrast, piezoelectric polymers offer a more flexible alternative. These materials can absorb significant strain, a crucial factor in energy harvesting applications [354, 355, 381]. and are therefore suitable for applications that require conformable or stretchable devices. Polyvinylidene fluoride (PVDF) stands out among piezoelectric polymers for its exceptional flexibility, light weight, low-cost processing, biocompatibility, long-lasting durability, excellent chemical resistance, and tunable properties [382-384]. The piezoelectric properties of PVDF primarily stem from its β-phase, which results from the dipole orientation within the crystalline structure of the polymer [79, 358, 385]. A widely used and effective method to increase the β-phase content in PVDF is the incorporation of nucleating nanofillers such as barium titanate (BT), graphene and MWCNTs [240, 384, 386-388]. MWCNTs in particular have attracted considerable attention as conductive fillers due to their ability to provide mechanical reinforcement, improve electrical conductivity and facilitate charge transport within the composite, ultimately leading to improved piezoelectric performance[389, 390].

On the other hand, beyond the inherent properties of piezoelectric materials, structural design featuring appealing flexibility has emerged as another way to improve piezoelectric conversion efficiency [391-393]. For example, micropatterns such as pyramids, pillars and shell arrays on thin films have succeeded in increasing the mechanical to electrical output voltage [394-396]. However, most of the above approaches are based on two-dimensional piezoelectric thin films, which exhibit a rather limited effective out-of-plane stress–strain response, resulting in unsatisfactory piezoelectric sensitivity over a wide pressure range. In contrast, 3D PEHs have attracted great interest recently as researchers recognize the promising potential to improve electromechanical response through appropriate 3D structural design [255]. For example, E. Mancuso et al. [397] fabricated porous scaffolds made of BT piezoceramics with

optimal porosity. This structure enabled high stress concentration, resulting in superior piezoelectric performance. Similarly, J. Li et al. [398] developed a 3D printed bulk structure consisting of periodically intercalated soft PVDF-HFP/Li-KNN ferroelectrics and hard electrode PLA/carbon layers. The resulting material exhibited a significantly improved d33 value of over 150 pC N−1 as well as superior mechanical toughness exceeding ~5.5 MPa $m^{1/2}$, more than three times higher than conventional piezoceramics.

Despite the ability of these 3D structures to generate high electrical voltage in d33 mode, they predominantly feature a unidirectional and unimodal piezoelectric system. Among the various piezoelectric modes, d31, d32, and d33 are preferred for voltage generation [399]. To achieve these modes, electrode placement, stress, and polarity orientation within the piezoelectric material must be carefully considered. While most piezoelectric energy harvesters in the literature activate either d31 mode or d33 mode, optimal device design requires effective coupling of mechanical energy into the harvester to maximize mechanical energy absorption.

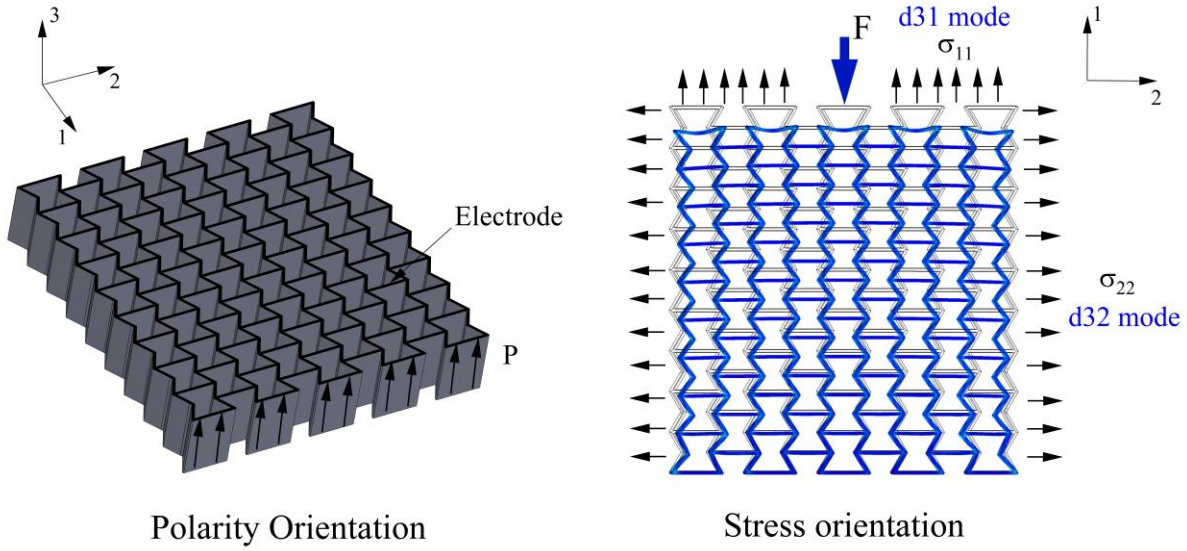

Figure 44: Operational principle of PEH with auxetic structure polarized in 3-direction in both d31 and d32 modes under a single excitation force.

In recent years, artificial materials and structures have made remarkable progress in various scientific and technological fields. In particular, auxetic structures characterized by a negative Poisson's ratio have attracted considerable attention due to their exceptional mechanical behavior [400, 401]. These materials and structures expand laterally when stretched and contract laterally when compressed, unlike conventional materials. This counterintuitive property allows the simultaneous activation of d31 and d32 modes by a single excitation force, as shown

in Figure 44. While the concept of exploiting the multidirectional motion of these structures for dual-mode energy harvesting is innovative, the integration of auxetic elements into energy harvesting systems remains an emerging area of research. The complexity and high porosity of these structures require reliable manufacturing techniques. Fused Deposition Modeling (FDM) 3D printing has emerged as a highly effective technique to produce piezoelectric devices. Its capacity for producing multi-materials and complex structures, including auxetic designs, makes it a preferred choice [368, 402]. FDM offers several advantages, including minimal waste generation and simplified manufacturing processes [367, 403, 404].

This study marks a breakthrough in the field of piezoelectric energy harvesting, encompassing the entire workflow from conceptual design to fabrication and experimental validation. We have developed a highly efficient PVDF/MWCNTs nanocomposite with an optimally tailored composition, which is then poled and shaped using FDM 3D printing. What sets our approach apart is the introduction of a carefully crafted three-dimensional, reentrant auxetic structure. This innovative network design promotes multidirectional and multimodal functionality. Using the negative Poisson's ratio of this structure, a single excitation in the x-direction triggers a biaxial displacement in both the x- and y-directions, simultaneously activating the d31 and d32 modes. Similarly, excitation in the z-direction enables activation of the d33 mode of the piezoelectric material. Consequently, this structure facilitates the exploitation of three different modes, enhancing the ability for elastic and dense energy recovery. By leveraging optimized materials, advanced manufacturing techniques and creative design, we have improved the performance of PVDF/MWCNTs PEHs to unprecedented levels. The integration of these PEHs plays a pivotal role in the development of a novel alarm system suitable for commercial, industrial, and residential applications. This innovative approach involves embedding the PVDF/MWCNTs PEH under the tiles of large businesses, factories, and residences to convert the compressive force of footsteps into electrical signals to trigger an integrated alarm system. This innovative system represents a substantial leap forward in security technology.

5.3 Experimental section

5.3.1 Materials

The materials utilized in this study include PVDF powder (Mw ≈ 64.04 g/mol), MWCNTs powder (Mw ≈ 16.043 g/mol), and N, N-dimethylformamide (DMF) with a purity of 99.8%. All these materials were sourced from Thermo Fisher Scientific.

5.3.2 Preparation of PVDF-Based Nanocomposite Filament

The preparation of the PVDF-MWCNTs nanocomposite starts by dissolving PVDF powder in DMF solvent. Then, different concentrations of MWCNTs (0, 0.3, 0.5, 0.7 and 1 wt%) were integrated into the solution. This mixture was continuously stirred at 60°C and 1500 rpm for 1 hour until complete dispersion was achieved. Following this, the obtained solution was dried at 130°C for 24 hours to ensure the complete evaporation of the DMF solvent. The resulting polymer composite was allowed to cool to ambient temperature before being cut into pellets. These pellets were then processed through a single-screw extruder (Wellzoom Type B Desktop Filament Extruder 3D Printer) operating at a rotation speed of 70 rpm and an extrusion temperature of 220°C.

Table 21: Printing parameters.

Parameters	Conditions
Nozzle temp (°C)	300
Build platform temp (°C)	110
Layer thickness (mm)	0.2
Infill density (%)	100
Raster angle (°)	90

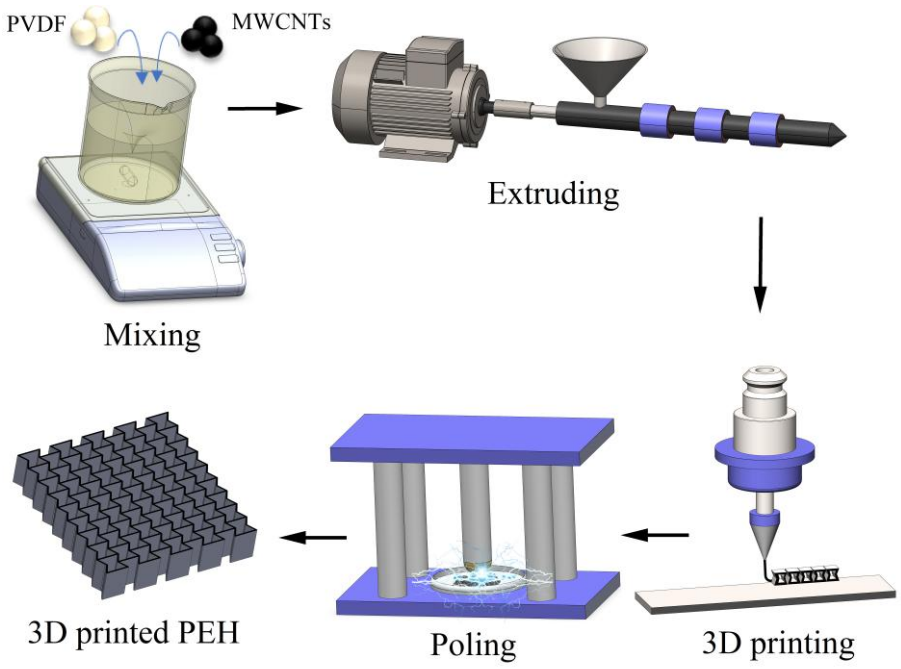

Figure 45: Schematic diagram of PVDF/MWCNTs PEH fabrication process.

The filament diameter was accurately maintained at 2.85 ± 0.05 mm using a conveyor belt system. Finally, a high-grade 3D printer (Ultimaker) was employed to print the PVDF-based nanocomposite PEH. Table 21 provides an overview of the main printing settings used in this study. A schematic representation of the synthesis process is shown in Figure 45.

The samples are labeled as follows: Pure PVDF, denoted as 'Pure PVDF'. The remaining samples are labeled C-x, where 'x' represents the weight percentage of MWCNTs in the composition.

5.3.3 Poling method

Before polarization, the samples were coated with a silver electrode to ensure proper electrical conductivity. Following this preparation, they were subjected to a polarization process using a high-voltage supply system. This procedure involved polarizing the samples for one hour at a temperature of 100°C, with the samples submerged in a silicone oil bath to maintain a controlled environment. During this process, a 100 kV/cm electric field was applied across the top and bottom electrodes during polarization to ensure the samples achieved the intended piezoelectric properties.

5.3.4 Characterization

5.3.4.1 Morphological and crystalline structure

The crystalline structure of the PVDF/MWCNTs nanocomposite was thoroughly investigated using a comprehensive set of analytical methods. Fourier transform infrared (FT-IR) spectroscopy, conducted at a high resolution of 4 cm^{-1} in ATR mode, was used to study characteristic bands across a spectral r ange from 4000 to 400 cm^{-1}.

To quantify the β-phase fraction within the PVDF/MWCNTs nanocomposite, Equation (16) was applied, leveraging the Lambert-Beer law as observed in the FT-IR spectra:

$$F(\beta) = \frac{A_\beta}{\left(\frac{k_\beta}{k_\alpha}\right)\cdot A_\alpha + A_\beta}, \qquad (16)$$

where A_α and A_β denote the absorbances corresponding to the α and β structural phases at 766 and 840 cm^{1}, respectively. K_β (6.1 × 10^4 cm^2/mol) and K_α (7.7 × 10^4 cm^2/mol) are the absorption coefficients at the corresponding wavenumber. This methodological approach allows for a precise determination of the β-phase's presence within the nanocomposite, which is critical for understanding its piezoelectric properties.

Scanning electron microscopy (SEM) was utilized for a detailed investigation of the sample morphology and the dispersion of the MWCNTs within the PVDF matrix. To further elucidate the crystalline phases and structural characteristics of PVDF, X-ray diffraction (XRD) analysis was performed. Scanning was performed in an angle range of 5-80°, with a controlled scan rate of 10°/min. Additionally, differential scanning calorimetry (DSC) was employed to determine the main thermal properties of the samples, with a specific focus on determining their melting point (Tm) and degree of crystallinity (Xc). These DSC measurements were performed over a temperature spectrum extending from 30 to 200°C, with a constant heating rate of 10°C/min, all within a nitrogen atmosphere to prevent oxidation and other atmospheric interference. The crystallinity (Xc) of the samples was determined using the following equation:

$$Xc=\frac{\Delta H_m}{(1-\varphi)\Delta H_{100\%}}\times 100\%, \qquad (17)$$

where ΔH_m is the melting enthalpy as recorded by the DSC, $\Delta H_{100\%}$ (105 J/g) is the melting enthalpy corresponding to the completely crystallized PVDF, and φ is the mass fraction of MWCNTs within the nanocomposite.

5.3.4.2 Piezoelectric and dielectric behavior

To evaluate the piezoelectric properties of the PVDF/BT nanocomposite, a quasi-static d33 meter, known by the name of Berlincourt Piezoelectric Meter (PKD3-2000 from PolyK USA), was employed. This device precisely measures piezoelectric coefficients by applying a controlled mechanical force onto the sample and then measuring the resultant electrical charge. Essentially, this process allows a quantitative analysis of the material's proficiency in converting mechanical energy to electrical energy.

Furthermore, the dielectric properties of the nanocomposites were accurately evaluated using an LCR meter (Electric Bridge Resistance Capacitance Tester Digital LCR Meter) through a double-probe method. This precise measurement approach facilitated the accurate determination of critical parameters, such as the dielectric constant and dielectric loss, providing valuable insights into the electrical behavior of the material. The dielectric constant was calculated using the following equation:

$$\varepsilon_r = \frac{C_P \times d}{\varepsilon_0 \times A}, \qquad (18)$$

where Cp is capacitance, ε_0 is permittivity of free space, A is the area, and d is the thickness of the material.

5.4 Results and discussion

5.4.1 Characterization results

Figure 46 shows a comprehensive visual representation with SEM images of the raw materials PVDF and MWCNTs as well as an XRD analysis of the as-received MWCNTs powder. In Figure 46(a), the SEM image shows that the PVDF particles exhibit generally spherical shapes. The inset in Figure 46(a) provides a high magnification SEM image of a single PVDF particle, showcasing a size of almost 200 microns and a surface with non-smooth features. This roughness is indicative of the presence of a high α-phase content in the as-received PVDF. The α-phase is known for its ordered and densely packed structure, which often manifests itself in surface irregularities and roughness.

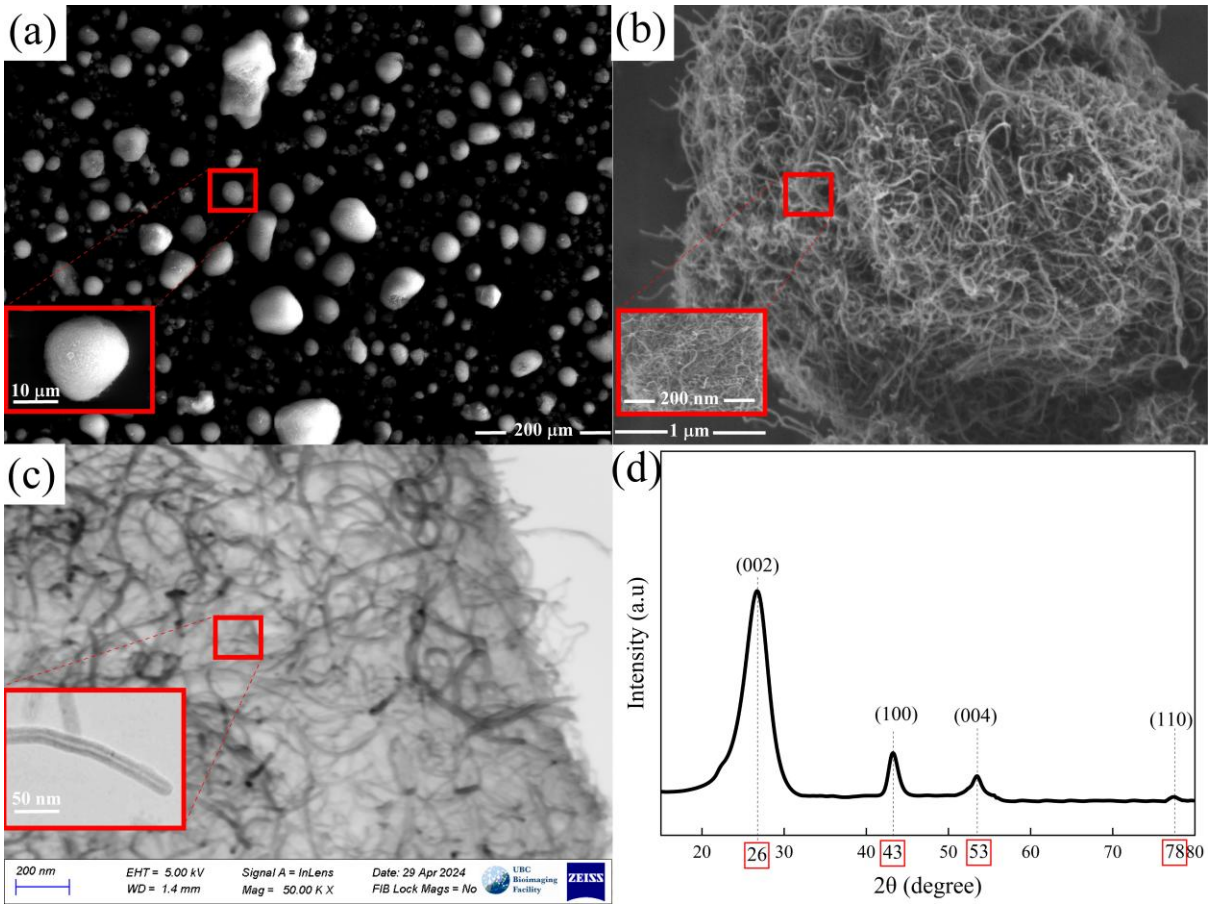

Figure 46: SEM images of as received (a) PVDF, and (b) MWCNTs; (c) high magnification TEM images of as received MWCNTs; and (d) X-ray diffraction patterns of as received MWCNTs.

Figure 46(b) shows both high and low magnification SEM images of the as-received MWCNTs, revealing their long, intertwined tubular structures. The structural morphology of MWCNT was confirmed by TEM analysis (Figure 46(c)). The inset of Figure 46(c) shows the

hollow inner cavity of the MWCNTs. This unique feature serves as a channel for the transport of ions within the nanocomposite material. The facilitated ion transport improves the poling efficiency of the material, resulting in higher piezoelectric performance. The XRD pattern of MWCNTs is shown in Figure 46(d). The pattern shows a prominent diffraction peak at about $2\theta = 26°$, accompanied by lower intensity diffraction peaks at about 43°, 53° and 78°. These peaks correspond to the (002), (100), (004) and (110) diffraction patterns of typical graphite, respectively. This observation indicates that the MWCNTs have a well graphitized structure. Such a structure is characterized by robust π-π interactions between adjacent graphene layers. These interactions improve mechanical, electrical and thermal properties of PVDF/MWCNTs nanocomposites, making them highly desirable for a variety of applications.

Figure 47(a) presents a low magnification SEM image showcasing the filament of nanocomposite C-0.3. It is clear that the particles are evenly distributed in the polymer matrix at lower MWCNT contents. To illustrate the threadlike fiber morphology of the MWCNTs, a high magnification SEM image is shown in Figure 47(b). Figure 47(c)-(f) provide a comparative insight into the distribution of MWCNTs within the PVDF matrix in the four nanocomposites investigated in this work. Particle detection analysis was performed to obtain more clarity on the distribution of nanoparticles.

The results indicate that agglomeration is more pronounced with increasing MWCNT content. Especially in sample C-1, considerable agglomeration and surface defects can be observed. To further illustrate these defects, Figure 47(g) shows an SEM image of sample C-1 at higher magnification, revealing prominent surface agglomerations. The particle detection analysis shown in Figure 47(h) provides additional insight into the detection of these agglomerations. In addition, high magnification SEM analysis reveals pores on the surface of sample C-0.1, as shown in Figure 47(i). These imperfections affect both the electrical and mechanical properties. The presence of defects can lead to localized stress concentrations, resulting in a reduction of the breakdown electric field and overall material integrity.

In addition, defects create pathways for energy dissipation increasing dielectric loss. Defects can also affect mechanical strength and stiffness. This reduction in mechanical properties could affect the durability and reliability of the PEH. Thus, to optimize the nanocomposite, a balance must be found between improved piezoelectric performance and mechanical robustness. Figure 47(j)-(l) show a comparison of the SEM images of the 3D-printed C-0.5 sample's cross-section at different printing temperatures (nozzle temperatures). At lower printing temperatures

(Figure 47(j)), the adhesion between successive layers of the printed object is weak, leading to the formation of interfaces where pores and defects are more likely to form.

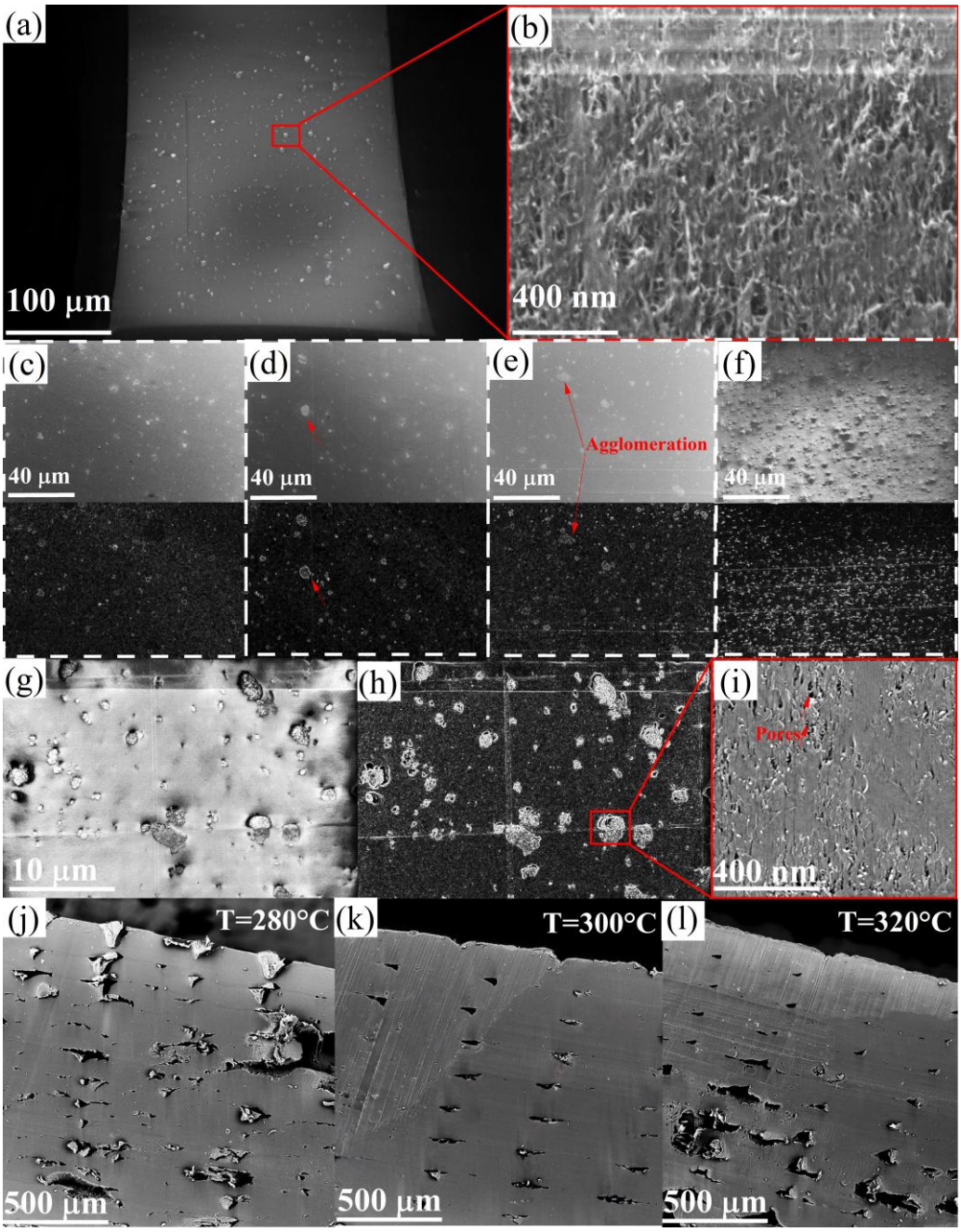

Figure 47: Morphology analysis of PVDF/MWCNTs composites and the effect of printing temperature : (a) Low and (b) high magnification SEM of the C-0.3 nanocomposite filament; SEM images and particle detection analysis of (c) C-0.3, (d) C-0.5, (e) C-0.7, and (f) C-1; (g) low magnification SEM, (h) particle detection analysis, and (i) high magnification SEM of C-0.1; cross-section SEM of the 3D-printed C-0.5 sample with nozzle temperature of (j) 280°C, (k) 300°C, and (l) 320°C.

Figure 47(k), on the other hand, shows no defects, indicating excellent adhesion between the successive layers and suggesting that a nozzle temperature of 300°C is optimal. However, when the temperature is further increased, the filament material becomes excessively fluid. This leads to excessive material flow during deposition, resulting in over-extrusion and the formation of blobs or irregularities in the printed layers. These irregularities contribute to the formation of pores and defects in the final printed structure, as depicted in Figure 47(l).

Figure 48(a) shows the FTIR spectrum, revealing the polymorphic phases of PVDF, where the α-phase is marked by characteristic absorption peaks at 765, 795, 976, 1150 and 1384 cm^{-1}, and the β-phase by peaks at 842 and 1274 cm^{-1}. As expected, the addition of MWCNTs sharpens the β-phase peaks and diminishes the α-phase peaks, indicating a shift from the α-phase to the more desirable β-phase, facilitated by the MWCNTs. This shift is likely due to MWCNTs fostering charge accumulation at the material interface during poling, which aligns the PVDF chains towards the β-phase.

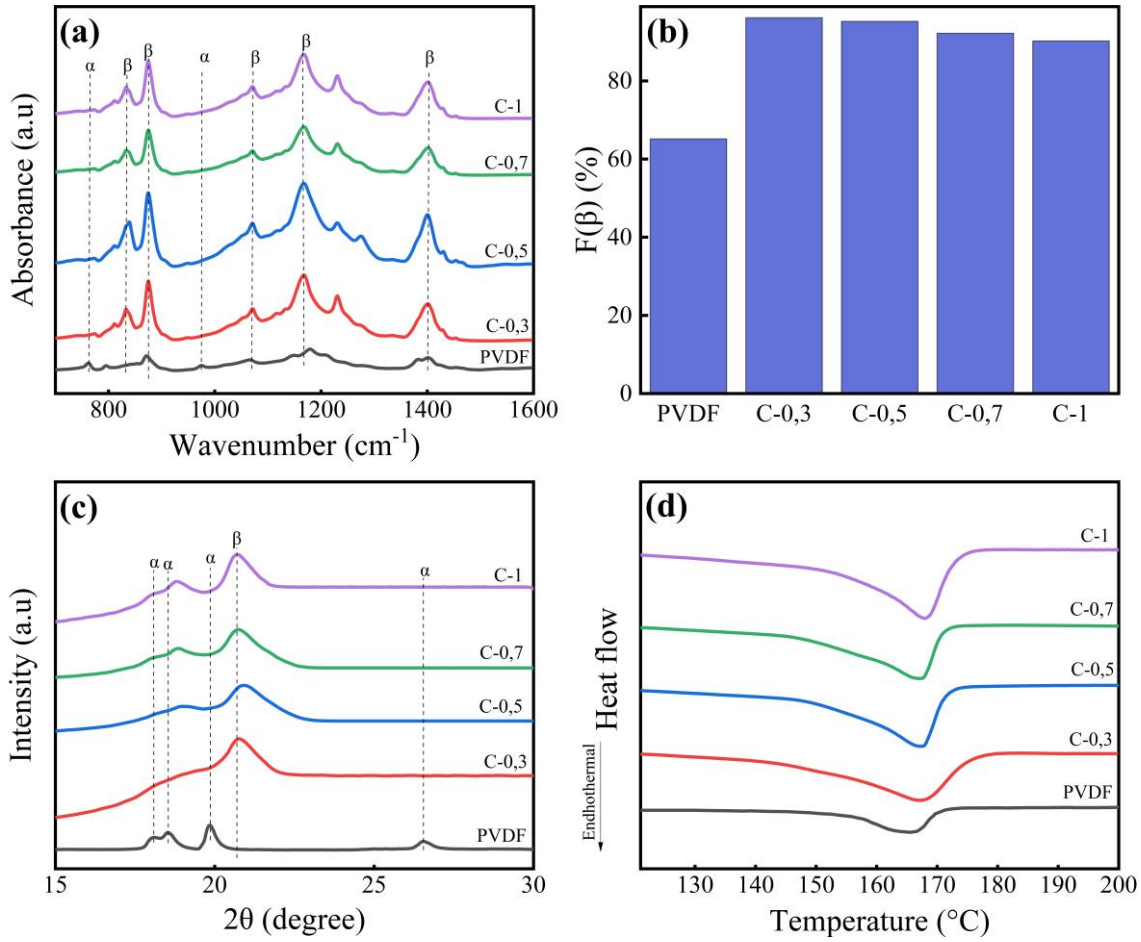

Figure 48: FTIR, XRD, and DSC characterization of PVDF/MWCNTs composites : (a) FT-IR spectra of the FDM 3D-printed PVDF and PVDF/MWCNTs samples (b) β-phase content of 3D-printed PVDF and PVDF/MWCNTs

samples (c) X-ray diffraction patterns of the FDM 3D-printed PVDF and PVDF/MWCNTs samples. (d) DSC curves of PVDF and PVDF/MWCNTs samples (heating curve).

The weight fractions of β-phase were determined using equation (16), and the results are shown in Figure 49(b). With 0.3 wt% MWCNTs addition, the β-phase fraction showed a remarkable increase from 65.15% to 95.23%. This increase is attributed to the electrostatic interactions between the MWCNTs functional groups and the CF2 groups of PVDF chains, which promotes the formation of the β-phase. However, higher MWCNTs content hinders the nucleation process, impeding the PVDF chain alignment into the β phase, hence a lower β-phase fraction at 90.22% for sample C-1. Figure 49(c) shows the XRD patterns of the five PVDF/MWCNTs samples under investigation. Pure PVDF exhibits distinct reflection peaks at 2θ angles of 17.6, 18.3, 19.9 and 26.5°, indicative of the α-phase, corresponding to the (100), (020), (110) and (021) reflections, respectively. However, upon introducing MWCNTs, the diffraction peaks associated with the α-crystal phase of PVDF, particularly at 2θ angles of 17.6 and 26.5°, show a reduction in intensity. Simultaneously, the β-crystal phase at 2θ = 20.6° becomes more prominent, which corresponds to the (110) reflection. This XRD analysis is in good agreement with the findings derived from the FT-IR results and confirms the transforming influence of MWCNTs incorporation on PVDF's crystalline phases.

The non-isothermal melting behavior of both pure PVDF and PVDF-based nanocomposites was investigated using DSC measurements, and the results are shown in Figure 48(d). The incorporation of MWCNTs exerts a minor influence on the melting temperature (Tm) of PVDF, with only a slight elevation in Tm, possibly due to enhanced thermal conductivity brought about by the MWCNTs.

Table 22: Thermal properties of PVDF and PVDF/ MWCNTs nanocomposites determined by DSC test and F(β) values measured with FT-IR data.

Sample	T_m (°C)	ΔH_m (J/g)	X_c (%)	F(β) (%)
Pure PVDF	166.15	57.66	54.92	65.15
C-0.3	167.83	59.44	56.78	96.15
C-0.5	167.90	59.68	57.12	95.23
C-0.7	167.92	60.57	58.09	92.17
C-1	168.05	61.13	58.81	90.22

Table 22 outlines the DSC parameters for all five samples alongside their corresponding β-phase fractions. The results indicate that the fusion enthalpy for the PVDF/MWCNTs composite samples surpasses that of pure PVDF. This phenomenon is attributed to the heterogeneous

nucleation triggered by the MWCNTs in PVDF. Consequently, a higher degree of crystallinity was observed in the composite material, with sample C-1 achieving a significantly higher crystallinity of 58.81% compared to the 54.92% crystallinity observed in pure PVDF.

Figure 49(a) shows the frequency-dependent behavior of the dielectric constant of the five examined samples, demonstrating that the dielectric constant of PVDF/MWCNT is higher than pure PVDF across the entire frequency spectrum. This increase can be attributed to the formation of microcapacitor structures favored by the interaction between MWCNTs and PVDF.

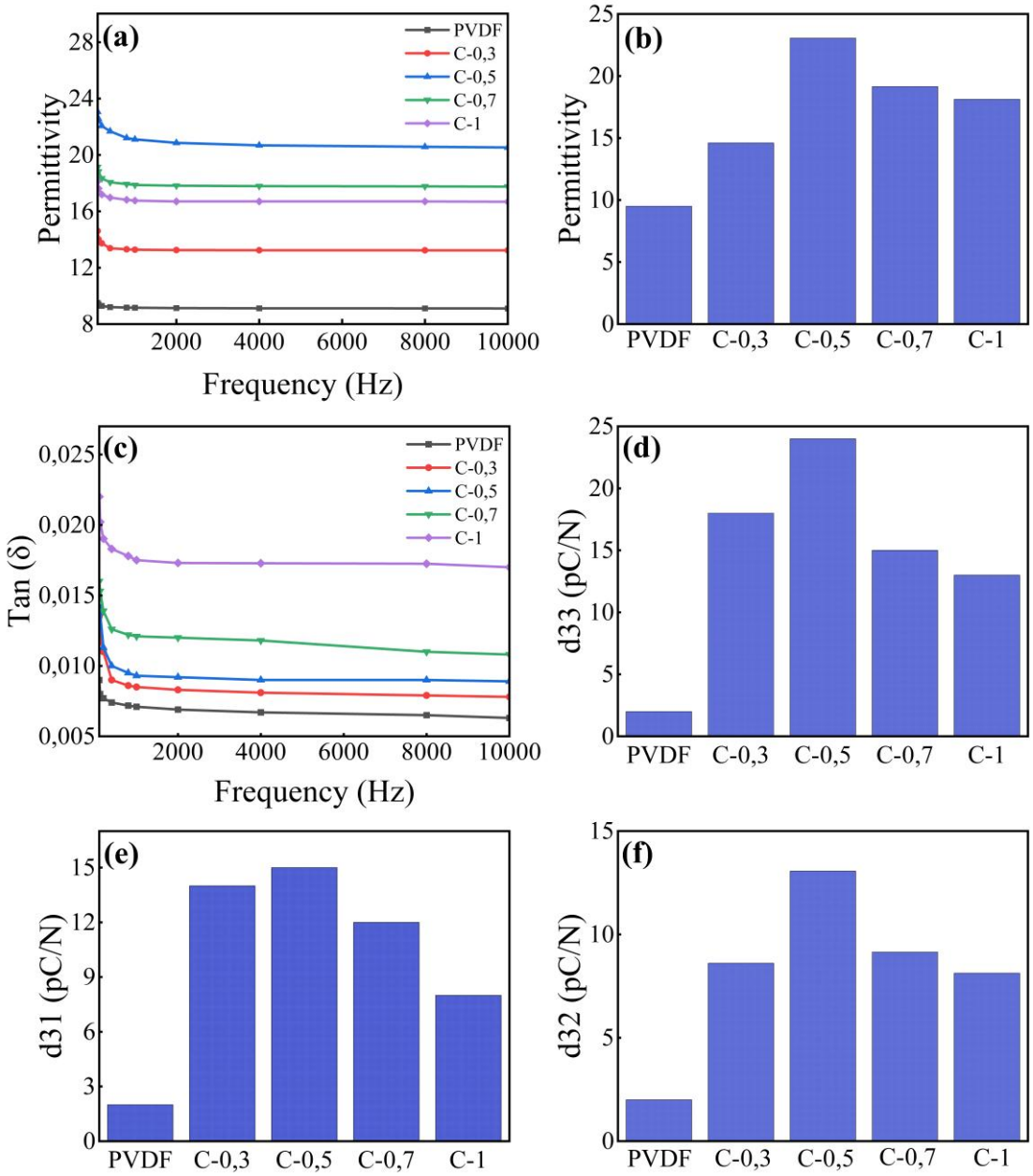

Figure 49: Dielectric and piezoelectric properties of PVDF/MWCNTs composites : (a) Frequency dependence of the permittivity; (b) permittivity of the five simples at 100 Hz; (c) frequency dependence of the dielectric loss; (d) d33, (e) d31, and (f) d32 coefficients of the piezoelectric nanocomposites.

In particular, the C-0.5 sample achieves a maximum dielectric constant of 24, marking a substantial increase from pure PVDF, which only reaches a value of 9 at a frequency of 100 Hz, as shown in Figure 49(b). Figure 49(c) shows that the addition of MWCNTs leads to an increase in dielectric loss, a trend that is more pronounced at lower frequencies and may be associated with ground fault currents. However, it is essential to highlight that even with MWCNTs addition, the maximum dielectric loss remains modest at 0.02 at 100 Hz for the C-1 sample. This dielectric loss is relatively low and unlikely to have a significant impact on practical applications.

As depicted in Figure 49(d), 50(e), and 50(f), the addition of MWCNTs leads to a notable improvement in the piezoelectric constants. In particular, the C-0.5 sample exhibits the highest d33 value of 24 pC/N, together with d31 and d32 values of 15 pC/N and 13 pC/N, respectively.

However, a further increase in MWCNTs content to 0.7 wt% leads to a decline in piezoelectric performances. This drop in performance can be attributed to the disruptive effects of higher amounts of MWCNTs on the alignment of the PVDF polymer chains, which is critical for effective polarization. Such disruption can impede the formation of the polar phase and, consequently, affect the overall piezoelectric response of the material.

5.4.2 Effective design and parametric study

In our investigation, numerical simulations using COMSOL software were performed to design and analyze three distinct metamaterial structures, comparing their performance with that of a traditional structure (Figure 50(a)). The studied metamaterial configurations include a honeycomb structure (Figure 50(b)), a reentrant shape structure (Figure 50(c)) and a tetrachiral structure (Figure 50(d)). Here, these metamaterials were specifically designed to amplify strain and deformation within the piezoelectric material, leveraging their unique mechanical properties to achieve amplified voltage outputs under identical mechanical loads compared to the conventional structure.

The results of the numerical simulation simultaneously show the stress, strain and output of each structure. To highlight the output voltage, a separate numerical study was performed to display the polarization of each structure. As depicted in Figure 50, the excitation was applied perpendicular to the polarization direction. The electric dipoles were aligned from the lower (ground) to the upper (terminal) electrodes. This alignment resulted in positive and negative voltage outputs on these surfaces, respectively.

It is important to note that the honeycomb structure has a positive Poisson's ratio, while the other two structures are classified as auxetic materials. Auxetic materials are known for their

superior vibration damping capabilities. Their exceptional lateral contraction under compression, enables them to absorb and distribute mechanical stress more effectively than the honeycomb structure, resulting in higher voltage outputs.

In addition, the reentrant shape provides a larger effective surface area for deformation compared to the tetrachiral structure. This larger surface area allows more piezoelectric material to be exposed to the excitation force, resulting in higher deformation and stress.

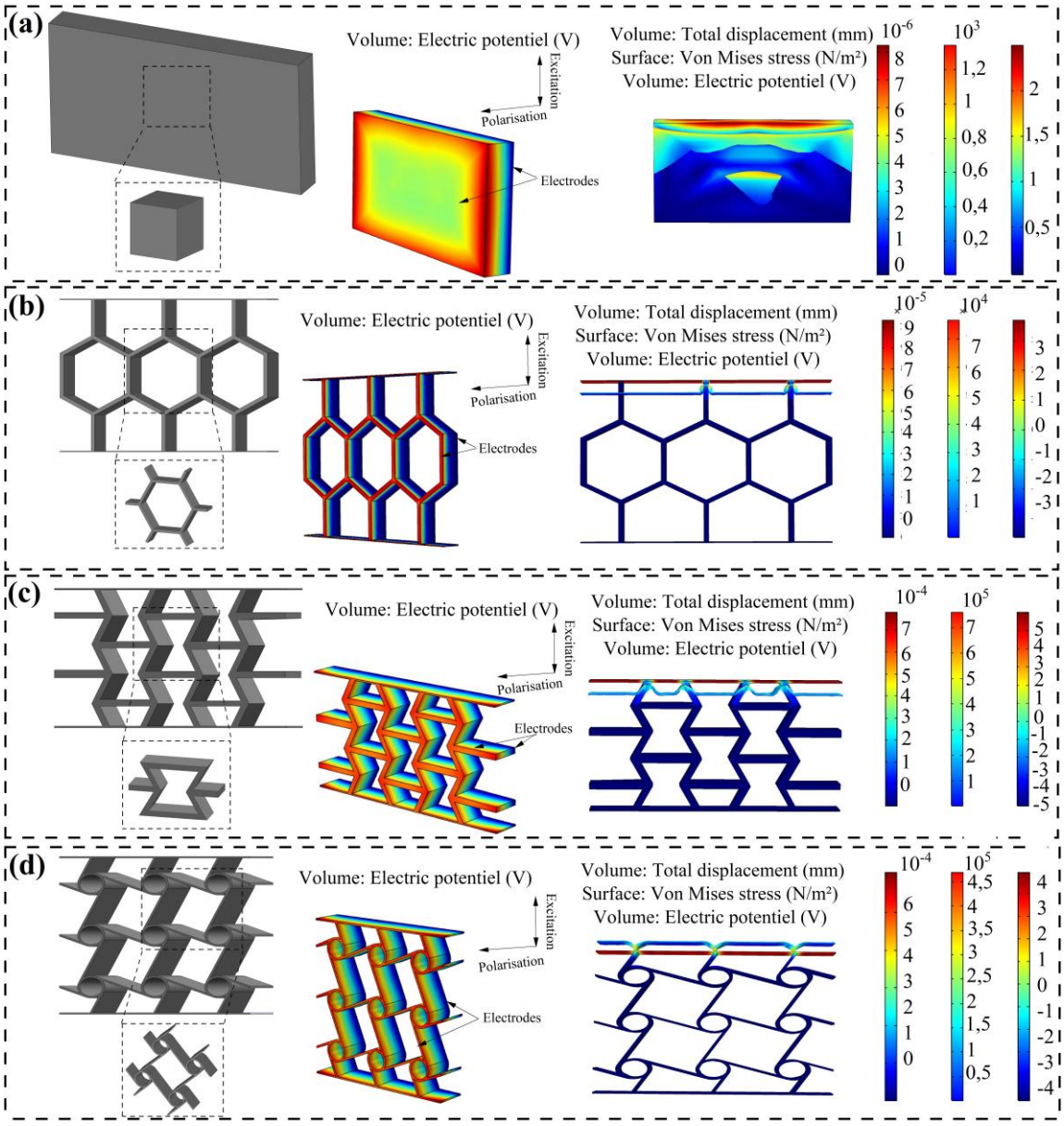

Figure 50: FEM-based structural optimization of various auxetic and conventional PEH geometries : Optimization of the PEH structure design based on the FEM simulation results of the mechanical and electrical performances of (a) the conventional structure, (b) the honeycomb structure, (c) the reentrant shape structure, and (d) the tetrarchical structure.

Therefore, the numerical simulations in Figure 50 demonstrated that the reentrant shape structure outperforms the other configurations in terms of strain, stress, and resultant voltage output, showcasing its potential for enhanced piezoelectric energy harvesting.

To enhance the efficiency of the PEH configuration, an optimization study was undertaken, involving meticulous adjustments to the dimensional parameters of the reentrant structure through numerical simulations. This investigation focused on three different element sizes to evaluate their influence on the structure's performance.

As depicted in Figure 51, a significant enhancement in the output voltage from 5 V to 12 V was observed when the element size was reduced by half. This reduction in size provides greater mechanical compliance, which means that the structure is easier to deform.

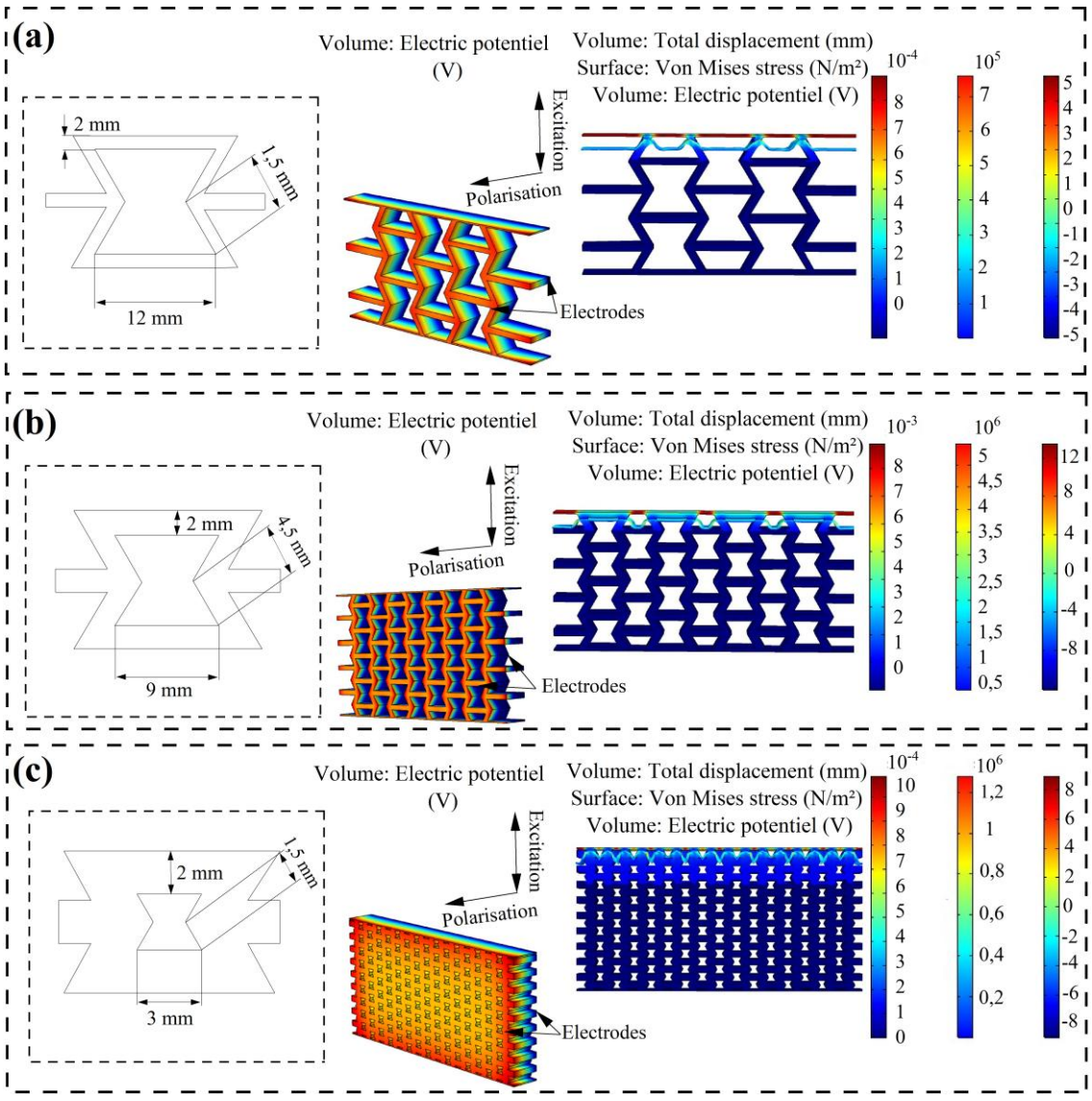

Figure 51: Optimization using three different sets of dimensional parameters of the reentrant shape structure using the FEM simulation results of the mechanical and electrical performances.

This greater compliance allows for greater deformation in response to the excitation force and therefore a higher voltage output.

However, an excessive reduction in element size can lead to over-stiffening of the structure, making it less susceptible to deformation under applied forces. This leads to lower strains and therefore a slight reduction in the output voltage to 8 V. This trend highlights the high sensitivity of the output voltage to the element size in the reentrant structure.

5.4.3 Fabrication, Piezoelectric tests, and application

FDM 3D printing process was used to fabricate PVDF-based PEHs with different concentrations of CNT nanoparticles. Figure 52(a) displays the five distinct 3D-printed PEHs. Figure 52(b) illustrates the remarkable flexibility of the C-0.5 sample (3×5 cm^2), emphasizing the material's suitability for applications necessitating mechanical flexibility. The structure of the PEHs, shown in Figure 52(c), features a piezoelectric core layer sandwiched between silver electrodes, all securely held together with Kapton tape, ensuring both efficient electrical conductivity and mechanical stability.

To evaluate the piezoelectric performance, a customized test setup (Figure 52(d)) was used, wherein the PEHs were subjected to oscillating pressure shocks using a computer-controlled excitation. The force was applied perpendicularly to the sample surface, which was fixed to a support platform. The piezoelectric responses were recorded with an oscilloscope and analyzed to obtain quantitative data on the electrical responses of the devices under mechanical stress. A detailed view of the actual testing apparatus is presented in Supplementary Figure S1.

The electrical outputs, specifically the current and voltage, presented in Figure 52(e) and 53(f), demonstrate a significant enhancement with an increasing MWCNTs content. This improvement is attributed to two main factors: First, the addition of MWCNTs enhances the piezoelectric properties of PVDF through improved polymer chain alignment and enhanced charge separation. Secondly, the incorporation of conductive MWCNTs into the PVDF matrix increases electrical conductivity, which facilitates efficient charge transport within the material, reducing losses and increasing overall electrical performance. At a MWCNTs concentration of 0.5 wt%, voltage and current reached peak values of 19.9 V and 2.58 µA, respectively, outperforming the metrics of pure PVDF (2.66 V for Voc and 0.42 µA for Isc). However, a further increase in MWCNTs concentration to 0.7 wt% resulted in a decrease in piezoelectric efficiency, possibly due to surface defects detected in samples with higher MWCNTs content that introduced localized resistance areas. This highlights the importance of maintaining a balance between

filler content and material morphology to optimize the piezoelectric performance of the nano-composites.

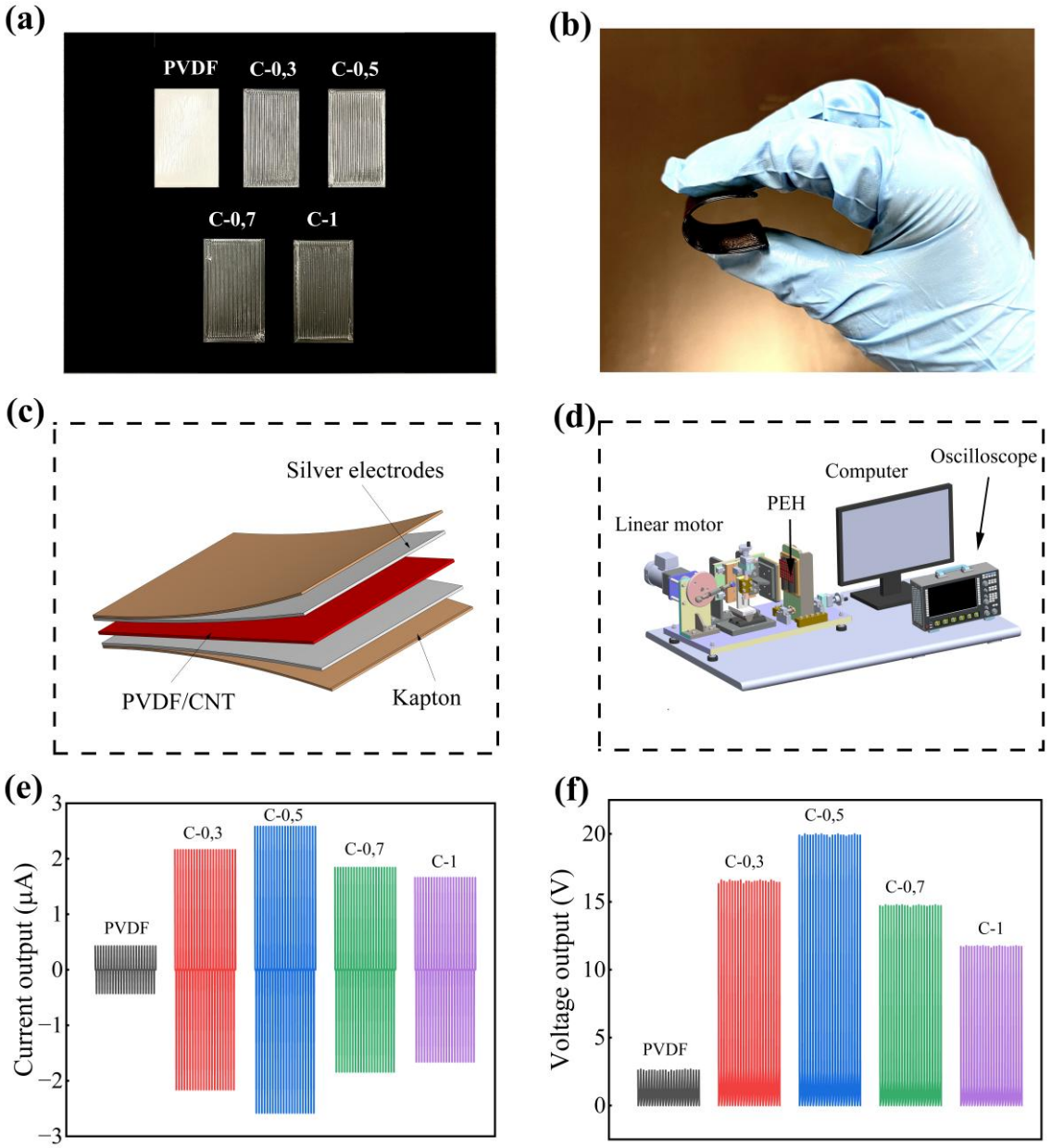

Figure 52: Fabrication and output signals of 3D-printed PVDF/MWCNTs PEHs : (a) Schematic diagram of the 3D printed PEHs with different compositions; (b) photo showing the high flexibility of the 3D printed C-0.5 sample; (b) schematic diagram of the PEHs; (d) schematic diagram of the piezoelectric testing system;(e) short circuit current and (f) open-circuit voltage signals of the PEHS with the four tested compositions.

To thoroughly assess the impact of various input parameters on the performance of PEHs, a set of experiments was carried out by altering the excitation frequencies (1 Hz, 2.5 Hz and 5 Hz)

and compression ratios of the sample (0.3 mm, 0.4 mm and 0.5 mm). The results, shown in Figures S2-S6, provide valuable insights.

Figure 53(a) reveals a clear relationship between the axial displacement and the PEHs' output voltages, indicating that greater displacements lead to higher voltage outputs. Furthermore, Figure 53(b) shows a remarkable increase in output voltage at elevated excitation frequencies. This phenomenon is likely due to the system approaching its natural frequency, thereby enhancing its vibration response.

Figure 54(c) presents the impressive performance of the optimal auxetic structure, achieving a Voc of 28.2 V under compressive excitation (d33 mode) and 14.8 V under tensile excitation (d31 and d32 modes). The inset of Figure 53(c) visually depicts the actual compression and tension tests conducted on the structure. The fabrication process of the auxetic structure is detailed in Figure S7.

Figure S8 demonstrates the exceptional flexibility of the 3D-printed auxetic structure. A comparative performance analysis between the auxetic structure and a conventional flat structure, as shown in Figure S9, highlights the superior efficacy of the auxetic design. The durability test, shown in Figure 53(d), emphasizes the robustness of the optimal structure. Even after 1400 compression cycles, the Voc value remained constant, emphasizing the exceptional durability and resistance of the structure. An energy storage experiment was performed, wherein the alternating current output from the PEH was converted into direct current using a bridge rectifier, subsequently used to charge a commercial capacitor. As shown in Figure 53(e), the PEH successfully charged a 1 μF 50 V capacitor to 22 V within 260 seconds. The inset in Figure 53(e) provides a schematic of the energy storage circuit used in this test. This study presents an innovative security system using PEHs, tailored for extensive application in large enterprises, industrial settings, and residential areas. This groundbreaking approach involves installing PVDF/MWCNTs nanocomposite based PEHs with an optimized auxetic structure beneath the flooring tiles of the designated environment.

This advanced system is engineered to deter theft and bolster property security effectively. The operational principle is based on the conversion of mechanical pressure from footsteps on the tiles into an electrical signal by the PEH, which then acts as a trigger for an integrated alarm system, as illustrated in Figure 53(f). The generated electrical signal serves as a switch mechanism: its presence signifies a "closed" switch state, activating the alarm system, whereas its absence represents an "open" switch state, indicating a lack of external pressure on the tiles

and, thus, a secure condition. The system's operational mechanism is detailed in Supplementary Figure S10.

By integrating PEHs into the flooring infrastructure, this novel application converts mechanical pressure into an effective and reliable security measure, offering a forward-looking defense against potential thefts and intrusions.

The schematic of the security system, depicted in Figure 53(g), outlines how the voltage produced by the PEH is rectified and subsequently stored in a capacitor.

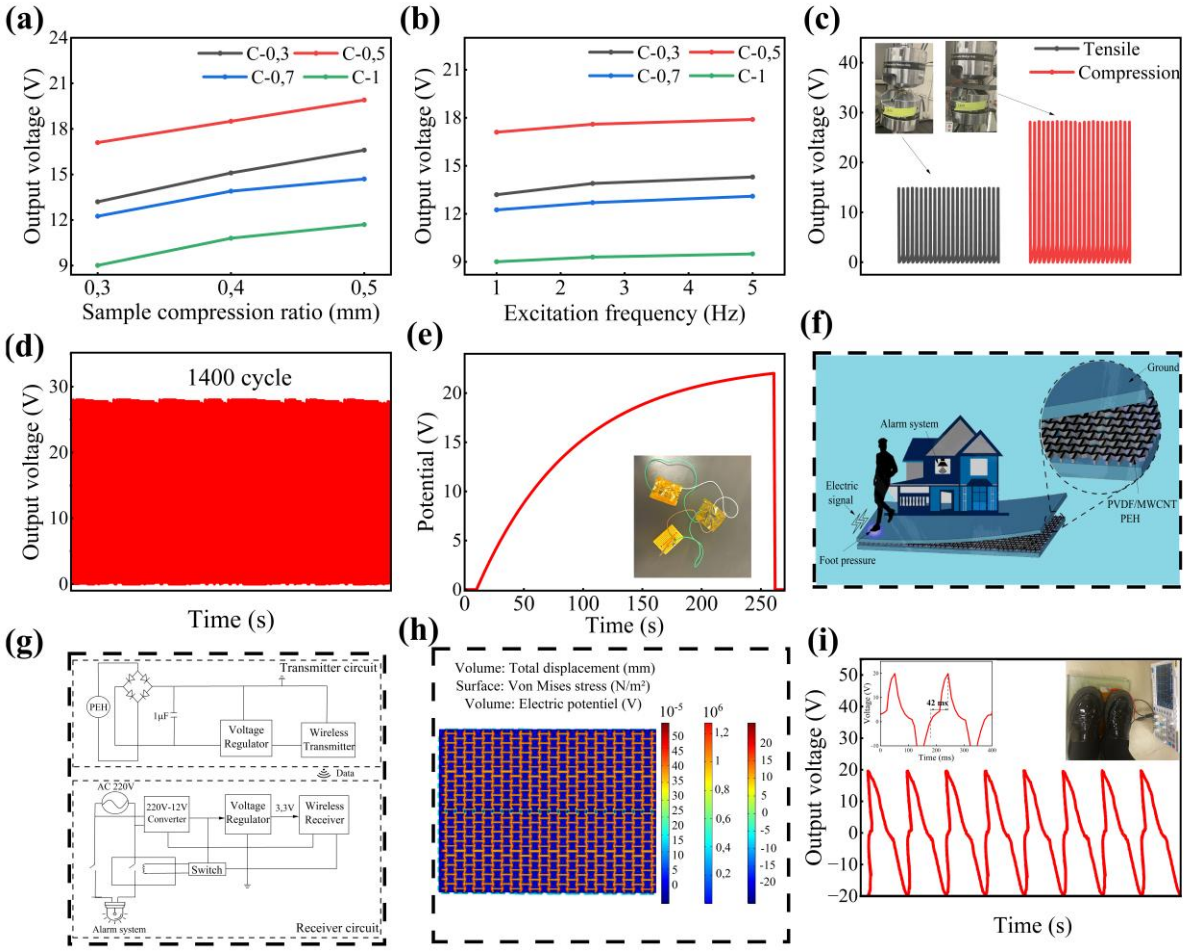

Figure 53: Evaluation of auxetic PEH structures in terms of performance, durability, and real-time application : (a) Sample compression ratio and (b) frequency dependence of the open-circuit voltage signals; (c) performances of the auxetic structure under both compressive and tensile excitation; (d) output voltage of 1400 cycles illustrating the durability of the auxetic structure; (e) curve of the PEH charging the capacitor for 250 s; (f) schematic of the PEH's application (g) schematic of the application's circuit of the PEH integrated into a smart security system; (h) numerical simulation of the application; (i) simulated open-circuit voltage signals of PEH in response to the footsteps of a 60 kg person.

This accumulated energy powers a wireless transmitter node, which is tasked with sending on/off signals to a corresponding wireless receiver. The system's final component is a relay circuit that manages the connection between a standard 220V power supply and the alarm system, enabling the activation or deactivation of the alarm as necessary. The numerical simulations, illustrated in Figure 53(h), project that the voltage generated from the pressure of a 60 kg individual's footsteps could reach up to 20 V. Detailed specifications and structural designs are provided in Supplementary Figure S11. These numerical predictions have been corroborated by experimental data under the same boundary conditions. The experimental findings, shown in Figure 53(i), demonstrate that the PEH can deliver an output voltage of 19.8 V with an impressively fast response time of 42 ms, emphasizing a remarkably small error of 1% between experimental and numerical results.

5.5 Conclusion

This study marks a significant breakthrough in the domain of piezoelectric energy harvesting, spanning the full spectrum from conceptualization and design to practical fabrication and rigorous experimental verification. A highly efficient nanocomposite of PVDF/MWCNTs has been developed, characterized by an optimally tailored composition. Leveraging FDM 3D printing technology, this nanocomposite was precisely engineered. A distinctive aspect of our methodology is the deployment of a meticulously devised reentrant auxetic lattice structure. This avant-garde lattice configuration facilitates the establishment of a system that is both multidirectional and multimodal, substantially amplifying its capacity for mechanical energy conversion. The structure exploits three distinct piezoelectric modes. Stretching along the x-axis initiates the first two modes, d31 and d32, capitalizing on the structure's negative Poisson's ratio, and achieving a notable open-circuit voltage of 14.8 V. In contrast, compressive stress along the z-axis activates the third d33 mode, culminating in an elevated open-circuit voltage of 28.2 V. This setup enables the energy harvester to charge a 1 μF capacitor to 22 V within a mere 260 seconds. Fundamentally, this research synergizes the potentials of refined materials, cutting-edge manufacturing processes, and groundbreaking design paradigms to elevate PVDF/MWCNTs PEHs to new heights of efficiency. In addition, the integration of PVDF/MWCNT PEHs is pivotal in the development of a novel alarm system tailored for large businesses, industries, and residential buildings. This pioneering application capitalizes on the inherent capability of PEHs to transmute the mechanical pressure from footsteps into electrical signals, thereby activating an integrated alarm system. This groundbreaking approach heralds

a significant advancement in security technologies, with the PEH showcasing exceptional performance by generating a voltage of 19.8 V in reaction to the footsteps of an individual weighing 60 kg, thereby affirming its viability and relevance in real-world settings.

5.6 Acknowledgements

The authors acknowledge the funding provided by the Natural Sciences and Engineering Research Council (NSERC) of Canada in the form of Discovery Grants (Grant Number: CRSNG – RGPIN -2021-02846).

5.7 References

[1] M. Safaei, H.A. Sodano, S.R. Anton, A review of energy harvesting using piezoelectric materials: state-of-the-art a decade later (2008–2018), Smart Mater. Struct. 28(11) (2019) 113001. 10.1088/1361-665X/ab36e4

[2] T. Li, P.S. Lee, Piezoelectric energy harvesting technology: from materials, structures, to applications, Small Struct. 3(3) (2022) 2100128. https://doi.org/10.1002/sstr.202100128.

[3] A. Aabid, B. Parveez, M.A. Raheman, Y.E. Ibrahim, A. Anjum, M. Hrairi, N. Parveen, J. Mohammed Zayan, A review of piezoelectric material-based structural control and health monitoring techniques for engineering structures: Challenges and opportunities, Actuators, MDPI, 2021, p. 101. https://doi.org/10.3390/act10050101.

[4] J. Yin, N. Liu, P. Jia, Z. Ren, Q. Zhang, W. Lu, Q. Yao, M. Deng, Y. Gao, MXene-enhanced environmentally stable organohydrogel ionic diode toward harvesting ultralow-frequency mechanical energy and moisture energy, SusMat 3(6) (2023) 859-876. https://doi.org/10.1002/sus2.169%20Go%20here%20for%20SFX

[5] M. Wu, Y. Wang, S. Gao, R. Wang, C. Ma, Z. Tang, N. Bao, W. Wu, F. Fan, W. Wu, Solution-synthesized chiral piezoelectric selenium nanowires for wearable self-powered human-integrated monitoring, Nano energy 56 (2019) 693-699. https://doi.org/10.1016/j.nanoen.2018.12.003.

[6] R. Li, S. Zhang, H. Chen, Y. Huang, B. Wang, X. Wu, Q. Jiang, S. Zhao, F. Wang, Y. Zhao, Multicolored structural coloration of carbon nanotube fibers, SusMat 3(1) (2023) 102-110. https://doi.org/10.1002/sus2.111.

[7] T.E. Hooper, J.I. Roscow, A. Mathieson, H. Khanbareh, A.J. Goetzee-Barral, A.J. Bell, High voltage coefficient piezoelectric materials and their applications, J. Eur. Ceram. Soc. 41(13) (2021) 6115-6129. https://doi.org/10.1016/j.jeurceramsoc.2021.06.022.

[8] Q. Guo, F. Li, F. Xia, P. Wang, X. Gao, H. Hao, H. Liu, H. Sun, S. Zhang, Piezoelectric ceramics with high piezoelectricity and broad temperature usage range, J. Materiomics 7(4) (2021) 683-692. https://doi.org/10.1016/j.jmat.2020.11.012.

[9] B. Xun, A. Song, J. Yu, Y. Yin, J.-F. Li, B.-P. Zhang, Lead-free BiFeO3-BaTiO3 ceramics with high Curie temperature: fine compositional tuning across the phase boundary for high piezoelectric charge and strain coefficients, ACS Appl. Mater. Interfaces. 13(3) (2021) 4192-4202. https://doi.org/10.1021/acsami.0c20381.

[10] J.-Y. Lee, H. Lee, H.-S. Kim, J. Jang, S.-H. Kim, J.-H. Ryu, J.-H. Jang, S.-L. Hwang, H. Ahn, D. Ha, Improving the efficiency of PZT-based piezoelectric energy harvesting by mixing MWCNTs under solar radiation, Mater. Today Sustainability 24 (2023) 100481. https://doi.org/10.1016/j.mtsust.2023.100481.

[11] H. Kim, S. Yun, K. Kim, W. Kim, J. Ryu, H.G. Nam, S.M. Han, S. Jeon, S. Hong, Breaking the elastic limit of piezoelectric ceramics using nanostructures: A case study using ZnO, Nano Energy 78 (2020) 105259.

[12] P.J. Liu, K. Wang, L. Li, R. Zhang, Z.P.G. Xu, Lead-free piezoelectric materials for musculoskeletal tissue engineering, Mater. Today Sustainability (2023) 100393. https://doi.org/10.1016/j.nanoen.2020.105259.

[13] M. Smith, S. Kar-Narayan, Piezoelectric polymers: theory, challenges and opportunities, Int. Mater. Rev. 67(1) (2022) 65-88. https://doi.org/10.1080/09506608.2021.1915935.

[14] L. Lu, W. Ding, J. Liu, B. Yang, Flexible PVDF based piezoelectric nanogenerators, Nano Energy 78 (2020) 105251. https://doi.org/10.1016/j.nanoen.2020.105251.

[15] T. Rodrigues-Marinho, N. Perinka, P. Costa, S. Lanceros-Mendez, Printable lightweight polymer-based energy harvesting systems: materials, processes, and applications, Mater. Today Sustainability 21 (2023) 100292. https://doi.org/10.1016/j.mtsust.2022.100292.

[16] X. Lv, Y. Liu, J. Yu, Z. Li, B. Ding, Smart fibers for self-powered electronic skins, Adv. Fiber Mater. 5(2) (2023) 401-428. https://doi.org/10.1007/s42765-022-00236-6

[17] S. Mishra, S. Mohanty, A. Ramadoss, Functionality of flexible pressure sensors in cardiovascular health monitoring: a review, Acs Sens. 7(9) (2022) 2495-2520. https://doi.org/10.1021/acssensors.2c00942.

[18] M. Pusty, P.M. Shirage, Insights and perspectives on graphene-PVDF based nanocomposite materials for harvesting mechanical energy, J. Alloys Compd. 904 (2022) 164060. https://doi.org/10.1016/j.jallcom.2022.164060.

[19] A. Kurakula, S.A. Graham, P. Manchi, M.V. Paranjape, J.S. Yu, Enhanced energy harvesting ability of bismuth sodium titanate/polyvinylidene fluoride composite film-based piezoelectric nanogenerators for mechanical energy scavenging and safety-walker applications, Mater. Today Sustainability 25 (2024) 100616. https://doi.org/10.1016/j.mtsust.2023.100616.

[20] Z. He, F. Rault, M. Lewandowski, E. Mohsenzadeh, F. Salaün, Electrospun PVDF nanofibers for piezoelectric applications: A review of the influence of electrospinning parameters on the β phase and crystallinity enhancement, Polym. 13(2) (2021) 174. https://doi.org/10.3390/polym13020174.

[21] A. Megdich, M. Habibi, L. Laperrière, A review on 3D printed piezoelectric energy harvesters: materials, 3D printing techniques, and applications, Mater. Today Commun. 35 (2023) 105541. https://doi.org/10.1016/j.mtcomm.2023.105541.

[22] J. Ma, U. Azhar, C. Zong, Y. Zhang, A. Xu, C. Zhai, L. Zhang, S. Zhang, Core-shell structured PVDF@ BT nanoparticles for dielectric materials: A novel composite to prove the dependence of dielectric properties on ferroelectric shell, Mater. Des. 164 (2019) 107556. https://doi.org/10.1016/j.matdes.2018.107556

[23] N. Bhaskar, M.C. Kachappilly, V. Bhushan, H.J. Pandya, B. Basu, Electrical field stimulated modulation of cell fate of pre-osteoblasts on PVDF/BT/MWCNT based

electroactive biomaterials, J. Biomed. Mater. Res. A 111(3) (2023) 340-353. https://doi.org/10.1002/jbm.a.37472.

[24] A. Megdich, M. Habibi, L. Laperrière, Modeling and optimization of piezoelectric and dielectric properties of poled PVDF/BT nanocomposites, Polym. Bull. (2024) 1-21. https://doi.org/10.1007/s00289-024-05157-5

[25] S. Song, Y. Li, Q. Wang, C. Zhang, Boosting piezoelectric performance with a new selective laser sintering 3D printable PVDF/graphene nanocomposite, Compos. - A: Appl. Sci. Manuf. 147 (2021) 106452. https://doi.org/10.1016/j.compositesa.2021.106452

[26] Z. Li, Z. Liu, H. Sun, C. Gao, Superstructured assembly of nanocarbons: fullerenes, nanotubes, and graphene, Chem. Rev. 115(15) (2015) 7046-7117. https://doi.org/10.1021/acs.chemrev.5b00102

[27] N. Nurazzi, F. Sabaruddin, M. Harussani, S. Kamarudin, M. Rayung, M. Asyraf, H. Aisyah, M. Norrrahim, R. Ilyas, N. Abdullah, Mechanical performance and applications of cnts reinforced polymer composites—A review, Nanomater. 11(9) (2021) 2186. https://doi.org/10.3390/nano11092186

[28] A.C. Hurtado, P. Peralta, R. Ruiz, M.M. Alamdari, E. Atroshchenko, Shape optimization of piezoelectric energy harvesters of variable thickness, J. Sound Vib. 517 (2022) 116503. https://doi.org/10.1016/j.jsv.2021.116503.

[29] C. Wang, G. Yu, H. Cao, S. Wang, Y. Li, Structure simulation optimization and test verification of piezoelectric energy harvester device for road, Sensor Actuat. A-Phys. 315 (2020) 112322. https://doi.org/10.1016/j.sna.2020.112322

[30] H. Yang, Y. Wei, W. Zhang, Y. Ai, Z. Ye, L. Wang, Development of piezoelectric energy harvester system through optimizing multiple structural parameters, Sens. 21(8) (2021) 2876. https://doi.org/10.3390/s21082876

[31] J. Seong, B.-U. Bak, D. Lee, J. Jin, J. Kim, Tribo-piezoelectric synergistic BaTiO3/PDMS micropyramidal structure for high-performance energy harvester and high-sensitivity tactile sensing, Nano Energy 122 (2024) 109264. https://doi.org/10.1016/j.nanoen.2024.109264

[32] X. Du, P. Li, Z. Li, X. Liu, W. Wang, Q. Feng, L. Du, H. Yu, J. Wang, X. Xie, Multi-Pillar Piezoelectric Stack Harvests Ocean Wave Energy with Oscillating Float Buoy, Energy (2024) 131347. https://doi.org/10.1016/j.energy.2024.131347

[33] S.M. AlTowireb, S. Goumri-Said, Core-Shell structures for the enhancement of energy harvesting in piezoelectric Nanogenerators: A review, Sustain. Energy Technol. 55 (2023) 102982. https://doi.org/10.1016/j.seta.2022.102982

[34] H. Pei, Y. Xie, Y. Xiong, Q. Lv, Y. Chen, A novel polarization-free 3D printing strategy for fabrication of poly (Vinylidene fluoride) based nanocomposite piezoelectric energy harvester, Compos. B Eng. 225 (2021) 109312. https://doi.org/10.1016/j.compositesb.2021.109312

[35] E. Mancuso, L. Shah, S. Jindal, C. Serenelli, Z.M. Tsikriteas, H. Khanbareh, A. Tirella, Additively manufactured BaTiO3 composite scaffolds: A novel strategy for load bearing bone tissue engineering applications, Mater. Sci. Eng. C. 126 (2021) 112192. https://doi.org/10.1016/j.msec.2021.112192

[36] J. Li, F. Yang, Y. Long, Y. Dong, Y. Wang, X. Wang, Bulk ferroelectric metamaterial with enhanced piezoelectric and biomimetic mechanical properties from additive

manufacturing, ACS nano 15(9) (2021) 14903-14914. https://doi.org/10.1021/acsnano.1c05003

[37] W. Zhou, D. Du, Q. Cui, C. Lu, Y. Wang, Q. He, Recent research progress in piezoelectric vibration energy harvesting technology, Energies 15(3) (2022) 947. https://doi.org/10.3390/en15030947

[38] X. Zhou, K. Parida, J. Chen, J. Xiong, Z. Zhou, F. Jiang, Y. Xin, S. Magdassi, P.S. Lee, 3D Printed Auxetic Structure-Assisted Piezoelectric Energy Harvesting and Sensing, Adv. Energy Mater. 13(34) (2023) 2301159. https://doi.org/10.1002/aenm.202301159

[39] K. Chen, S. Fang, Q. Gao, D. Zou, J. Cao, W.-H. Liao, Enhancing power output of piezoelectric energy harvesting by gradient auxetic structures, Appl. Phys. Lett. 120(10) (2022). https://doi.org/10.1063/5.0082015

[40] S. Vyavahare, S. Teraiya, S. Kumar, FDM manufactured auxetic structures: An investigation of mechanical properties using machine learning techniques, Int. J. Solids Struct. 265 (2023) 112126. https://doi.org/10.1016/j.ijsolstr.2023.112126

[41] A. Ziadia, M. Habibi, S. Kelouwani, Machine Learning Study of the Effect of Process Parameters on Tensile Strength of FFF PLA and PLA-CF, Eng 4(4) (2023) 2741-2763. https://doi.org/10.3390/eng4040156

[42] R. Patel, C. Desai, S. Kushwah, M. Mangrola, A review article on FDM process parameters in 3D printing for composite materials, Mater. Today Proc. 60 (2022) 2162-2166. https://doi.org/10.1016/j.matpr.2022.02.385

[43] Z. Abdelhamid, H. Mohamed, S. Kelouwani, The use of machine learning in process–structure–property modeling for material extrusion additive manufacturing: a state-of-the-art review, J. Braz. Soc. Mech. Sci. Eng. 46(2) (2024) 70. https://doi.org/10.1007/s40430-023-04637-5

[44] A. Megdich, M. Habibi, L. Laperrière, A review on 4D printing: Material structures, stimuli and additive manufacturing techniques, Mater. Lett. 337 (2023) 133977. https://doi.org/10.1016/j.matlet.2023.133977

Chapitre 6: Modélisation électromécanique des systèmes de récupération d'énergie piézoélectrique

Ce chapitre a fait l'objet d'une publication :

MEGDICH, Amal, HABIBI, Mohamed, and LAPERRIÈRE, Luc.

Electromechanical modelling of l-shaped bending-torsion piezoelectric energy harvesting systems. *Applied Mathematical Modelling*, 2025, vol. 138, p. 115755.

Il peut être consulté en ligne à l'adresse suivante :

https://doi.org/10.1016/j.apm.2024.115755

Après avoir exploré expérimentalement différentes formulations de nanocomposites piézoélectriques à base de PVDF et conçu des structures innovantes pour maximiser la récupération d'énergie, cette partie de la thèse se concentre sur le développement d'un modèle analytique pour prédire la tension de sortie d'un PEH. Contrairement aux travaux précédents, qui se concentraient principalement sur la caractérisation expérimentale et l'optimisation structurelle des nanocomposites et des dispositifs imprimés en 3D, cette étude adopte une approche théorique pour comprendre et quantifier le comportement électromécanique des PEH. Ce modèle analytique sera également utilisé dans le dernier chapitre de cette thèse pour affiner les analyses et optimiser davantage les performances des récupérateurs d'énergie.

L'article présente un modèle analytique avancé pour prédire la tension de sortie d'un PEH exploitant simultanément les modes piézoélectriques d_{31} (extension de face) et d_{36} (cisaillement de face). L'objectif principal de cette étude est d'élargir la bande de fréquence de fonctionnement des PEH en développant des géométries capables d'exploiter à la fois les mouvements de flexion et de torsion sous une seule excitation mécanique. L'utilisation du mode de cisaillement en torsion (d_{36}) en plus du mode traditionnel d_{31} améliore l'efficacité énergétique sur une plage de fréquence plus large.

Dans ce travail, trois configurations de PEH en L – H_1, H_2 et H_3 – sont étudiées pour comparer leur capacité à générer de l'énergie à partir de vibrations mécaniques. Un modèle analytique basé sur la théorie des poutres d'Euler-Bernoulli, le principe d'Hamilton et la méthode de

Galerkin, a été développé. Ce modèle permet d'établir une relation précise entre la déformation mécanique des structures et la tension de sortie générée. Les résultats analytiques montrent que l'exploitation du mode d_{36} améliore considérablement la puissance de sortie des PEH étudiés. Parmi les trois configurations, H_1 se distingue par sa capacité à induire simultanément des mouvements de flexion et de torsion sous une seule excitation, ce qui optimise la récupération d'énergie et conduit à une augmentation significative de l'efficacité énergétique.

L'approche analytique développée dans cet article constitue une avancée majeure pour la modélisation de structures complexes multimodales. En plus de fournir un puissant outil de prédiction, ce modèle sera utilisé dans le dernier chapitre de cette thèse pour affiner l'analyse des performances des PEH et guider les choix de conception vers des solutions plus efficaces et adaptées aux besoins des applications autonomes.

Electromechanical modelling of L-shaped bending-torsion piezoelectric energy harvesting systems

Amal Megdich[a], Mohamed Habibi[a,*], Luc Laperrière[a]

[a]Department of mechanical engineering, Université du Québec à Trois Rivières, 3351 Bd des Forges, G8Z 4M3, Trois-Rivières, Canada

6.1 Abstract

Piezoelectric energy harvesting (PEH) has become an important concept in recent years, aiming to harvest energy from various mechanical vibrations. However, a significant gap has been noticed in the multimodal and multidirectional analytics of PEHs. In this context, this paper proposes an innovative approach to introduce a novel multimodal and multidirectional PEH design, which exploits both the face extension mode (d31) and the face shear mode (d36), to target low-frequency environments. The study investigates three bending-torsion L-shaped bimorph PEHs, namely H_1, H_2, and H_3. To evaluate the performance of the proposed PEHs, a distributed parameter model is developed based on the assumptions of the Euler-Bernoulli beam. The validity of the model is confirmed by analytical, numerical, and experimental results from previous work. The exploitation of the d36 mode enhances the power output of H_1, H_2, and H_3 by 67.95%, 43.66%, and 31.83 respectively. The three PEHs performances are compared quantitatively and qualitatively, and H_1 is found to be the most efficient among them. The PEH H_1 requires a single excitation to perform the coupled bending-torsion motions, resulting in an outstanding average power output of 54.66 μW, which outperforms the other two PEHs by tenfold. The use of the d36 modes to expand the frequency bandwidth and improve the power output presents an excellent innovative and practical value for piezoelectric energy harvesting.

Keywords: Multimodal, face shear mode (d36), L-shaped bimorph PEHs, bending-torsion.

6.2 Introduction

With the rapid advances in microelectronics, research over the past decade has increasingly focused on energy-harvesting devices. This technology aims to build self-powered sensors by harnessing mechanical vibrations to reduce the cost of replacing batteries [303]. In this way, various approaches based on mechanical vibrations have been introduced, including electromagnetic [405, 406], triboelectric [407, 408], and piezoelectric [409, 410]. Due to its simple

configuration, ease of implementation, absence of electromagnetic interference, and high output power, the use of piezoelectric mechanisms for powering small actuators or sensors has attracted much attention. Three approaches can be taken to improve PEH performances: the material approach, the electrical approach, and the structural approach.

Selecting the right piezoelectric material is critical to optimizing energy harvesting performance. In particular, macrofiber composite (MFC)[282, 411], polyvinylidene fluoride (PVDF)[412], and lead zirconate titanate (PZT) [413, 414] are the most used piezoelectric materials in energy harvesting literature. Much of the literature on improving power generation deals with advancing materials by developing new materials with improved properties [415, 416] or using composite structures [250, 417] to improve energy harvesting capabilities. However, the resulting materials are complex and not commercially available. Efficient power conversion circuits are also important to maximize power transfer from the PEH to the load element. Techniques such as impedance matching [418, 419], maximum power point tracking (MPPT) [420, 421], and synchronized switching [422, 423] have been used to optimize power transfer efficiency. However, the main drawbacks of the existing AC-DC rectifiers include high energy losses due to poor conductivity (in the diodes), impedance matching difficulties, low bandwidth, and low sensitivity, resulting in low power conversion efficiency of the PEH system [424].

The third approach is to tune the natural frequency of the system by optimizing the structure of the PEH to achieve a larger effective bandwidth. Conventional piezoelectric energy PEHs are often designed as a simple cantilever beam structure with single or double piezoelectric layers because of its simple configuration. Therefore, the conventional cantilever beam configuration as a PEH has been extensively studied in the literature, and considerable efforts have been made to optimize this simple structure for improved electrical performance [425, 426]. Nevertheless, there are two main problems that limit the power that can be obtained from cantilever beams. First, the high strain is limited to the region near the clamped end. Therefore, energy cannot be harvested along the entire length of the beam, resulting in low power density. Second, energy can only be effectively harvested under resonant conditions, i.e., over a limited frequency bandwidth. The multibeam structure is suitable for multidirectional harvesting and have two or more resonant frequencies that are close to each other due to the multimodal and high utilization of each piezoelectric beam. The L-shaped structure is one of the most studied multibeam structures because of its high energy conversion capacity, large frequency bandwidth, significant deformation and strain in bending and torsional motions, ease of fabrication

and testing, and good scalability to fit specific application requirements. Yao et al. [427] investigated and optimised the performance of a bistable L-shaped PEH with a single PZT layer by introducing a tip mass and a nonlinear magnetic force. Liu et al. [428] controlled the bandwidth of frequency over which energy is harvested by properly adjusting beam lengths. Nie et al. [429] exploited a 1:2 internal resonance in an L-shaped beam-mass structure for broadband and highly efficient energy harvesting. Compared to a linear system, the L-shaped PEH with 1:2 internal resonance showed 215% and 405% improvement in energy harvesting efficiency and bandwidth, respectively. To further improve this PEH, Nie et al. [430] investigated the influence of load resistance on the nonlinear output response of the internal resonanced L-shaped PEH. Li et al. [431] introduced geometric, material, and damping nonlinearities to evaluate the performance of the L-shaped PEH under large deformations and high electric field conditions. Kouritem et al. [432] demonstrated that increasing the number of concentrated masses in L-shaped PEH increases the output power and broadband natural frequency. However, most previous studies on the L-shaped PEH focused mainly on energy harvesting in the bending mode. Torsional shear vibration is widely used in mechanical engineering, and this method of operation can realize highly efficient energy conversion [399]. However, it has not been sufficiently utilized in the field of energy harvesting, either because of the polarization direction and the position of the electrodes [433], or because the twist angle is too small to contribute to the energy harvesting [434].

Recently, a new pathway has emerged that warrants thorough exploration - the face shear mode (d36 mode). This intriguing mode promises to harness electrical energy from torsional motion, potentially revolutionizing energy conversion technologies. Despite its inherent potential to increase frequency bandwidth and boost energy output, the face shear mode has been largely overlooked until recently. This is because the piezoelectric constant d36 associated with face shear mode is too small to collect mechanical energy. Remarkably, in 2015, Miaw et al [435] succeeded in achieving d36 coefficients as high as 206pC/N by changing the symmetry of the poled PZT ceramic from transversely isotropic to orthogonal. Building on this breakthrough achievement, in 2020 Li et al [436] investigated the possibility of designing a bending-torsion L-shaped bimorph PEH (called H2) that utilizes both d31 and d36 modes to extend the frequency bandwidth and increase the power. The concept of using the inherent torsional motion in the second eigenmode of a structure to bring the resonant frequencies closer together is an intriguing proposal. This led us to design and analyze a PEH called H3, in which the main beam experiences torsion at its first resonant frequency. However, challenges arose in the form

of dual excitations required for bending and torsional motions in PEHs H2 and H3. In addition, the decoupling of bending and torsional motions limited the influence of the d36 mode, which manifested only at the second resonant frequency of H2 and the first resonant frequency of H3. This is where a breakthrough solution comes into play – the development of PEH H_1, which undergoes coupled bending and torsional motions through a single excitation. This ingenious design uses bending-torsion coupling to enable torsional motion in all natural modes. The key point of this research is to shed light on the effects of the d36 mode on the average harvested energy of the three PEHs while performing a comparative analysis of their performance.

Our seminal contribution lies in the pioneering development of an analytical model that ingeniously incorporates both d31 and d36 modes, using established analytical theories such as Euler-Bernoulli beam theory, the Hamilton's principle, and the Galerkin's technique. This sophisticated model is strategically designed to exploit the full potential of coupled motions by seamlessly merging bending and torsional dynamics, all with a single mechanical excitation. Unlike previous efforts, which often focused exclusively on separated bending and torsional motions constrained by the inherent decoupling limitations of the PEH, our method breaks through these barriers and creates a harmonious synergy between these two key modes that spans the entire frequency spectrum. This paradigm shift in approach stands in stark contrast to previous studies and their limited power generation capabilities, as evidenced by the earlier work [36] that serves as the fundamental benchmark for validating our analytical model. Our work not only bridges this critical gap, but also sets the stage for unprecedented advances in energy harvesting from both bending and torsional motions, positioning our research at the forefront of innovation in the field.

It is important to note that energy harvesters in the real world often exhibit complex, non-linear behaviour, whereas our initial modelling is intentionally linear. This choice was made to fulfil the primary goal of this study, which is to provide a basic understanding of the behaviour and performance of three multimodal and multidirectional L-shaped PEHs under simplified conditions. Linear modelling offers several advantages, including ease of interpretation, mathematical tractability, and computational efficiency, making it an ideal starting point for our analysis. By focusing on the linear aspects of the systems, we can provide a clear and structured insight into their fundamental behaviour, which can serve as a valuable basis for further investigation.

6.3 Analytical modeling

In this section, a comprehensive analysis of the dynamics of three L-shaped bimorph PEHs is presented by applying a distributed parameter model. This model accounts for both bending and torsional motions. The equations of motion and associated boundary conditions are derived using the Hamilton's principle, which provides a rigorous basis for understanding the dynamic responses of the PEHs. The electrical equations of the circuit with a parallel connection between the piezoelectric layers are also derived using Gauss's law.

6.3.1 Model description

This study investigates the dynamic behaviour of three L-shaped bimorph PEHs, designated H_1, H_2, and H_3. Each PEH configuration was carefully designed to optimize the energy harvesting efficiency. The structures consist of two composite beams with two PZT layers and one steel layer, and mass blocks m1 and m2 located at the corner and free end, respectively. For H_1 (Figure 54(a)), to initiate the motion, a harmonic excitation is applied in the y-direction at the clamped end of the main beam, defined by $Y(t) = Y_0 \sin(\Omega t)$, where Y_0 is the applied amplitude and Ω is the excitation frequency. This excitation causes the flexible beams to undergo coupled bending and torsional motions. The presence of the auxiliary beam and mass blocks results in a torsional motion in the main beam, while the transverse excitation forces bending motions in both beams.

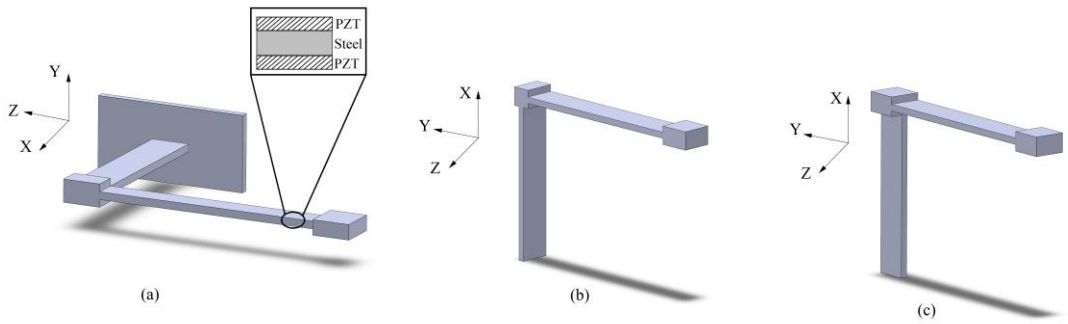

Figure 54: Schematic of the L-shaped bimorph PEHs (a) H_1, (b) H_2, and (c) H_3 with four PZT layers, two steel layers, and two lumped mass blocks.

The PEHs H_2 (Figure 54(b)) and H_3 (Figure 54(c)) are subjected to two different harmonic excitations: one in the x-direction ($X = X_0 \sin(\Omega t)$) and the other in the z-direction ($Z = Z_0 \sin(\Omega t)$), where X_0 and Z_0 represent the applied amplitudes and Ω stands for the excitation frequency. In the PEH H_2, the excitation in the x-direction results in bending motions in both

the main beam and the auxiliary beam, while the excitation in the z-direction leads to out-of-plane bending of the auxiliary beam, resulting in a torsional motion in the main beam. In the case of the PEH H_3, the excitation in the x-direction results in a bending motion of the auxiliary beam. Similarly, excitation in the z-direction triggers both bending in the main beam and out-of-plane bending in the auxiliary beam, which in turn results in torsional motion in the main beam. The dynamics of the three PEHs are comprehensively illustrated in Figure 55. The strategic installation of mass blocks significantly amplifies the vibration amplitudes and torsion angles, contributing to improved energy harvesting capabilities.

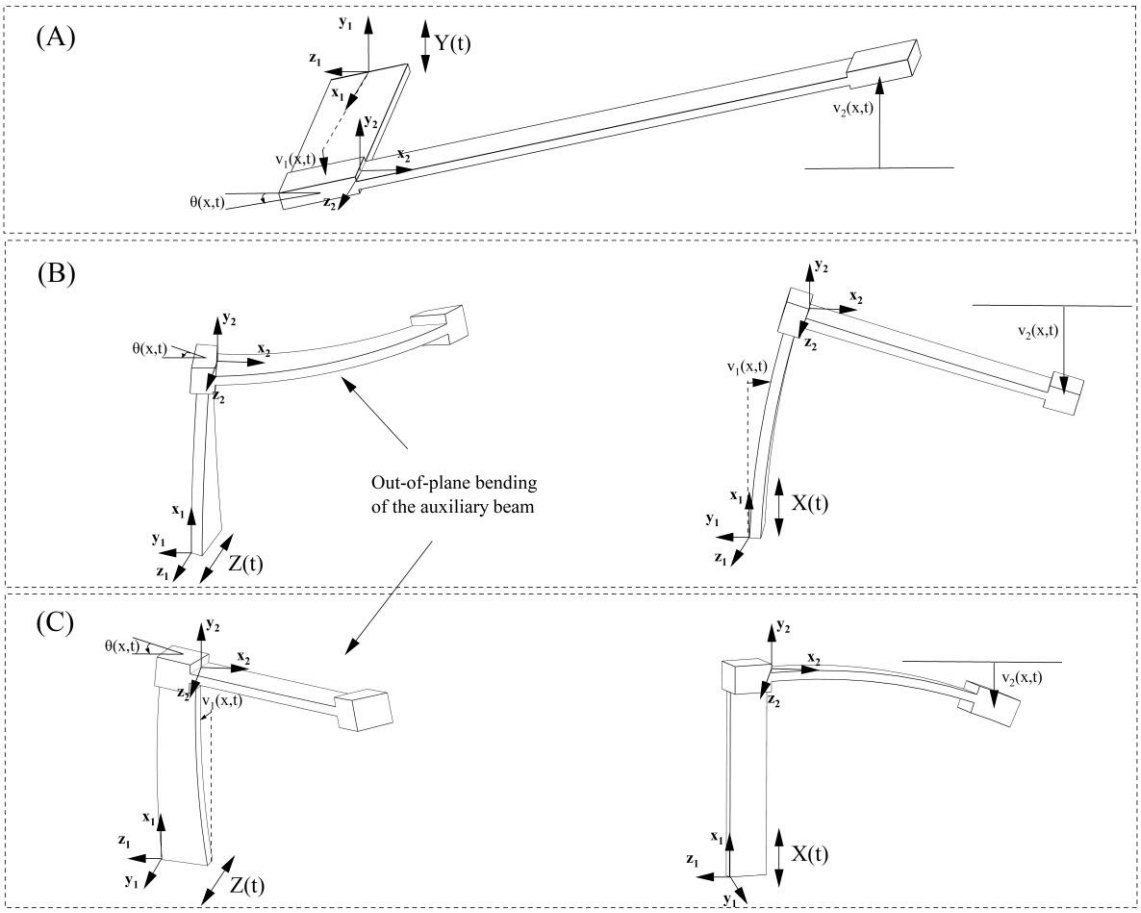

Figure 55: Schematic Illustration of the deformation patterns in PEHs (A) H_1 (B), H_2, and (C) H_3, undergoing bending and torsional motions, defined by the transverse displacement of the main and auxiliary beams ($v_1(x,t)$ and $v_2(x,t)$) and the torsional angle $\theta(x,t)$ of the main beam.

The three studied structures have identical material properties, ensuring a consistent and controlled comparison in the next sections. For each PEH, the material properties and the size of the piezoelectric and steel layers on both beams are identical. The geometrical and physical properties of the bimorph beams and the mass blocks of H_1 are shown in Table 23. The dimensions of the beams and masses of H_2 and H_3 are provided in Table 4 of the reference

[436]. To enable efficient energy conversion, the opposing surfaces of each piezoelectric layer are completely covered with highly conductive electrodes. These electrodes enable optimal electrical connection and ensure effective energy transfer. To enhance power generation, the two piezoelectric surfaces in each substructure are connected in a parallel configuration, to strategically exploit their combined potential. The electrical loads consist of two resistors, designated R_1 and R_2, connected respectively to the main beam and the auxiliary beam. The positions of the different layers inside the beams in the local coordinate system are illustrated in Figure 56.

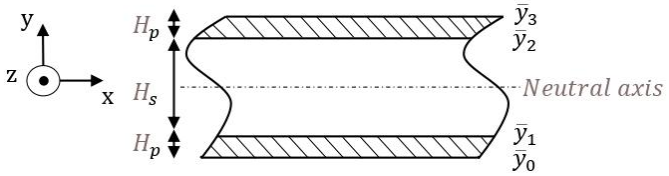

Figure 56: Layer positions of the composite cross-section in the beam's local coordinate system (x, y, z).

Table 23: Physical and geometric properties of the structure of H_1.

Es	Steel Young's modulus (GPa)	193
Ep	Piezoelectric material Young's modulus (GPa)	66
Gs	Steel Coulomb's modulus (GPa)	74.806
Gp	Piezoelectric material Coulomb's modulus (GPa)	25.19
L_1	Length of the main beam (mm)	100
L_2	Length of the auxiliary beam (mm)	150
Hs	Height of the steel layers (mm)	1
Hp	Height of the piezoelectric layers (mm)	0.2
b_1	Width of the main beam (mm)	20
b_2	Width of the auxiliary beam (mm)	10
ρ_s	Steel density (kg/m^3)	7930
ρ_p	Piezo density (kg/m^3)	5440
ρ_{m1}	Density of m1 (kg/m^3)	7850
ρ_{m2}	Density of m2 (kg/m^3)	11343.7
L_m	Length of m1 and m2 (mm)	20
h_m	Thickness of m1 and m2 (mm)	3
e31	Piezoelectric coupling coefficient (C/m^2)	-14.85
e36	Equivalent piezoelectric coupling coefficient (C/m^2)	6.876
ϵ33	Piezoelectric permittivity (nF/m)	32.15
R1, R2	Resistances attached to the beams (Ω)	-
Ξ	The modal damping ratio	0.002

The kinetic energies of the three PEHs H_1, H_2, and H_3 are respectively given by [429]:

$$T_{H1}(t) = \int_0^{L_1} \frac{1}{2}\Big[(\rho A)_1 \left(\dot{v}_1(x_1,t) + \dot{Y}(t)\right)^2 + J_{1x}\dot{\theta}(x_1,t)^2\Big]\mathrm{d}x + \frac{1}{2}m_1\dot{v}_1^2(L_1,t) + \frac{1}{2}m_2(\dot{v}_2(L_2,t) + \dot{v}_1(L_1,t)^2 + \int_0^{L_2} \frac{1}{2}\Big[(\rho A)_2\big(\dot{v}_2(x_2,t) + \dot{v}_1(L_1,t)\big)^2\Big]\mathrm{d}x + (J_{2z}L_2 + J_{m2z})\dot{\theta}^2(L_1,t), \quad (19)$$

$$\begin{aligned} T_{H2}(t) = {} & \int_0^{L_1} \frac{1}{2}\big[(\rho A)_1\dot{v}_1^2(x_1,t) + J_{1x}\dot{\theta}^2(x_1,t)\big]\mathrm{d}x + \frac{1}{2}m_1\dot{v}_1^2(L_1,t) + \frac{1}{2}\rho A L_2\dot{v}_1^2(L_1,t) \\ & + \frac{1}{2}J_1\dot{v}_1'^2(L_1,t) + \int_0^{L_2} \frac{1}{2}\big[(\rho A)_2\dot{v}_2(x_2,t) + (\rho A)_2\dot{X}(t) + m_2\delta(x_2 - L_2)\dot{X}(t)\big]^2\mathrm{d}x \\ & + \frac{1}{2}J_{2x}\dot{\theta}^2(L_1,t) - \frac{1}{2}J_{2y}\dot{Z}(t)\dot{\theta}(L_1,t) + \frac{1}{2}J_{m1x}\dot{\theta}^2(L_1,t) + \frac{1}{2}m_2(\dot{v}_1^2(L_1,t) + \\ & \dot{v}_2^2(L_2,t) + \frac{1}{2}J_2\dot{v}_2'^2(L_2,t) + \frac{1}{2}J_{m2x}\dot{\theta}^2(L_1,t) - \frac{1}{2}J_{m2}\dot{Z}(t)\theta(L_1,t), \end{aligned} \quad (20)$$

$$\begin{aligned} T_{H3}(t) = {} & \int_0^{L_1} \frac{1}{2}\big((\rho A)_1\dot{v}_1(x_1,t) + (\rho A)_1\dot{Z}(t) + m_1\delta(x_1 - L_1)\dot{Z}(t)\big)^2\mathrm{d}x + \int_0^{L_1} \frac{1}{2}J_{1x}\dot{\theta}^2(x_1,t)\mathrm{d}x \\ & + \int_0^{L_2} \frac{1}{2}\big((\rho A)_2\dot{v}_2(x_2,t) + (\rho A)_2\dot{X}(t) + m_2\delta(x_2 - L_2)\dot{X}(t)\big)^2\mathrm{d}x + \frac{1}{2}\big(J_{2x}\dot{\theta}^2(L_1,t) \\ & - J_{2y}\dot{Z}^2(t)\dot{\theta}(L_1,t) + \frac{1}{2}m_1\dot{v}_1^2(L_1,t) + \frac{1}{2}J_1\dot{v}_1'^2(L_1,t) + \frac{1}{2}m_2\dot{v}_2^2(L_2,t) + \frac{1}{2}J_2\dot{v}_2'^2(L_2,t) \\ & + \frac{1}{2}J_{m1x}\dot{\theta}^2(L_1,t) + \frac{1}{2}\big(J_{m2x}\dot{\theta}^2(L_1,t) - J_{m2}\dot{Z}(t)\theta(L_1,t)\big). \end{aligned} \quad (21)$$

where the over dot and the prime are derivatives with respect to time and space, respectively, δ is the Dirac delta function, $v_1(x,t)$ and $v_2(x,t)$ are the transverse deflections of the main and auxiliary beam, respectively, and $\theta(x,t)$ is the twist angle of the main beam, for each PEH. Also, $(\rho A)_i = b_i\big(2h_p\rho_p + h_s\rho_s\big)$ are the beams' masses by length unit, i=1, 2 is the beam's number, and the moments of inertia are given in Appendix B.

The total potential energy of each PEH is $U=U_1+U_2$, where U_1 and U_2 are the potential energy of the main and auxiliary beam, respectively, they are given by [437]

$$\begin{aligned} U_1(t) &= \frac{1}{2}\int_0^{L_1}\int_S (\sigma_{11}^1\varepsilon_{11}^1 + \sigma_{12}^1\varepsilon_{12}^1 + \sigma_{13}^1\varepsilon_{13}^1)\mathrm{d}S\mathrm{d}x, \\ U_2(t) &= \frac{1}{2}\int_0^{L_2}\int_S \sigma_{11}^2\varepsilon_{11}^2\mathrm{d}S\mathrm{d}x. \end{aligned} \quad (22)$$

Assuming an Euler-Bernoulli beam model and Hooke's law with a linear piezoelectric constitutive equation, and assuming that the electric field across the piezoelectric layers is $E_3^p = -\frac{V_i(t)}{h_p}[H(x) - H(x - L_i)]$, we end up with the following relations [438, 439]

$$\begin{aligned} & \varepsilon_{11}^i = -y_i v_i'', \varepsilon_{12}^i = -\frac{1}{2}z_i\theta', \varepsilon_{13}^i = \frac{1}{2}y_i\theta', \sigma_{11,s}^i = -E_s y_i v_i'', \sigma_{12,s}^i = -G_s z_i\theta', \sigma_{13,s}^i = G_s y_i\theta' \\ & \sigma_{11,p}^i = -E_p y_i v_i'' + e_{31}\frac{V_i}{h_p}U_{Li}, \sigma_{12,s}^i = -G_p z_i\theta', \sigma_{13,s}^i = G_p y_i\theta' + e_{36}\frac{V_i}{h_p}U_{Li}, \end{aligned} \quad (23)$$

where $U_{Li} = H(x) - H(x - Li)$, $H(x)$ is the Heaviside unit step function, i = 1, 2 is the beam's number, Vi is the voltages across beam i and s and p subscript denote the parameter associated with the steel and piezoelectric layers, respectively. The choice of Euler-Bernoulli beam theory is related to the fact that Euler-Bernoulli beam theory provides a simplified and accurate representation of beam deformation, allowing for a better understanding of the dynamics of the system. Since Euler-Bernoulli theory is widely used in both research and industry for beam

analysis, including piezoelectric energy PEHs, it embodies a well-accepted and established practice in our field.

Substituting Equation (23) into Equation (22), the potential energies of the two beams of each PEH are given by:

$$\begin{aligned} U_1(t) &= \tfrac{1}{2}\int_0^{L_1} \left(EIv_1''^2(x_1,t) + \Theta_1 V_1(t) U_{L1} v_1''(x_1,t) + GI\theta'^2(x_1,t) + \Theta_1 V_1(t) U_{L1}\theta'(x_1,t)\right)\mathrm{d}x_1, \\ U_2(t) &= \tfrac{1}{2}\int_0^{L_2} \left(EIv_2''^2(x_2,t) + \Theta_2 V_2(t) U_{L2} v_2''(x_2,t)\right)\mathrm{d}x_2. \end{aligned} \tag{24}$$

where the bending and torsion stiffnesses are given by:

$$\begin{aligned} EI_i &= \tfrac{1}{3}E_p b_i(\bar{y}_3^3 - \bar{y}_2^3) + \tfrac{1}{3}E_p b_i(\bar{y}_1^3 - \bar{y}_0^3) + \tfrac{1}{3}E_s b_i(\bar{y}_2^3 - \bar{y}_1^3), \\ GI_1 &= G_p\left(\tfrac{1}{12}h_p b_1^3 + \tfrac{1}{3}b_1(\bar{y}_3^3 - \bar{y}_2^3)\right) + G_p\left(\tfrac{1}{12}h_p b_1^3 + \tfrac{1}{3}b_1(\bar{y}_1^3 - \bar{y}_0^3)\right) + G_s\left(\tfrac{1}{12}h_s b_1^3 + \tfrac{1}{3}b_1(\bar{y}_2^3 - \bar{y}_1^3)\right), \end{aligned} \tag{25}$$

and the piezoelectric coupling coefficient Θi, for parallel configuration is calculated as

$$\begin{aligned} \Theta_1 &= -\tfrac{1}{2}b\left(e_{31}(\bar{y}_1 - \bar{y}_0) + e_{31}(\bar{y}_3 + \bar{y}_2)\right), \\ \Theta_2 &= -\tfrac{1}{2}b\left(e_{36}(\bar{y}_1 - \bar{y}_0) + e_{36}(\bar{y}_3 + \bar{y}_2)\right). \end{aligned} \tag{26}$$

To satisfy the continuity of the bending moment M_{b2} and the shear force T_{y2}, additional continuity conditions should be introduced. For the PEHs H_1 and H_2, these continuity conditions are considered by writing the works W_{H1} and W_{H2} of non-conservative M_{b2} and T_{y2}:

$$\begin{aligned} W_{H_1}(t) &= -M_{b2}(0,t)\theta(L_1,t) - T_{y2}(0,t)v_1(L_1,t), \\ W_{H_2}(t) &= -M_{b2}(0,t)v_1'(L_1,t), \end{aligned} \tag{27}$$

where $$M_{b2}(x_2,t) = EIv_2''(x_2,t) + \Theta_2 V_2(t) U_{L2} \text{ and } T_{y2}(x_2,t) = -M_{b2}'(x_2,t). \tag{28}$$

6.3.2 Equations of motion and boundary conditions

By applying Hamilton's principal, the equations of motion of each PEH can be written as follows

$$\begin{aligned} &(\rho A)_1 \ddot{v}_1(x_1,t) + EI_1 v_1''''(x_1,t) + \Theta_1 V_1(t) U_{L1}'' = F_1(t), \\ &(\rho A)_2 \ddot{v}_2(x_2,t) + EI_2 v_2''''(x_2,t) + \Theta_2 V_2(t) U_{L2}'' = F_2(t), \\ &J_{1x}\ddot{\theta}(x_1,t) - GI_1\theta''(x_1,t) + \Theta_3 V_1(t) U_{L1}' = 0, \end{aligned} \tag{29}$$

with the associated boundary conditions

$$\begin{aligned} &v_1(0,t) = 0, v_1'(0,t) = 0, \theta(0,t) = 0, v_2(0,t) = 0, v_2'(0,t) = 0, \\ &EIv_1''(L_1,t) = S_1, EIv_1'''(L_1,t) = S_2, EIv_2''(L_2,t) = S_3, EIv_2'''(L_2,t) = S_4, GI\theta'(L_1,t) = S_5. \end{aligned} \tag{30}$$

The expressions of F_i and S_i are defined in Table 24.

Table 24: Expressions of the parameters in the equation of motion and boundary conditions for each system.

PEH	H_1	H_2	H_3
F1	$-(\rho A)_1 a_y(t)$	0	$-\big((\rho A)_1 + m_1\delta(x-L_1)\big)a_z(t)$
F2	$-(\rho A)_2 \ddot{v}_1(L_1)$	$-\big((\rho A)_2 + m_2\delta(x-L_2)\big)a_x(t)$	$-\big((\rho A)_2 + m_2\delta(x-L_2)\big)a_x(t)$
S1	0	$EIv_2''(0) - J_1\ddot{v}_1'(L_1)$	$-J_1\ddot{v}_1'(L_1,t)$
S2	$EIv_2'''(0) + m_1\ddot{v}_1(L_1)$	$(m_1 + m_2 + (\rho A)_2 L_2)\ddot{v}_1(L_1)$	$m_1\ddot{v}_1(L_1,t)$
S3	0	$-J_2\ddot{v}_2'(L_2)$	$-J_2\ddot{v}_2'(L_2,t)$
S4	$m_2[\ddot{v}_2(L_2) + \ddot{v}_1(L_1)]$	$m_2\ddot{v}_2(L_2)$	$m_2\ddot{v}_2(L_2,t)$
S5	$EIv_2''(0,t) - (J_{2z}L_2 + J_{m2z})\ddot{\theta}(L_1,t)$	$-(J_{2x} + J_{m1x} + J_{m2x})\ddot{\theta}(L_1,t) + (J_{2y} + J_{m2})a_z(t)$	$-(J_{2x} + J_{m1x} + J_{m2x})\ddot{\theta}(L_1,t) + (J_{2y} + J_{m2})a_z(t)$

A comprehensive demonstration of this process is detailed in Appendix A.

6.3.3 Electromechanical coupling harmonic response analysis

The layers have a parallel configuration, and a load resistance noted Ri is connected to beam i. Applying Gauss's law, the electric current Ii through the resistance load for beam i is given by:

$$I_i = \frac{V_i}{R_i} = \frac{d}{dt}\int_{A_j} D_i^j \cdot n_j dA_j, \tag{31}$$

where n is the unit normal vector to the electrodes, and D_{ij} is the electric displacement of the j^{th} piezoelectric layer of beam i, given by [440]

$$D_i^j = e_{31}\varepsilon_{11}^i + e_{36}\varepsilon_{13}^i + \epsilon_{33}\frac{V_i}{h_p}U_{Li}. \tag{32}$$

Electromechanical equations of H_1

Substituting Equations (23) into (32), and applying Gauss's law, we end up with the following equations:

$$\begin{aligned} C_{p1}\dot{V}_1(t) + \frac{V_1(t)}{R_1} &= bk_1\big(\dot{v}_1'(L_1,t) - \dot{v}_1'(0,t)\big) + bk_3\left(\dot{\theta}(L_1,t) - \dot{\theta}(0,t)\right), \\ C_{p2}\dot{V}_2(t) + \frac{V_2(t)}{R_2} &= bk_2\big(\dot{v}_2'(L_2,t) - \dot{v}_2'(0,t)\big), \end{aligned} \tag{33}$$

where

$$C_{p1} = \left(\frac{\epsilon_{33}^{sp1}}{h_{p1}} + \frac{\epsilon_{33}^{sp2}}{h_{p2}}\right) bL_1,$$
$$C_{p2} = \left(\frac{\epsilon_{33}^{sp3}}{h_{p3}} + \frac{\epsilon_{33}^{sp4}}{h_{p4}}\right) bL_2 \quad (34)$$

are respectively the internal capacitances of the piezoelectric layers of the main and auxiliary composite beams, and k_1, k_2, and k_3 indicate constants related to material properties and beam geometries, which are represented by:

$$k_1 = -\left(h_{cp1}e_{31}^{p1} + h_{cp2}e_{31}^{p2}\right),$$
$$k_2 = -\left(h_{cp3}e_{31}^{p3} + h_{cp4}e_{31}^{p4}\right), \quad (35)$$
$$k_3 = -\left(h_{cp1}e_{36}^{p1} + h_{cp2}e_{36}^{p2}\right),$$

where h_{cpi} ($i \in \{1, 2, 3, 4\}$) are respectively the distances between the centre of piezoelectric layers and the neutral axis in the main and auxiliary composite beams, given by:

$$h_{cp1} = \frac{h_{s1}+h_{p1}}{2}, \quad h_{cp2} = \frac{h_{s1}+h_{p2}}{2},$$
$$h_{cp3} = \frac{h_{s2}+h_{p3}}{2}, \quad h_{cp4} = \frac{h_{s2}+h_{p4}}{2}. \quad (36)$$

Electromechanical equations of H_2 and H_3

Using the same demonstration, we get the electromechanical equations of the two PEHs H_2 and H_3

$$C_{p1}\dot{V}_1(t) + \frac{V_1(t)}{R_1} = bk_1\left(\dot{v}_1'(L_1,t) - \dot{v}_1'(0,t)\right),$$
$$C_{p2}\dot{V}_2(t) + \frac{V_2(t)}{R_2} = bk_2\left(\dot{v}_2'(L_2,t) - \dot{v}_2'(0,t)\right), \quad (37)$$
$$C_{p3}\dot{V}_3(t) + \frac{V_3(t)}{R_1} = bk_3\left(\dot{\theta}(L_1,t) - \dot{\theta}(0,t)\right),$$

where $C_{p3}=C_{p1}$

6.4 Structural natural frequencies and mode shapes

In this section, first, an analytical approach is used to formulate an eigenvalue problem (EVP) for each PEH. This analytical method can be used to derive the structural natural frequencies and corresponding eigenmodes, which provides important insight into the dynamic behaviour of the PEHs. We then take advantage of FE modelling to verify the accuracy and reliability of our analytical results. By developing a FE model, we can effectively validate the structural natural frequencies determined by the analytical approach. For further validation, we use the numerical data provided by Li et al. [436] for H_2 to ensure a comprehensive and rigorous assessment of our results.

6.4.1 Analytical mode shapes and natural frequencies

To derive the closed-circuit unforced and undamped EVP for the PEH, it is assumed that $V_i = 0$ and that $v_1(x_1,t) = \phi_{1k}(x_1)e^{i\omega t}, v_2(x_2,t) = \phi_{2k}(x_2)e^{i\omega t}, \theta(x_1,t) = \phi_{3k}(x_1)e^{i\omega t}$, where k=1, 2, 3 is the PEH number. The external excitations are set to zero, along with the voltages V_1 and V_2 (close circuit condition). As a result, the eigenvalue problem for each PEH H_k can be written as follows:

$$\phi_{1k}'''' - \frac{(\rho A)_1\omega^2}{EI}\phi_{1k} = 0, \phi_{2k}'''' - \frac{(\rho A)_2\omega^2}{EI}\phi_{2k} = 0, \phi_{3k}'' + \frac{J_{1x}\omega^2}{GI}\phi_{3k} = 0. \quad (38)$$

The general solutions of these equations are given by [441]:

$$\begin{aligned}\phi_{1k}(x_1) &= A_{1k}\cos(\beta_1 x_1) + B_{1k}\sin(\beta_1 x_1) + C_{1k}\cosh(\beta_1 x_1) + D_{1k}\sinh(\beta_1 x_1),\\ \phi_{2k}(x_2) &= A_{2k}\cos(\beta_2 x_2) + B_{2k}\sin(\beta_2 x_2) + C_{2k}\cosh(\beta_2 x_2) + D_{2k}\sinh(\beta_2 x_2),\\ \phi_{3k}(x_1) &= A_{3k}\cos(\beta_3 x_1) + B_{3k}\sin(\beta_3 x_1),\end{aligned} \quad (39)$$

where $\beta_1 = \sqrt[4]{\frac{(\rho A)_1\omega^2}{EI_1}}, \beta_2 = \sqrt[4]{\frac{(\rho A)_2\omega^2}{EI_2}}, \beta_3 = \sqrt{\frac{J_{1x}\omega^2}{GI_1}}$ and the coefficients are obtained using the associated boundary conditions for each PEH:

PEH H_1:
$$\begin{aligned}&\phi_{11}(0) = 0, \phi_{11}'(0) = 0, EI_1\phi_{11}''(L_1) = 0, EI_1\phi_{11}'''(L_1) - EI_2\phi_{21}'''(0) = 0, \phi_{31}(0) = 0,\\ &GI_1\phi_{31}'(L_1) - EI_2\phi_{21}''(0) = \omega^2 J_{2z}L_2\phi_{31}(L_1), EI_2\phi_{21}''(L_2) = 0, \phi_{21}(0) = \phi_{11}(L_1)\\ &\phi_{21}'(0) = \phi_{31}(L_1),\ EI_1\phi_{11}'''(L_1) = -\omega^2 m_1\phi_{11}(L_2), EI_2\phi_{21}'''(L_2) = -\omega^2 m_2\phi_{21}(L_2).\end{aligned} \quad (40)$$

PEH H_2:
$$\begin{aligned}&\phi_{12}(0) = 0, \phi_{12}'(0) = 0, EI\phi_{12}''(L_1) - EI\phi_{22}''(0) = \omega^2 J_1\phi_{12}'(L_1),\\ &EI\phi_{12}'''(L_1) = -\omega^2(m_1 + m_2 + \rho AL_2)\phi_{12}(L_1), EI\phi_{22}''(L_2) = \omega^2 J_2\phi_{22}'(L_2),\\ &EI\phi_{22}'''(L_2) = -\omega^2 m_2\phi_{22}(L_2), \phi_{22}(0,t) = 0, \phi_{22}'(0) = \phi_{12}'(L_1),\\ &\phi_{32}(0) = 0, GI\phi_{32}'(L_1) - \left(J_{2y} + J_{m1y} + J_{m2y}\right)\omega^2\phi_{32}(L_1) = 0.\end{aligned} \quad (41)$$

PEH H_3:
$$\begin{aligned}&\phi_{13}(0) = 0, \phi_{13}'(0) = 0, EI\phi_{13}''(L_1) - EI\phi_{23}''(0) = \omega^2 J_1\phi_{13}'(L_1),\\ &EI\phi_{13}'''(L_1) = -\omega^2(m_1 + m_2 + (\rho A)_2L_2)\phi_{13}(L_1), EI\phi_{23}''(L_2) = \omega^2 J_2\phi_{23}'(L_2),\\ &EI\phi_{23}'''(L_2) = -\omega^2 m_2\phi_{23}(L_2), \phi_{23}(0,t) = 0, \phi_{23}'(0) = \phi_{12}'(L_1),\\ &\phi_{33}(0) = 0, GI\phi_{33}'(L_1) - \left(J_{2y} + J_{m1y} + J_{m2y}\right)\omega^2\phi_{33}(L_1) = 0.\end{aligned} \quad (42)$$

6.4.2 Numerical mode shapes and natural frequencies

In this part, we performed a comprehensive analysis of the dynamic behavior of the three PEHs using ANSYS software. The main focus was on the calculation of the first three natural frequencies and the corresponding modes shapes for each PEH configuration. The results of these calculations were then compared with the analytical results, as shown in Table 25. The comparison revealed small relative errors between the theoretical model and the ANSYS simulations. This can be attributed to the use of different approaches in the two methods. The theoretical model relies on Euler-Bernoulli theory, while the finite element model uses three-

dimensional solid models. Despite this discrepancy, the close agreement between the two sets of results confirms the accuracy of our theoretical predictions.

Table 25: First three resonance frequencies of H_1, H_2, and H_3 obtained analytically and numerically under open circuit conditions.

PEH	Mode	Frequency (Theory) (Hz)	Frequency (ANSYS) (Hz)	Relative error (%)
H_1	1 (bending)	7.22	7.23	0.13
	2 (bending)	27.49	27.99	1.78
	3 (torsion)	118.74	111.94	-6.08
H_2	1 (bending)	36.83	35.89	-2.62
	2 (torsion)	55.49	55.28	-0.38
	3 (bending)	115.66	114.89	-0.67
H_3	1 (torsion)	37.89	33.59	-12.79
	2 (bending)	46.14	45.66	-1.04
	3 (bending)	126.05	110.47	-14.1

In addition, our investigation revealed interesting insights into the nature of the torsional motion in the PEHs. In the case of H_2, the torsional motion is aligned with the second natural frequency, while in H_3 it coincides with the first natural frequency. In the case of H_1, the torsional motion is present in all three modes, although it clearly dominates at the third natural frequency. Figure 57 shows the first three bending mode shapes of H_2 obtained from our analytical modal analysis, together with the numerical results from reference [436]. The remarkable agreement between these results supports our confidence in the accuracy of our analytical model.

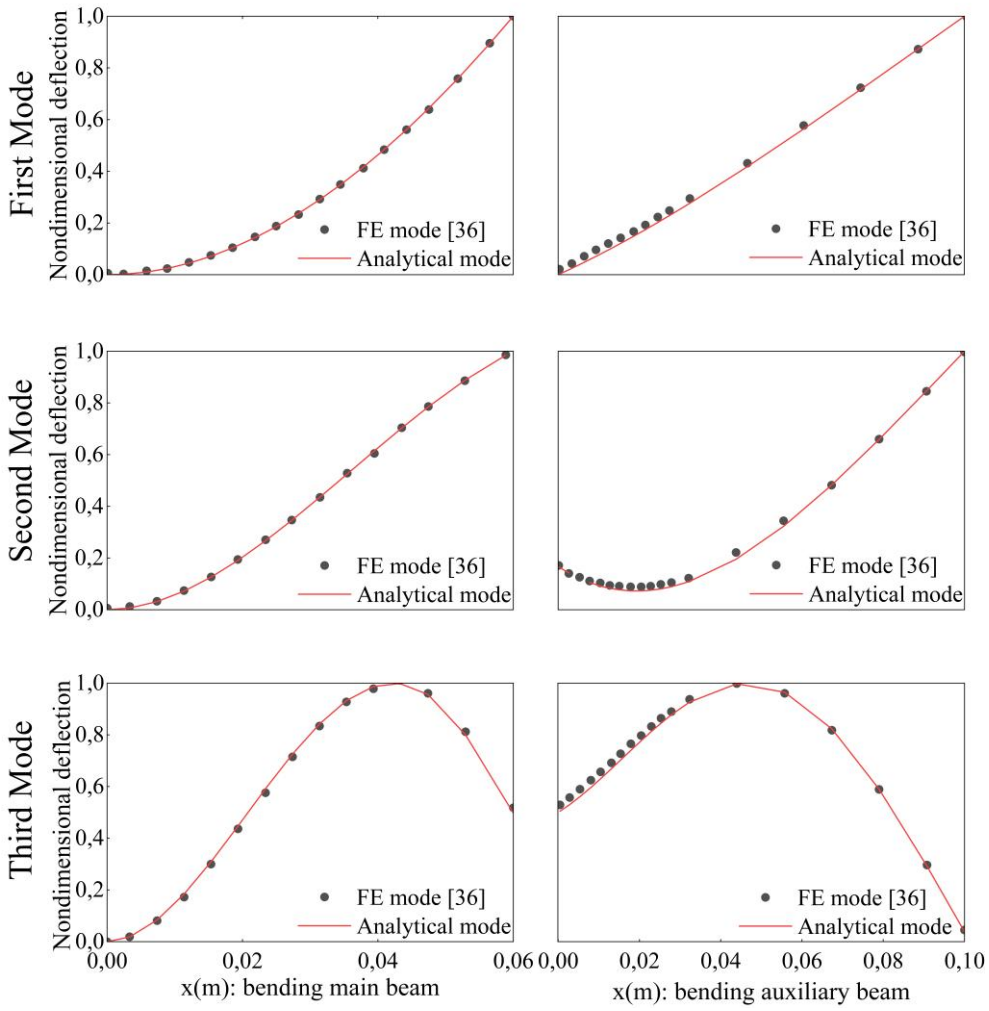

Figure 57: Comparison of the analytical and numerical results of the first three bending mode shapes of H_2.

6.5 Reduced order model and analytical solutions

In this section, we use the Galerkin procedure and the Euler-Lagrange method to discretize the governing equations for the considered PEHs. The calculated analytical mode shapes are used as a test function for the discretization procedure. Then the dynamic responses, electric voltages, and harvested electrical powers are obtained as closed-form formulas.

Using the Galerkin approximation, the orthogonality of the eigenvectors is useful to consider them as a complete set. Therefore, any function that satisfies the boundary conditions of the eigenvalue problem can be represented as a linear combination of the eigenvectors. Thus, the deflections *vi (x, t)* of the two beams and the twist angle θ(x,t) of the main beam are approximated for each PEH H_k [442]:

$$v_{1k} = \sum_{r=1}^{n} \phi_{1k}^{(r)}(x)\eta_{1k}^{(r)}(t), v_{2k} = \sum_{r=1}^{n} \phi_{2k}^{(r)}(x)\eta_{2k}^{(r)}(t), \theta_k = \sum_{r=1}^{n} \phi_{3k}^{(r)}(x)\eta_{3k}^{(r)}(t), \quad (43)$$

where n is the number of retained mode shapes, $\phi_{1k}(x), \phi_{2k}(x), and\ \phi_{3k}(x)$ are respectively the main beam bending eigenmodes, the auxiliary beam bending eigenmodes, and the main beam torsional eigenmodes of the PEH H_k, and η_{ik} are the corresponding modal coordinates.

For the PEH H_1, the three motions are coupled. Thus, we denote $\eta_{11}^{(r)} = \eta_{21}^{(r)} = \eta_{31}^{(r)} = \eta_r$. For the PEH H_2, the bending motions of the two beams are coupled. Thus, we denote $\eta_{12}^{(r)} = \eta_{22}^{(r)} = \eta_r$. The Euler-Lagrange approach is used here to derive the discretized equations of motion, defined by:

$$\frac{\mathrm{d}}{\mathrm{d}t}\frac{\partial \mathcal{L}_k}{\partial \eta_r} - \frac{\partial \mathcal{L}_k}{\partial \eta_r} = 0, \tag{44}$$

where $\mathcal{L}_k$ is Lagrangian of the PEH H_k, defined by by $\mathcal{L}_k = T_k - U_k$.

6.5.1 Reduced order model of H_1

Using the equations of motion and the boundary conditions developed in Equations (29) and (30) respectively, the corresponding orthogonality conditions are obtained as follows [443]:

$$\begin{aligned} &EI_1 \int_0^{L_1} \phi_{11}^{(r)''}(x)\phi_{11}^{(s)''}(x)\mathrm{d}x + EI_2 \int_0^{L_2} \phi_{21}^{(r)''}(x)\phi_{21}^{(s)''}(x)\mathrm{d}x + GI_1 \int_0^{L_1} \phi_{31}^{(r)'}(x)\phi_{31}^{(r)'}(x)\mathrm{d}x \\ &\qquad = \omega_r^2 \delta_{rs}, \\ &(\rho A)_1 \int_0^{L_1} \phi_{11}^{(r)}(x)\phi_{11}^{(s)}(x)\mathrm{d}x + (\rho A)_2 \int_0^{L_2} \phi_{21}^{(r)}(x)\phi_{21}^{(s)}(x)\mathrm{d}x + J_{1x} \int_0^{L_1} \phi_{31}^{(r)}(x)\phi_{31}^{(s)}(x)\mathrm{d}x \\ &+ m_2\phi_{2r}(L_2)\phi_{21}^{(s)}(L_2) + m_1\phi_{11}^{(r)}(L_1)\phi_{11}^{(s)}(L_1) + (J_{2z}L_2 + J_{m2z})\phi_{31}^{(r)}(L_1)\phi_{31}^{(s)}(L_1) = \delta_{rs}. \end{aligned} \tag{45}$$

Inserting the expressions of the kinetic energy (Equation 19) and potential energy (Equation 24) into the Euler-Lagrange equation (Equation 44) and applying the orthogonality conditions (Equation 45), we end up with the forced equation of motion in modal coordinates as follows [444]:

$$\ddot{\eta}_r + 2\xi_r\omega_r\dot{\eta}_r + \omega_r^2\eta_r + \chi_{1r}V_1 + \chi_{2r}V_2 = f_r, r \in \{1,2,3\}\,, \tag{46}$$

where ξ_r is the modal damping ratio of the r-th bending-torsion vibration mode, χ_{ir} are the modal electromechanical coupling terms, given by:

$$\begin{aligned} \chi_{1r} &= \Theta_1\left(\phi_{11}^{(r)'}(L_1) - \phi_{11}^{(r)'}(0)\right) + \Theta_3\left(\phi_{31}^{(r)}(L_1) - \phi_{31}^{(r)}(0)\right), \\ \chi_{2r} &= \Theta_2\left(\phi_{21}^{(r)'}(L_i) - \phi_{21}^{(r)'}(0)\right), \end{aligned} \tag{47}$$

and f_r is the modal force, given by:

$$f_r = -\left(\int_0^{L_1} (\rho A)_1 \phi_{11}^{(r)}(x)\mathrm{d}x\right) a_{by}. \tag{48}$$

Substituting Equation (43) into Equation (33), the governing circuit equations are written as

$$C_{p1}\dot{V}_1 + \frac{V_1}{R_1} = \sum_{r=1}^{3} (K_{1r} + K_{3r})\dot{\eta}_r,$$
$$C_{p2}\dot{V}_2 + \frac{V_2}{R_2} = \sum_{r=1}^{3} K_{2r}\dot{\eta}_r, \tag{49}$$

where K_{1r} and K_{3r} are the r-th modal coupling terms of the piezoelectric layers of the main beam, and K_{2r} is the r-th modal coupling term of the piezoelectric layers of the auxiliary beam, defined by:

$$K_{ir} = k_i b\left(\phi_{i1}^{(r)'}(L_i) - \phi_{i1}^{(r)'}(0)\right),$$
$$K_{3r} = k_3 b\left(\phi_{31}^{(r)}(L_1) - \phi_{31}^{(r)}(0)\right), \tag{50}$$

where i denotes the beam number.

6.5.2 Reduced order model of H_2

Applying the Galerkin procedure, the forced equations of motion in modal coordinates are deduced as follows:

$$\begin{aligned} &\ddot{\eta}_r + 2\xi_r\omega_r\dot{\eta}_r + \omega_r^2\eta_r + \chi_{1r}V_1 + \chi_{2r}V_2 = f_r, r \in \{1,3\} && (\text{Bending } mode),\\ &\ddot{\eta}_{3r} + 2\xi_{3r}\omega_{3r}\dot{\eta}_{3r} + \omega_{3r}^2\eta_{3r} + \chi_{3r}V_3 = f_{3r}, r = 2 && (\text{Torsional } mode). \end{aligned} \tag{51}$$

The modal electromechanical coupling terms are defined by:

$$\chi_{ir} = \Theta_i\left(\phi_{i2}^{(r)'}(L_i) - \phi_{i2}^{(r)'}(0)\right) \text{ (Bending } mode),$$
$$\chi_{3r} = \Theta_3\left(\phi_{32}^{(r)'}(L_1) - \phi_{32}^{(r)'}(0)\right) \text{ (Torsional } mode), \tag{52}$$

and the modal forces are given by:

$$f_r = -\left(\int_0^{L_2} (\rho A)_2\phi_{22}^{(r)}(x)\mathrm{d}x + m_2\phi_{22}^{(r)}(L_2)\right)a_x \text{ (Bending } mode),$$
$$f_{3r} = J_m a_z \phi_{32}^{(r)}(L_1) \text{ (Torsional } mode), \tag{53}$$

where J_m is the rotary inertia of the auxiliary beam and the mass block m_2

$$J_m = J_{2y} + J_{m2}. \tag{54}$$

The governing circuit equations in this case are:

$$C_{pi}\dot{V}_i + \frac{V_i}{R_i} = \sum_{r=1}^{3} K_{ir}\dot{\eta}_r, i \in \{1,2\} \text{ (Bending } mode),$$
$$C_{p3}\dot{V}_3 + \frac{V_3}{R_3} = \sum_{r=1}^{3} K_{3r}\dot{\eta}_{3r} \text{ (Torsional mode)}, \tag{55}$$

where

$$K_{ir} = k_i b\left(\phi_{i2}^{(r)'}(L_i) - \phi_{i2}^{(r)'}(0)\right),\ i \in \{1,2\} \text{ (Bending } mode),$$
$$K_{3r} = k_3 b\left(\phi_{32}^{(r)'}(L_1) - \phi_{32}^{(r)'}(0)\right) \text{ (Torsional } mode), \tag{56}$$

where *i* is the beam number.

6.5.3 Reduced order model of H_3

The forced equations of motion for this PEH in modal coordinates are defined as

$$\ddot{\eta}_{ir} + 2\xi_r\omega_r\dot{\eta}_{ir} + \omega_r^2\eta_{ir} + \chi_{ir}V_i = f_{ir}, \begin{cases} i = 1 \text{ and } r = 3 \text{ (Bending mode)} \\ i = 2 \text{ and } r = 2 \text{ (Bending mode)} \\ i = 3 \text{ and } r = 1 \text{ (Torsional mode)} \end{cases}, \tag{57}$$

where *i*=1 for the main beam bending, *i*=2 for the auxiliary beam bending, and *i*=3 for the main be torsion.

The modal electromechanical coupling terms are defined by:

$$\begin{aligned} \chi_{ir} &= \Theta_i \left(\phi_{i3}^{(r)'}(L_i) - \phi_{i3}^{(r)'}(0)\right) \text{ (Bending } mode\text{)}, \\ \chi_{3r} &= \Theta_3 \left(\phi_{33}^{(r)'}(L_1) - \phi_{33}^{(r)'}(0)\right) \text{ (Torsional } mode\text{)}, \end{aligned} \tag{58}$$

and the modal forces are given by:

$$\begin{aligned} f_{1r} &= -\left(\int_0^{L_1} (\rho A)_1 \phi_{13}^{(r)}(x)\mathrm{d}x + m_1\phi_{13}^{(r)}(L_1)\right) a_z \text{ (Bending mode)}, \\ f_{2r} &= -\left(\int_0^{L_2} (\rho A)_2 \phi_{23}^{(r)}(x)\mathrm{d}x + m_2\phi_{23}^{(r)}(L_2)\right) a_x \text{ (Bending mode)}, \\ f_{3r} &= J_m a_z \phi_{33}^{(r)}(L_1) \text{ (Torsional mode)}. \end{aligned} \tag{59}$$

In this case, the governing circuit equations are given by:

$$C_{pi}\dot{V}_i + \frac{V_i}{R_i} = \sum_{r=1}^{3} K_i\dot{\eta}_{ir}, i \in \{1,2,3\}, \tag{60}$$

where

$$\begin{aligned} K_{ir} &= k_i b \left(\phi_{i3}^{(r)'}(L_i) - \phi_{i3}^{(r)'}(0)\right), i \in \{1,2\}, \\ K_{3r} &= k_3 b \left(\phi_{33}^{(r)'}(L_1) - \phi_{33}^{(r)'}(0)\right). \end{aligned} \tag{61}$$

6.5.4 Analytical solutions of H_1

We note that $a_y = \Im\left(a_{by}e^{j\Omega t}\right)$, where $\Im$ stands for the imaginary part. Consequently, we seek the solutions of Equations (46) and (49) in the form:

$$\begin{aligned} \eta_r &= \Im(H_r e^{j\Omega t}), \quad r \in \{1,2,3\}, \\ V_i &= \Im(U_i e^{j\Omega t}), \quad i \in \{1,2\}. \end{aligned} \tag{62}$$

Substituting Equation (62) into Equation (46), we end up with

$$H_r = \frac{f_{r0} - \chi_i U_1 - \chi_2 U_2}{\omega_r^2 - \Omega^2 + 2\xi\omega_r\Omega j}, \tag{63}$$

where f_{r0} is the complex amplitude of the modal force function f_r.

$$f_{r0} = -\left(\int_0^{L_1} (\rho A)_1 \phi^{(r)}(x)\mathrm{d}x\right) a_{by}. \tag{64}$$

Considering Equation (49), the steady-state voltage outputs are given by:

$$\begin{aligned} U_1 &= \frac{Z_3 Z_5 - Z_2 Z_6}{Z_1 Z_5 - Z_2 Z_4} \\ U_2 &= \frac{Z_1 Z_6 - Z_3 Z_4}{Z_1 Z_5 - Z_2 Z_4} \end{aligned} \tag{65}$$

The expressions of Z_i are presented in Appendix C. Finally, the power generated by each beam i is given by:

$$P_i = \frac{(\Im U_i)^2}{2R_i}, i \in \{1,2\}. \tag{66}$$

6.5.5 Analytical solutions of H_2

Assuming that $a_z = \Im\left(a_{bz}e^{j\Omega t}\right)$ and $a_x = \Im\left(a_{bx}e^{j\Omega t}\right)$, we can write $V_i = \Im\left(U_i e^{j\Omega t}\right)$, i ∈ {1,2,3}, $\eta_r = \Im\left(H_r e^{j\Omega t}\right)$ and $\eta_{3r} = \Im\left(H_{3r} e^{j\Omega t}\right)$ and applying the same demonstration as dealt for the case of H_1. So, the steady state solutions of Equations (51) and (55) are given by:

$$\begin{aligned} \text{Bending mode: } H_r &= \frac{f_{r0} - \chi_i U_1 - \chi_2 U_2}{\omega_r^2 - \Omega^2 + 2\xi_r \omega_r \Omega j}, \\ U_1 &= \frac{Z_3 Z_5 - Z_2 Z_6}{Z_1 Z_5 - Z_2 Z_4}, \\ U_2 &= \frac{Z_1 Z_6 - Z_3 Z_4}{Z_1 Z_5 - Z_2 Z_4}. \\ \text{Torsional mode: } H_{3r} &= \frac{f_{3r0} - \chi_3 U_3}{\omega_r^2 - \Omega^2 + 2\xi_{3r} \omega_r \Omega j}, \\ U_3 &= \frac{\frac{f_{320} K_{32} \Omega j}{\omega_2^2 - \Omega^2 + 2\xi_2 \omega_2 \Omega j}}{Cp_3 \Omega j + \frac{1}{R} + \frac{K_{3r} \chi_{32} \Omega j}{\omega_2^2 - \Omega^2 + 2\xi_2 \omega_2 \Omega j}}, \end{aligned} \tag{67}$$

where Zi are defined in equations (C.1) -(C.6), taking $K_{3r} = 0$.

6.5.6 Analytical solutions of H_3

Since $V_i = \Im\left(U_i e^{j\Omega t}\right)$ and $\eta_{ir} = \Im\left(H_r e^{j\Omega t}\right)$, i, r ∈ {1,2,3}, we can apply the same demonstration, and we end up with

$$\begin{aligned} H_{ir} &= \frac{f_{ir0} - \chi_i U_i}{\omega_r^2 - \Omega^2 + 2\xi_r \omega_r \Omega j}. \\ \text{Torsional mode: } U_1 &= \frac{\frac{f_{130} K_{13} \Omega j}{\omega_3^2 - \Omega^2 + 2\xi_3 \omega_3 \Omega j}}{Cp_1 \Omega j + \frac{1}{R} + \frac{K_{13} \chi_{13} \Omega j}{\omega_3^2 - \Omega^2 + 2\xi_3 \omega_3 \Omega j}}. \\ \text{Bending mode: } U_2 &= \frac{\frac{f_{220} K_{22} \Omega j}{\omega_2^2 - \Omega^2 + 2\xi_2 \omega_2 \Omega j}}{Cp_2 \Omega j + \frac{1}{R} + \frac{K_{22} \chi_{22} \Omega j}{\omega_2^2 - \Omega^2 + 2\xi_2 \omega_2 \Omega j}}. \\ \text{Bending mode: } U_3 &= \frac{\frac{f_{310} K_{31} \Omega j}{\omega_1^2 - \Omega^2 + 2\xi_1 \omega_1 \Omega j}}{Cp_3 \Omega j + \frac{1}{R} + \frac{K_{31} \chi_{31} \Omega j}{\omega_1^2 - \Omega^2 + 2\xi_1 \omega_1 \Omega j}}. \end{aligned} \tag{68}$$

6.6 Results and discussions

In this section, we provide a comprehensive validation of our theoretical results using analytical and numerical simulations as well as experimental measurements of the performance of H_2 from reference [436]. The experimental data include the normalized voltage output corresponding to the first two bending modes and the first torsional mode at different load resistances. This rigorous validation process ensures the accuracy and reliability of our theoretical predictions. In addition, the significant impact of the d36 mode on the performances of the three PEHs studied is investigated, highlighting the potential benefits of this mode in improving energy harvesting efficiency and extending frequency bandwidth. In addition, effective design optimization is performed for H_2 and H3 to further maximize their energy harvesting capabilities. Then, the performances of the three PEHs are compared quantitatively and qualitatively to determine the most efficient configuration among them.

6.6.1 Analytical and numerical validations

For validation purposes, we compared the results of our analytical model for H_2 with the analytical and numerical results of Li et al [436]. As shown in Figure 58(a), our analytical performance results for H_2 closely match the analytical results from reference [436]. Moreover, the effectiveness of the L-shaped PEH in efficiently harvesting both bending and torsional vibration energy under harmonic excitation is demonstrated, indicating its ability to extract energy from multiple vibration modes Figure 58(b) compares the frequency responses of the output voltage of the main beam for both theoretical and numerical simulations under bidirectional harmonic excitation. The close agreement between the numerical and analytical results confirms the accuracy and reliability of our proposed theoretical studies in estimating the electromechanical frequency response. The small discrepancies between our analytical results and the numerical results are due to the simplifications and assumptions of analytical theories such as Euler-Bernoulli beam theory, which may not fully capture the subtleties of real-world scenarios. Although analytical techniques provide a robust framework for approximating system behaviour, these simplifications can lead to small errors, especially when dealing with complex systems such as PEHs. Numerical methods provide a more detailed and comprehensive approach and allow for the inclusion of additional complexities that analytical models may miss. However, numerical simulations are subject to discretization errors because they involve decomposition of the system into finite elements, which can lead to inaccuracies.

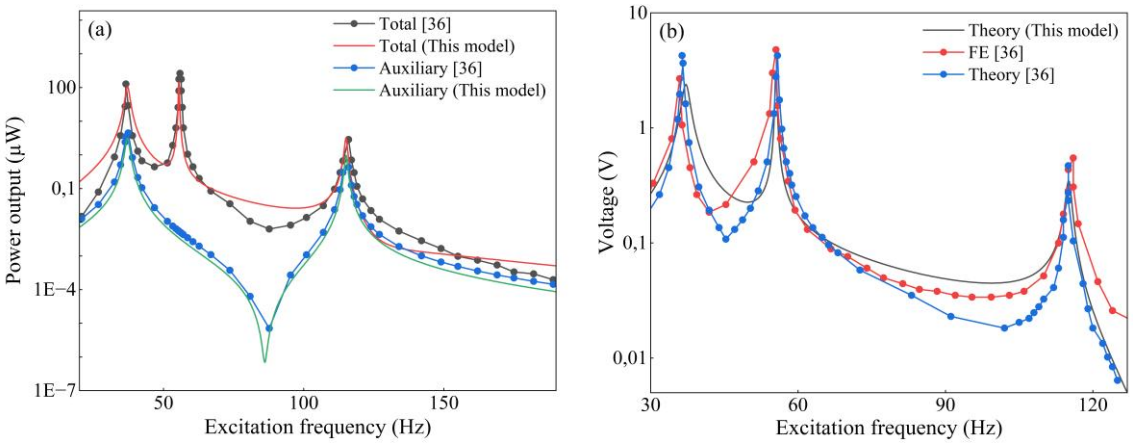

Figure 58: (a) Analytical and (b) numerical validations of the power output of H_2 with bending and torsional modes versus different excitation frequencies (20 Hz–200 Hz) under harmonic excitations abz = abx = 0.5 m/s^2 and load resistance R = 17 kΩ.

6.6.2 Experimental validations

6.6.2.1 Bending mode vibration energy harvesting

Figure 59 shows a comprehensive comparison between our theoretically predicted results and the experimental observations of Li et al. [436] regarding the normalized voltage output for the first two bending modes under different load resistances. The remarkable agreement between our analytical investigations and the experimental results, especially at the resonant frequencies, demonstrates the accuracy and validity of our proposed model.

Table 26 presents a quantitative comparison of the theoretical and experimental data for the first two resonant frequencies and output voltages at different load resistances. The table clearly shows that the experimental and analytical results for the first two resonant frequencies of the PEH have impressive consistency, with a maximum error of only 1.8%. This is further evidence of the accuracy of our theoretical model and proof of its reliability.

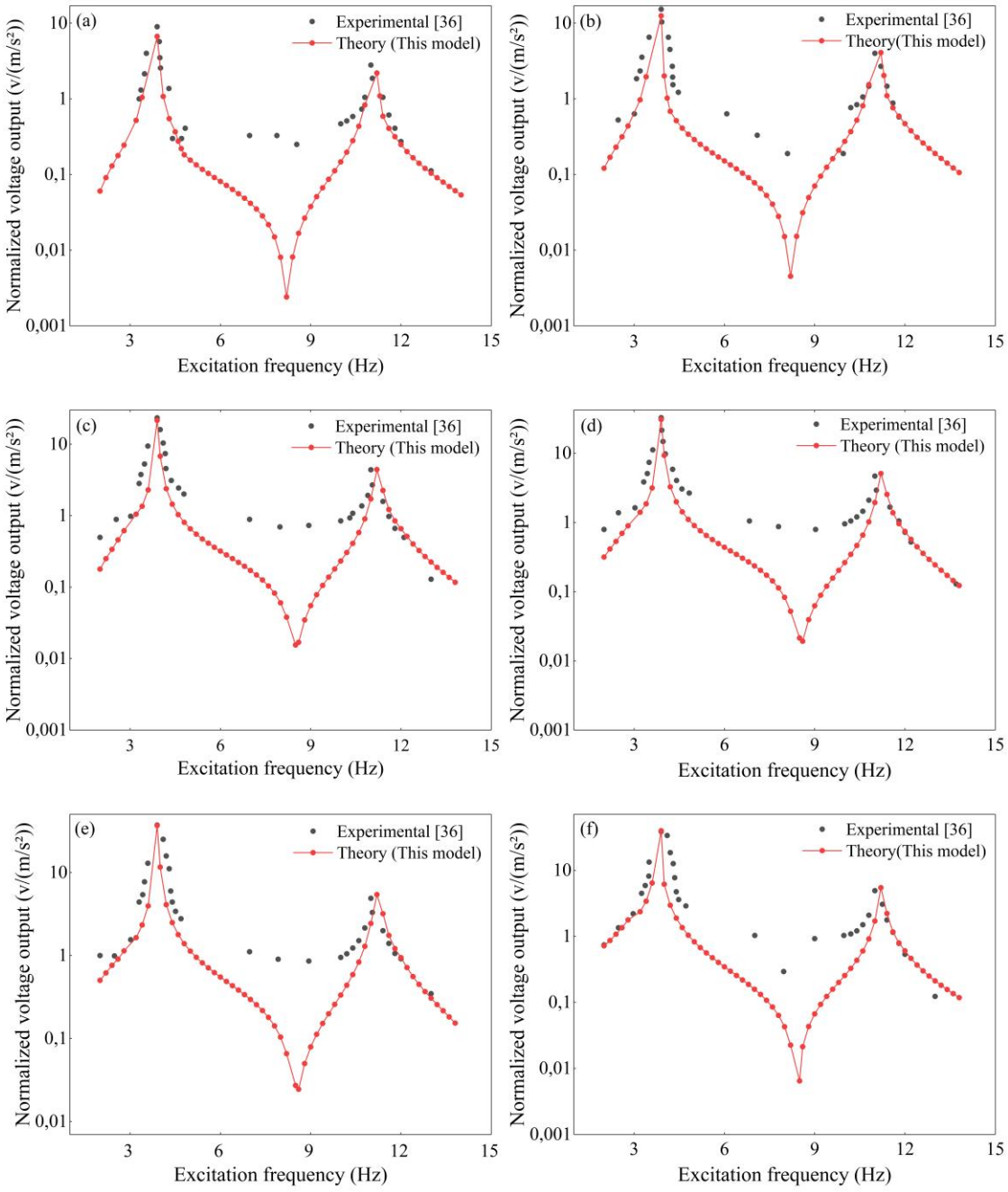

Figure 59: Voltage output comparison under bending mode and varying resistive loads : Comparisons of the theoretical model predictions and experimental measurements of normalized voltage output with bending mode of H_2 under different load resistances: (a) 50 kΩ, (b) 100kΩ, (c) 200kΩ, (d) 500kΩ, (e) 1000kΩ (f) open circuit.

However, the output voltage at resonant frequencies exhibits some significant errors between the analytical and experimental results. These errors are due to the simplifications and assumptions of the theories used. In addition, the measurement inaccuracies and the low precision of testing machine may introduce uncertainties in the experimental results.

Table 26: Quantitative comparisons of theoretical and experimental results of the first two resonance frequencies and output voltages with bending motions.

Load resistance (kΩ)	Resonance frequency (Hz)			Output voltage at resonance frequency		
	Experimental	Theory	Error (%)	Experiment (V/(m/s2))	Theory (V/(m/s2))	Error (%)
50	3.9/11	3.9/11.2	0/1.8	9.0/2.8	6.7/2.2	25.6/21.4
100	3.9/11	3.9/11.2	0/1.8	15.3/4.0	12.5/4.1	18.3/2.4
200	3.9/11	3.9/11.2	0/1.8	23.4/4.4	21.6/4.4	7.7/0
500	3.9/11	3.9/11.2	0/1.8	32.6/4.7	30.8/5.0	5.5/6.3
1000	3.9/11	3.9/11.2	0/1.8	37.2/4.8	36.8/5.4	1.1/12.5
Open circuit	3.9/11	3.9/11.2	0/1.8	38.5/4.9	39.6/ 5.4	2.8/9.2

6.6.2.2 Torsion mode vibration energy harvesting

Experimental data from the reference [436] were used to evaluate the accuracy of the predicted voltage outputs during torsional motions. Figure 60 shows a comparative analysis between the theoretical predictions and the experimental frequency responses of the normalized voltage output near the first resonant frequency at different load resistances. An encouraging degree of similarity was found, indicating the reliability of the theoretical model. Quantitative evaluations of the first torsional resonant frequencies and output voltages for different resistances were documented in Table 27.

The tabulated results provide a comprehensive overview of the correlation between the theoretical predictions and the experimental results. Remarkably, the data show close agreement between the two models and confirm the efficiency of exploiting the d36 mode as a viable option for energy harvesting applications.

It is impressive that all the relative errors between the analytical and experimental values of the resonant frequency are below the threshold of 3.7%. A detailed evaluation of the output voltage at resonant frequencies also reveals minor deviations, with the maximum error being only 10.3% for R = 100 kΩ. This indicates a high degree of agreement between theoretical calculations and experimental measurements, which supports the validity of the analytical model used. Furthermore, the relative error decreases with increasing load resistance, illustrating the sensitivity of PEH's performance to different load condition.

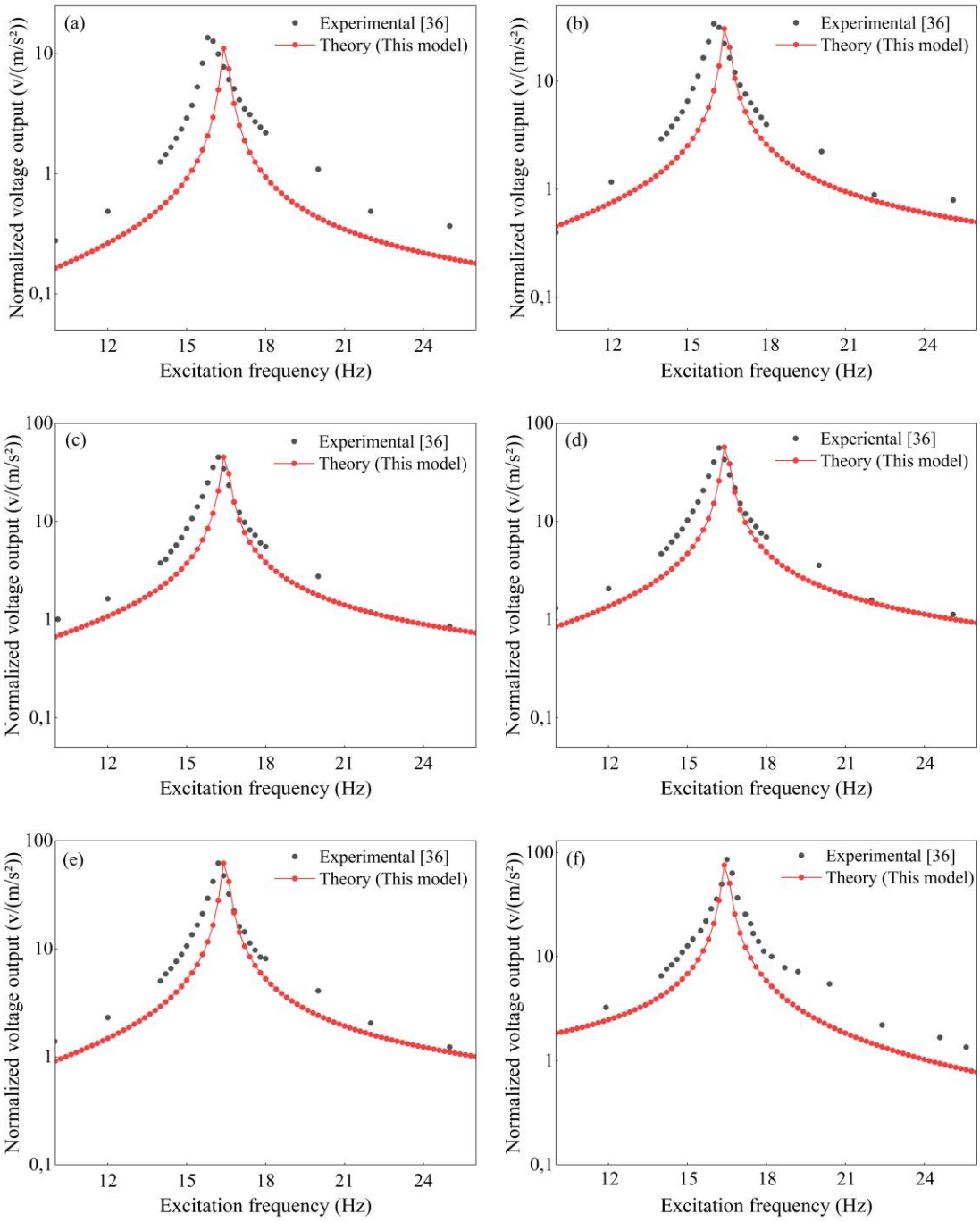

Figure 60: Voltage output comparison under torsional mode and varying resistive loads : Comparisons of the theoretical model predictions and experimental measurements of normalized voltage output with torsion mode of H_2 under different load resistances: (a) 50 kΩ, (b) 100kΩ, (c) 200kΩ, (d) 500kΩ, (e) 1000kΩ (f) open circuit.

Table 27: Quantitative comparisons of theoretical and experimental results on the first resonance frequencies and output voltages with torsional motion.

Load resistances (kΩ)	The resonance frequency (Hz)			Output voltages at resonance frequency		
	Experimental	Theory	Error (%)	Experiment (V/(m/s2))	Theory (V/(m/s2))	Error (%)
100	15.8	16.4	3.7	13.5	12.1	10.3
300	16	16.4	2.5	35.1	31.6	9.9
500	16.2	16.4	1.2	45.8	49.7	8.5
800	16.2	16.4	1.2	57.9	62.8	8.5
1000	16.2	16.4	1.2	64.7	68.0	5.1
Open circuit	16.4	16.4	0	84.1	82.8	1.5

6.6.3 Performances of H_1 and H_3

Since the performance of H_2 has already been discussed in the previous subsection, we now focus on the evaluation of the capabilities of H_1 and H_3. In the last part of this subsection, a breakthrough discovery is made that sheds light on the effect of the piezoelectric coefficient d36 on the energy generated by an L-shaped bimorph PEH by investigating the interplay between coupled bending and torsional motions. The importance of this result lies in its contribution to energy harvesting, as it represents a novel result in the field.

6.6.3.1 Frequency-response of the PEHs H1 and H3

The PEH H_1 demonstrates a remarkable ability to perform both bending and torsional vibrations when subjected to singular harmonic excitation. Figure 61(a) shows the power output of H_1 when subjected to a harmonic excitation of aby = 2 m/s², covering the frequency range from 2 Hz to 200 Hz. A major advantage of this PEH is the coupling between torsional and bending motions within the first three eigenmodes.

Figure 61(b) shows the power of H3 under the influence of two different harmonic excitations, denoted by $a_{bx} = a_{bz} = 2$ m/s². The power generated in the first resonant frequency results from the torsional motion of the main beam.

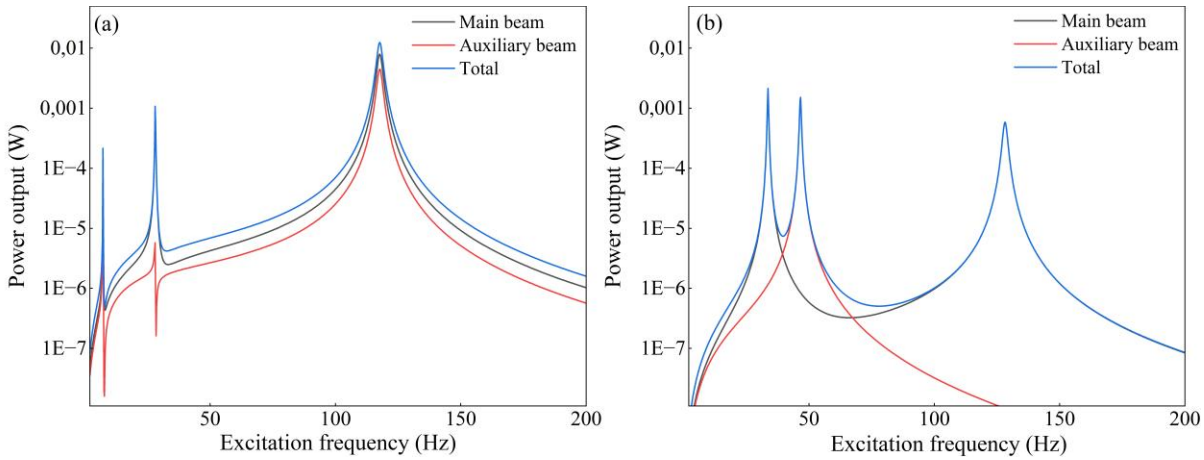

Figure 61: Power output analysis of PEHs H1 and H3 under dynamic excitation : Power output of (a) H_1 under harmonic excitation aby = 2 m/s^2, and (b) H_3 under harmonic excitations abx=abz=2 m/s^2 with bending and torsional modes versus different excitation frequencies (2 Hz-200 Hz) under load resistance R = 17 kΩ.

The power generated in the second and third resonant frequencies is due to the bending motions of the auxiliary and main beams, respectively. Despite the PEH's impressive capacity to collect multimodal and multidirectional vibration., it is essential to recognize that the maximum output power remains limited, reaching a threshold of 3×10^{-3} W. Consequently, a careful and effective design approach is essential in the development of PEHs H_2 and H_3.

6.6.3.2 Effect of exploiting d36 mode on the energy harvested by H_1

At this stage of our investigation, we are concerned with a crucial aspect: the effects of the d36 mode on a dynamically interwoven system characterized by simultaneous torsional and bending motions. Figure 62(a) shows a comprehensive overview of the power output of H_1 over a spectrum of excitation frequencies from 2 Hz to 200 Hz. Here the plot becomes particularly interesting when the effects of pure bending motion (represented by the black curve) are distinguished from the dynamic synergy between bending and torsional motions (represented by the red curve). The use of the d36 mode significantly affects the power output over the entire frequency bandwidth. Most striking is the pronounced effect in the third natural frequency region of the system, culminating in a 67.95% increase in average power output. Remarkably, this exploitation also eliminates the anti-resonances. For a more comprehensive examination of the offset between the two curves, we zoom in on the closer vicinity of the third resonance frequency and the anti-resonance frequencies. Table 28 provides a quantitative comparison that evaluates power generation at the first three resonant frequencies and the first two anti-resonant frequencies. A clear difference between the power generated exclusively by the d31 modes and the synergistic effect of the d31 and d36 modes was observed at both

resonant and anti-resonant frequencies. The results highlight the potential of the d36 mode in enhancing energy generation dynamics and open new possibilities for power generation from multimodal mechanical systems. Within the framework of the PEH H_2, the main beam experiences torsional movement in its second natural mode. Consequently, the energy derived from this motion comes into play when the excitation frequency aligns with the second natural frequency of the PEH. This causes the emergence of the second resonant peak in the power output, (Figure 62(b)) which results in an impressive 43.66% increase in average power generation. This increased power output illustrates the profound impact of the d36 mode on enhancing power generation efficiency.

Meanwhile, the main beam of the PEH H_3 undergoes torsional motion in its first natural mode. This pronounced behaviour leads to the manifestation of a power resonance peak at the PEH's first natural frequency. Here, the d36 mode effect becomes noticeable, as evidenced by the appearance of the first resonant peak in the power output, as shown in Figure 62(c). This effect contributes to a remarkable average power increase of 31.83%. A remarkable contrast results from the coupling/uncoupling between torsional and bending motions in these three PEHs. The torsional motion is generated only in the second resonance mode of PEH H_2 and in the first resonance mode of PEH H_3. As a result, the increase in average power is relatively modest and limited to a single resonant frequency. In stark contrast, the main beam of PEH H_1 experiences torsional motion that is intertwined with the bending motions during its first three eigenmodes. This intricate coupling allows the influence of the d36 mode to permeate the entire frequency bandwidth, resulting in a more significant improvement in PEH performance.

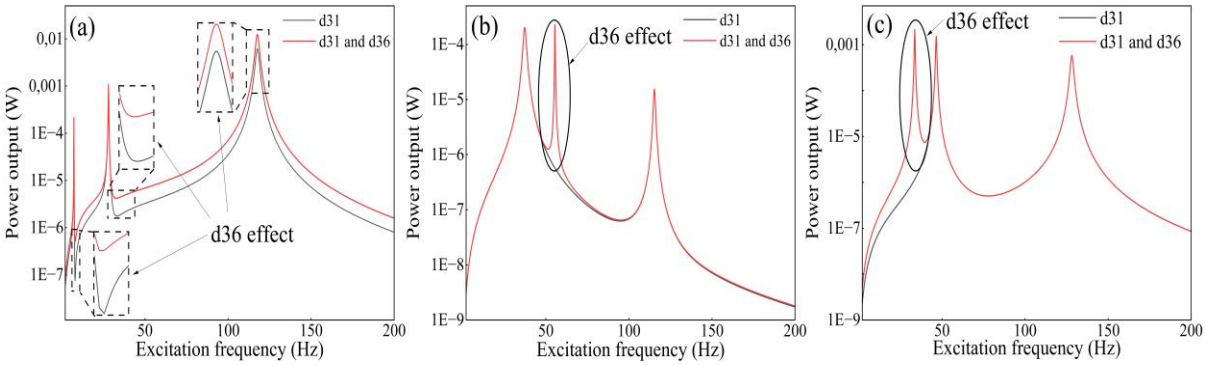

Figure 62: Comparison of PEH performance before and after activating d36 mode : Power output of the PEHs (a) H_1, (b) H_2, (c) H_3 before and after exploiting the d36 mode versus different excitation frequencies (2 Hz-200 Hz) under harmonic excitation aby = 2 m/s^2 and resistance R = 17 kΩ.

Table 28: Quantitative comparisons of the power output of H_1 with bending motion and with both bending and torsional motions on the first three resonance frequencies.

Frequency (Hz)	Power output (W)	
	d31 mode	d31 and d36 mode
7.23 (Resonance)	8.88 × 10−4	8.88 × 10−4
7.91 (Anti-resonance)	3.01 × 10−7	1.96 × 10−6
28.08 (Resonance)	2.2 × 10−3	2.2 × 10−3
32.99 (Anti-resonance)	7 × 10−6	1.68 × 10−5
117.64 (Resonance)	2.47 × 10−2	4.96 × 10−2

6.6.4 Effective design and comparative study

In this phase, an efficient design for both PEHs H_2 and H_3 was developed. A comprehensive evaluation with qualitative and quantitative analyses was then performed to compare the performance of the three L-shaped PEHs.

6.6.4.1 Effective design for the PEHs H_2 and H_3

A strategic approach was adopted to improve the performance of the two piezoelectric energy harvesters (PEH), namely H_2 and H_3, and to provide a comprehensive comparative analysis of the three PEHs' power generation capabilities.

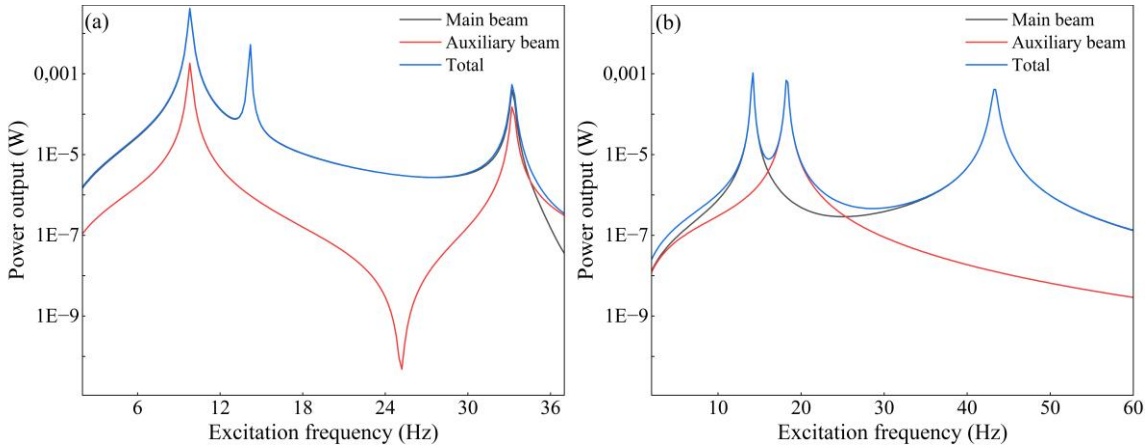

Figure 63: Power output improvements following effective PEH design : Power output of (a) H_2 and (b) H_3 with bending and torsional modes after performing an effective design under harmonic excitation abx = abz = 2 m/s^2 and resistance R = 17 kΩ.

The dimensions of H_2 and H_3 were systematically increased to provide uniform structural dimensions for all three systems. The results of this optimization process are visually represented in Figure 63(a), which shows the performance achieved by the refined H_2 configuration. A convincing contrast between the newly obtained results and the data presented in Figure 58(a) highlights a significant increase in the energy extracted, accompanied by a remarkable convergence of the first three natural frequencies. This positive trend is also evident in the case of H_3, as shown in Figure 61(b) and Figure 63(b), where an improvement in energy harvesting performance and frequency bandwidth is clearly visible.

6.6.4.2 Comparison of the performances of the three PEHs

The frequency response of the power of the three systems after applying the d36 mode is shown in Figure 64(a). The application of the d36 mode to PEHs H_2 and H_3 results in appearance of a resonant peak at the natural frequency associated with the torsional modes, causing the first three natural frequencies to converge. This convergence of resonant frequencies represents a remarkable similarity between these two PEHs. Conversely, the use of the d36 mode significantly increases the power output of PEH H_1, especially near its third natural frequency. As a result, the power output of PEH H_1 significantly exceeds that of its counterparts. A comparative analysis of the power output of the three PEHs is shown in Figs. 12(b), 12(c), 12(d), and 12(e), focusing on scenarios with single excitation for each PEH. With harmonic excitation in the x-direction, Figure 64(b) shows that the main beam of H_3 remains unproductive. Moreover, the energy recovery from the bending of the main beam of H_2 is remarkably small compared to the energy harvested by the main beam of H_1.

As shown in Figure 64(c), the auxiliary beam of PEH H_1 generates energy in its three eigenmodes. In contrast, the energy harvested from the bending of the auxiliary beams of PEHs H_2 and H_3 with harmonic excitation in the x-direction is generated exclusively in the first and second eigenmodes, respectively.

Considering the single excitation in the z-direction of the main beams of PEHs H_2 and H_3, a singular resonance peak in the second natural frequency is observed, as shown in Figure 64(d), originating from the torsional motion of the main beam of H_2. In contrast, PEH H3 exhibits two distinct resonance peaks due to the torsion and bending of its main beam, coinciding with the first and third natural frequencies, respectively.

As can be seen in Figure 64(e), the auxiliary beams of PEHs H_2 and H_3 do not generate energy under single excitation in the z-direction. Consequently, PEH H_1 represents a special case that

requires only a single excitation to effectively use its three interrelated motions (bending-bending-torsion) for energy generation.

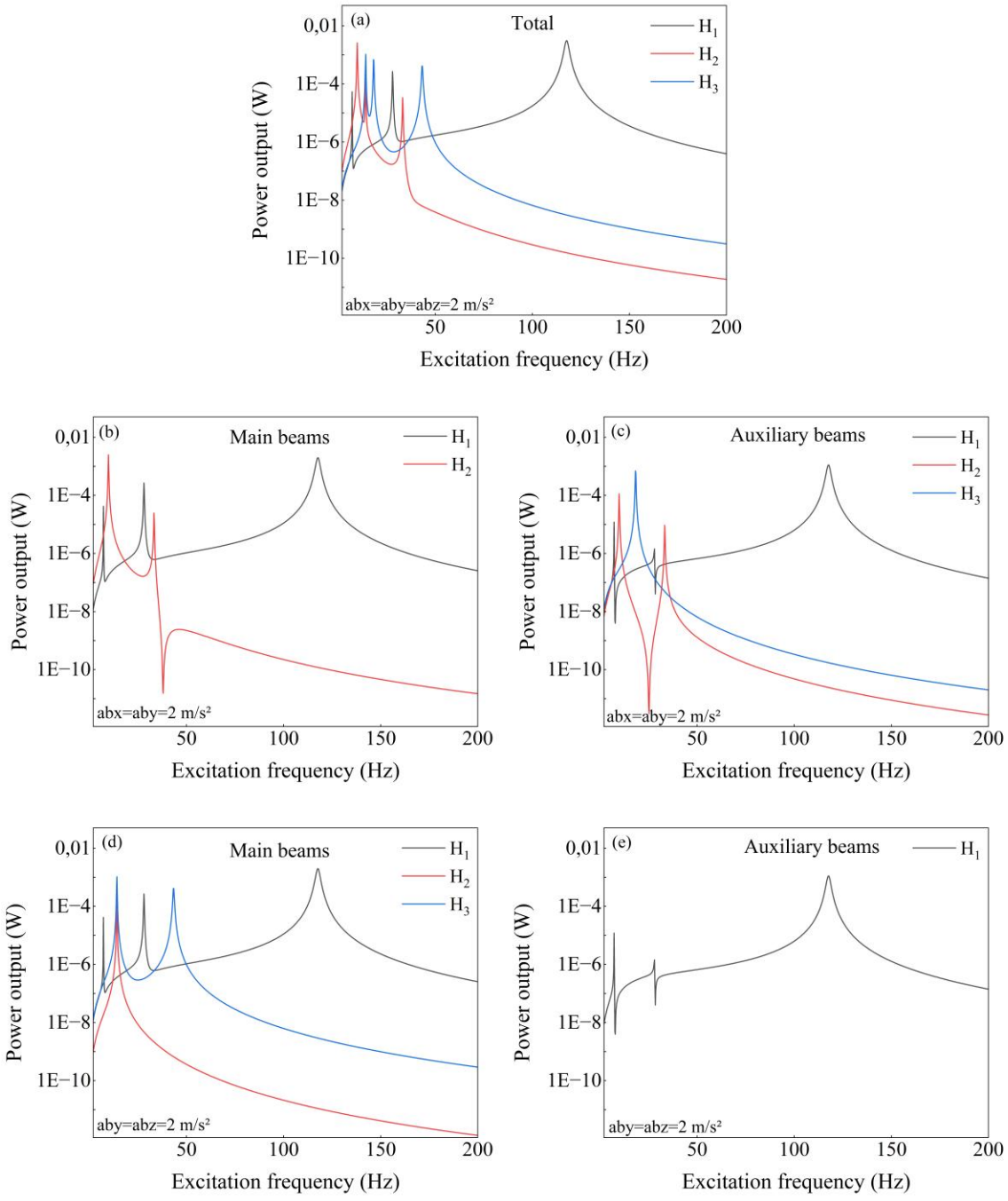

Figure 64: Comparative analysis of beam contributions to PEH power output under various excitations : Comparison of (a) the total power output of the three PEHs with bending and torsional modes in the case of double excitation frequency for H_2 and H_3 versus single excitation for H_1; and the power generated by (b), (d) the main beams and (c), (e) the auxiliary beams of the three PEHs under single excitation for each PEH and load resistance R = 17 kΩ.

In stark contrast, the other two PEHs require double excitation to achieve significant energy output due to their uncoupled motions.

The average power E_f of the PEH over a frequency range between f_1 and f_2 is defined as:

$$E_f = \frac{\int_{f_1}^{f_2} P_f \mathrm{d}f}{f_2 - f_1}, \tag{69}$$

where P_f is the power output of the PEH at excitation frequency *f*.

The PEH's mass energy density E_m and volume energy density E_v are given as

$$\begin{aligned} E_v &= \frac{E_f}{V_t} \\ E_m &= \frac{E_f}{M_t}, \end{aligned} \tag{70}$$

where V_t and M_t are the total volume and the total mass of the PEH, respectively.

As shown in Table 29, H_1 can create an average power nearly ten times that of the other two systems, even though H_1 works with a single excitation.

Table 29: Quantitative comparison of the three PEHs' performances.

PEH	Excitations	Average power (μW)	Volume energy density (W/m^3)	Mass energy density (μW/kg)
H_1	Ay	54.66	8.15	1055.55
H_2	ax and az	5.10	0.76	94.44
H_3	ax and az	5.89	0.87	111.11

6.7 Conclusions

Using the d31 and d36 modes, three broadband and high-efficiency L-shaped bimorph PEHs have been investigated. Taking advantage of these modes, we have developed a comprehensive approach to improve energy output and frequency response. The governing equations of motion and the associated boundary conditions under harmonic base excitations were developed using the Euler-Bernoulli beam theory and Hamilton's principle. The structure natural frequencies and the corresponding eigenmodes were calculated and validated using the Ansys program. The calculated eigenmodes were used as basic functions in a Galerkin procedure. The displacements, torsional angles, voltage outputs, and electrical power were then given in closed-form formulas. A comparative study was conducted analysing the performance profiles of the three PEHs before and after the integration of the d36 mode to reveal transformative effects. The introduction of piezoelectric shear coefficients (d36) had a profound effect on the

average power output in PEH H_1 and resulted in a resonant peak at the natural torsional mode frequency, broadening the bandwidth in PEHs H_2 and H_3. The proposed approach improved the average output of H_1, H_2, and H_3 by 67.95%, 43.66%, and 31.83%, respectively. A comparison of the performances of the three PEHs showed that the resonant frequencies in H_2 and H_3 exhibited a remarkable convergence, distinguishing them from H_1. Nevertheless, the harvested energy in H_1 exceeded its counterparts, indicating its superiority. The results show that H_1 can generate an average power of 54.66 μW between f1=2Hz and f2= 200 Hz with a single excitation along the y-axis. H_2 and H_3, on the other hand, which require two excitations along the x and z axes, produce average powers of 5.10 μW and 5.69 μW, respectively. Moreover, given the analytical model used in this study, a promising future perspective emerges, highlighting the strong recommendation for the manufacturing of the PEH H_1. This PEH features a practical and simple 2D structure in the xz-plane with a modest thickness of 1.2 mm, which offers significant potential for fabrication. These characteristics make it ideal for manufacturing processes such as 3D printing, which can produce the desired structure efficiently, easily, and precisely. H_1's practical design lends itself to a range of real-world applications, particularly those involving low-frequency vibrations, such as harnessing energy from human motion, structural vibration in buildings and infrastructure, environmental monitoring systems, and machinery health monitoring. Looking ahead, the use of H_1 could pave the way for innovative energy harvesting solutions and satisfy the growing need for sustainable energy sources in various fields.

6.8 Acknowledgment

The authors acknowledge the funding provided by the Natural Sciences and Engineering Research Council (NSERC) of Canada (grant number: CRSNG – RGPIN -2021-02846). The authors acknowledge Professor Fethi Abbassi from the Department of mechanical engineering of American University of the Middle East, Kuwait, for his support in numerical validation using Ansys.

Appendix A. Hamilton's principle

The Hamilton's principle is defined by

$$\int_{t_1}^{t_2} \delta\mathcal{L} + \delta W_{nc} \mathrm{d}t = 0, \tag{A.1}$$

where L is the Lagrangian of the system, Wnc is the work of the nonconservative forces and δ is the variation which describes infinitesimal changes in the virtual sense. The variation obeys the rules of differential calculus.

The lagrangian is defined by

$$\mathcal{L} = T - U, \tag{A.2}$$

where T and V are respectively the kinetic energy and the potential energy of the system.

Variation of the kinetic energy:

$$\begin{aligned}\int_{t1}^{t2} \delta T_{H1}\mathrm{d}t = &-\int_{t1}^{t2}\int_0^{L1} (\rho A)_1\left[\ddot{v}_1(x_1,t)+\ddot{Y}(t)\right]\delta v_1(x,t) + J_{1x}\ddot{\theta}_1(x_1,t)\delta\theta(x,t)\mathrm{d}x + \\ &(J_{2z}L_2 + J_{m2z})\ddot{\theta}_1(L_1,t)\delta\theta(L_1,t) + \int_0^{L_2}(\rho A)_2[\ddot{v}_2(x,t)+\ddot{v}_1(L_1,t)]\delta v_2(x,t)\mathrm{d}x + \\ &m_1\ddot{v}_1(L_1,t)\delta v_1(L_1,t) m_2[\ddot{v}_2(L_2,t)+\ddot{v}_1(L_1,t)]\delta v_2(L_2,t)\mathrm{d}t,\end{aligned} \tag{A.3}$$

$$\begin{aligned}\int_{t1}^{t2} \delta T_{H2}\mathrm{d}t = &-\int_{t1}^{t2}\int_0^{L_1} (\rho A)_1\ddot{v}_1(x_1,t)\delta v_1(x_1,t)\mathrm{d}x + J_{1x}\ddot{\theta}(x_1,t)\delta\theta(x_1,t)\mathrm{d}x + \\ &\int_0^{L_2}((\rho A)_2\ddot{v}_2(x_2,t) + (\rho A)_2 a_x(t) + m_2\delta(x_2-L_2)a_x(t))\delta v_2(x_2,t)\mathrm{d}x + \\ &(\rho A)_2 L_2\ddot{v}_1(L_1,t)\delta v_1(L_1,t) + \left(J_{2x}\ddot{\theta}(L_1,t) - J_{2y}a_z(t)\right)\delta\theta(L_1,t) + \\ &m_1\ddot{v}_1(L_1,t)\delta v_1(L_1,t) + J_1\ddot{v}_1'(L_1,t)\delta v_1'(L_1,t) + J_{m1x}\ddot{\theta}(L_1,t)\delta\theta(L_1,t) + \\ &m_2\ddot{v}_1(L_2,t)\delta v_1(L_1,t) + m_2\ddot{v}_2(L_2,t)\delta v_2(L_2,t) + J_2\ddot{v}_2'(L_2,t)\delta v_2'(L_2,t) + \\ &\left(J_{m2x}\ddot{\theta}(L_1,t) - J_{m2}a_z(t)\right)\delta\theta(L_1,t)\mathrm{d}t,\end{aligned} \tag{A.4}$$

$$\begin{aligned}\int_{t1}^{t2} \delta T_{H3}\mathrm{d}t = &-\int_{t1}^{t2}\int_0^{L_1}((\rho A)_1\ddot{v}_1(x_1,t) + (\rho A)_1 a_z(t) + m_1\delta(x_1-L_1)a_z(t))\delta v_1(x_1,t)\mathrm{d}x + \\ &\int_0^{L_2}((\rho A)_2\ddot{v}_2(x_2,t) + \rho A a_x(t) + m_2\delta(x_2-L_2)a_x(t))\delta v_2(x_2,t)\mathrm{d}x + \\ &\int_0^{L_1} J_{1x}\ddot{\theta}(x_1,t)\delta\theta(x_1,t)\mathrm{d}x + J_1\ddot{v}_1'(L_1,t)\delta v_1'(L_1,t) + J_{m1x}\ddot{\theta}(L_1,t)\delta\theta(L_1,t) + \\ &\left(J_{2x}\ddot{\theta}(L_1,t) - J_{2y}a_z(t)\right)\delta\theta(L_1,t) + m_1\ddot{v}_1(L_1,t)\delta v_1(L_1,t) + m_2\ddot{v}_2(L_2,t)\delta v_2(L_2,t) + \\ &J_2\ddot{v}_2'(L_2,t)\delta v_2'(L_2,t) + \left(J_{m2x}\ddot{\theta}(L_1,t) - J_{m2}a_z(t)\right)\delta\theta(L_1,t)\mathrm{d}t.\end{aligned} \tag{A.5}$$

Variation of the potential energy:

Considering Equation (7), the variations of potential energy of the main beam and the auxiliary beam of each PEH can be respectively written as

$$\begin{aligned}\delta U_1 = &\int_0^{L1}[EI_1 v_1''(x_1,t) + \Theta_1 V_1(t)U_{L1}]\delta v_1''(x_1,t)\mathrm{d}x + \int_0^{L_1}[GI_g\theta'(x_1,t) \\ &+\Theta_3 V_3(t)U_{L1}]\delta\theta'\mathrm{d}x \\ \delta U_2 = &\int_0^{L2}[EI_2 v_2''(x_2,t) + \Theta_2 V_2(t)U_{L2}]\delta v_2''(x_2,t)\mathrm{d}x.\end{aligned} \tag{A.6}$$

The total potential energy of the system is

$$\int_{t1}^{t2}\delta U\mathrm{d}t = \int_{t1}^{t2}\delta U_1\mathrm{d}t + \int_{t1}^{t2}\delta U_2\mathrm{d}t. \tag{A.7}$$

By substituting Equation (A.6) into Equation (A.7) and applying integration by parts, the variation of the potential energy of each PEH H_i can be written as

$$\int_{t1}^{t2} \delta U \mathrm{d}t = \int_{t1}^{t2} \int_{0}^{L1} [EI_1 v_1''''(x_1,t) + \Theta_1 V_1(t) U''_{L1}]\delta v_1(x_1,t) - [GI_g \theta''(x_1,t) + \Theta_3 V_3(t) U'_{L1}]\delta\theta(x_1,t)\mathrm{d}x + \left[(GI_g\theta'(x_1,t) + \Theta_3 V_3(t) U_{L1})\delta\theta(x_1,t)\right]_0^{L1} - [(EI_1 v_1'''(x_1,t) + \Theta_1 V_1(t) U'_{L1})\delta v_1(x_1,t)]_0^{L1} + [(EI_1 v_1''(x_1,t) + \Theta_1 V_1(t) U_{L1})\delta v_1'(x_1,t)]_0^{L1} + \int_0^{L2} [EI_2 v_2''''(x_2,t) + \Theta_2 V_2(t) U_{L2}]\delta v_2(x_2,t)\mathrm{d}x - [(EI_2 v_2'''(x_2,t) + \Theta_2 V_2(t) U'_{L2})\delta v_2(x_2,t)]_0^{L2} + [(EI_2 v_2''(x_2,t) + \Theta_2 V_2(t) U_{L2})\delta v_2'(x_2,t)]_0^{L2}\mathrm{d}t$$

(A.8)

Variation of the non-conservative forces:

$$\int_{t1}^{t2} \delta W_{H1}\mathrm{d}t = \int_{t1}^{t2} -[EIv_2''(0,t) + \Theta_2 V_2(t) U_{L2}]\delta\theta(L_1,t) - [EIv_2'''(0,t) + \Theta_2 V_2(t) U_{L2}]\delta v_1(L_1,t)\mathrm{d}t \quad \text{(A.9)}$$

$$\int_{t1}^{t2} \delta W_{H2}\mathrm{d}t = \int_{t1}^{t2} -[EIv_2''(0,t) + \Theta_2 V_2(t) U_{L2}]\delta v_1'(L_1,t)\mathrm{d}t \quad \text{(A.10)}$$

Finally, the equations of motion and boundary conditions of each PEH can be determined by substituting Equations (A.3)-(A.10) into Equation (A.1).

Appendix B. Moments of inertia

J_{2z} is the area moment of inertia of the auxiliary beam of the PEH H_1 related to the x-axis of the main beam:

$$J_{2z} = \sum_{i=1}^{3} \int_{-\frac{h_i}{2}}^{\frac{h_i}{2}} \int_{-\frac{b}{2}}^{\frac{b}{2}} \rho_i y^2 \mathrm{d}z\mathrm{d}y, \quad \text{(B.1)}$$

J_{m2z} is the rotary inertia of the mass block m_2 with respect to the x-local axis of the main beam of the PEH H_1.

$$J_{m2z} = \frac{1}{12} m_2 (h_m^2 + L_m^2) + m_2 \left(L_2 + \frac{L_m + L_m}{2}\right)^2, \quad \text{(B.2)}$$

J_1 is the rotary inertia of the mass block m_1 with respect to the z-local axis of the main beam and J_2 is the rotary inertia of the mass block m_2 with respect to the local z-axis of the auxiliary beams of the two PEHs H_2 and H_3

$$J_1 = \frac{1}{12} m_1 (h_m^2 + L_m^2) + m_1 \left(\frac{h_m}{2}\right)^2, \quad J_2 = \frac{1}{12} m_2 (h_m^2 + L_m^2) + m_2 \left(\frac{L_m}{2}\right)^2. \quad \text{(B.3)}$$

The rotary inertias of the mass block m_1, the mass block m_2, and the auxiliary beam with respect to the local x-axis of the main beam for the two PEHs H_2 and H_3 are defined as follows:

$$J_{m1x} = \frac{1}{12} m_1 (b^2 + L_m^2) \quad \text{(B.4)}$$

$$J_{m2x} = \frac{1}{12} m_2 (b^2 + L_m^2) + m_2 \left(L_2 + \frac{L_m + L_m}{2} \right)^2 \quad \text{(B.5)}$$

$$J_{m2} = m_2 (L_m + L_m + L_2) \quad \text{(B.6)}$$

$$J_{2x} = \frac{1}{3} \rho A \left(\left(L_2 + \frac{L_m}{2} \right)^3 - \left(\frac{L_m}{2} \right)^3 \right) \quad \text{(B.7)}$$

$$J_{2y} = \frac{1}{2} \rho A L_2 (L_m + L_2) \quad \text{(B.8)}$$

Table B.1: The values of the moments of inertia used in the analytical model.

Moments of inertia	Value (kg.m^2)
J_{2z}	6.680866×10^{-9}
J_{m2z}	0.000196931
J_1	2.044270×10^{-8}
J_2	3.875525×10^{-9}
J_{m1x}	2.044270×10^{-8}
J_{m2x}	0.0000121607
J_{m2}	0.000121370
J_{2x}	0.0000398515
J_{2y}	0.000582855

Appendix C. Parameters

$$Z_1 = jC_{p1}\Omega + \frac{1}{R_1} + \sum_{r=1}^{3} \frac{\Omega j}{\omega_r^2 - \Omega^2 + 2j\xi_r\omega_r\Omega} (K_{1r} + K_{3r}) \chi_{1r}^{\square} \quad \text{(C.1)}$$

$$Z_2 = \sum_{r=1}^{3} \frac{\Omega j}{\omega_r^2 - \Omega^2 + 2j\xi_r\omega_r\Omega} (K_{1r} + K_{3r}) \chi_{2r} \quad \text{(C.2)}$$

$$Z_3 = \sum_{r=1}^{3} \frac{\Omega j}{\omega_r^2 - \Omega^2 + 2j\xi_r\omega_r\Omega} (K_{1r} + K_{3r}) f_{r0} \quad \text{(C.3)}$$

$$Z_4 = \sum_{r=1}^{3} \frac{\Omega j}{\omega_r^2 - \Omega^2 + 2j\xi_r\omega_r\Omega} K_{2r} \chi_{1r}^{\square} \quad \text{(C.4)}$$

$$Z_5 = jC_{p2}\Omega + \frac{1}{R_2} + \sum_{r=1}^{3} \frac{\Omega j}{\omega_r^2 - \Omega^2 + 2j\xi_r\omega_r\Omega} K_{2r} \chi_{2r} \quad \text{(C.5)}$$

$$Z_6 = \sum_{r=1}^{3} \frac{\Omega j}{\omega_r^2 - \Omega^2 + 2j\xi_r\omega_r\Omega} K_{2r} f_{r0} \quad \text{(C.6)}$$

Table C.1: Mechanical and electrical parameters of the PEH H_1.

Parameters	Values
C_{p1}	6.431545×10^{-7}
C_{p2}	4.823659×10^{-7}
K_{11}	-0.00285941
K_{12}	-0.01193112
K_{13}	-0.06031375
K_{21}	-0.00211984
K_{22}	-0.00134278
K_{23}	-0.1426045
K_{31}	-0.00000557157
K_{32}	-0.0000410519
K_{33}	-0.0434889
χ_{11}	-0.00285941
χ_{12}	-0.0119311
χ_{13}	-0.0603137
χ_{21}	-0.00211984
χ_{22}	-0.00134278
χ_{23}	-0.1426045
f_{10}	0.0176750
f_{20}	0.074654
f_{30}	0.471333

6.9 References

[1] A. Megdich, M. Habibi, L. Laperrière, A Review on 3D printed piezoelectric energy harvesters: Materials, 3D printing techniques, and applications, Materials Today Communications (2023) 105541.

[2] H. Kim, S. Kim, K. Xue, J. Seok, Modeling and performance analysis of electromagnetic energy harvester based on torsional galloping phenomenon, Mechanical Systems and Signal Processing 195 (2023) 110287.

[3] T.I. Toluwaloju, C.K. Thein, D. Halim, J. Yang, Dynamic responses of the 2DOF electromagnetic vibration energy harvester through different electrical coil connections, Mechanical Systems and Signal Processing 184 (2023) 109709.

[4] H. Zhao, H. Ouyang, A vibro-impact triboelectric energy harvester with a magnetic bistable mechanism and grating-patterned films for dual power enhancement, Mechanical Systems and Signal Processing 178 (2022) 109318.

[5] Z. Liu, C. Zhao, G. Hu, Y. Yang, A multi-degree-of-freedom triboelectric energy harvester for dual-frequency vibration energy harvesting, Mechanical Systems and Signal Processing 188 (2023) 109951.

[6] S. Li, Z. Feng, X. He, Y. Ye, J. Li, An in-plane omnidirectional flutter piezoelectric wind energy harvester, Mechanical Systems and Signal Processing 200 (2023) 110637.

[7] Z. Zhang, Y. Gu, S. Wang, J. Wang, S. Li, F. Meng, J. Kan, Dynamic modeling and experimental validation of a low frequency piezoelectric vibration energy harvester via secondary excitation of pressured fluid, Mechanical Systems and Signal Processing 191 (2023) 110170.

[8] G. Sui, X. Shan, C. Hou, H. Tian, J. Hu, T. Xie, An underwater piezoelectric energy harvester based on magnetic coupling adaptable to low-speed water flow, Mechanical Systems and Signal Processing 184 (2023) 109729.

[9] Z. Wang, W. Wang, L. Tang, R. Tian, C. Wang, Q. Zhang, C. Liu, F. Gu, A.D. Ball, A piezoelectric energy harvester for freight train condition monitoring system with the hybrid nonlinear mechanism, Mechanical Systems and Signal Processing 180 (2022) 109403.

[10] X. Wang, Q. Du, Y. Zhang, F. Li, T. Wang, G. Fu, C. Lu, Dynamic characteristics of axial load bi-stable energy harvester with piezoelectric polyvinylidene fluoride film, Mechanical Systems and Signal Processing 188 (2023) 110065.

[11] A. Jamshiddoust, M. Avarzamani, A. Farrokhabadi, Experimental investigation of damages in the bimorph piezoelectric energy harvester with multilayer composite substrate, Mechanical Systems and Signal Processing 195 (2023) 110307.

[12] B. Zhao, J. Wang, G. Hu, A. Colombi, W.-H. Liao, J. Liang, Time-sharing Orbit Jump and Energy Harvesting in Nonlinear Piezoelectric Energy Harvesters Using a Synchronous Switch Circuit, arXiv preprint arXiv:2305.06016 (2023).

[13] S. Panda, H. Shin, S. Hajra, Y. Oh, W. Oh, J. Lee, P. Rajaitha, B.K. Panigrahi, J. Shukla, A.K. Sahu, Ferroelectric composite-based piezoelectric energy harvester for self-powered detection of obstructive sleep, Journal of Materiomics (2023).

[14] Y. Zhao, L.-C. An, K. Li, Y.-J. Gong, T.-M. Guo, F.-F. Gao, Y. Lei, Q. Li, W. Li, X.-H. Bu, A new piezoelectric hybrid metal thiocyanide for energy harvesting and human motion sensing, Science China Materials (2023) 1-7.

[15] X. Liu, Y. Shang, J. Liu, Z. Shao, C. Zhang, 3D printing-enabled in-situ orientation of BaTi2O5 nanorods in β-PVDF for high-efficiency piezoelectric energy harvesters, ACS Applied Materials & Interfaces 14(11) (2022) 13361-13368.

[16] Z. Wang, K. Maruyama, F. Narita, A novel manufacturing method and structural design of functionally graded piezoelectric composites for energy-harvesting, Materials & Design 214 (2022) 110371.

[17] M. Bonnin, F.L. Traversa, F. Bonani, An impedance matching solution to increase the harvested power and efficiency of nonlinear piezoelectric energy harvesters, Energies 15(8) (2022) 2764.

[18] L. Yang, T. Wei, N. Chen, High-Efficiency Energy Management Circuit Combining Synchronized Switch Harvesting on Inductor Rectifier and Impedance Matching for Impact-Type Piezoelectric Energy Harvester, Energy Technology 10(11) (2022) 2200434.

[19] J. Han, T. Maeda, H. Itakura, D. Kitazawa, Experimental study on the wave energy harvesting performance of a small suspension catamaran exploiting the maximum power point tracking approach, Ocean Engineering 243 (2022) 110176.

[20] R. Hua, S. Marin-Quiros, H.K. Mohan, Y. Wang, Maximum power point tracking for a multi-layered piezoelectric heel charger with a levered mechanism toward impact-based energy harvesting, Review of Scientific Instruments 93(9) (2022).

[21] M. Lallart, High gain, load-tolerant self-powered series–parallel synchronized switching technique for piezoelectric energy harvesting, IEEE Transactions on Power Electronics 37(7) (2022) 8649-8658.

[22] B. Zhang, H. Liu, B. Hu, S. Zhou, Analysis and optimization of self-powered parallel synchronized switch harvesting on inductor circuit for piezoelectric energy harvesting, Smart Materials and Structures 31(9) (2022) 095040.

[23] D. Li, C. Wang, X. Cui, D. Chen, C. Fei, Y. Yang, Recent progress and development of interface integrated circuits for piezoelectric energy harvesting, Nano Energy 94 (2022) 106938.

[24] M. Mousavi, S. Ziaei-Rad, A.H. Karimi, Piezoelectric-based energy harvesting from bridge vibrations subjected to moving successive vehicles by functionally graded cantilever beams–Theoretical and experimental investigations, Mechanical Systems and Signal Processing 188 (2023) 110015.

[25] C. Zhao, G. Hu, Y. Yang, A cantilever-type vibro-impact triboelectric energy harvester for wind energy harvesting, Mechanical Systems and Signal Processing 177 (2022) 109185.

[26] M. Yao, P. Liu, L. Ma, H. Wang, W. Zhang, Experimental study on broadband bistable energy harvester with L-shaped piezoelectric cantilever beam, Acta Mechanica Sinica 36 (2020) 557-577.

[27] D. Liu, M. Al-Haik, M. Zakaria, M.R. Hajj, Piezoelectric energy harvesting using L-shaped structures, Journal of Intelligent Material Systems and Structures 29(6) (2018) 1206-1215.

[28] X. Nie, T. Tan, Z. Yan, Z. Yan, M.R. Hajj, Broadband and high-efficient L-shaped piezoelectric energy harvester based on internal resonance, International Journal of Mechanical Sciences 159 (2019) 287-305.

[29] X. Nie, S. Pei, T. Tan, Z. Yan, Z. Yan, Nonlinear 1: 2 internal resonance response of L-shaped piezoelectric energy harvester under the influence of electrical damping, International Journal of Mechanical Sciences 225 (2022) 107365.

[30] H. Li, H. Sun, B. Song, D. Zhang, X. Shang, D. Liu, Nonlinear dynamic response of an L-shaped beam-mass piezoelectric energy harvester, Journal of Sound and Vibration 499 (2021) 116004.

[31] S.A. Kouritem, H.A. El-Gamal, K.T. Mohamed, Effect of major factors on broadband natural frequency energy harvesting for rectangular and L-shaped cantilever harvesters, Microsystem Technologies 29(5) (2023) 729-743.

[32] W. Zhou, D. Du, Q. Cui, C. Lu, Y. Wang, Q. He, Recent research progress in piezoelectric vibration energy harvesting technology, Energies 15(3) (2022) 947.

[33] S. Shi, W. Geng, K. Bi, Y. Shi, F. Li, J. He, X. Chou, High sensitivity MEMS accelerometer using PZT-based four L-shaped beam structure, IEEE Sensors Journal 22(8) (2022) 7627-7636.

[34] Y. Zheng, S. Sun, Global optimization of excitation directions for scavenging energy based on a cross-jointed L-shape multidirectional piezoelectric energy harvester, Sensors and Actuators A: Physical 342 (2022) 113651.

[35] H. Miao, X. Chen, H. Cai, F. Li, Comparative face-shear piezoelectric properties of soft and hard PZT ceramics, Journal of Applied Physics 118(21) (2015).

[36] H. Li, D. Liu, J. Wang, X. Shang, M.R. Hajj, Broadband bimorph piezoelectric energy harvesting by exploiting bending-torsion of L-shaped structure, Energy Conversion and Management 206 (2020) 112503.

[37] X. Li, D. Upadrashta, K. Yu, Y. Yang, Analytical modeling and validation of multi-mode piezoelectric energy harvester, Mechanical Systems and Signal Processing 124 (2019) 613-631.

[38] S. Rakici, J. Kim, A stabilized non-ordinary peridynamic model for linear piezoelectricity, Applied Mathematical Modelling (2023).

[39] S.-H. Jo, B.D. Youn, An improved analytical model that considers lateral effects of a phononic crystal with a piezoelectric defect for elastic wave energy harvesting, International Journal of Mechanical Sciences 205 (2021) 106593.

[40] J. Jia, X. Shan, D. Upadrashta, T. Xie, Y. Yang, R. Song, An asymmetric bending-torsional piezoelectric energy harvester at low wind speed, Energy 198 (2020) 117287.

[41] Y. Cao, D. Cao, G. He, X. Ge, Y. Hao, Vibration analysis and distributed piezoelectric energy harvester design for the L-shaped beam, European Journal of Mechanics-A/Solids 87 (2021) 104214.

[42] S. Osinaga, S. Machado, M. Febbo, An analytical model of the electromechanical coupling for a piezoelectric stepped buckled beam for energy harvesting applications, Mechanical Systems and Signal Processing 179 (2022) 109355.

[43] A. Homayouni-Amlashi, A. Mohand-Ousaid, M. Rakotondrabe, Analytical modelling and optimization of a piezoelectric cantilever energy harvester with in-span attachment, Micromachines 11(6) (2020) 591.

[44] Y. Chen, Z. Yang, Z. Chen, K. Li, L. Wang, S. Zhou, Theoretical and experimental investigations of multibifurcated piezoelectric energy harvesters with coupled bending and torsional vibrations, Acta Mechanica Sinica 38(5) (2022) 521434.

Partie II : Conception, optimisation et impression 4D de polymères et nanocomposites à mémoire de forme électroactifs pour dispositifs intelligents

Chapitre 7: Revue de littérature sur l'impression 4D

Ce chapitre a fait l'objet d'une publication :
MEGDICH, Amal, HABIBI, Mohamed, and LAPERRIÈRE, Luc.
A review on 4D printing: material structures, stimuli and additive manufacturing techniques. *Materials Letters*, 2023, vol. 337, p. 133977.
Il peut être consulté en ligne à l'adresse suivante :
https://doi.org/10.1016/j.matlet.2023.133977

Après avoir exploré et optimisé des nanocomposites piézoélectriques à base de PVDF pour la récupération d'énergie, cette deuxième partie de la thèse se concentre sur l'impression 4D, une technologie émergente qui combine l'impression 3D avec des matériaux intelligents capables de répondre à des stimuli externes. L'impression 4D ouvre de nouvelles perspectives pour le développement de structures adaptatives, auto-déployables et réactives aux changements environnementaux, offrant ainsi des opportunités sans précédent pour des applications avancées dans divers domaines tels que la robotique, la biomédecine et les appareils intelligents.

Cet article fournit une analyse approfondie des matériaux intelligents utilisés dans l'impression 4D, des différents types de stimuli qui activent leur transformation et des technologies de fabrication additive les plus couramment utilisées pour produire ces structures. L'objectif principal de cette revue est de fournir une compréhension globale des stratégies de conception des matériaux a mémoire de forme et des mécanismes de transformation qui leur permettent d'adopter des formes et des propriétés dynamiques en réponse à des stimuli externes tels que la chaleur, l'humidité, la lumière ou les champs électriques et magnétiques.

Dans cette étude, les structures des matériaux à mémoire de forme sont classées en trois grandes catégories : distribution uniforme, distribution en gradient et motifs spécifiques, chacune ayant des propriétés uniques en termes de réversibilité et de contrôle de la transformation. De plus, une attention particulière est accordée aux procédés de fabrication additive tels que le Fused Deposition Modeling (FDM) et le Direct Ink Writing (DIW), qui sont les plus utilisés dans le domaine en raison de leur flexibilité et de leur capacité à combiner plusieurs matériaux en une seule impression. L'article explore également les avantages et les limites de ces technologies,

ainsi que leur potentiel d'optimisation pour améliorer la précision et les performances des structures imprimées en 4D.

En synthétisant les recherches récentes dans ce domaine, cette revue met en évidence les défis et les perspectives actuels pour l'évolution de l'impression 4D, en identifiant les tendances émergentes et les stratégies les plus prometteuses pour la conception de matériaux intelligents aux propriétés programmables. Ces connaissances serviront de base à des développements expérimentaux et à des applications pratiques qui seront abordés dans les chapitres suivants de cette thèse.

A Review on 4D printing: Material structures, stimuli and additive manufacturing techniques

Amal Megdich[a], Mohamed Habibi[a*], Luc Laperrière[a]

[a]*Department of mechanical engineering, Université du Québec à Trois Rivières, 3351 Bd des Forges, G8Z 4M3, Trois-Rivières, Canada*

7.1 Abstract

Advances in 3D printable smart materials are leading to the development of four-dimensional printing (4DP). Assembling stimulus-responsive materials and combining their functionalities into a single printed construct is an efficient way to improve the shape recovery capability of the smart structure. Three types of multi- material structures are reported in the literature: uniform distribution, gradient distribution, and special patterns. Smart materials have the unique property of changing their shape and properties when activated by external stimuli such as heat, water, or pressure. This article provides an overview of current smart material structures, types of stimuli, and three-dimensional printing (3DP) technologies used to manufacture 4D smart structures.

Keywords: 4DP, stimuli-responsive materials, shape-recovery, stimulus.

7.2 Introduction

The development of improved smart structures with desirable properties is critical to the advancement of 4DP applications.Researchers have combined several materials to achieve this goal to create smart multi-material structures. Three types of multi-material structures are used in 4DP: uniform distribution, gradient distribution, and special patterns. When subjected to external stimuli such as heat, water, force, electric field, pH, etc., programmable materials can change their shape over time. Among the 3DP processes, Fused Deposition Modeling (FDM) and Direct Ink Writing (DIW) are the most widespread in the 4DP field. These technologies offer various advantages over traditional manufacturing processes, including faster production, unrestricted design, and combining multiple materials into a single object in a one-step manufacturing process. This reduces manufacturing costs and waste [445]. In this review, the different structures of smart materials are first discussed. Then, an overview of several types of stimuli is provided. Finally, current additive manufacturing (AM) technologies for 4DP are evaluated.

7.1. Material structures

Material structures are divided into single-material and multi-material structures (Figure 65). The single-material structure uses a single smart material with a gradient distribution. This anisotropy can produce shape-shifting behavior such as bending and twisting. Liu et al. [446] created a single-material smart structure using polylactic acid (PLA). This study's optimization of shape recovery behavior was based on a microstructural design by adjusting the FDM input parameters. The multi-material structure can be made of different smart materials or a combination of smart and conventional materials. Pandey et al. [447] created a biodegradable polymer composition by combining PLA with polycaprolactone (PCL). PLA was used as a fixed phase to maintain the original shape of the structure, while PCL was used as a reversible phase to facilitate temporary shape transition.

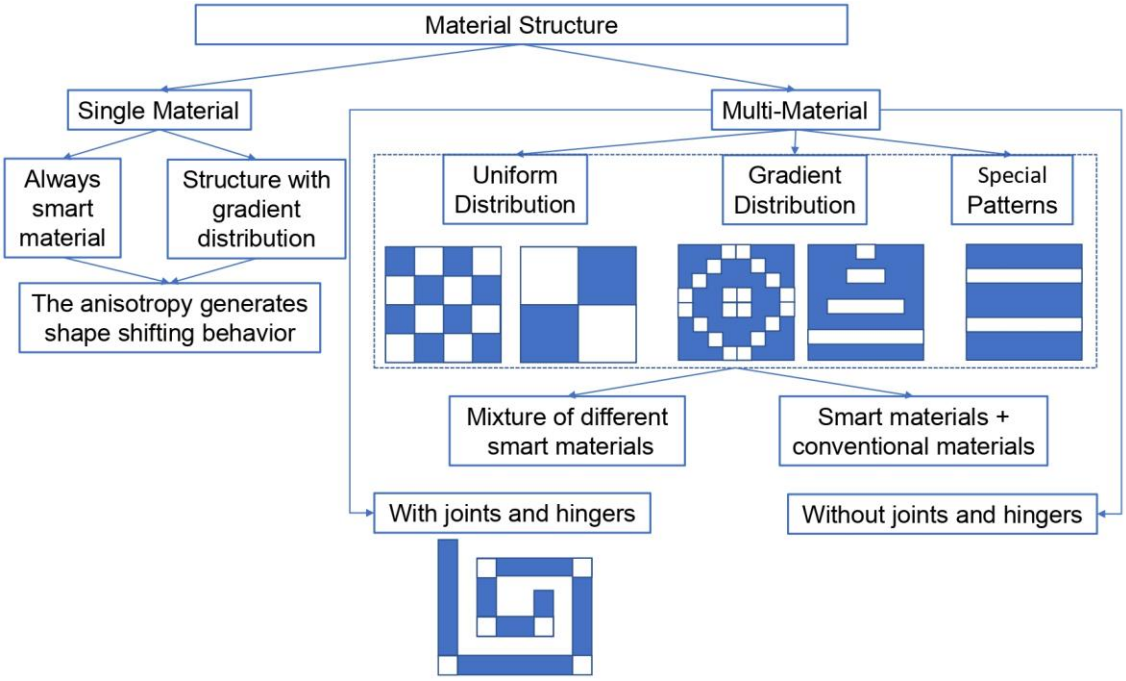

Figure 65: 4DP smart material structures.

Huang et al. [448] used cupric sulfate to reinforce and enhance the shape memory of PLA, resulting in an excellent shape recovery rate of 92.30%. Three types of multi-material structures are cited in the 4DP literature: uniform distribution, gradient distribution and special patterns. Composite structure is a major type of special patterns. This technique is used to improve the material's shape recovery capacity and mechanical properties. Gupta et al. [449] added short carbon fibers to polycarbonate with concentrations of 3 to 7.5 v%. The results showed that

increasing the reinforcement percentage significantly affected the material's hardness properties. Similarly, Mohan et al. [450] showed that adding 2 wt% graphene nanoplatelets to a cellulose matrix increased the tensile strength and elastic modulus of the composite by 20% and 37% respectively. Material structures can also be classified as structures with or without joints and hinges. Zolfagharian et al. [451] built a smart structure with 3D-printed actuation hinges using chitosan hydrogel ink. The hinges act as a heat source, absorbing a broad spectrum of light, especially infrared light, converting it into heat and causing thermal stress gradients to induce actuation.

7.3 Applied stimulus

Applied stimuli such as heat, water, stress, and pH (Figure 66) change stimuli-responsive materials' chain dynamics or internal atomic packing configurations, leading to shape-shifting behavior. When temperature is the external stimulus, the shape-shifting mechanism is called unconstrained-thermo-mechanism. This method requires two temperature levels: T_h (higher than the glass transition temperature (T_g) of the smart material) and T_L (lower than T_g). The desired shape is achieved when the printed structure is cooled to T_L. Then the structure is heated to T_H to resume its original shape. Nguyen and Kim [452] showed this method using polyurethane. In this work, two strategies are proposed to control the temperature: mixing the conductive carbon nanotubes into the polyurethane, or simultaneously printing the polyurethane and a conductive substance; and then heating with an electric current. Unconstrained-hydro-mechanism is another shape-shifting technique in which water is the stimulus.

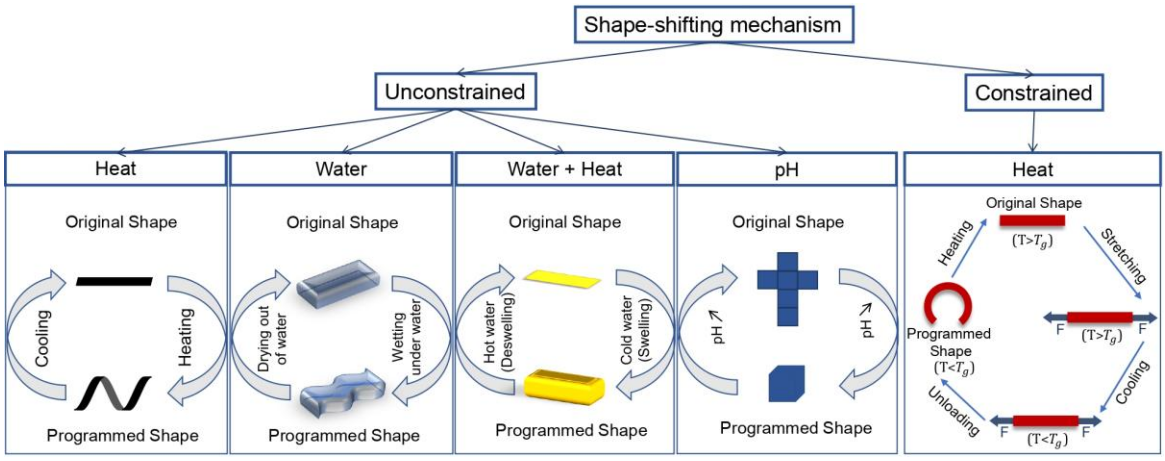

Figure 66: Schematic illustration of the shape-shifting mechanisms in 4DP.

The structure can change shape under water and return to its original shape after drying. In this context, Zhang et al. [453] created a water-sensitive film by altering Cellulose with

Stearyl. When the film is placed in water, it bends due to unequal water absorption. Another technique is the so-called Unconstrained-hydro-thermo-mechanism, which requires both heat and water stimuli. Ren et al. [454] formed a bi-layer structure using water-swellable polyurethane and thermal-shrinkable polyvinyl chloride. The strain generated by water-swelling or thermal-shrinkage causes the structure to create varied shapeshifting. Chemical stimuli such as pH can also be used for the shape-shifting process. PH-responsive hydrogels swell at one pH and shrink at another. Wu et al. [455] developed a pH sensor using acrylonitrile-butadiene-styrene and poly(4-vinylpyridine) based on this mechanism. The constrained-thermo-mechanism was demonstrated by Pandey et al. [447] using a PLA/PCL composite. The temporary shape was achieved by applying an external force at a deformation temperature higher than T_g. The deformed sample was then cooled to room temperature and fixed in temporary shape. Finally, the deformed sample was reheated at the same deformation temperature to illustrate the shape-memory effect.

7.4 AM methods for 4DP applications

Material extrusion technologies such as FDM and DIW are widely used in the 4DP industry. FDM melts a solid filament in a heating nozzle, and DIW drops a viscous ink, which can then be cured. The advantage of extrusion technologies is the ability to print different materials. However, the nozzle diameter, which is usually in the range of 100-200 μm, limits the resolution of these technologies.

Another limitation of extrusion-based processes is the low printing speed, although higher speed can be achieved if multiple nozzles are used. Powder bed fusion processes, such as Selective Laser Sintering (SLS), are rapidly emerging technologies for polymer 4DP. SLS has the advantage of producing complicated and large scaffolds. The main disadvantage of SLS is that the part's surface is not smooth because it is made by fusing spherical particles. Another 4DP technology for polymers is Vat photopolymerization, where a laser beam or UV light can be used as a light source to induce photocuring during the printing process. 3DP technology is known as Stereolithography (SLA) when a laser beam is used and Digital Light Processing (DLP) when a projector is used. DLP uses a digital micro-mirror device, which cures an entire layer of resin at once, printing objects quickly. The last common technology for polymer printing is Inkjet Printing (IJP). In this process, multiple print heads can be used to spray different photocurable liquid resins onto the printing bed simultaneously, followed by UV curing. This enables the fast and easy production of multi-material components. When printing a single-material, the

in-plane resolution of an IJP printer is 30-40 μm. However, when multiple materials are printed, the resolution drops to 200-400 μm.

Table 30: Materials, advantages and disadvantages of the most used 3DP technologies in 4DP.

Method	Materials	Advantages	Disadvantages	Ref
FDM	Thermoplastic	Low cost, fast printing process	Limited resolution, low printing speed	[456]
DIW	Polymers, metal particles, waxes, composites and ceramics	Multi-material printing, low material waste	High manufacturing cost	[456, 457]
SLS	Ceramics, thermoplastics, metals and composites	Complex scaffolds fabrication, no support is required	Unsmooth product surface.	[456, 458]
SLA	Photopolymers, ceramics, Composite	Complicated geometric shapes, high resolution (20 μm)	Unstable photopolymers over time	[456, 457, 459]
DLP	Elastomers, metamaterial	Rapid printing technology, great potentials in the future of 4DP, great resolution on both micro and nanoscales	High materials cost	[456, 457, 459]
IJP	Crystal	Multiple printing abilities, complex structure	Limited resolution for multi-materials structures	[456, 457]

Table 30 resumes the advantages and disadvantages of each 3DP technology described above.

Figure 67 illustrates that DIW and FDM are the most commonly used printing technologies in 4DP, followed by SLS and SLA.

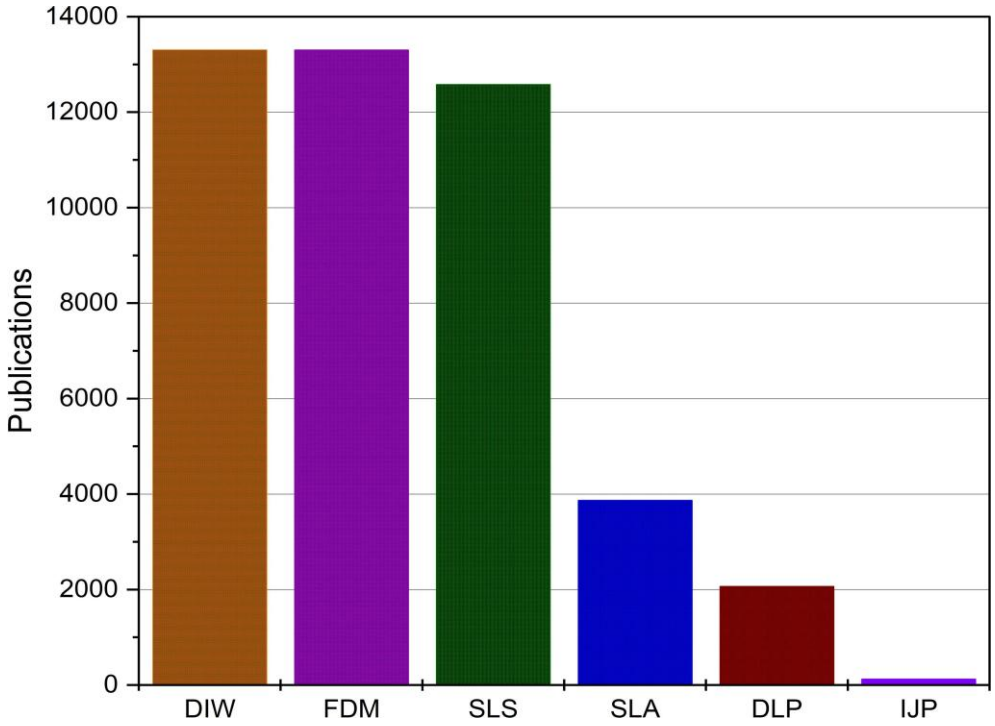

Figure 67: Publications for 4DP with different AM technologies in the past 5 years (from 2018 to September 2022).

7.5 Conclusion

4DP technology enables the production of smart single-material and multi-material structures. The single-material structure uses a single smart material. In contrast, the multi-material structure can be made of different smart materials or a combination of smart and conventional materials. Depending on the stimuli they are exposed to, 4D structures can change their shape over time. Among 3DP technologies, FDM and DIW are the most commonly used in 4DP.

7.6 Acknowledgment

The authors acknowledge the funding provided by the Natural Sciences and Engineering Research Council of Canada (NSERC) (grant number: CRSNG – RGPIN -2021-02846).

7.7 References

[1] A. Zolfagharian, A. Kaynak, M. Bodaghi, A. Z. Kouzani, S. Gharaie, S. Nahavandi, Control-based 4d printing: Adaptive 4d-printed systems, Applied Sciences 10 (2020) 3020.
[2] Y. Liu, F. Zhang, J. Leng, T.-W. Chou, Microstructural design of 4d printed angle-ply laminated strips with tunable shape memory properties, Materials Letters 285 (2021) 129197.
[3] H. Pandey, S. S. Mohol, R. Kandi, 4d printing of tracheal scaffold using shape-memory polymer composite, Materials Letters (2022) 133238.
[4] J. Huang, J. Fan, L. Cao, C. Xu, Y. Chen, A novel strategy to construct co-continuous pla/nbr

thermoplastic vulcan- izates: Metal-ligand coordination-induced dynamic vulcanization, balanced stiffness-toughness and shape memory effect, Chemical Engineering Journal 385 (2020) 123828.

[5] A. Gupta, S. Hasanov, I. Fidan, Processing and characterization of 3d-printed polymer matrix composites reinforced with discontinuous fibers, in: 2019 International Solid Freeform Fabrication Symposium, University of Texas at Austin, 2019.

[6] D. Mohan, T. Z. Khai, M. S. Sajab, H. Kaco, Well-dispersed cellulose-graphene in 4d printing biopolymer, Materials Letters 303 (2021) 130522.

[7] A. Zolfagharian, A. Kaynak, S. Y. Khoo, A. Kouzani, Pattern-driven 4d printing, Sensors and Actuators A: Physical 274 (2018) 231–243.

[8] T. T. Nguyen, J. Kim, 4d-printing—fused deposition modeling printing and polyjet printing with shape memory polymers composite, Fibers and Polymers 21 (2020) 2364–2372.

[9] K. Zhang, A. Geissler, M. Standhardt, S. Mehlhase, M. Gallei, L. Chen, C. Marie Thiele, Moisture-responsive films of cellulose stearoyl esters showing reversible shape transitions, Scientific reports 5 (2015) 1–13.

[10] L. Ren, B. Li, Q. Liu, L. Ren, Z. Song, X. Zhou, P. Gao, 4d printing dual stimuli-responsive bilayer structure toward multiple shape-shifting, Frontiers in Materials 8 (2021) 655160.

[11] C.-Y. Wu, J.-R. Chen, C.-K. Su, 4d-printed ph sensing claw, Analytica Chimica Acta 1204 (2022) 339733.

[12] M. Quanjin, M. Rejab, M. Idris, N. M. Kumar, M. Abdullah, G. R. Reddy, Recent 3d and 4d intelligent printing technologies: A comparative review and future perspective, Procedia Computer Science 167 (2020) 1210–1219.

[13] H. Chu, W. Yang, L. Sun, S. Cai, R. Yang, W. Liang, H. Yu, L. Liu, 4d printing: a review on recent progresses, Micromachines 11 (2020) 796.

[14] D. G. Tamay, T. Dursun Usal, A. S. Alagoz, D. Yucel, N. Hasirci, V. Hasirci, 3d and 4d printing of polymers for tissue engineering applications, Frontiers in bioengineering and biotechnology 7 (2019) 164.

[15] M. Rafiee, R. D. Farahani, D. Therriault, Multi-material 3d and 4d printing: a survey, Advanced Science 7 (2020) 1902307.

Chapitre 8: Caractérisation, conception, et impression 4D de nanocomposites électroactifs à mémoire de forme

Ce chapitre a fait l'objet d'une publication :
MEGDICH, Amal, HABIBI, Mohamed, LAPERRIÈRE, Luc, LI Zeshi, ABDIN Yasmine. Advanced nanocomposites for 4D printing: High-performance electroactive shape memory polymers for smart applications. *Applied Materials Today*, 2025, vol. 44, p. 102702.
Il peut être consulté en ligne à l'adresse suivante :
https://doi.org/10.1016/j.apmt.2025.102702

Après avoir fait une revue sur l'impression 4D et les matériaux intelligents utilisés dans cette technologie, cette partie de la thèse explore le développement et l'intégration de matériaux électroactifs pour des applications avancées en robotique souple et en systèmes intelligents adaptatifs. La plupart des travaux sur les polymères à mémoire de forme (SMP) se concentrent sur l'activation thermique, limitant ainsi le contrôle localisé et la réactivité des structures imprimées. Pour surmonter ces limitations, cette étude propose une approche innovante combinant l'optimisation de deux matériaux distincts : un nanocomposite PLA/MWCNTs optimisé pour la conversion électrothermique et un mélange de polymères à mémoire de forme PLA/PVDF conçu pour une récupération de forme efficace.

Cet article présente une approche d'impression multi-matériaux intégrant un nanocomposite PLA/MWCNTs, utilisé comme élément chauffant sous l'effet d'un champ électrique, et un mélange de polymères PLA/PVDF optimisé pour la mémoire de forme. Grâce à cette combinaison, une activation rapide et localisée de la mémoire de forme a été obtenue sous basse tension, permettant un contrôle précis et programmable des transformations structurelles. L'optimisation du composite PLA/MWCNTs a conduit à une conversion électrothermique efficace, atteignant 80 °C en seulement 10 s sous 10 V, tandis que le mélange PLA/PVDF a affiché d'excellentes performances en termes de récupération de forme et de fixation, avec des ratios de 98,56 % et 99,6 %, respectivement.

Dans cette étude, des simulations numériques ont été réalisées à l'aide du logiciel Abaqus pour modéliser le comportement électrothermique du nanocomposite et la dynamique de récupération de forme du SMP. Les résultats ont montré une excellente concordance entre les prédictions numériques et les observations expérimentales, validant ainsi l'efficacité du modèle

développé. Pour démontrer le potentiel de cette approche, des structures bio-inspirées et des mains robotiques souples ont été fabriquées à l'aide de l'impression multi-matériaux, mettant en évidence un actionnement précis, une grande flexibilité et une excellente robustesse structurelle.

Ainsi, cette étude marque une avancée majeure dans l'impression 4D en intégrant des matériaux fonctionnels optimisés dans une seule structure, permettant un contrôle adaptatif et intelligent des formes imprimées. Cette combinaison de conversion électrothermique et de récupération de forme ouvre de nouvelles perspectives pour le développement de systèmes autonomes et programmables, avec des applications potentielles en robotique douce, biomédecine et ingénierie adaptative.

Note : des informations complémentaires (supporting information) ont également été publiées pour cet article. Ils se retrouvent en Annexe 4 de cette thèse et sont identifiées par les références « Figure Si » ou « Table Si » dans cet article.

Advanced Nanocomposites for 4D Printing: High-Performance Electroactive Shape Memory Polymers for Smart Applications

Amal Megdich[1], Mohamed Habibi[1*], Luc Laperrière[1], Zeshi Li[2], and Yasmine Abdin[2]

[1] Department of mechanical engineering, Université du Québec à Trois-Rivières, Quebec, Canada.

[2] Department of Materials Engineering, The University of British Columbia, Vancouver, British Columbia V6T 1Z4, Canada.

8.1 Abstract

The potential of 4D printing to enable dynamic, programmable structures has been constrained by the reliance on heat and moisture as activation stimuli, limiting the complexity of shape transformations and hindering localized actuation. This study addresses these limitations by developing electroactive shape memory polymers (SMPs) by incorporating multi-walled carbon nanotubes (MWCNTs) into poly(lactic acid)/polyvinylidene fluoride (PLA/PVDF) blends. Using fused deposition modeling (FDM)-based 4D printing, the MWCNTs were strategically dispersed within the polymer matrix to enhance both electrothermal responsiveness and mechanical properties. The optimized composite, containing 7.5% MWCNTs, achieved a rapid temperature rise to 80°C in just 10 seconds under a low voltage, alongside outstanding shape recovery and fixity ratios of 98.56% and 99.6%, respectively. Numerical simulations developed in Abaqus accurately replicated the electrothermal behavior and shape recovery dynamics, with results aligning closely with experimental observations. The advanced SMPs were successfully implemented in bio-inspired origami structures and soft robotic hands, showcasing precise actuation, high flexibility, and robust structural integrity. These findings reveal the transformative potential of PLA/PVDF/MWCNT nanocomposites for next-generation applications in soft robotics, bio-inspired mechanisms, and adaptive intelligent systems.

Keywords: Electroactive shape memory polymers; Multi-Walled Carbon Nanotubes; 4D printing; Electrothermal response; Bio-inspired origami structures; Soft robotics.

8.2 Introduction

Smart materials have emerged as a cornerstone of modern technology due to their ability to respond to external stimuli, enabling applications in areas such as soft robotics [460, 461], biomedical devices [462-464], aerospace [465, 466], and adaptive structures [467, 468].

Among the various smart materials, shape memory polymers (SMPs) have gained much attention due to their light weight, high deformability, and programmable shape recovery. These properties have led to their use in applications that require adaptive, reconfigurable and deployable structures.

C. Lin et al. [469] developed a PLA-based shape memory blocker for the treatment of congenital atrial septal defects. The device was able to deploy rapidly and was activated within 16.0 seconds under a remote magnetic field. To evaluate biocompatibility, the shape memory blocker was successfully implanted subcutaneously in male rats, demonstrating its potential for minimally invasive medical applications. Y. Wang et al. [470] developed SMP-based cardiac constructs with highly aligned microstructure and adjustable curvature to mimic cardiac muscle tissue at both macroscopic and microscopic levels. JG. Choi et al. [471] developed smart flexible fibers made of a shape memory polymer and a thermosensitive hydrogel that can be fabricated into various types of actuators to perform complex motions involving torsion, tension/compression, and bending in soft robots.

Despite their potential, conventional SMP-based systems are mainly activated by thermal or moisture stimuli [472-477]. While these activation methods are effective, they limit the versatility of SMP and restrict their use in more programmable and complex designs [478]. To overcome these limitations, researchers have explored alternative stimuli such as light [479-483], magnetic fields [484-487], and electric fields [488].

Zhang et al. [489] developed light-responsive metal-polymer composites (LMPCs) that exhibit rapid and repeatable shape transformations under near-infrared (NIR) irradiation. These LMPCs demonstrate significant potential for applications in advanced fields such as soft robotics, artificial muscles, and aerospace materials, where tasks like object manipulation (e.g., grasping and releasing) require precision and adaptability. Similarly, H. Liu et al. [490] investigated the enhancement of polymer materials by integrating iron oxide (Fe_3O_4) into a blend of polylactic acid (PLA) and thermoplastic polyurethane (TPU). This integration not only improved the material's mechanical strength but also increased its thermal conductivity, expanding its functionality and applicability in advanced engineering domains. The improved thermal conductivity of the PLA/TPU/Fe_3O_4 composite facilitated rapid heat transfer within the matrix when exposed to a magnetic field, enabling efficient shape memory activation.

Additionally, X. Dong et al. [491] studied an electroresponsive PLA/carbon nanotube (CNT) shape memory polymer composite, utilizing fused deposition modeling (FDM) to print U-shaped structures with varying infill directions (0°, 45°, and 90°). Their results revealed that the 0° infill direction provided the most uniform heat distribution and required the lowest

activation voltage, while the 90° infill direction exhibited the most uneven heat distribution and the highest activation voltage. This underscores the importance of optimizing infill patterns to enhance thermal management and energy efficiency in shape memory applications. Similarly, K. Dong et al. [492] demonstrated the potential of CNTs in enhancing thermal responsiveness by incorporating 6 wt% CNTs into a PLA/TPU (90:10) blend. This composite achieved a rapid temperature increase from 22.3°C to 74.3°C within just 25 seconds under a voltage of 10 V. These results highlight the role of CNTs in significantly improving the conductivity and thermal response of polymer composites, making them highly suitable for advanced applications requiring rapid thermal activation.

The ability to trigger SMPs with electrical energy offers significant advantages, including faster response times, precise control and compatibility with energy harvesting systems.

However, the development of electroactive SMPs is still relatively under-researched compared to thermoresponsive systems [493]. To close this gap, material innovations are needed to improve the electrical responsiveness of SMPs while maintaining their mechanical and thermal performance.

In addition, numerical simulation models were used to predict the deformation behavior of SMP-based structures during heat activation [494-496]. S. Ladakhan et al. [497] simulated 4D-printed metastructures made of PLA blended with thermoplastic polyurethane (TPU) using ABAQUS. The S-shaped metastructure was designed with a unit cell configuration optimized for load retention and shape recovery. B. Goo et al. [498] used numerical simulations to investigate the thermal deformation of anisotropic 3D-printed thermoplastic parts made of acrylonitrile butadiene styrene (ABS) filaments. The structure consisted of rods printed with different combinations of longitudinal and transverse layers, creating anisotropic thermal properties. Numerical simulations with ANSYS Workbench® were used to model the temperature distribution and thermally induced deformation, focusing on the effects of the different pressure ratios between transverse and longitudinal directions. Despite these advances, there is still a critical gap in numerical simulations using electroresponsive SMPs [499, 500]. To date, there are no studies that have modeled the heat distribution in SMP composites induced by electrical stimuli. This unexplored area represents a valuable research opportunity, as understanding electrothermal behavior is essential for optimizing activation efficiency, reducing energy consumption, and enabling precise control in real-world applications. Bridging this gap could pave the way for the development of the next generation of electroactive SMP-based devices with improved functionality and wider applicability.

This study builds on this emerging field by presenting an electroactive SMP composite based on a PLA/PVDF/MWCNT blend. The incorporation of multi-walled carbon nanotubes (MWCNTs) improves the electrothermal behavior of the material by increasing its conductivity and heat transfer efficiency. The resulting composite shows significant potential for applications requiring rapid and programmable shape change. To comprehensively investigate this material system, we adopted a multi-step approach involving material synthesis, additive manufacturing via FDM (Fused Deposition Modeling) and advanced characterization techniques. We also performed numerical simulations using finite element analysis to model the electrothermal behavior and shape recovery of electroresponsive SMPs under an applied voltage of 10V. This was achieved through thermoelectric coupled analysis and viscoelastic models integrated in Abaqus, effectively validating the experimental results. The versatility of the proposed electroactive SMP is demonstrated through two application-oriented case studies: bio-inspired origami structures and a 3D-printed robotic hand with human-inspired joints. These examples illustrate the potential of the material for dynamic actuation in soft robotics and intelligent systems. By integrating material innovation, advanced characterization, numerical modeling and practical demonstrations, this study aims to open a new perspective for the development of electroactive SMPs for 4D printing. In the following sections, provide detailed insights into the materials, methods, results and their further implications for future applications.

8.3 Materials and methods

8.3.1 Materials

The materials used in this study included poly(lactic acid) (PLA) pellets with an average molecular weight (Mw) of 60,000 g/mol, obtained from Millipore Sigma. Polyvinylidene fluoride (PVDF) powder with an average molecular weight of 530,000 g/mol, multi-walled carbon nanotubes (MWCNTs) with an average molecular weight of 16.043 g/mol, Graphene nanoplatelets 2-10 nm (GNPs), and N,N-dimethylformamide (DMF) with a purity of 99.8% were purchased from Thermo Fisher Scientific.

8.3.2 Materials processing

The fabrication of the PLA-MWCNT nanocomposite began with dissolving PLA pellets in ethyl acetate. Subsequently, varying amounts of MWCNTs (5, 7.5, and 10 wt%) were added to the solution. This mixture was stirred continuously at 50°C and 1500 rpm for 1 hour to ensure

complete dissolution. The resulting solution was dried at 80°C for 24 hours to remove residual solvent. This method was also adapted in our previous works, where similar procedures were followed to prepare different nanocomposites [388, 501, 502].

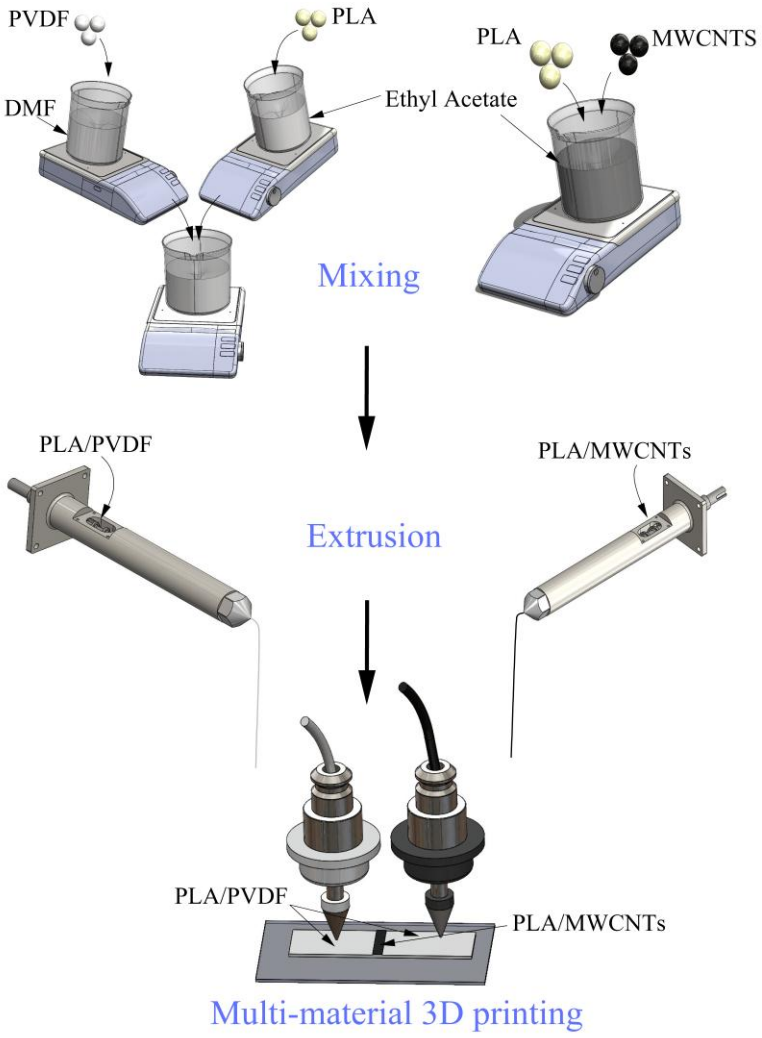

Figure 68: Preparation and multi-material 3d printing process for electroresponsive SMPs using PLA/PVDF blends and PLA/MWCNT nanocomposite joints.

To prepare the shape memory polymer (SMP) blend, PVDF and PLA were mixed in different proportions (30/70, 50/50, and 70/30). The PVDF powder was first dissolved in N, N-dimethylformamide (DMF) by stirring at 60°C and 1500 rpm for 1 hour. Simultaneously, PLA pellets were dissolved in ethyl acetate under continuous stirring at 50°C until fully dissolved. Once the solutions of PLA and PVDF were prepared, the PLA solution was slowly added to the PVDF solution with constant stirring to ensure uniform mixing. This blended solution was dried at 130°C for 24 hours to remove the solvents completely.

The resulting polymer composite (PLA/MWCNTs) and polymer blend (PLA/PVDF) were cooled to room temperature and cut into pellets. These pellets were processed using a single-screw extruder (Wellzoom Type B Desktop Filament Extruder) operating at a rotation speed of 70 rpm and an extrusion temperature of 220°C. The filament diameter was carefully controlled to 2.85 ± 0.05 mm with the assistance of a conveyor belt system.

The final step involved using a professional FDM 3D printer (Ultimaker) to fabricate the shape memory polymer structures. The key 3D printing parameters utilized in this study are summarized in Table 31. The selected printing parameters have been optimized to ensure proper material processing and high-quality printed structures. A graphical representation of the synthesis and processing workflow is provided in Figure 68.

Table 31: Printing parameters.

Parameters	PLA/PVDF	PLA/MWCNTs
Nozzle temperature (°C)	260	275
Build platform temperature (°C)	100	100
Layer thickness (mm)	0.4	0.4
Infill density (%)	100	100
Raster angle (deg)	90	90

Table 32 summarizes the material compositions used to develop the electroresponsive SMP blends and nanocomposites tested in this study. Two distinct material categories are included: PLA/PVDF SMP blends and PLA/MWCNT nanocomposites. Pure PLA and PVDF serve as baseline materials. The PLA/PVDF blends (P3F7, P5F5, and P7F3) feature varying PLA-to-PVDF ratios. The PLA/MWCNT nanocomposites (C-5, C-7.5, and C-10) integrate increasing concentrations of MWCNTs, from 5% to 10%, to enhance thermal conductivity and electrothermal responsiveness.

Table 32: PLA/PVDF SMP blends and PLA/MWCNTs nanocomposites with varying compositions.

Sample	PLA	PVDF	MWCNTs
Pure PLA	100	0	0
Pure PVDF	0	100	0
P3F7	30	70	0
P5F5	50	50	0
P7F3	70	30	0
C-5	95	0	5
C-7.5	92.5	0	7.5
C-10	90	0	10

8.3.3 Experimental Characterization

8.3.3.1 Morphological, Crystalline Structure and Rheology Characterization

The morphological, crystalline structures and Rheology characteristics of the PLA/PVDF blends and PLA/MWCNTs nanocomposites were thoroughly investigated using a combination of analytical techniques to understand their physical and chemical properties.

Scanning Electron Microscopy (SEM) SEM offered valuable insights into the surface morphology and microstructure of the PLA/PVDF blends and PLA/MWCNT nanocomposites, shedding light on the distribution and dispersion of the different material phases. The SEM analysis revealed critical details about the interface quality between PLA and PVDF, identifying potential phase separation that could affect mechanical compatibility and thermal stability. Furthermore, it provided a detailed examination of MWCNT dispersion within the PLA matrix, identifying any signs of aggregation that might hinder the uniformity of the nanocomposite. The SEM results also facilitated the evaluation of interfacial bonding between MWCNTs and the PLA matrix, a key factor influencing the composite's mechanical strength, thermal conductivity, and electrical performance.

Differential Scanning Calorimetry (DSC) DSC has been updated to ensure accurate thermal characterization of the PLA/PVDF belnds. The analysis is performed under the following conditions: Samples are heated at a rate of 20°C/min to Tmax=200°C, followed by a 3-minute isothermal holding time to stabilize the temperature. The samples are then cooled at a rate of 10°C/min to Tmin=-45°C, followed by a 5-minute isothermal pause to ensure uniform cooling. Finally, samples are heated at a reduced rate of 10°C/min to Tmax=200°C to capture detailed thermal transitions. These conditions provide a comprehensive thermal profile that can be used to analyze the thermal transitions of the PLA/PVDF blends, including the glass transition temperature (Tg), melting temperature (Tm), and crystallization behavior. This analysis was conducted for blends with varying compositions (30/70, 50/50, and 70/30) to assess how the ratio of PLA to PVDF influences thermal properties.

X-ray Diffraction (XRD) XRD analysis was conducted to investigate the crystalline phases and structural properties of the PLA/PVDF blends and PLA/MWCNT nanocomposites. The XRD results provided critical information on phase composition and crystalline structures, enabling the identification of distinct crystalline phases of PLA, PVDF, and MWCNTs. This analysis was instrumental in assessing the compatibility of the materials and how their interactions influence the crystallinity of the composites. Furthermore, XRD offered valuable

insights into the effect of material composition on thermal stability, highlighting the role of crystalline structures in determining the overall performance of the blends and nanocomposites.

Fourier Transform Infrared Spectroscopy (FTIR) FTIR was conducted in ATR mode with a resolution of 4 cm^{-1} across a spectral range of 4000–400 cm^{-1} to identify the functional groups and chemical interactions present in the PLA/PVDF blends and PLA/MWCNT nanocomposites. This technique provided a comprehensive chemical fingerprint of the materials, enabling precise identification of molecular interactions between PLA, PVDF, and MWCNTs. The FTIR analysis was particularly crucial for detecting shifts in characteristic absorption peaks, indicating the formation of new bonds or the enhancement of interfacial compatibility. These insights were fundamental to understanding the chemical synergy and the role of each component in influencing the overall performance of the blends and nanocomposites.

8.3.3.2 Mechanical characterization

To enhance the softness and flexibility of PLA, PVDF was incorporated into the polymer matrix, forming PLA/PVDF blends. The mechanical properties of these blends were assessed through tensile tests conducted following ASTM D638 Type IV standards, with the specimen dimensions detailed in Figure S1a.

The tensile tests enabled the determination of critical mechanical parameters, including modulus of elasticity, tensile strength, and elongation at break. The study identified the optimal composition that balances mechanical strength with flexibility by examining blends with different PLA-to-PVDF ratios. This mechanical characterization is essential for tailoring the material properties to suit applications such as electroresponsive SMPs, where specific mechanical and structural attributes are crucial for functionality and durability.

8.4 Results and discussion

8.4.1 Scanning Electron Microscopy (SEM)

The SEM analysis provided detailed insights into the morphology and compatibility of the PLA/PVDF blends and PLA/MWCNTs nanocomposites. Figure 69(a) shows the surface morphology of pure PLA, which appears smooth and uniform without visible defects, highlighting its high printability. In contrast, Figure 69(b) illustrates a single PVDF particle with a size of approximately 200 μm and a non-smooth surface, reflecting its distinct crystalline

properties. Figure 69(c) reveals the as-received MWCNTs, displaying long, intertwined tubular structures essential for enhancing thermal and electrical properties in nanocomposites.

The PLA/PVDF blends exhibited varying degrees of phase separation depending on their composition. Figure 69(d) shows the morphology of the P3F7 blend. At high magnification (200x), the surface shows a rough and uneven morphology, suggesting limited interaction between the PLA and PVDF phases. At lower magnification (50x), distinct phase separation is evident, with visible domains of PLA and PVDF forming separate regions.

Figure 69(e) highlights the improved morphology of the P5F5 blend, where smaller voids and a smoother, more homogeneous surface at both high and low magnifications suggest better interaction between PLA and PVDF, although some phase separation remains. Figure 69(f) further demonstrates enhanced compatibility in the P7F3 blend. At high magnification (200x), fewer voids and rough areas are visible, while at lower magnification (50x), the surface appears more uniform, indicating stronger interactions between the two polymers despite incomplete miscibility.

The improved miscibility observed in the P5F5 blend can be attributed to the balanced ratio of PLA and PVDF, which maximizes the intermolecular interactions between the two polymers. In this composition, sufficient PVDF is present to act as a compatibilizer for PLA, which promotes better interfacial adhesion and reduces phase separation. In contrast, the P3F7 blend contains an excess of PVDF, resulting in a dominance of PVDF domains and limited interactions with the smaller amount of PLA. Similarly, the P7F3 blend has a higher PLA content, which reduces the ability of PVDF to effectively interact with and disperse in the PLA matrix. The balanced polymer ratio in P5F5 thus creates a more favorable environment for interphase interaction and improved compatibility.

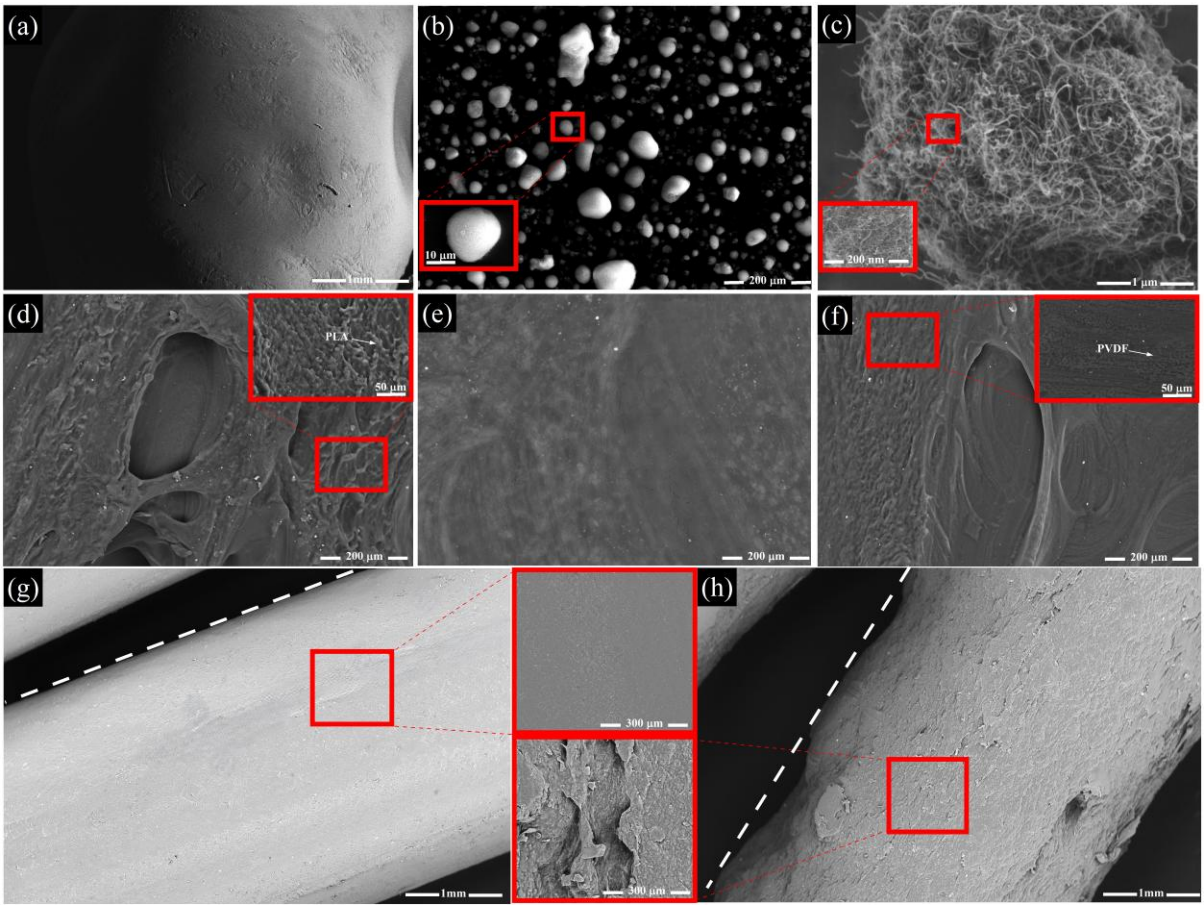

Figure 69: SEM images of as received (a) PLA, (b) PVDF, and (c) MWCNTs; high and low magnification SEM of (d) P7F3, (e) P5F5, (f) P3F7, and the extruded filaments of (g) C-7,5, and (h) C-10.

For the PLA/MWCNTs nanocomposites, Figure 69(g) shows the extruded filament of the C-7.5 sample, which features a smooth surface and uniform cross-section. This indicates the effective dispersion of MWCNTs within the PLA matrix, leading to enhanced reinforcement without compromising extrusion quality. Conversely, Figure 69(h) illustrates the filament of the C-10 nanocomposite, which displays significant defects, including an uneven surface and non-uniform cross-section. These imperfections result from the excessive concentration of MWCNTs, surpassing the PLA matrix's dispersion capacity and causing aggregation and reduced mechanical performance.

These findings underline the importance of optimizing composition to achieve desired morphology and functionality. The P5F5 and P7F3 blends, as well as the C-7.5 nanocomposite, demonstrate a favorable balance between compatibility and performance. However, the challenges observed in the P3F7 blend and C-10 nanocomposite highlight the critical need to

address phase separation and filler aggregation to improve overall material properties and processing quality.

8.4.2 Differential Scanning Calorimetry (DSC)

The thermal parameters of PLA, PVDF, and their blends (P3F7, P5F5, and P7F3) are summarized in Table 33, providing key insights into their glass transition temperature (Tg), melting temperature (Tm), and cold crystallization temperature (Tc). Differential Scanning Calorimetry (DSC) was used to analyze these parameters, allowing for an evaluation of miscibility and the influence of PVDF on PLA's thermal behavior.

For pure PLA (Figure 70(a)), a prominent Tg was observed at approximately 69.99 °C, reflecting the characteristic transition of its amorphous region. Similarly, pure PVDF (Figure 3b) exhibited a Tg at -44.69 °C, consistent with its flexible amorphous phase. These baseline transitions served as reference points for analyzing the PLA/PVDF blends.

In the P3F7 blend (Figure 70(c)), the DSC curve revealed two distinct Tg values: ~69.97 °C for PLA and ~-43.73 °C for PVDF. This separation indicates immiscibility between the two polymers. Similarly, the P7F3 blend (Figure 70(e)) exhibited Tg values of ~69.99 °C for PLA and ~-44.17 °C for PVDF, further confirming the immiscibility of the polymers in this composition.

Conversely, the P5F5 blend (Figure 70(d)) showed a significant reduction in the Tg of PLA to ~50.02 °C, suggesting partial miscibility or molecular interactions between PLA and PVDF. The closer ratio of the two polymers likely promotes interfacial interactions, reflected in this thermal transition.

The melting temperatures (Tm) and cold crystallization temperatures (Tc) provided additional insights. The Tm and Tc values for PLA in the P3F7 and P7F3 blends were similar to those of pure PLA, indicating limited interaction between the phases. However, in the P5F5 blend, the Tm of PLA decreased slightly, and its Tc shifted, reflecting enhanced interactions between the phases at this composition. These findings highlight how composition affects thermal transitions and polymer behavior, which is crucial for optimizing blends for specific applications.

8.4.3 X-ray Diffraction (XRD)

The XRD patterns of the PLA/PVDF SMP blends, shown in Figure 70(f), reveal important information about their crystalline structures. Peaks at 2θ = 17.8°, 18.5°, and 19.9° are characteristic reflections of PVDF, corresponding to the (100), (020), and (110) planes,

respectively. These peaks confirm the presence of crystalline PVDF, which may exist in the α-phase or β-phase, depending on the processing conditions and composition. Additionally, the peak at 2θ = 24°, attributed to the (110) / (200) planes of PLA, first appears prominently in the P3F7 blend and grows significantly in intensity within the P5F5 blend. Compared to the XRD pattern of pure PLA, the intensity of this peak is markedly higher in blends with higher PVDF content. This suggests that PVDF contributes to enhanced crystallization of PLA by acting as a plasticizer, lowering its glass transition temperature (Tg), and improving the mobility of PLA chains, which align into more crystalline structures. This interaction increases the overall crystallinity of the PLA matrix within these blends.

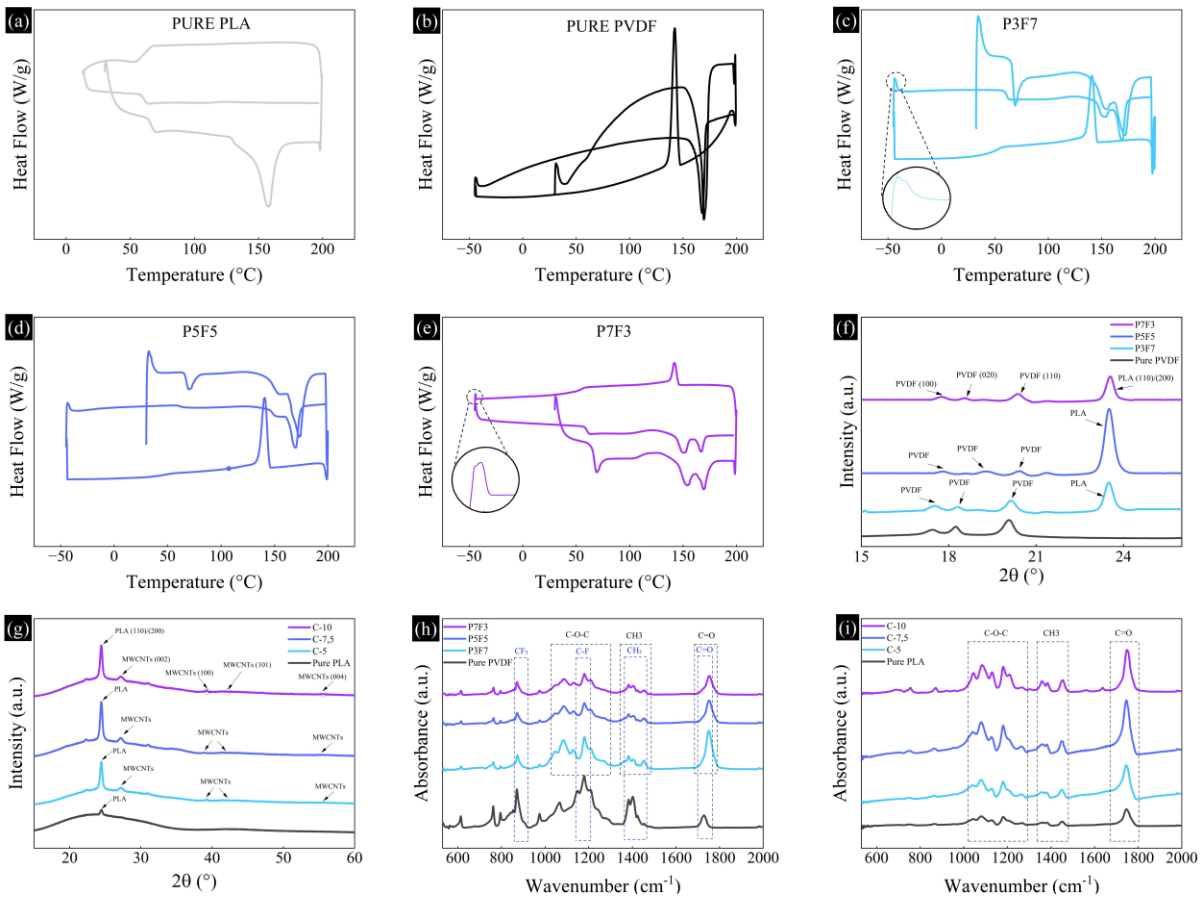

Figure 70: Thermal and structural characterization of PLA/PVDF and PLA/MWCNTs samples : Heating and cooling curves of (a) Pure PLA, (b) Pure PVDF, (c) P3F7, (d) P5F5, (e) P7F3. X-ray diffraction patterns of the FDM 3D-printed (f) PLA/PVDF and (g) PLA/MWCNTs samples. FTIR spectra of the FDM 3D-printed (h) PLA/ PVDF and (i) PLA/MWCNTs samples.

The XRD patterns of the 3D-printed PLA/MWCNTs nanocomposites, displayed in Figure 70(g), further elucidate the influence of MWCNTs on the crystalline properties of the PLA matrix. The crystalline PLA peak at 2θ = 24°, corresponding to the (110)/(200) planes, becomes

more pronounced with the addition of MWCNTs, while the amorphous peak in the range of 16° to 30° diminishes. This observation confirms that MWCNTs act as nucleation sites, promoting enhanced crystallinity within the PLA matrix. This higher crystallinity contributes to improved mechanical stability, better shape fixity performance, and enhanced structural properties of the nanocomposite. Additionally, distinct peaks associated with MWCNTs are observed. The sharp peak at 2θ = 26° corresponds to the graphitic (002) planes, representing the characteristic structure of MWCNTs. Further peaks at 2θ = 40° and 43° correspond to the (100) and (101) planes, respectively, indicative of the hexagonal arrangement of carbon atoms in graphene layers. The peak at 2θ = 55° signifies higher-order reflections, providing additional structural details about the MWCNTs.

Table 33: Thermal properties of PVDF, PLA and PLA/PVDF SMP blends determined by DSC test.

Sample	Tg (PLA) (°C)	Tg (PVDF) (°C)	Tc (PVDF) (°C)	Tm (PLA) (°C)	Tm (PVDF) (°C)
Pure PLA	69.99	-	-	157.72	-
Pure PVDF	-	-44.69	142.28	-	169.45
P7F3	69.97	-43.73	141.75	154.60	170.65
P5F5	50.02	-44.81	141.93	153.84	171.13
P7F3	69.99	-44.17	142.52	153.15	169.04

These XRD results highlight the synergistic interactions between the components in PLA/PVDF blends and PLA/MWCNTs nanocomposites. The presence of PVDF enhances the crystallinity of PLA in SMP blends, while MWCNTs act as effective nucleating agents, further improving the crystalline properties of PLA nanocomposites. These structural modifications are critical for achieving mechanical and thermal performance in electroresponsive SMP applications.

8.4.4 Fourier Transform Infrared Spectroscopy (FTIR)

The Fourier Transform Infrared Spectroscopy (FTIR) analysis provided valuable insights into the chemical interactions and molecular structure of the PLA/PVDF blends and PLA/MWCNTs nanocomposites. Figure 70(h) highlights the FTIR spectra of pure PVDF and PLA/PVDF blends with varying PLA content. In pure PVDF, distinct peaks were observed at 840 cm^{-1}, corresponding to CF_2 stretching vibrations, and 1180 cm^{-1}, associated with C-F stretching vibrations. These peaks are characteristic of PVDF's high fluorine content, while additional peaks in the 1400–1450 cm^{-1} range were attributed to CH_2 bending vibrations. A minor peak at 1750 cm^{-1}, linked to the C=O bond, was also detected.

For the PLA/PVDF blends, the dominance of PVDF peaks diminished as PLA content increased. In blends with higher PVDF content (P3F7), the CF_2 and C-F vibrations dominated the spectrum. However, a shift toward PLA-dominant features was evident as PLA content increased in P5F5 and P7F3. This transition, illustrated by the decreasing intensity of PVDF peaks and the emergence of PLA peaks, suggests a changing molecular balance and structural transformation within the blends. The coexistence of crystalline and amorphous phases in higher PLA content blends indicates improved compatibility between the two polymers.

Figure 70(i) compares the FTIR spectra of pure PLA and PLA/MWCNT nanocomposites with varying MWCNT concentrations (0.5%, 7.5%, and 10%). In pure PLA, a strong peak at 1750 cm^{-1}, corresponding to the carbonyl (C=O) stretching vibration, and peaks between 1050–1300 cm^{-1}, representing ester bond (C-O-C) stretching, were observed. Methyl group bending vibrations (CH_3) appeared at 1450 cm^{-1} and 1380 cm^{-1}.

With the incorporation of MWCNTs, new peaks associated with MWCNTs become more prominent, especially in the low wavenumber region between 600-900 cm^{-1}, where C-C vibrations and other interactions typical of MWCNTs are observed.

Incorporating MWCNTs introduced new peaks in the low wavenumber region (600–900 cm^{-1}) associated with C-C vibrations and MWCNT-polymer interactions. The ester bond region (1050–1300 cm^{-1}) showed broadening, reflecting strong interactions between MWCNTs and PLA chains. Additionally, the intensity of the C=O stretching peak at 1750 cm^{-1} increased with higher MWCNT content, suggesting enhanced crystallinity in the PLA matrix. This increased crystallinity aligns with XRD findings, indicating that MWCNTs act as nucleation sites, promoting molecular order and structural stability in the nanocomposites. These results underscore the role of MWCNTs in improving the material's crystalline and molecular structure, paving the way for enhanced mechanical and thermal properties.

8.4.5 Mechanical properties

The tensile test results provide a detailed understanding of how PVDF content influences the mechanical properties of PLA in the polymer blends. The stress-strain curves for pure PLA, P7F3, P5F5, and P3F7, illustrated in Figure 71(a)-(d), reveal the relationship between stress and strain for each material. From these curves, key mechanical parameters, including Young's modulus, tensile strength, and tensile elongation, were extracted and analyzed to assess the balance between stiffness, strength, and flexibility.

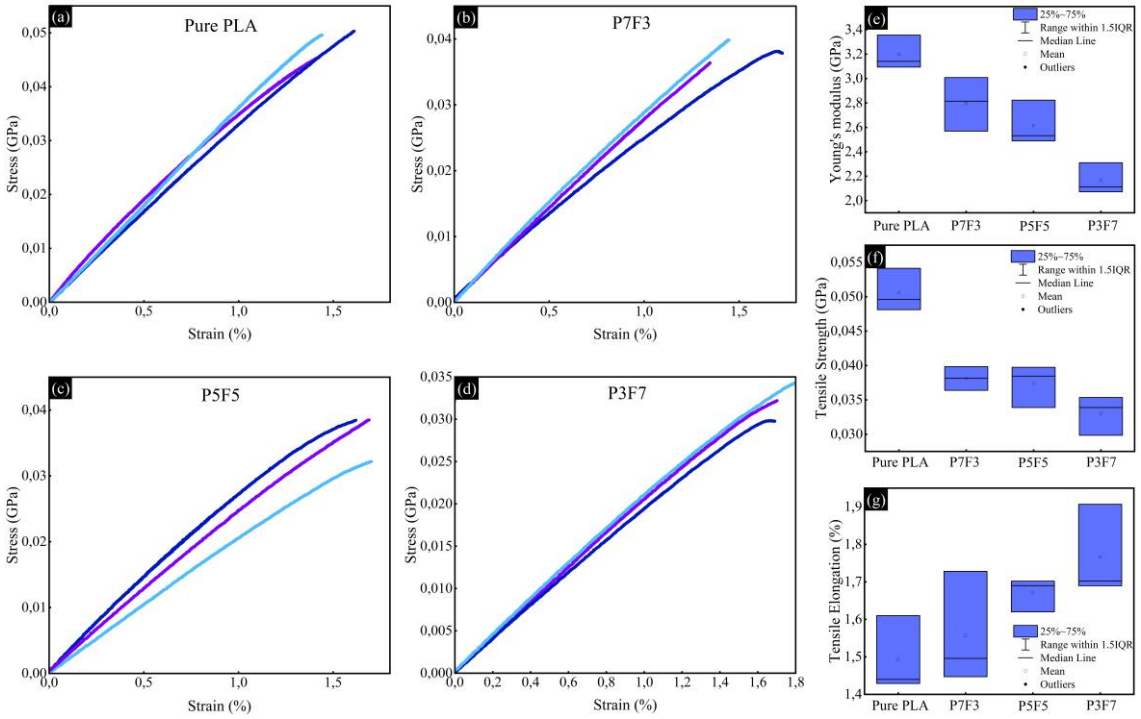

Figure 71: Mechanical performance of different PLA/PVDF blend ratios : (a) Stress-strain curve of (a) Pure PLA, (b) P7F3, (c) P5F5, (d) P3F7. (e) Young's modulus, (f) Tensile strength, and (g) Tensile elongation of PLA/PVDF samples.

As depicted in Figure 71(e), pure PLA exhibits the highest Young's modulus among the samples, demonstrating that it is the stiffest material in the group. However, the modulus decreases progressively with the increasing addition of PVDF, reflecting a trade-off between stiffness and flexibility. This trend indicates that incorporating PVDF into PLA reduces rigidity and enhances the material's deformability, making it more suitable for flexible applications.

Figure 71(f) highlights the tensile strength of the samples, with pure PLA showing the highest value. As PVDF is added, the tensile strength decreases, with P7F3 and P5F5 exhibiting intermediate values and P3F7 showing the lowest strength. This gradual decline in strength confirms that while PVDF improves flexibility, it compromises the material's ability to resist high levels of stress.

In contrast, tensile elongation follows an opposite trend. Pure PLA demonstrates the lowest elongation at break, indicating it has the least capacity to deform before failure. Increasing PVDF content increases the elongation capacity, reflecting enhanced flexibility and ductility. Notably, blends such as P7F3 and P5F5 offer a balanced mechanical profile, where flexibility is substantially improved without dramatically reducing tensile strength.

Overall, these results suggest that moderate PVDF content, as in the P7F3 or P5F5 blends, effectively enhances the flexibility and ductility of the material while maintaining a reasonable level of stiffness and strength.

8.4.6 Thermal and electrothermal performance of PLA/MWCNT nanocomposites

Figure 72(a) presents the infrared thermal images illustrating the temperature evolution of PLA/MWCNT nanocomposites containing different MWCNT concentrations (5%, 7.5%, and 10%) under a constant voltage of 10 V and a current of 0.1 A. The thermal responses were recorded at intervals of 2s, 4s, 6s, 8s, and 10s to capture the heating behavior of the materials. The results demonstrate a clear dependence of thermal performance on MWCNT content, with the C-10 sample exhibiting the highest temperature rise, followed by C-7.5 and C-5. This trend suggests that increasing the MWCNT content enhances thermal response, likely due to improved electrical conductivity and more effective Joule heating.

The progressive temperature increase across the samples confirms their ability to efficiently convert electrical energy into heat. This characteristic is critical for triggering the shape memory effect in electroresponsive SMPs. The superior thermal response of PLA/MWCNT nanocomposites underscores their suitability for applications requiring precise and efficient thermal activation.

A comparative analysis of MWCNTs and graphene nanoplatelets (GNPs) as fillers in PLA matrices was also conducted. Equal amounts of GNPs were added to PLA, and the thermal responses of both composites were recorded and compared (see Figure S2). The PLA/MWCNT samples consistently achieved higher maximum temperatures than the PLA/GNP samples. This behavior is attributed to the superior electrical conductivity of MWCNTs, as further evidenced by conductivity measurements shown in Figure S3. This comparison highlights the advantages of MWCNTs in enhancing the thermal performance of polymer composites, making them more effective for applications requiring rapid and uniform heating.

Figure 72(b) illustrates the visual appearance of the 3D-printed PLA/MWCNT nanocomposites with varying MWCNT concentrations (C-5, C-7.5, and C-10). The samples exhibit uniform and smooth structures, suggesting that adding MWCNTs does not significantly impair the printability of the PLA matrix. The variations in coloration, corresponding to the differing MWCNT content, indicate successful dispersion of the MWCNTs within the PLA matrix. This dispersion is critical for achieving consistent electrothermal properties across the printed components. The inset in the figure shows the dimensions of the samples (45 × 15 mm^2), providing a clear reference for the size of the specimens used in this study.

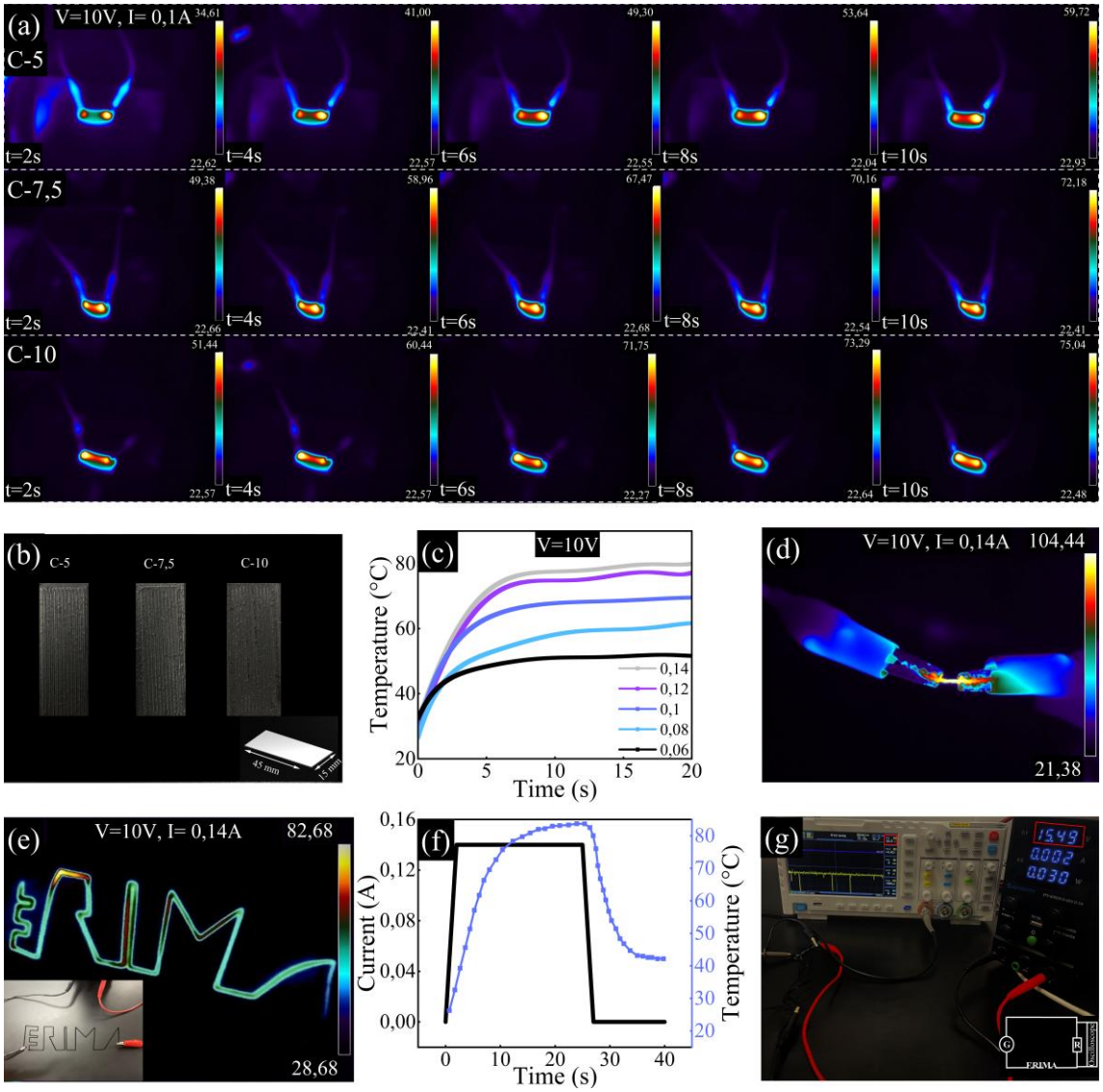

Figure 72: Electrothermal performance of PLA/MWCNTs nanocomposites under electrical stimulus : (a) Heat distribution maps of PLA/MWCNTs nanocomposite with different MWCNTs content under voltage of 20 V and current of 0.1 A; (b) Visual appearance of the 3D-printed PLA/MWCNTs samples; (c) Influence of applied current on the heating rate of the PVDF/MWCNTs hinge with optimal composition; (d) Heat distribution maps of optimal PVDF/MWCNTs hinge cross-section under optimal inputs conditions (e) Heat distribution map of optimal PLA/MWCNTs composition under optimal inputs conditions; (f) Relationship between the applied current and the resulting temperature profile in the "ERIMA" pattern; (g) Conductivity test of optimal PLA/MWCNTs composition.

Figure 72(c) presents the temperature-time curves for the C-7.5 nanocomposite under an applied voltage of 10 V and varying currents (0.06 A, 0.08 A, 0.1 A, 0.12 A, and 0.14 A). The data demonstrate a pronounced temperature rise at higher currents, confirming that the applied current directly influences the electrothermal performance. The rapid temperature increase followed by a plateau highlights the material's efficiency in reaching the activation temperature required for the shape memory effect without overheating, ensuring practical reliability. The

supporting video SV1 shows the rapid thermal heating of the C-5 sample under a current of 0.14 A.

Figure 72(d) provides an infrared thermal image of a joint made from the PLA/MWCNT nanocomposite (C-7.5) under an applied voltage of 10 V and a current of 0.14 A. The image reveals a localized and substantial temperature rise at the joint, reaching 104.44 °C. This demonstrates the material's capability to effectively convert electrical energy into heat at targeted locations. Such localized heating is essential for activating shape memory behavior in complex multi-material structures, allowing precise temperature control at specific joints to achieve desired shape transformations.

Figure 72(e) presents an infrared thermal image of a 3D-printed circuit featuring the "ERIMA" pattern, fabricated using the C-7.5 nanocomposite under 10 V and 0.14 A. The thermal image reveals a uniform temperature distribution across the structure, emphasizing the homogeneity of the electrothermal properties of the nanocomposite material. The inset provides a visual reference of the printed pattern, showcasing the material's capability to create intricate designs while maintaining its functional performance. This consistent heating behavior is critical to ensuring uniform activation of shape memory effects throughout the structure, which is particularly important for complex applications.

Figure 72(f) illustrates the current-temperature-time relationship in the "ERIMA" pattern, highlighting the material's thermal response. The graph shows a rapid temperature rise corresponding to the initial increase in current, followed by a stabilization phase, demonstrating efficient energy conversion and thermal management within the material. After the current is switched off, the gradual decrease in temperature reflects effective heat dissipation, an essential feature for preventing overheating and ensuring the long-term durability of the shape memory polymer in cyclic operations.

Figure 72(g) depicts a circuit setup comprising a generator, the "ERIMA" feature made from the C-7.5 nanocomposite, a resistor, and an oscilloscope designed to demonstrate the high conductivity of the PLA/MWCNT nanocomposite. In this configuration, the current flows through the PLA/MWCNT sample from the generator to the resistor. The generator applies a voltage of 15.5 V, while the oscilloscope measures 15 V across the resistor. The minimal voltage drop across the PLA/MWCNT sample highlights its excellent conductivity, underscoring its suitability for efficient electrical conduction applications.

8.4.7 Evaluation of Electroresponsive SMP Structure Design

The design of the electroresponsive SMP structure was proposed by comparing three configurations (S_1, S_2, and S_3), as detailed in Figures S5–S7. The dimensions of configurations S2 and S3 are presented in Figures S1 (c) and (d), respectively. Figure 73(a) shows the visual appearance of the optimal 3D-printed electroactive SMP structure (S_1), fabricated with different PLA/PVDF blend ratios: P3F7, P5F5, and P7F3. The chosen structure ensures the effective integration of both mechanical and electrothermal functionalities.

Figure 73(b) provides a schematic diagram of the multilayer SMP structure. It highlights the joint's design, comprising three layers: two outer layers made of PLA/PVDF blends and a central PLA/MWCNTs layer. The central layer serves as a conductive element that heats up under an applied voltage, activating the shape memory effect. The number of layers and their configuration in S1 were optimized experimentally, as outlined in Figures S8 and S9, with the detailed dimensions shown in Figures S1 (e)-(h).

The shape memory behavior of the structure is demonstrated in Figure 73(c), which illustrates the programming and recovery process of the SMP. During programming, the joint is heated above its glass transition temperature (T > Tg) under an applied voltage, deforming it from its original angle (θ_0=180º) to a programmed angle (θ_p =0º). The shape is then fixed by cooling the joint, resulting in a bent angle (θ_f). The shape fixation ratio (SFR) is calculated as:

$$\text{SFR}\ (\%) = \frac{\theta_0 - \theta_f}{\theta_0} \times 100. \qquad (71)$$

During the recovery phase, the joint is reheated, returning to its original shape with a recovered angle (θ_r). This highlights the electroactive response enabled by the PLA/MWCNTs conductive layer. The shape recovery ratio (SRR) is defined as:

$$\text{SRR}\ (\%) = \frac{\theta_r - \theta_f}{\theta_0 - \theta_f} \times 100. \qquad (72)$$

This process demonstrates the material's ability to achieve precise, reversible shape changes, a crucial feature for applications requiring controlled actuation. Figure 73(d) provides a sequence of thermal images and corresponding photographs depicting the shape recovery process of the P5F5 SMP structure under an applied voltage of 10 V. The images show temperature distribution at various time intervals (1s, 5s, 9s, 13s, 17s), highlighting localized heating within the PLA/MWCNTs layer containing 7.5% MWCNTs. The temperature rises from 67.66 °C to 80.28 °C, demonstrating efficient heat generation and transfer through the conductive layer. This thermal behavior activates the shape recovery mechanism within the PLA/PVDF blend layers, with detailed thermal and electrical responses presented in Figure S4.

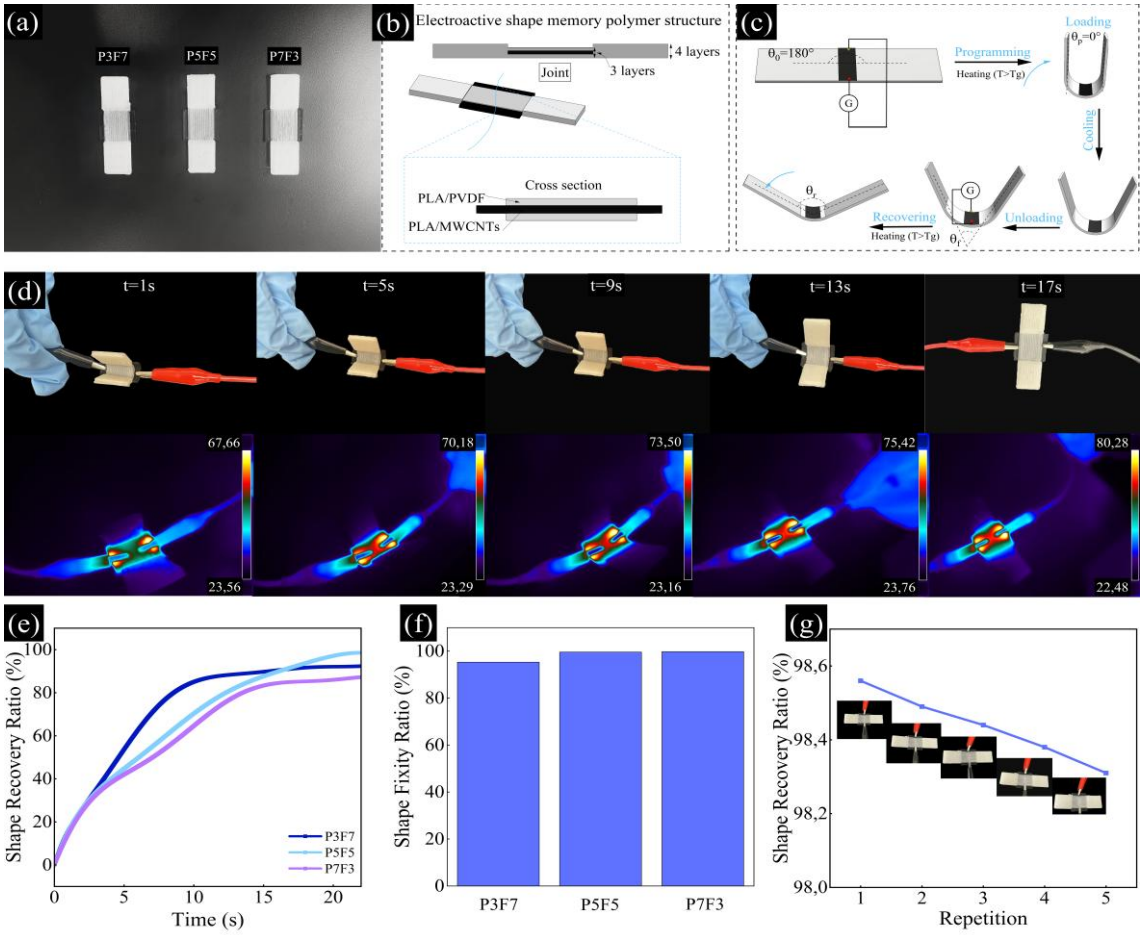

Figure 73: Evaluation of electroactive SMPs : (a) Different SMP blends (P3F7, P5F5, P7F3) with 7.5% MWCNTs; (b) Schematic representation of the electroactive shape memory polymer structure; (c) Shape memory cycle: Programming, cooling, and recovery; (d) Temperature distribution during the recovery process over time; (e) Shape recovery ratio over time for different SMP blends; (f) Shape fixity ratio for different SMP blends; (g) Shape recovery ratio over multiple cycles.

Figure 73(e) presents the shape recovery ratio (SRR) over time for the three SMP blends: P3F7, P5F5, and P7F3. The results show that all samples recover rapidly within the first few seconds. Among them, P3F7 and P5F5 exhibit slightly higher SRR values compared to P7F3. Notably, increasing PVDF content enhances SRR, improving from 87.23% to 98.56%, as higher PVDF concentrations improve the material's flexibility. This enhanced flexibility allows the polymer chains to realign more easily when heated above the transition temperature, resulting in faster and more complete shape recovery. However, a further increase in PVDF content reduces SRR to 92.34%. This decline is attributed to the reduced PLA content, which limits the availability of active molecules critical for achieving full recovery. Figure 73(f) illustrates the shape fixity ratio (SFR) for the different SMP blends. All samples show a high degree of fixity, with P3F7 achieving the highest SFR at 99.8%, closely followed by P5F5 at 99.6%. Conversely, P7F3,

the most flexible blend, has a slightly lower SFR of 95.3%. This trend aligns with expectations, as stiffer SMPs, such as P3F7, can better "lock in" and maintain the deformed shape when cooled below the transition temperature. The higher stiffness of these samples minimizes relaxation, resulting in superior shape fixity.

The P5F5 composition was selected as the optimal choice due to its superior thermal and mechanical properties, as described in the previous section, in combination with its excellent shape recovery and fixity performances. The supporting video SV2 demonstrates the fast recovery speed of the P5F5 sample with an applied voltage of 10 V and a current of 0.14 A. Figure 73(g) provides the SRR of over multiple deformation and recovery cycles the P5F5 sample. The graph shows a slight but consistent decline in SRR, decreasing from 98.56% to 98.31% over five cycles. This corresponds to a minimal loss of 0.25° in shape recovery. The accompanying visual graph captures the state of the SMP structure during each cycle, correlating effectively with the observed reduction in SRR. This analysis highlights the material's durability and long-term reliability, which are critical metrics for evaluating its suitability in practical applications requiring repeated actuation.

8.4.8 Finite Element Electrothermal and Thermomechanical Simulation

To achieve precise control of the electrothermal PLA/MWCNTs nanocomposite, a comprehensive multiphysics simulation model of the heating process was developed using finite element analysis in ABAQUS software. This model integrates electrical and thermal effects, enabling a detailed analysis of the material's behavior under applied voltage (see Equations S1-S4). Figure Figure 74(a) illustrates the simulated electrothermal processes, including internal heat generation through current flow, conduction along the material's length, and heat dissipation into the surrounding air via convection.

In addition, a thermoviscoelastic multi-branch model (Figure 74(b)) was constructed to describe the thermo-mechanical response of the P5F5 SMP. This model incorporates two equilibrium branches representing the contributions of P5F5 and C-7.5, along with several thermoviscoelastic non-equilibrium branches (number n), to capture the polymer's multiple relaxation processes. Detailed heat transfer calculations, including Joule heating in the C-7.5 sample, thermal conduction within the joints, and convection with the surrounding air, are provided in Equations 1-5 in the Supporting Information. The model also predicts the resulting total stress (σ) as a function of time (t).

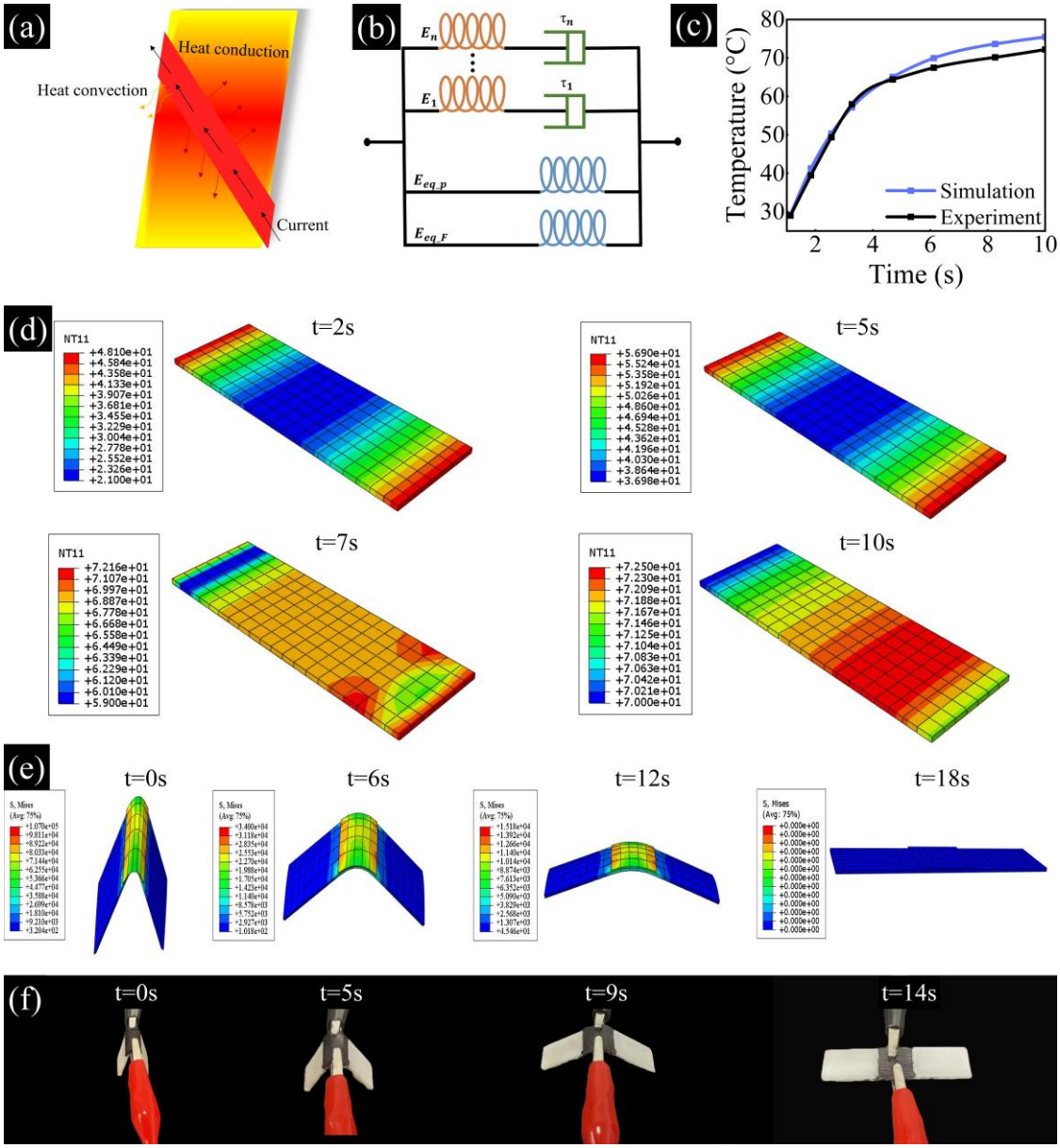

Figure 74: Electrothermal simulations and experimental validation of shape memory behavior : Numerical simulations and experimental validation of the electrothermal and shape recovery behaviors: (a) The multiphysics model of the proposed electrothermal joint; (b) Thermoviscoelastic multibranch model for thermomechanical response analysis; (c) Comparison of simulated and experimental temperature rise versus time; (d) Numerical simulation of temperature distribution in electrothermal nanocomposite ; (e) Numerical simulation and (f) Experimental observation of shape recovery process versus time, under electrical heating.

Figure 74(c) presents a comparison between the numerical simulations and experimental measurements of temperature rise over time. The data exhibit close agreement, validating the accuracy of the numerical model. The results reveal rapid temperature increases during the initial seconds, followed by a gradual stabilization, consistent with the expected behavior of the PLA/MWCNTs nanocomposite under electrical heating. Figure 74(d) illustrates the

simulated temperature distribution within a C-7.5 sample at various time intervals (2s, 5s, 7s, 10s). The simulation highlights a uniform thermal distribution, with temperatures reaching 70°C to 72.5°C within 10 seconds under an applied voltage of 10 V. This rapid and uniform temperature rise underscores the material's efficiency in thermal activation, a critical feature for shape memory effect applications. The dimensions of the simulated sample are provided in Figure S1b.

The shape memory behavior of the P5F5 SMP under electrical heating was also simulated (Figure 74(e)), demonstrating the material's deformation over time (0s, 6s, 12s, 18s) as it transitioned from its programmed to recovered shape. The simulation showed a gradual restoration to the original shape, completed within 18 seconds, highlighting the SMP's effective response to thermal stimuli. Figure 74(f) presents a series of photographs experimentally validating the shape recovery process, captured at different time intervals (0s, 5s, 9s, 14s). The experimental images show the gradual restoration of the SMP structure to its original shape, closely mirroring the numerical simulation results depicted in Figure 74(g). This strong correlation between experimental and simulated outcomes confirms the accuracy of the numerical model and demonstrates the effective conversion of electrical heating into shape recovery in the SMP.

8.4.9 3D printing of bio-inspired multi-material structures using PLA/PVDF SMP blends and PLA/MWCNTs nanocomposites

This study successfully demonstrated the 3D printing of bio-inspired multi-material structures using a combination of P5F5 and C-7.5 composites, showcasing the versatility and printability of these advanced materials. The intricate designs, inspired by natural processes, included the unfolding of butterfly wings (Figure 75(a)), the blooming of flowers (Figure 75(b)), the aging of leaves (Figure 75(c)), and the movement of snakes (Figure 75(d)). These structures highlight the composites' ability to form complex shapes while maintaining excellent structural integrity. Each bio-inspired design was carefully modeled, programmed, and numerically validated through simulations that mapped stress distribution and thermal effects. The detailed dimensions of each model are provided in Figure S1i. The results revealed the remarkable responsiveness of the structures to applied electrical voltage, enabling controlled deformations and transformations closely mimicking their biological counterparts.

For example, the butterfly and flower designs unfolded and bloomed precisely, while the leaf design replicated the natural rippling effect in aging leaves.

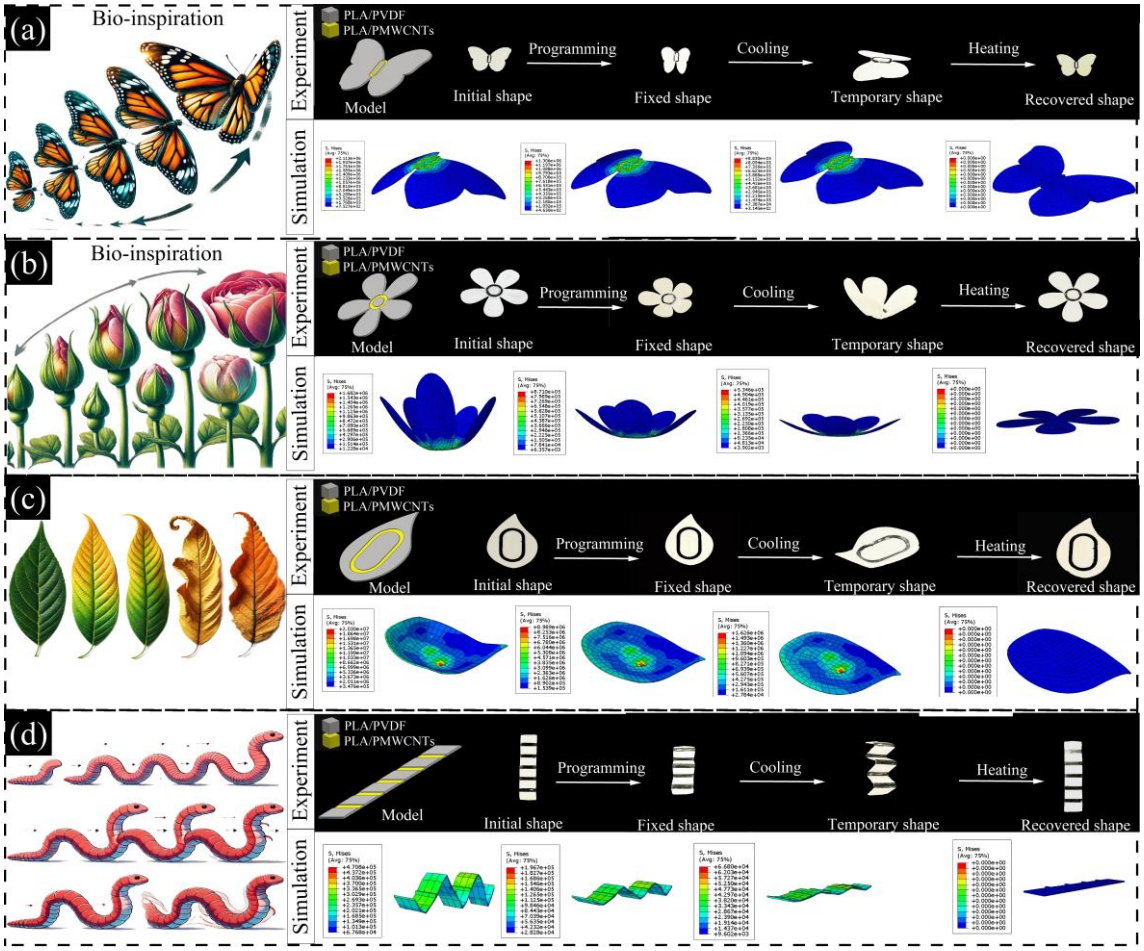

Figure 75: Demonstration of bioinspired shape morphing using electroactive SMPs : Simulations and experimental validation of bio-inspired shape change with electroactive shape memory polymers: (a) Butterfly wing unfolding, (b) flower blooming, (c) leaf curling and aging behavior, and (d) snake movement.

Similarly, the snake design successfully mimicked undulating motion, demonstrating the adaptability of these materials for dynamic and programmable movements. The numerical results of these bio-inspired designs are presented in the supporting videos SV3, SV4, SV5 and SV6, respectively.

The close agreement between numerical simulations and experimental results emphasizes the computational models' reliability. These findings underscore the potential of P5F5 and C-7.5 composites for creating dynamic, programmable materials for various innovative applications.

8.4.10 3D printing of robotic hand with human-inspired joints using PLA/PVDF SMP blends and PLA/MWCNTs nanocomposites

Figure 76 demonstrates the application of the SMP blend P5F5 in combination with the electroresponsive C-7.5 nanocomposite to fabricate a 3D-printed robotic hand with human-inspired joints. Heat is generated by selectively applying an electric current to the PLA/MWCNTs joints, enabling controlled finger movements that replicate all degrees of freedom (DOF). The robotic hand's performance highlights the versatility and precision achievable with these materials. In the first phase of the process, a current of 0.14 A was applied to each joint, elevating the temperature to approximately 80°C. This heating facilitated joint mobility, allowing the fingers to achieve their desired positions. Cooling the joints to ambient temperature effectively "froze" the fingers in place, demonstrating the material's high shape fixity ratio (SFR), as detailed in Figure S10a.

During the recovery phase, an electric current of 0.14 A was reapplied to specific joints, triggering precise and responsive shape recovery to pre-programmed positions. The results, shown in Figure 77, illustrate the controlled actuation of individual joints, enabling the robotic hand to perform various human-like finger movements. Each row in the figure corresponds to a distinct test scenario, where unique combinations of joints were activated, showcasing the material's responsiveness and precision. The shape recovery ratios (SRRs) of each joint are presented in Figure S10b, further confirming the system's effectiveness.

This setup underscores the robotic hand's ability to execute complex and dexterous movements with a high degree of control. The findings emphasize the potential of using PLA/MWCNTs nanocomposites for applications in robotics and prosthetics, where fine motor skills, adaptability, and responsiveness to electrical stimuli are essential. This innovative approach opens avenues for creating advanced robotic systems that accurately mimic human motion.

8.5 Conclusion

This study highlights the significant advancements achieved with PLA/PVDF/MWCNT composites in 4D printing, particularly for electroactive shape memory polymers (SMPs). The incorporation of MWCNTs enhanced the electrothermal response, mechanical properties, and shape memory performance of the materials, effectively overcoming the limitations of conventional heat and water-triggered SMPs. The optimized composite containing 7.5% MWCNTs (C-7.5) achieved a rapid temperature rise from 22.3°C to 80.28°C within 10 seconds under an applied voltage of 10V and current of 0.14A, ensuring efficient activation of the shape memory

effect. The composite also exhibited a high shape recovery ratio (SRR) of 98.56% and a shape fixity ratio (SFR) of 99.6%, highlighting its exceptional precision and reliability for reversible shape transformations.

The development of a robust numerical model further reinforced the practicality of these composites. The model accurately predicted the electrothermal behavior, with simulations aligning closely with experimental results, such as the observed steady-state temperature of approximately 72.5°C after 10 seconds of heating. These predictive capabilities provide critical insights for designing and optimizing structures for real-world applications.

Figure 76: Shape fixity test of a 3D-printed PLA/PVDF-based robotic hand with PLA/MWCNTs joints using 0.14A electric current.

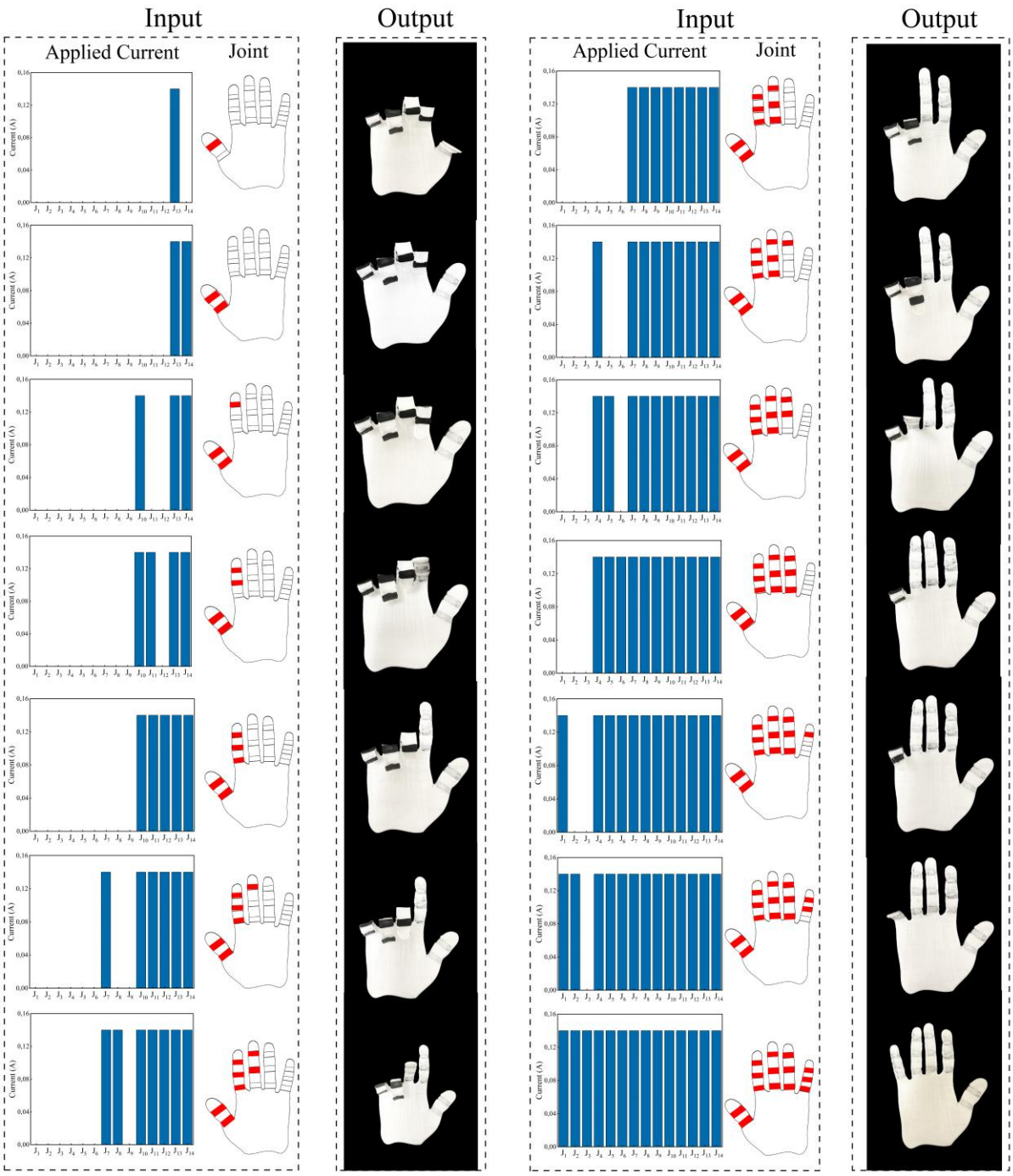

Figure 77: Shape recovery test of a 3D-printed PLA/PVDF-based robotic hand with PLA/MWCNTs joints using 0.14A electric current.

The successful integration of these materials into complex designs, such as bio-inspired systems and a robotic hand with human-like dexterity, demonstrates their versatility. The robotic hand showcased precise joint control, maintaining SFR values above 99% and achieving SRR values consistently above 98% across multiple cycles. This demonstrates the composite's suitability for creating advanced, programmable devices with fine-tuned actuation.

In conclusion, the PLA/PVDF/MWCNT nanocomposite represents a transformative step in 4D printing technology. Its adaptability, high performance, and scalability make it a promising candidate for next-generation smart devices. The results highlight its potential for diverse applications, including robotics, healthcare, and dynamic material systems, with future research opportunities to enhance durability under cyclic conditions and expand its multifunctionality.

8.6 Acknowledgment

The authors acknowledge the funding provided by the Natural Sciences and Engineering Research Council (NSERC) of Canada in the form of Discovery Grants (Grant Number: CRSNG – RGPIN -2021-02846).

8.7 References

[1] X. Wang, Y. He, Y. Liu, J. Leng, Advances in shape memory polymers: Remote actuation, multi-stimuli control, 4D printing and prospective applications, Materials Science and Engineering: R: Reports 151 (2022) 100702.
[2] A. Subash, B. Kandasubramanian, 4D printing of shape memory polymers, European Polymer Journal 134 (2020) 109771.
[3] J. Zhang, Z. Yin, L. Ren, Q. Liu, L. Ren, X. Yang, X. Zhou, Advances in 4D printed shape memory polymers: from 3D printing, smart excitation, and response to applications, Advanced Materials Technologies 7(9) (2022) 2101568.
[4] W. Zhao, C. Yue, L. Liu, Y. Liu, J. Leng, Research progress of shape memory polymer and 4D printing in biomedical application, Advanced Healthcare Materials 12(16) (2023) 2201975.
[5] Y. Chen, C. Chen, H.U. Rehman, X. Zheng, H. Li, H. Liu, M.S. Hedenqvist, Shape-memory polymeric artificial muscles: Mechanisms, applications and challenges, Molecules 25(18) (2020) 4246.
[6] M. Herath, J. Epaarachchi, Shape memory polymer composites and their smart structural applications, Composite Materials, Elsevier2021, pp. 581-610.
[7] L. Luo, F. Zhang, L. Wang, Y. Liu, J. Leng, Recent Advances in Shape Memory Polymers: Multifunctional Materials, Multiscale Structures, and Applications, Advanced Functional Materials 34(14) (2024) 2312036.
[8] S. Rodinò, C. Maletta, Design Considerations and Applications of Shape Memory Alloy-Based Actuation in Morphing Structures: A Systematic Review, Progress in Engineering Science (2024) 100021.
[9] G. Scalet, Two-way and multiple-way shape memory polymers for soft robotics: An overview, Actuators, MDPI, 2020, p. 10.
[10] C. Lin, J. Lv, Y. Li, F. Zhang, J. Li, Y. Liu, L. Liu, J. Leng, 4D-printed biodegradable and remotely controllable shape memory occlusion devices, Advanced Functional Materials 29(51) (2019) 1906569.
[11] Y. Wang, H. Cui, Y. Wang, C. Xu, T.J. Esworthy, S.Y. Hann, M. Boehm, Y.-L. Shen, D. Mei, L.G. Zhang, 4D printed cardiac construct with aligned myofibers and adjustable curvature for myocardial regeneration, ACS applied materials & interfaces 13(11) (2021) 12746-12758.
[12] J.G. Choi, G.M. Spinks, S.J. Kim, Mode shifting shape memory polymer and hydrogel composite fiber actuators for soft robots, Sensors and Actuators A: Physical 342 (2022) 113619.

[13] K. Bouguermouh, M. Habibi, L. Laperrière, Z. Li, Y. Abdin, 4D-printed PLA-PETG polymer blends: comprehensive analysis of thermal, mechanical, and shape memory performances, Journal of Materials Science (2024) 1-18.
[14] B. Karima, M. Habibi, L. Laperrière, 4D printing of fiber-reinforced auxetic structures: the building blocks: a review, Smart Material Structures 33(6) (2024) 063001.
[15] R. Purwar, R. Sachan, Thermoresponsive shape memory polymers for smart textiles, Advances in functional and protective textiles, Elsevier2020, pp. 37-62.
[16] M. Wang, F. Yang, Y.J. Zhang, Tunable Thermo-Responsive Shape Memory Materials Enabled by Poly (E-Caprolactone)-Poly (2-Vinyl) Ethylene Glycol Copolymers Via Facile Thiol-Ene Photo-Crosslink, Available at SSRN 4956901.
[17] X. Yang, X. He, L. Wang, C. Zhao, D. Xiang, H. Li, J. Lai, G. Yan, Z. Li, L. Sun, Durable semi-interpenetrating polymer network containing dynamic boroxine bonds for multi-shape manipulated deformation, Chemical Engineering Journal 491 (2024) 151905.
[18] W. Liu, D. Kong, W. Zhao, J. Leng, Multi-stimulus responsive shape memory polyurea incorporating stress-mismatching structure for soft actuators and reversible deployable structures, Composite Structures 334 (2024) 117966.
[19] A. ISLAM, J. HASAN, K.R. HOSSAIN, Intelligent materials in 3D printing: A journey from additive manufacturing to 4D printing, Journal of Advanced Manufacturing Science and Technology 4(4) (2024).
[20] Y.-F. Shih, W.-C. Hou, C.-W. Chang, C.-H. Wu, R.-J. Jeng, Y.-H. Chen, Carbon nanotube/microcapsule/polyurethane nanocomposites for multistimuli responsive shape memory polymers.
[21] A. Concellón, P. Mainik, C. Vazquez-Martel, C. Álvarez-Solana, E. Blasco, 4D Printing of Liquid Crystal Emulsions for Smart Structures with Multiple Functionalities, Angewandte Chemie e202421162.
[22] J. zhang, Q. Zhang, W. Pan, M. Jiao, Y. Chen, H. Pei, X. Li, Y. Qi, J. Zhao, Ethylene vinyl acetate/copper sulphide with near-infrared light active shape memory behavior, Journal of Elastomers & Plastics (2024) 00952443241297450.
[23] S. Nandha, D. Rajan, U. Shivakumar, Nanocellulose Incorporated Liquid Crystal Elastomers as Soft Actuators, ACS Applied Polymer Materials 6(20) (2024) 12842-12853.
[24] Z. Liu, Y. Li, S. Ma, C. Liu, Y. Zhang, X. Lu, Z. Lin, Y. Liang, Near-infrared light-driven programmable shape memory polymer for self-shaping 3D printing methods, Virtual and Physical Prototyping 19(1) (2024) e2422384.
[25] N. Phetnoi, L. Amornkitbamrung, K. Charoensuk, C. Sapcharoenkun, C. Jubsilp, S. Ekgasit, S. Rimdusit, Fast magnetic-responsive shape memory composites from bio-based benzoxazine/polyglycerol polyglycidyl ether copolymers highly filled with iron oxide nanoparticles, Composites Part A: Applied Science and Manufacturing 186 (2024) 108398.
[26] J. Liu, S. Wang, S. Huang, K. Zhang, Z. Chen, C. Huang, Y. Zhang, S. Du, T. Xu, Magnetic and radio frequency dual-responsive shape-programmable robots for adaptive aneurysm embolization, Cell Reports Physical Science 5(9) (2024).
[27] A. Ahangari, H. Doostmohammadi, M. Baniassadi, M. Bodaghi, M. Baghani, Development and 4D printing of magneto-responsive PMMA/TPU/Fe3O4 nanocomposites with superior shape memory and toughness properties, European Polymer Journal 220 (2024) 113495.
[28] K. Ruenpanya, P. Mora, P. Karagiannidis, K. Bunyanuwat, S. Rimdusit, Magnetic-responsive triple shape memory polymer from bio-based benzoxazine/urethane polymer alloys with iron oxide nanoparticles, Advanced Industrial and Engineering Polymer Research (2024).
[29] P. Kumar, P. Suryavanshi, S.K. Dwivedy, S. Banerjee, Stimuli-responsive materials for 4D Printing: Mechanical, Manufacturing, and Biomedical Applications, Journal of Molecular Liquids (2024) 125553.

[30] L. Zhang, X. Huang, T. Cole, H. Lu, J. Hang, W. Li, S.-Y. Tang, C. Boyer, T.P. Davis, R. Qiao, 3D-printed liquid metal polymer composites as NIR-responsive 4D printing soft robot, Nature Communications 14(1) (2023) 7815.
[31] H. Liu, F. Wang, W. Wu, X. Dong, L. Sang, 4D printing of mechanically robust PLA/TPU/Fe3O4 magneto-responsive shape memory polymers for smart structures, Composites Part B: Engineering 248 (2023) 110382.
[32] X. Dong, F. Zhang, L. Wang, Y. Liu, J. Leng, 4D printing of electroactive shape-changing composite structures and their programmable behaviors, Composites Part A: Applied Science and Manufacturing 157 (2022) 106925.
[33] K. Dong, M. Panahi-Sarmad, Z. Cui, X. Huang, X. Xiao, Electro-induced shape memory effect of 4D printed auxetic composite using PLA/TPU/CNT filament embedded synergistically with continuous carbon fiber: A theoretical & experimental analysis, Composites Part B: Engineering 220 (2021) 108994.
[34] A.D.B. Ferreira, P.R. Nóvoa, A.T. Marques, Multifunctional Material Systems: A state-of-the-art review, Composite Structures 151 (2016) 3-35.
[35] W. Zhao, L. Liu, J. Leng, Y. Liu, Thermo-mechanical behavior prediction of particulate reinforced shape memory polymer composite, Composites Part B: Engineering 179 (2019) 107455.
[36] K.K. Westbrook, P.H. Kao, F. Castro, Y. Ding, H.J. Qi, A 3D finite deformation constitutive model for amorphous shape memory polymers: a multi-branch modeling approach for nonequilibrium relaxation processes, Mechanics of Materials 43(12) (2011) 853-869.
[37] W. Zhao, L. Liu, X. Lan, J. Leng, Y. Liu, Thermomechanical constitutive models of shape memory polymers and their composites, Applied Mechanics Reviews 75(2) (2023) 020802.
[38] S.H. Ladakhan, R.B. Sreesha, S.M. Adinarayanappa, 4D printing of polylactic acid (PLA)/PLA-thermoplastic polyurethane (TPU)-based metastructure: examining the mechanical, thermal, and shape memory properties, Smart Materials and Structures 33(10) (2024) 105037.
[39] B. Goo, C.-H. Hong, K. Park, 4D printing using anisotropic thermal deformation of 3D-printed thermoplastic parts, Materials & Design 188 (2020) 108485.
[40] C. Shuai, W. Xu, H. He, F. Yang, J. Liu, P. Feng, Layered co-continuous structure in bone scaffold fabricated by laser additive manufacturing for enhancing electro-responsive shape memory properties, Journal of Materials Research and Technology 30 (2024) 61-69.
[41] C. Zeng, L. Liu, W. Bian, Y. Liu, J. Leng, 4D printed electro-induced continuous carbon fiber reinforced shape memory polymer composites with excellent bending resistance, Composites Part B: Engineering 194 (2020) 108034.
[42] A. Megdich, M. Habibi, L. Laperrière, Z. Li, Y. Abdin, Advanced 3D-printed PVDF/BT piezoelectric energy harvester with a bio-inspired 3D structure for a self-powered smart mouse, Nano Energy (2024) 109876.
[43] A. Megdich, M. Habibi, L. Laperrière, Z. Li, Y. Abdin, Enhanced piezoelectric performance of PVDF/MWCNTs energy harvester through a 3D-printed multimodal auxetic structure for smart security systems, Materials Today Sustainability 27 (2024) 100847.
[44] A. Megdich, M. Habibi, L. Laperrière, Modeling and optimization of piezoelectric and dielectric properties of poled PVDF/BT nanocomposites, Polymer Bulletin (2024) 1-21.

Partie III : Intégration de l'impression 4D et des technologies MEMS piézoélectriques – Vers des dispositifs autonomes et adaptatifs

Chapitre 9: Revue de littérature sur l'impression 4D des MEMS piézoélectriques

Ce chapitre a fait l'objet d'une publication :
MEGDICH, Amal, HABIBI, Mohamed, LAPERRIÈRE.
Review of progress in 4D printing of piezoelectric energy harvesters, accepté au journal *Materials Science and Engineering: R: Reports.*

Avant d'entamer nos investigations expérimentales, ce chapitre présente une revue détaillée des avancées réalisées dans l'impression 4D et dans l'impression 3D de matériaux piézoélectriques. Une comparaison systématique entre ces deux technologies est réalisée en analysant les techniques d'impression utilisées, les stimuli d'activation, ainsi que les matériaux impliqués. L'objectif de cette revue est de mettre en lumière les convergences et les divergences entre ces deux domaines, tout en identifiant les défis et opportunités liés à leur intégration.
Dans un premier temps, l'article examine les principales technologies d'impression 3D employées dans chacun de ces domaines telles que le Fused Deposition Modeling (FDM), la stéréolithographie (SLA) et le Digital Light Processing (DLP), et le Direct Ink Writing (DIW).
L'article compare également les différents stimuli activant ces technologies. L'impression 4D repose sur des stimuli tels que la température, l'humidité, les champs magnétiques et électriques, tandis que les récupérateurs d'énergie piézoélectriques fonctionnent grâce aux contraintes mécaniques et aux vibrations. Cette analyse met en évidence les synergies potentielles entre ces mécanismes, ouvrant la voie à des dispositifs hybrides combinant mémoire de forme et récupération d'énergie.
Un autre point central de cette revue est l'analyse des matériaux utilisés dans les deux domaines, qui se répartissent en trois grandes catégories :
Les polymères, qui comprennent les polymères à mémoire de forme (SMP) pour l'impression 4D et les polymères piézoélectriques tels que le PVDF et ses dérivés pour la récupération d'énergie.
Les céramiques, qui sont largement utilisées dans l'impression 3D de matériaux piézoélectriques, notamment le titanate de baryum (BTO) et le titanate de zirconate de plomb (PZT), mais qui commencent également à être explorées pour certaines applications d'impression 4D.

Les composites, qui combinent des charges fonctionnelles (nanotubes de carbone, nanoparticules céramiques) avec des matrices polymères pour améliorer les performances mécaniques et électromécaniques des dispositifs imprimés.

Enfin, la revue explore les travaux récents qui combinent l'impression 4D avec la technologie piézoélectrique, en mettant en avant les approches expérimentales et les concepts émergents. Ces études montrent comment l'intégration de matériaux piézoélectriques dans des structures imprimées en 4D permet d'améliorer la récupération d'énergie ou de concevoir des capteurs capables de s'adapter à leur environnement. L'examen des articles existants souligne les avantages de cette combinaison, tout en identifiant les défis à relever, notamment en termes de stabilité des propriétés piézoélectriques après transformation de la structure et d'optimisation des performances des dispositifs imprimés.

Cette revue sert ainsi de base à nos travaux expérimentaux en identifiant les meilleures stratégies pour concevoir et optimiser des structures imprimées en 4D intégrant des matériaux piézoélectriques. Le prochain et dernier chapitre de cette thèse s'appuiera sur ces connaissances pour développer des prototypes fonctionnels et explorer leurs applications potentielles dans des systèmes autonomes et intelligent

Review of progress in 4D printing of piezoelectric energy harvesters

Amal Megdich[1], Mohamed Habibi[1*], Luc Laperrière[1]

[1]Department of mechanical engineering, Université du Québec à Trois-Rivières, Quebec, Canada

9.1 Abstract

The fabrication of piezoelectric energy harvesters (PEHs) has evolved significantly over the past three decades, transitioning from mechanization to automation and computerization. Additive manufacturing (AM), a forefront technology in advanced manufacturing, has been extensively used to design and produce complex components from piezoelectric materials. By integrating the fourth dimension, we can improve the fabrication of PEHs, allowing them to alter their shape while converting mechanical stress into electrical energy, thus adding dynamic functionality and broadening their application spectrum. Despite the extensive literature on 3D printing of piezoelectric materials and 4D printing technology, a notable research gap exists in merging these two fields. This review aims to bridge this gap by providing a comparative analysis of 3D printed piezoelectric materials and shape memory materials, discussing the relevant AM technologies, stimuli, and smart materials, and highlighting innovative integration methods. Furthermore, we explore a novel approach termed '4D printing of piezoelectric energy harvesters.' This innovative method merges the principles of 4D printing with the advanced capabilities of 3D printing of piezoelectric materials, resulting in multifunctional devices that can adapt and respond to external stimuli over time.

The article also addresses the challenges and opportunities in optimizing AM processes to enhance the performance and functionality of these advanced materials and devices.

Keywords: Piezoelectric energy harvesters, 3D printing, shape memory materials, 4D printing.

9.2 Introduction

Additive manufacturing (AM), commonly known as 3D printing (3DP), has revolutionized the production of complex shapes and structures by enabling precise material placement and minimizing waste [503, 504]. Within the myriad advancements in this field, two areas particularly notable for their innovative integration of functionalities: 3D printing of piezoelectric materials and 4D printing, which involves the 3D printing of shape-memory materials [346, 358, 404, 457].

3D printing of piezoelectric materials focuses on developing devices that convert mechanical energy into electrical energy. Leveraging the precise control over material composition and architecture afforded by 3D printing, researchers can improve the performance and efficiency of piezoelectric devices [505-507]. Recent advances in the 3D printing of piezoelectric energy harvesters (PEHs) have significantly broadened the range of materials and applications for these devices. Researchers have developed advanced polymer, ceramic, and composites to improve the efficiency and functionality of PEHs. Polymers such as polyvinylidene fluoride (PVDF) and its copolymers are favored fortheir inherent piezoelectric properties and flexibility [165, 354]. Ceramics like barium titanate (BTO) and lead zirconate titanate (PZT) are used to enhance the piezoelectric response [508, 509], while composite materials combine the strengths of both polymers and ceramics to create high-performance, durable and adaptable PEHs [335, 510, 511]. These materials are designed to respond to various stimuli, converting vibrations from the human body, vehicles, and ambient energy sources into electrical energy. Such stimuli include footsteps [512, 513], heartbeats [514, 515], vehicle movements [280, 516], and environmental vibrations, such as wind [517], highlighting the versatility and potential of 3D-printed PEHs in harvesting energy from diverse sources. These innovations pave the way for new applications in wearable technology, smart sensors, and sustainable energy solutions [351, 518, 519].

4D printing extends the capabilities of conventional 3D printing by incorporating time-dependent behaviors through the use of intelligent shape-memory materials [520]. This process typically utilizes standard 3D printing techniques, including fused deposition modeling (FDM), stereolithography (SLA), and direct ink writing (DIW) direct light printing (DLP) to produce structures with pre-programmed shapes and functions. 4D printing employs smart materials such as shape memory polymers (SMP) [460, 462, 463], shape memory ceramics [521, 522], and shape memory composites [523, 524], whichcan be reshaped in a controlled manner in response to external stimuli. These materials can change their shape or properties in response to external stimuli such as heat, light, electric or magnetic fields, making them well-suited for applications in biomedical devices, soft robotics and adaptive structures [463, 525-528]. Shape memory polymers, for instance, often respond to temperature changes that induce phase transitions, leading to alterations in shape. Specifically, heating an SMP above its glass transition temperature allows it to recover its original shape [529]. Photopolymers can alter their properties or shape when exposed to specific wavelengths of light [530], enabling precise remote control of the material's behavior. Additionally, the integration n of magnetic

nanoparticles or conductive fillers such as carbon nanotubes (CNTs) and graphene into polymers makes it possible to control the movement and deformation through magnetic or electric fields [523, 531]. Despite the extensive literature on advancements in 4D printing technology and the numerous studies on 3D printing of piezoelectric materials, a significant gap remains in research that directly compares these two technologies. Most existing reviews focus either on the dynamic, stimuli-responsive capabilities of 4D printing or on the energy conversion efficiency and functional applications of 3D printed piezoelectric materials [457, 532-534]. However, the potential for integrating these technologies into a cohesive system that leverages both shape memory properties and piezoelectric effects has not been sufficiently explored. Such an integrated approach could unlock new possibilities for innovative applications, combining the programmable deformation of shape memory materials with the self-powering and sensing capabilities of piezoelectric materials. This review aims to bridge this gap by providing a comparative analysis of 4D printing and 3D printing of piezoelectric materials and highlighting the potential for their synergistic integration.

This review article contrasts 4D printing and 3D printing of piezoelectric materials by examining the 3D printing technologies employed, the stimuli applied, and the characteristics of the materials used. Additionally, the article explores instances where these two technologies have been synergistically combined, offering insights into their collaborative potential and envisioning future applications.

9.3 AM processes

Additive manufacturing (AM) encompasses a variety of processes, each with distinctive capabilities and applications [535]. Among these, fused deposition modeling (FDM), stereolithography (SLA), digital light processing (DLP) and direct ink writing (DIW) are the most commonly used methods for both 4D printing and the production of piezoelectric energy harvesters (PEHs). Fused deposition modeling (FDM) a prevalent AM technique that extrudes thermoplastic material layer by layer to create parts, known for its simplicity and cost-effectiveness, making it popular for producing prototypes and small batches [367, 368, 403, 536, 537]. Stereolithography (SLA) utilizes a laser to cure liquid resin into solid parts, offering high precision and an excellent surface finish, ideal for intricate and complex geometries [538-540]. Digital Light Processing (DLP) is similar to SLA but employs a digital light projector to cure the resin, allowing for faster build times and finer resolution [541, 542]. Direct Ink Writing (DIW) involves extruding a material, typically a paste or gel, through a nozzle to create structures [543,

544]. DIW is highly versatile, facilitating the incorporation of various materials, including ceramics, polymers, and composites, and is particularly useful for the manufacture of complex, multi-material, and functional components [545, 546]. Each of these AM processes offers unique advantages, meets different requirements, and expands the possibilities for innovative manufacturing solutions. Further details on the materials, performances, advantages, and limitations of each AM method are provided in Table 34.

Table 34: Materials, Performances, advantages, and limitations of the most used 3DP technologies for both 4D printing and PEHs fabrication.

AM process	Materials	Feed state	Resolution (um)	Advantages	Limitations	Ref
FDM	Thermoplastic polymers such as ABS, PLA, PETG, and composite materials containing reinforcements like carbon fiber.	Solid	200–300	Low cost of materials. Wide range of material options. Straightforward and widely accessible technology	Lower dimensional accuracy and finish quality Limited mechanical performance	[547-549]
SLA	Photopolymer	Liquid	18-150	High precision and resolution. Smooth surface finishes suitable for detailed models and prototypes.	Limited range of materials Materials can be brittle and expensive	[550-552]
DLP	Photopolymers	Liquid	4-20	Fast processing High accuracy and smooth surfaces.	Material limitations include brittleness and cost. Post-processing requirements for cleaning and curing	[261, 553, 554]
DIW	A wide range of viscoelastic inks, including ceramics, metals, and polymers.	Liquid	30-100	Ability to deposit materials with controlled architecture. Suitable for multi-material printing.	Limited to materials that can be formulated into inks. Often requires post-processing such as sintering or curing	[555-557]

9.3.1 Fused Deposition Modeling (FDM)

9.3.1.1 Introduction to FDM

Fused Deposition Modeling (FDM), developed in the late 1980s, is a prominent method in the AM landscape, appealing significantly to both researchers and industry professionals [558, 559]. As an AM technique, FDM operates by melting raw material filaments and extruding them to form new shapes layer by layer. In this process, the filament is fed through a drive wheel into a temperature-controlled nozzle head, where it is heated to a semi-liquid state. The nozzle then precisely applies the material in wafer-thin layers, following the contours defined by CAD programs and building structural elements from the ground up. The filament properties are crucial as it ensures the proper bonding between the layers during printing. Various processing parameters, including layer thickness, width and filament type, significantly impact the mechanical properties of the printed parts [560, 561]. The inherent complexity of FDM requires careful material development and represents a major challenge for the advancement of filament technology.

9.3.1.2 FDM in 3D Printing of piezoelectric energy harvesting systems

3D printing represents a transformative approach in the manufacture of piezoelectric energy harvesting devices [127]. This advanced manufacturing technique facilitates the production of complex geometries and customized structures that conventional methods struggle to achieve. By depositing materials layer by layer, 3D printing allows precise control over the composition and architecture of piezoelectric materials, leading to enhanced performance and efficiency. FDM technology is particularly effective for crafting intricate structures and fine-tuning material properties [562]. It enables the desirable alignment of anisotropic fillers along specific print paths, driven by the strong shear and tensile stresses at the narrow nozzle walls, as shown in Figure 78(a) [250, 364]. During filament production and FDM printing, the molecular chains of the piezoelectric polymer are stretched in the direction of extrusion due to the shearing and stretching flow field generated during extrusion. Concurrently, the fillers align parallel to the polymer melt flow direction, influenced by the shear and stretching forces during melt extrusion. This results in a high degree of alignment and a controlled stacking density, as verified by the SEM/TEM morphology observations depicted in Figure 78(b).

On the other hand, the printing parameters of FDM significantly influence the performances of PEHs. Parameters such as layer thickness, printing speed, bed temperature and nozzle temperature are crucial in determining the mechanical and functional properties of the printed

piezoelectric structures. For example, Figure 78(c) presents a comparison of the SEM images of the cross-section of a 3D-printed PVDF/MWCNT sample at different nozzle temperatures [502]. At lower printing temperatures, the adhesion between successive layers is weak, leading to the formation of interfaces where pores and defects are more likely to appear. Conversely, at a nozzle temperature of 300°C, there are no observable defects, indicating excellent layer adhesion. However, increasing the temperature beyond this point causes the filament material to become overly fluid. This results in excessive material flow during deposition, leading to over-extrusion and the formation of blobs or irregularities in the printed layers. These irregularities contribute to pores and defects formation in the final printed structure.

Therefore, careful optimization of printing parameters is essential to achieve the desired balance between the piezoelectric and mechanical properties of the PEHs, ensuring their reliability and effectiveness in practical applications.

In addition, innovations in material composition have significantly advanced the capabilities of 3D-printed piezoelectric energy harvesting devices. Researchers have focused on developing novel composite materials that improve the piezoelectric properties and functional performance of these devices. Y. Du et al. [563], for example, have introduced a hybrid printing method combining tellurium nanowires (Te NW) and silver nanowires (Ag NW) to fabricate wearable piezoelectric devices. This method utilizes aerosol jet printing and extrusion printing to enable precise deposition of nanomaterials and the formation of complex device structures, as shown in Figure 78(d). The synergy of Te NW and Ag NW harnesses their unique properties, resulting in improved electrical conductivity and mechanical flexibility. Such innovative approaches in material composition not only improve the efficiency and durability of piezoelectric devices but also facilitate the seamless integration of functional and structural materials, resulting in highly integrated and sophisticated wearable electronic systems. These advances in material composition are critical for the development of next-generation piezoelectric energy harvesting technologies, opening new avenues for applications in wearable electronics and other adaptive systems.

Optimization of FDM process has led to significant advancements in the performance and functionality of 3D-printed piezoelectric energy harvesting devices. Researchers have focused on refining printing parameters and incorporating innovative techniques to enhance the mechanical properties, electrical performance, and overall efficiency of these devices.

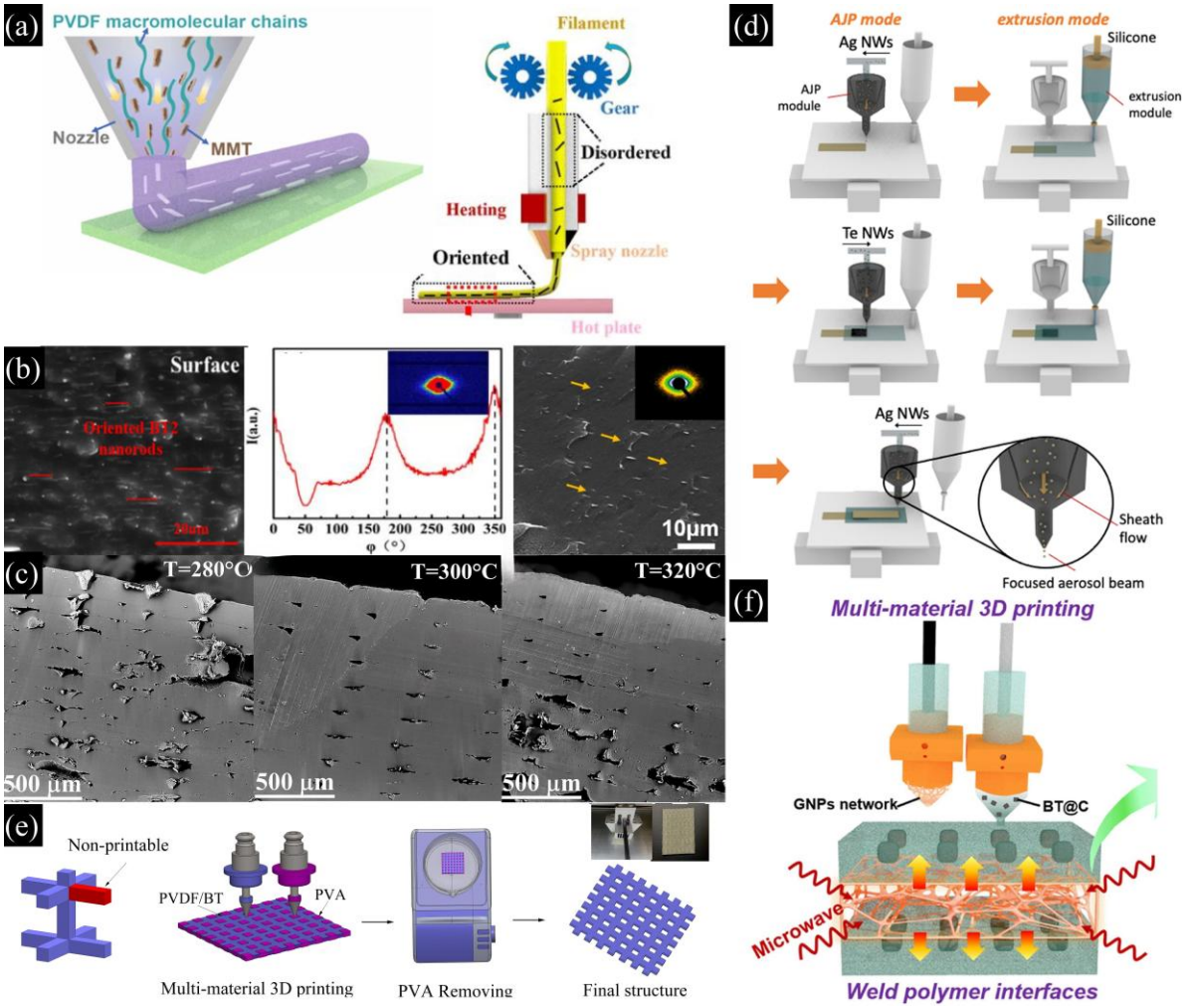

Figure 78: Advanced multi-material 3D printing techniques for piezoelectric device fabrication : (a) schematic diagram of the fillers alignment during 3D printing, (b) SEM and SAXS analysis indicating the orientation of fillers in the piezoelectric polymer [250, 364], (c) Cross-section SEM of 3D-printed PVDF/MWCNT sample with different nozzle temperatures, (d) Hybrid printing process of the piezoelectric device using the aerosol jet printer module (left) and the extrusion printing module (right) [563], (e) Multi-material printing of piezoelectric high porous lattice structure [501], (f) Microwave-assisted FDM multi-material 3D printing technology [564].

A. Megdich et al. [501] have proposed a novel method for fabricating complex piezoelectric lattice structures with high porosity, such as grid structures, using FDM technology. This approach employs multi-material 3D printing, where polyvinyl alcohol (PVA) is used to fill the voids within the layers, ensuring the printability of subsequent layers. PVA is chosen for its water solubility, which guarantees the integrity of the piezoelectric material during the dissolution process. This dissolution, which takes about 3 hours at 70°C and high stirring speed, results inthe desired final structure. The entire printing process is illustrated in Figure 78(e), with an inset showing the real structure during and after printing. Additionally, H. Pei et al. [564] developed a microwave-assisted FDM multi-material 3D printing strategy to address

common issues such as weak welds within parts and insufficient polarization, as shown in Figure 78(f). This method uses microwave energy to increase the bond strength between layers and improve the polarization of piezoelectric materials, resulting in more robust and efficient devices. Furthermore, precise control of nozzle temperature, deposition speed and layer thickness during the FDM process has been shown to significantly affect the orientation and distribution of piezoelectric fillers, optimizing their piezoelectric properties.

These innovations in FDM optimization not only improve the structural integrity and performance of printed components but also expand the potential applications of 3D-printed piezoelectric materials in fields such as wearable electronics and adaptive systems.

9.3.1.3 FDM in 4D Printing

FDM has become a pivotal technology in 4D printing, noted for its accessibility and versatility in producing complex, time-dependent structures [565]. 4D printing advances beyond traditional 3D printing by incorporating smart materials that can change their shape or properties in response to external stimuli such as heat, moisture, or light. The FDM process is particularly apt for this application, as it processes a variety of thermoplastics, including shape memory polymers (SMP), which are crucial for achieving shape-changing capabilities [473]. This method enables the production of structures that evolve over time, finding applications in fields such as biomedical devices, soft robotics and adaptive structures [566]. The simplicity and precision of FDM allow for the embedding of pre-stressed elements into printed objects, facilitating programmable and controllable deformation behavior [566]. These features position FDM as a promising technique for producing smart materials and devices that adapt their functionality over time, including adaptive composite structures that transition from 1D to 2D and 2D to 3D shapes [567].

Recent innovations in FDM-based 4D printing have significantly enhanced the functional capabilities of printed structures through advances in material composition. Researchers have developed new composite materials, creating structures with customized properties that respond dynamically to external stimuli [568]. A notable breakthroughs include dual-material lattice-based metastructures that combine soft and hard components to achieve reversible plastic deformation when heated, has demonstrated by M. Bodaghi et al. [569]. Similarly, the development of digital material (DM) filaments by S.-J. Ahn et al. [570] (shown in Figure 79(a)) has facilitated the fabrication of functionally graded materials by blended FDM (b-FDM). This

technique allows for precise spatial control of material properties within a single print, marking a major advancement in the field of additive manufacturing.

Optimizing FDM for 4D printing has resulted in significant improvements in the functionality and performance of printed structures. Researchers have refined printing parameters and introduced new techniques to improve the precision, mechanical properties, and responsiveness of 4D-printed materials. Notably, UV-assisted FDM strategies, as demonstrated by C. Y. Cheng et al. [571], employ UV LEDs to facilitate photo-crosslinking during printing, enhancing the strength of the layered composite and shape memory properties (illustrated in Figure 79(b)). Additionally, M. Barletta et al. [572] have established correlations between FDM parameters such as nozzle temperature, deposition rate and layer thickness and the properties of PLA-based components. Further innovations in shape memory programming during the FDM process, presented by M. Hosseinzadeh et al. [573]., have streamlined programming steps and ensure controlled shape recovery during reheating. Figure 79(c) and 2d contrast the traditional shape memory cycle of shape memory polymers (SMP) with this innovative FDM-based method of shape memory programming. F. Wang et al. [574] introduced an efficient and cost-effective 4D printing process using FDM at varying speeds to embed differentiated strain within flat patterns. As detailed in Figure 79(e), upon heated, the top layers printed at high speed shrink more than the bottom layers printed at low speed, inducing bending due to the strain mismatch. Thus, the degree of bending can be modulated by varying the built-in strain between the top and bottom layers. R. Noroozi et al. [575] conducted experimental, analytical and numerical studies to explore how printing speed in FDM fabrication influences the functionally graded pre-strain regime, shape recovery and self-bending properties of the active elements. As shown in Figure 79(f), the findings indicated that the faster printed 4D elements exhibited greater curvature upon thermal activation, facilitating the control and expansion of band gaps crucial for applications in vibration mitigation and acoustic damping.

Advancements in FDM hardware and design have expanded the versatility and complexity of 4D-printed structures. Modifications to standard FDM printers, enabling printing on curved surfaces and facilitating more intricate designs, have stimulated the development of reconfigurable materials and devices that exhibit sophisticated shape change behavior.

These innovations have unlocked new applications in fields such as robotics, biomedical devices, and adaptive systems.

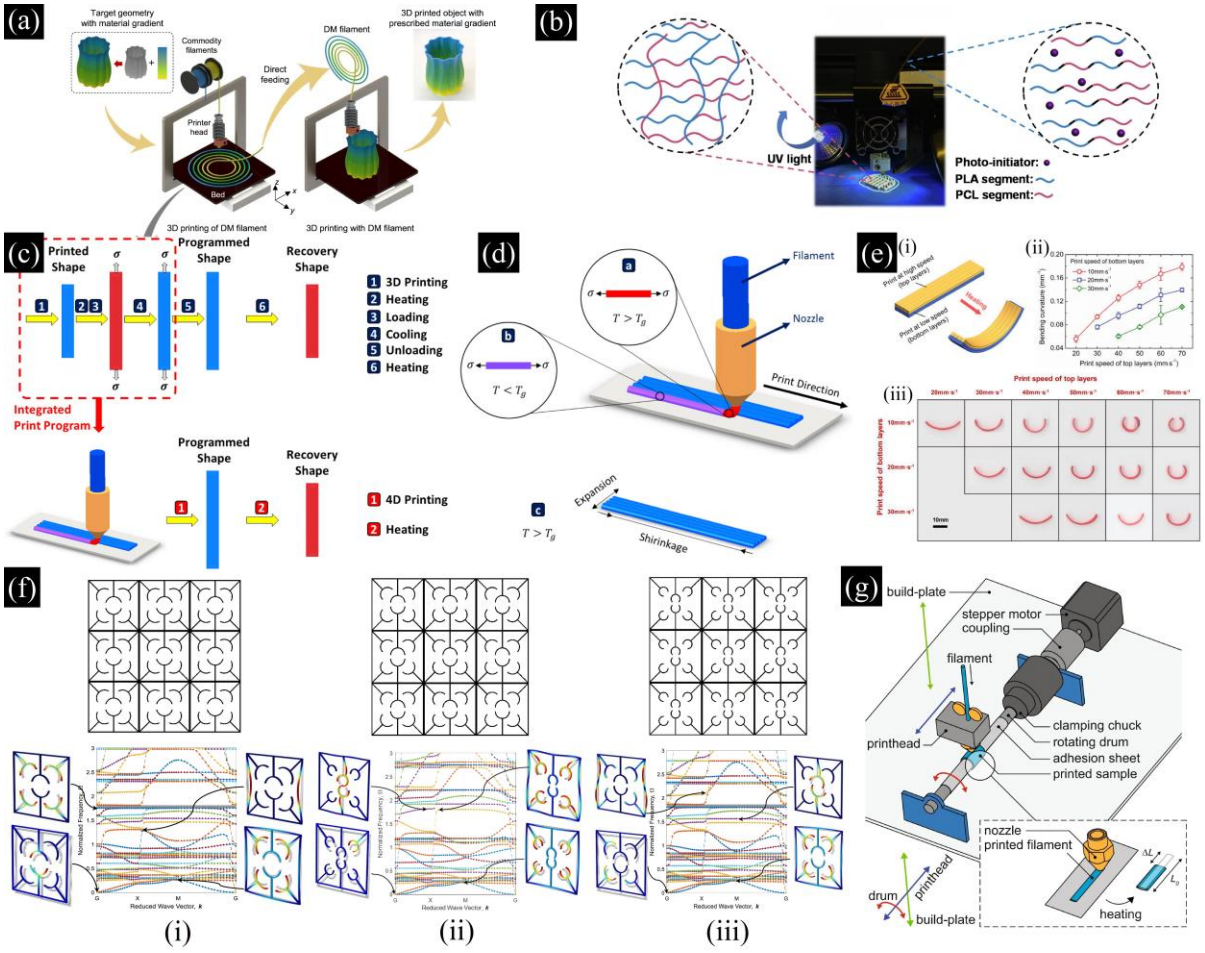

Figure 79: Innovative FDM-based 4D printing methods for shape memory networks and actuators : (a) b-FDM 3D printing with a DM filament [570], (b) 4D printing the shape memory networks via an FDM-based 3D printer equipped with UV lamp[571], (c) Traditional shape memory cycle of SMP, (d) New FDM-shape memory programming method [573],(e) Basic mechanism of direct 4D printing by multispeed FDM fabrication. (i) Schematic illustration of the heat-induced bending of PLA samples whose top and bottom layers are printed by different speeds. (ii) Bending curvature and (iii) profile of PLA fabricated under different combinations of printing speed [574], (f) Band structure and mode shape configuration of adaptive periodic diagonal metastructure after heating–cooling process for three different printing speeds: (i) 20, (ii) 40, and (iii) 70 mm/s [575], (g) Schematic illustration of the methodology used for the fabrication of curved shape-shifting specimens [576].

A notable example s is the modified FDM printer by T. van Manen et al. [576], which capable of printing on curved surfaces, as illustrated in Figure 79(g). Through these advancements, FDM continues to play a pivotal role in the field of 4D printing, offering unmatched flexibility and precision in the production of smart materials and adaptive structures, and cementing its role as a foundational technology in the evolution of additive manufacturing.

FDM continues to be an important technology in the field of 4D printing, offering unparalleled flexibility and precision in the production of smart materials and adaptive structures [577].

Continuous advances in material composition, parameter optimization and hardware design are not only paving the way for new and innovative applications but also solidifying FDM's role as a cornerstone in the evolution of additive manufacturing.

9.3.2 Stereolithography (SLA)

9.3.2.1 Introduction to SLA

Stereolithography, also known as photo-solidification, is a three-dimensional printing technique that uses a photochemical process to produce objects, prototypes, or samples layer by wafer-thin layer [578]. In this process, chemical monomers, or oligomers cross-link under UV radiation to form a stable three-dimensional structure. This technology is used for manufacturing a wide range of products, from computer hardware to medical models. SLA, one of the oldest technologies, was first developed in 1981 by Dr. Hideo Kodama [579], who method it as a novel meth for the rapid reconstruction of 3D models using a holographic technique. Since its inception, SLA has evolved to produce not only polymers but also composites and ceramics samples. It offers adequate resolution, smaller feature sizes, fast production and better surface quality [580]. In SLA, layers of liquid precursor in the vat are exposed to ultraviolet (UV) radiation, which selectively solidifies them. The photo-initiator (PI) molecule in the resin reacts to the incident light, activating the chemical polymerization reaction during irradiation. This causes the exposed areas to harden, building the part layer by layer. The resin is solidified by irradiation either from above or from below through a transparent tank [461].

9.3.2.2 SLA in 3D Printing of piezoelectric energy harvesting systems

The use of SLA for fabricating piezoelectric nanoceramics represents a significant advancement in the field [581]. Known for its high dimensional resolution and precision, SLA is ideally suited for creating complex geometries and intricate features in ceramic components. W. Wang et al. [582] have demonstrated the potential of this technology by presenting various complex piezoelectric geometries, such as transducers with fine features and hollow structures, which are challenging to achieve with conventional fabrication methods (illustrated in Figure 80(a)).

Innovations in material composition have significantly improved the capabilities of 3D-printed piezoelectric energy harvesting (PEH) devices using SLA technology. K. Zheng et al. [583] developed textured piezoelectric ceramics using SLA 3D printing technology, offering a novel

approach to fabricate piezoelectric materials with improved properties. Their study introduced a method where BaTiO3 (BT) templates are aligned during printing process to mimic the shear force effect typically seen in conventional tape casting processes. This alignment is critical to achieve the desired texture and improved piezoelectric properties. Furthermore, H. Lu et al. [584] introduced advanced piezoceramic printing and processing strategies to fabricate highly sensitive piezoelectric micro-transducers operating at ultrasonic frequencies (shown in Figure 80(b)). A UV-sensitive piezocomposite colloid was prepared using PZT nanoparticles (lead zirconate titanate), lead nitrate (as a liquid-phase sintering agent) and a UV-sensitive resin made from a mixture of monomers (polyethylene glycol diacrylate, PEGDA) and a photo-initiator. The colloid, heavily loaded with PZT (35 vol%) and 5 vol% lead nitrates, ensures high piezoelectric properties while maintaining printability.

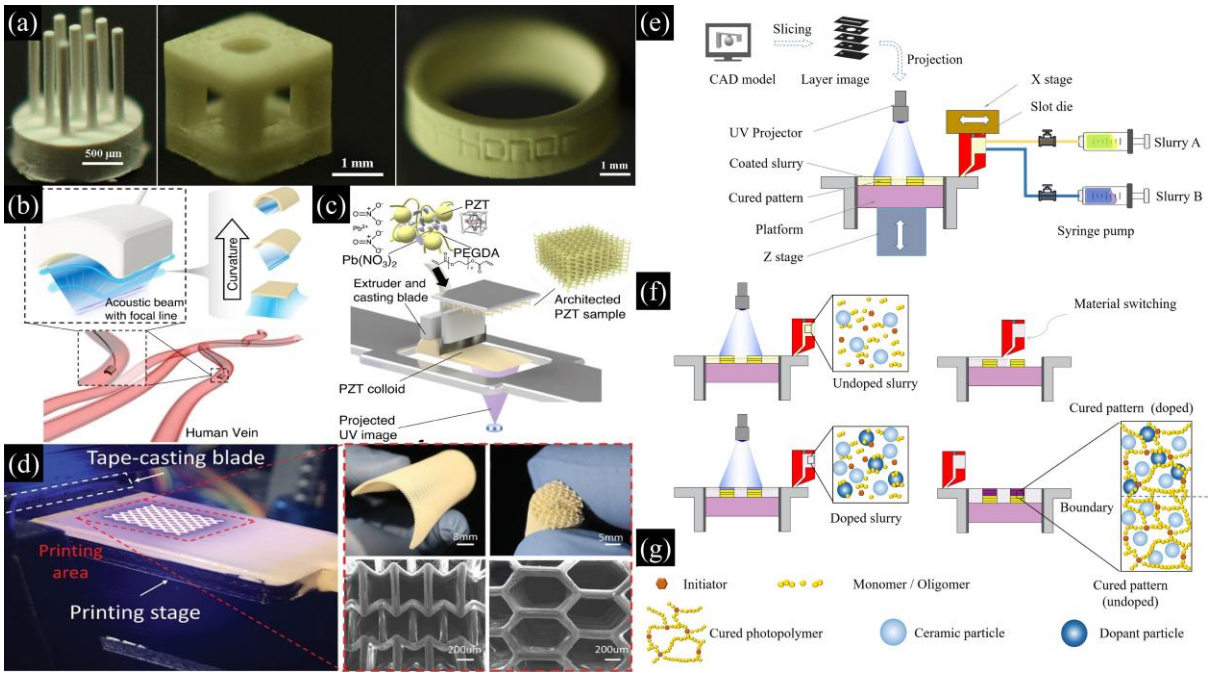

Figure 80: SLA and PuSL techniques for fabricating miniature piezoelectric transducers : (a) Different 3D structures SLA printed by 40 vol% BT suspensions [582], (b) Schematic of the fabricated miniatured ultrasound transducer with curved PZT elements, (c) Fabrication process of PZT-based piezoelectric microtransducer using SLA [584], (d) Custom PuSL fabrication system for piezoelectric nanocomposite [587] (e) A schematic of the SEPS process with material switching, (f) The printing process of SEPS, (g) Different material ingredients [585].

Additionally, L. He et al. [585] introduced an innovative AM process called Suspension-Enclosing Projection Stereolithography (SEPS). This process facilitates the fabrication of piezoelectric ceramics with tunable properties through selective doping. SEPS is a stereolithography-based AM process designed for multi-material printing (illustrated in Figure 80(e)). The system comprises a customized light engine, a shear-controlled layer applicator.

And a cooling build platform. The ceramic slurry is evenly distributed on the cooling platform, where it is immediately cooled to enhance the yield strength. A digital micromirror device (DMD) then projects a digital image onto the slurry, curing it layer by layer. The starting material can be dynamically switched to introduce different dopants into predefined areas, allowing for the creation of complex 3D structures with varied properties (shown in Figure 80(f) and Figure 80(g)).

Moreover, the optimization of SLA processes has led to significant improvements in the production of PEH components. A. Sotov et al. [586] developed and optimized a process for 3D printing of piezoceramic materials using liquid crystal display stereolithography (LCD-SLA). This involved determining optimal parameters for LCD-SLA 3D printing, such as the correct UV exposure time and viscosity of the ceramic slurry, to produce high-quality green models without significant defects. Additionally, a precise thermal debinding process based on TGA-DSC analysis was developed to prevent cracking and delamination of the printed models, which is crucial for the effective removal of the photopolymer resin while preserving the structural integrity of the ceramic parts.

Innovations in the SLA process have notably enhanced the capabilities of 3D-printed PEH devices. For instance, as illustrated in Figure 80(c), H. Lu et al. [584] used a customized high-resolution PμSL system that integrates a tape-casting deposition process. This integration enables precise control over layer thickness and ensures high-resolution feature detailing. The manufacturing process includes several key steps designed to optimize piezoelectric performance and precise microscale features. D. Yao et al. [587] developed a highly efficient, flexible and tunable piezoelectric nanocomposite material using advanced 3D printing techniques. Their study utilized a customized PμSL system for 3D printing nanocomposites, incorporating a tape-casting recoating process that ensures precise control of the thickness of the colloidal paste before UV pattern exposure. This method enables the creation of intricate and high-resolution structures, as detailed in Figure 80(d).

These innovations in material composition, SLA optimization, and process improvements have significantly boosted the performance and broadened the application possibilities of 3D printed PEH devices, paving the way for more efficient, precise and versatile piezoelectric systems.

9.3.2.3 SLA in 4D Printing

Recent advances in 4D printing with SLA have focused on developing new materials to improve the functionality and performance of printed structures [565]. T. Brossier et al. [588]

developed two new thermoresponsive hydrogel systems based on copolymers of poly(oxazoline) and poly(acrylamide) (illustrated in Figure 81(a)). In each system, the thermosensitive component is either poly(2-isopropyl-2-oxazoline) (PiPrOx) or poly(N-isopropylacrylamide) (PNIPAM), with crosslinking facilitated by the poly(oxazoline) comonomer blocks. As shown in Figure 81(b), these synthesized hydrogels demonstrate the ability to contract at body temperature, highlighting their substantial t potential for application in biomedical devices. Additionally, S. Miao et al. [589] developed a novel fabrication technique that combines photolithography and stereolithography (shown in Figure 81(c)). This tandem approach exploits the strengths of both techniques to fabricate complex hierarchical 4D micropatterns. Photolithography is employed to rapidly develop films with different thicknesses and induce a gradient of cross-linking density, which enables self-bending of the scaffold. Concurrently, stereolithography is used to create intricate surface micropatterns with high resolution and precision, enhancing the overall structural complexity.

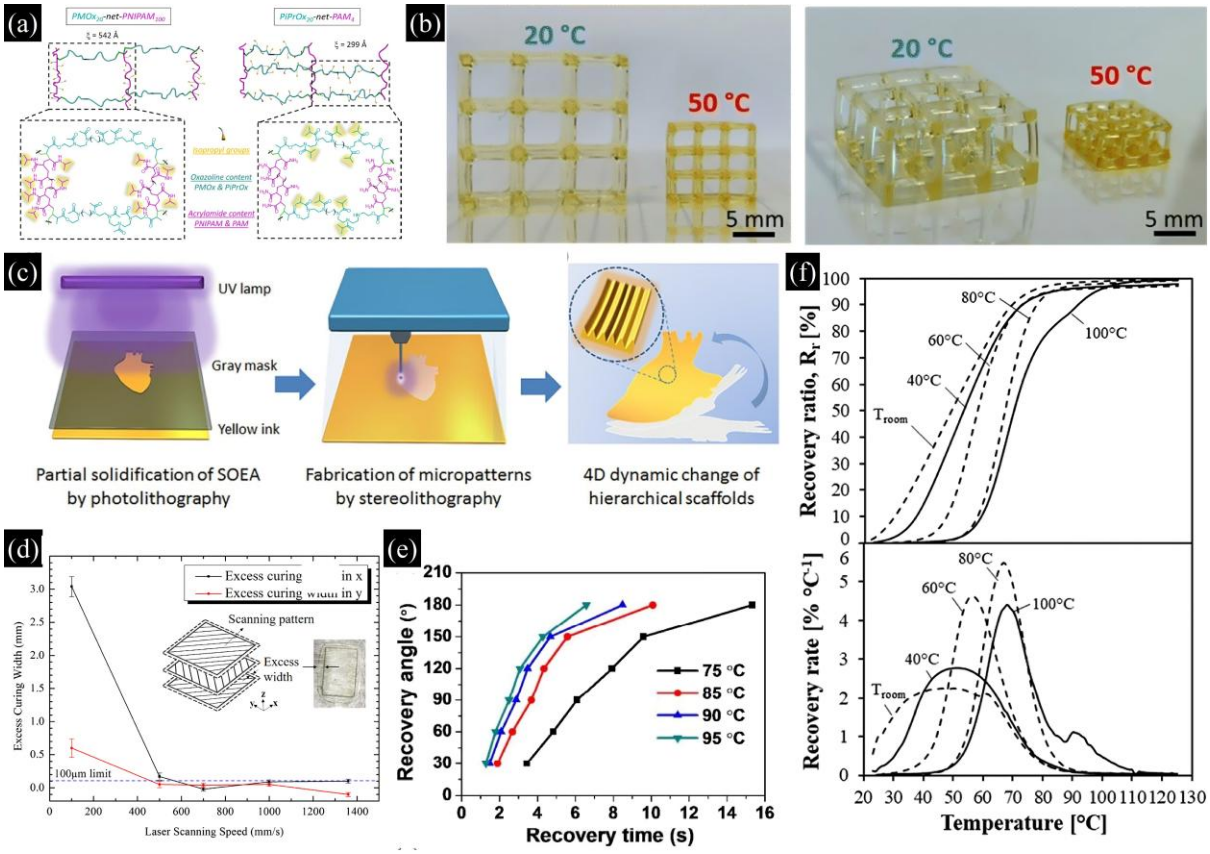

Figure 81: Design and performance of thermoresponsive hydrogels and photolithography-based processes : (a) Synthesis of the hydrogels based on copolymers PMOx20-net-PNIPAM100 (5/1) and PiPrOx20-net-PAM4 (5/1), and illustration of the resulting networks. Blue corresponds to POx blocks, purple for acrylamide units and green for methacrylate moieties, (b) thermos-responsive effect of the hydrogel PiPrOx20-net-PAM4 [588], (c) Schematic illustration of the photolithographic-stereolithographic-tandem process [589], (d) excess curing width in x

and y directions as a function of laser scanning speeds [590], (e) recovery angle with time in water bath at different temperatures [592], (f) Recovery ratio and recovery rate for the as-printed samples [593].

The optimization of stereolithography (SLA) processes has significantly improved the precision, efficiency and functionality of 4D-printed structures. Researchers have concentrated on refining laser scanning speeds, curing depths and crosslinker concentrations to improve the spatial accuracy and mechanical properties of printed parts. For instance, Y.Y.C. Choong et al. [590] optimized the laser scanning speed to maintain an excess cure width of less than 100 μm, achieving high-dimensional accuracy as shown in Figure 81(d).

They also measured the curing depths to determine the optimal number of layers required for precise printing. In a separate study [591], adjustments in the crosslinker concentration and curing time for specific models demonstrated that 15% crosslinker concentration and 3 seconds of layer-by-layer curing yielded the best resolution, enabling the printing of 1mm diameter spikes and 0.2mm diameter through-holes. These optimized parameters provide a robust framework for the printed architecture while preserving the desired flexibility.

Moreover, J. Chowdhury et al. [594] established a correlation between the properties of shape memory polymer (SMP)— such as tensile stress, surface roughness, recovery time, strain fixation and glass transition temperature— - and micro-SLA printing parameters, including laser pulse frequency, and printing speed. Their results indicated that optimizing printing speed and laser pulse frequency can significantly enhance these properties, achieving a shape fixity percentage of approximately 86.3% and a recovery time of 6.95 seconds. Similarly, R. Yu et al. [592] investigated the evolution of recovery angles at different temperatures, demonstrating that that higher temperatures increase the mobility of the switching segments, which leads to faster recovery times (illustrated in Figure 81(e)). Moreover, as shown in Figure 81(f), N. Inverardi et al. [593] demonstrated that the deformation temperature (Tdef) significantly influences the recovery behavior of SMPs, providing a way to control the transformation temperature, an effect known as the temperature memory effect. These advancements in SLA process, including the precise control of printing parameters and a deepened understanding of material behavior under varying conditions, have led to the development of more efficient, adaptable and high-performance 4D-printed structures,broadening their potential applications across various sectors.

9.3.3 Direct Light Printing (DLP)

9.3.3.1 Introduction to DLP

Direct Light Printing (DLP) is a UV-driven, localized photopolymerization technique that operates in a liquid environment, using liquid monomers, photo-initiators and oligomers [461]. It is a superior 3D printing technology for producing porous or hollow structures, making it ideal for lattice metamaterials, pneumatically actuated soft robots, and other hollow or truss-based structures and devices [595]. DLP offers enhanced uniformity and control over layer thickness because the part is suspended upside down on the build platform, providing superior process control compared to other 3D printing techniques. Evolving from stereolithography, DLP is a high-resolution prototyping technology with a pixel-based exposure mechanism, making it particularly effective for illuminating sharp corners [596]. The Digital Micrometer Device (DMD) serves as a dynamic mask, facilitating the production of complex structures, especially in tissue engineering. The short printing times and nozzle-free approach help maintain cell viability at impressive rates of 85–95%, significantly enhancing the potential for biomedical applications.

9.3.3.2 DLP in 3D Printing of piezoelectric energy harvesting systems

Recent advances in the material composition of 3D-printed piezoelectric energy harvesters (PEH) using DLP technology have led to significant improvements in their performance and versatility. Researchers have focused on developing novel materials and composites that benefit from the precision and flexibility of DLP to create optimized structures with improved properties. For example, C. Liu et al. [597] introduced a novel approach for fabricating PZT-based piezoceramics with DLP technology. As depicted in Figure 82(a), this approach enables the production of Pb1− xLax(Zr0.52Ti0.48)O3 green bodies with complex geometries, illustrating potential for structural optimization in piezoceramic fabrication. Similarly, Q. He et al. [598] developed a composite material for smart monitoring devices that merges mechanical protection with piezoelectric sensing capabilities. Inspired by the microstructure of the cuttlefish bone's chambered wall septa (shown in Figure 82(b) (i)), this composite material exhibits high stiffness, energy absorption and porosity, making it suited for multifunctional sensors (depicted Figure 82(b) (ii) and (iii)). DLP technology enables the precise fabrication of these high-resolution structures, offering advanced mechanical reinforcement and electrical self-recognition capabilities. These developments in material composition highlight the versatility

and potential of DLP technology in the producing innovative, high-performance piezoelectric materials and devices.

Furthermore, optimization of the DLP process has been essential in enhancing the performance and functionality of 3D-printed PEH devices.

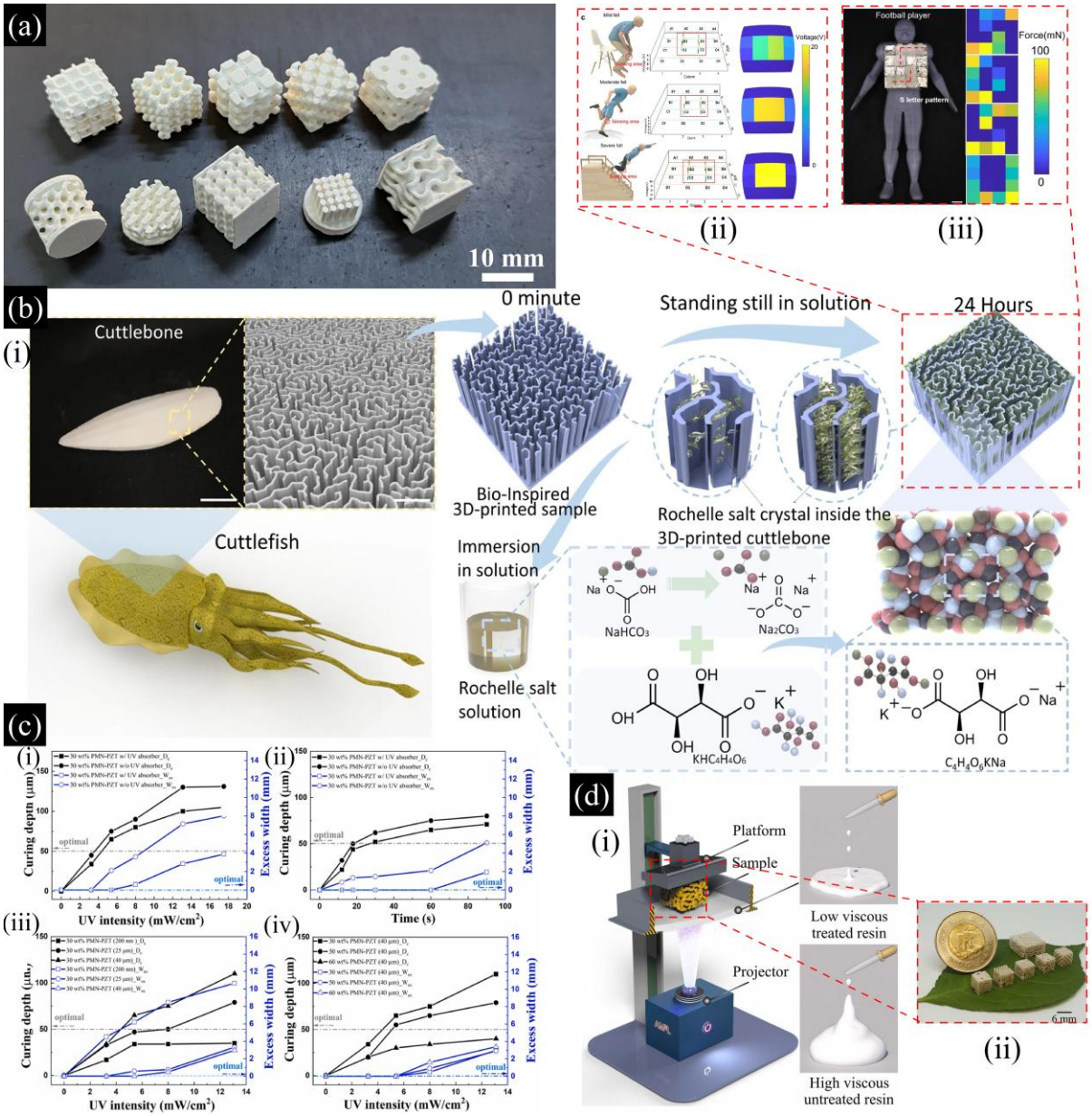

Figure 82: DLP-based fabrication of complex bio-inspired piezoelectric structures : (a) Pb1−xLax(Zr0.52Ti0.48)O3 green bodies with complex geometries fabricated by DLP technology [597], (b) (i) 3D printing of piezoelectric composite Inspired by the cuttlefish bone's chambered wall-septa microstructure using DLP technology, Application of the bio-inspired composites smart sensor armor for (ii) fall alarm knee pads for the elderly, and (iii) football players [598], (c) Curing depth (Dc) and excess width (Wex) for 30 wt% PMN–PZT polymer resin with and without 0.2 wt% photo-absorber at (i) 60 s UV laser exposure time and (ii) 5.4 mW/cm2 UV laser intensity, The curing depth and excess width depending on (iii) particle sizes and (iv) particle concentrations at 60 s, UV laser exposure time [505], (d) DLP printing process of complex shell-based structures

[599].

S-M. Chang et al. [505] focused on optimizing UV laser processing parameters, specifically aiming to control the depth of cure (Dc) and excess width (Wex) of the ceramic-polymer suspensions during the DLP photopolymerization process, as illustrated in. This optimization is crucial to achieve high-resolution 3D printing with good accuracy and quality. Moreover, J. Shi et al. [599] have developed a customized platform for AM of piezoceramics to produce complex shell-based structures (shown in Figure 82(d) (i)). This platform utilizes DLP 3D printing to enable freeform fabrication (depicted Figure 82(d) (ii)), effectively overcoming the challenges of conventional methods pose in producing intricate and precisely defined topologies. This technique is particularly suitable for applications requiring high precision and complex geometries. These advancements in material composition and DLP process optimization illustrate the significant progress in 3D printing PEH devices using DLP technology. By refining materials and processes, researchers have expanded the application possibilities of DLP 3D printing, leading to the creation of more efficient, versatile, and higher-performing structures and devices

9.3.3.3 DLP in 4D Printing

Innovations in material composition have significantly expanded the capabilities of 4D printing using DLP technology. Researchers have developed advanced resin formulations and photopolymerizable systems to achieve diverse mechanical properties and functional responses. L. Yue et al. [600] introduced a resin design strategy for grayscale DLP 3D printing, utilizing light intensity to locally control monomer conversion. This approach enables the production of materials ranging from soft organogels to stiff thermosets within a single layer, as illustrated in Figure 83(a). N. Paunović et al. [601] have developed photopolymers that blend poly(D,L-lactide) and trimethylene carbonate, exhibiting shape memory properties suitable for medical applications, as shown in Figure 83(b) (i). These materials maintain a deformed shape at room temperature and recover at body temperature (37°C), depicted in Figure 83(b) (ii). A. Cosola et al. [602] formulated a versatile three-component system using 2-hydroxyethyl methacrylate (HEMA) and poly(ethylene glycol methyl ether methacrylate) (PEGMEMA), with a bis(acyl)phosphine oxide derivative serving as both photo-initiator and crosslinking agent, shown in Figure 83(c). This system produces SMPs with excellent thermally triggered shape memory responses and a strain recovery of 99%. Additionally, Y. He et al. [603] developed highly conductive, strong and transparent hydrogels using DLP, encapsulated with

elastomers to retain moisture and maintain properties over time. These advances in material composition pave the way for the creation of multifunctional, adaptable structures with applications in biomedical devices, soft robotics and beyond.

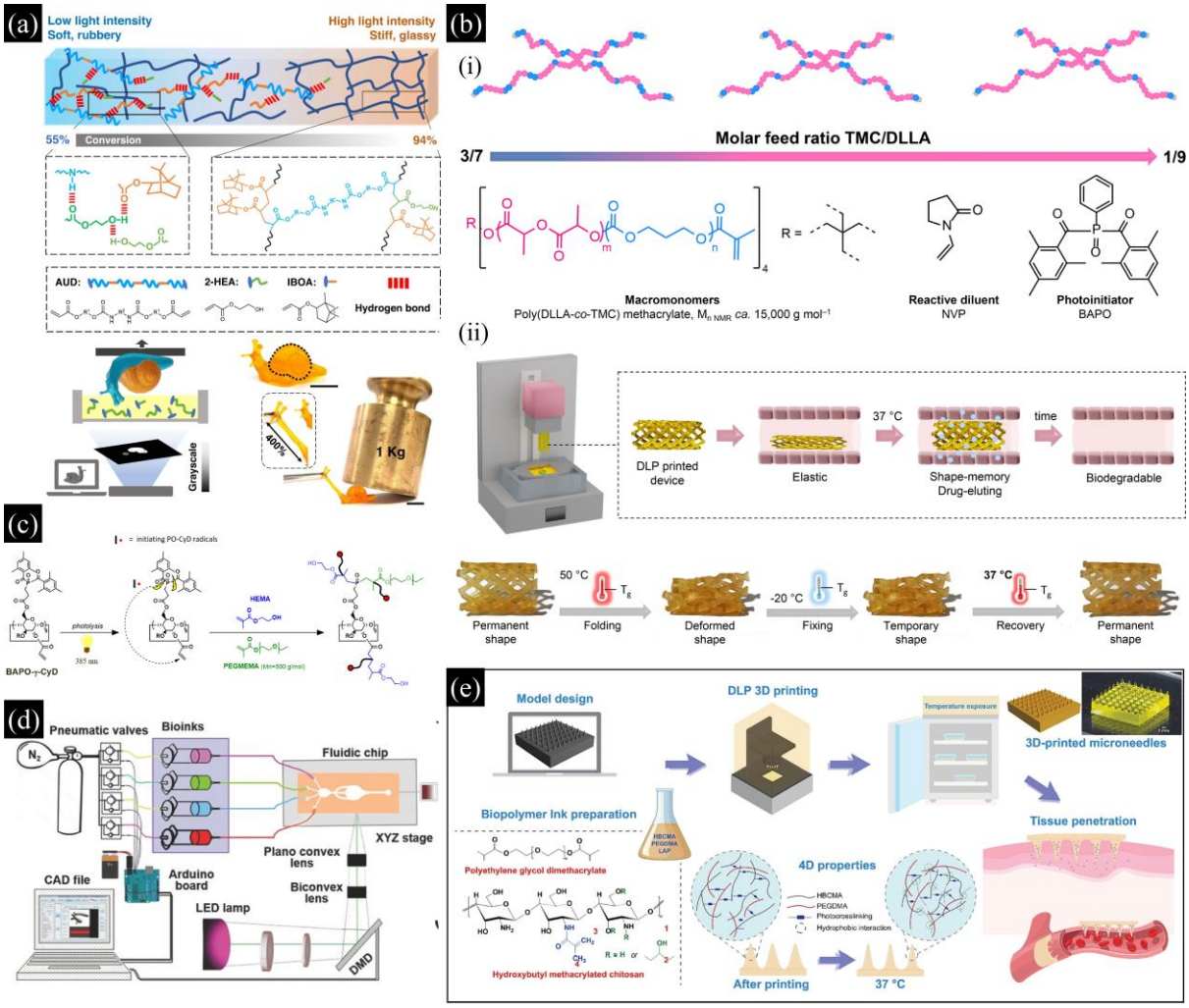

Figure 83: Advanced DLP printing strategies for multifunctional 4D printed materials : (a) Using light to control mechanical properties in g-DLP printing [600], (b) 4D printing of biodegradable shape-memory elastomers with tailored transition temperature and tunable drug release kinetics via DLP [601], (c) Crosslinked covalent PHEMA-co-PEGMEMA network generated either via PO-CyD groups or residual acrylate functions of the multifunctional photo-initiator BAPO-γ-CyD [602], (d) Microfluidics enabled multi-material maskless DLP 3D printing [604], (e) Four-dimensional printing of HBCMA-based microneedles using a DLP 3D printer [605].

Optimizing the DLP process is critical to improving the performance and functionality of 4D printed structures. A.K. Miri et al. [604] have developed an innovative bioprinting platform that combines a microfluidic device with a Digital Micromirror Device (DMD) based DLP bioprinter. As shown in Figure 83(d), this platform can rapidly switch between different cell-loaded hydrogel bioinks using a microfluidic device equipped with four pneumatic on/off valves. This capability enables the creation of complex, heterogeneous hydrogel constructs

layer by layer, which is essential for 4D printing of multi-material structures. Furthermore, the application of DLP printing to microstructures such as microneedles has made significant progress. As detailed in Figure 83(e), Q.T. Che et al. [605] used DLP 4D printing technology to fabricate microneedles from a novel biopolymer ink formulation based on hydroxybutyl methacrylated chitosan (HBCMA). This method allows the microneedles to be dynamically modified after fabrication to achieve the required needle sharpness and structural integrity. These innovations in DLP optimization, including the integration of advanced bioprinting platforms and the development of high-resolution printing techniques, have expanded the application potential of DLP-4D printing, leading to the creation of more accurate, versatile and effective structures and devices.

9.3.4 Direct Ink Writing (DIW)

9.3.4.1 Introduction to DIW

Direct Ink Writing (DIW) is an advanced 3D printing technique that precisely deposits material through a nozzle to construct structures layer by layer [543]. Unlike conventional 3D printing processes, DIW utilizes a diverse range of materials, including ceramics, polymers and composites, which are formulated into viscous inks [546, 606]. These inks are extruded under controlled pressure through a nozzle, enabling the production of complex geometries with high resolution and accuracy. DIW is particularly valuable for applications that require customized material properties and intricate designs, making it adapted for the fabrication of structures using smart materials [607]. The versatility and precision of DIW enables the development of advanced materials and structures with enhanced performance and meeting specific functional requirements.

9.3.4.2 DIW in 3D Printing of piezoelectric energy harvesting systems

Direct Ink Writing (DIW) is a versatile 3D printing technique where ink is extruded through a nozzle to create precise, layered structures. This method is particularly advantageous for the producing piezoelectric energy harvesters (PEH) due to its ability to print complex geometries with high precision and control over material composition and properties.

Innovations in material composition have significantly improved the performance of 3D printed PEHs using DIW technology. For instance, B. Wang et al. [608] used a freeze-drying assisted DIW 3D printing technique to fabricate a CNF/MXen-based hierarchical architecture (shown in Figure 84(a)). This method ensures the formation of a free-standing aerogel scaffold

with high shape fidelity and an improved porous structure, which is essential for improving the piezoelectric properties and overall performance of the piezoelectric sensor. Furthermore, F. Chen et al. [609] developed a novel multi-material DIW 3D printing technique to fabricate piezoelectric nanogenerators with a voxel-isolated conducting network , as depicted in Figure 84(b). This method allows for the alternating arrangement of piezoelectric and conductive inks, optimizing the polarization path and ensuring uniform distribution of the polarization field. The resulting voxel structure substantially improves the piezoelectric effect and the output power of the nanogenerators, achieving an open-circuit voltage (VOC) of 150 V and a short-circuit current (ISC)of 16 μA.

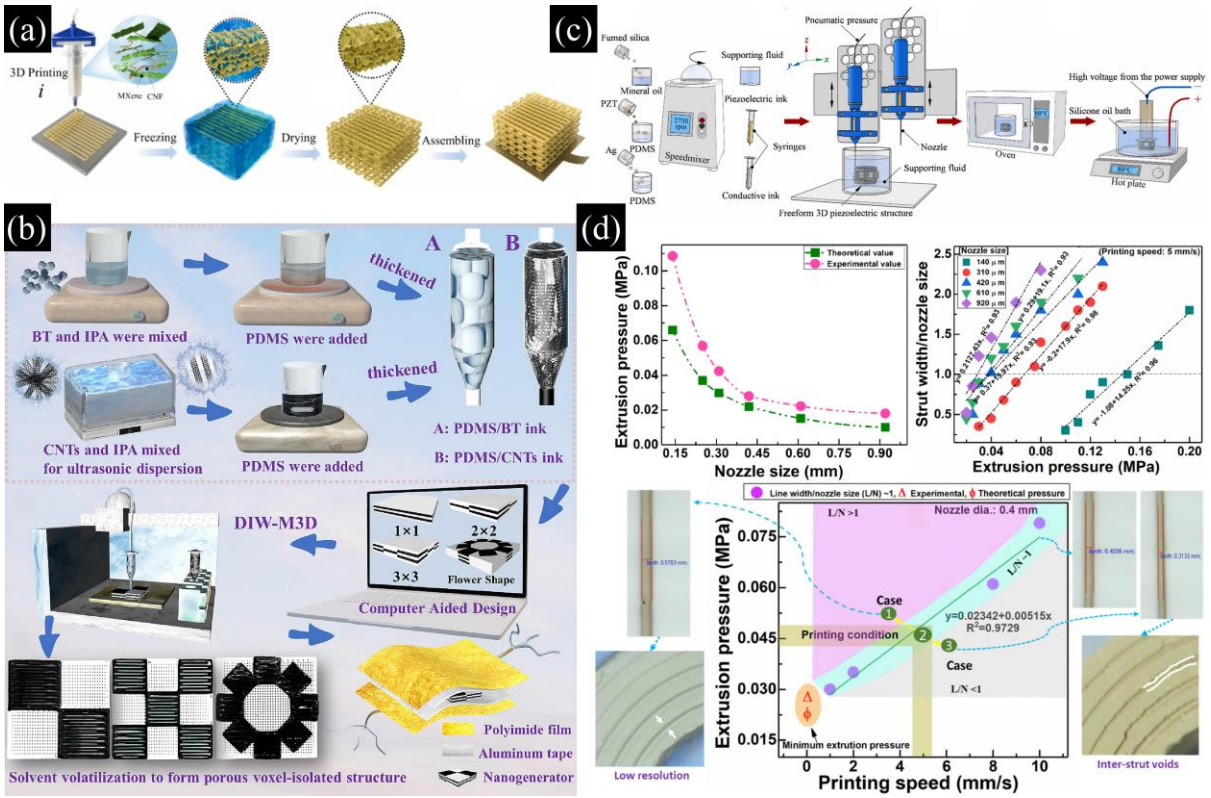

Figure 84: Direct Ink Writing and freeze-drying-assisted multi-material 3D printing for piezo-composites : (a) Freeze-drying assisted DIW 3D printing technique [608], (b) multi-material DIW 3D printing of piezoelectric and conductive inks [609], (c) Supporting Fluid-Assisted Multi-Material Extrusion-Based 3D Printing Process for Flexible Piezoelectric Composite Sensors with Integrated Electrodes [610], (d) printing parameters optimization [611].

R. Tao et al. [610] introduced a novel fluid-assisted multi-material extrusion-based 3D printing technique to fabricate flexible, conformal and free-form piezoelectric composite sensors with integrated electrodes , as illustrated in Figure 84(c). This technique enables the production of complex geometries that are difficult to achieve with conventional fabrication techniques.

Further optimization of the DIW process has been crucial for improving the precision and functionality of 3D-printed PEH devices. For example, S. Hossain et al. [611] optimized the printing parameters, including extrusion pressure, nozzle size, and printing speed, to minimize defects such as voids between struts and tail defects , shown in Figure 84(d). By fine-tuning these parameters, they significantly improved the structural integrity and resolution of the printed ceramics. Understanding the relationships between various printing dynamics, such as extrusion pressure, nozzle size and printing speed, is crucial for a defect-free printing process.

These innovations in material composition and DIW process optimization demonstrate substantial advances in 3D printing of PEH devices using DIW technology. By refining the materials and techniques, researchers have expanded the applications of DIW 3D printing, leading to the creation of more efficient, versatile and high-performance piezoelectric structures and devices.

9.3.4.3 DIW in 4D Printing

DIW is particularly beneficial for 4D printing applications as it allows complex geometries to be printed with high precision and control over material composition and properties. The subsequent sections present the latest innovations in material composition and DIW optimization for 4D printing.

Significant advancements in material composition have broadened the possibilities of 4D printing with DIW technology. Y. Zhou et al. [612] developed dual-curing DIW 4D printing inks that combine commercially available benzoxazine with synthetic diglycidyl ether bisphenol A monoacrylate (DGEBAMA), as illustrated in Figure 85(a). This dual-curing approach, involving UV crosslinking followed by thermal curing, addresses the limitations of conventional benzoxazine resins, resulting in structures with enhanced thermal properties and mechanical strength. A. Sun et al. [613] used DIW to produce thermochromic smart materials that exhibit both shape memory and color-changing properties, allowing precise control over the composition and geometry of the printed structures. Moreover, Y. Li et al. [614] introduced a shape memory polymer (SMP) based on bismaleimide (BMI) for 4D printing , utilizing a two-step curing process that combines UV-assisted DIW and thermal curing to enhance mechanical properties and shape memory performance , as depicted in Figure 85(b). These advances enable the production of multifunctional, responsive structures suited for a diverse range of applications.

Optimization of the DIW process has been essential for improving the precision and functionality of 4D-printed structures. E. Liao et al. [615] developed a method to actively mix two-component silicone inks at the molecular level during extrusion using a specially designed print head, as shown in Figure 85(c).

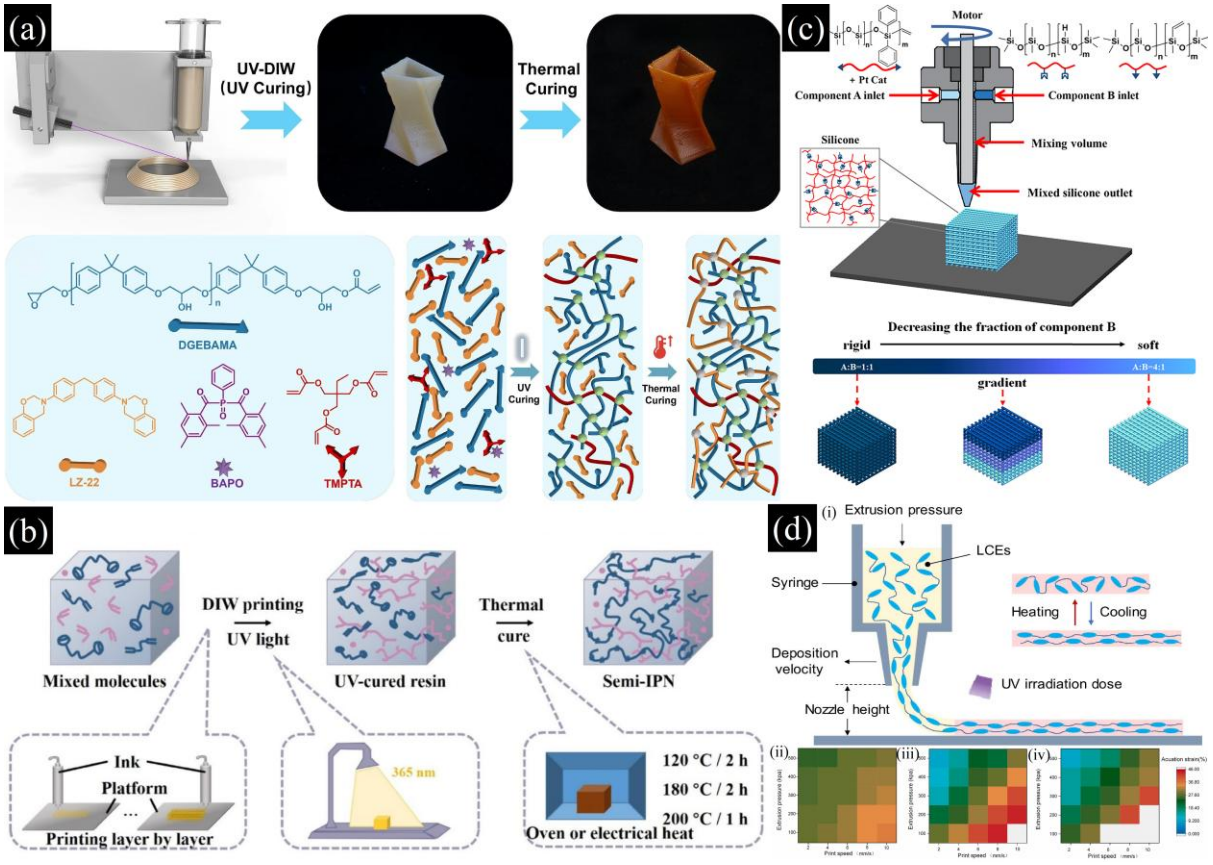

Figure 85: DIW-printed bio-inspired composites and microfluidics-enabled 4D printing systems : (a) UV-assisted DIW 3D printing of BZs with chemical reactions occurring in BZs during the entire process [612], (b) Schematic diagram of the two-step curing process [614], (c) Schematic diagram of the active mixing of two-component silicone ink and printing of cellular silicones [615], (d) (i) Schematic diagram of multi-parameter-encoded 4D printing method, Actuation strain of printed LCEs filament under varying combination of print speed, extrusion pressure and the print height of (ii) 0.3 mm, (iii) 0.6 mm, and (iv) 0.9 mm [616].

This innovative approach ensures continuous and precise control of ink properties, facilitating the production of silicone structures with varied compositions and customized properties, addressing the issue of viscosity changes over time in premixed inks. Additionally, L. Ren et al. [616] introduced a multi-parameter encoded 4D printing method that that systematically programs the shape morphing behavior of liquid crystal elastomers (LCEs). By adjusting printing parameters such as printing speed, extrusion pressure, printing height and UV light intensity, this method allows precise modulation of the deformation characteristics within the printed structures, as shown in Figure 85(d). These optimizations in the DIW process expand

the possibilities for producing highly customizable and programmable materials with improved performance and consistency.

9.4 Applied stimuli

9.4.1 Applied stimuli in piezoelectric energy harvesting

9.4.1.1 Human motion

The human body is a source of mechanical vibrations and movements during everyday activities, such as walking, running, breathing and even minor gestures such as speaking or smiling. These biomechanical activities consistently generate mechanical energy, which can be effectively harvested using PEHs. Integrating PEHs into wearable devices or smart clothing transforms this otherwise wasted energy into electrical energy, providing a sustainable and self-sufficient power source for various low-power electronic devices [617, 618]. This innovative approach improves the functionality and efficiency of wearable technologies and promotes the development of self-powered systems for health monitoring, fitness tracking and other intelligent applications [619].

Y. Huang et al. [620] have developed a PEH tailored specifically for monitoring subtle physiological activities and human movements. This PEH was designed for real-time tracking of various small body signals, such as breathing and speech, as illustrated in Figure 86(a). A practical application of this technology includes measuring subtle changes in arterial pressure. Specifically, the PEH can detect radial artery augmentation index and pulse pressure velocity by sensing pressure variations associated with blood flow in surface arteries. The ability to measure these parameters non-invasively and continuously offers significant value for emergency care, the early detection of cardiovascular diseases, and ongoing health assessment [621]. In addition, the PEH can detect various flexion and joint movements (shown in Figure 86(b)), making it useful for posture monitoring and gait analysis, which are critical for health and fitness tracking systems. Similarly, M. Fahad et al. [622] have shown that PEHs can harvest mechanical energy from various human activities such as finger tapping, walking and other movements (as shown in Figure 86(c)). The harvested energy can then be used to power low-power electronic devices such as smartwatches [623]For practical applications, B. Wang et al. [624] developed a bionic smartwatch with a dual-layered band inspired by the structure of the woodpecker's hyoid bone, as shown in the Figure 86(d). A piezoelectric array was integrated into the outer layer of the watch continuously generates energy through wrist movements and

impacts, providing a reliable and sustainable energy source. Additionally, PEH can be integrated into shoes to monitor various types of human movement. In this setup, foot pressure acts as a mechanical force that excites the piezoelectric material, leading to the generation of electrical energy [625-627]. These signals are then used to map the pressure distribution across the foot [628, 629] , as shown Figure 86(e), making this technology useful for applications such as foot health diagnostics, customized orthopedic solutions, and gait analysis [630], as illustrated in Figure 86(f). Moreover, R. Tao et al. [631] demonstrated the capability to 3D print a multi-material piezoelectric shoe sole with an octet filling pattern. This innovative sole generates a peak-to-peak voltage of about 20 V from a typical human footstep, showcasing the potential for energy harvesting from human motion. Such technology can power LED shoes, enhancing worker visibility in low light conditions [632]. Additionally, the human body, including internal organs like the heart, is a continuous source of mechanical energy. The rhythmic contractions of the heart, for instance, generate significant mechanical forces that can be harnessed by piezoelectric materials to produce electrical voltage [633, 634]. This harvested energy can power devices such as pacemakers, potentially reducing or eliminating the need for conventional batteries [293, 294].

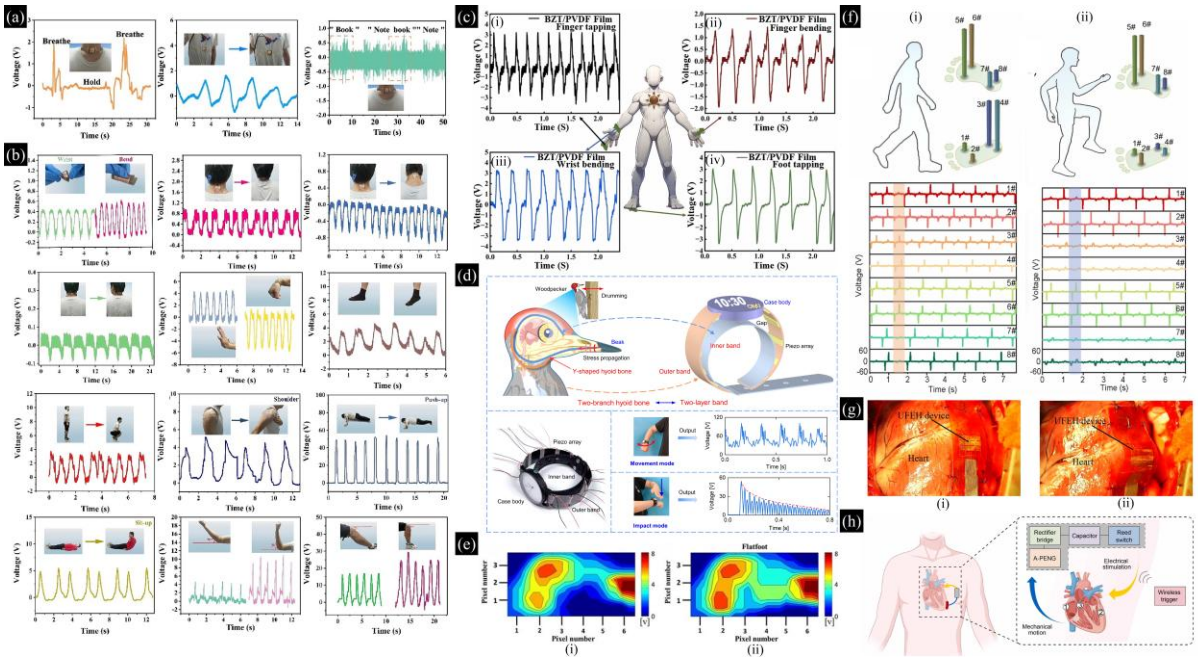

Figure 86: DIW-printed bio-inspired composites and microfluidics-enabled 4D printing systems : (a) Piezoelectric energy harvesting from various small body signals [620], (b) PE harvesting from joint motions [620], (c) Energy harvesting from (i) finger tapping, (ii) finger bending, (iii) wrist bending, and (iv) foot tapping [622], (d) Design and application of bio-inspired smartwatch powered using PEH [624], (e) Pressure mapping of (i) normal foot and (ii) flat foot [628], (f) Pressure distribution and output signals of four sensors distributed on the insoles during

(i) straight walking and (ii) during in-place walking [630], (g) (i) Image of device when the heart relaxes in diastoles. (ii) Image of device when the heart contracts in systole [635], (f) self-powered pacemaker turned on by wireless trigger [636].

By utilizing the natural mechanical movements of the heart, this approach not only provides a reliable source of energy, but also enhances the sustainability and longevity of life-saving medical implants.

B. Lu et al. [635] designed a PZT-based PEH specifically to harvest biomechanical energy from cardiac motion that is regular, lifelong, and relatively insensitive to external environmental changes , as illustrated in Figure 86(g). The device can achieve a peak-to-peak voltage of up to 3 V, demonstrating its ability to generate sufficient power for medical implants such as pacemakers. This technology not only provides a reliable energy source for pacemakers, thereby reducing the need for battery replacements and the associated risky surgeries, but also incorporates multifunctional properties for in vivo diagnosis and treatment [636]. As shown in Figure 86(h), the electrical energy harvested by the PEH is stored in a commercially available capacitor via a full-wave rectifier bridge. This stored energy releases electrical pulses when the wireless trigger placed outside the body approaches the reed switch. The wireless trigger allows medical personnel to selectively activate the pacemaker during diagnostic procedures. This controlled activation is instrumental in assessing how the heart responds to various stimuli and provides valuable information about the heart's condition and functionality.

9.4.1.2 Ambient energy

PEHs can effectively harness various forms of environmental energy, including acoustic [637, 638], vibration [639, 640] and wind [641]. In acoustic excitation, sound waves are converted into electrical energy using either excess ambient noise or specific sound frequencies to drive the piezoelectric materials [642-644].

M. Jin et al. [645] developed an ultrathin planar metasurface-based acoustic energy harvester that employs piezoelectric materials to convert acoustic energy into electrical energy , as depicted in Figure 87(a). This design incorporates a piezoelectric plate placed at the point of maximum strain energy within the metasurface structure to achieve highly efficient energy conversion. This piezoelectric plate is essential for the functionality of the energy harvester, enabling the generation of electricity from incident airborne sound waves. Vibration energy, sourced from mechanical vibrations in industrial machinery, transportation systems or

structural vibrations, provides a dynamic and continuous input for PEHs. . This allows for the consistent generation of electricity, tapping into an underutilized energy resource that is abundantly available in many environments [646].

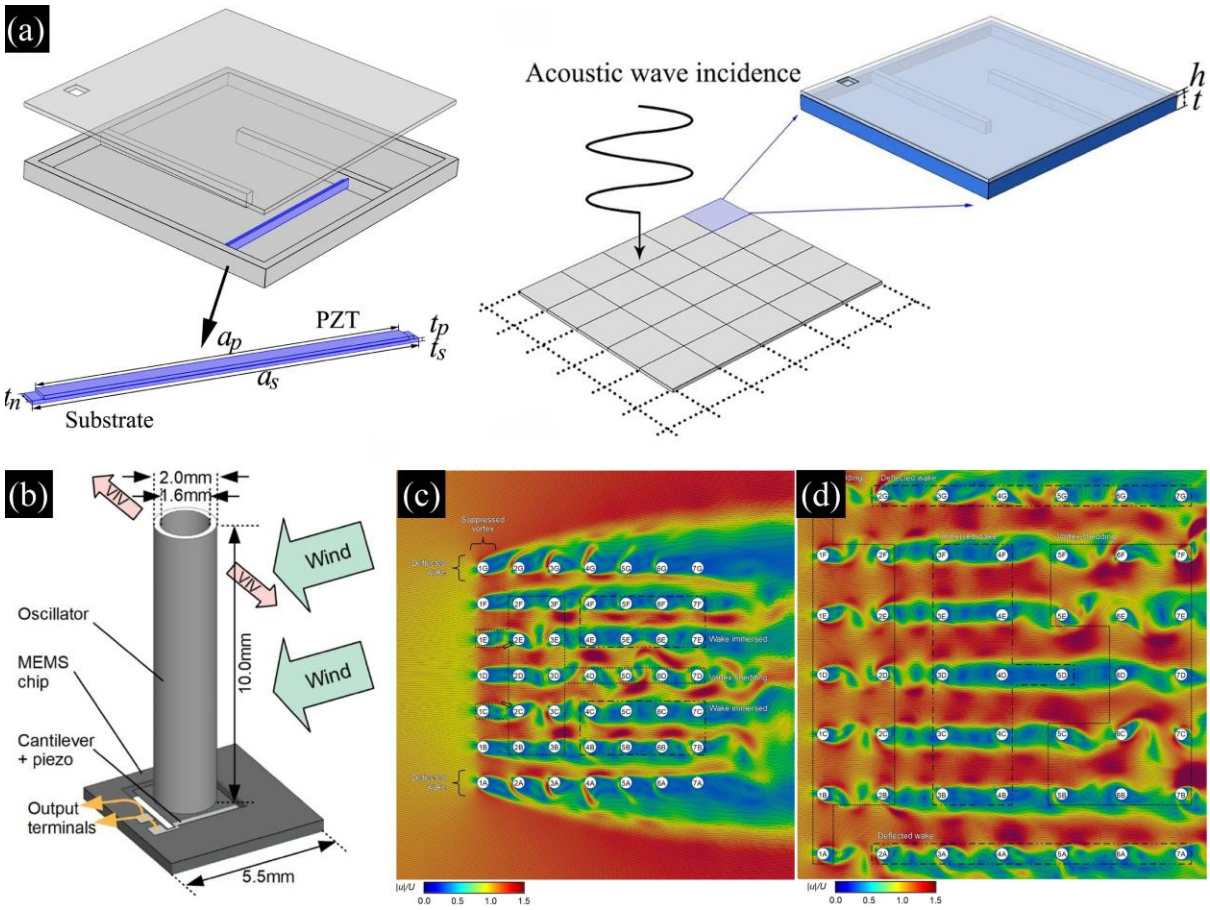

Figure 87: 4D-printed composites for soft robotics and bioinspired sensor applications : (a) Schematic illustration of the design of ultra-thin planar acoustic energy harvester for harvesting airborne sound [645], (b) Schematic drawing of the wind energy harvester [650], Contours of normalised velocity magnitude encountered by the cylinders in a 7×7 formation with (c) L/D=3 , and (d) L/D=5 [84].

One of the main benefits of harnessing mechanical vibrations with PEHs is the capability of real-time monitoring of structural health [647, 648]. M. Iqbal et al. [649] focused on monitoring the structural health of bridges by employing PEHs. These harvesters were specifically developed to convert mechanical vibrations and wind energy into electrical energy, which in turn powers wireless sensor nodes (WSNs). These WSNs are used for continuous monitoring of bridge conditions, enabling the early detection of damage, enhancing safety, and reducing maintenance costs.

Wind energy, characterized by air currents and turbulence, can induce mechanical stresses in piezoelectric materials, effectively converting the kinetic energy of the wind into usable electrical energy. Utilizing these diverse environmental energy sources, PEHs provide a versatile

and sustainable solution for powering small electronic devices and sensors in various applications. Y. Lee et al. [650] investigated the potential of PEHs to harness wind energy through vortex-induced vibration (VIV). The device they developed consists of a cylindrical oscillator attached to a MEMS platform with a silicon cantilever coated with piezoelectric material, as shown in Figure 87(b). The oscillator is activated into VIV by wind, generating mechanical vibrations that the piezoelectric layer then converts into electrical energy. Their study revealed that arranging multiple devices in a specific formation significantly increases the power output by exploiting vortex interactions between the cylinders. This amplifies the vibrational forces on downstream cylinders. Figure 87(c) and (d) illustrate this formation effect, showing how varying the spacing between cylinders relative to their diameter (L/D = 3 and L/D = 5) influences wind flow patterns and vortex shedding. This demonstrates optimized VIV performance and enhanced energy recovery, as shown in Figure 87(c) and (d).

M. Iqbal et al. [651] developed a PEH that stands out by its capability to simultaneously convert three different types of ambient energy — sound, vibration and wind — into electrical energy. This ability to utilize multiple energy sources marks a significant advancement over conventional energy harvesters, which typically harness on only one or two energy sources. The research and development of PEHs to exploit ambient energy sources such as sound, vibration and wind demonstrates the vast potential and versatility of these devices. By integrating advanced materials and optimizing the design, researchers have significantly improved the efficiency and functionality of PEHs. These innovations not only improve energy harvesting capabilities, but also open up new applications in areas like structural health monitoring, flexible electronics and sustainable power generation for small devices. The capability of PEHs to harvest energy from multiple sources represents a crucial step towards developing robust and adaptable energy solutions, setting a promising direction for future research and development in this dynamic field.

9.4.1.3 Vehicles vibrations

PEHs can be effectively integrated into vehicles to generate energy from the mechanical deformation of tires. As the tire deforms, it creates the necessary mechanical vibrations to excite the piezoelectric material, thereby generating electrical energy, as shown in Figure 88(a). This energy is then utilized to power strain sensors and a wireless data transmission system, facilitating continuous monitoring and real-time data transmission [652]. Research has demonstrated that PEH can generate up to 6 V from the compressive forces exerted by vehicle tires, , as depicted in Figure 88(b) [653]. Additionally, Figure 88(c) illustrates the integration of

piezoelectric sensors in tractor tires under various operational conditions. This figure includes optical images of a tractor equipped with various agricultural implements, alongside the corresponding output voltage waveforms of the sensors [654].

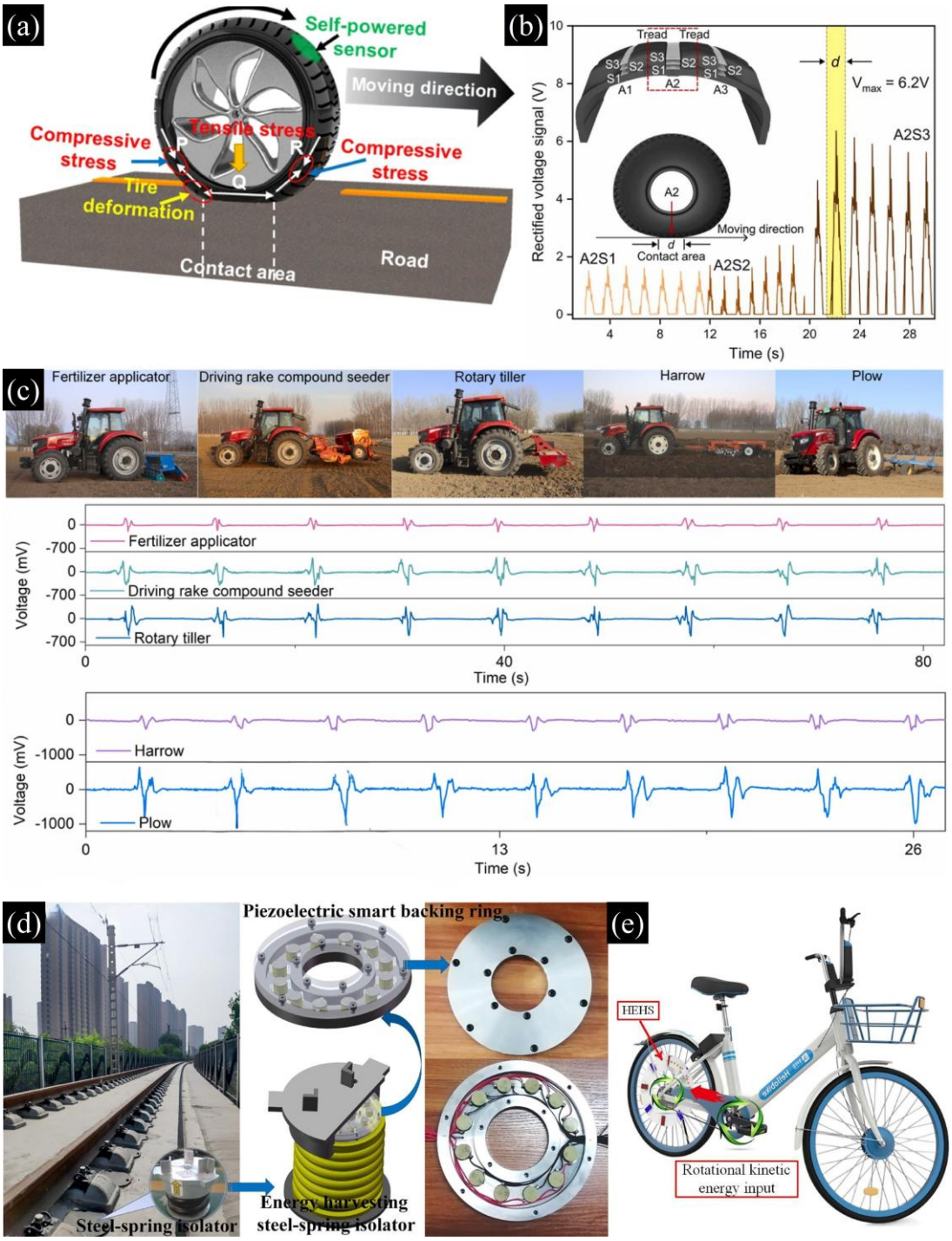

Figure 88: Adaptive multi-material systems for intelligent actuators and wearable sensors : (a) Schematics of the tire deformation with different types of strain [652], (b) Maximum output voltage of PEH under tire compression force [653], (c) Real-time monitoring of tractor tire strain using flexible multilayer piezoelectric sensors under various agricultural conditions [654], (d) Schematic diagram and fabricated prototype of piezoelectric smart

backing ring [655], (f) Rotational kinetic energy on the wheels of bicycles [658].

Trains generate considerable mechanical vibrations while traveling, which can be harnessed by PEHs to generate electrical energy. By embedding piezoelectric materials into the railroad infrastructure, these devices can capture the mechanical stress caused by passing trains and convert it into electrical power. This harvested energy can be used to power wireless sensor nodes that monitor critical parameters such as track integrity, train speed and environmental conditions. Real-time monitoring systems powered by PEHs enhance safety, reduce maintenance costs, and improve the overall efficiency of railroad operations. J. Wang et al. [655] developed a piezoelectric smart backing ring designed to capture kinetic energy from train-induced forces acting on steel spring insulators in railroad systems. The prototype, consisting of a concave-shaped hollow base, a convex-shaped hollow cover plate, and twelve piezoelectric stacks (as shown in Figure 88(d)), can generate an average power output of up to 500 mW under the forces experienced by the steel springs, with the potential to reach up to 1 W when optimized. This represents a significant improvement over most existing piezoelectric energy harvesters used in railroad systems, which typically generate power in the milliwatt range.

As bicycles continue to grow in popularity for transportation and recreation, the mechanical vibrations generated by cycling provide a valuable source of ambient energy. PEHs can be integrated into various bicycle components, such as the frame [656], wheels [657, 658], or pedals [659, 660], to harness these vibrations and convert them into electrical power [658]. As illustrated in Figure 88(e), the rotational kinetic energy generated while riding a bicycle can be effectively utilized as an energy source.

The generated power can be used to operate on-board electronics, such as lighting systems [661], GPS devices [662], and sensors that monitor riding performance and environmental conditions [658]. Additionally, the harvested energy can be stored in batteries for later use or transferred directly to mobile devices. By exploiting the kinetic energy of bicycles, PEHs contribute to greener transportation solutions by reducing reliance on conventional power sources and improving the functionality of bicycles with self-sustaining power systems. This technology not only promotes environmentally friendly transportation, but also supports the development of smart, energy-efficient urban mobility solutions.

9.4.2 Applied stimuli in 4d printing

9.4.2.1 Thermo-responsive materials

The development of thermos-responsive materials in 4D printing has revolutionized the creation dynamic and functional structures [663]. These materials are sensitive to temperature changes and enable programmed transformations, making them suitable for a diverse range of applications, from biomedical devices to energy storage solutions [664-667]. Recent advances have focused on improving the properties and performance of these materials to achieve more precise control and improved functionality. C. Ni et al. [668] have developed a shape-memory hydrogel that can revert to its original shape at room temperature, featuring programmable onset of recovery. While the shape recovery is naturally triggered at room temperature, the initial phase separation and programming require precise control through heating, as shown in Figure 89(a) (i). The extent of phase separation, which influences the delay in recovery onset of, is controlled during the programming phase through precise heating. Notably, although recovery begins 10 minutes post-programming, infrared temperature monitoring indicates that the sample reaches equilibrium temperature within 10 seconds, as depicted in Figure 89(a) (ii).

Cold-programming shape-changing structures present an innovative approach for temperature-triggered transformations, eliminating the need for heating during the programming phase. L. Yue et al. [669] have developed such structures that can be cold programmed at room temperature. Cold programming involves stretching the printed structure to a desired strain to achieve a temporary shape. Following deformation, the structure retains the temporary shape due to the mechanical properties of the materials used, which consist of a combination of glassy and rubbery phases, as illustrated in Figure 89(b) (i). The glassy thermoset materials within the composite play a crucial role in fixing the temporary shape by restricting molecular mobility and trapping the internal stress. The original shape is subsequently restored when the temperature is elevated above the transition temperature (Tc) of the materials used in the structure, as shown in Figure 89(b) (ii) and (iii).

Thermoreactive MXene hydrogels represent a breakthrough in the field of smart materials, combining excellent mechanical properties with adaptable functionalities. K. Li et al. [670] have developed a universal 4D printing technology specifically for the fabrication of thermoreactive MXene hydrogels. This innovation approach leverages the unique properties of MXenes to create hydrogels with customizable geometries and enhanced performance characteristics, particularly suited for energy storage applications. The cross-linked hydrogels

are synthesized through a heat-stimulated self-assembly process, as shown in Figure 89(c). This process not only improves the mechanical strength of the hydrogels and but also optimizes the distribution and interaction of the conductive components within the material. These resulting MXen hydrogels offer presents a porous 3D architecture, large specific surface areas, high electrical conductivities and robust mechanical properties, making them exceptionally suitable for advanced energy storage systems.

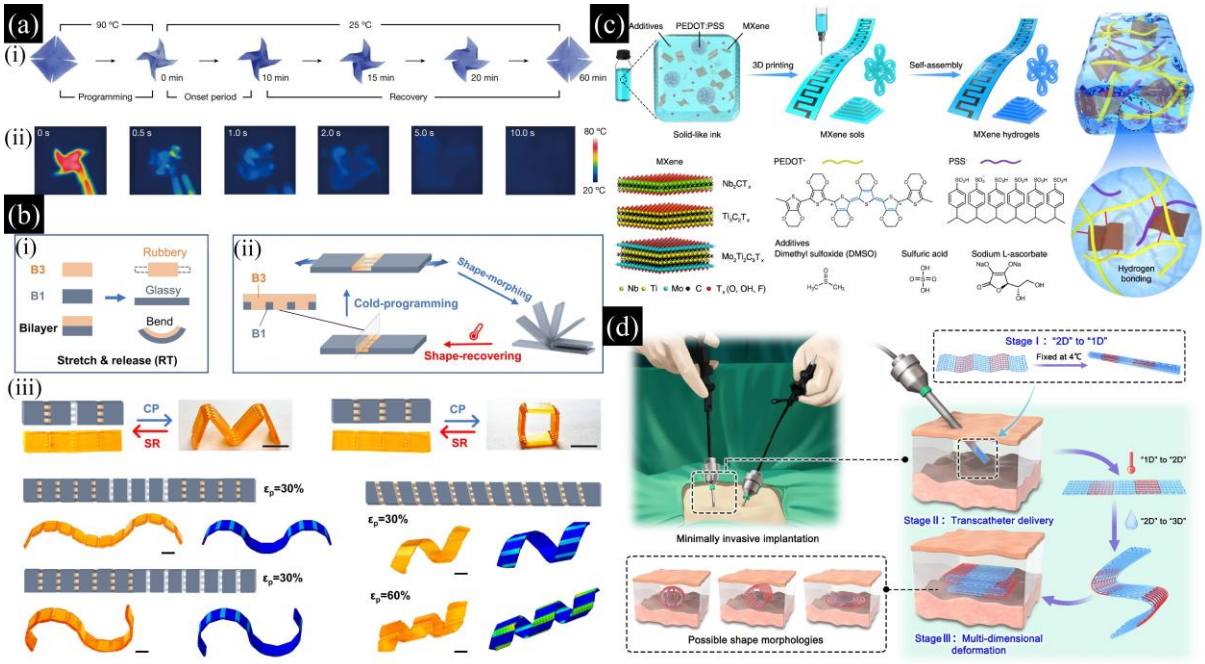

Figure 89: Structural optimization of 4D-printed lattice networks using DLP and direct writing : (a) (i) shape recovery process at 25 °C, with a programming time of 60 min, (ii) Infrared images of the hydrogel at 25 °C [668], (b) cold-programmable of thermos-responsive SMP [669], (c) Heat-stimulated self-assembly of MXene hydrogels [670], (d) Body temperature-triggering of the DTPUs shape memory behavior [671].

Thermoresponsive materials play a pivotal role in various sectors, especially in medicine and healthcare, where they are used to create intelligent implants and devices that adapt to body temperature, enhancing both comfort and treatment efficacy. For example, shape memory polymers are employed to develop stents that expand at body temperature, significantly reducing the need for invasive procedures and thereby improving patient outcomes. In healthcare, thermoresponsive hydrogels are used in drug delivery systems, where they enable the controlled release of medications in response to body heat. Furthermore, these materials are instrumental in tissue engineering, where they are used to fabricate scaffolds that not only support cell growth but also aid in tissue regeneration. The ability to program and control the

behavior of thermoresponsive materials in response to temperature variations provides significant advantages for applications requiring high precision and adaptability.

B. Liu et al. [671] introduced a novel approach to fabricate hydrogel scaffolds through 4D multi-material printing. This innovation focuses on the development of dynamic thermoset polyurethanes (DTPUs), which are engineered to combine shape memory properties, programmable deformability, and swelling stiffening capabilities. This combination is particularly advantageous for minimally invasive implantation. As illustrated in Figure 89(d), the DTPUs are capable of exhibiting shape memory behavior that is triggered by body temperature: The dry-printed 2D patterns are fixed in a temporary 1D shape at room temperature and, upon implantation, body temperature activates the transformation, restoring the original 2D pattern. This characteristic allows for the DTPUs to be inserted minimally invasively and then adapt to their intended form within the body, enhancing the effectiveness and applicability of medical implants.

9.4.2.2 Photoresponsive materials

Recent advances in 4D printing with photosensitive materials have paved the way forto the development of various innovative materials and applications. For instance, hydrogels developed by J. Liu et al. [672], utilize a photocontrolled metallopolymer adhesive composed of a Ru-containing polymer and a thioether-containing polymer, as illustrated in Figure 90(a) (i). These adhesive forms reversible cross-links via Ru–S coordination bonds, enabling reconfigurable hydrogel assemblies tailored for numerous customized functions, as shown in Figure 90(a) (ii). Y. Zheng et al. [673] have advanced the field of photosensitive materials by developing a novel photosensitive hydrogel system using oxazine (OX) compounds. These hydrogels are designed to perform complex and precise movements at the water-air interface when exposed to light. By integrating OX compounds into the hydrogel network through a free radical copolymerization strategy, the researchers created capable of converting light energy into thermal energy. As depicted in Figure 90(b), this conversion induces temperature changes that drive Marangoni propulsion, showcasing the dynamic potential of these materials for innovative applications in soft robotics and beyond.

L. Zhang et al. [489] introduced metal-polymer composites (LMPCs) that respond to near-infrared (NIR) light, demonstrating rapid and repeatable shape changes under NIR irradiation, as depicted in Figure 90(c) (i). These LMPCs have significant potential for advanced applications in soft robotics, artificial muscles and aerospace materials, capable of performing

complex tasks such as grasping and releasing objects, illustrated in Figure 90(c) (ii), (iii), and (iv). In addition, K. Qian et al. [674] developed a photosensitive liquid crystal polymer network (LCN) that incorporates cyanostilbene (CS) and spiropyran (SP), as shown in Figure 90(d). This LCN can perform multi-element encryption and stepwise decryption using light and heat stimuli, offering dual functionality through photodeformation and reversible photochromism.

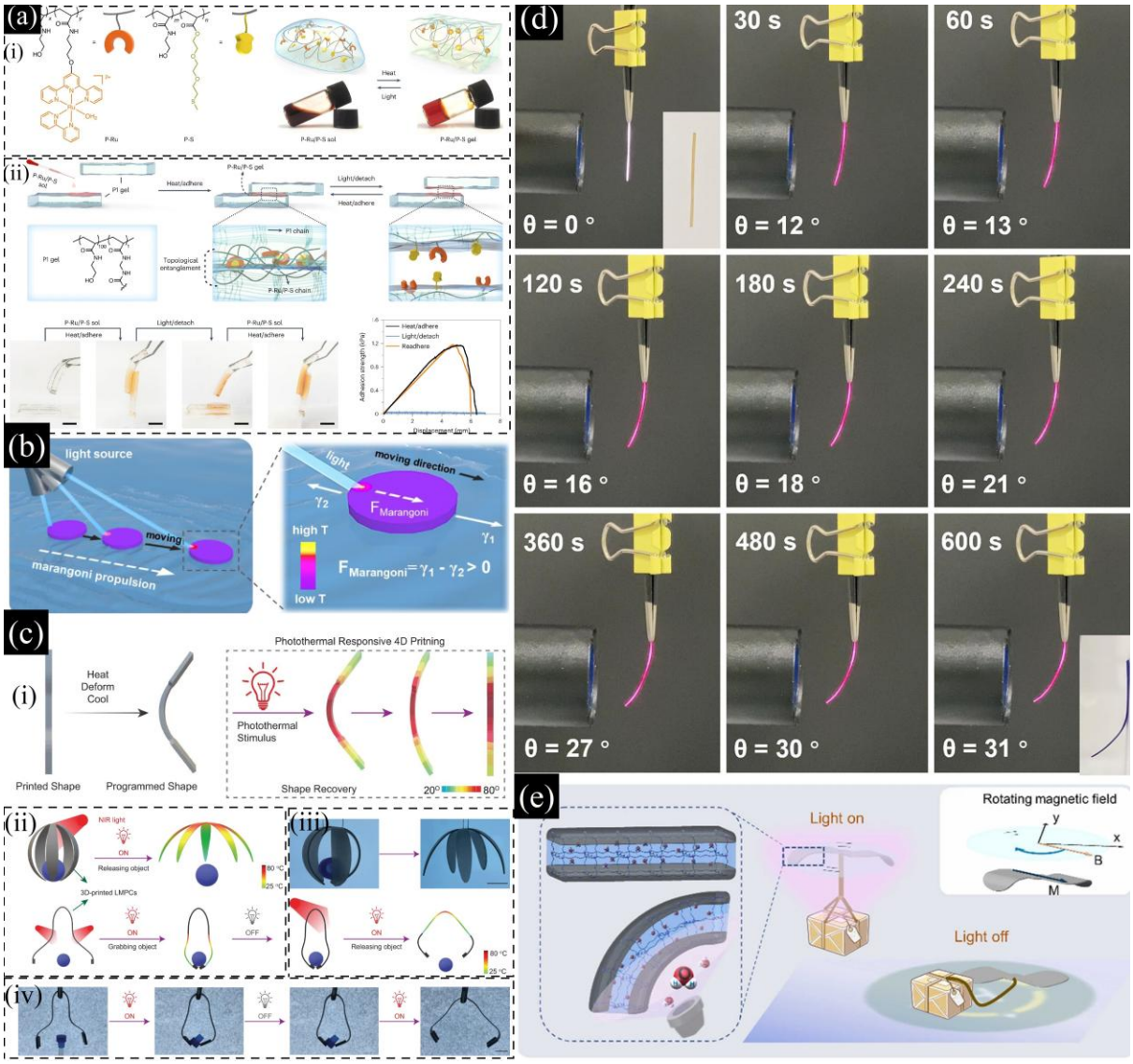

Figure 90: SLA-printed piezoelectric structures and self-morphing mechanisms in smart ceramics : (a) (i) Chemical structures of photocontrolled metallopolymer adhesive, (ii) Schematic, and photos showing reversible adhesion of two hydrogels using the adhesive [672], (b) Schematic representation of a light-fueled unidirectional swimming of OX hydrogel driven by Marangoni propulsion at the water-air interface [673], (c) (i) diagram of photothermally induced 4D printing [489], (ii), (iii), and (iv) diagram and demonstration of gripping and releasing an object via using NIR light controlled LMPCs [489], (d) Photographs of CS-SP-LCN (CS:SP = 7:3) film under UV irradiation for different times [674], (e) Schematic diagram of the motion of the light-controllable variable pitch micro-propeller [675].

Furthermore, M. Wang et al. [676] expanded the scope of photosensitive materials with a Cu2I2-based 2D metal-organic framework (MOF) that includes spiropyran (SP) groups. This MOF displays dynamic photochromic behavior with multicolor states and tunable retention times, making it ideal for applications requiring precise control over color changes and information states. A notable application of these innovative materials is the bioinspired propeller robot developed by W. Yang et al. [675] (Figure 90(e)), which combines magnetic and optical fields with photothermal conversion materials such as carbon nanotubes (CNTs). This robot achieves controllable pitch by efficiently converting light energy into thermal energy, demonstrating the extensive potential of photoresponsive materials for creating dynamic and multifunctional systems. These innovations highlight the versatility and transformative potential of photosensitive materials in 4D printing, opening new avenues forapplications and enhancing performance across various sectors.

9.4.2.3 Electrorespensive material

The development of electroresponsive materials in 4D printing has led to significant advances in the fabrication of dynamic structures and devices capable of altering their shape or properties in response to electrical stimuli [677]. A prevalent method for creating these materials involves incorporating nanoparticles or fibers that can convert electrical current into heat. This heat generationis crucial for initiating the shape memory effect and other responsive behaviors in the materials.

For example, X. Dong et al. [491] explored the properties of PLA/CNT shape memory polymer composites with varying CNT contents. They utilized FDM technology o 3D print a U-structure with two long legs, experimenting with different filling directions (0°, 45°, 90°). As illustrated in Figure 91(a), the specimen with 0° infill direction exhibited the most uniform internal heat distribution and required the lowest activation voltage. Conversely, the specimen with a 90° filling direction displayed the most uneven internal heat distribution and necessitated the highest activation voltage. These findings underscore the significance of optimizing filling patterns to ensure uniform heat distribution and efficient activation. This optimization is crucial for the practical application of electroresponsive materials in creating dynamic devices that respond predictably and effectively to electrical stimuli.

Furthermore, K. Dong et al. [492] enhanced the electrothermal responsiveness of 4D-printed structures by incorporating carbon nanotubes (CNTs) at a proportion of 6 wt% into a mixture of polylactic acid and thermoplastic urethane (PLA/TPU) with a ratio of 90:10. The high

conductivity of CNTs enabled rapid heating of the structure, increasing the temperature from 22.3°C to 74.3°C in just 25 seconds under a voltage of 10 V, as shown in Figure 91(b). This rapid heating allowed the structure to regain its original shape with a recovery rate (Rr) of 94%, showcasing the effectiveness of CNTs in enhancing the electrothermal responsiveness of 4D-printed structures. In addition, Y. Wang et al. [678] introduced a novel method using continuous carbon fibers (CCFs) to fabricate and control active origami structures through 4D printing technology. These origami structures can precisely control their unfolding and modulate their properties on demand, facilitated by the integration of continuous carbon fibers (CCFs) for electrothermal activation, as illustrated in Figure 91(c). When an electric current is applied, the CCFs generate heat due to their electrical resistance, inducing a phase transition in the SPM that triggers the shape-changing behavior. Similarly, A. Fallah et al. [679] developed a coaxial AM process for 4D printing with continuous carbon fiber reinforced shape memory polymers (SMP).

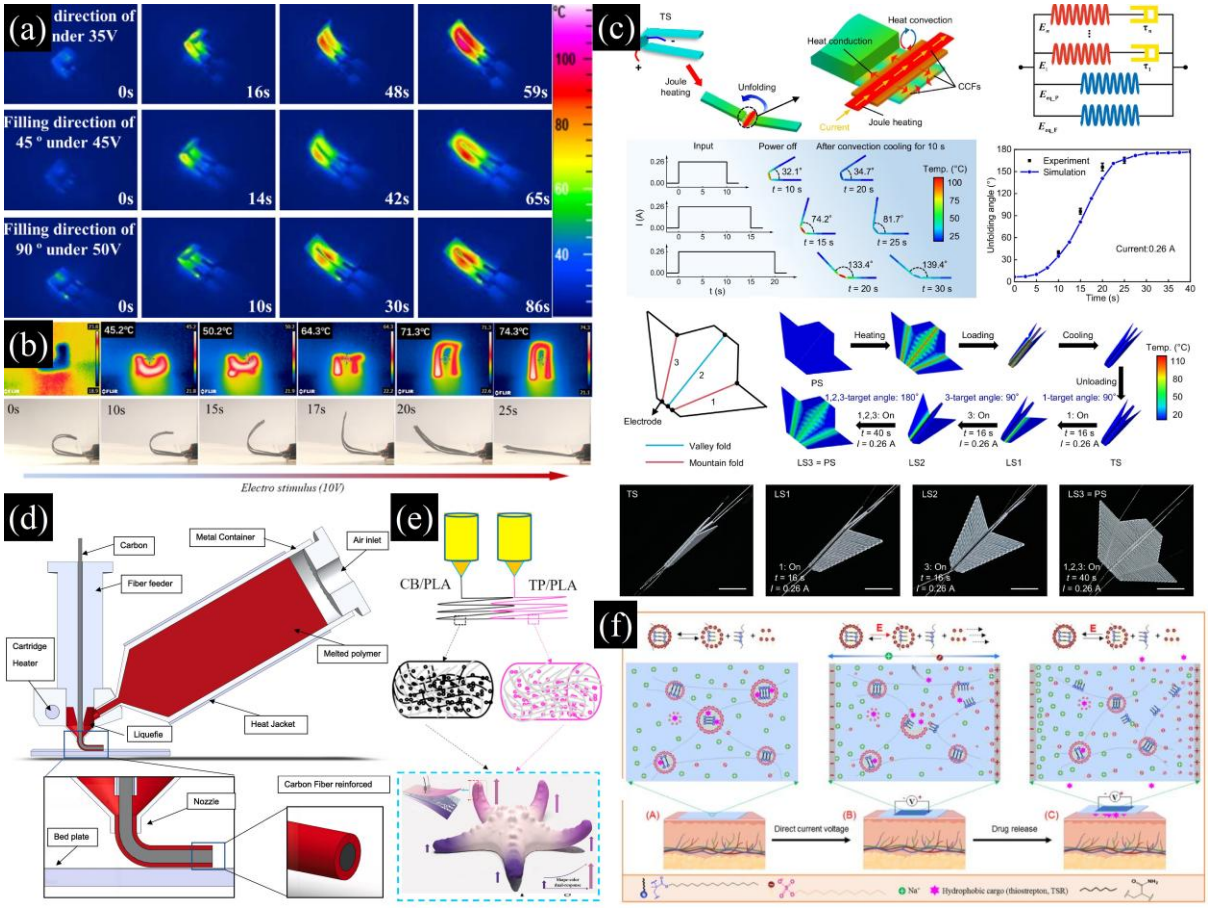

Figure 91: Electrothermal responses and actuation mechanisms in 4D printed smart structures : (a) Heat distribution maps of U-shaped structures: 0◦ infill direction, 45◦ infill direction, and 90◦ infill direction during the

electroactive shape recovery process [491], (b) electro-induced behavior of the printed PLA/TPU/CNT under an applied voltage of 10V [492], (c) Working principle of electrothermal responsive origami [678], (d) Schematic figure of designed coaxial nozzle [679], (e) 4D-printing programmable electroactive shape-color double-responsive process [680], (f) rearrangement of SDS micelles under direct current voltage (DCV) allowing for release of encapsulated hydrophobic drugs to the skin surface [681].

As illustrated in Figure 91(d), they introduced a novel coaxial nozzle designed to simultaneously feed both continuous carbon fibers and thermoplastic polymers, enabling the fabrication of continuous carbon fiber reinforced composites (CCFRPs). This integration of continuous carbon fiber reinforcement allows for the use of Joule heating to achieve shape recovery, providing a a precise and controlled method of inducing shape changes through the application of voltage.

X. Zhou et al. [681] have developed and synthesized a novel class of electro-responsive hydrogels (ERHs) capable of releasing drugs on demand. These hydrogels are prepared using a process where a direct current voltage (DCV) induces a rearrangement of sodium dodecyl sulfate (SDS) micelles. This rearrangement tunes the hydrogel networks, which are initially sustained by hydrophobic interactions supported by SDS micelles, as illustrated in Figure 91(f). Upon application of an electric field, the hydrogels respond by altering the configuration of SDS micelles within the polymer network. This change increases the mesh size of the hydrogel, thereby enabling a controlled release of encapsulated hydrophobic drugs.

9.4.2.4 Magneto-responsive materials

Magneto-responsive materials are at the cutting edge of development in dynamic and intelligent structures within 4D printing, opening new avenues for innovative applications in flexible electronics, biomedical devices and soft robotics [682, 683]. Recent advancements have focused on enhancing the mechanical properties, responsiveness and programmability of these materials to expand their functionality and versatility.

Magneto-responsive SMPs represent a unique class of materials undergo shape changes in response to magnetic fields. H. Liu et al. [490] investigated the integration of these SMPs into 4D printing, leveraging the distinctive properties of polylactic acid (PLA), thermoplastic polyurethane (TPU) and iron oxide (Fe3O4) composites. The addition of Fe3O4 not only increases the mechanical robustness of the materials, but also enhances their thermal conductivity. This enhancement allows the heat generated by a magnetic field to be quickly conducted through the matrix, leading to efficient and responsive shape recovery. The performance of these

materials improves with increasing Fe3O4 content, as shown in Figure 92(a). The ability to precisely control the shape recovery process makes these composites particularly suitable for smart structures and applications that require precise control.

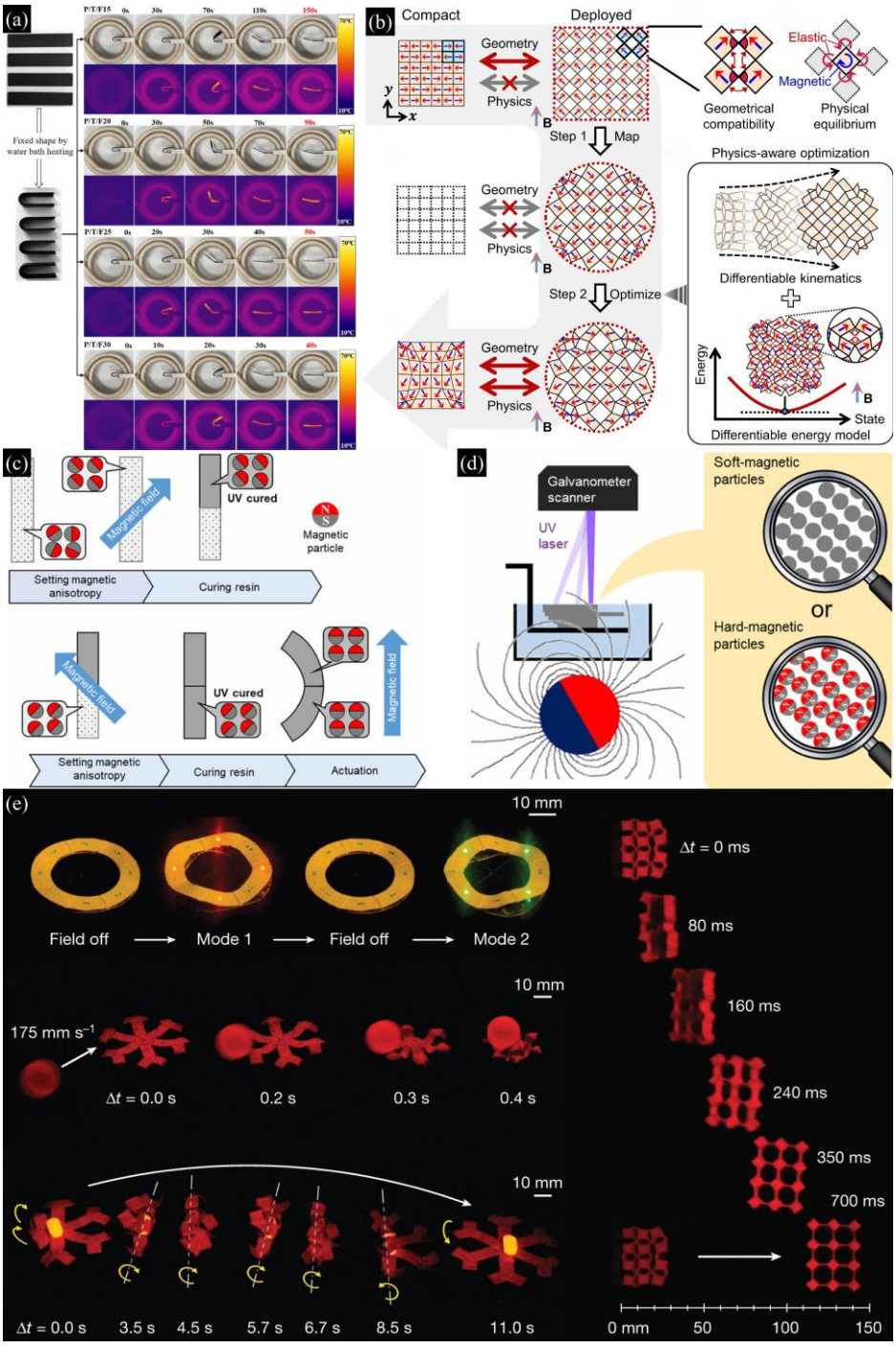

Figure 92: Magnetic actuation and shape recovery behavior of smart printed composites : (a) shape recovery process including the instantaneous shapes and thermal distribution with different Fe3O4 contents [490], (b) Simultaneous Design of Cuts and Magnetization Orientations in Magnetically Actuated Kirigami [684], (c) Fabrication and Actuation System for Magnetic Anisotropy in 3D-Printed Gel Structures [685], (d) Schematic Illustration

of 3D Printing System with Magnetic Powder Dispersion [685], (e) Diverse Functional Demonstrations of Magnetically Actuated 3D-Printed Soft Materials [686].

An innovative application of magneto-responsive materials involves the design of magnetically actuated kirigami structures. L. Wang et al. [684] introduced a differentiable inverse design concept that merges both geometric and physical principles to create complex kirigami designs. These designs can transform into predetermined shape upon magnetic excitation, as shown in Figure 92(b). This innovative framework automates the design process while ensuring kinematic and physical feasibility. By optimizing the cuts and the orientations of magnetization in the Kirigami panels, these structures can achieve precise shape transformations, making them suitable for applications in flexible electronics and adaptive structures.

Magnetic soft actuators represent a significant area of application in the field of 4D printing. H. Shinoda et al. [685] have developed a 4D printing process specifically for these actuators, enabling them to deform predictably in response to magnetic field. During the curing process, a magnetic field is applied as depicted in Figure 92(c) and (d), creating magnetic anisotropy within each part of the printed structure. This anisotropy allows the actuators to mimic biological movements, such as crawling and wave propagation. The fluid, adaptive movements of these magnetic soft actuators make them exceptionally suited for biologically inspired robotics and medical devices that require sophisticated, lifelike motion capabilities. Y. Kim et al. [686] have significantly advanced the capabilities of magnetically responsive materials by focusing on 3D printing of programmed ferromagnetic domains within soft materials. This innovative technology facilitates rapid transformations between complex 3D shapes through magnetic actuation. As illustrated in Figure 92(e), the printed structures can be used to create reconfigurable soft electronics and mechanical metamaterials capable of jumping, as well as soft robots that can crawl, roll, pick up fast-moving objects and transport pharmaceutical cans. These dynamic functionalities highlight the potential for wide-ranging applications in flexible electronics, biomedical devices, and soft robotics.

These progress in magneto-responsive SMPs and their applications in kirigami structures, soft actuators and ferromagnetic domains, demonstrates the transformative potential of 4D printing with magnetic fields. By harnessing the unique properties of these materials, researchers are developing innovative solutions that merge precise actuation with multifunctionality. This integration is paving the way for groundbreaking technological advances across various fields,

driving forward the development of devices and systems that adapt and react to their environments in revolutionary ways.

9.5 Smart materials

Smart materials, such as shape memory materials and piezoelectric materials, represent a significant breakthrough in materials science and engineering due to their dynamic responsiveness to environmental stimuli [687]. Piezoelectric materials, which encompass polymers, ceramics, and composites, have the remarkable ability to generate electrical energy from mechanical stress. This functionality makes them particularly valuable for a wide range of applications in sensors, actuators, and energy harvesting devices. The capacity of piezoelectric materials to convert mechanical energy into electrical energy makes them indispensable across various applications, including healthcare, automotive, aerospace and consumer electronics. For example, in the healthcare industry, piezoelectric sensors are crucial in medical devices for monitoring physiological parameters [688-690]. In precision mechanics, piezoelectric actuators are employed due to their accuracy and reliability [691, 692].

Shape memory materials constitute another class of smart materials renowned for their remarkable capability to return to a predefined shape when exposed to specific stimuli such as heat, light, or magnetic fields. Shape memory polymers (SMP) are particularly valuable due to their low cost, ease of processing and high formability [693]. Conversely, shape memory ceramics provide high temperature stability and robust mechanical properties, making them suitable for applications requiring high thermal resistance[694]. Shape memory composites, which merge the beneficial attributes of both polymers and ceramics, offer enhanced mechanical properties and increased design flexibility. These composites are particularly effective in environments that demand durability and adaptability.

Furthermore, the innovative integration of piezoelectric materials with shape memory materials has led to the development of multifunctional devices capable of simultaneous shape transformation and generate energy. This synergy has significantly broadened the scope of applications for smart materials, propelling their use in advanced technological solutions.

9.5.1 Smart Polymers

9.5.1.1 Polymers based PEH

Piezoelectric polymers are crucial in various applications due to their flexibility, light weight and ability to be processed into different shapes [165, 695]. Unlike conventional piezoelectric

ceramics, piezoelectric polymers, such as Polyvinylidene fluoride (PVDF), can be easily integrated into flexible and wearable electronics, leading them immense versatility for a broad spectrum of innovative applications [696]. PVDF is one of the most prominent piezoelectric polymers, favored for its robust piezoelectric response and excellent mechanical properties. It can be processed into thin films, fibers, and coatings, making it adaptable to various applications. PVDF exhibits a significant piezoelectric effect when it is properly poled and stretched, which aligns its molecular dipoles and enhances its piezoelectric characteristics [327, 388].

K. Bannuru et al. [697] developed piezoelectric 3D sensors made of PVDF using a novel electro-printing technique. This method combines mechanical stretching and electric field-assisted poling to improve the electroactive crystalline phases in PVDF, specifically the β and γ phases which are essential for its piezoelectric properties, as depicted in Figure 93(a). The refined electro-printing process results in 3D PVDF structures that respond sensitivity to different load profiles at different frequencies, exhibiting a piezoelectric voltage coefficient (g33) ranging from 1.72E-4 to 4.08E-4 V.m/N.

Moreover, H. Kim et al. [253] have developed a novel process that combines 3D printing with a corona poling technique to enhance the fabrication of piezoelectric layers of PVDF. Called the "Integrated 3D printing and corona poling process" (IPC), this innovative method significantly improves the piezoelectric properties of PVDF films by facilitating the transformation of the polymer from its non-electroactive α-phase to the electroactive β-phase during the printing process. The IPC process is achieved by applying a high electrical voltage between the nozzle of the 3D printer and the heating bed, which aligns the PVDF molecular chains as they are deposited layer by layer.

PVDF-TrFE, a copolymer of PVDF and trifluoroethylene, is renowned for its enhanced piezoelectric and ferroelectric properties compared to pure PVDF. The addition of trifluoroethylene in the copolymer stabilizes the piezoelectric β-phase, which is crucial for the material's high performance. X. Yuan et al. [698] have developed PVDF-TrFE films that feature multiple, alternating tilt-polarized regions created using a pair of dislocated interdigital (ID) electrodes, as depicted in Figure 93(b) (i). As shown in Figure 93(b) (ii), this novel polarization method optimizes the piezoelectric effect by aligning the dipoles in a tilted orientation, consequently enhancing the electric dipole moment. The alternating tilt-polarized regions exhibit increased sensitivity to external stresses, making them highly effective in

dynamic environments. Experimental results demonstrate that the ID tilt-polarized PVDF-TrFE film can generate a stable peak voltage of 73.5 V under dynamic compressive load, corresponding to a pressure sensitivity of 1.47 V/kPa, as shown in Figure 93(b) (iii). This performance is significantly superior to films polarized by conventional thickness polarization (CTPPF) and in-plane polarization (ID-IPPF).

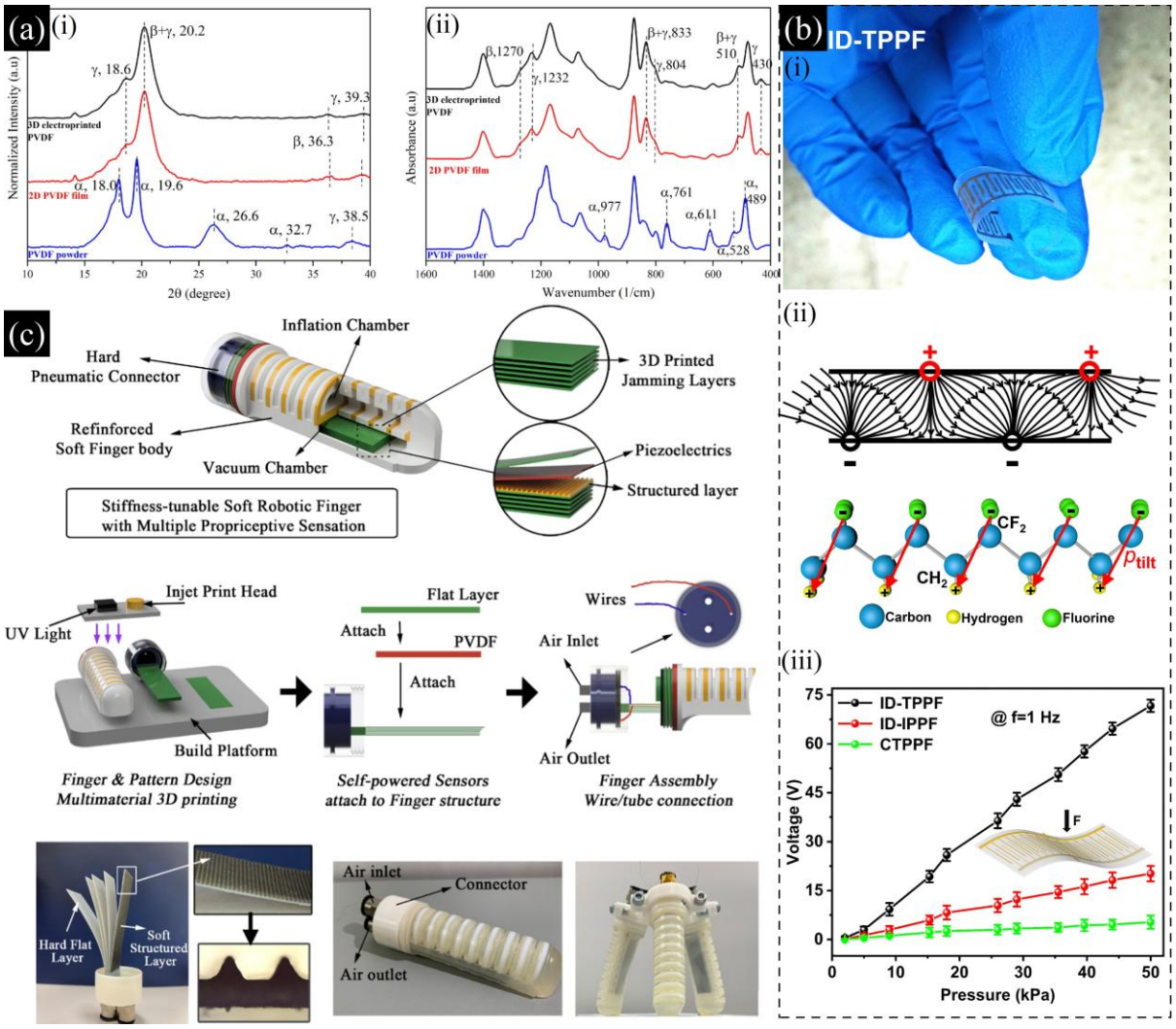

Figure 93: Structural and electrical characterization of PVDF-based piezoelectric devices : (a) (i) X-ray diffractogram and (ii) FTIR spectra of commercial PVDF powder, solution cast PVDF film, and electroprinted PVDF structures, highlighting the peaks corresponding to different phases [697], (b) (i) ID tilt-polarized PVDF-TrFE film, (ii) Distribution of electric field lines and tilt dipole orientation during poling in ID-TPPF, (iii) The output voltages of ID-TPPF, ID-IPPF, and CTPPF as a function of dynamic compressive pressure at 1 Hz [698], (c) Stiffness variable soft finger with built-in multifunctional self-powered PVDF-based sensor by multi-material 3D printing [699].

Y. Li et al. [198] have developed an in-situ fabrication and functionalization process for PVDF-TrFE piezopolymer coatings , focusing on systematically optimizing processing conditions to enhance their performance. This research carefully examines and fine-tunes parameters such as annealing temperature and time, as well as poling voltage and duration. The primary goal of these optimizations is to enhance the crystallinity, ferroelectric phase, morphology, polarization and ultimately the piezoelectric properties of the PVDF-TrFE coatings. The study also compares the performance of PVDF-TrFE coatings with conventional piezoceramic sensors (PZT wafers) in structural health monitoring (SHM) applications. Findings reveal that the piezopolymer coatings exhibit superior conformability to specific waves, consistent performance, and minimal interference with wave propagation. These characteristics make PVDF-TrFE coatings an excellent choice for large-area and flexible sensor networks.

Recent developments in polymer science have sparked a significant interest in exploring new polymer materials for their potential piezoelectric properties, with polyacrylonitrile (PAN) gaining particular attention. Although PAN itself does not naturally exhibit piezoelectric characteristics, innovative methods of aligning PAN nanofibers have led to a substantial improvement in piezoelectric properties. For example, C. Zhao et al. [700] have introduced a novel technique for the multi-plane alignment of PAN nanofibers. This alignment considerably improves the piezoelectric capabilities of the material, enhancing its efficiency in energy conversion. By optimizing the alignment of the PAN nanofibers, the researchers were able to significantly elevate the material's piezoelectric performance. Such advancements are pivotal for the effective transformation of mechanical energy into electrical energy, broadening the potential applications of PAN in energy harvesting and smart materials technology.

The research and development of advanced polymer materials have significantly broadened the applications spectrum for piezoelectric devices. These materials are crucial for creating flexible, lightweight, and high-performance piezoelectric sensors, actuators and energy harvesting devices.

M. Xie et al. [699] used multi-material 3D printing technology to develop a flexible, self-powered multifunctional sensor integrated into a soft robotic gripper with adjustable stiffness. As shown in Figure 93(c), the sensor incorporates a piezoelectric polyvinylidene fluoride (PVDF) film combined with a micro-structured accumulation layer, enabling simultaneous detection of bending curvature and stiffness. This dual sensing capability is crucial for soft

robotic grippers, enhancing their ability to perform safe and dexterous gripping through passive proprioceptive sensations.

Furthermore, G. Ce et al. [701] developed a high-performance, environmentally friendly, and manufacturable piezoelectric polymer MEMS accelerometer. This device rivals conventional PZT-based devices and offers new opportunities for flexible and organic electronics. The accelerometer achieves high sensitivity, with 21.82 pC/g, corresponding to an open-circuit voltage sensitivity of 126.32 mV/g), a flat 5% band of 58.5 Hz and low noise density (6.02 μg/√Hz). These performance metrics not only compete with modern PZT-based MEMS accelerometers but also outperform several commercial MEMS accelerometers.

9.5.1.2 Shape memory polymers

Recent advances in shape memory polymers (SMPs) have primarily focused on improving their material composition to enhance performance and functionality. Researchers have experimented with various combinations of polymers, resins and additives to develop SMPs with improved thermomechanical properties and responsiveness [472, 702]. These innovations in material composition are critical to the evolution of more versatile and efficient SMPs, broadening their applicability across aa wider range of applications and enhancing their utility in 4D printing processes. F. Alam et al. [703] have made significant strides by integrating a liquid crystal (RM257) with a photocurable resin to produce SMPs that are sensitive to temperature changes, as illustrated in Figure 94(a). This innovative blend allows for the direct 3D printing of thermoresponsive structures, eliminating the complexities traditionally associated with SMP resin preparation. Innovations in 3D printing technology have significantly broadened the functional scope of shape memory polymers (SMPs), facilitating the creation of complex, high-resolution structures tailored with customized properties. Advanced techniques such as two-photon polymerization lithography and projection micro-stereolithography have facilitated the precise control of SMP microstructures, resulting in improved shape memory effects and enabled more sophisticated applications. These technological advancements have not only expanded the design and manufacturing possibilities for SMP-based devices but have also pushed the boundaries of what can be achieved with smart materials, opening up new avenues for innovation in various industries. W. Zhang et al. [704] have developed a new SMP photoresist that significantly enhances4D printing capabilities, achieving submicron resolution through two-photon polymerization lithography (TPL). As illustrated in Figure 94(b), this advance allows for the creation of complex nanostructures with shape memory effects, achieving resolutions as fine as 300 nm half pitch. This level of detail

in SMP fabrication opens up possibilities for highly precise biomedical applications and nanotechnology. Similarly, M. Hippler et al. [705] introduced a versatile single photoresist formulation for the fabrication of hetero-microstructures with tunable properties. This is achieved by varying the local exposure dose during three-dimensional laser lithography. As depicted in Figure 94(c), the resulting microstructures respond dynamically to temperature changes and can undergo large amplitude deformations, allowing for the construction of sophisticated 3D architectures. Additionally, as shown in Figure 94(d), localized responses within these structures can be precisely controlled through two-photon absorption, which selectively increase the temperature in targeted areas of the material. H. Yang et al. [706] have employed an innovative approach using two 3D printable polymeric materials that, intriguingly, do not rely on intrinsic shape memory effect to generate a robust shape memory response.. This multimaterial 4D printing technique allows for the creation of heterogeneous structures with custom-tailored shape memory properties, as shown in Figure 94(e), opening up new possibilities in designing mechanical metamaterials that can perform complex motions and transformations. In another study, Q. Ge et al. [707] have successfully fabricated high-resolution SMP-based multimaterial structures using projection microstereolithography, as shown in Figure 94(f). This technique significantly enhances functionality of the produced structures through varied thermomechanical properties, achieving a rubber modulus ranging from approximately 1 MPa to 100 MPa, glass transition temperatures spanning from -50 °C to 180 °C and elongation at break reaching up to 300%. Such versatility is crucial for the precise production of 3D structures that exhibit specific and controlled shape memory behavior. Advances in shape memory polymers (SMPs) and 3D printing technologies have significantly broadened their application spectrum. SMPs are particularly valued for their unique ability to change shape in response to external stimuli such as heat, light and magnetic fields, making them suitable for a range of innovative applications. These include dynamically adaptive metamaterials and multifunctional devices that merge energy storage with shape-changing capabilities, showcasing SMPs' versatility and potential in tackling complex engineering challenges and crafting intelligent, responsive systems. K.-H. Lee et al. [708] have developed autonomous light-triggered shape-reconfigurable and rechargeable power sources (SL-PSs) , as depicted in Figure 94(h). These SL-PSs are fabricated by integrating quasi-solid-state supercapacitors (SCs) with thermoresponsive liquid crystalline polymer networks (LCNs) through a device-adapted printing process. This novel integration facilitates the dual functionality of energy storage and shape transformation within a single device. By combining these capabilities, the combined SCs and LCNs not only store energy but also adapt

dynamically to their environment, capable of powering electronic devices while autonomously changing shape in response to external stimuli like light or heat.

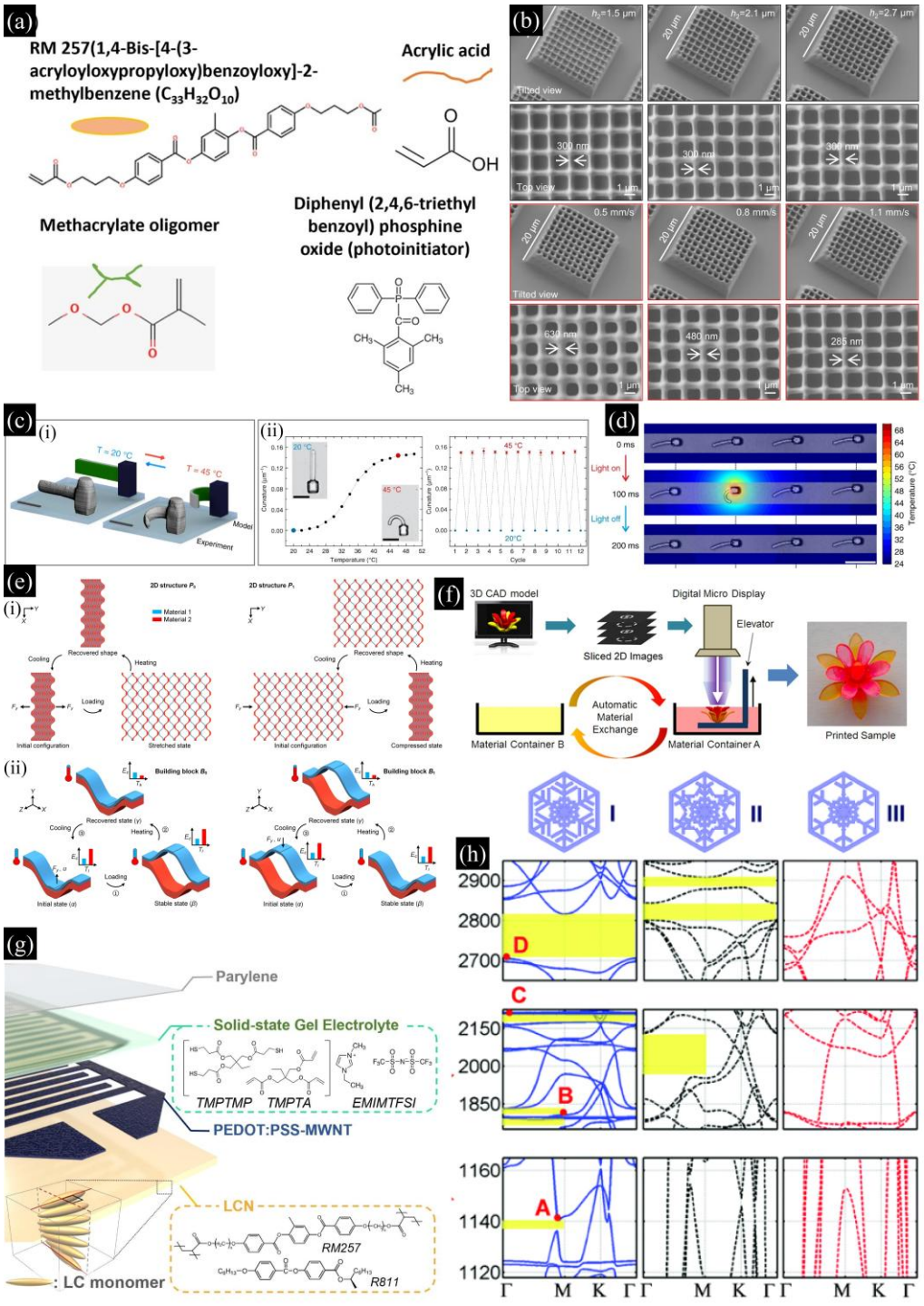

Figure 94: Fabrication and design strategies for high-resolution shape memory and photothermal polymers : (a) Schematic illustration of the preparation of a shape-memory polymer by utilizing a liquid crystal (RM257) [703], (b) SEM images of grid structure showing the high resolution of TPL [704], (c) (i) Scheme of bi-material hetero-

structures with the two materials highlighted in green and gray, lower and higher dose exposure, respectively, (ii) Curvature versus temperature. The right-hand side panel shows the result of twelve temperature cycles without deterioration [705], (d) Light-induced actuation [705], (e) Design strategies of (i) 2D, and (ii) 3D bimaterial metamaterial structures based on polymeric materials [706], (f) Schematics of multimaterial additive manufacture system [707], (g) Schematic representation depicting the structure and components of the SL-PS [708], (h) Comparisons of bandgap characteristics at different stages in shape recovery (Unit cells I, II, III) [709].

This innovative synergy of energy storage and dynamic shape change significantly enhances the application potential of SMP-based devices, particularly in wearable electronics, robotics, and smart materials. In a related advancement, B. Li et al. [709] have used shape memory polymers (SMPs) to create 4D printed metamaterials capable of dynamically switching vibrational band gaps and guiding elastic waves during their recovery process. As depicted in Figure 94(g), unit cell I demonstrates a series of full or directional bandgaps around 1140 Hz, 1790 Hz, 2150 Hz, and between 2700–2800 Hz. These band gaps block wave propagation and significantly attenuate wave transmission at these specific frequencies. However, in unit cells II and III, these band gaps shift or even disappear due to structural reconfiguration induced by the SMP's shape memory effect. Such changes can transform regions with band gaps in the initial structure (unit cell I) into passbands for the temporary structures (unit cells II and III) and vice versa, all controllable through the shape memory recovery process. This ability to tune the behavior of SMP-based metamaterials demonstrates their potential for applications that require dynamic control of wave propagation, such as acoustic filtering and vibration isolation.

Table 35 gives a comprehensive overview of different shape memory polymers (SMP) used in 3D printing technologies and describes their response to stimuli, fixity ratios (Rf) and recovery ratios (Rr).

Table 35: Overview of Shape Memory Polymers in 3D Printing: Stimuli Response, Performances, and Applications.

Materials	3D printing technology	Stimulus	Response time (Rt)	Features	Application	Ref
poly(glycerol dodecanoate) acrylate (PGDA)	FDM	Heat	1.4s	Rf= 100% Rr=98%	Treatment of vascular disease	[710]
tert-Butyl acrylate (tBA)/aliphatic urethane diacrylate (AUD)	DLP	Heat	-	Rf=100% Rr=90%	Soft robotics	[711]
tert-Butyl acrylate (tBA)/ Phenylbis (2,4,6-	DLP	Heat	12s	Rf=100% Rr=90-97%	-	[712]

trimethylbenzoyl) phosphine oxide (BAPO)						
poly (D,L-lactide-co-trimethylene carbonate) (PLMC)/poly (trimethylene carbonate) (PTMC)/Fe3O4	DIW	Heat/ Magnetic field	~8s	Rf=100% Rr=99.8%	biomedical applications	[713]

Table 35: Overview of Shape Memory Polymers in 3D Printing: Stimuli Response, Performances, and Applications. (suite)

Benzyl methacrylate (BMA)/ methacrylate poly (ethylene glycol) dimethacrylate (PEGDMA)	SLA	Heat	5s	Rf=99%	-	[714]
Epoxy-Acrylate Hybrid Photopolymer	SLA	Heat	<20 s	Rf: 97.44% / Rr: 100%	Shape memory devices	[592]
Polyurethane Acrylate	SLA	Heat	<20 s	Rf: 96.77% / Rr: 100%	Shape memory devices	[715]
Methacrylated Polycaprolactone Monomers	Multi-material 3D Printing	Heat, Light	<20 s	Rf: >90% / Rr: >85%	Soft robotic devices	[716]
Methacrylate-Based Monomers	Radical Polymerization	Heat, Light	<20 s	Rf: >91% / Rr: 89.5-98.6%	Biomedical applications	[717]
Polyurethane Shape Memory Polymer	DLP	Heat	7-13 s	Rf: 96.4% / Rr: 99.3%	Shape memory applications	[718]
Zinc-Neutralized Poly(ethylene-co-methacrylic acid)	FDM	Heat	<20 s	Rr: 83-100%	Shape memory applications	[719]
Epoxy-Anhydride SMPs	Various	Heat	<20 s	-	Shape memory applications	[720]
Polyurethane Shape Memory Polymer	Various	Heat	<20 s	Rf: 98% / Rr: 90-99%	Industrial applications	[710]

9.5.2 Smart Ceramics

Smart ceramic materials, including piezoelectric ceramics and shape memory ceramics, mark a significant advance in modern materials science, offering exceptional functionalities for a variety of high-tech applications. Recent advances in the manufacture and processing of these smart ceramics have further enhanced their capabilities [721, 722]. Techniques such as AM and advanced sintering processes have enabled the production of complex geometries and the fine-tuning of material properties, thereby broadening the potential applications of these materials [723]. The integration of smart ceramic materials into multifunctional devices leverages their unique properties to create systems that are more efficient, responsive, and adaptable. This integration is driving innovation across multiple fields, from healthcare to aerospace, highlighting the transformative impact of these materials. The ongoing development and refinement of shape memory and piezoelectric ceramics are set to open new frontiers in the application of smart materials, underscoring their essential role in advancing modern technology and enhancing the capabilities of future devices.

9.5.2.1 Ceramics-based PEH

Piezoelectric ceramics are an essential in a wide array of applications due to their robust piezoelectric properties. Among these materials, lead zirconate titanate (PZT) is particularly notable for its outstanding performance [724, 725].

PZT is one of the most widely used piezoelectric ceramics due to its high piezoelectric coefficients, dielectric constant and electromechanical coupling factors [349, 356, 726]. These characteristics make PZT exceedingly efficient at converting mechanical energy into electrical energy and vice versa, which is crucial for applications that require high sensitivity and precision. It is widely employed in devices such as medical ultrasonic transducers [727], piezoelectric actuators [728, 729], sensors [730, 731], and a variety of industrial applications [732]. However, the environmental and health concerns associated with the lead content in PZT have prompted a significant shift towards the development of lead-free alternatives that maintain similar piezoelectric properties [733]. Barium titanate (BT) has emerged as one of the most promising lead-free piezoelectric ceramics [734]. Known for its environmental friendliness and advantageous piezoelectric properties, BT has garnered considerable attention as a viable substitute for PZT. BT exhibits a high dielectric constant, good ferroelectric properties and good piezoelectric coefficients. BT's piezoelectric performance can be enhanced

through doping and compositional modifications, making it a versatile and safer option for various applications.

K. Chen et al. [735] have developed 3D-printed scaffolds that combine hydroxyapatite (HAp) and barium titanate ($BaTiO_3$). These scaffolds are designed to leverage the piezoelectric properties of $BaTiO_3$ to enhance both immunomodulatory and osteogenic responses. As illustrated in Figure 95(a), the incorporation of $BaTiO_3$ imparts piezoelectric properties to the scaffold, which actively stimulate bone tissue regeneration and enhance osteogenic differentiation. The research further explores how the piezoelectric properties of these scaffolds influence immune responses, potentially reducing inflammation and promoting a conducive environment for bone healing. In a related study, Z. Jiang et al. [736] employed digital light processing (DLP) 3D printing technology to fabricate porous scaffolds from piezoelectric BT ceramics.. The porosity of these scaffolds was systematically varied from 10% to 90%, enabling precise control of their mechanical and piezoelectric properties. With increasing porosity, both the compressive strength and the piezoelectric coefficient (d_{33}) of the scaffolds gradually decreased. This adjustment resulted in a uniform and gradually decreasing potential distribution across the scaffolds, as shown in Figure 95(b), ensuring the reliable performance of the piezoelectric ceramics.

Advancements in the processing techniques for 3D printing piezoelectric ceramics are crucial to optimizing the final properties and performance of the materials. Y. Hong et al. [737] developed a Surface Tension Assisted Two-Step (STATS) process, an efficient method for fabricating 3D-architected cellular piezoceramics as illustrated in Figure 95(c). In the STATS process, 3D-printed organic lattices are first immersed in a precursor solution, then dried to form a gel precursor, and finally sintered to produce compact ceramics. This method allows for the creation of cellular ceramics with varied cell sizes, geometries, relative densities, and constituents, effectively combining the constituent loading efficiency of Direct Ink Writing (DIW) with the fabrication speed and resolution of Stereolithography (SLA)/Digital Light Processing (DLP).

CL. Liu et al. [738] enhanced the curing behavior and layer adhesion of PZT ceramic slurry by incorporating soluble starch. This modification improves printability and the interlayer bonding of PZT green bodies. Their findings indicate that PZT ceramics printed with 20 vol% soluble starch achieve a relative density of approximately 89.51% of the theoretical density

and exhibit outstanding dielectric constants, residual polarization, piezoelectric voltage constants, figures of merit, and electromechanical coupling factors.

Furthermore, Z. Li et al. [739] introduced a novel method combining DIW with secondary molding techniques to fabricate complex piezoelectric ceramic structures.. This approach overcomes the limitations of traditional DIW, which often struggles with unsupported structures. This used PZT ink exhibits shear-thinning behavior and adequate viscoelasticity, allowing the green body to remain flexible and be shaped into complex shapes such as bends and twists before final sintering, as shown in Figure 95(d). The sintered PZT ceramics demonstrate robust piezoelectric properties, with an average d33 value of 265 pC/N.

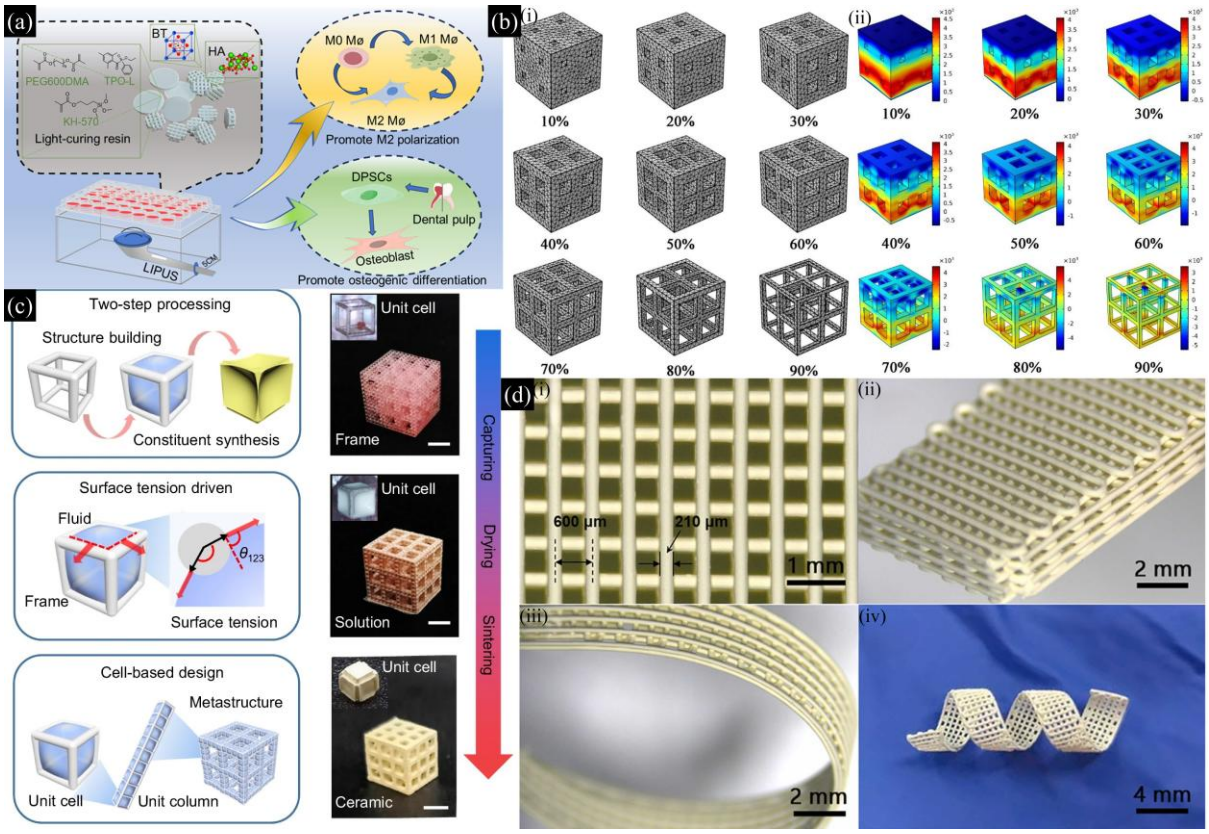

Figure 95: Architectured piezoceramics and immunomodulatory scaffolds for bio-applications : (a) Immunomodulatory Effects of HA/BT Piezoelectric Ceramic Scaffolds on Macrophage Polarization [735], (b) (i) Grid division, (ii) and Potential distribution of 10% - 90% porosity BaTiO3 piezoelectric ceramics [736], (c) Surface Tension-Assisted Two-Step (STATS) Manufacturing Process for 3D-Architected Cellular piezoceramics [737], (d) Optical photos of ceramic green bodies: (i) top view and (ii) side view of 3D woodpile structure, (iii) green body bent into an annulus and (iv) green body twisted into ribbon spiral [739].

9.5.2.2 Shape memory ceramics

Recent advancements in 4D printing have significantly broadened the spectrum of materials that can be used, particularly in the field of shape memory ceramics. These innovative materials exhibit the remarkable ability to change shape in response to external stimuli, such as temperature changes, in a precise and controlled manner [740]. Researchers are actively exploring various compositions and combinations of ceramics to enhance their performance and broaden their potential applications. A notable development by P. Zhao et al. [741] has marked a significant leap forward in 4D printing, enabling the creation of complex, self-deforming ceramic structures. This self-deformation is driven by the formation of a dense alumina-silica (Al_2O_3-SiO_2) mixed region that occurs during the infiltration of molten SiO_2. This process, conducted at high temperatures, induces a notable shrinkage discrepancy between the mixed region and the adjacent pure Al_2O_3 region. Strategic programming of the SiO_2 pattern on the Al_2O_3 substrate allows for precise control over this deformation process, facilitating the creation of intricate shapes and complex structures. As illustrated in Figure 96 (a), the infiltration process increases the density and enhances bonding at the interface, significantly bolstering the structural integrity and preventing cracking at elevated temperatures (1500°C), though these enhancements are less pronounced at lower temperatures (1400°C).

Advanced processing techniques are pivotal in 4D printing of shape memory ceramics, ensuring the achievement of specific material properties and functionalities. These methods facilitate precise control over the geometry, composition, and structural transformation of ceramic materials. Prominent techniques such as direct light processing (DLP) 3D printing, hydrogel ceramic laminates and vat photopolymerization are leading this innovation. R. Wang et al. [742] have developed a novel method that significantly enhances the ability to fabricate complex ceramic structures using 4D printing technology , as illustrated in Figure 96(b) (i). This method utilizes DLP 3D printing to produce hydrogel ceramic laminates, enabling precise control over the geometry and composition of the structures. This capability allows for the transformation of originally flat patterns into complex 3D shapes. The transformation process is detailed in Figure 96(b) (ii), where the flat hydrogel ceramic laminate first undergoes deformation due to dehydration-induced shrinkage of the hydrogel layer. This is followed by a debinding phase at 550°C, which remove the hydrogel and organic components within the ceramic elastomer. the process concludes with a sintering step at 1450°C, which densify the ceramic. The ceramic elastomer slurry used in this process is notably ductile, capable of

enduring tensile elongations of up to 700%. Such ductility is critical to achieve the desired deformations during the 4D printing process, expanding the design possibilities, and enhancing the functional applications of shape memory ceramics.

D. Kong et al. [743] have developed a highly programmable 4D printing process based on vat photopolymerization to produce polymer-derived ceramics (PDCs) with reconfigurable properties and inherent shape memory. This method allows for the creation of intricate ceramic structures with high solid content and resolution. As depicted in Figure 96(c), the printed ceramic structures can undergo autonomous shape changes triggered by their shape memory properties, eliminating the need for external mechanical stresses or complex control systems to enact transformations.

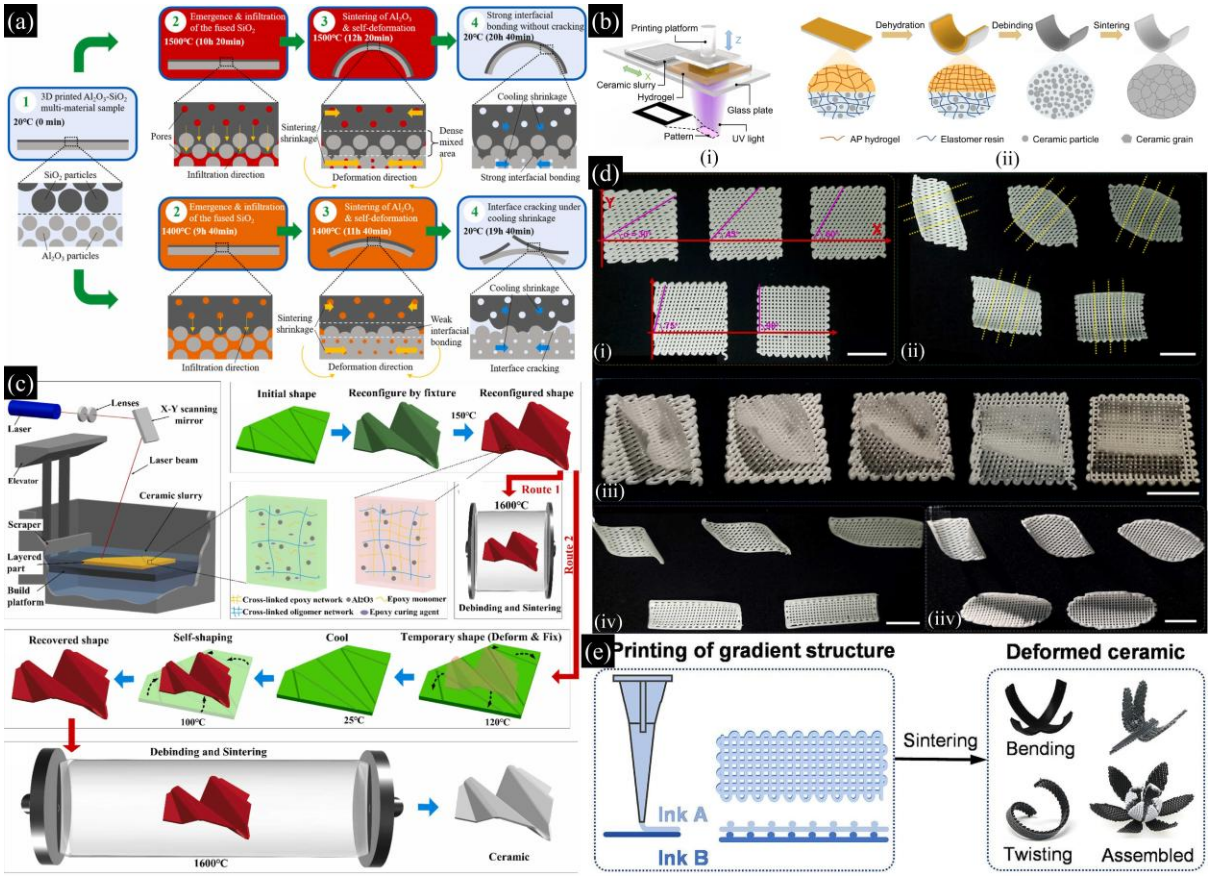

Figure 96: Architectured piezoceramics and immunomodulatory scaffolds for bio-applications : (a) Generation mechanism of self-deformation during the sintering process and the occurrence of cooling cracks at different temperatures [741], (b) (i) Illustration of multimaterial 3D printing a hydrogel-ceramic laminate, (ii) Processes to convert a hydrogel-ceramic laminate to a pure curved ceramic beam. The upper orange layer and lower grey layer in the laminate represent the AP hydrogel and ceramic elastomer, respectively [742], (c) PDCPs Preparation and

Transformation Process in VPP [743], (d) Self-morphing of ceramic bilayers in sintering, (i) Bilayer ceramic squares are printed in different paths, (ii) The shape changes of bilayer ceramic squares after sintering, (iii) The comparison of ceramic squares before and after sintering. (iv) The geometries of bilayer ceramic rectangles after sintering, (iiv) The geometries of bilayer ceramic ellipses after sintering. The scale bare is 10 mm [744], (e) Direct 4D Printing of Bilayer Ceramic Structures and Autonomous Shape Morphing During Sintering [745].

Sintering plays a pivotal role in the 4D printing of ceramics, critically influencing the final properties and functionalities of the printed structures. This process involves heating the ceramic particles to a temperature below their melting point, which facilitates bonding and densification, thereby enhancing the mechanical strength and stability of the material. In the context of 4D printing, sintering is often used to induce differential shrinkage, a key mechanism for enabling shape change in ceramics. F. Wang et al. [744] have demonstrated that by programming the solid content of the ceramic inks and the printing paths, they can precisely control the shape-changing behavior of the ceramic structures during sintering . Their method involves printing two-layer zirconia (ZrO2) ceramics where each layer has a different solid content -high in the bottom layer and low in the top layer. This configuration leads to a shrinkage mismatch during sintering process, causing the flat structures to self-morphize and evolve into complex shapes, as shown in Figure 96(d).

L. Wan et al. [745] presented a novel direct 4D printing approach to fabricate complex ceramic structures that autonomously transform into predetermined shapes, without external stimuli or manual intervention. In their method, a gradient two-layer structure is printed, cured, and sintered, enabling the shape to alter due to differential shrinkage. The printing process uses polydimethylsiloxane (PDMS) inks mixed with varying concentrations of aluminum oxide nanoparticles to create gradient bilayer structures. The different concentrations of aluminum oxide in each layer lead to varying degrees of shrinkage during sintering, facilitating controlled deformation and the formation of intricate shapes, as depicted in Figure 96(e).

9.5.3 Smart Composites

9.5.3.1 Composites-based PEH

Recent advances in piezoelectric energy harvesting have led to significant progress in the development of piezoelectric composites, thereby enhancing their performance and broadening their application scope[399, 746]. N. Shepelin et al. [747] highlights a novel phenomenon known as polarization locking in poly(vinylidene fluoride–co–trifluoroethylene) (PVDF-TrFE) when combined with Ti3C2Tx MXene nanosheets. This polarization locking arises from strong

electrostatic interactions between the PVDF-TrFE and the MXene nanosheets, resulting in superior energy harvesting performance compared to conventional electric poling methods (Figure 97(a)). The piezoelectric charge coefficient (d33) achieved by this composite reaches -52.0 pC/N, which significantly surpasses the -38 pC/N typically observed in electrically polarized PVDF-TrFE.

Ceramic-polymer composites represent one of the most effective classes of piezoelectric materials. These composites blend piezoelectric ceramic nanoparticles into a polymer matrix, merging the high piezoelectric response of ceramics with the mechanical flexibility and durability of polymers. By synthesizing these distinct materials, the resulting composite benefits from the best properties of both constituents.

Z. Wang et al. [748] presented a high flexible ceramic-polymer composite (Figure 97(b)), with (0-3) interconnects consisting of an elastomeric polydimethylsiloxane (PDMS) matrix doped with Ag-coated PNN-PZT (0.55Pb(Ni1/3Nb2/3)O3-0.135PbZrO3-0.315PbTiO3) ceramic heterojunction particles. This combination improves both the flexibility and the electromechanical coupling of the material and resolves the traditional trade-off between mechanical flexibility and piezoelectric performance.

Significant progress in piezoelectric composite technology has been achieved by S. M. A. Z. Shawon et al. [749], who developed an innovative piezoelectric composite material by incorporating doped ZnSnO3 nanocubes with aluminum (Al) nanoparticles into a polydimethylsiloxane (PDMS) matrix. This novel composite results in a flexible piezoelectric film, as depicted in Figure 97(c). The unique combination of ZnSnO3 nanocubes, known for their high piezoelectric potential, with the flexibility and durability of PDMS, makes this material exceptionally suited for use in flexible electronics and wearable devices. The structure and operating principle of this piezoelectric system are illustrated in Figure 97(c).

In addition, Z. Hanani et al. [750] have introduced a highly efficient, lead-free, bio-flexible piezoelectric nanocomposite using Ba0.85Ca0.15Zr0.10Ti0.90O3 (BCZT) nanoparticles functionalized with polydopamine and embedded in a biodegradable polylactic acid (PLA) polymer matrix. This nanogenerator is capable of generating an open-circuit voltage of 14.4 V and a short-circuit current of 0.55 μA under light finger pressure, achieving a maximum power density of 7.54 mW/cm³ at a low resistive load of 3.5 MΩ and retains its high mechanical robustness and stable performance even after a year. Further contributing to the field, J. Villafuerte et al. [751] developed flexible piezoelectric dynamic strain sensors by integrating

Sb-doped ZnO nanowires encapsulated in PMMA, grown on PDMS substrate. This approach demonstrates the significant potential of these materials for use in medical devices, where flexibility and durability are crucial.

In another innovative development, S. Kang et al. [752] crafted a composite material by combining poly(vinylidene fluoride-co-trifluoroethylene) (P(VDF-TrFE)) with surface-modified carbon nanotubes (SMC) and zinc stannate ($ZnSnO_3$) nanoparticles. The $ZnSnO_3$ nanoparticles are anchored onto the SMCs, which are then embedded in the P(VDF-TrFE) matrix, as illustrated in Figure 97(d). This peapod inspired hierarchical design optimally the distributes and integrates the components, resulting to a marked improvement in piezoelectric performance and flexibility.

Overall, these studies highlight the remarkable advancements in 3D printing of piezoelectric composites and demonstrate their potential for energy harvesting, flexible electronics, and wearable technology.

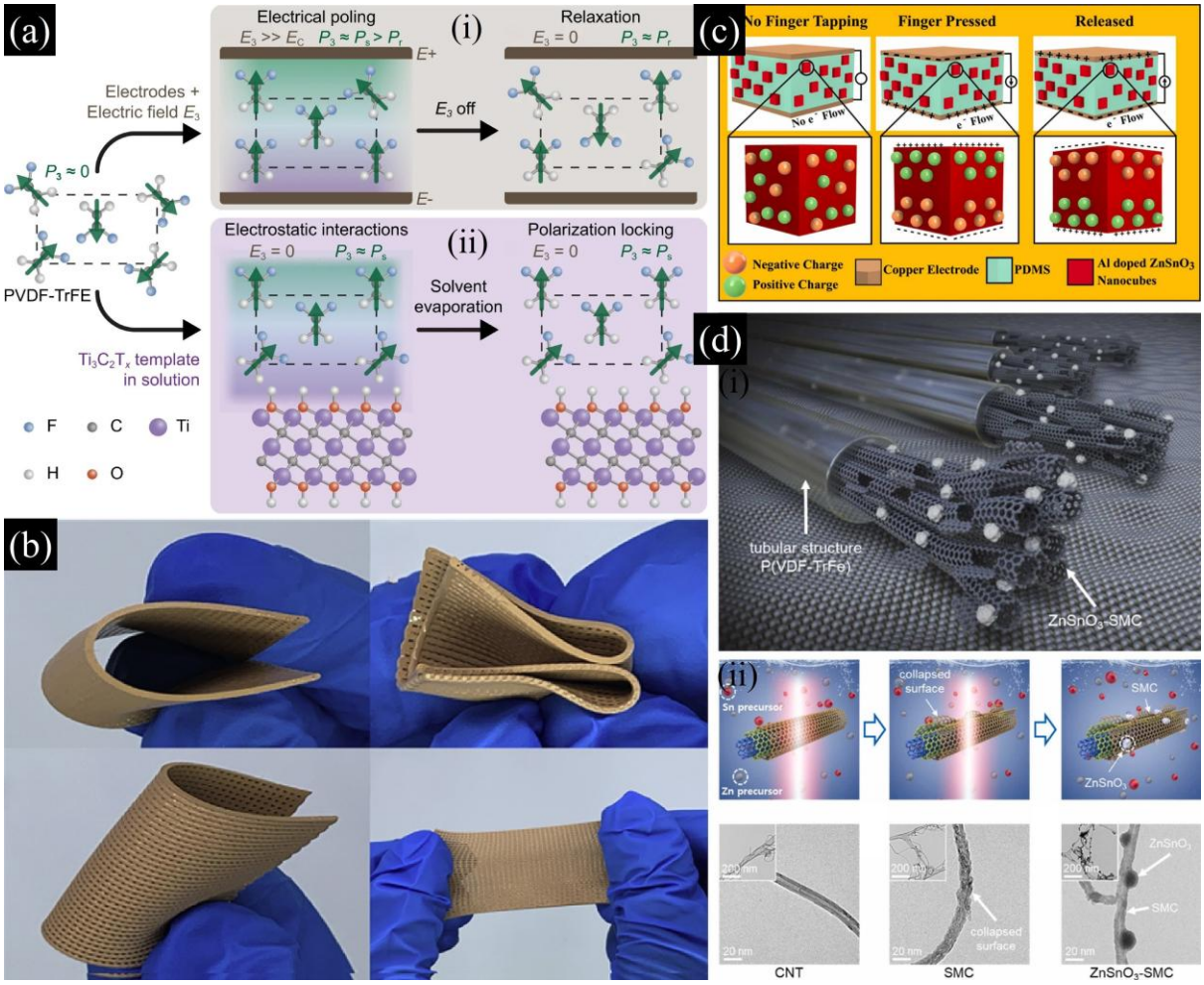

Figure 97: Printed nanocomposites with induced polarization, mechanical flexibility, and hybrid structures : (a) (i) Conventional electrical poling compared to (ii) nanomaterial-Induced polarization locking mechanism in PVDF-TrFE [747], (b) Flexibility and stretching of printed composite presented by bending, twisting, and stretching [748], (c) working principle of the piezoelectric film with the Al–doped $ZnSnO_3$ encapsulated by the PDMS matrix [749], (d) (i) Conceptual illustration showing the ZnSnO3-SMCP(VDF-TrFE) composite, (ii) Schematic depiction of the ZnSnO3-SMC preparation, HR-TEM images showing the formation of ZnSnO3-SMC [752].

9.5.3.2 Shape memory composites

Recent advancement in 3D printing technology have significantly broadened the scope and capabilities of additive manufacturing. A key innovation in this field is the development of continuous fiber-reinforced composites, which enhance the mechanical properties of 4D-printed structures [753]. Q. Wang et al. [754] have introduced a groundbreaking 4D printing method to fabricate continuous fiber-reinforced liquid crystal elastomer (LCE) composites capable of achieving programmable spatial deformation. The proposed method uses a Direct Ink Writing (DIW)-based 4D printing process that allows precise control of fiber placement and orientation within the composite material, as illustrated in Figure 98(a) (i). By adjusting the

off-center distribution of continuous fibers within the composite filament, as shown in Figure 98(a) (ii), the researchers can precisely control the direction and amplitude of bending deformation. This innovative feature provides programmable deformation capabilities, enabling the creation of customized shapes that can dynamically respond to external stimuli such as heat. Similarly, C. Zeng et al. [142] have developed continuous fiber reinforced composite honeycomb structures (CFRCHS) that exhibit excellent shape memory properties. These structures are produced using fused filament fabrication (FFF) technology, based on the co-extrusion process of continuous fibers and polymers. The printer involved features two feed channels connected to the extrusion head, as illustrated in Figure 98(b). Mold recovery tests on these 3D-printed CFRCHS demonstrate their significant potential as crucial components in lightweight smart systems and adaptive energy-absorbing devices. These advancements highlight the versatility and potential of continuous fiber-reinforced composites in various sectors requiring adaptable and responsive materials, from aerospace to automotive and beyond.

Moreover, B. Winhard et al. [755] have pioneered a remarkable advancement in 4D printing technology with the development of nacre-inspired composites through a direct writing strategy. This method innovatively aligns micrometer-sized aluminum oxide platelets along a common plane, effectively replicating the intricate natural structure of nacre. The study introduces a cutting-edge 4D printing that leverages suspension spreading to precisely align the particles. Subsequent solvent evaporation triggers the polycondensation of monomers, culminating in the formation of a vinylogous urethane vitrimer after extrusion, as illustrated in Figure 98(c). The resulting composites have a covalent, adaptable network that facilitates rapid and mechanically loss-free self-healing, reshaping and shape memory capabilities. These properties make the materials suitable for a range of high-value applications, including biomedicine and aerospace.

Innovations in 3D and 4D printing technologies continue to drive the development of advanced materials expanding their potential applications across various industries.

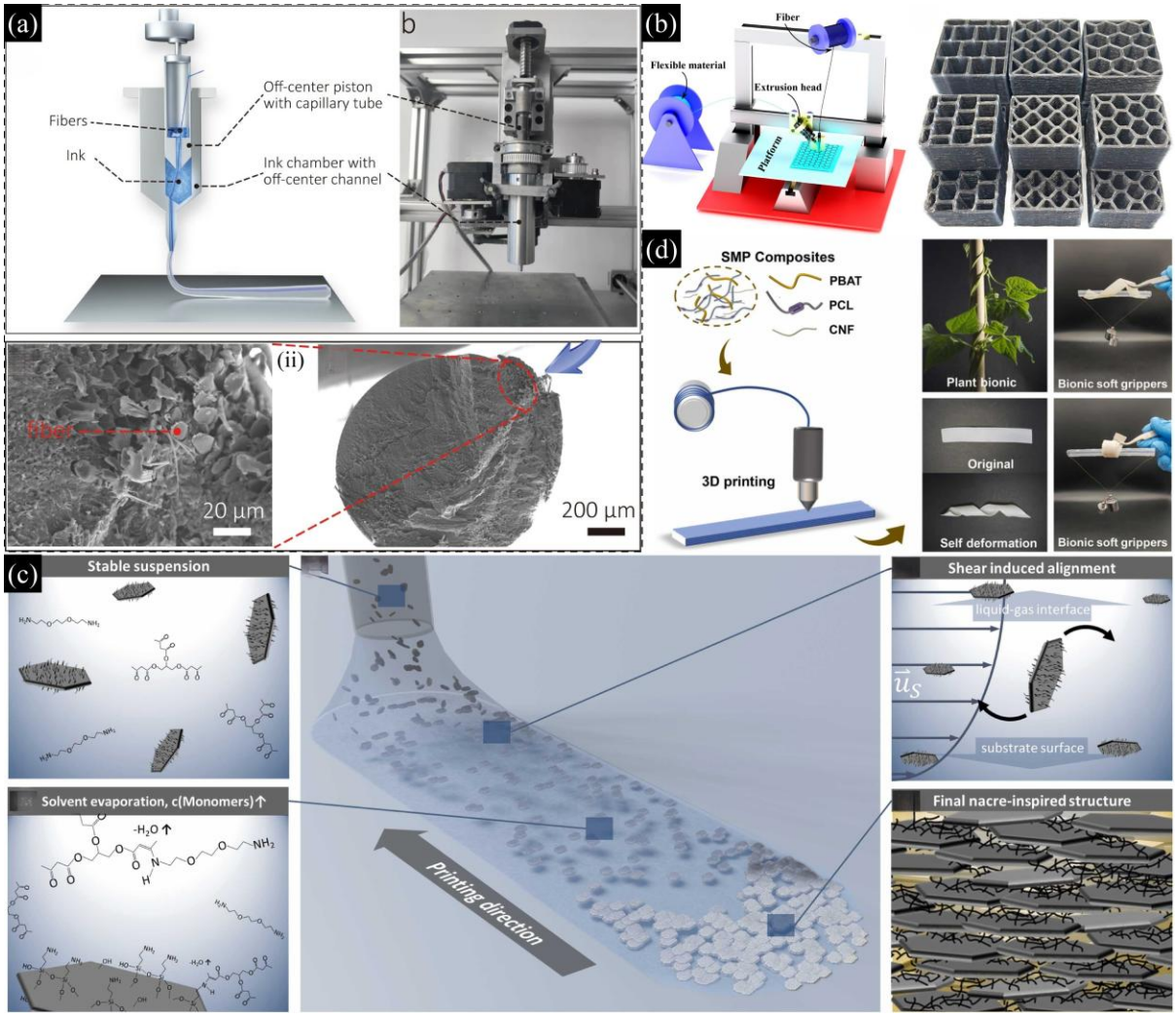

Figure 98: Bioinspired 3D-printed composites with off-center and layered architectures : (a) (i) Preparation of off-center CFRLCE materials [754], (ii) SEM image of the cross section of the composite, indicating the off-center distribution effect of the fiber bundle, (b) Scheme of 3D printing for CFRCHSs [756] (c) Nacre-inspired composites using a direct write printing technology [755], (d) 4D Printing of Shape Memory Polymer (SMP) Composites for Bio-Inspired Self-Deforming Soft Grippers [757].

An outstanding example is the creation of bio-inspired soft grippers using of 4D-printed composites. T. Gu et al. [141] have developed 4D-printed composites combining cellulose nanofibers with shape memory polymers (SMP, which enhance both themechanical properties and functionality of the materials. These advanced composites are intended for use in self-deforming bionic plant grippers that replicate the adaptive movements of plants, as depicted in Figure 98(d). These bionic grippers are particularly suited for fields such as robotics and biomedical devices, where they can handle delicate objects with a high degree of precision and adaptability.

9.6 4DP of Piezoelectric energy harvesters

Piezoelectric materials can be classified as shape memory materials by leveraging their reverse piezoelectric effect, where the application of an electric field induces a shape change. This unique characteristic enables what is commonly referred to as 4D printing, where the fourth dimension stands for the material's ability to evolve over time in response to an external electric field.

In this innovative approach, the reverse piezoelectric effect is utilized, allowing printed structures to programmably change their shape, thereby enhancing their functionality and broadening their utility.

The capacity for piezoelectric materials to undergo shape transformations under electric fields makes them exceptionally suited for advanced applications in smart actuators, adaptive systems, and reconfigurable devices. G. Sossou et al. [758] showcases the potential of this technology through the design and evaluation of smart structures capable of altering their shape or generating mechanical responses when subjected to electric stimuli.

Furthermore, the integration of piezoelectric ceramics with shape memory polymers (SMP) through advanced 3D printing techniques marks a significant advancement in the development of multifunctional materials. This combination utilizes the distinct properties of both materials, resulting in composite that possess both piezoelectric and shape memory functionalities. Such materials can generate electrical signals in response to mechanical deformation and reverting to their original shape upon exposure to specific stimuli, such as temperature changes.

H. Cui et al. [759] have detailed a method for merging piezoelectric ceramics with SMPs through 3D printing technique. The piezoelectric nanocomposite is combined with SMP to produce materials that not only exhibit piezoelectric properties but also have shape memory. This combination leverages the strengths of both materials of each material type, offering a unique approach to fabricating materials that are exceptionally versatile and capable of enhanced performance.

R. Sharma et al. [760] have developed a cutting-edge composite material that integrates polyvinylidene fluoride (PVDF) with barium titanate (BTO) and graphene (Gr) for enhanced multifunctional properties. PVDF is selected for its inherent piezoelectric properties, which are significantly amplified by the addition BTO. Graphene is incorporated to improve the mechanical, thermal, and electrical properties of the composite. This innovative material is

designed for 4D printing applications, capable of responding to external stimuli such as temperature, pressure, or electric fields to adaptively change its shape or properties. The PVDF/BTO/Gr composite exemplifies the convergence of smart material functionalities, making it a prime candidate for advanced manufacturing technologies that require responsive, adaptable materials.

Building on similar principles, S. Bodkhe et al. [761] used polylactic acid (PLA) and polyesteramide (PEA) to fabricate shape memory composites. In this composite, PLA provides the structural rigidity while PEA contributes flexibility, enabling the material to transition states upon heating. To introduce piezoelectric properties, barium titanate (BT) nanoparticles are embedded within the PLA matrix. These nanoparticles facilitate the generation of electrical charges under mechanical deformation, effectively combining shape memory and piezoelectric functionalities in a single material. This synergy not only simplifies the manufacturing process but also enhances the compatibility and functionality of the resulting printed structures.

Furthering this technology, S. Bodkhe et al. [762] developed a PLA/BT nanocomposite that combines multiple functions, including shape memory and piezoelectric properties. This innovation is designed to create materials that can perceive, process, and respond to environmental stimuli, mirroring the adaptive capabilities of natural systems.

The combination of piezoelectric and shape memory effects through advanced 4D printing techniques offers groundbreaking opportunities in fields such as biomedical devices, robotics, and adaptive structures. One promising application is the development of vascular stents that are designed to be compressible for easy insertion and expansible at the target site within the body. These stents could also incorporate built-in sensors to continuously monitor vital signs like blood pressure, enhancing patient care by providing real-time data and potentially reducing the need for invasive follow-up surgeries.

D. Grinberg et al. [763] have combined 4D printing technology with piezoelectric materials to produce advanced medical devices. The 4D printing process involves fabricating objects from piezoelectric composite materials that dynamically alter their shape or properties in response to external stimuli, such as mechanical stress or electric fields. A key focus of this technology is the creation of intelligent medical implants and prostheses. For instance, the development of a knee prosthesis equipped with integrated piezoelectric sensors is underway. These sensors are designed to monitor mechanical loads in real-time, generating electrical signals that provide

crucial insights into the performance and durability of the implant under various stress conditions.

Moreover, H.B. Lee et al. [764] have introduced a new and effective approach for the development of a 3D and soft elastic human interface system based on a piezoelectric mechanical sensor. This system incorporates a piezoelectric layer made from poly(vinylidene fluoride trifluoroethylene) and dual polydimethylsiloxane (PDMS) substrates, with Au-sputtered electrodes enhancing its conductivity and flexibility. The sensor is adept at detecting various physical stimuli, ranging from tactile forces to subtle skin deformations caused by a pulse, highlighting its potential for sensitive, wearable health monitoring devices.

In addition, an underwater acoustic transducer was developed by K. Liu et al. [765] using piezoelectric PZT composites via Direct Ink Writing (DIW). This transducer autonomously modifies its electrical output in response to acoustic stimulation, showcasing the adaptability of piezoelectric devices fabricated via 4D printing and opening new avenues for their use in advanced sensory applications. Despite these advancements, the domain of 4D printing piezoelectric energy harvesters (PEHs) remains underexplored compared to its 3D printing counterpart, which has seen extensive research and numerous technological breakthroughs. The potential of 4D printing for creating adaptable, responsive, and multifunctional PEHs is vast and yet to be fully tapped. The existing research gap presents a significant opportunity for future investigations to harness 4D printing's capabilities to enhance the performance and functionalities of PEHs. Addressing this gap could lead to revolutionary applications and drive further innovations in the field of smart materials and energy harvesting.

9.7 Outlook and perspective

The integration of 4D printing with piezoelectric energy harvesting represents a promising development in materials science and manufacturing technology. This integration enables the production of devices that not only generate electrical energy from mechanical stimuli but also dynamically adapt their shape in response to environmental changes. Such capabilities herald a wide array of applications across biomedicine, robotics, and adaptive systems. Future research should focus on the optimization of AM processes and material formulations to enhance the performance and functionality of 4D-printed PEHs. Furthermore, interdisciplinary collaboration will be crucial to overcome the challenges and unlock the full potential of this technology. With advances in this field, we can expect significant progress in smart materials

and intelligent systems, paving the way for innovative solutions for energy harvesting and adaptive functionality.

9.8 Future Research and Development Priorities

The most important areas of future research and development in the field of 4D printing of piezoelectric materials are described below:

- *Development of new materials:*

-Hybrid materials: development of hybrid materials that combine piezoelectric ceramics and SMP to exhibit both piezoelectric and shape memory effects.

-Nanotechnology composites: enhancing piezoelectric polymer matrices with nanomaterials like graphene and carbon nanotubes to impart enhanced electro- and thermoreactivity.

- *Innovative structures:*

-Metamaterials: development of piezoelectric metamaterials with programmable properties that respond dynamically to external stimuli, enabling novel functionalities.

-Lattice structures: Development of complex lattice structures designs that optimize both energy harvesting capabilities and shape memory features.

- *Multi-material 3D printing technologies:*

-Advanced printing techniques: Integration of advanced multi-material 3D printing techniques such as Direct Ink Writing (DIW), Stereolithography (SLA), and Digital Light Processing (DLP) to fabricate complex, multi-functional piezoelectric devices.

-Sequential layering: Exploring sequential layering strategies to produce multilayer structures with varied material properties to enhance device performance.

- *New applications:*

-Biomedical devices: developing smart, self-powered implants, sensors, and actuators that adapt to bodily movements and harvest energy from physiological activities.

-Wearable Technology: Development of flexible and wearable piezoelectric devices that can monitor health, support sports and fitness applications, and adapt to body temperature.

-Robotics: The integration of 4D-printed piezoelectric materials in soft robotics for adaptable, responsive and energy-efficient components.

-Environmental monitoring: Deployment of piezoelectric sensors in systems that monitor and react to environmental changes like pressure, temperature, and vibration.

- *Optimization and standardization:*

-Process optimization: continuous improvement and optimization of 4D printing processes to achieve higher precision, efficiency, and scalability.

-Standardization: Establishment of standards and guidelines for the production and testing of 4D printed piezoelectric materials to ensure consistent quality and performance.

6. Interdisciplinary collaboration:

-Collaborative research: encouraging interdisciplinary collaboration among materials scientists, engineers, biologists and computer scientists to address complex challenges and foster innovations in 4D printing technologies.

9.9 Conclusion

This review article has highlighted the cutting-edge field of 4D printing of piezoelectric energy harvesters (PEHs), a domain where the traditional capabilities of 3D printing intersect innovatively with the dynamic functionalities of 4D printing. The discourse explored various additive manufacturing (AM) techniques, including fused deposition modeling (FDM), stereolithography (SLA), digital light processing (DLP), and direct ink writing (DIW). Each technique plays a crucial role in fabricating complex and high-performance smart materials that are pivotal in this field.

We discussed recent material advances, focusing on polymers, ceramics, and composites, and their ability to actively respond to a range of stimuli such as heat, light, electrical and magnetic fields, and mechanical vibrations originating from diverse sources like the human body, vehicles, and environmental energy. While the realm of 3D printing of PEHs is well-researched and rich in scholarly contributions, the integration of these advancements with 4D printing technologies remains underexplored.

This review aims to bridge this gap by providing an exhaustive analysis of the current landscape and projecting potential future trajectories for the development of 4D printed PEHs. By doing so, it seeks to spur further research and innovation in this promising area, opening new avenues for the application of these smart materials in various fields such as biomedical devices, adaptive robotics, and sustainable energy solutions. Through continued interdisciplinary

collaboration and technological innovation, 4D printing of PEHs is poised to revolutionize the way we harness energy and interact with our environment, paving the way for the next generation of smart systems and technologies.

9.10 Acknowledgment

The authors acknowledge the funding provided by the Natural Sciences and Engineering Research Council (NSERC) of Canada in the form of Discovery Grants (Grant Number: CRSNG – RGPIN -2021-02846).

9.11 References

[1] R. Krishna, M. Manjaiah, C. Mohan, Developments in additive manufacturing, Additive manufacturing, Elsevier2021, pp. 37-62.
[2] T.D. Ngo, A. Kashani, G. Imbalzano, K.T. Nguyen, D. Hui, Additive manufacturing (3D printing): A review of materials, methods, applications and challenges, Composites Part B: Engineering 143 (2018) 172-196.
[3] A. Megdich, M. Habibi, L. Laperrière, A review on 3D printed piezoelectric energy harvesters: materials, 3D printing techniques, and applications, Materials Today Communications 35 (2023) 105541.
[4] C. Chen, X. Wang, Y. Wang, D. Yang, F. Yao, W. Zhang, B. Wang, G.A. Sewvandi, D. Yang, D. Hu, Additive manufacturing of piezoelectric materials, Advanced Functional Materials 30(52) (2020) 2005141.
[5] H. Chu, W. Yang, L. Sun, S. Cai, R. Yang, W. Liang, H. Yu, L. Liu, 4D printing: a review on recent progresses, Micromachines 11(9) (2020) 796.
[6] A. Megdich, M. Habibi, L. Laperrière, A review on 4D printing: Material structures, stimuli and additive manufacturing techniques, Materials Letters 337 (2023) 133977.
[7] S.-M. Chang, S. Hur, J. Park, D.-G. Lee, J. Shin, H.S. Kim, S.E. Song, J.M. Baik, M. Kim, H.-C. Song, Optimization of piezoelectric polymer composites and 3D printing parameters for flexible tactile sensors, Additive Manufacturing 67 (2023) 103470.
[8] A. Ahmadpour, A.K. Yetisen, S. Tasoglu, Piezoelectric metamaterial blood pressure sensor, ACS Applied Electronic Materials 5(6) (2023) 3280-3290.
[9] S. Gao, A.K. Gain, L. Zhang, A metamaterial for wearable piezoelectric energy harvester, Smart Materials and Structures 30(1) (2020) 015026.
[10] L. Lu, W. Ding, J. Liu, B. Yang, Flexible PVDF based piezoelectric nanogenerators, Nano Energy 78 (2020) 105251.
[11] S. Sukumaran, S. Chatbouri, D. Rouxel, E. Tisserand, F. Thiebaud, T. Ben Zineb, Recent advances in flexible PVDF based piezoelectric polymer devices for energy harvesting applications, J. Intell. Mater. Syst. Struct. 32(7) (2021) 746-780.
[12] A. Meshkinzar, A. M. Al-Jumaily, Cylindrical piezoelectric PZT transducers for sensing and actuation, Sensors 23(6) (2023) 3042.
[13] G. Song, Z. Liu, F. Zhang, F. Liu, Y. Gu, Z. Liu, Y. Li, High-throughput synthesis and electrical properties of BNT–BT–KNN lead-free piezoelectric ceramics, Journal of Materials Chemistry C 8(11) (2020) 3655-3662.
[14] X. Du, Z. Zhou, Z. Zhang, L. Yao, Q. Zhang, H. Yang, Porous, multi-layered piezoelectric composites based on highly oriented PZT/PVDF electrospinning fibers for high-performance piezoelectric nanogenerators, Journal of Advanced Ceramics 11 (2022) 331-344.

[15] N. Chamankar, R. Khajavi, A.A. Yousefi, A. Rashidi, F. Golestanifard, A flexible piezoelectric pressure sensor based on PVDF nanocomposite fibers doped with PZT particles for energy harvesting applications, Ceramics International 46(12) (2020) 19669-19681.
[16] J.-X. Chen, J.-W. Li, C.-C. Cheng, C.-W. Chiu, Piezoelectric property enhancement of PZT/Poly (vinylidenefluoride-co-trifluoroethylene) hybrid films for flexible piezoelectric energy harvesters, ACS omega 7(1) (2021) 793-803.
[17] P. Bhatele, S. Mali, A. Mali, M. Chrungoo, A. Mali, R. Makode, Energy Generation Via Footsteps Using Piezoelectric Sensor, International Research Journal of Engineering and Technology (2022) 9-12.
[18] M. Logeshwaran, J.J.J. Sheela, A.P. Priya, A High-Efficiency Power Generator by Footsteps Using Piezoelectric Effect, 2022 Second International Conference on Artificial Intelligence and Smart Energy (ICAIS), IEEE, 2022, pp. 1547-1553.
[19] H.D. Mayekol Mayck, A.M.R. Fath El-Bab, E. Murimi, P. Moukala Mpele, A human heartbeat frequencies based 2-DOF piezoelectric energy harvester for pacemaker application, Energy Harvesting and Systems 8(1) (2021) 1-11.
[20] Y. Luo, Y. Xiao, J. Liu, Y. Wu, Z. Zhao, Design and application of a flexible nano cardiac sound sensor based on P (VDF-TrFE)/KNN/GR composite piezoelectric film for heart disease diagnosis, Nanotechnology 35(7) (2023) 075502.
[21] D. Al-Yafeai, T. Darabseh, A.-H. I. Mourad, A state-of-the-art review of car suspension-based piezoelectric energy harvesting systems, Energies 13(9) (2020) 2336.
[22] Y.L. Morangueira, J.C.d.C. Pereira, Energy harvesting assessment with a coupled full car and piezoelectric model, Energy 210 (2020) 118668.
[23] A. Ali, S. Ali, H. Shaukat, E. Khalid, L. Behram, H. Rani, W.A. Altabey, S.A. Kouritem, M. Noori, Advancements in piezoelectric wind energy harvesting: A review, Results in Engineering (2024) 101777.
[24] Y. Wu, Y. Ma, H. Zheng, S. Ramakrishna, Piezoelectric materials for flexible and wearable electronics: A review, Materials & Design 211 (2021) 110164.
[25] S.D. Mahapatra, P.C. Mohapatra, A.I. Aria, G. Christie, Y.K. Mishra, S. Hofmann, V.K. Thakur, Piezoelectric materials for energy harvesting and sensing applications: roadmap for future smart materials, Advanced Science 8(17) (2021) 2100864.
[26] N.M. Nor, H.H. Hamzah, K.A. Razak, Recent advancement in sustainable energy harvesting using piezoelectric materials, Sustainable Materials for Next Generation Energy Devices, Elsevier2021, pp. 221-248.
[27] I. Akbar, M. El Hadrouz, M. El Mansori, D. Lagoudas, Toward enabling manufacturing paradigm of 4D printing of shape memory materials: Open literature review, European Polymer Journal 168 (2022) 111106.
[28] J. Zhang, Z. Yin, L. Ren, Q. Liu, L. Ren, X. Yang, X. Zhou, Advances in 4D printed shape memory polymers: from 3D printing, smart excitation, and response to applications, Advanced Materials Technologies 7(9) (2022) 2101568.
[29] W. Zhao, C. Yue, L. Liu, Y. Liu, J. Leng, Research progress of shape memory polymer and 4D printing in biomedical application, Advanced Healthcare Materials 12(16) (2023) 2201975.
[30] X. Wang, Y. He, Y. Liu, J. Leng, Advances in shape memory polymers: Remote actuation, multi-stimuli control, 4D printing and prospective applications, Materials Science and Engineering: R: Reports 151 (2022) 100702.
[31] G. Liu, X. Zhang, X. Lu, Y. Zhao, Z. Zhou, J. Xu, J. Yin, T. Tang, P. Wang, S. Yi, 4D additive–subtractive manufacturing of shape memory ceramics, Advanced Materials 35(39) (2023) 2302108.
[32] S. Chen, J. Li, H. Shi, X. Chen, G. Liu, S. Meng, J. Lu, Lightweight and geometrically complex ceramics derived from 4D printed shape memory precursor with reconfigurability and

programmability for sensing and actuation applications, Chemical Engineering Journal 455 (2023) 140655.
[33] X. Huang, M. Panahi-Sarmad, K. Dong, R. Li, T. Chen, X. Xiao, Tracing evolutions in electro-activated shape memory polymer composites with 4D printing strategies: a systematic review, Composites Part A: Applied Science and Manufacturing 147 (2021) 106444.
[34] M.A. Kouka, F. Abbassi, M. Habibi, F. Chabert, A. Zghal, C. Garnier, 4D printing of shape memory polymers, blends, and composites and their advanced applications: a comprehensive literature review, Advanced Engineering Materials 25(4) (2023) 2200650.
[35] M. Ramezani, Z. Mohd Ripin, 4D printing in biomedical engineering: Advancements, challenges, and future directions, Journal of functional biomaterials 14(7) (2023) 347.
[36] K. McLellan, Y.-C. Sun, H.E. Naguib, A review of 4D printing: Materials, structures, and designs towards the printing of biomedical wearable devices, Bioprinting 27 (2022) e00217.
[37] S.Y. Hann, H. Cui, M. Nowicki, L.G. Zhang, 4D printing soft robotics for biomedical applications, Additive Manufacturing 36 (2020) 101567.
[38] M.Y. Khalid, Z.U. Arif, W. Ahmed, R. Umer, A. Zolfagharian, M. Bodaghi, 4D printing: Technological developments in robotics applications, Sensors and Actuators A: Physical 343 (2022) 113670.
[39] S. Gopinath, N.N. Adarsh, P. Radhakrishnan Nair, S. Mathew, Recent trends in thermo-responsive elastomeric shape memory polymer nanocomposites, Polymer Composites 44(8) (2023) 4433-4458.
[40] A. Andreu, P.-C. Su, J.-H. Kim, C.S. Ng, S. Kim, I. Kim, J. Lee, J. Noh, A.S. Subramanian, Y.-J. Yoon, 4D printing materials for vat photopolymerization, Additive Manufacturing 44 (2021) 102024.
[41] H. Wang, J. Zhao, Z. Luo, Z. Li, Recent research developments of 4D printing technology for magnetically controlled smart materials: a review, Magnetochemistry 9(8) (2023) 204.
[42] F. Momeni, X. Liu, J. Ni, A review of 4D printing, Materials & design 122 (2017) 42-79.
[43] X. Yuan, Z. Mai, Z. Li, Z. Yu, P. Ci, S. Dong, A 3D-printing approach toward flexible piezoelectronics with function diversity, Materials Today (2023).
[44] S. Bodkhe, P. Ermanni, Challenges in 3D printing of piezoelectric materials, Multifunctional Materials 2(2) (2019) 022001.
[45] J. Fan, L. Zhang, S. Wei, Z. Zhang, S.-K. Choi, B. Song, Y. Shi, A review of additive manufacturing of metamaterials and developing trends, Materials Today 50 (2021) 303-328.
[46] A. Ziadia, M. Habibi, S. Kelouwani, Machine Learning Study of the Effect of Process Parameters on Tensile Strength of FFF PLA and PLA-CF, Eng 4(4) (2023) 2741-2763.
[47] I.J. Solomon, P. Sevvel, J. Gunasekaran, A review on the various processing parameters in FDM, Materials Today: Proceedings 37 (2021) 509-514.
[48] A. Dey, N. Yodo, A systematic survey of FDM process parameter optimization and their influence on part characteristics, Journal of Manufacturing and Materials Processing 3(3) (2019) 64.
[49] Z. Abdelhamid, H. Mohamed, S. Kelouwani, The use of machine learning in process–structure–property modeling for material extrusion additive manufacturing: a state-of-the-art review, Journal of the Brazilian Society of Mechanical Sciences and Engineering 46(2) (2024) 70.
[50] R. Patel, C. Desai, S. Kushwah, M. Mangrola, A review article on FDM process parameters in 3D printing for composite materials, Materials Today: Proceedings 60 (2022) 2162-2166.
[51] A. Kafle, E. Luis, R. Silwal, H.M. Pan, P.L. Shrestha, A.K. Bastola, 3D/4D printing of polymers: fused deposition modelling (FDM), selective laser sintering (SLS), and stereolithography (SLA), Polymers 13(18) (2021) 3101.

[52] J. Huang, Q. Qin, J. Wang, A review of stereolithography: Processes and systems, Processes 8(9) (2020) 1138.
[53] M. Mukhtarkhanov, A. Perveen, D. Talamona, Application of stereolithography based 3D printing technology in investment casting, Micromachines 11(10) (2020) 946.
[54] Z. Zhao, X. Tian, X. Song, Engineering materials with light: recent progress in digital light processing based 3D printing, Journal of Materials Chemistry C 8(40) (2020) 13896-13917.
[55] J. Zhang, Q. Hu, S. Wang, J. Tao, M. Gou, Digital light processing based three-dimensional printing for medical applications, International journal of bioprinting 6(1) (2020).
[56] M. Saadi, A. Maguire, N.T. Pottackal, M.S.H. Thakur, M.M. Ikram, A.J. Hart, P.M. Ajayan, M.M. Rahman, Direct ink writing: a 3D printing technology for diverse materials, Advanced Materials 34(28) (2022) 2108855.
[57] R.Y. Tay, Y. Song, D.R. Yao, W. Gao, Direct-ink-writing 3D-printed bioelectronics, Materials Today (2023).
[58] S. Tagliaferri, A. Panagiotopoulos, C. Mattevi, Direct ink writing of energy materials, Materials Advances 2(2) (2021) 540-563.
[59] N.W. Solís Pinargote, A. Smirnov, N. Peretyagin, A. Seleznev, P. Peretyagin, Direct ink writing technology (3d printing) of graphene-based ceramic nanocomposites: A review, Nanomaterials 10(7) (2020) 1300.
[60] M.K. Kim, I.H. Lee, H.-C. Kim, Effect of fabrication parameters on surface roughness of FDM parts, International Journal of Precision Engineering and Manufacturing 19 (2018) 137-142.
[61] V. Shanmugam, O. Das, K. Babu, U. Marimuthu, A. Veerasimman, D.J. Johnson, R.E. Neisiany, M.S. Hedenqvist, S. Ramakrishna, F. Berto, Fatigue behaviour of FDM-3D printed polymers, polymeric composites and architected cellular materials, International Journal of Fatigue 143 (2021) 106007.
[62] A.M. Arefin, N.R. Khatri, N. Kulkarni, P.F. Egan, Polymer 3D printing review: Materials, process, and design strategies for medical applications, Polymers 13(9) (2021) 1499.
[63] F. Jelínek, P. Breedveld, Design for additive manufacture of fine medical instrumentation—DragonFlex case study, Journal of Mechanical Design 137(11) (2015) 111416.
[64] E.M. Maines, M.K. Porwal, C.J. Ellison, T.M. Reineke, Sustainable advances in SLA/DLP 3D printing materials and processes, Green Chemistry 23(18) (2021) 6863-6897.
[65] M. Pagac, J. Hajnys, Q.-P. Ma, L. Jancar, J. Jansa, P. Stefek, J. Mesicek, A review of vat photopolymerization technology: materials, applications, challenges, and future trends of 3D printing, Polymers 13(4) (2021) 598.
[66] J. Borrello, P. Nasser, J.C. Iatridis, K.D. Costa, 3D printing a mechanically-tunable acrylate resin on a commercial DLP-SLA printer, Additive manufacturing 23 (2018) 374-380.
[67] Z. Chen, Z. Li, J. Li, C. Liu, C. Lao, Y. Fu, C. Liu, Y. Li, P. Wang, Y. He, 3D printing of ceramics: A review, Journal of the European Ceramic Society 39(4) (2019) 661-687.
[68] H. Quan, T. Zhang, H. Xu, S. Luo, J. Nie, X. Zhu, Photo-curing 3D printing technique and its challenges, Bioactive materials 5(1) (2020) 110-115.
[69] S.P. Stier, H. Böse, Ablative Laser Structuring for Stretchable Multilayer and Multi-Material Electronics and Sensor Systems, Proceedings, MDPI, 2020, p. 21.
[70] J. Gopinathan, I. Noh, Recent trends in bioinks for 3D printing, Biomaterials research 22(1) (2018) 11.
[71] Y.L. Yap, S.L. Sing, W.Y. Yeong, A review of 3D printing processes and materials for soft robotics, Rapid Prototyping Journal 26(8) (2020) 1345-1361.
[72] T. Sathies, P. Senthil, M. Anoop, A review on advancements in applications of fused deposition modelling process, Rapid Prototyping Journal 26(4) (2020) 669-687.

[73] S.C. Daminabo, S. Goel, S.A. Grammatikos, H.Y. Nezhad, V.K. Thakur, Fused deposition modeling-based additive manufacturing (3D printing): techniques for polymer material systems, Materials today chemistry 16 (2020) 100248.
[74] A.J. Sheoran, H. Kumar, Fused Deposition modeling process parameters optimization and effect on mechanical properties and part quality: Review and reflection on present research, Materials Today: Proceedings 21 (2020) 1659-1672.
[75] R.B. Kristiawan, F. Imaduddin, D. Ariawan, Ubaidillah, Z. Arifin, A review on the fused deposition modeling (FDM) 3D printing: Filament processing, materials, and printing parameters, Open Engineering 11(1) (2021) 639-649.
[76] N. Sezer, M. Koç, A comprehensive review on the state-of-the-art of piezoelectric energy harvesting, Nano energy 80 (2021) 105567.
[77] M. Lalegani Dezaki, M.K.A. Mohd Ariffin, S. Hatami, An overview of fused deposition modelling (FDM): Research, development and process optimisation, Rapid Prototyping Journal 27(3) (2021) 562-582.
[78] X. Liu, Y. Shang, J. Liu, Z. Shao, C. Zhang, 3D printing-enabled in-situ orientation of BaTi2O5 nanorods in β-PVDF for high-efficiency piezoelectric energy harvesters, ACS Applied Materials & Interfaces 14(11) (2022) 13361-13368.
[79] H. Pei, J. Jing, Y. Chen, J. Guo, N. Chen, 3D printing of PVDF-based piezoelectric nanogenerator from programmable metamaterial design: Promising strategy for flexible electronic skin, Nano Energy 109 (2023) 108303.
[80] A. Megdich, M. Habibi, L. Laperrière, Z. Li, Y. Abdin, Enhanced piezoelectric performance of PVDF/MWCNTs energy harvester through a 3D-printed multimodal auxetic structure for smart security systems, Materials Today Sustainability 27 (2024) 100847.
[81] Y. Du, R. Wang, M. Zeng, S. Xu, M. Saeidi-Javash, W. Wu, Y. Zhang, Hybrid printing of wearable piezoelectric sensors, Nano Energy 90 (2021) 106522.
[82] A. Megdich, M. Habibi, L. Laperrière, Z. Li, Y. Abdin, Advanced 3D-printed PVDF/BT piezoelectric energy harvester with a bio-inspired 3D structure for a self-powered smart mouse, Nano Energy (2024) 109876.
[83] H. Pei, Y. Chen, Q. Lv, Z. Peng, X. Wang, N. Chen, H. Zhang, A novel microwave assisted multi-material 3D printing strategy to architect lamellar piezoelectric generators for intelligent sensing, Composites Part B: Engineering 280 (2024) 111529.
[84] M.Q. Zafar, H. Zhao, 4D printing: future insight in additive manufacturing, Metals and Materials International 26 (2020) 564-585.
[85] B. Karima, M. Habibi, L. Laperrière, 4D printing of fiber-reinforced auxetic structures: the building blocks: a review, Smart Material Structures 33(6) (2024) 063001.
[86] J. Carrell, G. Gruss, E. Gomez, Four-dimensional printing using fused-deposition modeling: a review, Rapid Prototyping Journal 26(5) (2020) 855-869.
[87] M. Bodaghi, R. Noroozi, A. Zolfagharian, M. Fotouhi, S. Norouzi, 4D printing self-morphing structures, Materials 12(8) (2019) 1353.
[88] P. Fu, H. Li, J. Gong, Z. Fan, A.T. Smith, K. Shen, T.O. Khalfalla, H. Huang, X. Qian, J.R. McCutcheon, 4D printing of polymers: Techniques, materials, and prospects, Progress in Polymer Science 126 (2022) 101506.
[89] M. Bodaghi, A. Serjouei, A. Zolfagharian, M. Fotouhi, H. Rahman, D. Durand, Reversible energy absorbing meta-sandwiches by FDM 4D printing, International Journal of Mechanical Sciences 173 (2020) 105451.
[90] S.-J. Ahn, H. Lee, K.-J. Cho, 3D printing with a 3D printed digital material filament for programming functional gradients, Nature Communications 15(1) (2024) 3605.
[91] C.-Y. Cheng, H. Xie, Z.-y. Xu, L. Li, M.-N. Jiang, L. Tang, K.-K. Yang, Y.-Z. Wang, 4D printing of shape memory aliphatic copolyester via UV-assisted FDM strategy for medical protective devices, Chemical Engineering Journal 396 (2020) 125242.

[92] M. Barletta, A. Gisario, M. Mehrpouya, 4D printing of shape memory polylactic acid (PLA) components: Investigating the role of the operational parameters in fused deposition modelling (FDM), Journal of Manufacturing Processes 61 (2021) 473-480.
[93] M. Hosseinzadeh, M. Ghoreishi, K. Narooei, 4D printing of shape memory polylactic acid beams: An experimental investigation into FDM additive manufacturing process parameters, mathematical modeling, and optimization, Journal of Manufacturing Processes 85 (2023) 774-782.
[94] F. Wang, F. Luo, Y. Huang, X. Cao, C. Yuan, 4D printing via multispeed fused deposition modeling, Advanced Materials Technologies 8(2) (2023) 2201383.
[95] R. Noroozi, M. Bodaghi, H. Jafari, A. Zolfagharian, M. Fotouhi, Shape-adaptive metastructures with variable bandgap regions by 4D printing, Polymers 12(3) (2020) 519.
[96] T. van Manen, S. Janbaz, K.M. Jansen, A.A. Zadpoor, 4D printing of reconfigurable metamaterials and devices, Communications Materials 2(1) (2021) 56.
[97] S.K. Melly, L. Liu, Y. Liu, J. Leng, On 4D printing as a revolutionary fabrication technique for smart structures, Smart Materials and Structures 29(8) (2020) 083001.
[98] H.A. Alshahrani, Review of 4D printing materials and reinforced composites: Behaviors, applications and challenges, Journal of Science: Advanced Materials and Devices 6(2) (2021) 167-185.
[99] J. Saroia, Y. Wang, Q. Wei, M. Lei, X. Li, Y. Guo, K. Zhang, A review on 3D printed matrix polymer composites: its potential and future challenges, The international journal of advanced manufacturing technology 106 (2020) 1695-1721.
[100] K. Mohammad-Jafari, S.M. Naghib, 3D Printing of Microfluidic-assisted Liposomes Production for Drug Delivery and Nanobiomedicine: A Review, Current Medicinal Chemistry (2024).
[101] A. Subash, B. Kandasubramanian, 4D printing of shape memory polymers, European Polymer Journal 134 (2020) 109771.
[102] D. Sun, Y. Lu, T. Karaki, Review of the applications of 3D printing technology in the field of piezoelectric ceramics, Resources Chemicals and Materials 2(2) (2023) 128-142.
[103] W. Wang, J. Sun, B. Guo, X. Chen, K.P. Ananth, J. Bai, Fabrication of piezoelectric nano-ceramics via stereolithography of low viscous and non-aqueous suspensions, Journal of the European Ceramic Society 40(3) (2020) 682-688.
[104] K. Zheng, D. Ding, Y. Quan, J. Zhuang, C. Fei, J. Zhao, L. Wang, T. Zhao, Z. Wang, M. Liu, 3D printing orientation controlled PMN-PT piezoelectric ceramics, Journal of the European Ceramic Society 43(6) (2023) 2408-2416.
[105] H. Lu, H. Cui, G. Lu, L. Jiang, R. Hensleigh, Y. Zeng, A. Rayes, M.K. Panduranga, M. Acharya, Z. Wang, 3D Printing and processing of miniaturized transducers with near-pristine piezoelectric ceramics for localized cavitation, Nature communications 14(1) (2023) 2418.
[106] L. He, X. Wang, F. Fei, L. Chen, X. Song, Selectively doped piezoelectric ceramics with tunable piezoelectricity via suspension-enclosing projection stereolithography, Additive manufacturing 48 (2021) 102407.
[107] A. Sotov, A. Kantyukov, A. Popovich, V. Sufiiarov, LCD-SLA 3D printing of BaTiO3 piezoelectric ceramics, Ceramics International 47(21) (2021) 30358-30366.
[108] D. Yao, H. Cui, R. Hensleigh, P. Smith, S. Alford, D. Bernero, S. Bush, K. Mann, H.F. Wu, M. Chin-Nieh, Achieving the upper bound of piezoelectric response in tunable, wearable 3D printed nanocomposites, Advanced Functional Materials 29(42) (2019) 1903866.
[109] T. Brossier, M. Habib, B.T. Benkhaled, G. Volpi, V. Lapinte, S. Blanquer, 4D printing of hydrogels based on poly (oxazoline) and poly (acrylamide) copolymers by stereolithography, Materials Advances (2024).

[110] S. Miao, H. Cui, M. Nowicki, S.-j. Lee, J. Almeida, X. Zhou, W. Zhu, X. Yao, F. Masood, M.W. Plesniak, Photolithographic-stereolithographic-tandem fabrication of 4D smart scaffolds for improved stem cell cardiomyogenic differentiation, Biofabrication 10(3) (2018) 035007.
[111] Y.Y.C. Choong, S. Maleksaeedi, H. Eng, J. Wei, P.-C. Su, 4D printing of high performance shape memory polymer using stereolithography, Materials & Design 126 (2017) 219-225.
[112] A.S. Mathews, S. Abraham, S.K. Kumaran, J. Fan, C. Montemagno, Bio nano ink for 4D printing membrane proteins, RSC advances 7(66) (2017) 41429-41434.
[113] J. Chowdhury, P.V. Anirudh, C. Karunakaran, V. Rajmohan, A.T. Mathew, K. Koziol, W.F. Alsanie, C. Kannan, A.S. Balan, V.K. Thakur, 4D printing of smart polymer nanocomposites: integrating graphene and acrylate based shape memory polymers, Polymers 13(21) (2021) 3660.
[114] R. Yu, X. Yang, Y. Zhang, X. Zhao, X. Wu, T. Zhao, Y. Zhao, W. Huang, Three-dimensional printing of shape memory composites with epoxy-acrylate hybrid photopolymer, ACS Applied Materials & Interfaces 9(2) (2017) 1820-1829.
[115] N. Inverardi, S. Pandini, F. Bignotti, G. Scalet, S. Marconi, F. Auricchio, Sequential motion of 4D printed photopolymers with broad glass transition, Macromolecular Materials and Engineering 305(1) (2020) 1900370.
[116] Q. Ge, B. Jian, H. Li, Shaping soft materials via digital light processing-based 3D printing: A review, Forces in Mechanics 6 (2022) 100074.
[117] M. Yang, K. Kowsari, N.O. Myrie, D. Espinosa-Hoyos, A. Jagielska, S. Kim, N.X. Fang, K.J. Van Vliet, Additive manufacturing of high aspect-ratio structures with self-focusing photopolymerization, Light: Advanced Manufacturing 3(3) (2022) 542-571.
[118] C.-L. Liu, Q. Du, J.-M. Wu, G. Zhang, Y.-S. Shi, Novel 3D printed PZT-based piezoceramics for piezoelectric energy harvesting via digital light processing, Chemical Engineering Journal 492 (2024) 152004.
[119] Q. He, Y. Zeng, L. Jiang, Z. Wang, G. Lu, H. Kang, P. Li, B. Bethers, S. Feng, L. Sun, Growing recyclable and healable piezoelectric composites in 3D printed bioinspired structure for protective wearable sensor, Nature Communications 14(1) (2023) 6477.
[120] J. Shi, K. Ju, H. Chen, A. Mirabolghasemi, S. Akhtar, A. Sasmito, A. Akbarzadeh, 3D Printed Architected Shell-based Ferroelectric Metamaterials with Programmable Piezoelectric and Pyroelectric properties, Nano Energy (2024) 109385.
[121] L. Yue, S. Macrae Montgomery, X. Sun, L. Yu, Y. Song, T. Nomura, M. Tanaka, H. Jerry Qi, Single-vat single-cure grayscale digital light processing 3D printing of materials with large property difference and high stretchability, Nature communications 14(1) (2023) 1251.
[122] N. Paunović, D. Meyer, A. Krivitsky, A.R. Studart, Y. Bao, J.-C. Leroux, 4D printing of biodegradable elastomers with tailorable thermal response at physiological temperature, Journal of Controlled Release 361 (2023) 417-426.
[123] A. Cosola, M. Sangermano, D. Terenziani, R. Conti, M. Messori, H. Grützmacher, C.F. Pirri, A. Chiappone, DLP 3D–printing of shape memory polymers stabilized by thermoreversible hydrogen bonding interactions, Applied Materials Today 23 (2021) 101060.
[124] Y. He, R. Yu, X. Li, M. Zhang, Y. Zhang, X. Yang, X. Zhao, W. Huang, Digital light processing 4D printing of transparent, strong, highly conductive hydrogels, ACS Applied Materials & Interfaces 13(30) (2021) 36286-36294.
[125] A.K. Miri, D. Nieto, L. Iglesias, H. Goodarzi Hosseinabadi, S. Maharjan, G.U. Ruiz-Esparza, P. Khoshakhlagh, A. Manbachi, M.R. Dokmeci, S. Chen, Microfluidics-enabled multimaterial maskless stereolithographic bioprinting, Advanced Materials 30(27) (2018) 1800242.

[126] Q.T. Che, J.W. Seo, K. Charoensri, M.H. Nguyen, H.J. Park, H. Bae, 4D-printed microneedles from dual-sensitive chitosan for non-transdermal drug delivery, International Journal of Biological Macromolecules 261 (2024) 129638.
[127] X. Wan, L. Luo, Y. Liu, J. Leng, Direct ink writing based 4D printing of materials and their applications, Advanced Science 7(16) (2020) 2001000.
[128] K.R. Ryan, M.P. Down, C.E. Banks, Future of additive manufacturing: Overview of 4D and 3D printed smart and advanced materials and their applications, Chemical Engineering Journal 403 (2021) 126162.
[129] B. Wang, M. Gao, X. Fu, M. Geng, Y. Liu, N. Cheng, J. Li, L. Li, Z. Zhang, Y. Song, 3D printing deep-trap hierarchical architecture-based non-contact sensor for multi-direction motion monitoring, Nano Energy 107 (2023) 108135.
[130] F. Chen, Z. An, Y. Chen, Y. Li, X. Liu, N. Chen, Y. Ru, D. Gao, Multi-material 3D printing of piezoelectric and triboelectric integrated nanogenerators with voxel structure, Chemical Engineering Journal 471 (2023) 144770.
[131] R. Tao, F. Granier, D. Therriault, Multi-material freeform 3D printing of flexible piezoelectric composite sensors using a supporting fluid, Additive Manufacturing 60 (2022) 103243.
[132] S.S. Hossain, S. Jang, S. Park, C.-J. Bae, Understanding ink design and printing dynamics of extrusion-based 3D printing: Defect-free dense piezoelectric ceramics, Journal of Manufacturing Processes 92 (2023) 1-11.
[133] Y. Zhou, G. Wei, J. Yuan, X. Sang, J.-T. Miao, R. Liu, UV-assisted direct ink writing 4D printing of benzoxazine/epoxy thermosets, Chemical Engineering Journal 477 (2023) 147221.
[134] A. Sun, S. Ma, X. Shi, C. Chu, J. Guo, H. Jing, G. Xu, Y. Cheng, 4D printing of temperature-responsive composites with programmable thermochromic deformation bifunctional, Sensors and Actuators A: Physical (2024) 115138.
[135] Y. Li, F. Zhang, Y. Liu, J. Leng, 4D printed shape memory bismaleimide resin with high storage modulus and low shrinkage rate via second-stage curing, Chemical Engineering Journal 491 (2024) 152196.
[136] E. Liao, Y. Zhang, Y. Su, C. Zhang, C. Geng, C. Li, X. Liu, Y. Liu, A. Lu, Active mixing of two-component viscoelastic silicone ink at molecular level for spatiotemporally controlled 3D/4D printing of cellular silicones, Polymer 302 (2024) 127053.
[137] L. Ren, Y. He, L. Ren, Z. Wang, X. Zhou, Q. Wu, K. Wang, B. Li, Q. Liu, Multi-parameter-encoded 4D printing of liquid crystal elastomers for programmable shape morphing behaviors, Additive Manufacturing 61 (2023) 103376.
[138] P. Bhatnagar, S.H. Zaferani, N. Rafiefard, B. Baraeinejad, A.R. Vazifeh, R. Mohammadpour, R. Ghomashchi, H. Dillersberger, D. Tham, D. Vashaee, Advancing personalized healthcare and entertainment: Progress in energy harvesting materials and techniques of self-powered wearable devices, Progress in Materials Science (2023) 101184.
[139] H. Zhou, Y. Zhang, Y. Qiu, H. Wu, W. Qin, Y. Liao, Q. Yu, H. Cheng, Stretchable piezoelectric energy harvesters and self-powered sensors for wearable and implantable devices, Biosensors and Bioelectronics 168 (2020) 112569.
[140] L. Sun, L. He, G. Yu, X. Zheng, H. Wang, D. Yu, J. Lin, Recent developments in wearable piezoelectric energy harvesters, Review of Scientific Instruments 95(4) (2024).
[141] Y. Huang, S. Chen, Y. Li, Q. Lin, Y. Wu, Q. Shi, Flexible piezoelectric sensor based on PAN/MXene/PDA@ ZnO composite film for human health and motion detection with fast response and highly sensitive, Chemical Engineering Journal 488 (2024) 150997.
[142] C. Dagdeviren, Y. Su, P. Joe, R. Yona, Y. Liu, Y.-S. Kim, Y. Huang, A.R. Damadoran, J. Xia, L.W. Martin, Conformable amplified lead zirconate titanate sensors with enhanced

piezoelectric response for cutaneous pressure monitoring, Nature communications 5(1) (2014) 4496.
[143] M. Fahad, A. Waqar, B. Kim, Effective-performance of inorganic and organic (barium zirconium titanate/polyvinylidene fluoride) piezoelectric composite for energy harvesting and self-powered smart IoT-based electronics, Journal of Alloys and Compounds (2024) 174033.
[144] G. Shi, X. Liang, Y. Xia, S. Jia, X. Hu, M. Yuan, H. Xia, B. Wang, A novel dual piezoelectric-electromagnetic energy harvester employing up-conversion technology for the capture of ultra-low-frequency human motion, Applied Energy 368 (2024) 123479.
[145] B. Wang, Z. Long, Y. Hong, Q. Pan, W. Lin, Z. Yang, Woodpecker-mimic two-layer band energy harvester with a piezoelectric array for powering wrist-worn wearables, Nano Energy 89 (2021) 106385.
[146] S. Asano, S. Nishimura, Y. Ikeda, T. Morita, H. Hosaka, Energy harvester for safety shoes using parallel piezoelectric links, Sensors and Actuators A: Physical 309 (2020) 112000.
[147] A. Mahapatra, R. Ajimsha, M. Ittoop, A. Sharma, S. Karmakar, A. Shaikh, P.R. Sankar, P. Misra, Flexible ZnO: PVDF based free standing piezoelectric nanogenerator for vibrational energy harvesting and wearable shoe insole pedometer sensor, Journal of Alloys and Compounds 960 (2023) 170898.
[148] Z. Yin, S. Gao, L. Jin, S. Guo, Q. Wu, Z. Li, A shoe-mounted frequency up-converted piezoelectric energy harvester, Sensors and Actuators A: Physical 318 (2021) 112530.
[149] Y.K. Fuh, B.S. Wang, C.-Y. Tsai, Self-powered pressure sensor with fully encapsulated 3D printed wavy substrate and highly-aligned piezoelectric fibers array, Scientific Reports 7(1) (2017) 6759.
[150] A.C. Turkmen, C. Celik, Energy harvesting with the piezoelectric material integrated shoe, Energy 150 (2018) 556-564.
[151] C. Su, X. Huang, L. Zhang, Y. Zhang, Z. Yu, C. Chen, Y. Ye, S. Guo, Robust superhydrophobic wearable piezoelectric nanogenerators for self-powered body motion sensors, Nano Energy 107 (2023) 108095.
[152] R. Tao, J. Shi, F. Granier, M. Moeini, A. Akbarzadeh, D. Therriault, Multi-material fused filament fabrication of flexible 3D piezoelectric nanocomposite lattices for pressure sensing and energy harvesting applications, Applied Materials Today 29 (2022) 101596.
[153] S.Y. Jeong, W.S. Hwang, J.Y. Cho, J.C. Jeong, J.H. Ahn, K.B. Kim, S. Do Hong, G.J. Song, D.H. Jeon, T.H. Sung, Piezoelectric device operating as sensor and harvester to drive switching circuit in LED shoes, Energy 177 (2019) 87-93.
[154] S. Vyas, S. Saxena, Piezoelectric power generation using vibrations from human heart, Materials Today: Proceedings (2023).
[155] J. An, H. Park, Y.H. Jung, S. Min, D.H. Kim, D.J. Joe, S.-G. Lee, D.Y. Hyeon, Y. Je, H.-S. Seo, In vivo flexible energy harvesting on porcine heart via highly-piezoelectric PIN–PMN–PT single crystal, Nano Energy 121 (2024) 109227.
[156] S. Azimi, A. Golabchi, A. Nekookar, S. Rabbani, M.H. Amiri, K. Asadi, M.M. Abolhasani, Self-powered cardiac pacemaker by piezoelectric polymer nanogenerator implant, Nano Energy 83 (2021) 105781.
[157] L. Dong, A.B. Closson, M. Oglesby, D. Escobedo, X. Han, Y. Nie, S. Huang, M.D. Feldman, Z. Chen, J.X. Zhang, In vivo cardiac power generation enabled by an integrated helical piezoelectric pacemaker lead, Nano Energy 66 (2019) 104085.
[158] B. Lu, Y. Chen, D. Ou, H. Chen, L. Diao, W. Zhang, J. Zheng, W. Ma, L. Sun, X. Feng, Ultra-flexible piezoelectric devices integrated with heart to harvest the biomechanical energy, Scientific reports 5(1) (2015) 16065.
[159] Y. Zhang, L. Zhou, C. Liu, X. Gao, Z. Zhou, S. Duan, Q. Deng, L. Song, H. Jiang, L. Yu, Self-powered pacemaker based on all-in-one flexible piezoelectric nanogenerator, Nano Energy 99 (2022) 107420.

[160] G. Ji, J. Huber, Recent progress in acoustic metamaterials and active piezoelectric acoustic metamaterials-a review, Applied Materials Today 26 (2022) 101260.
[161] Y.H. Jung, S.K. Hong, H.S. Wang, J.H. Han, T.X. Pham, H. Park, J. Kim, S. Kang, C.D. Yoo, K.J. Lee, Flexible piezoelectric acoustic sensors and machine learning for speech processing, Advanced Materials 32(35) (2020) 1904020.
[162] P. Shivashankar, S. Gopalakrishnan, Review on the use of piezoelectric materials for active vibration, noise, and flow control, Smart materials and structures 29(5) (2020) 053001.
[163] Z. Zhao, J. Zhu, W. Chen, Size-dependent vibrations and waves in piezoelectric nanostructures: a literature review, International Journal of Smart and Nano Materials 13(3) (2022) 391-431.
[164] C. Lu, X. Jiang, L. Li, H. Zhou, A. Yang, M. Xin, G. Fu, X. Wang, Wind energy harvester using piezoelectric materials, Review of Scientific Instruments 93(3) (2022).
[165] W. Sun, K. Zhong, Y. Liu, H. Xiao, D. Zhao, Z. Yan, T. Tan, Enhanced metamaterial vibration for high-performance acoustic piezoelectric energy harvesting, Composites Communications 35 (2022) 101342.
[166] T. Weimann, A. Molter, L. Fernandez, M. He, Structural vibration control based on the effect of acoustic black holes and piezoelectric actuators, Finite Elements in Analysis and Design 224 (2023) 103992.
[167] C.S. Schimidt, L.P.R. de Oliveira, C.D.M. Junior, Vibro-acoustic performance of graded piezoelectric metamaterial plates, Composite Structures 327 (2024) 117656.
[168] M. Jin, B. Liang, J. Yang, J. Yang, J.-c. Cheng, Ultrathin planar metasurface-based acoustic energy harvester with deep subwavelength thickness and mechanical rigidity, Scientific reports 9(1) (2019) 11152.
[169] R. Gomasa, V. Talakokula, S.K.R. Jyosyula, T. Bansal, A review on health monitoring of concrete structures using embedded piezoelectric sensor, Construction and Building Materials 405 (2023) 133179.
[170] S. Du, J. Zhou, F. Li, Dynamic deformation monitoring of cantilever beams using piezoelectric sensors: Theory and experiment, Measurement (2024) 114305.
[171] C. Wu, Q. Xiao, D. Zhu, Piezoelectric ceramic sensor-based structural health monitoring of diagonally braced H-shaped steel structures, Scientific Reports 13(1) (2023) 14964.
[172] M. Iqbal, F.U. Khan, Hybrid vibration and wind energy harvesting using combined piezoelectric and electromagnetic conversion for bridge health monitoring applications, Energy conversion and management 172 (2018) 611-618.
[173] Y.J. Lee, Y. Qi, G. Zhou, K.B. Lua, Vortex-induced vibration wind energy harvesting by piezoelectric MEMS device in formation, Scientific reports 9(1) (2019) 20404.
[174] M. Iqbal, F. Khan, Hybrid acoustic, vibration, and wind energy harvester using piezoelectric transduction for self-powered wireless sensor node applications, Energy Conversion and Management 277 (2023) 116635.
[175] D. Maurya, S. Khaleghian, R. Sriramdas, P. Kumar, R.A. Kishore, M.G. Kang, V. Kumar, H.-C. Song, S.-Y. Lee, Y. Yan, 3D printed graphene-based self-powered strain sensors for smart tires in autonomous vehicles, Nature communications 11(1) (2020) 5392.
[176] K.K. Meena, I. Arief, A.K. Ghosh, H. Liebscher, S. Hait, J. Nagel, G. Heinrich, A. Fery, A. Das, 3D-printed stretchable hybrid piezoelectric-triboelectric nanogenerator for smart tire: Onboard real-time tread wear monitoring system, Nano Energy 115 (2023) 108707.
[177] C.-X. Xing, Q.-B. Zhang, Z.-H. Wang, J.-X. Guo, M.-L. Li, D.-H. Yu, Y.-D. Wang, Q. Zhou, W. Tang, Z. Li, Soft-metal bonding-enabled recyclable and anti-interference flexible multilayer piezoelectric sensor for tractor tire strain monitoring, Nano Energy 127 (2024) 109704.

[178] J. Wang, Y. Cao, H. Xiang, Z. Zhang, J. Liang, X. Li, D. Ding, T. Li, L. Tang, A piezoelectric smart backing ring for high-performance power generation subject to train induced steel-spring fulcrum forces, Energy Conversion and Management 257 (2022) 115442.
[179] P. Bharanitharan, R. Anbalagan, T. Mani, V. Arumugam, Electric Bikes as Exercise Equipment: A Technical Study on Design and Energy Recovery for Home and Fitness Center Use, SAE Technical Paper, 2023.
[180] C. Jettanasen, P. Songsukthawan, A. Ngaopitakkul, Development of micro-mobility based on piezoelectric energy harvesting for smart city applications, Sustainability 12(7) (2020) 2933.
[181] X. Dai, H. Wang, H. Wu, Y. Pan, D. Luo, A. Ahmed, Z. Zhang, A hybrid energy harvesting system for self-powered applications in shared bicycles, Sustainable Energy Technologies and Assessments 51 (2022) 101891.
[182] M.C. Arellano-Sánchez, J. Reyes-Reyes, M. Ponce-Silva, V. Olivares-Peregrino, C. Astorga-Zaragoza, Static technologies associated with pedaling energy harvesting through rotary transducers, a review, Applied Energy 263 (2020) 114607.
[183] M. Shelke, S. Sole, S. Bhatlawande, Automatic Piezoelectric Bicycle Headlight, 2023 14th International Conference on Computing Communication and Networking Technologies (ICCCNT), IEEE, 2023, pp. 1-5.
[184] C. Jettanasen, P. Songsukthawan, A. Ngaopitakkul, Conversion of mechanical energy to electrical energy using piezoelectric materials for bicycle lane lighting systems, Applied Sciences 12(14) (2022) 7237.
[185] P. Chen, Y. Yang, Design, dynamics modeling, and experiments of a vibration energy harvester on bicycle, IEEE/ASME Transactions on Mechatronics 28(5) (2023) 2670-2678.
[186] J. Patdiya, B. Kandasubramanian, Progress in 4D printing of stimuli responsive materials, Polymer-Plastics Technology and Materials 60(17) (2021) 1845-1883.
[187] F. Doberenz, K. Zeng, C. Willems, K. Zhang, T. Groth, Thermoresponsive polymers and their biomedical application in tissue engineering–a review, Journal of Materials Chemistry B 8(4) (2020) 607-628.
[188] S. Pardeshi, F. Damiri, M. Zehravi, R. Joshi, H. Kapare, M.K. Prajapati, N. Munot, M. Berrada, P.S. Giram, S. Rojekar, Functional thermoresponsive hydrogel molecule to material design for biomedical applications, Polymers 14(15) (2022) 3126.
[189] M. Li, Z. Chen, Thermo-responsive polymers for thermal regulation in electrochemical energy devices, Journal of Polymer Science 59(20) (2021) 2230-2245.
[190] Z. Wei, L. Yu, S. Lu, Y. Zhao, Reversibly thermo-responsive materials applied in lithium batteries, Energy Storage Materials (2023) 102901.
[191] C. Ni, D. Chen, Y. Yin, X. Wen, X. Chen, C. Yang, G. Chen, Z. Sun, J. Wen, Y. Jiao, Shape memory polymer with programmable recovery onset, Nature 622(7984) (2023) 748-753.
[192] L. Yue, X. Sun, L. Yu, M. Li, S.M. Montgomery, Y. Song, T. Nomura, M. Tanaka, H.J. Qi, Cold-programmed shape-morphing structures based on grayscale digital light processing 4D printing, Nature Communications 14(1) (2023) 5519.
[193] K. Li, J. Zhao, A. Zhussupbekova, C.E. Shuck, L. Hughes, Y. Dong, S. Barwich, S. Vaesen, I.V. Shvets, M. Möbius, 4D printing of MXene hydrogels for high-efficiency pseudocapacitive energy storage, Nature Communications 13(1) (2022) 6884.
[194] B. Liu, H. Li, F. Meng, Z. Xu, L. Hao, Y. Yao, H. Zhu, C. Wang, J. Wu, S. Bian, 4D printed hydrogel scaffold with swelling-stiffening properties and programmable deformation for minimally invasive implantation, Nature Communications 15(1) (2024) 1587.
[195] J. Liu, Y.-S. Huang, Y. Liu, D. Zhang, K. Koynov, H.-J. Butt, S. Wu, Reconfiguring hydrogel assemblies using a photocontrolled metallopolymer adhesive for multiple customized functions, Nature Chemistry (2024) 1-10.

[196] Y. Zheng, C. Li, Photothermally-driven oxazine hydrogel actuators at the water-air interface, Giant 16 (2023) 100192.
[197] L. Zhang, X. Huang, T. Cole, H. Lu, J. Hang, W. Li, S.-Y. Tang, C. Boyer, T.P. Davis, R. Qiao, 3D-printed liquid metal polymer composites as NIR-responsive 4D printing soft robot, Nature Communications 14(1) (2023) 7815.
[198] K. Qian, Y. Shao, Z. Yang, S. Jiang, A multi-element encrypted and decrypted photoresponsive liquid crystal polymer network through the cooperation of cyanostilbene and spiropyran, Chemical Engineering Journal (2024) 152713.
[199] M.-J. Wang, B. Li, Y.-L. Wei, S.-N. Zhao, S.-Q. Zang, The guest CH3CN molecule triggers solid-state photochromism in a Cu2I2-based MOF for advanced time-dependent encryption and inkless erasable printing, Chinese Chemical Letters 35(3) (2024) 108491.
[200] W. Yang, Z. Wang, X. Wang, Y. Chen, Z. Ge, H. Yu, Bio-inspired propeller robot with controllable pitch driven by magnetic and optical coupling field, Sensors and Actuators B: Chemical 382 (2023) 133509.
[201] E. Yarali, M. Baniasadi, A. Zolfagharian, M. Chavoshi, F. Arefi, M. Hossain, A. Bastola, M. Ansari, A. Foyouzat, A. Dabbagh, Magneto-/electro-responsive polymers toward manufacturing, characterization, and biomedical/soft robotic applications, Applied Materials Today 26 (2022) 101306.
[202] X. Dong, F. Zhang, L. Wang, Y. Liu, J. Leng, 4D printing of electroactive shape-changing composite structures and their programmable behaviors, Composites Part A: Applied Science and Manufacturing 157 (2022) 106925.
[203] K. Dong, M. Panahi-Sarmad, Z. Cui, X. Huang, X. Xiao, Electro-induced shape memory effect of 4D printed auxetic composite using PLA/TPU/CNT filament embedded synergistically with continuous carbon fiber: A theoretical & experimental analysis, Composites Part B: Engineering 220 (2021) 108994.
[204] Y. Wang, H. Ye, J. He, Q. Ge, Y. Xiong, Electrothermally controlled origami fabricated by 4D printing of continuous fiber-reinforced composites, Nature Communications 15(1) (2024) 2322.
[205] A. Fallah, S. Asif, G. Gokcer, B. Koc, 4D printing of continuous fiber-reinforced electroactive smart composites by coaxial additive manufacturing, Composite Structures 316 (2023) 117034.
[206] D. Chen, Q. Liu, P. Geng, S. Tang, J. Zhang, S. Wen, Y. Zhou, C. Yan, Z. Han, Y. Shi, A 4D printing strategy and integrated design for programmable electroactive shape-color double-responsive bionic functions, Composites Science and Technology 208 (2021) 108746.
[207] X. Zhou, N. Zhang, S. Kandalai, H. Li, F. Hossain, S. Zhang, J. Zhu, J. Zhang, J. Cui, Q. Zheng, Dynamic and wearable electro-responsive hydrogel with robust mechanical properties for drug release, ACS Applied Materials & Interfaces 15(13) (2023) 17113-17122.
[208] E. Yarali, M.J. Mirzaali, A. Ghalayaniesfahani, A. Accardo, P.J. Diaz-Payno, A.A. Zadpoor, 4D printing for Biomedical Applications, Advanced Materials (2024) 2402301.
[209] R. Sajjad, S.T. Chauhdary, M.T. Anwar, A. Zahid, A.A. Khosa, M. Imran, M.H. Sajjad, A Review of 4D Printing-Technologies, Shape Shifting, Smart Materials, and Biomedical Applications, Advanced Industrial and Engineering Polymer Research (2023).
[210] H. Liu, F. Wang, W. Wu, X. Dong, L. Sang, 4D printing of mechanically robust PLA/TPU/Fe3O4 magneto-responsive shape memory polymers for smart structures, Composites Part B: Engineering 248 (2023) 110382.
[211] L. Wang, Y. Chang, S. Wu, R.R. Zhao, W. Chen, Physics-aware differentiable design of magnetically actuated kirigami for shape morphing, Nature Communications 14(1) (2023) 8516.

[212] H. Shinoda, S. Azukizawa, K. Maeda, F. Tsumori, Bio-mimic motion of 3D-printed gel structures dispersed with magnetic particles, Journal of The Electrochemical Society 166(9) (2019) B3235-B3239.
[213] Y. Kim, H. Yuk, R. Zhao, S.A. Chester, X. Zhao, Printing ferromagnetic domains for untethered fast-transforming soft materials, Nature 558(7709) (2018) 274-279.
[214] P. Cataldi, M. Liu, M. Bissett, I.A. Kinloch, A review on printing of responsive smart and 4D structures using 2D materials, Advanced Materials Technologies 7(11) (2022) 2200025.
[215] A. Zaszczyńska, A. Gradys, P. Sajkiewicz, Progress in the applications of smart piezoelectric materials for medical devices, Polymers 12(11) (2020) 2754.
[216] M. Qu, X. Chen, D. Yang, D. Li, K. Zhu, X. Guo, J. Xie, Monitoring of physiological sounds with wearable device based on piezoelectric MEMS acoustic sensor, Journal of Micromechanics and Microengineering 32(1) (2021) 014001.
[217] S. Min, D.H. Kim, D.J. Joe, B.W. Kim, Y.H. Jung, J.H. Lee, B.Y. Lee, I. Doh, J. An, Y.N. Youn, Clinical validation of a wearable piezoelectric blood-pressure sensor for continuous health monitoring, Advanced Materials 35(26) (2023) 2301627.
[218] S. Mohith, A.R. Upadhya, K.P. Navin, S. Kulkarni, M. Rao, Recent trends in piezoelectric actuators for precision motion and their applications: A review, Smart Materials and Structures 30(1) (2020) 013002.
[219] X. Gao, J. Yang, J. Wu, X. Xin, Z. Li, X. Yuan, X. Shen, S. Dong, Piezoelectric actuators and motors: materials, designs, and applications, Advanced Materials Technologies 5(1) (2020) 1900716.
[220] S.K. Melly, L. Liu, Y. Liu, J. Leng, Active composites based on shape memory polymers: overview, fabrication methods, applications, and future prospects, Journal of Materials Science 55 (2020) 10975-11051.
[221] W. Zheng, Y. Shi, L. Zhao, S. Jia, L. Li, C.L. Gan, D. Zhang, Q. Guo, Realizing reversible phase transformation of shape memory ceramics constrained in aluminum, Nature Communications 14(1) (2023) 7103.
[222] M.A. Ansari, P. Somdee, Piezoelectric polymeric foams as flexible energy harvesters: a review, Advanced Energy and Sustainability Research 3(9) (2022) 2200063.
[223] Z. Zhao, Y. Dai, S. Dou, J. Liang, Flexible nanogenerators for wearable electronic applications based on piezoelectric materials, Materials Today Energy 20 (2021) 100690.
[224] Z. Jin, D. Lei, Y. Wang, L. Wu, N. Hu, Influences of poling temperature and elongation ratio on PVDF-HFP piezoelectric films, Nanotechnology Reviews 10(1) (2021) 1009-1017.
[225] A. Megdich, M. Habibi, L. Laperrière, Modeling and optimization of piezoelectric and dielectric properties of poled PVDF/BT nanocomposites, Polymer Bulletin (2024) 1-21.
[226] K.K.R. Bannuru, A.R.P. Mathai, P.V. y Alvarado, H.Y. Low, Freestanding 3D piezoelectric PVDF sensors via electroprinting, Materials Today: Proceedings 70 (2022) 447-453.
[227] H. Kim, F. Torres, Y. Wu, D. Villagran, Y. Lin, T.-L.B. Tseng, Integrated 3D printing and corona poling process of PVDF piezoelectric films for pressure sensor application, Smart Materials and Structures 26(8) (2017) 085027.
[228] X. Yuan, X. Gao, X. Shen, J. Yang, Z. Li, S. Dong, A 3D-printed, alternatively tilt-polarized PVDF-TrFE polymer with enhanced piezoelectric effect for self-powered sensor application, Nano Energy 85 (2021) 105985.
[229] Y. Li, W. Feng, L. Meng, K.M. Tse, Z. Li, L. Huang, Z. Su, S. Guo, Investigation on in-situ sprayed, annealed and corona poled PVDF-TrFE coatings for guided wave-based structural health monitoring: From crystallization to piezoelectricity, Materials & Design 199 (2021) 109415.

[230] C. Zhao, J. Xu, J. Tao, C. Xiao, X. Jin, W. Wang, X. Liu, J. Chen, Z. Zhu, Multi-scale alignment in highly piezoelectric polyacrylonitrile nanofibers separator for advanced self-charging supercapacitor, Nano Energy 116 (2023) 108812.
[231] M. Xie, M. Zhu, Z. Yang, S. Okada, S. Kawamura, Flexible self-powered multifunctional sensor for stiffness-tunable soft robotic gripper by multimaterial 3D printing, Nano Energy 79 (2021) 105438.
[232] C. Ge, E. Cretu, A polymeric piezoelectric MEMS accelerometer with high sensitivity, low noise density, and an innovative manufacturing approach, Microsystems & Nanoengineering 9(1) (2023) 151.
[233] L.J. Tan, W. Zhu, K. Zhou, Recent progress on polymer materials for additive manufacturing, Advanced Functional Materials 30(43) (2020) 2003062.
[234] K. Bouguermouh, M. Habibi, L. Laperrière, Z. Li, Y. Abdin, 4D-printed PLA-PETG polymer blends: comprehensive analysis of thermal, mechanical, and shape memory performances, Journal of Materials Science (2024) 1-18.
[235] F. Alam, J. Ubaid, H. Butt, N. El-Atab, Swift 4D printing of thermoresponsive shape-memory polymers using vat photopolymerization, NPG Asia Materials 15(1) (2023) 65.
[236] W. Zhang, H. Wang, H. Wang, J.Y.E. Chan, H. Liu, B. Zhang, Y.-F. Zhang, K. Agarwal, X. Yang, A.S. Ranganath, Structural multi-colour invisible inks with submicron 4D printing of shape memory polymers, Nature Communications 12(1) (2021) 112.
[237] M. Hippler, E. Blasco, J. Qu, M. Tanaka, C. Barner-Kowollik, M. Wegener, M. Bastmeyer, Controlling the shape of 3D microstructures by temperature and light, Nature communications 10(1) (2019) 232.
[238] H. Yang, N. D'Ambrosio, P. Liu, D. Pasini, L. Ma, Shape memory mechanical metamaterials, Materials Today 66 (2023) 36-49.
[239] Q. Ge, A.H. Sakhaei, H. Lee, C.K. Dunn, N.X. Fang, M.L. Dunn, Multimaterial 4D printing with tailorable shape memory polymers, Scientific reports 6(1) (2016) 31110.
[240] K.-H. Lee, J. Jeon, W. Cho, S.-W. Kim, H. Moon, J.J. Wie, S.-Y. Lee, Light-triggered autonomous shape-reconfigurable and locomotive rechargeable power sources, Materials Today 55 (2022) 56-65.
[241] B. Li, C. Zhang, F. Peng, W. Wang, B.D. Vogt, K. Tan, 4D printed shape memory metamaterial for vibration bandgap switching and active elastic-wave guiding, Journal of Materials Chemistry C 9(4) (2021) 1164-1173.
[242] M. Staszczak, M. Nabavian Kalat, K.M. Golasiński, L. Urbański, K. Takeda, R. Matsui, E.A. Pieczyska, Characterization of polyurethane shape memory polymer and determination of shape fixity and shape recovery in subsequent thermomechanical cycles, Polymers 14(21) (2022) 4775.
[243] B. Zhang, H. Li, J. Cheng, H. Ye, A.H. Sakhaei, C. Yuan, P. Rao, Y.F. Zhang, Z. Chen, R. Wang, Mechanically robust and UV-curable shape-memory polymers for digital light processing based 4D printing, Advanced Materials 33(27) (2021) 2101298.
[244] Y.Y.C. Choong, S. Maleksaeedi, H. Eng, S. Yu, J. Wei, P.-C. Su, High speed 4D printing of shape memory polymers with nanosilica, Applied Materials Today 18 (2020) 100515.
[245] X. Wan, Y. He, Y. Liu, J. Leng, 4D printing of multiple shape memory polymer and nanocomposites with biocompatible, programmable and selectively actuated properties, Additive Manufacturing 53 (2022) 102689.
[246] M. Han, Y. Yang, L. Li, Energy consumption modeling of 4D printing thermal-responsive polymers with integrated compositional design for material, Additive Manufacturing 34 (2020) 101223.
[247] T. Zhao, R. Yu, X. Li, B. Cheng, Y. Zhang, X. Yang, X. Zhao, Y. Zhao, W. Huang, 4D printing of shape memory polyurethane via stereolithography, European Polymer Journal 101 (2018) 120-126.

[248] E. Sachyani Keneth, R. Lieberman, M. Rednor, G. Scalet, F. Auricchio, S. Magdassi, Multi-material 3D printed shape memory polymer with tunable melting and glass transition temperature activated by heat or light, Polymers 12(3) (2020) 710.
[249] K. Wang, Y.-G. Jia, X. Zhu, Biocompound-based multiple shape memory polymers reinforced by photo-cross-linking, ACS Biomaterials Science & Engineering 1(9) (2015) 855-863.
[250] H. Wu, P. Chen, C. Yan, C. Cai, Y. Shi, Four-dimensional printing of a novel acrylate-based shape memory polymer using digital light processing, Materials & Design 171 (2019) 107704.
[251] Z. Zhao, F. Peng, K.A. Cavicchi, M. Cakmak, R. Weiss, B.D. Vogt, Three-dimensional printed shape memory objects based on an olefin ionomer of zinc-neutralized poly (ethylene-co-methacrylic acid), ACS applied materials & interfaces 9(32) (2017) 27239-27249.
[252] X.L. Wu, S.F. Kang, X.J. Xu, F. Xiao, X.L. Ge, Effect of the crosslinking density and programming temperature on the shape fixity and shape recovery in epoxy–anhydride shape-memory polymers, Journal of Applied Polymer Science 131(15) (2014).
[253] M. Dadkhah, J.-M. Tulliani, A. Saboori, L. Iuliano, Additive manufacturing of ceramics: Advances, challenges, and outlook, Journal of the European Ceramic Society (2023).
[254] C.L. Cramer, E. Ionescu, M. Graczyk-Zajac, A.T. Nelson, Y. Katoh, J.J. Haslam, L. Wondraczek, T.G. Aguirre, S. LeBlanc, H. Wang, Additive manufacturing of ceramic materials for energy applications: Road map and opportunities, Journal of the European Ceramic Society 42(7) (2022) 3049-3088.
[255] Y. Lakhdar, C. Tuck, J. Binner, A. Terry, R. Goodridge, Additive manufacturing of advanced ceramic materials, Progress in Materials Science 116 (2021) 100736.
[256] Y. Huang, L. Zhang, R. Jing, M. Tang, D. Alikin, V. Shur, X. Wei, L. Jin, Lead zirconate titanate-based ceramics with high piezoelectricity and broad usage temperature range, Chemical Engineering Journal 477 (2023) 147192.
[257] L. Song, S. Glinsek, E. Defay, Toward low-temperature processing of lead zirconate titanate thin films: Advances, strategies, and applications, Applied Physics Reviews 8(4) (2021).
[258] P. Eltouby, I. Shyha, C. Li, J. Khaliq, Factors affecting the piezoelectric performance of ceramic-polymer composites: A comprehensive review, Ceramics International 47(13) (2021) 17813-17825.
[259] J. Huang, M. Yao, X. Yao, A novel approach to improving the electromechanical properties of PZT-based piezoelectric ceramics via a grain coating modification strategy, Ceramics International 47(11) (2021) 16294-16302.
[260] Y. Yan, L.D. Geng, H. Liu, H. Leng, X. Li, Y.U. Wang, S. Priya, Near-ideal electromechanical coupling in textured piezoelectric ceramics, Nature communications 13(1) (2022) 3565.
[261] Z. Jiang, R.J. Dickinson, T.L. Hall, J.J. Choi, A PZT–PVDF stacked transducer for short-pulse ultrasound therapy and monitoring, IEEE Transactions on Ultrasonics, Ferroelectrics, and Frequency Control 68(6) (2021) 2164-2171.
[262] J. Li, L. He, J. Cai, Y. Hu, J. Wen, J. Ma, N. Wan, A walking type piezoelectric actuator based on the parasitic motion of obliquely assembled PZT stacks, Smart Materials and Structures 30(8) (2021) 085030.
[263] S. Yan, C. Sun, Q. Cui, M. He, R. Wang, J. Hao, X. Chu, Dielectric, piezoelectric and dc bias characteristics of Bi-doped PZT multilayer ceramic actuator, Materials Chemistry and Physics 255 (2020) 123605.
[264] M. Sawane, M. Prasad, MEMS piezoelectric sensor for self-powered devices: A review, Materials Science in Semiconductor Processing 158 (2023) 107324.

[265] H.H. Pan, J.-C. Guan, Stress and strain behavior monitoring of concrete through electromechanical impedance using piezoelectric cement sensor and PZT sensor, Construction and Building Materials 324 (2022) 126685.
[266] A. Aabid, M.A. Raheman, Y.E. Ibrahim, A. Anjum, M. Hrairi, B. Parveez, N. Parveen, J. Mohammed Zayan, A systematic review of piezoelectric materials and energy harvesters for industrial applications, Sensors 21(12) (2021) 4145.
[267] J. Li, X. Liu, G. Zhao, Z. Liu, Y. Cai, S. Wang, C. Shen, B. Hu, X. Wang, Piezoelectric materials and techniques for environmental pollution remediation, Science of The Total Environment 869 (2023) 161767.
[268] R. Damamme, L. Seveyrat, A. Borta-Boyon, V.-C. Nguyen, M.-Q. Le, P.-J. Cottinet, 3D printing of doped barium-titanate using robocasting-Toward new generation lead-free piezoceramic transducers, Journal of the European Ceramic Society 43(8) (2023) 3297-3306.
[269] K. Chen, Y. Wang, C. Wu, Y. Du, H. Tang, S. Zheng, Z. Zhou, H. Zheng, G. Wu, ln vitro assessment of immunomodulatory and osteogenic properties in 3D-printed hydroxyapatite/barium titanate piezoelectric ceramic scaffolds, Ceramics International 50(6) (2024) 8751-8759.
[270] Z. Jiang, L. Cheng, Y. Zeng, Z. Zhang, Y. Zhao, P. Dong, J. Chen, 3D printing of porous scaffolds BaTiO3 piezoelectric ceramics and regulation of their mechanical and electrical properties, Ceram. Int. 48(5) (2022) 6477-6487.
[271] Y. Hong, S. Liu, X. Yang, W. Hong, Y. Shan, B. Wang, Z. Zhang, X. Yan, W. Lin, X. Li, A bioinspired surface tension-driven route toward programmed cellular ceramics, Nature Communications 15(1) (2024) 5030.
[272] C.-L. Liu, Q. Du, H. Zhou, S. Chen, J.-M. Wu, G. Zhang, Y.-S. Shi, 3D printing of lead zirconate titanate piezoelectric ceramics via digital light processing (DLP), Ceramics International 49(17) (2023) 28492-28499.
[273] Z. Li, J. Li, H. Luo, X. Yuan, X. Wang, H. Xiong, D. Zhang, Direct ink writing of 3D piezoelectric ceramics with complex unsupported structures, Journal of the European Ceramic Society 42(9) (2022) 3841-3847.
[274] W. Zheng, L. Li, L. Zhao, Q. Guo, Design of Shape Memory Ceramics: Principles, Strategies and Perspectives, JOM (2024) 1-18.
[275] P. Zhao, K. Hu, Q. Wang, Z. Lu, Programmable ceramic 4D printing via multi-material vat photopolymerization, Additive Manufacturing (2024) 104235.
[276] R. Wang, C. Yuan, J. Cheng, X. He, H. Ye, B. Jian, H. Li, J. Bai, Q. Ge, Direct 4D printing of ceramics driven by hydrogel dehydration, Nature Communications 15(1) (2024) 758.
[277] D. Kong, A. Guo, H. Wu, X. Li, J. Wu, Y. Hu, P. Qu, S. Wang, S. Guo, Four-Dimensional Printing of Polymer-Derived Ceramics with High-resolution, Reconfigurability, and Shape Memory Effects, Additive Manufacturing (2024) 104050.
[278] F. Wang, C. Liu, H. Yang, H. Wang, H. Zhang, X. Zeng, C. Wang, W. Zhang, W. Lv, P. Zhu, 4D printing of ceramic structures, Additive Manufacturing 63 (2023) 103411.
[279] L. Wan, Z. Mao, H. Liu, Y. Xie, F. Lyu, Z. Cao, Y. He, J. Yin, X. Han, W.Y.K. Chan, Direct 4D printing of gradient structure of ceramics, Chemical Engineering Journal 465 (2023) 142804.
[280] W. Zhou, D. Du, Q. Cui, C. Lu, Y. Wang, Q. He, Recent research progress in piezoelectric vibration energy harvesting technology, Energies 15(3) (2022) 947.
[281] F. Mokhtari, B. Azimi, M. Salehi, S. Hashemikia, S. Danti, Recent advances of polymer-based piezoelectric composites for biomedical applications, Journal of the Mechanical Behavior of Biomedical Materials 122 (2021) 104669.
[282] N.A. Shepelin, P.C. Sherrell, E.N. Skountzos, E. Goudeli, J. Zhang, V.C. Lussini, B. Imtiaz, K.A.S. Usman, G.W. Dicinoski, J.G. Shapter, Interfacial piezoelectric polarization

locking in printable Ti3C2T x MXene-fluoropolymer composites, Nature communications 12(1) (2021) 3171.
[283] Z. Wang, X. Yuan, J. Yang, Y. Huan, X. Gao, Z. Li, H. Wang, S. Dong, 3D-printed flexible, Ag-coated PNN-PZT ceramic-polymer grid-composite for electromechanical energy conversion, Nano Energy 73 (2020) 104737.
[284] S.M.A.Z. Shawon, Z.D. Carballo, V.S. Vega, C. Lin, M.S. Rafaqut, A.X. Sun, J.J. Li, M.J. Uddin, Surface modified hybrid ZnSnO3 nanocubes for enhanced piezoelectric power generation and wireless sensory application, Nano Energy 92 (2022) 106653.
[285] Z. Hanani, I. Izanzar, M.b. Amjoud, D. Mezzane, M. Lahcini, H. Uršič, U. Prah, I. Saadoune, M. El Marssi, I.A. Luk'yanchuk, Lead-free nanocomposite piezoelectric nanogenerator film for biomechanical energy harvesting, Nano Energy 81 (2021) 105661.
[286] J. Villafuerte, X. Zhang, E. Sarigiannidou, F. Donatini, O. Chaix-Pluchery, L. Rapenne, M.-Q. Le, L. Petit, J. Pernot, V. Consonni, Boosting the piezoelectric coefficients of flexible dynamic strain sensors made of chemically-deposited ZnO nanowires using compensatory Sb doping, Nano Energy 114 (2023) 108599.
[287] S. Kang, S.H. Kim, H.B. Lee, S. Mhin, J.H. Ryu, Y.W. Kim, J.L. Jones, Y. Son, N.K. Lee, K. Lee, High-power energy harvesting and imperceptible pulse sensing through peapod-inspired hierarchically designed piezoelectric nanofibers, Nano Energy 99 (2022) 107386.
[288] P. Cheng, Y. Peng, S. Li, Y. Rao, A. Le Duigou, K. Wang, S. Ahzi, 3D printed continuous fiber reinforced composite lightweight structures: A review and outlook, Composites Part B: Engineering 250 (2023) 110450.
[289] Q. Wang, X. Tian, D. Zhang, Y. Zhou, W. Yan, D. Li, Programmable spatial deformation by controllable off-center freestanding 4D printing of continuous fiber reinforced liquid crystal elastomer composites, Nature Communications 14(1) (2023) 3869.
[290] B.F. Winhard, P. Haida, A. Plunkett, J. Katz, B. Domènech, V. Abetz, K.P. Furlan, G.A. Schneider, 4D-printing of smart, nacre-inspired, organic-ceramic composites, Additive manufacturing 77 (2023) 103776.
[291] C. Zeng, L. Liu, W. Bian, J. Leng, Y. Liu, Compression behavior and energy absorption of 3D printed continuous fiber reinforced composite honeycomb structures with shape memory effects, Additive Manufacturing 38 (2021) 101842.
[292] T. Gu, H. Bi, H. Sun, J. Tang, Z. Ren, X. Zhou, M. Xu, Design and development of 4D-printed cellulose nanofibers reinforced shape memory polymer composites: Application for self-deforming plant bionic soft grippers, Additive Manufacturing 70 (2023) 103544.
[293] G. Sossou, F. Demoly, H. Belkebir, H.J. Qi, S. Gomes, G. Montavon, Design for 4D printing: A voxel-based modeling and simulation of smart materials, Materials & Design 175 (2019) 107798.
[294] H. Cui, R. Hensleigh, D. Yao, D. Maurya, P. Kumar, M.G. Kang, S. Priya, X. Zheng, Three-dimensional printing of piezoelectric materials with designed anisotropy and directional response, Nature materials 18(3) (2019) 234-241.
[295] R. Sharma, R. Singh, A. Batish, Study on barium titanate and graphene reinforced PVDF matrix for 4D applications, Journal of Thermoplastic Composite Materials 34(9) (2021) 1234-1253.
[296] S. Bodkhe, P. Ermanni, 3D printing of multifunctional materials for sensing and actuation: Merging piezoelectricity with shape memory, European Polymer Journal 132 (2020) 109738.
[297] S. Bodkhe, T. Frei, P. Ermanni, 4D printing of multifunctional materials, Proceedings of the 2019 International Conference on Composite Materials, RMIT University, 2019, p. 152.
[298] D. Grinberg, S. Siddique, M.Q. Le, R. Liang, J.F. Capsal, P.J. Cottinet, 4D Printing based piezoelectric composite for medical applications, Journal of Polymer Science Part B: Polymer Physics 57(2) (2019) 109-115.

[299] H.B. Lee, Y.W. Kim, J. Yoon, N.K. Lee, S.-H. Park, 3D customized and flexible tactile sensor using a piezoelectric nanofiber mat and sandwich-molded elastomer sheets, Smart Materials and Structures 26(4) (2017) 045032.
[300] K. Liu, Q. Zhang, C. Zhou, Y. Shi, C. Sun, H. Sun, C. Yin, J. Hu, S. Zhou, Y. Zhang, 4D printing of lead zirconate titanate piezoelectric composites transducer based on direct ink writing, Frontiers in Materials 8 (2021) 659441.

Chapitre 10: Impression 4D d'un système de récupération d'énergie piézoélectrique adaptatif à fréquences naturelles variables

Ce chapitre a fait l'objet d'une publication :
MEGDICH, Amal, HABIBI, Mohamed, LAPERRIÈRE, Luc, LI Zeshi, and ABDIN Yasmine. 4D-Printed Multi-Responsive Shape Memory Composite for Enhanced Piezoelectric Energy Harvesting: Adaptive Design and Analytical Modeling, soumis au journal *Energy Conversion and Management.*

Après avoir fait une revue approfondie des MEMS piézoélectriques et de l'impression 4D dans le chapitre précédent, cette partie de la thèse explore l'intégration de ces deux technologies pour concevoir des systèmes dynamiques de récupération d'énergie. La plupart des travaux actuels se concentrent soit sur l'amélioration des MEMS en améliorant leur efficacité énergétique et leur bande passante, soit sur le développement de structures imprimées en 4D adaptables. Cependant, il existe très peu d'études qui ont cherché à exploiter la synergie entre ces deux approches pour concevoir des dispositifs capables de modifier leur composition en réponse à des stimuli externes, améliorant ainsi l'efficacité de conversion énergétique.

Cet article présente une approche innovante qui combine l'impression 4D et les systèmes MEMS piézoélectriques en développant un récupérateur d'énergie piézoélectrique à mémoire de forme multi-réponses (MSMC-PEH). Ce dispositif est construit à partir d'un nanocomposite PVDF/BT, qui assure la conversion électromécanique, et d'un polymère à mémoire de forme PLA/MWCNTs, capable d'adopter différentes configurations sous l'influence de stimuli électriques et thermiques. Grâce à cette conception géométrique, le MSMC-PEH peut passer d'une structure en porte-à-faux classique à des formes en L, V ou U, améliorant ainsi sa réponse en fréquence et augmentant la gamme de vibrations pouvant être utilisées pour la récupération d'énergie. Les tests expérimentaux ont montré d'excellentes performances en termes de récupération de forme et de stabilité, atteignant respectivement 98% et 99%, tout en offrant une adaptabilité exceptionnelle.

Dans cette étude, un modèle analytique basé sur la théorie d'Euler-Bernoulli a été développé pour prédire le comportement du MSMC-PEH en fonction de ses différentes configurations. Ces modèles théoriques ont été validés par des simulations numériques et des tests

expérimentaux, révélant une forte corrélation entre les résultats prédits et les observations réelles. L'analyse a également montré que la structure adaptative du MSMC-PEH lui permet d'atteindre un large spectre de fréquences (2-120 Hz) et une meilleure efficacité de conversion par rapport aux systèmes MEMS piézoélectriques statiques.

Ainsi, cette étude représente une avancée significative dans le domaine de la récupération d'énergie en intégrant l'impression 4D et les matériaux piézoélectriques dans une seule structure dynamique. L'approche proposée ouvre de nouveaux horizons pour le développement de systèmes autonomes intelligents en robotique, de capteurs embarqués et d'appareils portables, où l'adaptation structurelle est essentielle pour atteindre une efficacité énergétique maximale.

Note : des informations complémentaires (supporting information) ont également été publiées pour cet article. Ils se retrouvent en Annexe 5 de cette thèse et sont identifiées par les références « Figure Si » ou « Table Si » dans cet article.

4D-Printed Multi-Responsive Shape Memory Composite for Enhanced Piezoelectric Energy Harvesting: Adaptive Design and Analytical Modeling

Amal Megdich[1], Mohamed Habibi[1*], Luc Laperrière[1], Zeshi Li[2], and Yasmine Abdin[2]

[1] Department of mechanical engineering, Université du Québec à Trois-Rivières, Quebec, Canada.

[2] Department of Materials Engineering, The University of British Columbia, Vancouver, British Columbia V6T 1Z4, Canada.

10.1 Abstract

Adaptive energy harvesting systems that combine multifunctionality with high efficiency are increasingly in demand for advanced applications in robotics and sensor devices. However, achieving both adaptability and energy conversion efficiency in a single structure remains a great challenge. This study introduces a 4D-printed, multiresponsive shape memory composite piezoelectric energy harvester (MSMC-PEH) enabling dynamic reconfiguration and improved energy harvesting performance. The innovative design integrates a piezoelectric part of PVDF/BT nancomposite and a shape memory composite (SMC) of PLA/MWCNTs that enables smooth transitions between cantilevered, L-, V- and U-shaped configurations in response to electrical or thermal stimuli.

The MSMC-PEH was fabricated using an FDM 3D printer with optimized piezoelectric and SMC compositions and tested under two different stimuli. Experimental results revealed excellent shape recovery and fixity ratios exceeding 98% and 99%, respectively. To evaluate the energy harvesting performances, an analytical model based on Euler-Bernoulli theory was developed. This model was validated by numerical simulations and experimental tests, showing a strong correlation between the theoretical predictions and the observed results. The adaptive and reconfigurable design enables it to achieve a broad bandwidth over a wide frequency range (2 to 120 Hz), emphasizing its versatility and immense potential for various practical applications.

Keywords: 4D printing, multiresponsive SMC, MSMC-PEH, analytical model, energy harvesting performances.

10.2 Introduction

Piezoelectric energy harvesters (PEHs) have attracted considerable attention due to their ability to convert ambient mechanical vibrations into electrical energy and power self-sustaining

systems in applications such as robotics [358, 766, 767], sensing [114, 115, 502, 518], and wearable technologies [164, 768-770]. Among the various designs studied in the literature, the cantilever beam remains the most widely used structure due to its simplicity, ease of fabrication and well-documented behavior [771-774]. However, its narrow frequency bandwidth significantly limits its efficiency in harvesting energy from a wide range of real-world vibrations such as human motion, vehicle vibrations and wind-induced oscillations [775-777].

To overcome this limitation, recent advances in piezoelectric energy harvesting have focused on innovative design strategies to improve the frequency bandwidth and overall performance of these devices. Structural optimization has emerged as a key approach, with researchers investigating alternative geometries and configurations to extend the operating range of PEHs and improve their adaptability to different excitation frequencies. For example, K. Chen et al. [778] introduced a clamped-clamped beam design incorporating auxetic structures characterized by a negative Poisson's ratio. This unique property allows the structure to expand laterally when compressed longitudinally, significantly improving the ability to harvest energy. As a result, bandwidth could be increased by an impressive 1556%-2142%, while power output could be increased by up to 173% compared to conventional designs. Further research into auxetic structures by L. He et al [779] demonstrated their potential to reduce resonant frequencies, improve multimode operation and increase output power. Another innovative approach by a et al [780] involved the introduction of an Arc-Shaped Branch Beam Harvester (ASBBH), a novel design that increases the efficiency and extends the operating bandwidth of PEHs, especially for ultra-low frequency vibrations. Similarly, I.E Piyarathan et al [437] proposed a harvester design with multiple cantilevers and tip masses strategically placed to generate closely spaced resonant peaks. This design resulted in improved power density and broader bandwidth.

In parallel with structural optimization, the integration of nonlinear dynamics has been shown to be effective in increasing the bandwidth of PEHs. For example, Z. Wang et al [781] investigated a spring-based bistable energy harvester (SBEH) which leverages nonlinear dynamics to improve bandwidth and efficiency. This configuration achieved an 838% increase in bandwidth compared to its linear counterpart. Similarly, R. Dauksevicius et al [782] presented a nonlinear harvester that utilizes vibro-impact interaction achieving a frequency tuning ratio of 2:1, which significantly increases the broadband performance, especially in the low frequency range below 50 Hz. In the field of MEMS-based designs, S. Nabavi et al [783]

utilized nonlinear mechanisms in combination with uniform mass distribution to improve both bandwidth and energy harvesting efficiency, further enhancing the potential of these systems.

Hybrid energy harvesting systems that combine multiple mechanisms have also been explored to further improve efficiency and bandwidth. C. Wang et al [784] developed a tri-hybrid energy harvester that integrates piezoelectric, electromagnetic and triboelectric mechanisms to enable superior performance in low frequency environments. This approach significantly extended the operating bandwidth while improving the overall energy harvesting efficiency. Similarly, Z. Xu et al [785] proposed a hybrid harvester that combines piezoelectric and electromagnetic mechanisms with magnetic interaction, resulting in a broader operating bandwidth and improved power output. Finally, multimodal energy harvesting systems have also gained attention. For example, A. Megdich et al [786] integrated the piezoelectric mode d36 to harvest energy from torsional vibrations. This design brought the first three natural frequencies closer together, further optimizing the bandwidth and performance of multimodal PEH systems. Overall, these developments represent a significant advance in improving the efficiency and bandwidth of PEHs and open up new possibilities for low-frequency vibration energy harvesting applications.

Despite these advances, most PEHs developed and studied to date feature static forms with only a single configuration, which limits their adaptability to different excitation frequencies. In addition, the majority of existing PEHs use lead zirconate titanate (PZT) as the primary piezoelectric material due to its high energy conversion efficiency [724, 787-792]. However, PZT ceramics are inherently rigid and brittle, which poses a challenge for applications requiring flexibility and durability [388, 793-796]. These limitations emphasize the need for innovative designs and material choices to develop more versatile and efficient energy harvesters.

In this work, we propose a novel approach to overcome these challenges by developing a personalized PEH that integrates advanced materials and 4D printing technology. The piezoelectric component is composed of a PVDF/BT nanocomposite utilizing polyvinylidene fluoride (PVDF) for its flexibility and barium titanate (BT) for its superior piezoelectric performance. In addition, the introduction of 4D printing enables the creation of an adaptive PEH that can dynamically change its shape in response to external stimuli. This adaptive capability allows the PEH to tune its resonant frequencies to match the excitation frequencies, significantly improving its voltage output over a wide frequency range.

By utilizing these innovations, our study not only addresses the limitations of conventional PEHs, but also demonstrates the potential of 4D printing and advanced composite materials for the development of multifunctional, high-performance energy harvesters suitable for real-world applications.

10.3 Analytical modeling

10.3.1 Models description

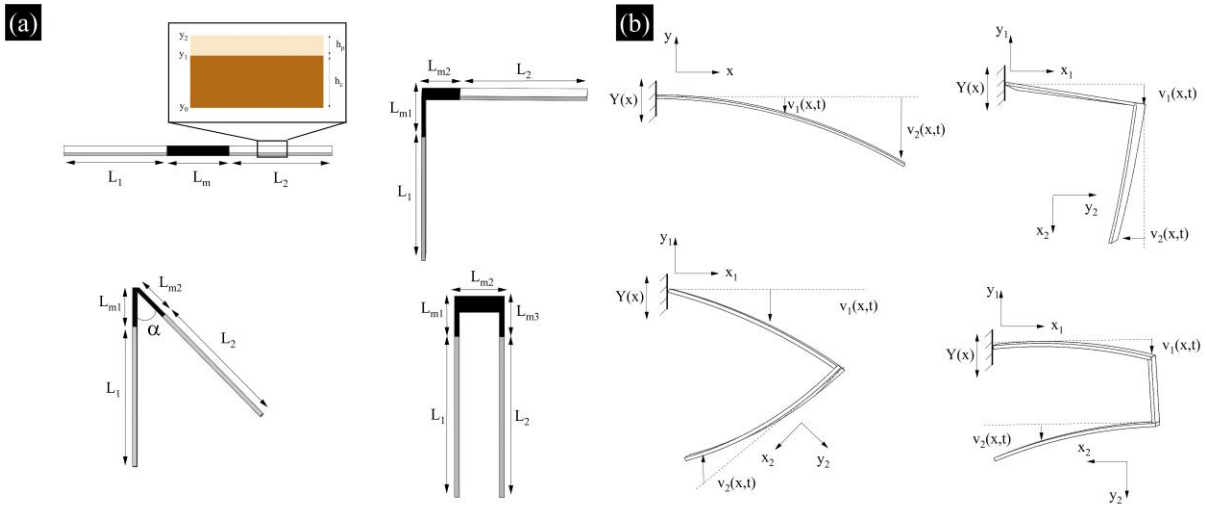

Figure 99: Bioinspired 3D-printed composites with off-center and layered architectures : (a) Schematic of MSMC-PEH in its different temporary shapes, Featuring a SMC component of PLA/MWCNTs (Black part) and a piezoelectric component of PVDF/BT layer and copper layer (gray part) (b) Schematic Illustration of the deformation patterns in the MSMC-PEH in its different configurations undergoing bending motions, defined by the transverse displacement of the main and auxiliary beams $v_1(x,t)$ and $v_2(x,t)$.

The structure analyzed in this study can change its shape due to its shape-memory capability transitioning from a simple cantilever beam to different configurations (L-, V- and U-shape). The piezoelectric components consist of two layers: a piezoelectric layer made of PVDF/BT and a copper layer. The second face of the piezoelectric layer is entirely covered with a silver electrode paste that is assumed to be perfectly conductive. The shape memory component consists of an electro-thermo-responsive material based on PLA/MWCNTs. Each structure is divided into three parts: a main beam, a section of shape memory composite (SMC) that considered as a rigid mass block, and an auxiliary beam. The piezoelectric layers on each of the two beams have the same material parameters and dimensions. The dimensions of the individual components in the different configurations are shown in Figure 99(a).

The structures are clamped at the end of the main beam, where a harmonic excitation Y(t) is applied, allowing both the main and auxiliary flexible beams to bend, with deflections $v_1(x,t)$, and $v_2(x,t)$, respectively, as shown in Figure 99(b). The electrical loads consist of a resistance R_1 attached to the main beam and another one denoted by R_2 that is attached to the auxiliary beam.

10.3.2 Constitutive equations

Assuming an Euler-Bernoulli beam model and Hooke's law, the mechanical strain for both main and auxiliary beams and the stress tensor for the copper layer of the two beams can be written as follows

$$\varepsilon_{\mathrm{i}} = \begin{pmatrix} -yv_{\mathrm{i}}''(x,t) & 0 & 0 \\ 0 & 0 & 0 \\ 0 & 0 & 0 \end{pmatrix},\ \sigma_c = \begin{pmatrix} -E_c y v''(x,t) & 0 & 0 \\ 0 & 0 & 0 \\ 0 & 0 & 0 \end{pmatrix}, y \in [y_0, y_1]. \qquad (73)$$

For electromechanical coupling effect of piezoelectric material, we assumed linear constitutive equations for the unbounded piezoelectric continuum

$$\sigma_p = E_p : \varepsilon^p - e^p . E^p \qquad (74)$$

$$D^p = e^p : \varepsilon^p + \epsilon^{\varepsilon^p} \cdot E^p, \quad (75)$$

where D^p denotes the electric displacement matrix, ϵ^{ε^p} denotes the permittivity matrix at constant strain, E^p denotes the electric field matrix, ε^p denotes the strain matrix of piezoelectric layer, σ_p denotes the stress matrix, E_p denotes the elastic stiffness constant matrix, symbol "." and ":" denote dot product and double contraction-point multiplication respectively, e^p denotes the piezoelectric constant matrix at constant stress, which is given by

$$e^p = d^p : E_p, \quad (76)$$

Considering only the coefficient e_{31}, the mechanical stress σ_{pi} and the electric displacement D^{pi} of each piezoelectric layer i, can be written as follows:

$$\sigma_{pi} = \begin{pmatrix} -E_{pi} y v_i''(x,t) - e_{31}^{pi} E_3^{pi} & 0 & 0 \\ 0 & 0 & 0 \\ 0 & 0 & 0 \end{pmatrix},\ y \in [y_1, y_2] \quad (77)$$

$$D^{pi} = \begin{pmatrix} 0 \\ 0 \\ e_{31}^{pi} \cdot \varepsilon_{11}^{pi} + \epsilon_{33}^{\varepsilon^{pi}} \cdot E_3^{pi} \end{pmatrix}. \quad (78)$$

In the following subsections, the analytical solutions of the electromechanical coupling equations of the MSMC-PEHs with bending modes are deduced.

10.3.3 Hamilton's principle

In this section, Hamilton's principle is applied to formulate a distributed-parameter model for the MSMC-PEHs and derive the governing equations of motion and the corresponding boundary conditions. The demonstration focuses specifically on the first configuration (a cantilever beam), which consists of a main beam, an auxiliary beam and an SMC section considered as a rigid mass block positioned between the two beams. However, the governing equations of motion and boundary conditions are developed for the four configurations. The complete analytical model for the three temporary shapes (L-, V- and U-shaped configurations) can be found in the supporting information (Equations S1 to S160).

10.3.3.1 Kinetic energy

We used the the extended Hamilton's principle, defined by

$$\int_{t_1}^{t_2} \delta(\mathcal{L} + W_{nc})dt = 0, \qquad (79)$$

where $\mathcal{L}$ is the Lagrangian of the system, W_{nc} is the work of the nonconservative forces and δ is the variation which describes infinitesimal changes in the virtual sense. The variation obeys the rules of differential calculus.
The lagrangian is defined by:

$$L = T - U, \qquad (80)$$

where T and V are respectively the kinetic energy and the potential energy of the system.

The kinetic energy of the main and auxiliary beams can be written respectively as follows

$$T_1 = \int_0^{L_1} \frac{1}{2}\rho A(\dot{v}_1(x,t) + \dot{Y}(t))^2 dx, \quad T_2 = \int_0^{L_2} \frac{1}{2}\rho A\left(\dot{v}_2(x,t) + \dot{v}_1(L_1,t)\right)^2 dx, \qquad (81)$$

where the terms ρ, and A are respectively the density, and the cross section of the composite beams, and the term ρA is given by

$$\rho A = \sum_{i=1}^{2} \int_{-\frac{h_i}{2}}^{\frac{h_i}{2}} \int_{-\frac{b}{2}}^{\frac{b}{2}} \rho_i dz dy, \qquad (82)$$

with the terms h_i is the thickness of the ist layer.

The SMC component here is considered as a rigid mass block, thus its kinetic energy can be written as follows:

$$T_m = \frac{1}{2}M\left(\dot{v}_1(L_1,t)\right)^2 + \frac{1}{2}J_m\left(\dot{v}'_1(L_1,t)\right)^2 + M\frac{L_m}{2}\left(\dot{v}_1(L_1,t)\right)\left(\dot{v}'_1(L_1,t)\right), \qquad (83)$$

where J_m is the mass moment of inertia.

The variation of the kinetic energy is obtained by applying the differential to Equations (81) and (83).

$$\begin{aligned}\int_{t1}^{t2} \delta T dt = -\int_{t1}^{t2} \int_0^{L1} \rho A\left[\ddot{v}_1(x,t) + \ddot{Y}(t)\right]\delta v_1(x,t)dx + \int_0^{L2} \rho A[\ddot{v}_2(x,t) + \ddot{v}_1(L_1,t)] \\ \delta v_2(x,t)dx + \mathrm{M}\left(\ddot{v}_1(L_1,t)\right)\delta v_1(L_1,t) + \mathrm{M}\frac{L_\mathrm{m}}{2}\left(\ddot{v}_1(L_1,t)\right)\delta v'_1(L_1,t) \\ +\mathrm{M}\frac{L_\mathrm{m}}{2}\left(\ddot{v}'_1(L_1,t)\right)\delta v_1(L_1,t) + J_m\left(\ddot{v}'_1(L_1,t)\right)\delta v'_1(L_1,t).\end{aligned} \quad (84)$$

10.3.3.2 Potential energy

The potential energy of the main and auxiliary beam U_1 and U_2 can be expressed respectively as follows:

$$U_1 = \frac{1}{2}\int_v \sigma_{p1}:\varepsilon + \sigma_{c1}:\varepsilon dV, U_2 = \frac{1}{2}\int_v \sigma_{p2}:\varepsilon + \sigma_{c2}:\varepsilon dV. \quad (85)$$

Replacing the strain and stress matrix with their expressions, and assuming that the electric field across the piezoelectric layers is

$$E_3^{pi} = -\frac{V_i(t)}{h_{pi}}\left[H(x) - H\left(x - L_j\right)\right], i \in \{1,2\}, \quad (86)$$

where $V_1(\mathrm{t})$ and $V_2(\mathrm{t})$ are the respective output voltages from the main and auxiliary beams. Equation (85) becomes

$$U_1 = \frac{1}{2}\int_0^{L_1} EI_1 v_1''^2(x,t) + \Theta_1 V_1(t)[H(x) - H(x - L_1)]v_1''(x,t)dx \quad (87)$$

and

$$U_2 = \frac{1}{2}\int_0^{L_2} EI_2 v_2''^2(x,t) + \Theta_2 V_2(t)[H(x) - H(x - L_2)]v_2''(x,t)dx, \quad (88)$$

where H (.) designates the Heaviside function, which is added for mathematical reasons. The bending stiffness EI_i of the composite cross section of the i-th beam are given by

$$EI_1 = \frac{1}{3}E_{p1}b(y_2^3 - y_1^3) + \frac{1}{3}E_{c1}b(y_1^3 - y_0^3) \quad (89)$$

$$EI_2 = \frac{1}{3}E_{p2}b(y_2^3 - y_1^3) + \frac{1}{3}E_{c2}b(y_1^3 - y_0^3), \quad (90)$$

and the piezoelectric coupling term Θ_i for parallel connection is expressed as

$$\begin{aligned}\Theta_1 &= -\frac{1}{2}b\left[e_{31}^{p1}(y_1 + y_2)\right] \\ \Theta_2 &= -\frac{1}{2}b\left[e_{31}^{p2}(y_1 + y_2)\right].\end{aligned} \quad (91)$$

The variation of the potential energy of the system is

$$\begin{aligned}\int_{t1}^{t2} \delta U dt = \int_{t1}^{t2} \int_0^{L1} M_{b1}''(x,t)\delta v_1(x,t)dx - \\ [M_{b1}'(x,t)\delta v_1(x,t)]_0^{L1} + [M_{b1}(x,t)\delta v_1'(x,t)]_0^{L1} + \int_0^{L2} M_{b2}''(x,t)\delta v_2(x,t)dx - \\ [M_{b2}'(x,t)\delta v_2(x,t)]_0^{L_2} + [M_{b2}(x,t)\delta v_2'(x,t)]_0^{L_2}dt,\end{aligned} \quad (92)$$

where $M_{b1}, and\ M_{b2}$ are respectively the bending moment of the main beam and the auxiliary beam.

$$\begin{matrix} M_{b1}(x,t) = EI_1 v_1''(x,t) + \Theta_1 V_1(t)[H(x) - H(x-L_1)] \\ M_{b2}(x,t) = EI_2 v_2''(x,t) + \Theta_2 V_2(t)[H(x) - H(x-L_2)]. \end{matrix} \quad (93)$$

10.3.3.3 Variation of the non-conservative forces

The auxiliary beam stimulates the main beam's bending in x = L_1 by applying a shear force opposing to its internal shear force ($T_{y2}(0,t)$) in x=0. and a bending moment opposite to its internal bending moment ($M_{b2}(0,t)$). As a result, the variation of the non-conservative forces for this MSMC-PEH can be written as follows:

$$\int_{t1}^{t2} \delta W_{nc} dt = \int_{t1}^{t2} - M_{b2}(0,t)\delta v'_1(L_1,t) - T_{y2}(0,t)\delta v_1(L_1,t)dt. \quad (94)$$

10.3.4 Equations of motion and boundary conditions

From (79), (80), (84), (92) and (94), we can deduce the equations of motions:

$$\rho A \ddot{v}_1(x,t) + EI_1 v_1''''(x,t) + \Theta_1 V_1(t)[H''(x) - H''(x-L_1)] = -\rho A \ddot{Y}(t) \quad (95)$$

$$\rho A[\ddot{v}_2(x,t)] + EI_2 v_2''''(x,t) + \Theta_2 V_2(t)[H''(x) - H''(x-L_2)] = 0, \quad (96)$$

and the associated boundary conditions

- For the cantilever beam:

$$\begin{matrix} v_1(0,t) = 0 \\ v_1'(0,t) = 0 \\ EI_1 v_1''(L_1,t) = -J_m \left(\ddot{v}'_1(L_1,t)\right) - \mathrm{M}\frac{L_\mathrm{m}}{2}\left(\ddot{v}_1(L_1,t)\right) + EI_2 v_2''(0,t) \\ EI_1 v_1'''(L_1,t) = \mathrm{M}\left(\ddot{v}_1(L_1,t)\right) + \mathrm{M}\frac{L_\mathrm{m}}{2}\left(\ddot{v}'_1(L_1,t)\right) + EI_2 v_2'''(0,t) \\ v_2(0,t) = v_1(L_1,t) \\ v_2'(0,t) = v_1'(L_1,t) \\ EI_2 v_2''(L_2,t) = 0 \\ EI_{gz} v_2'''(L_2,t) = 0, \end{matrix} \quad (97)$$

where $J_m = \frac{1}{12}\mathrm{M}(h_\mathrm{m}^2 + L_\mathrm{mc}^2) + \mathrm{M}(\frac{L_\mathrm{m}}{2})^2$.

- For the L-shaped structure

$$
\begin{gathered}
v_1(0,t)=0 \\
v_1'(0,t)=0 \\
EI_1 v_1''(L_1,t)=-J_{m1}\left(\ddot{v}'_1(L_1,t)\right)-M_1\tfrac{L_\mathrm{m}}{4}\left(\ddot{v}_1(L_1,t)\right)+EI_2 v_2''(0,t)
\end{gathered}
$$

- $$EI_1 v_1'''(L_1,t)=(\mathrm{M}+\rho AL_2)\left(\ddot{v}_1(L_1,t)\right)+M_1\tfrac{L_\mathrm{m}}{4}\ddot{v}'_1(L_1,t)+M_2\left(\tfrac{L_\mathrm{m}}{2}+\tfrac{h_\mathrm{m}}{2}\right)\ddot{v}'_1(L_1,t) \quad (98)$$

$$
\begin{gathered}
v_2(0,t)=0 \\
v_2'(0,t)=0 \\
EI_2 v_2''(L_2,t)=0 \\
EI_{gz} v_2'''(L_2,t)=0.
\end{gathered}
$$

- For the V-shaped structure:

$$
\begin{gathered}
v_1(0,t)=0 \\
v_1'(0,t)=0 \\
EI_1 v_1''(L_1,t)=-J_{m1}\left(\ddot{v}'_1(L_1,t)\right)-M_1\tfrac{L_\mathrm{m}}{4}\left(\ddot{v}_1(L_1,t)\right)+EI_2 v_2''(0,t)
\end{gathered}
$$

$$
\begin{gathered}
EI_1 v_1'''(L_1,t)=(\mathrm{M}+\rho AL_2)\left(\ddot{v}_1(L_1,t)\right)+M_1\tfrac{L_\mathrm{m}}{4}\ddot{v}'_1(L_1,t)+M_2(\tfrac{L_\mathrm{m}}{4}cos\,(\alpha)+\tfrac{h_\mathrm{m}}{2})\ddot{v}'_1(L_1,t) \quad (99) \\
v_2(0,t)=0 \\
v_2'(0,t)=0 \\
EI_2 v_2''(L_2,t)=0 \\
EI_{gz} v_2'''(L_2,t)=0,
\end{gathered}
$$

where $J_{m1}=\frac{1}{12}M_1\left(h_\mathrm{m}^2+\frac{{L_\mathrm{m}}^2}{4}\right)+M_1(\frac{L_\mathrm{m}}{4})^2$, and $\alpha=45°$ is the angle between the two beams, as shown in Figure 100(a).

- For the U-structure:

$$
\begin{gathered}
v_1(0,t)=0 \\
v_1'(0,t)=0 \\
EI_1 v_1''(L_1,t)=-J_{m1}\left(\ddot{v}'_1(L_1,t)\right)-M_1\tfrac{L_\mathrm{c}}{8}\left(\ddot{v}_1(L_1,t)\right)+EI_2 v_2''(0,t) \\
EI_1 v_1'''(L_1,t)=M\left(\ddot{v}_1(L_1,t)\right)+M_1\tfrac{L_\mathrm{c}}{8}\ddot{v}'_1(L_1,t)+M_2\left(\tfrac{L_\mathrm{m}}{4}+\tfrac{h_\mathrm{m}}{2}\right)\ddot{v}'_1(L_1,t) \\
+M_3\tfrac{L_\mathrm{m}}{8}\ddot{v}'_1(L_1,t)+EI_2 v_2'''(0,t) \quad (100) \\
v_2(0,t)=0 \\
v_2'(0,t)=0 \\
EI_2 v_2''(L_2,t)=0 \\
EI_{gz} v_2'''(L_2,t)=0,
\end{gathered}
$$

where $J_{m1}=\frac{1}{12}M_1\left(h_\mathrm{m}^2+\frac{{L_\mathrm{m}}^2}{16}\right)+M_1(\frac{L_\mathrm{m}}{8})^2$

10.3.5 Electrical equations

The electric current I is given by applying Gauss's and Kirchhoff's laws:

$$I_i=\tfrac{\mathrm{d}}{\mathrm{d}t}\int_A D_3^{pi}\,\mathrm{d}A, i\in\{1,2\}. \quad (101)$$

Using the expression of the electric displacement (Equation (87)), the electric currents generated by piezoelectric layers of the MSMC-PEH can be written as follows

$$\begin{aligned} -\left(h_{cp1}e_{31}\right)b\int_0^{L_1}\dot{v}_1''\mathrm{d}x-\left(\frac{\epsilon_{33}^{sp1}}{h_{p1}}\right)bL_1\dot{V}_1(t)=\frac{V_1(t)}{R_1} \\ -\left(h_{cp2}e_{31}\right)b\int_0^{L_2}\dot{v}_2''\mathrm{d}x-\left(\frac{\epsilon_{33}^{sp2}}{h_{p2}}\right)bL_2\dot{V}_2(t)=\frac{V_2(t)}{R_2} \end{aligned}, \quad (102)$$

where h_{cpi} ($\mathrm{i}\in\{1,2\}$) are given by

$$h_{cp1}=\frac{h_{s1}+h_{p1}}{2}, h_{cp2}=\frac{h_{s2}+h_{p2}}{2}. \quad (103)$$

Equation (102) can be written as

$$\begin{aligned} C_{p1}\dot{V}_1(t)+\frac{V_1(t)}{R_1}=bk_1\left(\dot{v}_1'(L_1,t)-\dot{v}_1'(0,t)\right) \\ C_{p2}\dot{V}_2(t)+\frac{V_2(t)}{R_2}=bk_2\left(\dot{v}_2'(L_2,t)-\dot{v}_2'(0,t)\right) \end{aligned}, \quad (104)$$

where

$$\begin{aligned} C_{p1}=\left(\frac{\epsilon_{33}^{sp1}}{h_{p1}}\right)bL_1 \\ C_{p2}=\left(\frac{\epsilon_{33}^{sp2}}{h_{p2}}\right)bL_2 \end{aligned} \quad (105)$$

are respectively the internal capacitances of the piezoelectric layers of the main and auxiliary composite beams, and $k_1, and\ k_2$ indicate constants related to material properties and beam geometries, which are represented by

$$\begin{aligned} k_1=-h_{cp1}e_{31}^{p1} \\ k_2=-h_{cp2}e_{31}^{p2} \end{aligned}. \quad (106)$$

10.3.6 Structural natural frequencies and mode shapes

To calculate the natural frequencies and corresponding mode shapes, the deflections $v_i(\mathrm{x},\mathrm{t})$ of the two composite beams are represented by separable functions of time and space.

$$\begin{aligned} v_1(x,t)=\phi_1(x)exp\ (i\omega t) \\ v_2(x,t)=\phi_2(x)exp\ (i\omega t) \end{aligned}, \quad (107)$$

where $\phi_1(x), and\ \phi_2(x)$ are respectively the eigenfunctions of the bending of the main and auxiliary beams.

The eigenvalue problem that results is written as follows:

$$\phi_1''''(x)-\frac{\rho A\omega^2}{EI_1}\phi_1(x)=0 \quad (108)$$

$$\phi_2''''(x)-\frac{\rho A\omega^2}{EI_2}\phi_2(x)=0, \quad (109)$$

and the associated boundary conditions are:

- For the cantilever beam:

$$\begin{gathered}\phi_1(0)=0\\ \phi_1'(0)=0\\ EI_1\phi_1''(L_1)=J_m\omega^2\phi_1'(L_1)+\mathrm{M}\tfrac{L_\mathrm{m}}{2}\omega^2\phi_1(L_1)+EI_2\phi_2''(0)\\ EI_1\phi_1'''(L_1)=-M\omega^2\phi_1(L_1)+\mathrm{M}\tfrac{L_\mathrm{m}}{2}\omega^2\phi_1'(L_1)+EI_2\phi_2'''(0,t)\\ \phi_2(0)=\phi_1(L_1)\\ \phi_2'(0)=\phi_1'(L_1)\\ EI_2\phi_2''(L_2)=0\\ EI_2\phi_2'''(L_2)=0.\end{gathered}\quad(110)$$

- For the L-shaped structure:

$$\begin{gathered}\phi_1(0)=0\\ \phi_1'(0)=0\\ EI_1\phi_1''(L_1)=-J_{m1}\omega^2\phi_1'(L_1)-M_1\tfrac{L_\mathrm{m}}{4}\omega^2\phi_1(L_1)\\ +EI_2\phi_2''(0)\\ EI_1\phi_1'''(L_1)=(\mathrm{M}+\rho AL_2)\omega^2\phi_1(L_1)+M_1\tfrac{L_\mathrm{m}}{4}\omega^2\phi'_1(L_1)+M_2\left(\tfrac{L_\mathrm{m}}{2}+\tfrac{h_\mathrm{m}}{2}\right)\omega^2\phi'_1(L_1)\\ \phi_2(0)=0\\ \phi_2'(0)=0\\ EI_2\phi_2''(L_2)=0\\ EI_2\phi_2'''(L_2)=0.\end{gathered}\quad(111)$$

- For the V-structure:

$$\begin{gathered}\phi_1(0)=0\\ \phi_1'(0)=0\\ EI_1\phi_1''(L_1)=-J_{m1}\omega^2\phi_1'(L_1)-M_1\tfrac{L_\mathrm{m}}{4}\omega^2\phi_1(L_1)\\ +EI_2\phi_2''(0)\\ EI_1\phi_1'''(L_1)=(\mathrm{M}+\rho AL_2)\omega^2\phi_1(L_1)+M_1\tfrac{L_\mathrm{m}}{4}\omega^2\phi'_1(L_1)+M_2(\tfrac{L_\mathrm{m}}{4}cos\,(\alpha)+\tfrac{h_\mathrm{m}}{2})\omega^2\phi'_1(L_1)\\ \phi_2(0)=0\\ \phi_2'(0)=0\\ EI_2\phi_2''(L_2)=0\\ EI_2\phi_2'''(L_2)=0.\end{gathered}\quad(112)$$

- For the U-structure:

$$\begin{gathered}\phi_1(0)=0\\ \phi_1'(0)=0\\ EI_1\phi_1''(L_1)=-J_{m1}\omega^2\phi_1'(L_1)-M_1\tfrac{L_\mathrm{c}}{8}\omega^2\phi_1(L_1)+EI_2\phi_2''(0)\\ EI_1\phi_1'''(L_1)=M\omega^2\phi_1(L_1)+M_1\tfrac{L_\mathrm{c}}{8}\omega^2\phi_1'(L_1)+M_2\left(\tfrac{L_\mathrm{m}}{4}+\tfrac{h_\mathrm{m}}{2}\right)\omega^2\phi_1'(L_1)+M_3\tfrac{L_\mathrm{m}}{8}\omega^2\phi_1'(L_1)+EI_2\phi_2'''(0)\\ \phi_2(0)=0\\ \phi_2'(0)=0\\ EI_2\phi_2''(L_2)=0\\ EI_2\phi_2'''(L_2)=0.\end{gathered}$$

(113)

The general solutions of Equations (108), and (109) are given by

$$\begin{matrix}\phi_1(x) = A_1 cos\,(\beta_1 x) + B_1 sin\,(\beta_1 x) + C_1 cosh\,(\beta_1 x) + D_1 sinh\,(\beta_1 x)\\ \phi_2(x) = A_2 co\,s(\beta_2 x) + B_2 si\,n(\beta_2 x) + C_2 cos\,h(\beta_2 x) + D_2 sin\,h(\beta_2 x),\end{matrix} \quad (114)$$

where A_i, B_i, C_i and D_i are the modal coefficients of the eigenfunctions, which are obtained using the associated boundary conditions (Equation (110)). And β_i are the frequency number, which are obtained as

$$\beta_1 = \sqrt[4]{\frac{\rho A\omega^2}{EI_1}}, \beta_2 = \sqrt[4]{\frac{\rho A\omega^2}{EI_2}}. \quad (115)$$

The analytical first two resonant frequencies and the corresponding mode shapes for each configuration were numerically validated using COMSOL software, as shown in Table 36. The comparison revealed minimal relative errors between the theoretical model and the numerical simulations. These discrepancies can be attributed to the differences in the methods used: The theoretical model is based on Euler-Bernoulli beam theory, while the finite element model in COMSOL uses three-dimensional solid modeling. Despite these methodological differences, the close agreement of the results demonstrates the robustness and accuracy of the theoretical predictions.

Table 36: First two resonance frequencies of the different configurations obtained analytically and numerically under open circuit conditions.

Configuration	Cantilever beam	L-shaped	V-shaped	U-shaped
Analytical	17.8/111.6	23.7/64.6	29.3/73.9	13.4/39.6
Numerical	17.2/110.7	22.9/63.9	28.4/73.2	12.7/39.1
Error (%)	3.370/0.806	3.375/1.083	3.071/0.947	5.223/1.262

10.3.7 Reduced-order model and analytical solution

In this section, we use the Galerkin procedure and the Euler-Lagrange method to discretize the Reduced-order model (ROM) for the considered configurations, based on exploiting the systems' natural frequencies and corresponding mode shapes in bending movements. Then the dynamic responses, and the electric voltage outputs are presented in terms of closed-form formulas.

10.3.7.1 Reduced order model

Using the Galerkin, we can define the deflections $v_i(x,t)$ of the two composite beams as an absolutely and uniformly convergent series of the eigenfunctions

$$\begin{matrix}v_1(x,t) = \sum_{r=1}^{\infty} \phi_{1r}(x)\eta_r(t)\\ v_2(x,t) = \sum_{r=1}^{\infty} \phi_{2r}(x)\eta_r(t),\end{matrix} \quad (116)$$

where $\phi_{1r}(\mathrm{x}), and\ \phi_{2r}(\mathrm{x})$ are the eigenfunctions of respectively the bending of the main beam, and the bending of the auxiliary beam, and $\eta_r(\mathrm{t})$ are the modal coordinates of the displacements $v_1\ and\ v_2$ in the orthogonal base formed by the the eigenfunction for the r-th mode. The aim of this subsection is to create a reduced-order model of the structure using the Euler Lagrange approach, so, we limit ourselves to the first two structural mode shapes to discretize the system. This choice is linked to the application of applied excitation frequencies, which are generally lower than the third structural natural frequency. The Euler-Lagrange approach is defined as follows:

$$\frac{d}{dt}\frac{\partial \mathcal{L}}{\partial \dot{\eta}_s} - \frac{\partial \mathcal{L}}{\partial \eta_s} = 0, \quad (117)$$

where $\mathcal{L}$ is Lagrangian of the system which is introduced in Equation (80). Using the expressions of kinetic energy and potential energy developed in the previous chapter, the Lagrangian can be written as follows:

$$L = \frac{1}{2}\int_0^{L_1} \rho A\left(\dot{v}_1(x,t) + \dot{Y}(t)\right)^2 - EI_1 v_1''^2(x,t) - \Theta_1 V_1(t) v_1''(x,t)dx + \frac{1}{2}\int_0^{L_2} \rho A(\dot{v}_2(x,t) + \dot{v}_1(L_1,t))^2 - EI_2 v_2''^2(x,t) - \Theta_2 V_2(t) v_2''(x,t)dx + \frac{1}{2}M\left(\dot{v}_1(L_1,t)\right)^2 + \frac{1}{2}J_m\left(\dot{v}'_1(L_1,t)\right)^2 + \mathrm{M}\frac{L_\mathrm{m}}{2}\left(\dot{v}_1(L_1,t)\right)\left(\dot{v}'_1(L_1,t)\right). \quad (118)$$

Substituting Equation (116) into Equation (118), we obtain

$$\begin{aligned} L = {} & \frac{1}{2}\int_0^{L_1} \rho A\left(\sum_{r=1}^{2} \phi_{1r}(x)\dot{\eta}_r(t) + \dot{Y}(t)\right)^2 - EI_1 \sum_{r=1}^{2} \phi_{1r}''^2(x)\eta_r^2(t) - \\ & \Theta_1 V_1(t) \sum_{r=1}^{2} \phi_{1r}''(x)\eta_r(t) + \frac{1}{2}\int_0^{L_2} \rho A \sum_{r=1}^{2} (\phi_{2r}(x)\dot{\eta}_r(t) + \phi_{1r}(L_1)\dot{\eta}_r(t))^2 \\ & -EI_2 \sum_{r=1}^{2} \phi_{2r}''^2(x)\eta_r^2(t) - \Theta_2 V_2(t) \sum_{r=1}^{2} \phi_{2r}''(x)\eta_r(t)dx + \frac{1}{2}\mathrm{M}\sum_{r=1}^{2} \phi_{1r}^2(L_1)\dot{\eta}_r^2(t) \\ & +\frac{1}{2}J_m \sum_{r=1}^{2} \phi_{1r}'^2(L_1)\dot{\eta}_r^2(t) + \mathrm{M}\frac{L_\mathrm{m}}{2}\left(\sum_{r=1}^{2} \phi_{1r}^2(L_1)\dot{\eta}_r^2(t)\right)\left(\sum_{r=1}^{2} \phi_{1r}'^2(L_1)\dot{\eta}_r^2(t)\right). \end{aligned} \quad (119)$$

Using the orthogonality conditions for the L-shaped bimorph beam-mass structure with torsional and bending mode

$$\begin{gathered} EI_1 \int_0^{L_1} \phi_{1r}''(x)\phi_{1s}''(x)dx + EI_2 \int_0^{L_2} \phi_{2r}''(x)\phi_{2s}''(x)dx = \omega_r^2 \delta_{rs} \\ \int_0^{L_1} (\rho A)\phi_{1r}\phi_{1s}\,\mathrm{d}x + \int_0^{L_2} (\rho A)(\phi_{2r}\phi_{2s} + \phi_{2r}\phi_{1s}(L_1) + \phi_{1r}(L_1)\phi_{1s}(L_1))\mathrm{d}x + M\phi_{1r}(L_1)\phi_{1s}(L_1) + J_\mathrm{m}\phi'_{1\mathrm{r}} \\ (L_1)\phi'_{1s}(L_1) + J_\mathrm{m}\phi'_{1r}(L_1)\phi'_{1s}(L_1) + \frac{1}{2}\mathrm{M}L_\mathrm{m} \\ \left(\phi'_{1r}(L_1)\phi_{1s}(L_1) + \phi_{1r}(L_1)\phi'_{1s}(L_1)\right) = \delta_{rs}, \end{gathered} \quad (120)$$

we obtain the forced equation of motion in modal coordinates

$$\ddot{\eta}_r(t) + 2\xi_r\omega_r\dot{\eta}_r(t) + \omega_r^2\eta_r(t) + \chi_{1r}V_1(t) + \chi_{2r}V_2(t) = f_r(t), r \in \{1,2\}, \quad (121)$$

where ξ_r is the modal damping ratio of the r-th bending vibration mode, χ_{ir} are the modal electromechanical coupling terms, which are given by

$$\begin{matrix}\chi_{1r} = \Theta_1(\phi'_{1r}(L_1) - \phi'_{1r}(0)) \\ \chi_{2r} = \Theta_2(\phi'_{2r}(L_i) - \phi'_{2r}(0))\end{matrix}, \quad (122)$$

and $f_r(\mathrm{t})$ is the modal force given by

$$f_r(t) = -\int_0^{L_1} \rho A \phi_{1r}(x) dx \ddot{Y}(t). \quad (123)$$

Substituting Equation (116) into equation (104), the governing circuit equations are written as

$$\begin{matrix}C_{p1}\dot{V}_1(t) + \frac{V_1(t)}{R_1} = \sum_{r=1}^{2} K_{1r}\,\dot{\eta}_r(t) \\ C_{p2}\dot{V}_2(t) + \frac{V_2(t)}{R_2} = \sum_{r=1}^{2} K_{2r}\dot{\eta}_r(t)\end{matrix}, \quad (124)$$

where K_{1r} and K_{3r} are the r-th modal coupling terms of the piezoelectric layers of the main beam, and K_{2r} is the r-th modal coupling term of the piezoelectric layers of the auxiliary beam

$$K_{ir} = k_i b(\phi'_{ir}(L_i) - \phi'_{ir}(0)), i \in \{1,2\}. \quad (125)$$

10.3.7.2 Analytical solution

We note that $Y(t) = \Im\left[Y_0 e^{j\Omega t}\right]$, where $\Im$ stands for the imaginary part. Consequently, we seek the solutions of Equations (121), and (124) in the form

$$\begin{matrix}\eta_r(t) = \Im[H_r e^{j\Omega t}], r \in \{1,2\} \\ V_i(t) = \Im[U_i e^{j\Omega t}], i \in \{1,2\}\end{matrix}. \quad (126)$$

Substituting Equation (162) into Equation (121),

$$H_r = \frac{f_{r0} - \chi_i U_1 - \chi_2 U_2}{\omega_r^2 - \omega^2 + 2\xi\omega_r\omega j}, \quad (127)$$

where f_{r0} is the complex amplitude of the modal force function $f_r(t)$

$$f_{r0}(t) = -\int_0^{L_1} \rho A \phi_{1r}(x) dx \ddot{Y}_0. \quad (128)$$

Considering Equation (142), we obtain the following equation system

$$\begin{cases}U_1 Z_1 = Z_3 - Z_2 U_2 \\ U_2 Z_5 = Z_6 - Z_4 U_1\end{cases}. \quad (129)$$

Finally, the steady state voltage outputs are given by

$$\begin{matrix}U_1 = \frac{Z_3 Z_5 - Z_2 Z_6}{Z_1 Z_5 - Z_2 Z_4} \\ U_2 = \frac{Z_1 Z_6 - Z_3 Z_4}{Z_1 Z_5 - Z_2 Z_4}\end{matrix}, \quad (130)$$

where

$$
\begin{aligned}
Z_1 &= jC_{p1}\Omega + \frac{1}{R_1} + \sum_{r=1}^{2} \frac{\Omega j}{\omega_r^2 - \Omega^2 + 2j\xi_r\omega_r\Omega}(K_{1r})\chi'_{1r} \\
Z_2 &= \sum_{r=1}^{2} \frac{\Omega j}{\omega_r^2 - \Omega^2 + 2j\xi_r\omega_r\Omega}(K_{1r})\chi_{2r} \\
Z_3 &= \sum_{r=1}^{2} \frac{\Omega j}{\omega_r^2 - \Omega^2 + 2j\xi_r\omega_r\Omega}(K_{1r})f_{r0} \\
Z_4 &= \sum_{r=1}^{2} \frac{\Omega j}{\omega_r^2 - \Omega^2 + 2j\xi_r\omega_r\Omega}K_{2r}\chi'_{1r} \\
Z_5 &= jC_{p2}\Omega + \frac{1}{R_2} + \sum_{r=1}^{2} \frac{\Omega j}{\omega_r^2 - \Omega^2 + 2j\xi_r\omega_r\Omega}K_{2r}\chi_{2r} \\
Z_6 &= \sum_{r=1}^{2} \frac{\Omega j}{\omega_r^2 - \Omega^2 + 2j\xi_r\omega_r\Omega}K_{2r}f_{r0}.
\end{aligned}
\tag{131}
$$

10.4 Experimental section

10.4.1 Materials

PLA pellets (Mw ≈ 60,000 g/mol) was purchased from Millipore Sigma, PVDF (Mw ≈ 530,000 g/mol) powder, MWCNTS (Mw ≈ 16.043 g/mol) powder, BT powder (Mw ≈ 233.24 g/mol) and N,N-dimethylformamide (DMF, 99.8+%) were purchased from Thermo Fisher Scientific, ethyl acetate was purchased from Alfa Chemistry.

10.4.2 Materials synthesis

First, PVDF powder was mixed with varying proportions of BT (0, 20, 30, and 40 wt%) and dissolved in DMF solvent. The mixture was stirred at 60 ◦C at a speed of 1500 rpm for 1 h until completely dissolved. Following this, the mixture was dried at a temperature of 100◦C for a duration of 24 h to ensure complete evaporation of the DMF solvent.

To produce the PLA/MWCNT nanocomposite, we first dissolved PLA pellets in ethyl acetate. Then different amounts of MWCNTs (5, 7.5 and 10 wt%) were added to the solution. This mixture was stirred continuously at 50°C and 1500 rpm for 1 hour until it was completely dissolved. The resulting solution was then dried at 80°C for 24 hours until the solvent was completely evaporated.

The resulting nanocomposites PVDF/BT and PLA/MWCNTs were cooled to room temperature before being cut into pellets. These pellets were fed into a single-screw extruder (Wellzoom Type B Desktop Filament Extruder 3D Printer) operating at a rotation speed of 70 rpm and an extrusion temperature of 220°C. The filament diameter was precisely adjusted to 2.85 ± 0.05 mm using a conveyor belt. Finally, a professional 3D printer (FDM, Ultimaker) was used to print the MSMC-PEH. Table 37 gives an overview of the main 3D printing settings used in this study. A visual representation of the synthesis process can be found in Figure 100.

Table 37: Printing parameters.

Parameters	PVDF/BT	PLA/MWCNTs
Nozzle temperature (°C)	280	275
Build platform temperature (°C)	100	100
Layer thickness (mm)	0.4	0.4
Infill density (%)	100	100
Raster angle (deg)	90	90

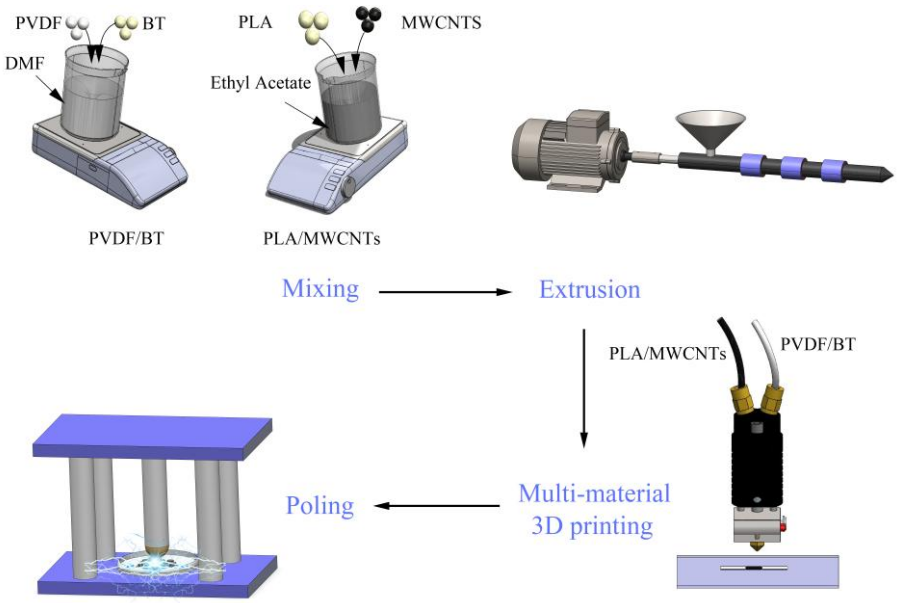

Figure 100: Preparation process and multi-material 3D printing of PVDF/BT-based PEH combined with multi-responsive SMC using PLA/MWCNTs nanocomposites.

Table 38 provides a detailed overview of the compositions of the sample.

Table 38: PLA/MWCNTs and PVDF/BT nanocomposites with varying compositions.

Sample	PLA	MWCNTs	PVDF	BT
Pure PVDF	0	0	100	0
BT-20	0	0	80	20
BT-30	0	0	70	30
BT-40	0	0	60	40
C-5	95	5	0	0
C-7.5	92.5	7.5	0	0
C-10	90	10	0	0

10.4.3 Characterization

10.4.3.1 Morphological and crystalline structure

The crystalline structure of PVDF/BT and PLA/MWCNTs nanocomposites has been thoroughly characterized using a range of advanced analytical techniques. Scanning electron microscopy (SEM) was used to study the surface morphology and microstructural properties of both nanocomposites, allowing a detailed analysis of the distribution and dispersion of the fillers in the matrices. Fourier transform infrared spectroscopy (FT-IR), performed in ATR mode with a high resolution of 4 cm^{-1} over the spectral range of 4000–400 cm^{-1}, provided precise insights into the chemical structure and functional groups present in the nanocomposites.

Equation (132) derived from the Lambert-Beer law, was utilized to quantify the β-phase fraction within the nanocomposite based on the intensities of the characteristic absorption bands in the FT-IR spectra.

$$F(\beta) = \frac{A_\beta}{\left(\frac{k_\beta}{k_\alpha}\right)\cdot A_\alpha + A_\beta}. \qquad (132)$$

In addition, X-ray diffraction (XRD) was used to determine the crystalline phases and structural properties of PVDF, BT, PLA and MWCNTs, providing a comprehensive understanding of their phase composition and crystalline structure. Differential scanning calorimetry (DSC) analysis was performed to investigate the thermal properties, phase transitions and crystallization behavior of the components, allowing precise determination of critical thermal parameters such as glass transition temperature (Tg), melting temperature (Tm) and crystallization characteristics.

10.4.3.2 Piezoelectric and dielectric behavior

In order to evaluate the piezoelectric properties of the PVDF/BT nanocomposites, the piezoelectric coefficient (d33) was measured using a quasi-static measuring device. This instrument determines the value by exerting a controlled mechanical force on the sample and measuring the resulting electrical charge. This provides a quantitative measure of the material's ability to convert mechanical energy into electrical energy.

The dielectric behavior of the nanocomposites, which includes the dielectric constant and the dielectric loss, was characterized using an LCR meter. The dielectric constant was calculated using Equation (133), which provides a comprehensive understanding of the electrical storage capacity and energy dissipation properties of the material.

$$\varepsilon_p = \frac{C_p \times d}{\varepsilon_0 \times A} \qquad (133)$$

Where ε_0 is the permittivity of free space, A is the area, and d is the thickness of the material.

10.5 Results and discussion

10.5.1 Analytical modeling results

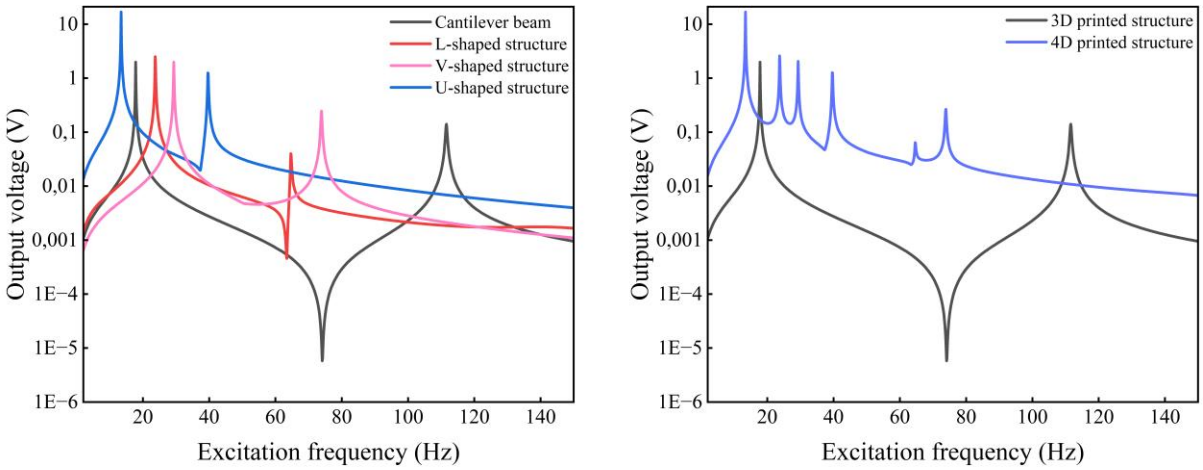

Figure 101: (a) Output voltage of the MSMC-PEH in its various shapes. (b) Comparison of the output voltages between a simple 3D-printed cantilever beam and a 4D-printed one.

Figure 101(a) shows the output voltage of the MSMC-PEH in different temporary configurations, including cantilever beam, L-shaped, V-shaped and U-shaped structures. Each configuration corresponds to a distinct resonance behavior, with specific excitation frequencies leading to peak output voltage values. It is noteworthy that the cantilever beam has the lowest output voltage levels, and the narrowest frequency bandwidth compared to the other configurations. This can be attributed to its simpler geometry, which leads to less effective energy harvesting. In contrast, the other structures show improved performance with the first two natural frequencies closer to each other. This characteristic contributes to a wider operating range and higher output voltages, as the overlapping frequency bands increase energy harvesting efficiency across multiple frequencies.

Figure 101(b) compares the output of the 4D printed MSMC-PEH with a conventional 3D printed cantilever beam. The 4D printed MSMC-PEH consistently outperforms its 3D printed counterpart, exhibiting a wider frequency bandwidth. This improved bandwidth is mainly due to the ability of the structure to dynamically adjust its shape and effectively match its natural frequencies to the excitation frequencies. As a result, the 4D printed MSMC-PEH achieves excellent voltage output generation across the entire frequency spectrum from 2 to 120 Hz,

which aligns well with the excitation frequencies commonly applied in real-world applications. This significant performance improvement is due to the unique ability of the 4D printed system to change its shape and optimize its structural dynamics in response to different stimuli. The increased resonance peaks and wider operating range highlight the potential of integrating 4D printing technologies with piezoelectric materials to create highly efficient and adaptable energy harvesting solutions.

10.5.2 Morphological and crystalline structure

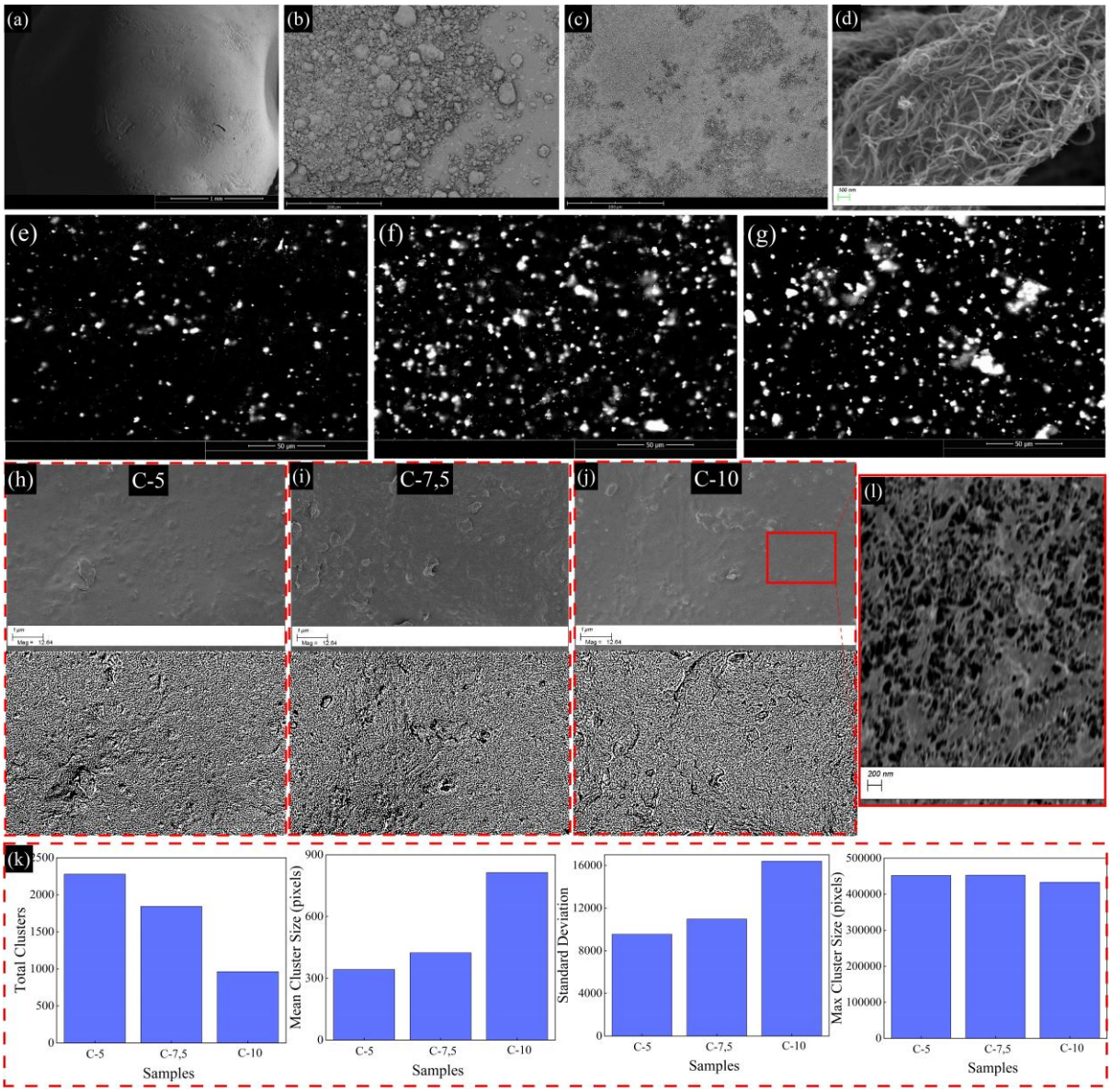

Figure 102: SEM and image-based analysis of component morphology and dispersion in PVDF/BT and PLA/MWCNTs : SEM images of as received (a) PLA, (b) PVDF, and (c)BT, (d) MWCNTs; SEM images of (e) BT-20, (f) BT-30, and (g) BT-40; low magnification SEM and segmented images (MWCNT Regions In White) of (h) C-5, (i) C-7.5, and (j) C-10; (k) total clusters, mean cluster size, standard deviation, and max cluster size

for the three compositions (C-5, C-7.5, and C-10) ; (l) high magnification SEM of C-10.

Figure 102(a) shows the SEM image of the as received PLA. The surface of the pure PLA appears smooth and uniform, with no visible defects. Figure 102(b) shows a high magnification SEM image of the as received PVDF. Figure 102(c) presents the as-received barium titanate powder in its raw form. Figure 102(d) shows both high magnification SEM images of the as-received MWCNTs, revealing their long, intertwined tubular structures. Figure 103(e) shows SEM images of the BT-20 sample, which reveal a uniform distribution of BT nanoparticles in the PVDF matrix and excellent interfacial adhesion. The observed homogeneous dispersion is attributed to the efficient incorporation of the fillers into the polymer matrix, which ensures both structural integrity and functional performance. Figure 103(f) shows the BT-30 sample where the SEM image reveals a slight increase in agglomeration of the nanoparticles, likely due to the higher filler loading. Nevertheless, the overall dispersion remains relatively uniform, indicating a controlled distribution of nanoparticles even at higher filler concentrations. Figure 102(g), which corresponds to the BT-40 sample, shows clear a pronounced agglomeration of the nanoparticles. The strong agglomeration of particles disturbs the uniformity of the nanocomposite structure, which may have a negative impact on the functional properties, especially on the piezoelectric and mechanical performance.

Figures 102(h), (i) and (j) show low magnification SEM images and corresponding segmented images of C-5, C-7.5 and C-10, respectively. Figure 4(h) shows a relatively smoother surface with less visible nanotube structures, indicating better dispersion but possibly less interconnectivity between the nanotubes.

Figure 102(i) shows more noticeable MWCNTs structures, indicating moderate dispersion with increasing interconnectivity. Figure 102(j) shows that C-10 has distinct nanotube networks but also visible agglomerations, implying that the dispersion is less uniform due to the increased MWCNTs content. Figure 102(k) compares the total number of clusters, mean cluster size, standard deviation and maximum cluster size for the three compositions. The C-10 sample has the largest mean cluster size, confirming the observation that higher nanotube content leads to agglomeration. The cluster size increases with MWCNTs content, indicating that the dispersion becomes less uniform with increasing concentration. A similar maximum cluster size in all samples means that some agglomerates may present in all cases but are more frequent at higher MWCNT contents.

The high magnification SEM image of C-10 in Figure 102(l) shows a close-up of the nanotube network within the PLA matrix. The intertwined nanotube structures are clearly visible, confirming that MWCNTs form interconnected networks that can improve electrical and mechanical properties. However, agglomeration can also be seen. Thus, C-5 has the best dispersion but probably the lowest nanotube interconnectivity. C-7.5 achieves a balance between dispersion and interconnectivity. C-10 has the most interconnected nanotube networks but suffers from strong agglomeration.

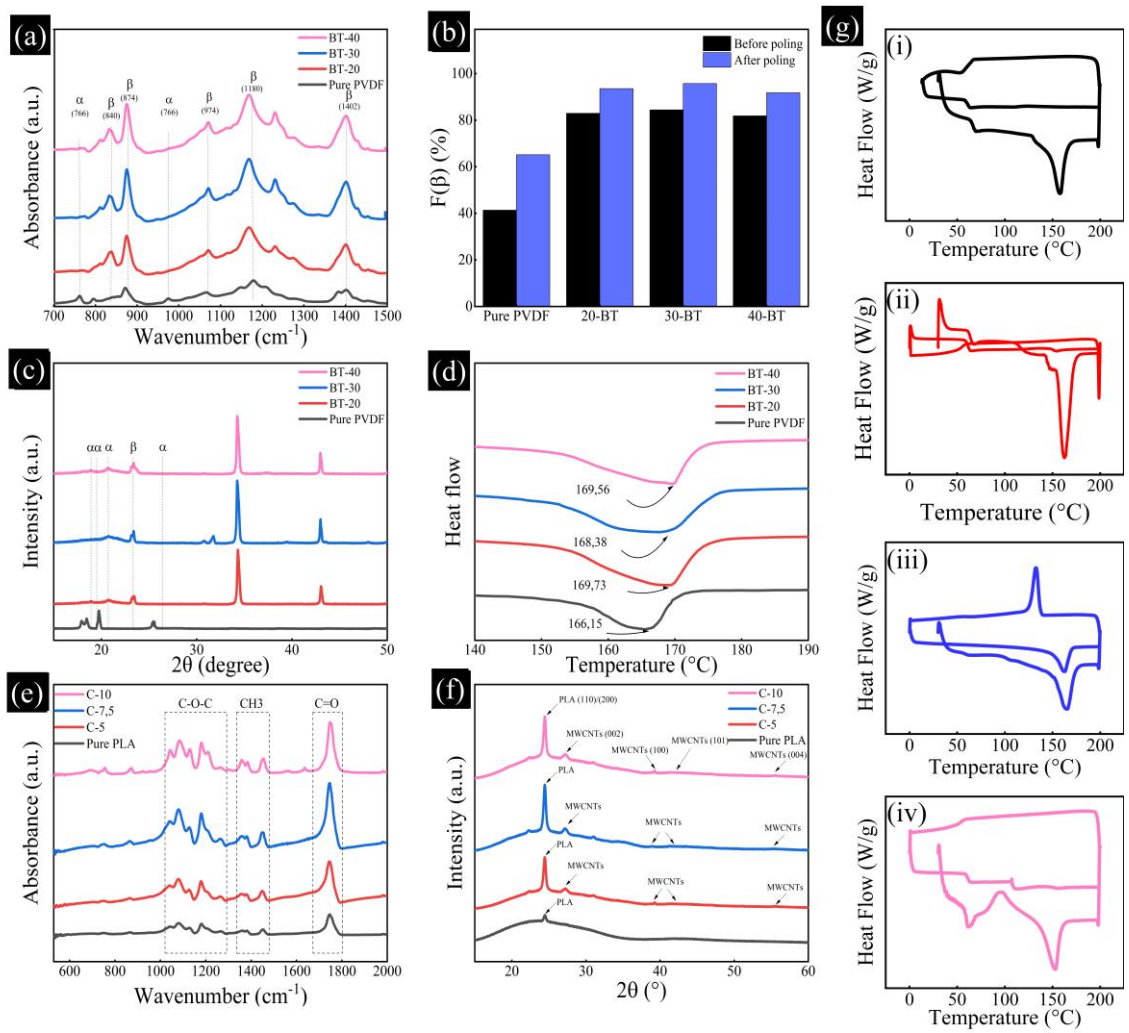

Figure 103: FTIR, XRD, and DSC characterization of 3D-printed nanocomposites before and after electrical poling : FT-IR spectra of PVDF, and PVDF/BT 3D printed samples (b) β-phase content of 3D-printed PVDF and PVDF/BT samples before and after poling (c) Xray diffraction patterns of the FDM 3D-printed PVDF and PVDF/BT samples. (d) DSC curves of PVDF and PVDF/BT samples (heating curve). (e) FT-IR spectra of PLA and PLA/MWCNTs samples 3D-printed. (f) X-ray diffraction patterns of PLA and PLA/MWCNTs samples 3D-printed. (g) DSC curves of PVDF/MWCNT samples: heating and cooling curves of (i) Pure Pla, (ii) C-5, (iii) C-7.5, and (iv) C-10.

Table 39: Thermal properties of PLA and PLA/MWCNTs SMC determined by DSC test.

Sample	Tg (°C)	Tm (°C)	Tc (°C)
Pure PLA	69.99	157.72	-
C-5	69.91	162.28	-
C-7.5	69.92	166.91	199.64
C-10	69.96	154.05	-

As shown in Figure 103(a), FT-IR spectral analysis highlights the phase transitions in PVDF. With increasing BT content, a significant reduction in the absorption peaks associated with the α-phase of PVDF (at 766 and 974 cm^{-1}) is observed. At the same time, the absorption peaks corresponding to the β-phase of PVDF, found at 840, 874, 1067, 1180 and 1402 cm^{-1}, become more pronounced. These results confirm enhanced crystallization in the piezoelectrically favorable β-phase.

Using Equation (132), the crystallization fraction of the β-phase was calculated. The results—- both before and after poling— - are shown in Figure 103 (b). While pure PVDF has a β-phase content of 41.357, the incorporation of 20 wt% BT coupled with the poling process significantly increases the β-phase content to 93.524%. This improvement is attributed to the role of BT nanoparticles as nucleating agents that align the PVDF molecules in the β-phase structure. The highest β-phase fraction of 95.727% is achieved with 30 wt% BT, which is the optimal filler concentration for inducing the β-phase transition.

Figure 103(c) shows the XRD patterns of pure PVDF and its nanocomposites with different BT concentrations. The pure PVDF sample exhibits distinct reflection peaks at $2\theta = 17.6°$, 18.3°, 19.9°, and 26.5°, which correspond to the crystallographic planes (100), (020), (110), and (021) of the α-phase, respectively. The incorporation of BT nanoparticles reduces the intensity of these α-phase peaks, while a prominent peak occurs at $2\theta = 20.6°$, which is associated with the β-phase. The XRD patterns also show diffraction peaks at $2\theta = 23.1°$, 33.3°, 39.2° and 44.09°, corresponding to the (100), (110), (200) and (210) reflections of BT, respectively. In addition, new phases appear in the BT-30 composite at $2\theta = 30.84°$ and 31.7°, which are due to electrostatic interactions between the polar fluorine atoms in PVDF and the polarizable oxygen and barium ions in BT. These newly formed interfacial phases improve the interaction between PVDF and BT, which facilitates the transfer of stresses and improves the

conversion of mechanical energy into electrical energy. The 30% BT composition provides an optimal balance that promotes the nucleation and growth of these phases while improving the piezoelectric performance of the material.

Figure 103(d) shows the differential scanning calorimetry (DSC) analysis revealing the melting behavior of the samples. The DSC curves show a shift in the melting temperature (Tm) of the PVDF/BT nanocomposites to higher values as the BT content increases. This shift reflects the increased thermal stability exhibited by the BT nanoparticles due to their ceramic nature and high melting point.

Figure 103(e) compares the FTIR spectra of pure PLA and PLA/MWCNT nanocomposites with different MWCNT concentrations (0.5%, 7.5% and 10%). In pure PLA, characteristic peaks include a strong band at 1750 cm^{-1}, which corresponds to the stretching vibration of the carbonyl group (C=O), and bands between 1050–1300 cm^{-1}, which are attributed to the stretching of the ester bond (C-O-C). In addition, bending vibrations of the methyl group (CH_3) are observed at 1450 cm^{-1} and 1380 cm^{-1}. The incorporation of MWCNTs gives rise to new peaks in the low wavenumber region (600–900 cm^{-1}), which are associated with C-C vibrations and MWCNT-polymer interactions. The ester bond region (1050–1300 cm^{-1}) shows a broadening, indicating strong interfacial interactions between the MWCNTs and the PLA chains. In addition, the intensity of the C=O stretching peak at 1750 cm^{-1} increases with higher MWCNT content, indicating increased crystallinity in the PLA matrix. These results emphasize the contribution of MWCNTs in improving the crystalline and molecular structure of the material and pave the way for improved mechanical and thermal properties.

The XRD patterns of the 3D-printed PLA/MWCNTs nanocomposites, shown in Figure 103(f), further illustrate the influence of MWCNTs on the crystalline properties of the PLA matrix. The crystalline PLA peak at $2\theta = 24°$, which corresponds to the (110)/(200) planes, becomes more prominent with increasing MWCNTs content, while the amorphous peak decreases in the range of 16° to 30°. This observation confirms that MWCNTs act as nucleation sites and promote higher crystallinity within the PLA matrix. The higher crystallinity contributes to improved mechanical stability, better shape fixity performance, and improved structural integrity of the nanocomposite.

Distinct peaks associated with MWCNTs can also be seen. The sharp peak at $2\theta = 26°$ corresponds to the graphitic (002) planes, representing the characteristic structure of MWCNTs. Additional peaks at $2\theta = 40°$ and 43° are attributed to the (100) and (101) planes,

respectively, indicating the hexagonal arrangement of carbon atoms in the graphene layers. The peak at 2θ = 55° represents higher order reflections that provide further insight into the structural details of MWCNTs. These observations emphasize the dual role of MWCNTs in enhancing the crystallinity of the PLA matrix and introducing their intrinsic structural properties into the nanocomposite.

Figure 103(g) shows the differential scanning calorimetry (DSC) curves for PLA/MWCNTs composites with 5 %, 7.5 % and 10 % MWCNTs, which give an insight into their thermal behavior. For pure PLA (graph i), a clear Tg was observed at around 69.99 °C, reflecting the characteristic transition of the amorphous region

In the case of the C-5 sample (graph ii), the DSC curve shows a Tg at 69.91°C, which is comparable to that of pure PLA, indicating that the addition of 5% MWCNTs has a minimal effect on the glass transition behavior. However, the melting temperature (Tm) is 162.28°C, which is slightly higher than that of pure PLA, indicating a moderate nucleation effect due to the dispersed MWCNTs. The endothermic peak remains relatively sharp, indicating that the MWCNTs are well dispersed at this concentration but do not significantly alter the crystallization kinetics of PLA. This concentration represents an intermediate state where the thermal stability is slightly improved without significantly changing the melting behavior.

The DSC curve for the C-7.5 sample (graph ii) shows a broader and slightly shifted endothermic peak corresponding to the melting temperature. The higher melting temperature at 176.91°C, indicates improved thermal stability compared to the C-5 sample. The broader endothermic peak also reflects a more heterogeneous melting behavior, possibly due to better dispersion of the MWCNTs in the PLA matrix, which enhances the nucleation effect. The glass transition temperature is observed at 69.92°C, which is in line with the expected range for PLA-based composites. This balance between dispersion and interaction leads to an improved thermal response, highlighting C-7.5 as an effective filler concentration.

For the C-10 sample (graph iii), the DSC curve shows a shift of the endothermic peak corresponding to the melting temperature to a lower temperature (154.05°C) compared to pure PLA. This decrease in Tm suggests that the higher MWCNT content disrupts the crystalline structure of PLA, reducing its overall crystallinity. The glass transition temperature is 69.96°C, which is consistent with the other samples and indicates that the addition of MWCNTs does not significantly change the softening behavior of the PLA matrix.

For the C-7.5 sample (graph ii), the DSC curve shows a clear exothermic peak corresponding to the crystallization temperature at 199.64°C. This exothermic peak indicates the release of energy as the polymer chains reorganize into a crystalline structure during cooling. Interestingly, this peak is not observed in the 5% or 10% MWCNT samples, suggesting that the 7.5% MWCNT concentration provides an optimal environment for crystallization.

The occurrence of the exothermic peak in the C-7.5 sample can be attributed to the effective dispersion of MWCNTs in the PLA matrix, which enhances their role as nucleating agents. This dispersion promotes the alignment and crystallization of the polymer chains, resulting in a well-defined exothermic peak. In contrast, the absence of this peak in the C-10 sample is likely due to agglomeration of the MWCNTs at higher concentrations, which disrupts the reorganization of the chains and reduces the degree of crystallinity. Similarly, the MWCNT content of the C-5 sample might not be sufficient to significantly affect the crystallization process. The presence of this exothermic peak in the C-7.5 sample highlights its superior crystallization behavior compared to the other compositions and makes it a promising candidate for applications requiring improved crystalline structure and thermal properties. The thermal parameters of the four samples are shown in detail in Table 39, providing a detailed comparison of the glass transition temperatures (Tg), cold crystallization temperatures (Tc) and melting temperatures (Tm).

10.5.3 Piezoelectric and dielectric behavior

As shown in Figure 104(a), the dielectric properties of PVDF/BT nanocomposites were investigated over a frequency range of (10^2-10^4 Hz). The dielectric constant was found to decrease significantly with increasing frequency, especially at lower frequencies. This behavior is primarily attributed to the Maxwell-Wagner-Sillars (MWS) interfacial polarization that occurs at the interfaces between PVDF and BT nanoparticles. In Figure 104 (b), pure PVDF exhibits a moderate dielectric constant (ε=9.50 at 100 Hz). The addition of BT nanoparticles leads to a progressive increase in the dielectric constant of the nanocomposites, reaching a peak value of 24.8 for the BT-40 sample. However, the addition of BT also leads to an increase in dielectric loss, as shown in Figure 104 (c). Across the entire frequency spectrum, the dielectric loss in the nanocomposites exceeds that of pure PVDF, with the strongest effects observed at lower frequencies. Despite the increase in dielectric loss with higher BT content, the peak value remains relatively low (0.022 at 100 Hz), implying only a small negative impact on the practical applicability of the material. Figure 104 (d) shows the values of the piezoelectric coefficient

(d33) for the nanocomposites. The BT-30 sample has the highest d33 value of 28 pC/N. However, increasing the BT content to 40 wt% leads to a decrease in d33 to 22 pC/N. This decrease can be attributed to excessive BT content leading to defects in the PVDF matrix. These defects interfere with the correct alignment of the PVDF chains, reducing the degree of polarization and affecting the piezoelectric performance.

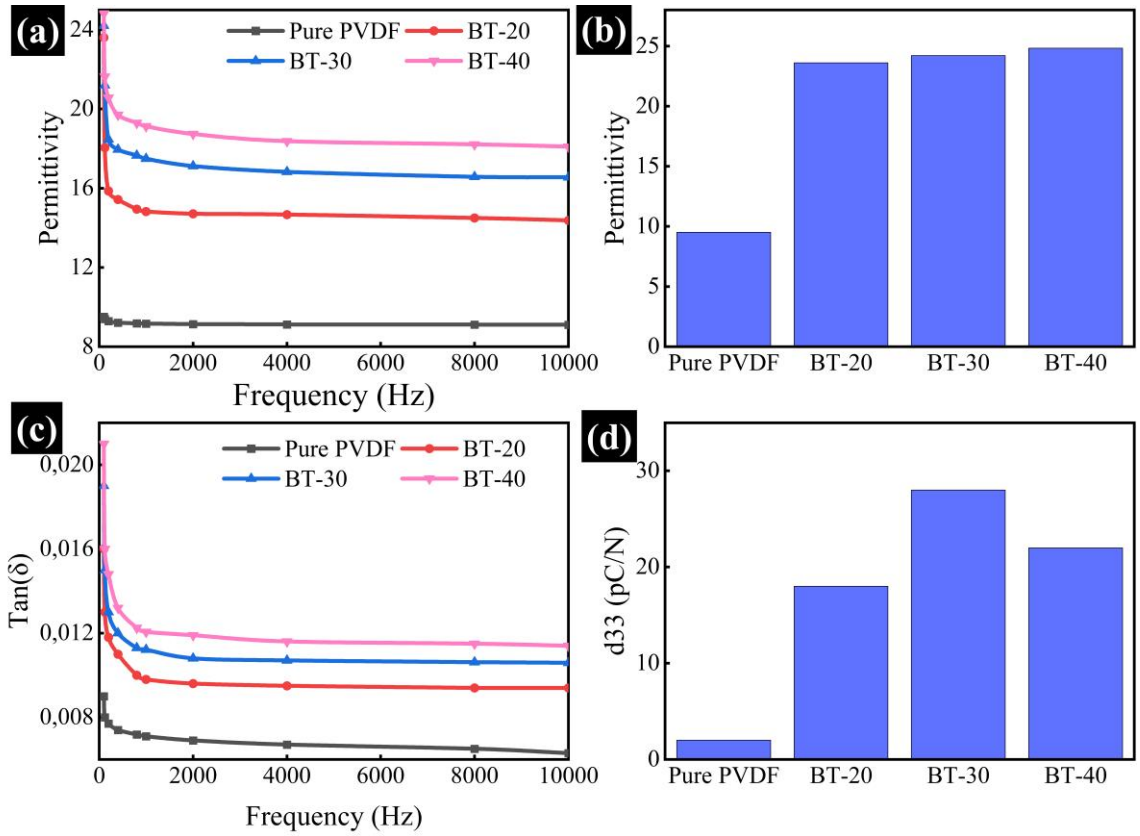

Figure 104: Dielectric and piezoelectric performance comparison of 3D-printed PVDF-based composites : (a) Frequency dependence of the dielectric constant (b) dielectric constant of the four PVDF/BT samples at 100 Hz (c) Frequency dependence of the dielectric loss (d) d33 coefficients of the piezoelectric nanocomposites

10.5.4 Heat transfer and shape memory performances

Figure 105(a) shows the visual appearance of 3D-printed PLA/MWCNTs nanocomposites with different MWCNT contents (C-5, C-7.5 and C-10). The uniformity and smooth surface of the printed structures show that the incorporation of MWCNTs does not significantly affect the printability of the PLA matrix. Figure 105(b) shows the temperature-time curves for the C-7.5 nanocomposite at an applied voltage of 10 V and different currents (0.06 A, 0.08 A, 0.1 A, 0.12 A and 0.14 A). As expected, higher currents lead to a stronger temperature rise, which shows

that the electrothermal performance is directly dependent on the applied current. Therefore, a current of 0.14 A was chosen for the further experiments in this study.

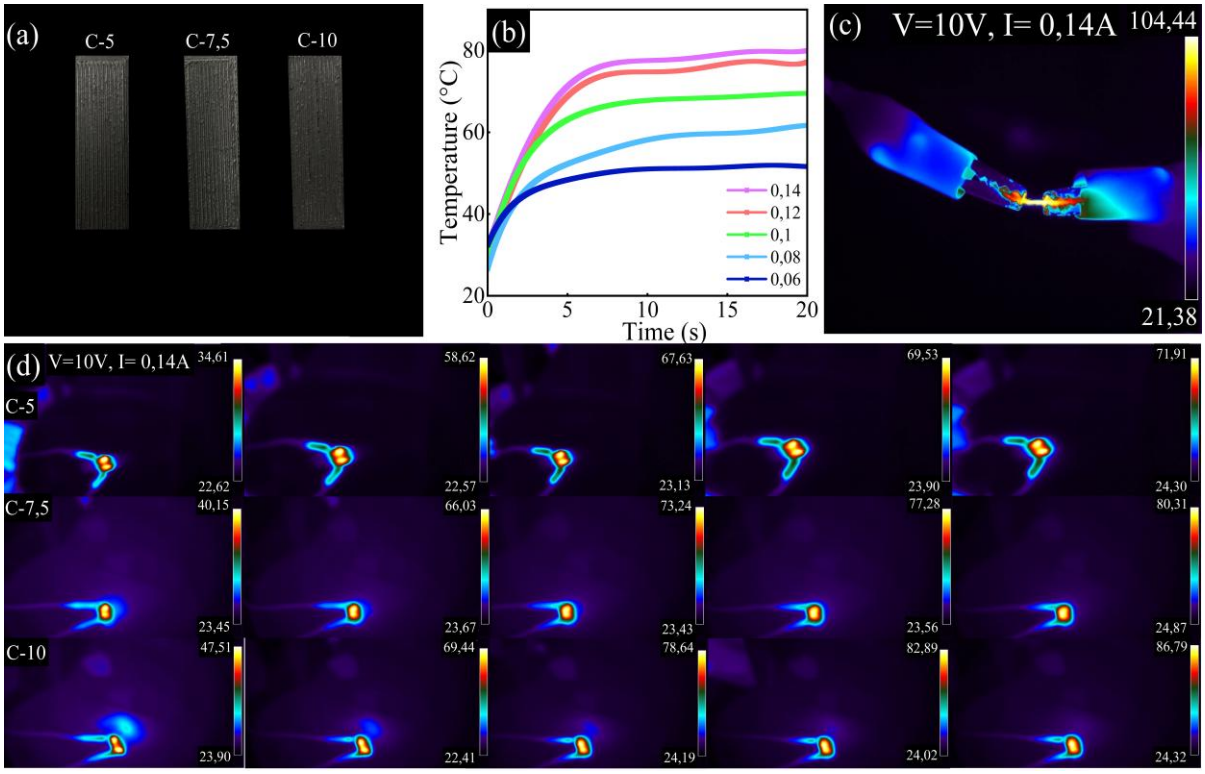

Figure 105: Current to heat conversion performances of PLA/MWCNTs nanocomposites : (a) Visual appearance of the 3D-printed PLA/MWCNTs samples; (b) Influence of applied current on the heating rate of the C-7.5 sample. (c) Heat distribution maps of the C-7.5 sample cross section under optimal inputs conditions (0.14 A). (d) Heat distribution maps of PLA/MWCNTs nanocomposite with different MWCNTs content under voltage of 10 V and current of 0.14 A.

Figure 105(c) shows an infrared thermal image of the cross-section of the C-7.5 sample at a voltage of 10 V and a current of 0.14 A. The image shows a localized and significant temperature rise, reaching 104.44 °C. This result confirms the ability of the material to efficiently convert electrical energy into heat at specific locations. Such precise and localized heating is essential for the activation of shape memory behavior in complex multi-material structures, where a controlled temperature at the joints ensures the desired shape change. Figure 105(d) shows infrared thermal images recording the temperature evolution of PLA/MWCNTs nanocomposites with different MWCNT contents (5 %, 7.5 % and 10 %) at a constant voltage of 10 V and a current of 0.14 A. The thermal responses were recorded at different time intervals (2

s, 4 s, 6 s, 8 s and 10 s) to illustrate the heating behavior of the nanocomposites. The results show a clear temperature difference between the samples, with C-10 exhibiting the highest temperature increase, followed by C-7.5 and C-5. This trend indicates that higher MWCNT content improves the thermal response, likely due to improved electrical conductivity and more efficient Joule heating. The progressive increase in temperature confirms the ability of the material to convert electrical energy into heat, a crucial attribute for triggering the shape memory effect in the electroresponsive SMC. Although the C-10 sample showed better efficiency in converting electricity to heat, reaching 86.79°C in only 10 seconds, the C-7.5 sample was selected as the optimal composition due to its better crystalline behavior, as explained in the previous subsection. Moreover, the C-7.5 sample was able to reach a temperature of up to 80°C, which significantly exceeds its Tg. To further confirm this choice, SEM analysis of the extruded filaments of both the C-7.5 and C-10 samples was performed. The results, shown in Figure S1, reveal the excellent surface quality and smoothness of the C-7.5 sample compared to the rough surface of C-10, further supporting its selection as the ideal composition.

Figure 106 (a) shows the visual appearance of the 3D printed electroactive SMC structure with different MWCNTs fractions, labeled as C-5, C-7.5 and C-10. Figure 106 (b) illustrates the programming and recovery process of the shape memory cycle. The structure is first heated above the glass transition temperature (T=80∘C) under an applied electric current, which deforms it from its original angle θ_0=180∘ to a programmed angle θ_p =0. The shape is then fixed by cooling the structure, resulting in a bent angle θ_f. The shape fixation ratio is defined as:

$$\text{SFR}\ (\%) = \frac{\theta_0 - \theta_f}{\theta_0} \times 100.$$

In the recovery phase, the sample is returned to its original shape by reheating, resulting in a recovered angle θ_r that emphasizes the electroactive response enabled by the conductive PLA/MWCNTs SMC. The shape recovery ratio is defined as:

$$\text{SRR}\ (\%) = \frac{\theta_r - \theta_f}{\theta_0 - \theta_f} \times 100.$$

This process demonstrates the material's ability to make precise and reversible shape changes, which is essential for applications requiring controlled actuation. Figure 106(c) shows a programmed temporary shape of the composite pattern and illustrates its ability to maintain a deformed shape until recovery is triggered. Figure 106(d) shows the SFR for the different SMC. All samples exhibit a high degree of fixity, with C-7.5 achieving the highest SFR at 97.6%,

closely followed by C-5 at 96.9%. In contrast, the sample, C-10, has a slightly lower SFR of 96.5%. Figure 8(e) illustrates the shape recovery ratio (SRR) over time for the three SMC samples: C-5, C-7.5, and C-10.

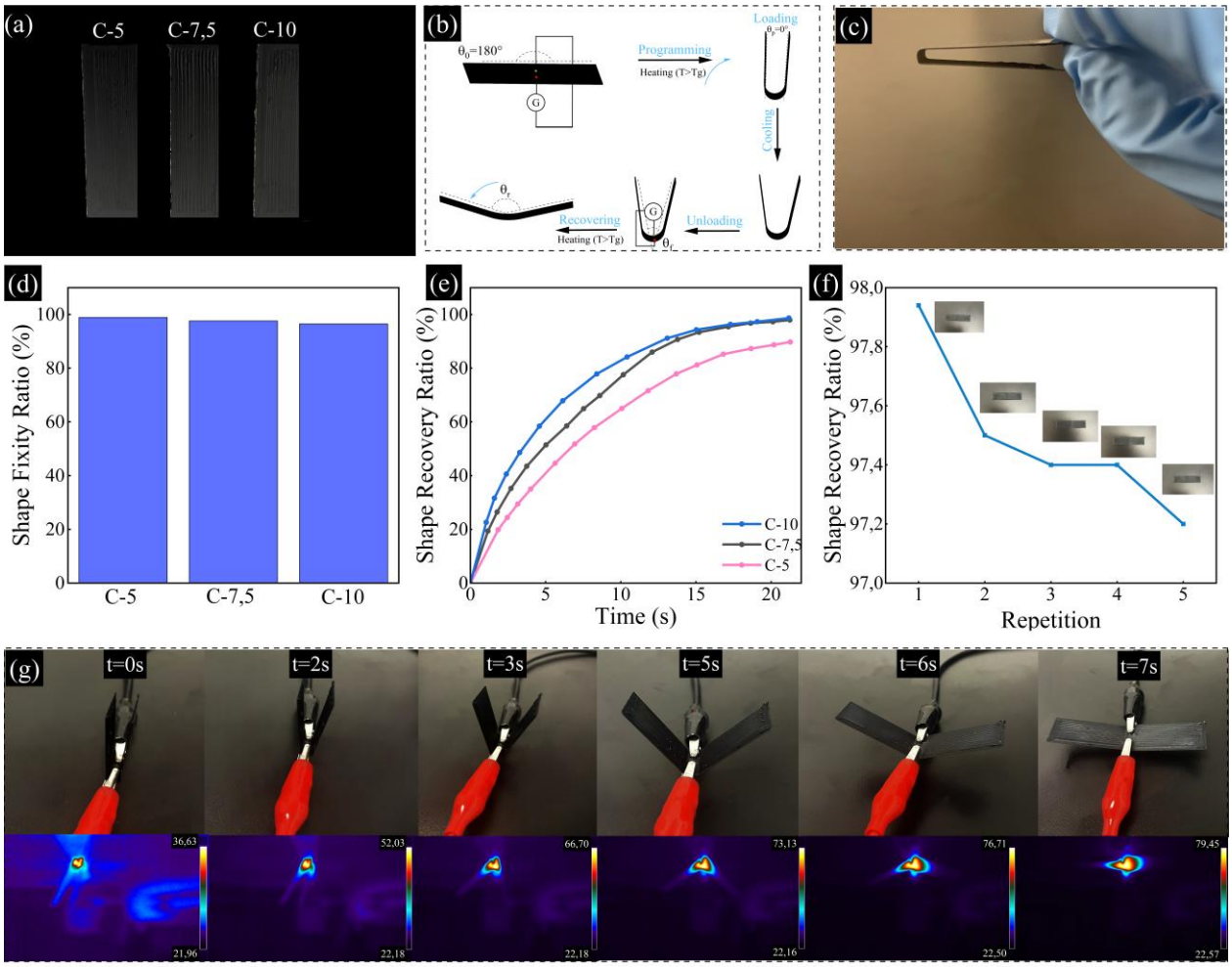

Figure 106: Shape memory behavior of PLA/MWCNTs composites under thermal and electric activation : (a) 3D printed PLA/MWCNTs composite samples (C-5, C-7.5, C-10). (b) Programming and recovery mechanism for shape memory behavior. (c) Demonstration of programmed temporary shape. (d) Shape fixity ratio for C-5, C-7.5 and C-10 samples. (e) Shape recovery ratio over time for C-5, C-7.5 and C-10 samples. (f) Evolution of shape recovery ratio with repeated shape memory cycles. (g) Thermal image sequence showing temperature evolution during shape recovery.

The data show that the C-10 sample exhibits the highest recovery rate and recovery ratio (98.77%), followed by C-7.5 (95.94%) and C-5 (79.91%). These results indicate that higher MWCNTs content increases the thermal conductivity and thus accelerates the shape recovery process. The slower recovery rate of C-5 can be attributed to its lower efficiency in converting electric current into heat. The recovered shapes of the three SMC are presented in Figure S2.

Figure 106(f) shows the SRR of C-7.5 over multiple cycles of deformation and recovery. The graph shows a slight decrease in SRR with each cycle, dropping from 97.94% to 97.85% over five cycles, which corresponds to a minimal loss of 0.1% in shape recovery. The accompanying images visually document the state of the SMC structure during each cycle and effectively correlate with the observed decline in SRR. This analysis is critical for evaluating the durability and long-term reliability of the SMC. Figure 106(g) shows a sequence of thermal images and corresponding photographs taken during the process of shape recovery of the C-7.5 SMC structure under an applied voltage of 10V and current of 0.14. The sequence shows the temperature distribution at different time intervals (0s, 2s, 3s, 5s, 6s, 9s). The temperature increases from 36.63°C to 79.45°C, indicating efficient heat generation and transfer through the PLA/MWCNTs sample.

To demonstrate the multiresponsive behavior of our developed SMC, hot water was used as an additional stimulus to activate the shape change of the material. Figure S3 illustrates the recovery process of the structure at a temperature of 80°C. The results show an excellent shape recovery, which was achieved in only 4 seconds. In addition, the shape fixity and recovery ratios under the two stimuli were compared in Figure S4. The data show an excellent shape fixity ratio of 97.4% and a shape recovery ratio of 98.9% when the sample is exposed to hot water, which exceeds the shape memory performance observed under an electric field.

10.5.5 Fabrication, test, and experimental validations

Figure 107 comprehensively illustrates the development and performance of the 4D-printed MSMC-PEH. Figure 107(a) shows the multi-material 3D printing process used to produce the MSMC-PEH using an FDM ULTIMAKER 3D printer, with the integration of PLA/MWCNTs SMC joint. Figure 107(b) shows the high flexibility of the piezoelectric layer made of PVDF/BT, a crucial component to improve the energy conversion efficiency of the system. Figure 107(c) shows a detailed schematic of the final structure of the MSMC-PEH, including the piezoelectric core layer between the copper layer and the silver electrode, all secured together with Kapton tape. Figure 107(d) explains the shape memory principle used in this work, describing the programming and recovery cycles that transform the MSMC-PEH into its different temporary configurations (L-, V- and U-shape). with θ_p is the pre-programmed angle achieved at a temperature of 80°C. This mechanism highlights the system's ability to achieve controlled shape changes in response to external stimuli (heat or electric field) and demonstrates the unique advantages of combining 4D printing with piezoelectric energy harvesting.

The Programming and recovery mechanism for shape memory behavior of the MSMC-PEH is detailed in Figure S5.

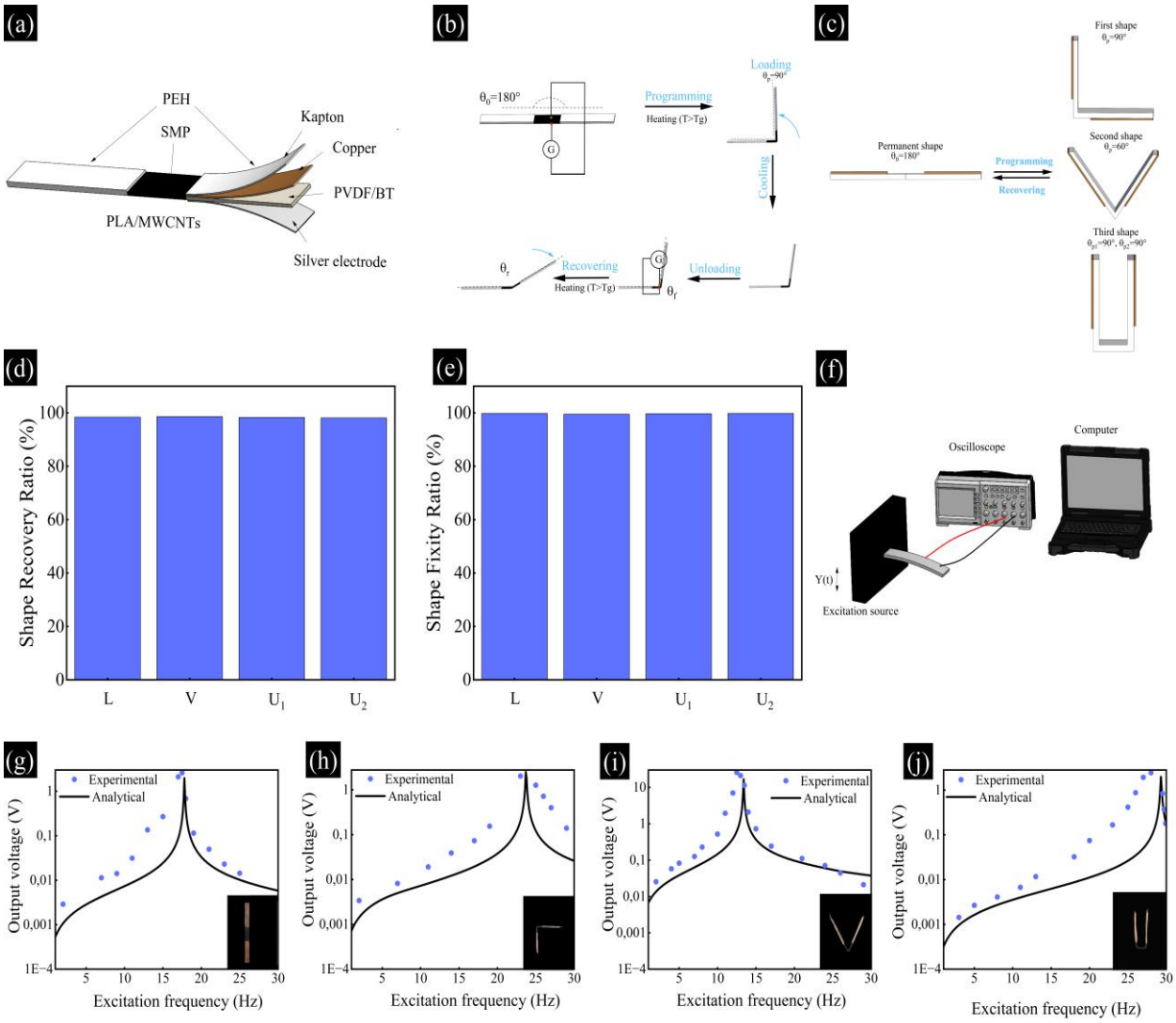

Figure 107: Fabrication and performance evaluation of MSMC-PEH in multiple configurations : (a) Multi-material 3D printing process for MSMC-PEH fabrication. (b) Demonstration of the high flexibility of the MSMC-PEH. (c) Structural composition of the MSMC-PEH with SMC and piezoelectric layers. (d) Shape programming and recovery process of the MSMC-PEH with temporary configurations. (e) Shape recovery ratio for different configurations (L, V, U), where U_1 and U_2 correspond to the two joints of the U-shaped structure. (f) Shape fixity ratio for different configurations (L, V, U) where U_1 and U_2 correspond to the two joints of the U-shaped structure. Experimental and analytical voltage output for (g) the cantilever beam, (h) the L-shaped configuration, (i) the V-shaped configuration and (j) the U-shaped configuration.

Table 40: Quantitative comparisons of theoretical and experimental results of the first resonance frequencies and output voltages of each configuration with bending motions.

Configuration	Cantilever	L-shaped	V-shaped	U-shaped

Analytical	17.8/1.979V	23.7/2.502V	29.3/1.976V	13.4/17.752V
Experimental	17.5/2.4V	23/2.1V	28/2.44V	12.5/22.8V
Error (%)	1.685/21.273	2.953/16.067	4.436/23.481	6.716/28.436

The performance of MSMC-PEH in terms of shape recovery and fixity is quantified in Figures 108 (e) and (f). The results show a near-perfect shape recovery ratio (over 98%) and fixity ratio (over 99%) for all tested configurations, highlighting the exceptional material properties and structural integrity of the system under dynamic transformations. These results confirm the reliability and effectiveness of the MSMC-PEH in maintaining its programmed and recovered shapes under different conditions. Finally, Figures 108 (g), (h), (i) and (j) show the experimental validation of the energy harvesting performance of the MSMC-PEH at the first natural frequency for each configuration. The insets in these sub-figures visually represent the corresponding shapes during the test and illustrate the remarkable functional adaptability of the system. The actual experimental setup used to test the piezoelectric performance of each configuration is shown in Figure S6. The numerical comparison between experimental and analytical results, summarized in Table, shows an excellent agreement of the resonant frequency values, underlining the reliability of the design and the precision of the prediction models. The observed discrepancies in the voltage output between the analytical and experimental results can be attributed to the simplifications and assumptions in the theoretical models, especially in the modeling of the SMC components. Furthermore, measurement inaccuracies and the limited precision of the test equipment can introduce additional uncertainties into the experimental results.

10.6 Conclusion

In this study, a 4D-printed multiresponsive shape memory composite (MSMC-PEH) was developed to overcome the dual challenge of achieving adaptability and high energy conversion efficiency in a single structure. The innovative design integrates a piezoelectric PVDF/BT nanocomposite component with a SMC of PLA/MWCNTs that enables seamless transitions between different configurations (cantilever beam, L-, V- and U-shaped) in response to electrical or thermal stimuli.

The selection of nanocomposite compositions was determined by extensive characterization testing as well as current-to-heat conversion and shape memory performance tests under different stimuli for the SMC part.

The MSMC-PEH was fabricated using multi-material FDM 3D printing technology and tested under two different stimuli. The results showed excellent performance, with a shape recovery and fixity ratios exceeding 98% and 99% respectively, confirming the reliability and adaptability of the system. To evaluate the energy harvesting capabilities of the MSMC-PEH, an analytical model was developed using established theories such as Euler-Bernoulli beam theory, Hamilton's principle and Galerkin's technique. This model was validated by numerical simulations and experimental tests. This revealed a strong correlation between the theoretical predictions and the observed results.

By achieving a wide operating bandwidth in a frequency range from 2 to 120 Hz the MSMC-PEH exhibits remarkable versatility, making it ideal for various practical applications such as robotics, wearable devices and sensor systems.

This work lays a solid foundation for future innovation in adaptive energy harvesting technologies and highlights the transformative potential of 4D printing in the development of multifunctional, high-performance systems.

10.7 Acknowledgment

The authors acknowledge the funding provided by the Natural Sciences and Engineering Research Council (NSERC) of Canada in the form of Discovery Grants (Grant Number: CRSNG – RGPIN -2021-02846).

10.8 References

[1] L. Persano, A. Camposeo, F. Matino, R. Wang, T. Natarajan, Q. Li, M. Pan, Y. Su, S. Kar-Narayan, F. Auricchio, Advanced materials for energy harvesting and soft robotics: Emerging frontiers to enhance piezoelectric performance and functionality, Advanced Materials 36(45) (2024) 2405363.

[2] M. Han, H. Wang, Y. Yang, C. Liang, W. Bai, Z. Yan, H. Li, Y. Xue, X. Wang, B. Akar, Three-dimensional piezoelectric polymer microsystems for vibrational energy harvesting, robotic interfaces and biomedical implants, Nature Electronics 2(1) (2019) 26-35.

[3] A. Megdich, M. Habibi, L. Laperrière, A review on 3D printed piezoelectric energy harvesters: materials, 3D printing techniques, and applications, Materials Today Communications 35 (2023) 105541.

[4] S.D. Mahapatra, P.C. Mohapatra, A.I. Aria, G. Christie, Y.K. Mishra, S. Hofmann, V.K. Thakur, Piezoelectric materials for energy harvesting and sensing applications: roadmap for future smart materials, Advanced Science 8(17) (2021) 2100864.

[5] S. Panda, S. Hajra, K. Mistewicz, P. In-na, M. Sahu, P.M. Rajaitha, H.J. Kim, Piezoelectric energy harvesting systems for biomedical applications, Nano Energy 100 (2022) 107514.

[6] F. Ali, W. Raza, X. Li, H. Gul, K.-H. Kim, Piezoelectric energy harvesters for biomedical applications, Nano Energy 57 (2019) 879-902.

[7] A. Megdich, M. Habibi, L. Laperrière, Z. Li, Y. Abdin, Enhanced piezoelectric performance of PVDF/MWCNTs energy harvester through a 3D-printed multimodal auxetic structure for smart security systems, Materials Today Sustainability 27 (2024) 100847.
[8] A. Ali, H. Shaukat, S. Bibi, W.A. Altabey, M. Noori, S.A. Kouritem, Recent progress in energy harvesting systems for wearable technology, Energy Strategy Reviews 49 (2023) 101124.
[9] S.V. Fernandez, F. Cai, S. Chen, E. Suh, J. Tiepelt, R. McIntosh, C. Marcus, D. Acosta, D. Mejorado, C. Dagdeviren, On-body piezoelectric energy harvesters through innovative designs and conformable structures, ACS Biomaterials Science & Engineering 9(5) (2021) 2070-2086.
[10] F. Mokhtari, M. Shamshirsaz, M. Latifi, J. Foroughi, Nanofibers-based piezoelectric energy harvester for self-powered wearable technologies, Polymers 12(11) (2020) 2697.
[11] R. Hesham, A. Soltan, A. Madian, Energy harvesting schemes for wearable devices, AEU-International Journal of Electronics and Communications 138 (2021) 153888.
[12] A.I. Sadaf, R.U. Ahmed, H. Ahmed, Cantilever configurations in vibration-based piezoelectric energy harvesting: A comprehensive review on beam shapes and multi-beam formations, Smart Materials and Structures (2024).
[13] Q. Xu, A. Gao, Y. Li, Y. Jin, Design and optimization of piezoelectric cantilever beam vibration energy harvester, Micromachines 13(5) (2022) 675.
[14] X. He, D. Li, H. Zhou, X. Hui, X. Mu, Theoretical and experimental studies on MEMS variable cross-section cantilever beam based piezoelectric vibration energy harvester, Micromachines 12(7) (2021) 772.
[15] J.-X. Wang, W.-B. Su, J.-C. Li, C.-M. Wang, A rotational piezoelectric energy harvester based on trapezoid beam: Simulation and experiment, Renewable Energy 184 (2022) 619-626.
[16] J. Song, G. Sun, X. Zeng, X. Li, Q. Bai, X. Zheng, Piezoelectric energy harvester with double cantilever beam undergoing coupled bending-torsion vibrations by width-splitting method, Scientific Reports 12(1) (2022) 583.
[17] M.S. Salem, S. Ahmed, A. Shaker, M.T. Alshammari, K.A. Al-Dhlan, A. Alanazi, A. Saeed, M. Abouelatta, Bandwidth broadening of piezoelectric energy harvesters using arrays of a proposed piezoelectric cantilever structure, Micromachines 12(8) (2021) 973.
[18] J. Wang, Z. Xue, C. Cai, D. Wang, A novel piezoelectric energy harvester with different circular arc spiral cantilever beam, IEEE Sensors Journal 22(11) (2022) 11016-11022.
[19] K. Chen, Q. Gao, S. Fang, D. Zou, Z. Yang, W.-H. Liao, An auxetic nonlinear piezoelectric energy harvester for enhancing efficiency and bandwidth, Applied Energy 298 (2021) 117274.
[20] L. He, H. Kurita, F. Narita, Multimode auxetic piezoelectric energy harvester for low-frequency vibration, Smart Materials and Structures 33(3) (2024) 035020.
[21] I.E. Piyarathna, A.M. Thabet, M. Ucgul, C. Lemckert, Y.Y. Lim, Z.S. Tang, Linear segmented arc-shaped piezoelectric branch beam energy harvester for ultra-low frequency vibrations, Sensors 23(11) (2023) 5257.
[22] X. Li, D. Upadrashta, K. Yu, Y. Yang, Analytical modeling and validation of multi-mode piezoelectric energy harvester, Mechanical Systems and Signal Processing 124 (2019) 613-631.
[23] Z. Wang, T. Li, Y. Du, Z. Yan, T. Tan, Nonlinear broadband piezoelectric vibration energy harvesting enhanced by inter-well modulation, Energy Conversion and Management 246 (2021) 114661.
[24] R. Dauksevicius, R. Gaidys, V. Ostasevicius, R. Lockhart, A.V. Quintero, N. De Rooij, D. Briand, Nonlinear piezoelectric vibration energy harvester with frequency-tuned impacting resonators for improving broadband performance at low frequencies, Smart Materials and Structures 28(2) (2019) 025025.

[25] S. Nabavi, L. Zhang, Nonlinear multi-mode wideband piezoelectric MEMS vibration energy harvester, IEEE Sensors Journal 19(13) (2019) 4837-4848.
[26] C. Wang, S.-K. Lai, Z.-C. Wang, J.-M. Wang, W. Yang, Y.-Q. Ni, A low-frequency, broadband and tri-hybrid energy harvester with septuple-stable nonlinearity-enhanced mechanical frequency up-conversion mechanism for powering portable electronics, Nano Energy 64 (2019) 103943.
[27] Z. Xu, X. Shan, D. Chen, T. Xie, A novel tunable multi-frequency hybrid vibration energy harvester using piezoelectric and electromagnetic conversion mechanisms, Applied Sciences 6(1) (2015) 10.
[28] A. Megdich, M. Habibi, L. Laperriere, Electromechanical modelling of l-shaped bending-torsion piezoelectric energy harvesting systems, Applied Mathematical Modelling 138 (2025) 115755.
[29] B. Tiwari, T. Babu, R. Choudhary, Piezoelectric lead zirconate titanate as an energy material: A review study, Materials Today: Proceedings 43 (2021) 407-412.
[30] L. Hou, Y. Huan, M. Zheng, Y. Liu, C. Wang, X. Wang, C. Li, Z. Wang, T. Wei, 3D vertically aligned microchannel structure to enhance piezoelectric energy harvesting performance of PZT/PVDF&CNTs piezoelectric composites, Journal of Materiomics 10(5) (2024) 1063-1070.
[31] V. Ogbonna, A. Popoola, O. Popoola, Piezoelectric ceramic materials on transducer technology for energy harvesting: A review, Frontiers in Energy Research 10 (2022) 1051081.
[32] J. Wang, X. Qin, Z. Liu, G. Ding, G. Cai, Experimental study on fatigue degradation of piezoelectric energy harvesters under equivalent traffic load conditions, International Journal of Fatigue 150 (2021) 106320.
[33] T. Satyanarayana, Y. Nikhitha, C.N. Kumar, K.J.N. Sai, V. Lohitha, Optimization of bimorph cantilever based piezoelectric energy harvester for high efficiency, Materials Today: Proceedings 80 (2023) 2883-2887.
[34] M. Rashmi, K.T. Sairam, A. Suresh, Energy harvesting through piezoelectric technology, Materials Today: Proceedings (2023).
[35] Y. Huang, L. Zhang, R. Jing, M. Tang, D. Alikin, V. Shur, X. Wei, L. Jin, Lead zirconate titanate-based ceramics with high piezoelectricity and broad usage temperature range, Chemical Engineering Journal 477 (2023) 147192.
[36] A. Megdich, M. Habibi, L. Laperrière, Modeling and optimization of piezoelectric and dielectric properties of poled PVDF/BT nanocomposites, Polymer Bulletin (2024) 1-21.
[37] R. Wang, E. Tang, G. Yang, Y. Han, C. Chen, Dynamic fracture behavior of piezoelectric ceramics under impact: force-electric response and electrical breakdown, Journal of The European Ceramic Society 41(16) (2021) 139-150.
[38] R. Lay, G.S. Deijs, J. Malmström, The intrinsic piezoelectric properties of materials–a review with a focus on biological materials, RSC advances 11(49) (2021) 30657-30673.
[39] M. Abbasipour, R. Khajavi, A.H. Akbarzadeh, A comprehensive review on piezoelectric polymeric and ceramic nanogenerators, Advanced Engineering Materials 24(6) (2022) 2101312.
[40] I. Mendoza, D. Drury, A. Matejunas, J. Ivy, S. Koumlis, P. Jewell, G. Brennecka, L. Lamberson, Quasi-static and dynamic fracture behavior of lead zirconate titanate: a study of poling and loading rate, Engineering Fracture Mechanics 247 (2021) 107669.

Chapitre 11: Conclusions et Perspectives

11.1 Conclusions

Cette thèse a exploré la conception, la modélisation et la fabrication de dispositifs micro-électromécaniques (MEMS) piézoélectriques avancés en exploitant les potentialités de l'impression 4D. L'objectif était de surmonter les limitations des MEMS traditionnels en intégrant des matériaux intelligents capables d'adapter leur géométrie et leurs propriétés en fonction de stimuli externes, améliorant ainsi l'efficacité de récupération d'énergie mécanique.

Dans cette perspective, plusieurs contributions scientifiques et technologiques majeures ont été réalisées.

Nous avons tout d'abord concentré nos efforts sur l'étude et l'optimisation des systèmes micro-électromécaniques (MEMS) piézoélectriques pour la récupération d'énergie. L'objectif était d'améliorer leurs performances en travaillant sur plusieurs aspects fondamentaux : le choix des matériaux, l'optimisation des structures et le contrôle des paramètres de polarisation. Nous avons étudié en détail les nanocomposites piézoélectriques à base de PVDF, en intégrant divers additifs tels que le titanate de baryum et les nanotubes de carbone, afin d'améliorer leurs propriétés piézoélectriques et mécaniques. Par ailleurs, nous avons développé des modèles analytiques pour simuler et optimiser les structures des MEMS, permettant ainsi d'ajuster leurs fréquences naturelles afin de maximiser leur efficacité énergétique. L'impression 3D a été exploitée comme une alternative de fabrication pour garantir une précision accrue et une flexibilité structurelle optimisée, rendant ces dispositifs plus adaptés aux applications réelles.

En parallèle, nous avons mené des travaux spécifiques sur l'impression 4D, qui offre une approche révolutionnaire pour concevoir des structures dynamiques capables de modifier leur forme en réponse à des stimuli externes. Nous avons d'abord exploré les matériaux à mémoire de forme, notamment les polymères électroactifs et thermo-sensibles, afin de comprendre et maîtriser leurs comportements sous l'effet de champs électriques ou de variations thermiques.

Ces recherches ont impliqué la caractérisation des propriétés mécaniques, thermiques et électromécaniques des nanocomposites développés, ainsi que la modélisation numérique de leur capacité de transformation structurelle. L'objectif était d'optimiser les processus d'impression 4D en définissant les paramètres idéaux pour obtenir des structures programmables et réactives. Cette étude approfondie a permis de poser les bases nécessaires à l'intégration future de ces matériaux dans les MEMS afin de leur conférer des propriétés adaptatives et intelligentes.

Cette approche méthodologique, qui a consisté à étudier séparément les MEMS et l'impression 4D, s'est révélée essentielle pour garantir une maîtrise approfondie des deux technologies avant leur intégration. En développant une compréhension fine des matériaux, des structures et des processus de fabrication propres à chaque domaine, nous avons pu identifier les synergies possibles et concevoir des stratégies d'hybridation optimales. Cette démarche progressive a ouvert la voie à la conception de MEMS imprimés en 4D, capables d'ajuster dynamiquement leurs propriétés en fonction des conditions externes.

Les résultats obtenus ont démontré que l'association des MEMS piézoélectriques et de l'impression 4D représente une avancée significative dans le domaine de la récupération d'énergie. Cette approche permet non seulement d'accroître le rendement des dispositifs, mais également d'élargir leurs applications potentielles, notamment dans les systèmes autonomes, la biomédecine et l'électronique portable.

En conclusion, cette recherche apporte une contribution novatrice à la conception de MEMS adaptatifs et intelligents, tout en ouvrant la voie à de nouvelles investigations. L'optimisation des matériaux et des processus de fabrication, couplée aux avancées en intelligence artificielle pour la modulation des réponses électromécaniques, constitue une piste prometteuse pour le développement futur de dispositifs encore plus performants et polyvalents.

11.2 Perspectives

Ce projet de recherche ouvre des perspectives prometteuses pour le développement futur des technologies MEMS piézoélectriques et de l'impression 4D, ainsi que pour leur intégration synergique au sein de dispositifs intelligents et adaptatifs. Les axes suivants sont identifiés comme prioritaires pour consolider les avancées réalisées et étendre leur application à des dispositifs intelligents et autonomes :

- Amélioration de la densité de puissance énergétique

Afin d'augmenter l'efficacité des dispositifs piézoélectriques développés, il serait pertinent d'explorer de nouvelles architectures multimodales, capables de combiner plusieurs modes de

vibration (flexion, torsion, compression) dans une seule structure. Cette approche permettrait de capter un spectre plus large d'énergie mécanique ambiante. En parallèle, l'intégration de matériaux piézoélectriques alternatifs — tels que le PVDF-TrFE, le ZnO ou encore le PZT flexible — offrirait des points de comparaison sur le plan du rendement énergétique, et ouvrirait la voie à des structures optimisées selon les conditions vibratoires spécifiques de l'application visée.

- Co-design matériau/géométrie/procédé par intelligence artificielle

Le recours à des approches d'intelligence artificielle avancée constitue une piste prometteuse pour optimiser simultanément les paramètres du matériau, la géométrie fonctionnelle de la structure, et les conditions de fabrication additive (paramètres d'impression 3D/4D). Ce co-design intégré, fondé sur des algorithmes de type machine learning, permettrait d'accélérer la recherche de configurations optimales en matière de performance énergétique, de stabilité mécanique, et d'adaptabilité.

- Applications dans l'environnement réel

Les performances des dispositifs doivent être validées dans des contextes réels d'usage, afin de garantir leur pertinence fonctionnelle. Parmi les applications envisagées figurent les chaussures intelligentes, les capteurs embarqués dans des prothèses adaptatives, ou encore les systèmes de surveillance de structures dans les domaines du bâtiment, du transport ou de l'aéronautique. Ces démonstrateurs permettront de confronter les dispositifs à des contraintes dynamiques et environnementales variées, et d'évaluer leur robustesse et durabilité à long terme.

- Exploration de nouvelles structures multi-réactives

L'extension du concept vers des structures multi-stimuli constitue une voie d'évolution naturelle. Il s'agira notamment d'étudier des matériaux ou composites capables de répondre simultanément à plusieurs stimuli externes : lumière, humidité, champ magnétique, etc. En particulier, l'association de polymères à mémoire de forme (SMP) avec des hydrogels réactifs pourrait permettre d'obtenir une réactivité plus fine et différenciée selon l'environnement, ouvrant ainsi la voie à des dispositifs plus intelligents et autonomes.

Vers une nouvelle génération de MEMS 4D intelligents et adaptatifs :

- Couplage avec l'intelligence artificielle pour le pilotage adaptatif

L'évolution vers des MEMS 4D intelligents passera nécessairement par le pilotage embarqué via l'intelligence artificielle. En intégrant des algorithmes d'apprentissage automatique (machine learning) directement dans le système, ces MEMS seront capables de :

-Détecter en temps réel l'état vibratoire, thermique ou environnemental,

-Activer automatiquement les transformations 4D optimales (en termes de forme, d'orientation ou de fréquence),

-Co-optimiser en continu leur géométrie, leur rendement énergétique et leur comportement fonctionnel.

Cette adaptabilité dynamique permettra une réponse plus efficace aux stimuli changeants et favorisera l'autonomie décisionnelle des dispositifs dans des contextes réels.

- Applications dans l'environnement réel

Les perspectives applicatives incluent le développement de systèmes embarqués pour l'aéronautique et le spatial, dans lesquels la masse, la consommation énergétique et la fiabilité sont critiques. Des microrobots autonomes reconfigurables en temps réel, des implants biomédicaux adaptatifs, et des capteurs d'impact pour textiles intelligents, capables de s'auto-calibrer selon l'activité de l'utilisateur, représentent autant de débouchés concrets pour ces technologies MEMS 4D. Ces dispositifs pourraient ainsi répondre à des besoins spécifiques dans les domaines de la santé, de la surveillance et de l'interaction homme-environnement.

LISTE DE RÉFÉRENCES GLOBALE DES 9 ARTICLES

[1] S. Chalasani, J.M. Conrad, A survey of energy harvesting sources for embedded systems, IEEE SoutheastCon 2008, IEEE, 2008, pp. 442-447.
[2] M. Guan, W. Liao, On the efficiencies of piezoelectric energy harvesting circuits towards storage device voltages, Smart Materials and Structures 16(2) (2007) 498.
[3] H.A. Sodano, G. Park, D. Inman, Estimation of electric charge output for piezoelectric energy harvesting, Strain 40(2) (2004) 49-58.
[4] H.A. Sodano, D.J. Inman, G. Park, A review of power harvesting from vibration using piezoelectric materials, Shock and Vibration Digest 36(3) (2004) 197-206.
[5] S. Li, J. Yuan, H. Lipson, Ambient wind energy harvesting using cross-flow fluttering, Journal of applied physics 109(2) (2011).
[6] M.A. Weimer, T.S. Paing, R.A. Zane, Remote area wind energy harvesting for low-power autonomous sensors, 2006 37th IEEE Power Electronics Specialists Conference, IEEE, 2006, pp. 1-5.
[7] S. Li, H. Lipson, Vertical-stalk flapping-leaf generator for wind energy harvesting, Smart materials, adaptive structures and intelligent systems, 2009, pp. 611-619.
[8] Z. Abdin, M.A. Alim, R. Saidur, M.R. Islam, W. Rashmi, S. Mekhilef, A. Wadi, Solar energy harvesting with the application of nanotechnology, Renewable and sustainable energy reviews 26 (2013) 837-852.
[9] V. Raghunathan, A. Kansal, J. Hsu, J. Friedman, M. Srivastava, Design considerations for solar energy harvesting wireless embedded systems, IPSN 2005. Fourth International Symposium on Information Processing in Sensor Networks, 2005., IEEE, 2005, pp. 457-462.
[10] E.-J. Yoon, C.-G. Yu, Power management circuits for self-powered systems based on micro-scale solar energy harvesting, International Journal of Electronics 103(3) (2016) 516-529.
[11] D. Dondi, A. Bertacchini, L. Larcher, P. Pavan, D. Brunelli, L. Benini, A solar energy harvesting circuit for low power applications, 2008 IEEE International Conference on Sustainable Energy Technologies, IEEE, 2008, pp. 945-949.
[12] E.H.H. Al-Qadami, Z. Mustaffa, M.E. Al-Atroush, Evaluation of the pavement geothermal energy harvesting technologies towards sustainability and renewable energy, Energies 15(3) (2022) 1201.
[13] P.A. Østergaard, H. Lund, A renewable energy system in Frederikshavn using low-temperature geothermal energy for district heating, Applied Energy 88(2) (2011) 479-487.
[14] W.E. Glassley, Geothermal energy: renewable energy and the environment, CRC press2014.
[15] K. Wang, B. Yuan, G. Ji, X. Wu, A comprehensive review of geothermal energy extraction and utilization in oilfields, Journal of Petroleum Science and Engineering 168 (2018) 465-477.
[16] D. Jiang, M. Xu, M. Dong, F. Guo, X. Liu, G. Chen, Z.L. Wang, Water-solid triboelectric nanogenerators: An alternative means for harvesting hydropower, Renewable and Sustainable Energy Reviews 115 (2019) 109366.
[17] D.L. Vu, C.D. Le, K.K. Ahn, Functionalized graphene oxide/polyvinylidene fluoride composite membrane acting as a triboelectric layer for hydropower energy harvesting, International Journal of Energy Research 46(7) (2022) 9549-9559.
[18] J. Maas, C. Graf, Dielectric elastomers for hydro power harvesting, Smart Materials and Structures 21(6) (2012) 064006.

[19] S. Pobering, N. Schwesinger, A novel hydropower harvesting device, 2004 International Conference on MEMS, NANO and Smart Systems (ICMENS'04), IEEE, 2004, pp. 480-485.
[20] D. Abbas, D. Current, M. Phillips, R. Rossman, H. Hoganson, K.N. Brooks, Guidelines for harvesting forest biomass for energy: A synthesis of environmental considerations, Biomass and Bioenergy 35(11) (2011) 4538-4546.
[21] R. Singh, A.D. Setiawan, Biomass energy policies and strategies: Harvesting potential in India and Indonesia, Renewable and Sustainable Energy Reviews 22 (2013) 332-345.
[22] C.-H. Ko, S. Chaiprapat, L.-H. Kim, P. Hadi, S.-C. Hsu, S.-Y. Leu, Carbon sequestration potential via energy harvesting from agricultural biomass residues in Mekong River basin, Southeast Asia, Renewable and Sustainable Energy Reviews 68 (2017) 1051-1062.
[23] C.B. Field, J.E. Campbell, D.B. Lobell, Biomass energy: the scale of the potential resource, Trends in ecology & evolution 23(2) (2008) 65-72.
[24] A. Erturk, J. Hoffmann, D.J. Inman, A piezomagnetoelastic structure for broadband vibration energy harvesting, Applied Physics Letters 94(25) (2009).
[25] S.P. Beeby, R.N. Torah, M.J. Tudor, P. Glynne-Jones, T. O'Donnell, C.R. Saha, S. Roy, A micro electromagnetic generator for vibration energy harvesting, Journal of Micromechanics and microengineering 17(7) (2007) 1257.
[26] L. Zuo, X. Tang, Large-scale vibration energy harvesting, Journal of intelligent material systems and structures 24(11) (2013) 1405-1430.
[27] L. Gammaitoni, I. Neri, H. Vocca, Nonlinear oscillators for vibration energy harvesting, Applied Physics Letters 94(16) (2009).
[28] V.R. Challa, M.G. Prasad, Y. Shi, F.T. Fisher, A vibration energy harvesting device with bidirectional resonance frequency tunability, Smart Materials and Structures 17(1) (2008) 015035.
[29] L. Mateu, F. Moll, Review of energy harvesting techniques and applications for microelectronics, VLSI Circuits and Systems II, SPIE, 2005, pp. 359-373.
[30] P. Basset, D. Galayko, F. Cottone, R. Guillemet, E. Blokhina, F. Marty, T. Bourouina, Electrostatic vibration energy harvester with combined effect of electrical nonlinearities and mechanical impact, Journal of Micromechanics and Microengineering 24(3) (2014) 035001.
[31] P. Podder, A. Amann, S. Roy, Combined effect of bistability and mechanical impact on the performance of a nonlinear electromagnetic vibration energy harvester, IEEE/ASME Transactions On Mechatronics 21(2) (2015) 727-739.
[32] D. Cao, W. Xia, W. Hu, Low-frequency and broadband vibration energy harvester driven by mechanical impact based on layer-separated piezoelectric beam, Applied Mathematics and Mechanics 40(12) (2019) 1777-1790.
[33] G. Shi, D. Tong, Y. Xia, S. Jia, J. Chang, Q. Li, X. Wang, H. Xia, Y. Ye, A piezoelectric vibration energy harvester for multi-directional and ultra-low frequency waves with magnetic coupling driven by rotating balls, Applied Energy 310 (2022) 118511.
[34] Y. Hu, J. Yang, Q. Jing, S. Niu, W. Wu, Z.L. Wang, Triboelectric nanogenerator built on suspended 3D spiral structure as vibration and positioning sensor and wave energy harvester, ACS nano 7(11) (2013) 10424-10432.
[35] N.V. Viet, X. Xie, K.M. Liew, N. Banthia, Q. Wang, Energy harvesting from ocean waves by a floating energy harvester, Energy 112 (2016) 1219-1226.
[36] C.H. Wong, Z. Dahari, Development of vibration-based piezoelectric raindrop energy harvesting system, Journal of Electronic Materials 46 (2017) 1869-1882.
[37] L.E. Helseth, Harvesting electrical energy from water drops falling on a vibrating cantilever, Smart Materials and Structures 31(3) (2022) 035031.
[38] R. Guigon, J.-J. Chaillout, T. Jager, G. Despesse, Harvesting raindrop energy: experimental study, Smart Materials and Structures 17(1) (2008) 015039.

[39] X. Jiang, Y. Li, J. Li, J. Wang, J. Yao, Piezoelectric energy harvesting from traffic-induced pavement vibrations, Journal of Renewable and Sustainable Energy 6(4) (2014).
[40] D.B. Ashebo, C.A. Tan, J. Wang, G. Li, Feasibility of energy harvesting for powering wireless sensors in transportation infrastructure applications, Nondestructive Characterization for Composite Materials, Aerospace Engineering, Civil Infrastructure, and Homeland Security 2008, SPIE, 2008, pp. 265-272.
[41] Y. Pan, T. Lin, F. Qian, C. Liu, J. Yu, J. Zuo, L. Zuo, Modeling and field-test of a compact electromagnetic energy harvester for railroad transportation, Applied Energy 247 (2019) 309-321.
[42] X. Xie, Q. Wang, Energy harvesting from a vehicle suspension system, Energy 86 (2015) 385-392.
[43] C. Saha, T. O'donnell, N. Wang, P. McCloskey, Electromagnetic generator for harvesting energy from human motion, Sensors and Actuators A: Physical 147(1) (2008) 248-253.
[44] I. Izadgoshasb, Y.Y. Lim, N. Lake, L. Tang, R.V. Padilla, T. Kashiwao, Optimizing orientation of piezoelectric cantilever beam for harvesting energy from human walking, Energy conversion and management 161 (2018) 66-73.
[45] M. Renaud, P. Fiorini, R. van Schaijk, C. Van Hoof, Harvesting energy from the motion of human limbs: the design and analysis of an impact-based piezoelectric generator, Smart Materials and Structures 18(3) (2009) 035001.
[46] K. Xia, Z. Zhu, H. Zhang, C. Du, Z. Xu, R. Wang, Painting a high-output triboelectric nanogenerator on paper for harvesting energy from human body motion, Nano Energy 50 (2018) 571-580.
[47] M.V. Tholl, A. Haeberlin, B. Meier, S. Shaheen, L. Bereuter, B. Becsek, H. Tanner, T. Niederhauser, A. Zurbuchen, An intracardiac flow based electromagnetic energy harvesting mechanism for cardiac pacing, IEEE transactions on biomedical engineering 66(2) (2018) 530-538.
[48] A. Nanda, M.A. Karami, Energy harvesting from arterial blood pressure for embedded brain sensing, International Design Engineering Technical Conferences and Computers and Information in Engineering Conference, American Society of Mechanical Engineers, 2016, p. V003T11A015.
[49] H. Ouyang, Z. Liu, N. Li, B. Shi, Y. Zou, F. Xie, Y. Ma, Z. Li, H. Li, Q. Zheng, Symbiotic cardiac pacemaker, Nature communications 10(1) (2019) 1821.
[50] M. Ansari, M.A. Karami, Modeling and experimental verification of a fan-folded vibration energy harvester for leadless pacemakers, Journal of Applied Physics 119(9) (2016).
[51] M. Amin Karami, D.J. Inman, Powering pacemakers from heartbeat vibrations using linear and nonlinear energy harvesters, Applied Physics Letters 100(4) (2012).
[52] Q. Zheng, B. Shi, F. Fan, X. Wang, L. Yan, W. Yuan, S. Wang, H. Liu, Z. Li, Z.L. Wang, In vivo powering of pacemaker by breathing-driven implanted triboelectric nanogenerator, Advanced materials 26(33) (2014) 5851-5856.
[53] S. Wang, Y. Jiang, H. Tai, B. Liu, Z. Duan, Z. Yuan, H. Pan, G. Xie, X. Du, Y. Su, An integrated flexible self-powered wearable respiration sensor, Nano Energy 63 (2019) 103829.
[54] A. Panahi, A. Hassanzadeh, A. Moulavi, Design of a low cost, double triangle, piezoelectric sensor for respiratory monitoring applications, Sensing and Bio-Sensing Research 30 (2020) 100378.
[55] M.P. Mahmud, S.R. Bazaz, S. Dabiri, A.A. Mehrizi, M. Asadnia, M.E. Warkiani, Z.L. Wang, Advances in mems and microfluidics-based energy harvesting technologies, Advanced Materials Technologies 7(7) (2022) 2101347.
[56] S.P. Beeby, T. O'Donnell, Electromagnetic energy harvesting, Energy Harvesting Technologies (2009) 129-161.

[57] W. Shen, S. Zhu, Harvesting energy via electromagnetic damper: Application to bridge stay cables, Journal of Intelligent Material Systems and Structures 26(1) (2015) 3-19.
[58] Y.-J. Wang, C.-D. Chen, C.-K. Sung, System design of a weighted-pendulum-type electromagnetic generator for harvesting energy from a rotating wheel, IEEE/ASME Transactions on Mechatronics 18(2) (2012) 754-763.
[59] X. Zhao, J. Cai, Y. Guo, C. Li, J. Wang, H. Zheng, Modeling and experimental investigation of an AA-sized electromagnetic generator for harvesting energy from human motion, Smart Materials and Structures 27(8) (2018) 085008.
[60] H. Liu, Y. Qian, C. Lee, A multi-frequency vibration-based MEMS electromagnetic energy harvesting device, Sensors and Actuators A: Physical 204 (2013) 37-43.
[61] Y. Zhang, T. Wang, A. Luo, Y. Hu, X. Li, F. Wang, Micro electrostatic energy harvester with both broad bandwidth and high normalized power density, Applied energy 212 (2018) 362-371.
[62] X. Guo, Y. Zhang, K. Fan, C. Lee, F. Wang, A comprehensive study of non-linear air damping and "pull-in" effects on the electrostatic energy harvesters, Energy conversion and management 203 (2020) 112264.
[63] D. Liu, X. Yin, H. Guo, L. Zhou, X. Li, C. Zhang, J. Wang, Z.L. Wang, A constant current triboelectric nanogenerator arising from electrostatic breakdown, Science advances 5(4) (2019) eaav6437.
[64] Y. Naito, K. Uenishi, Electrostatic MEMS vibration energy harvesters inside of tire treads, Sensors 19(4) (2019) 890.
[65] B. Vysotskyi, D. Aubry, P. Gaucher, X. Le Roux, F. Parrain, E. Lefeuvre, Nonlinear electrostatic energy harvester using compensational springs in gravity field, Journal of Micromechanics and Microengineering 28(7) (2018) 074004.
[66] B. Shi, Z. Li, Y. Fan, Implantable energy-harvesting devices, Advanced Materials 30(44) (2018) 1801511.
[67] H. Liang, G. Hao, O.Z. Olszewski, A review on vibration-based piezoelectric energy harvesting from the aspect of compliant mechanisms, Sensors and Actuators A: Physical 331 (2021) 112743.
[68] H. Shao, G. Chen, H. He, Elastic wave localization and energy harvesting defined by piezoelectric patches on phononic crystal waveguide, Physics Letters A 403 (2021) 127366.
[69] Z. Liu, L. Wang, X. Yu, J. Zhang, R. Yang, X. Zhang, Y. Ji, M. Wu, L. Deng, L. Li, Piezoelectric-effect-enhanced full-spectrum photoelectrocatalysis in p–n heterojunction, Advanced Functional Materials 29(41) (2019) 1807279.
[70] A. Rahman, O. Farrok, M.R. Islam, W. Xu, Recent progress in electrical generators for oceanic wave energy conversion, IEEE Access 8 (2020) 138595-138615.
[71] D.K. Khatua, S.-J. Kim, Perspective on the development of high performance flexible piezoelectric energy harvesters, Journal of Materials Chemistry C 10(8) (2022) 2905-2924.
[72] K. Kapat, Q.T. Shubhra, M. Zhou, S. Leeuwenburgh, Piezoelectric nano-biomaterials for biomedicine and tissue regeneration, Advanced Functional Materials 30(44) (2020) 1909045.
[73] K.K. Sappati, S. Bhadra, Flexible piezoelectric 0–3 PZT-PDMS thin film for tactile sensing, IEEE Sensors Journal 20(9) (2020) 4610-4617.
[74] T.P. Comyn, P.I. Cowin, T. Stevenson, High strength piezoelectric materials for extreme environments, 2021 IEEE Sensors, IEEE, 2021, pp. 1-4.
[75] A. Anand, D. Meena, M. Bhatnagar, Synthesis and characterization of flexible PVDF/Bi2Al4O9/RGO based piezoelectric materials for nanogenerator application, Journal of Alloys and Compounds 843 (2020) 156019.
[76] T. Vijayakanth, D.J. Liptrot, E. Gazit, R. Boomishankar, C.R. Bowen, Recent advances in organic and organic–inorganic hybrid materials for piezoelectric mechanical energy harvesting, Advanced Functional Materials 32(17) (2022) 2109492.

[77] C. Zhang, W. Fan, S. Wang, Q. Wang, Y. Zhang, K. Dong, Recent progress of wearable piezoelectric nanogenerators, ACS Applied Electronic Materials 3(6) (2021) 2449-2467.
[78] Z. Yin, B. Tian, Q. Zhu, C. Duan, Characterization and application of PVDF and its copolymer films prepared by spin-coating and Langmuir–Blodgett method, Polymers 11(12) (2019) 2033.
[79] Z. He, F. Rault, M. Lewandowski, E. Mohsenzadeh, F. Salaün, Electrospun PVDF nanofibers for piezoelectric applications: A review of the influence of electrospinning parameters on the β phase and crystallinity enhancement, Polymers 13(2) (2021) 174.
[80] M.S.A. Salem, A.H. El-Shazly, M.R. El-Marghany, M.N. Sabry, N. Nady, Effect of adding functionalized graphene on the performance of PVDF membrane in direct contact membrane distillation, Key Engineering Materials 801 (2019) 337-342.
[81] A. Ahmad, U. Farooqui, N. Hamid, Effect of graphene oxide (GO) on Poly (vinylidene fluoride-hexafluoropropylene)(PVDF-HFP) polymer electrolyte membrane, Polymer 142 (2018) 330-336.
[82] F. Ram, P. Kaviraj, R. Pramanik, A. Krishnan, K. Shanmuganathan, A. Arockiarajan, PVDF/BaTiO3 films with nanocellulose impregnation: Investigation of structural, morphological and mechanical properties, Journal of Alloys and Compounds 823 (2020) 153701.
[83] J. Zhou, W. Zhou, D. Cao, C. Zhang, W. Peng, T. Yao, J. Zuo, J. Cai, Y. Li, PVDF reinforced with core–shell structured Mo@ MoO3 fillers: effects of semi-conductor MoO3 interlayer on dielectric properties of composites, Journal of Polymer Research 29(3) (2022) 72.
[84] S. Kalani, R. Kohandani, R. Bagherzadeh, Flexible electrospun PVDF–BaTiO 3 hybrid structure pressure sensor with enhanced efficiency, RSC advances 10(58) (2020) 35090-35098.
[85] S. Mirjalali, A. Mahdavi Varposhti, S. Abrishami, R. Bagherzadeh, M. Asadnia, S. Huang, S. Peng, C.H. Wang, S. Wu, A review on wearable electrospun polymeric piezoelectric sensors and energy harvesters, Macromolecular Materials and Engineering 308(1) (2023) 2200442.
[86] A.S.M.I. Uddin, D. Lee, C. Cho, B. Kim, Impact of multi-walled CNT incorporation on dielectric properties of PVDF-BaTiO3 nanocomposites and their energy harvesting possibilities, Coatings 12(1) (2022) 77.
[87] L. Wu, Z. Jin, Y. Liu, H. Ning, X. Liu, Alamusi, N. Hu, Recent advances in the preparation of PVDF-based piezoelectric materials, Nanotechnology Reviews 11(1) (2022) 1386-1407.
[88] P. Fakhri, B. Amini, R. Bagherzadeh, M. Kashfi, M. Latifi, N. Yavari, S.A. Kani, L. Kong, Flexible hybrid structure piezoelectric nanogenerator based on ZnO nanorod/PVDF nanofibers with improved output, RSC advances 9(18) (2019) 10117-10123.
[89] W. Feng, Y. Chen, W. Wang, D. Yu, A waterproof and breathable textile pressure sensor with high sensitivity based on PVDF/ZnO hierarchical structure, Colloids and Surfaces A: Physicochemical and Engineering Aspects 633 (2022) 127890.
[90] H. Elahi, K. Munir, M. Eugeni, M. Abrar, A. Khan, A. Arshad, P. Gaudenzi, A review on applications of piezoelectric materials in aerospace industry, Integrated Ferroelectrics 211(1) (2020) 25-44.
[91] F.C. Bolat, S. Basaran, S. Sivrioglu, Piezoelectric and electromagnetic hybrid energy harvesting with low-frequency vibrations of an aerodynamic profile under the air effect, Mechanical Systems and Signal Processing 133 (2019) 106246.
[92] H. Elahi, The investigation on structural health monitoring of aerospace structures via piezoelectric aeroelastic energy harvesting, Microsystem Technologies 27(7) (2021) 2605-2613.
[93] M. Akbar, A.R. Firdaus, S. Wibowo, N. Wirawan, Piezoelectric energy harvesting from a fixed-wing unmanned aerial vehicle, 2019 2nd International Conference on Applied Engineering (ICAE), IEEE, 2019, pp. 1-4.

[94] J. Wang, T. He, C. Lee, Development of neural interfaces and energy harvesters towards self-powered implantable systems for healthcare monitoring and rehabilitation purposes, Nano Energy 65 (2019) 104039.
[95] M. Wu, K. Yao, D. Li, X. Huang, Y. Liu, L. Wang, E. Song, J. Yu, X. Yu, Self-powered skin electronics for energy harvesting and healthcare monitoring, Materials Today Energy 21 (2021) 100786.
[96] Y. Huang, P. Yang, Z. Zhang, An ecg acquisition system with piezoelectric energy harvesting for low power healthcare devices, 2021 IEEE 14th International Conference on ASIC (ASICON), IEEE, 2021, pp. 1-4.
[97] W. Deng, Y. Zhou, A. Libanori, G. Chen, W. Yang, J. Chen, Piezoelectric nanogenerators for personalized healthcare, Chemical Society Reviews 51(9) (2022) 3380-3435.
[98] R. Esmaeeli, H. Aliniagerdroudbari, S.R. Hashemi, A. Nazari, M. Alhadri, W. Zakri, A.H. Mohammed, C. Batur, S. Farhad, A rainbow piezoelectric energy harvesting system for intelligent tire monitoring applications, Journal of Energy Resources Technology 141(6) (2019) 062007.
[99] S. Du, Y. Jia, E. Arroyo, S. Fernandez, S.T. Riches, A.A. Seshia, MEMS piezoelectric energy harvester powered wireless sensor module driven by noisy base excitation, 2019 20th International Conference on Solid-State Sensors, Actuators and Microsystems & Eurosensors XXXIII (TRANSDUCERS & EUROSENSORS XXXIII), IEEE, 2019, pp. 350-353.
[100] S. Kassan, J. Gaber, P. Lorenz, Autonomous energy management system achieving piezoelectric energy harvesting in wireless sensors, Mobile Networks and Applications 25(2) (2020) 794-805.
[101] Z.J. Chew, T. Ruan, M. Zhu, Power management circuit for wireless sensor nodes powered by energy harvesting: On the synergy of harvester and load, IEEE Transactions on Power Electronics 34(9) (2018) 8671-8681.
[102] P. Cahill, A. Mathewson, V. Pakrashi, Experimental validation of piezoelectric energy-harvesting device for built infrastructure applications, Journal of Bridge Engineering 23(8) (2018) 04018056.
[103] Z. Zhang, H. Xiang, Z. Shi, J. Zhan, Experimental investigation on piezoelectric energy harvesting from vehicle-bridge coupling vibration, Energy Conversion and Management 163 (2018) 169-179.
[104] P. Cahill, B. Hazra, R. Karoumi, A. Mathewson, V. Pakrashi, Vibration energy harvesting based monitoring of an operational bridge undergoing forced vibration and train passage, Mechanical Systems and Signal Processing 106 (2018) 265-283.
[105] Z. Zhao, T. Wang, J. Shi, B. Zhang, R. Zhang, M. Li, Y. Wen, Analysis and application of the piezoelectric energy harvester on light electric logistics vehicle suspension systems, Energy Science & Engineering 7(6) (2019) 2741-2755.
[106] D.H. Jeon, J.Y. Cho, J.P. Jhun, J.H. Ahn, S. Jeong, S.Y. Jeong, A. Kumar, C.H. Ryu, W. Hwang, H. Park, A lever-type piezoelectric energy harvester with deformation-guiding mechanism for electric vehicle charging station on smart road, Energy 218 (2021) 119540.
[107] W. Tian, Y. Shi, H. Cui, J. Shi, Research on piezoelectric energy harvester based on coupled oscillator model for vehicle vibration utilizing a L-shaped cantilever beam, Smart Materials and Structures 29(7) (2020) 075014.
[108] B. Bao, Q. Wang, A rain energy harvester using a self-release tank, Mechanical Systems and Signal Processing 147 (2021) 107099.
[109] M. Shi, E.M. Yeatman, A.S. Holmes, Energy harvesting piezoelectric wind speed sensor, Journal of Physics: Conference Series, IOP Publishing, 2019, p. 012044.
[110] S. Bhuvaneswari, K. Maheswari, K. Chandraprakash, S. Deepak, Piezo electric rainfall energy harvester with proactive protection mechanism with Integrated IOT device, IOP Conference Series: Materials Science and Engineering, IOP Publishing, 2021, p. 012105.

[111] X. Cao, Y. Xiong, J. Sun, X. Zhu, Q. Sun, Z.L. Wang, Piezoelectric nanogenerators derived self-powered sensors for multifunctional applications and artificial intelligence, Advanced Functional Materials 31(33) (2021) 2102983.
[112] Y.-C. Wang, E. Kohtanen, A. Erturk, Characterization of a multifunctional bioinspired piezoelectric swimmer and energy harvester, Smart Materials, Adaptive Structures and Intelligent Systems, American Society of Mechanical Engineers, 2020, p. V001T06A012.
[113] E. Kar, N. Bose, B. Dutta, N. Mukherjee, S. Mukherjee, Ultraviolet-and microwave-protecting, self-cleaning e-skin for efficient energy harvesting and tactile mechanosensing, ACS applied materials & interfaces 11(19) (2019) 17501-17512.
[114] S. Panda, S. Hajra, K. Mistewicz, P. In-na, M. Sahu, P.M. Rajaitha, H.J. Kim, Piezoelectric energy harvesting systems for biomedical applications, Nano Energy 100 (2022) 107514.
[115] F. Ali, W. Raza, X. Li, H. Gul, K.-H. Kim, Piezoelectric energy harvesters for biomedical applications, Nano Energy 57 (2019) 879-902.
[116] A. Ballo, M. Bottaro, A.D. Grasso, A review of power management integrated circuits for ultrasound-based energy harvesting in implantable medical devices, Applied Sciences 11(6) (2021) 2487.
[117] P. Gljušćić, S. Zelenika, D. Blažević, E. Kamenar, Kinetic energy harvesting for wearable medical sensors, Sensors 19(22) (2019) 4922.
[118] H.-T. Deng, Y.-L. Wang, D.-L. Wen, X.-R. Zhang, P. Huang, X.-S. Zhang, Progress of biomechanical energy harvesters for wearable electronic applications, Journal of Micromechanics and Microengineering 32(8) (2022) 083001.
[119] X. Mo, H. Zhou, W. Li, Z. Xu, J. Duan, L. Huang, B. Hu, J. Zhou, Piezoelectrets for wearable energy harvesters and sensors, Nano Energy 65 (2019) 104033.
[120] Y.-W. Chong, W. Ismail, K. Ko, C.-Y. Lee, Energy harvesting for wearable devices: A review, IEEE Sensors Journal 19(20) (2019) 9047-9062.
[121] P. Panda, Environmental friendly lead-free piezoelectric materials, Journal of materials science 44(19) (2009) 5049-5062.
[122] M.T. Chorsi, E.J. Curry, H.T. Chorsi, R. Das, J. Baroody, P.K. Purohit, H. Ilies, T.D. Nguyen, Piezoelectric biomaterials for sensors and actuators, Advanced Materials 31(1) (2019) 1802084.
[123] H.A. Sodano, D.J. Inman, G. Park, Comparison of piezoelectric energy harvesting devices for recharging batteries, Journal of intelligent material systems and structures 16(10) (2005) 799-807.
[124] A. Nechibvute, A. Chawanda, P. Luhanga, Piezoelectric energy harvesting devices: an alternative energy source for wireless sensors, Smart Materials Research 2012(1) (2012) 853481.
[125] R. Li, Y. Yu, B. Zhou, Q. Guo, M. Li, J. Pei, Harvesting energy from pavement based on piezoelectric effects: Fabrication and electric properties of piezoelectric vibrator, Journal of Renewable and Sustainable Energy 10(5) (2018).
[126] C.N. Kumar, Energy collection via Piezoelectricity, Journal of Physics: Conference Series, IOP Publishing, 2015, p. 012031.
[127] N. Sezer, M. Koç, A comprehensive review on the state-of-the-art of piezoelectric energy harvesting, Nano energy 80 (2021) 105567.
[128] H.S. Kim, J.-H. Kim, J. Kim, A review of piezoelectric energy harvesting based on vibration, International journal of precision engineering and manufacturing 12 (2011) 1129-1141.
[129] Y. Shu, I. Lien, Analysis of power output for piezoelectric energy harvesting systems, Smart materials and structures 15(6) (2006) 1499.

[130] I. Coondoo, N. Panwar, H. Maiwa, A.L. Kholkin, Improved piezoelectric and energy harvesting characteristics in lead-free Fe 2 O 3 modified KNN ceramics, Journal of Electroceramics 34 (2015) 255-261.
[131] B.A. Seddik, G. Despesse, E. Defay, Wideband mechanical energy harvester based on piezoelectric longitudinal mode, 10th IEEE International NEWCAS Conference, IEEE, 2012, pp. 453-456.
[132] S. Manotham, P. Jaita, P. Butnoi, N. Lertcumfu, G. Rujijanagul, Improvements of depolarization temperature, piezoelectric and energy harvesting properties of BNT-based ceramics by doping an interstitial dopant, Journal of Alloys and Compounds 897 (2022) 163021.
[133] S. Manotham, P. Butnoi, P. Jaita, D. Tantraviwat, N. Boothrawong, G. Rujijanagul, Role of ZnO nanoparticle doping on depolarization temperature, piezoelectric and energy harvesting properties of lead-free Bi0. 5 (Na0. 84K0. 16) 0.5 TiO3 ceramics, Materials Research Bulletin 128 (2020) 110859.
[134] X. Yang, F. Zhuo, C. Wang, Y. Liu, Z. Wang, C. He, X. Long, Tunable pyroelectricity, depolarization temperature and energy harvesting density in Pb (Lu0. 5Nb0. 5) O3-xPbTiO3 ceramics, Acta Materialia 186 (2020) 523-532.
[135] H.-T. Kim, J.-H. Ji, B.S. Kim, J.-H. Koh, Strain related curie temperature and improved piezoelectric properties of lead-free (1-x) Ba (Sn, Ti) O3-x (Ba, Ca) TiO3 ceramics, Ceramics International 46(16) (2020) 25050-25057.
[136] T.P. Pham Thi, Z. Yan, G. Nick, K. Hamideh, H.D. Nguyen Phuc, Z. Xuefan, Z. Dou, Z. Kechao, D. Steve, B. Chris, Demonstration of enhanced piezo-catalysis for hydrogen generation and water treatment at the ferroelectric curie temperature, Iscience 23(5) (2020).
[137] H.-C. Song, P. Kumar, D. Maurya, M.-G. Kang, W.T. Reynolds, D.-Y. Jeong, C.-Y. Kang, S. Priya, Ultra-low resonant piezoelectric MEMS energy harvester with high power density, Journal of Microelectromechanical Systems 26(6) (2017) 1226-1234.
[138] A. Morel, G. Pillonnet, Y. Wanderoild, A. Badel, Dielectric losses considerations for piezoelectric energy harvesting, Journal of Low Power Electronics 14(2) (2018) 244-254.
[139] J. Liang, H.S.-H. Chung, W.-H. Liao, Dielectric loss against piezoelectric power harvesting, Smart materials and structures 23(9) (2014) 092001.
[140] W. Wang, J. Cao, C.R. Bowen, S. Zhou, J. Lin, Optimum resistance analysis and experimental verification of nonlinear piezoelectric energy harvesting from human motions, Energy 118 (2017) 221-230.
[141] M.-G. Kang, W.-S. Jung, C.-Y. Kang, S.-J. Yoon, Recent progress on PZT based piezoelectric energy harvesting technologies, Actuators, MDPI, 2016, p. 5.
[142] D.-J. Shin, S.-J. Jeong, C.-E. Seo, K.-H. Cho, J.-H. Koh, Multi-layered piezoelectric energy harvesters based on PZT ceramic actuators, Ceramics international 41 (2015) S686-S690.
[143] K. Morimoto, I. Kanno, K. Wasa, H. Kotera, High-efficiency piezoelectric energy harvesters of c-axis-oriented epitaxial PZT films transferred onto stainless steel cantilevers, Sensors and Actuators A: Physical 163(1) (2010) 428-432.
[144] A.K. Batra, S. Bhattacharjee, A.K. Chilvery, M.D. Aggarwal, M.E. Edwards, A. Bhalla, Simulation of energy harvesting from roads via pyroelectricity, Journal of Photonics for Energy 1(1) (2011) 014001-014001-12.
[145] R. Tu, B. Zhang, H.A. Sodano, Lead titanate nanowires/polyamide-imide piezoelectric nanocomposites for high-temperature energy harvesting, Nano Energy 97 (2022) 107175.
[146] K. Kim, J. Yoo, H.G. Lim, M. Lee, S.-M. Park, H.H. Kim, Lead-free piezoelectric composite with lithium niobate and barium titanate fabricated by interdigital pair bonding technique, IEEE Access 9 (2021) 85894-85902.

[147] B.B. Bohara, A.K. Batra, C. Bowen, Lanthanum-modified lead zirconate titanate based paint for sensor and energy harvesting applications, Journal of Materials Science: Materials in Electronics 29 (2018) 20931-20941.
[148] J. Sun, H. Guo, J. Ribera, C. Wu, K. Tu, M. Binelli, G. Panzarasa, F.W. Schwarze, Z.L. Wang, I. Burgert, Sustainable and biodegradable wood sponge piezoelectric nanogenerator for sensing and energy harvesting applications, ACS nano 14(11) (2020) 14665-14674.
[149] S. Banerjee, S. Bairagi, S.W. Ali, A critical review on lead-free hybrid materials for next generation piezoelectric energy harvesting and conversion, Ceramics International 47(12) (2021) 16402-16421.
[150] Z. Butt, S.U. Rahman, R.A. Pasha, S. Mehmood, S. Abbas, H. Elahi, Characterizing barium titanate piezoelectric material using the finite element method, Transactions on Electrical and Electronic materials 18(3) (2017) 163-168.
[151] J. Lin, Y. Cao, K. Zhu, F. Yan, C. Shi, H. Bai, G. Ge, J. Yang, W. Yang, G. Li, Ultrahigh energy harvesting properties in temperature-insensitive eco-friendly high-performance KNN-based textured ceramics, Journal of Materials Chemistry A 10(14) (2022) 7978-7988.
[152] Z. Chen, Y. Zhang, P. Huang, X. Li, J. Du, W. Bai, L. Li, F. Wen, P. Zheng, W. Wu, Enhanced piezoelectric properties and thermal stability in Mo/Cr co-doped CaBi2Nb2O9 high-temperature piezoelectric ceramics, Journal of Physics and Chemistry of Solids 136 (2020) 109195.
[153] Q. Lu, L. Liu, X. Lan, Y. Liu, J. Leng, Dynamic responses of SMA-epoxy composites and application for piezoelectric energy harvesting, Composite Structures 153 (2016) 843-850.
[154] B. Toroń, P. Szperlich, M. Kozioł, SbSI composites based on epoxy resin and cellulose for energy harvesting and sensors—The influence of SBSI nanowires conglomeration on piezoelectric properties, Materials 13(4) (2020) 902.
[155] Z. Zeng, L. Gai, A. Petitpas, Y. Li, H. Luo, D. Wang, X. Zhao, A flexible, sandwich structure piezoelectric energy harvester using PIN-PMN-PT/epoxy 2-2 composite flake for wearable application, Sensors and Actuators A: Physical 265 (2017) 62-69.
[156] S. Anwar, M. Hassanpour Amiri, S. Jiang, M.M. Abolhasani, P.R. Rocha, K. Asadi, Piezoelectric nylon-11 fibers for electronic textiles, energy harvesting and sensing, Advanced Functional Materials 31(4) (2021) 2004326.
[157] A. Datta, Y.S. Choi, E. Chalmers, C. Ou, S. Kar-Narayan, Piezoelectric nylon-11 nanowire arrays grown by template wetting for vibrational energy harvesting applications, Advanced Functional Materials 27(2) (2017) 1604262.
[158] F. Ram, S. Radhakrishnan, T. Ambone, K. Shanmuganathan, Highly flexible mechanical energy harvester based on nylon 11 ferroelectric nanocomposites, ACS Applied Polymer Materials 1(8) (2019) 1998-2005.
[159] D. Zabek, R. Pullins, M. Pearson, A. Grzebielec, T. Skoczkowski, Piezoelectric-silicone structure for vibration energy harvesting: Experimental testing and modelling, Smart Materials and Structures 30(3) (2021) 035002.
[160] T. Ali, F.U. Khan, A silicone based piezoelectric and electromagnetic hybrid vibration energy harvester, Journal of Micromechanics and Microengineering 31(5) (2021) 055003.
[161] M. Tascan, Optimization of process parameters of wet-spun solid PVDF fibers for maximizing the tensile strength and applied force at break and minimizing the elongation at break using the Taguchi method, Journal of Engineered Fibers and Fabrics 9(1) (2014) 155892501400900119.
[162] S. Mohammadpourfazeli, S. Arash, A. Ansari, S. Yang, K. Mallick, R. Bagherzadeh, Future prospects and recent developments of polyvinylidene fluoride (PVDF) piezoelectric polymer; fabrication methods, structure, and electro-mechanical properties, RSC advances 13(1) (2023) 370-387.

[163] B. Jaleh, A. Jabbari, Evaluation of reduced graphene oxide/ZnO effect on properties of PVDF nanocomposite films, Applied Surface Science 320 (2014) 339-347.
[164] F. Mokhtari, M. Shamshirsaz, M. Latifi, J. Foroughi, Nanofibers-based piezoelectric energy harvester for self-powered wearable technologies, Polymers 12(11) (2020) 2697.
[165] S. Sukumaran, S. Chatbouri, D. Rouxel, E. Tisserand, F. Thiebaud, T. Ben Zineb, Recent advances in flexible PVDF based piezoelectric polymer devices for energy harvesting applications, J. Intell. Mater. Syst. Struct. 32(7) (2021) 746-780.
[166] L. Li, M. Zhang, M. Rong, W. Ruan, Studies on the transformation process of PVDF from α to β phase by stretching, Rsc Advances 4(8) (2014) 3938-3943.
[167] H. Wang, Q. Chen, W. Xia, X. Qiu, Q. Cheng, G. Zhu, Electroactive PVDF thin films fabricated via cooperative stretching process, Journal of Applied Polymer Science 135(22) (2018) 46324.
[168] Y. Ting, Suprapto, C.W. Chiu, H. Gunawan, Characteristic analysis of biaxially stretched PVDF thin films, Journal of Applied Polymer Science 135(36) (2018) 46677.
[169] S. Men, Z. Gao, R. Wen, J. Tang, J.M. Zhang, Effects of annealing time on physical and mechanical properties of PVDF microporous membranes by a melt extrusion-stretching process, Polymers for Advanced Technologies 32(6) (2021) 2397-2408.
[170] N. Jahan, F. Mighri, D. Rodrigue, A. Ajji, Enhanced electroactive β phase in three phase PVDF/CaCO3/nanoclay composites: effect of micro-CaCO3 and uniaxial stretching, Journal of Applied Polymer Science 134(24) (2017).
[171] Y. Zhou, W. Liu, B. Tan, C. Zhu, Y. Ni, L. Fang, C. Lu, Z. Xu, Crystallinity and β phase fraction of PVDF in biaxially stretched PVDF/PMMA films, Polymers 13(7) (2021) 998.
[172] C. Mi, Z. Ren, H. Li, S. Yan, X. Sun, Synergistic effect of hydrogen bonds and diffusion on the β-crystallization of poly (vinylidene fluoride) on poly (methyl methacrylate) interface, Industrial & Engineering Chemistry Research 58(17) (2019) 7389-7396.
[173] S. Mishra, R. Sahoo, L. Unnikrishnan, A. Ramadoss, S. Mohanty, S.K. Nayak, Investigation of the electroactive phase content and dielectric behaviour of mechanically stretched PVDF-GO and PVDF-rGO composites, Materials Research Bulletin 124 (2020) 110732.
[174] F. Khan, T. Kowalchik, S. Roundy, R. Warren, Stretching-induced phase transitions in barium titanate-poly (vinylidene fluoride) flexible composite piezoelectric films, Scripta Materialia 193 (2021) 64-70.
[175] Y. Bormashenko, R. Pogreb, O. Stanevsky, E. Bormashenko, Vibrational spectrum of PVDF and its interpretation, Polymer testing 23(7) (2004) 791-796.
[176] R. Gregorio, M. Cestari, F. Bernardino, Dielectric behaviour of thin films of β-PVDF/PZT and β-PVDF/BaTiO 3 composites, Journal of Materials Science 31 (1996) 2925-2930.
[177] J. Martín, D. Zhao, T. Lenz, I. Katsouras, D.M. de Leeuw, N. Stingelin, Solid-state-processing of δ-PVDF, Materials Horizons 4(3) (2017) 408-414.
[178] C.K. McGinn, K.A. Kam, M.-M. Laurila, K. Lozano Montero, M. Mäntysalo, D. Lupo, I. Kymissis, Formulation, printing, and poling method for piezoelectric films based on PVDF–TrFE, Journal of Applied Physics 128(22) (2020).
[179] C. Lee, J.A. Tarbutton, Polyvinylidene fluoride (PVDF) direct printing for sensors and actuators, The International Journal of Advanced Manufacturing Technology 104(5) (2019) 3155-3162.
[180] J. Fan, D. Gonzalez, J. Garcia, B. Newell, R.A. Nawrocki, The effects of additive manufacturing and electric poling techniques on PVdF thin films: Towards 3D printed functional materials, Smart Materials, Adaptive Structures and Intelligent Systems, American Society of Mechanical Engineers, 2020, p. V001T04A010.

[181] J. Fan, B. Newell, J. Garcia, R.M. Voyles, R.A. Nawrocki, Contact-poling enhanced, fully 3d printed pvdf pressure sensors: towards 3d printed functional materials, Smart Materials, Adaptive Structures and Intelligent Systems, American Society of Mechanical Engineers, 2021, p. V001T02A007.
[182] A. Sasmal, S. Sen, P.S. Devi, Frequency dependent energy storage and dielectric performance of Ba–Zr Co-doped BiFeO3 loaded PVDF based mechanical energy harvesters: Effect of corona poling, Soft Matter 16(36) (2020) 8492-8505.
[183] S.K. Mahadeva, J. Berring, K. Walus, B. Stoeber, Effect of poling time and grid voltage on phase transition and piezoelectricity of poly (vinyledene fluoride) thin films using corona poling, Journal of physics D: applied physics 46(28) (2013) 285305.
[184] V. Sencadas, S. Lanceros-Mendez, D. Chinaglia, A. Pouzada, Influence of the processing conditions and corona poling on the morphology of/spl beta/-pvdf, 2005 12th International Symposium on Electrets, IEEE, 2005, pp. 161-164.
[185] G. Rui, Y. Huang, X. Chen, R. Li, D. Wang, T. Miyoshi, L. Zhu, Giant spontaneous polarization for enhanced ferroelectric properties of biaxially oriented poly (vinylidene fluoride) by mobile oriented amorphous fractions, Journal of Materials Chemistry C 9(3) (2021) 894-907.
[186] L. Ruan, X. Yao, Y. Chang, L. Zhou, G. Qin, X. Zhang, Properties and applications of the β phase poly (vinylidene fluoride), Polymers 10(3) (2018) 228.
[187] I. Pariy, A. Ivanova, V. Shvartsman, D. Lupascu, G. Sukhorukov, M. Surmeneva, R. Surmenev, Poling and annealing of piezoelectric Poly (Vinylidene fluoride) micropillar arrays, Materials Chemistry and Physics 239 (2020) 122035.
[188] A. Gaur, C. Kumar, S. Tiwari, P. Maiti, Efficient energy harvesting using processed poly (vinylidene fluoride) nanogenerator, ACS Applied Energy Materials 1(7) (2018) 3019-3024.
[189] R. Tu, E. Sprague, H.A. Sodano, Precipitation-printed high-β phase poly (vinylidene fluoride) for energy harvesting, ACS Applied Materials & Interfaces 12(52) (2020) 58072-58081.
[190] C.M. Costa, V. Sencadas, J.F. Mano, S. Lanceros-Méndez, Effect of poling on the mechanical properties of β-poly (vinylidene fluoride), Materials science forum, Trans Tech Publ, 2006, pp. 951-955.
[191] I.O. Pariy, A.A. Ivanova, V.V. Shvartsman, D.C. Lupascu, G.B. Sukhorukov, T. Ludwig, A. Bartasyte, S. Mathur, M.A. Surmeneva, R.A. Surmenev, Piezoelectric response in hybrid micropillar arrays of poly (vinylidene fluoride) and reduced graphene oxide, Polymers 11(6) (2019) 1065.
[192] Y.P. Su, L.N. Sim, H.G. Coster, T.H. Chong, Incorporation of barium titanate nanoparticles in piezoelectric PVDF membrane, Journal of Membrane Science 640 (2021) 119861.
[193] Y. Ahn, J.Y. Lim, S.M. Hong, J. Lee, J. Ha, H.J. Choi, Y. Seo, Enhanced piezoelectric properties of electrospun poly (vinylidene fluoride)/multiwalled carbon nanotube composites due to high β-phase formation in poly (vinylidene fluoride), The Journal of Physical Chemistry C 117(22) (2013) 11791-11799.
[194] R.S. Kumar, T. Sarathi, K. Venkataraman, A. Bhattacharyya, Enhanced piezoelectric properties of polyvinylidene fluoride nanofibers using carbon nanofiber and electrical poling, Materials Letters 255 (2019) 126515.
[195] G.H. Kim, S.M. Hong, Y. Seo, Piezoelectric properties of poly (vinylidene fluoride) and carbon nanotube blends: β-phase development, Physical chemistry chemical physics 11(44) (2009) 10506-10512.
[196] H. Song, H. Li, S. Lim, Fast 3D digital light process printing of PVDF-HFP composite with electric in situ poling system for piezoelectric applications, Macromolecular Materials and Engineering 306(10) (2021) 2100266.

[197] R. Liu, Q. Liu, D. He, G. Sun, Z. Li, Y. Zhu, Enhancement of the piezoelectric property of polyvinylidene fluoride through electroactive phase enrichment and the application in piezoelectric generators, ACS Applied Electronic Materials 3(4) (2021) 1804-1812.
[198] Y. Li, W. Feng, L. Meng, K.M. Tse, Z. Li, L. Huang, Z. Su, S. Guo, Investigation on in-situ sprayed, annealed and corona poled PVDF-TrFE coatings for guided wave-based structural health monitoring: From crystallization to piezoelectricity, Materials & Design 199 (2021) 109415.
[199] A. Ikei, J. Wissman, K. Sampath, G. Yesner, S.N. Qadri, Tunable in situ 3d-printed pvdf-trfe piezoelectric arrays, Sensors 21(15) (2021) 5032.
[200] G. Xue, Y. Zhang, T. Xie, Z. Zhang, Q. Liu, X. Li, X. Gou, Cell adhesion-mediated piezoelectric self-stimulation on polydopamine-modified poly (vinylidene fluoride) membranes, ACS Applied Materials & Interfaces 13(15) (2021) 17361-17371.
[201] R. Mansour, O. Omoniyi, R. O'Leary, J.F. Windmill, Fabrication of ultraviolet-curable piezoelectric composite for sensor and actuator applications, 2018 IEEE SENSORS, IEEE, 2018, pp. 1-4.
[202] B. Tiller, A. Reid, B. Zhu, J. Guerreiro, R. Domingo-Roca, J.C. Jackson, J. Windmill, Piezoelectric microphone via a digital light processing 3D printing process, Materials & Design 165 (2019) 107593.
[203] S. Bodkhe, G. Turcot, F.P. Gosselin, D. Therriault, One-step solvent evaporation-assisted 3D printing of piezoelectric PVDF nanocomposite structures, ACS applied materials & interfaces 9(24) (2017) 20833-20842.
[204] H. Kim, F. Torres, D. Villagran, C. Stewart, Y. Lin, T.L.B. Tseng, 3D printing of BaTiO3/PVDF composites with electric in situ poling for pressure sensor applications, Macromolecular Materials and Engineering 302(11) (2017) 1700229.
[205] S. Song, Y. Li, Q. Wang, C. Zhang, Facile preparation of high loading filled PVDF/BaTiO 3 piezoelectric composites for selective laser sintering 3D printing, RSC advances 11(60) (2021) 37923-37931.
[206] J. Jiang, S. Tu, R. Fu, J. Li, F. Hu, B. Yan, Y. Gu, S. Chen, Flexible piezoelectric pressure tactile sensor based on electrospun BaTiO3/poly (vinylidene fluoride) nanocomposite membrane, ACS applied materials & interfaces 12(30) (2020) 33989-33998.
[207] A. Ferri, S. Barrau, R. Bourez, A. Da Costa, M.-H. Chambrier, A. Marin, J. Defebvin, J.-M. Lefebvre, R. Desfeux, Probing the local piezoelectric behavior in stretched barium titanate/poly (vinylidene fluoride) nanocomposites, Composites Science and Technology 186 (2020) 107914.
[208] S.H. Lee, Y.C. Choi, M.S. Kim, K.M. Ryu, Y.G. Jeong, Fabrication and characterization of piezoelectric composite nanofibers based on poly (vinylidene fluoride-co-hexafluoropropylene) and barium titanate nanoparticle, Fibers and Polymers 21 (2020) 473-479.
[209] N. Shehata, R. Nair, R. Boualayan, I. Kandas, A. Masrani, E. Elnabawy, N. Omran, M. Gamal, A.H. Hassanin, Stretchable nanofibers of polyvinylidenefluoride (PVDF)/thermoplastic polyurethane (TPU) nanocomposite to support piezoelectric response via mechanical elasticity, Scientific Reports 12(1) (2022) 8335.
[210] M.M. Abolhasani, M. Naebe, A. Jalali-Arani, Q. Guo, Crystalline structures and α→ β and γ polymorphs transformation induced by nanoclay in PVDF-based nanocomposite, Nano 9(06) (2014) 1450065.
[211] Y. Xin, X. Qi, H. Tian, C. Guo, X. Li, J. Lin, C. Wang, Full-fiber piezoelectric sensor by straight PVDF/nanoclay nanofibers, Materials Letters 164 (2016) 136-139.
[212] S. Tiwari, A. Gaur, C. Kumar, P. Maiti, Enhanced piezoelectric response in nanoclay induced electrospun PVDF nanofibers for energy harvesting, Energy 171 (2019) 485-492.

[213] Y.-J. Kim, T.-V. Dang, H.-J. Choi, B.-J. Park, J.-H. Eom, H.-A. Song, D. Seol, Y. Kim, S.-H. Shin, J. Nah, Piezoelectric properties of CH 3 NH 3 PbI 3 perovskite thin films and their applications in piezoelectric generators, Journal of Materials Chemistry A 4(3) (2016) 756-763.
[214] V. Jella, S. Ippili, J.-H. Eom, J. Choi, S.-G. Yoon, Enhanced output performance of a flexible piezoelectric energy harvester based on stable MAPbI3-PVDF composite films, Nano Energy 53 (2018) 46-56.
[215] A. Tuluk, T. Mahon, S. van der Zwaag, P. Groen, Estimating the true piezoelectric properties of BiFeO3 from measurements on BiFeO3-PVDF terpolymer composites, Journal of Alloys and Compounds 868 (2021) 159186.
[216] C. Li, W. Luo, X. Liu, D. Xu, K. He, PMN-PT/PVDF nanocomposite for high output nanogenerator applications, Nanomaterials 6(4) (2016) 67.
[217] C. Shamitha, A. Mahendran, S. Anandhan, Effect of polarization switching on piezoelectric and dielectric performance of electrospun nanofabrics of poly (vinylidene fluoride)/Ca–Al LDH nanocomposite, Journal of Applied Polymer Science 137(20) (2020) 48697.
[218] A. Wang, J. Liu, C. Shao, Y. Zhang, C. Chen, Electro-assisted 3d printing multi-layer PVDF/CaCl2 composite films and sensors, Coatings 12(6) (2022) 820.
[219] A. Wang, C. Chen, J. Qian, F. Yang, L. Wang, M. Zhang, Enhanced electrical properties of PVDF thin film by addition of NaCl by near-electric-field 3D printing, Journal of Electronic Materials 50(8) (2021) 4781-4786.
[220] S. Badatya, D.K. Bharti, N. Sathish, A.K. Srivastava, M.K. Gupta, Humidity sustainable hydrophobic poly (vinylidene fluoride)-carbon nanotubes foam based piezoelectric nanogenerator, ACS Applied Materials & Interfaces 13(23) (2021) 27245-27254.
[221] J. Li, S. Chen, W. Liu, R. Fu, S. Tu, Y. Zhao, L. Dong, B. Yan, Y. Gu, High performance piezoelectric nanogenerators based on electrospun ZnO nanorods/poly (vinylidene fluoride) composite membranes, The Journal of Physical Chemistry C 123(18) (2019) 11378-11387.
[222] D. Ponnamma, M.M. Chamakh, A.M. Alahzm, N. Salim, N. Hameed, M.A.A. AlMaadeed, Core-shell nanofibers of polyvinylidene fluoride-based nanocomposites as piezoelectric nanogenerators, Polymers 12(10) (2020) 2344.
[223] N. Abzan, M. Kharaziha, S. Labbaf, Development of three-dimensional piezoelectric polyvinylidene fluoride-graphene oxide scaffold by non-solvent induced phase separation method for nerve tissue engineering, Materials & Design 167 (2019) 107636.
[224] C.-T. Pan, S.-Y. Wang, C.-K. Yen, A. Kumar, S.-W. Kuo, J.-L. Zheng, Z.-H. Wen, R. Singh, S.P. Singh, M.T. Khan, Polyvinylidene fluoride-added ceramic powder composite near-field electrospinned piezoelectric fiber-based low-frequency dynamic sensors, ACS omega 5(28) (2020) 17090-17101.
[225] Y. Hong, B. Wang, Z. Long, Z. Zhang, Q. Pan, S. Liu, X. Luo, Z. Yang, Hierarchically interconnected piezoceramic textile with a balanced performance in piezoelectricity, flexibility, toughness, and air permeability, Advanced Functional Materials 31(42) (2021) 2104737.
[226] A. Lopes, J. Gutiérrez, J. Barandiarán, Direct fabrication of a 3D-shape film of polyvinylidene fluoride (PVDF) in the piezoelectric β-phase for sensor and actuator applications, European Polymer Journal 99 (2018) 111-116.
[227] L. Song, R. Dai, Y. Li, Q. Wang, C. Zhang, Polyvinylidene fluoride energy harvester with boosting piezoelectric performance through 3D printed biomimetic bone structures, ACS Sustainable Chemistry & Engineering 9(22) (2021) 7561-7568.
[228] J. Zhang, D. Liu, Q. Han, L. Jiang, H. Shao, B. Tang, W. Lei, T. Lin, C.H. Wang, Mechanically stretchable piezoelectric polyvinylidene fluoride (PVDF)/Boron nitride

nanosheets (BNNSs) polymer nanocomposites, Composites Part B: Engineering 175 (2019) 107157.
[229] J. Zhang, H. Wang, P. Blanloeuil, G. Li, Z. Sha, D. Wang, W. Lei, C. Boyer, Y. Yu, R. Tian, Enhancing the triboelectricity of stretchable electrospun piezoelectric polyvinylidene fluoride/boron nitride nanosheets composite nanofibers, Composites Communications 22 (2020) 100535.
[230] S. Song, Y. Li, Q. Wang, C. Zhang, Facile preparation of high loading filled PVDF/$BaTiO_3$ piezoelectric composites for selective laser sintering 3D printing, (2021).
[231] P.K. Mishra, P. Senthil, Prediction of in-plane stiffness of multi-material 3D printed laminate parts fabricated by FDM process using CLT and its mechanical behaviour under tensile load, Materials Today Communications 23 (2020) 100955.
[232] A. Ahmed, A. Azam, Y. Wang, Z. Zhang, N. Li, C. Jia, R.T. Mushtaq, M. Rehman, T. Gueye, M.B. Shahid, Additively manufactured nano-mechanical energy harvesting systems: advancements, potential applications, challenges and future perspectives, Nano convergence 8 (2021) 1-42.
[233] C. Kaynak, S.D. Varsavas, Performance comparison of the 3D-printed and injection-molded PLA and its elastomer blend and fiber composites, Journal of Thermoplastic Composite Materials 32(4) (2019) 501-520.
[234] O. Machida, A. Shimofuku, R. Tashiro, A. Takeuchi, Y. Akiyama, E. Ohta, Fabrication of lead zirconate titanate films by inkjet printing, Japanese Journal of Applied Physics 51(9S1) (2012) 09LA11.
[235] B. Andò, S. Baglio, A.R. Bulsara, T. Emery, V. Marletta, A. Pistorio, Low-cost inkjet printing technology for the rapid prototyping of transducers, Sensors 17(4) (2017) 748.
[236] C. Chen, F. Cai, Y. Zhu, L. Liao, J. Qian, F.-G. Yuan, N. Zhang, 3D printing of electroactive PVDF thin films with high β-phase content, Smart Materials and Structures 28(6) (2019) 065017.
[237] N.A. Shepelin, V.C. Lussini, P.J. Fox, G.W. Dicinoski, A.M. Glushenkov, J.G. Shapter, A.V. Ellis, 3D printing of poly (vinylidene fluoride-trifluoroethylene): a poling-free technique to manufacture flexible and transparent piezoelectric generators, MRS Communications 9(1) (2019) 159-164.
[238] Y.-Y. Li, L.-T. Li, B. Li, Direct ink writing of 3–3 piezoelectric composite, Journal of Alloys and Compounds 620 (2015) 125-128.
[239] C. Yang, S. Song, F. Chen, N. Chen, Fabrication of PVDF/BaTiO3/CNT piezoelectric energy harvesters with bionic balsa wood structures through 3D printing and supercritical carbon dioxide foaming, ACS Applied Materials & Interfaces 13(35) (2021) 41723-41734.
[240] S. Song, Y. Li, Q. Wang, C. Zhang, Boosting piezoelectric performance with a new selective laser sintering 3D printable PVDF/graphene nanocomposite, Composites Part A: Applied Science and Manufacturing 147 (2021) 106452.
[241] C. Shuai, G. Liu, Y. Yang, F. Qi, S. Peng, W. Yang, C. He, G. Wang, G. Qian, A strawberry-like Ag-decorated barium titanate enhances piezoelectric and antibacterial activities of polymer scaffold, Nano Energy 74 (2020) 104825.
[242] F. Qi, Z. Zeng, J. Yao, W. Cai, Z. Zhao, S. Peng, C. Shuai, Constructing core-shell structured BaTiO3@ carbon boosts piezoelectric activity and cell response of polymer scaffolds, Materials Science and Engineering: C 126 (2021) 112129.
[243] C. Yang, F. Chen, J. Sun, N. Chen, Boosted mechanical piezoelectric energy harvesting of polyvinylidene fluoride/barium titanate composite porous foam based on three-dimensional printing and foaming technology, ACS omega 6(45) (2021) 30769-30778.
[244] M.-L. Seol, R. Ivaškevičiūtė, M.A. Ciappesoni, F.V. Thompson, D.-I. Moon, S.J. Kim, S.J. Kim, J.-W. Han, M. Meyyappan, All 3D printed energy harvester for autonomous and sustainable resource utilization, Nano Energy 52 (2018) 271-278.

[245] U.J. Yang, J.W. Lee, J.P. Lee, J.M. Baik, Remarkable output power enhancement of sliding-mode triboelectric nanogenerator through direct metal-to-metal contact with the ground, Nano Energy 57 (2019) 293-299.
[246] Z. Chen, X. Song, L. Lei, X. Chen, C. Fei, C.T. Chiu, X. Qian, T. Ma, Y. Yang, K. Shung, 3D printing of piezoelectric element for energy focusing and ultrasonic sensing, Nano Energy 27 (2016) 78-86.
[247] Y. Chen, X. Bao, C.-M. Wong, J. Cheng, H. Wu, H. Song, X. Ji, S. Wu, PZT ceramics fabricated based on stereolithography for an ultrasound transducer array application, Ceramics International 44(18) (2018) 22725-22730.
[248] X. Liu, Y. Shang, J. Zhang, C. Zhang, Ionic liquid-assisted 3D printing of self-polarized β-PVDF for flexible piezoelectric energy harvesting, ACS Applied Materials & Interfaces 13(12) (2021) 14334-14341.
[249] J. Liu, Y. Shang, Z. Shao, X. Liu, C. Zhang, Three-Dimensional Printing to Translate Simulation to Architecting for Three-Dimensional High Performance Piezoelectric Energy Harvester, Industrial & Engineering Chemistry Research 61(1) (2021) 433-440.
[250] X. Liu, Y. Shang, J. Liu, Z. Shao, C. Zhang, 3D printing-enabled in-situ orientation of BaTi2O5 nanorods in β-PVDF for high-efficiency piezoelectric energy harvesters, ACS Applied Materials & Interfaces 14(11) (2022) 13361-13368.
[251] H. Pei, S. Shi, Y. Chen, Y. Xiong, Q. Lv, Combining solid-state shear milling and FFF 3D-printing strategy to fabricate high-performance biomimetic wearable fish-scale PVDF-based piezoelectric energy harvesters, ACS Applied Materials & Interfaces 14(13) (2022) 15346-15359.
[252] X. Liu, J. Liu, L. He, Y. Shang, C. Zhang, 3D printed piezoelectric-regulable cells with customized electromechanical response distribution for intelligent sensing, Advanced Functional Materials 32(26) (2022) 2201274.
[253] H. Kim, F. Torres, Y. Wu, D. Villagran, Y. Lin, T.-L.B. Tseng, Integrated 3D printing and corona poling process of PVDF piezoelectric films for pressure sensor application, Smart Materials and Structures 26(8) (2017) 085027.
[254] L. He, J. Lu, C. Han, X. Liu, J. Liu, C. Zhang, Electrohydrodynamic pulling consolidated high-efficiency 3D printing to architect unusual self-polarized β-PVDF arrays for advanced piezoelectric sensing, Small 18(15) (2022) 2200114.
[255] H. Pei, Y. Xie, Y. Xiong, Q. Lv, Y. Chen, A novel polarization-free 3D printing strategy for fabrication of poly (Vinylidene fluoride) based nanocomposite piezoelectric energy harvester, Composites Part B: Engineering 225 (2021) 109312.
[256] H. Kim, T. Fernando, M. Li, Y. Lin, T.-L.B. Tseng, Fabrication and characterization of 3D printed BaTiO3/PVDF nanocomposites, Journal of Composite Materials 52(2) (2018) 197-206.
[257] A. Ambrosi, M. Pumera, 3D-printing technologies for electrochemical applications, Chemical society reviews 45(10) (2016) 2740-2755.
[258] J.U. Pucci, B.R. Christophe, J.A. Sisti, E.S. Connolly Jr, Three-dimensional printing: technologies, applications, and limitations in neurosurgery, Biotechnology advances 35(5) (2017) 521-529.
[259] Q. Yan, H. Dong, J. Su, J. Han, B. Song, Q. Wei, Y. Shi, A review of 3D printing technology for medical applications, Engineering 4(5) (2018) 729-742.
[260] Z. Lyu, G.J. Lim, J.J. Koh, Y. Li, Y. Ma, J. Ding, J. Wang, Z. Hu, J. Wang, W. Chen, Design and manufacture of 3D-printed batteries, Joule 5(1) (2021) 89-114.
[261] H. Quan, T. Zhang, H. Xu, S. Luo, J. Nie, X. Zhu, Photo-curing 3D printing technique and its challenges, Bioactive materials 5(1) (2020) 110-115.
[262] F. Zhang, M. Wei, V.V. Viswanathan, B. Swart, Y. Shao, G. Wu, C. Zhou, 3D printing technologies for electrochemical energy storage, Nano Energy 40 (2017) 418-431.

[263] M. Pei, H. Shi, F. Yao, S. Liang, Z. Xu, X. Pei, S. Wang, Y. Hu, 3D printing of advanced lithium batteries: a designing strategy of electrode/electrolyte architectures, Journal of Materials Chemistry A 9(45) (2021) 25237-25257.
[264] C. Yang, S. Song, F. Chen, N. Chen, Fabrication of PVDF/$BaTiO_3$/CNT Piezoelectric Energy Harvesters with Bionic Balsa Wood Structures through 3D Printing and Supercritical Carbon Dioxide Foaming, (2021).
[265] H. Kim, E. Park, S. Kim, B. Park, N. Kim, S. Lee, Experimental study on mechanical properties of single-and dual-material 3D printed products, Procedia Manufacturing 10 (2017) 887-897.
[266] H.K. Sezer, O. Eren, FDM 3D printing of MWCNT re-inforced ABS nano-composite parts with enhanced mechanical and electrical properties, Journal of manufacturing processes 37 (2019) 339-347.
[267] R.F. Quero, B.M. de Castro Costa, J.A.F. da Silva, D.P. de Jesus, Using multi-material fused deposition modeling (FDM) for one-step 3D printing of microfluidic capillary electrophoresis with integrated electrodes for capacitively coupled contactless conductivity detection, Sensors and Actuators B: Chemical 365 (2022) 131959.
[268] D. Espalin Jr, Development of a multi-material, multi-technology FDM system for process improvement experimentation, The University of Texas at El Paso2012.
[269] D. Yadav, D. Chhabra, R.K. Garg, A. Ahlawat, A. Phogat, Optimization of FDM 3D printing process parameters for multi-material using artificial neural network, Materials Today: Proceedings 21 (2020) 1583-1591.
[270] S.H. Ji, Y.-S. Cho, J.S. Yun, Wearable core-shell piezoelectric nanofiber yarns for body movement energy harvesting, Nanomaterials 9(4) (2019) 555.
[271] Y. Liu, H. Khanbareh, M.A. Halim, A. Feeney, X. Zhang, H. Heidari, R. Ghannam, Piezoelectric energy harvesting for self-powered wearable upper limb applications, Nano Select 2(8) (2021) 1459-1479.
[272] D. Sarkar, N. Das, M.M. Saikh, P. Biswas, S. Das, S. Das, N.A. Hoque, R. Basu, Development of a sustainable and biodegradable sonchus asper cotton pappus based piezoelectric nanogenerator for instrument vibration and human body motion sensing with mechanical energy harvesting applications, ACS omega 6(43) (2021) 28710-28717.
[273] Y. Yang, H. Pan, G. Xie, Y. Jiang, C. Chen, Y. Su, Y. Wang, H. Tai, Flexible piezoelectric pressure sensor based on polydopamine-modified BaTiO3/PVDF composite film for human motion monitoring, Sensors and Actuators A: Physical 301 (2020) 111789.
[274] S. Siddiqui, D.-I. Kim, E. Roh, T.Q. Trung, M.T. Nguyen, N.-E. Lee, A durable and stable piezoelectric nanogenerator with nanocomposite nanofibers embedded in an elastomer under high loading for a self-powered sensor system, Nano Energy 30 (2016) 434-442.
[275] M. Zhu, Q. Shi, T. He, Z. Yi, Y. Ma, B. Yang, T. Chen, C. Lee, Self-powered and self-functional cotton sock using piezoelectric and triboelectric hybrid mechanism for healthcare and sports monitoring, ACS nano 13(2) (2019) 1940-1952.
[276] X. Rui, Y. Li, X. Zheng, Z. Sha, Z. Zeng, Design and experimental study of a piezoelectric energy harvester in automotive spokes, Journal of Physics D: Applied Physics 52(35) (2019) 355501.
[277] R. Esmaeeli, H. Aliniagerdroudbari, A. Nazari, S.R. Hashemi, M. Alhadri, W. Zakri, A.H. Mohammed, C. Batur, S. Farhad, Optimization of a rainbow piezoelectric energy harvesting system for tire monitoring applications, Energy Sustainability, American Society of Mechanical Engineers, 2018, p. V001T02A004.
[278] R. Esmaeeli, H. Aliniagerdroudbari, S.R. Hashemi, M. Alhadri, W. Zakri, C. Batur, S. Farhad, Design, modeling, and analysis of a high performance piezoelectric energy harvester for intelligent tires, International Journal of Energy Research 43(10) (2019) 5199-5212.

[279] X. Rui, Z. Zeng, Y. Zhang, Y. Li, H. Feng, X. Huang, Z. Sha, Design and experimental investigation of a self-tuning piezoelectric energy harvesting system for intelligent vehicle wheels, IEEE Transactions on Vehicular Technology 69(2) (2019) 1440-1451.
[280] Y.L. Morangueira, J.C.d.C. Pereira, Energy harvesting assessment with a coupled full car and piezoelectric model, Energy 210 (2020) 118668.
[281] M.V. Lopes, J.J. Eckert, T.S. Martins, A.A. dos Santos, Multi-objective optimization of piezoelectric vibrational energy harvester orthogonal spirals for ore freight cars, Journal of the Brazilian Society of Mechanical Sciences and Engineering 43(6) (2021) 295.
[282] Z. Wang, W. Wang, L. Tang, R. Tian, C. Wang, Q. Zhang, C. Liu, F. Gu, A.D. Ball, A piezoelectric energy harvester for freight train condition monitoring system with the hybrid nonlinear mechanism, Mechanical Systems and Signal Processing 180 (2022) 109403.
[283] B. Dziadak, M. Kucharek, J. Starzyński, Powering the WSN node for monitoring rail car parameters, using a piezoelectric energy harvester, Energies 15(5) (2022) 1641.
[284] F. Yang, M. Gao, P. Wang, J. Zuo, J. Dai, J. Cong, Efficient piezoelectric harvester for random broadband vibration of rail, Energy 218 (2021) 119559.
[285] L. Jiang, Y. Yang, R. Chen, G. Lu, R. Li, J. Xing, K.K. Shung, M.S. Humayun, J. Zhu, Y. Chen, Ultrasound-induced wireless energy harvesting for potential retinal electrical stimulation application, Advanced Functional Materials 29(33) (2019) 1902522.
[286] F. Xie, X. Qian, N. Li, D. Cui, H. Zhang, Z. Xu, An experimental study on a piezoelectric vibration energy harvester for self-powered cardiac pacemakers, Annals of translational medicine 9(10) (2021).
[287] T. Zhang, H. Liang, Z. Wang, C. Qiu, Y.B. Peng, X. Zhu, J. Li, X. Ge, J. Xu, X. Huang, Piezoelectric ultrasound energy–harvesting device for deep brain stimulation and analgesia applications, Science advances 8(15) (2022) eabk0159.
[288] P. Mangaiyarkarasi, P. Lakshmi, V. Sasrika, Grey wolf optimization based flexible piezoelectric energy harvester for hearing aid applications, 2019 IEEE International Systems Conference (SysCon), IEEE, 2019, pp. 1-8.
[289] Y. Hong, L. Jin, B. Wang, J. Liao, B. He, T. Yang, Z. Long, P. Li, Z. Zhang, S. Liu, A wood-templated unidirectional piezoceramic composite for transmuscular ultrasonic wireless power transfer, Energy & Environmental Science 14(12) (2021) 6574-6585.
[290] S. Gururaj, A. Applequist, S. Bhattarai, A.M. Appaji, P. Kadambi, Self-powered cardiac pacemaker: the viability of a piezoelectric energy harvester, 2020 International Conference on COMmunication Systems & NETworkS (COMSNETS), IEEE, 2020, pp. 70-75.
[291] A. Anand, S. Kundu, Design of mems based piezoelectric energy harvester for pacemaker, 2019 Devices for Integrated Circuit (DevIC), IEEE, 2019, pp. 465-469.
[292] Z. Xu, C. Jin, A. Cabe, D. Escobedo, N. Hao, I. Trase, A.B. Closson, L. Dong, Y. Nie, J. Elliott, Flexible energy harvester on a pacemaker lead using multibeam piezoelectric composite thin films, ACS applied materials & interfaces 12(30) (2020) 34170-34179.
[293] S. Azimi, A. Golabchi, A. Nekookar, S. Rabbani, M.H. Amiri, K. Asadi, M.M. Abolhasani, Self-powered cardiac pacemaker by piezoelectric polymer nanogenerator implant, Nano Energy 83 (2021) 105781.
[294] L. Dong, A.B. Closson, M. Oglesby, D. Escobedo, X. Han, Y. Nie, S. Huang, M.D. Feldman, Z. Chen, J.X. Zhang, In vivo cardiac power generation enabled by an integrated helical piezoelectric pacemaker lead, Nano Energy 66 (2019) 104085.
[295] L. Jiang, G. Lu, Y. Zeng, Y. Sun, H. Kang, J. Burford, C. Gong, M.S. Humayun, Y. Chen, Q. Zhou, Flexible ultrasound-induced retinal stimulating piezo-arrays for biomimetic visual prostheses, Nature communications 13(1) (2022) 3853.
[296] J.S. Perlmutter, J.W. Mink, Deep brain stimulation, Annu. Rev. Neurosci. 29(1) (2006) 229-257.

[297] A. Delnavaz, J. Voix, Energy harvesting for in-ear devices using ear canal dynamic motion, IEEE Transactions on Industrial Electronics 61(1) (2013) 583-590.
[298] A. Delnavaz, J. Voix, Ear canal dynamic motion as a source of power for in-ear devices, Journal of Applied Physics 113(6) (2013).
[299] W. Liu, X. Cheng, X. Fu, C. Stefanini, P. Dario, Preliminary study on development of PVDF nanofiber based energy harvesting device for an artery microrobot, Microelectronic engineering 88(8) (2011) 2251-2254.
[300] Q. Liu, Q. Li, Z. Fang, X. Zhou, R. Wang, C. Zuo, Piezoelectric energy harvesting for flapping wing micro air vehicle and flapping wing sensing based on flexible polyvinylidene fluoride, Applied Sciences 11(3) (2021) 1166.
[301] P.-K. Yang, S.-A. Chou, C.-H. Hsu, R.J. Mathew, K.-H. Chiang, J.-Y. Yang, Y.-T. Chen, Tin disulfide piezoelectric nanogenerators for biomechanical energy harvesting and intelligent human-robot interface applications, Nano Energy 75 (2020) 104879.
[302] K. Ibtehaj, M.H.H. Jumali, S. Al-Bati, A novel facile preparation method of self-polarized Poly (vinylidene fluorides) nanofiber for high-performance piezoelectric nanogenerator, Polymer 208 (2020) 122956.
[303] A. Megdich, M. Habibi, L. Laperrière, A Review on 3D printed piezoelectric energy harvesters: Materials, 3D printing techniques, and applications, Materials Today Communications (2023) 105541.
[304] E. Brunengo, G. Luciano, G. Canu, M. Canetti, L. Conzatti, M. Castellano, P. Stagnaro, Double-step moulding: An effective method to induce the formation of β-phase in PVDF, Polymer 193 (2020) 122345.
[305] X. Hu, Z. Ding, L. Fei, Y. Xiang, Y. Lin, Wearable piezoelectric nanogenerators based on reduced graphene oxide and in situ polarization-enhanced PVDF-TrFE films, Journal of materials science 54 (2019) 6401-6409.
[306] J. Yang, X. Yao, Z. Meng, Investigation of molecular mechanisms of polyvinylidene fluoride under the effects of temperature, electric poling, and mechanical stretching using molecular dynamics simulations, Polymer 245 (2022) 124691.
[307] M.T. Darestani, T.C. Chilcott, H. Coster, Effect of poling time on filtration properties of PVDF membranes treated in intense electric fields, Polymer bulletin 71 (2014) 951-964.
[308] D. Lei, N. Hu, L. Wu, H. Ning, Y. Wang, Z. Jin, Y. Liu, Improvement of the piezoelectricity of PVDF-HFP by CoFe2O4 nanoparticles, Nano Materials Science (2023).
[309] H. Gade, S. Bokka, G.G. Chase, Polarization treatments of electrospun PVDF fiber mats, Polymer 212 (2021) 123152.
[310] Y.P. Su, L.N. Sim, X. Li, H.G. Coster, T.H. Chong, Anti-fouling piezoelectric PVDF membrane: Effect of morphology on dielectric and piezoelectric properties, Journal of Membrane Science 620 (2021) 118818.
[311] B. Peng, D. Andriukaitis, C. Ravikumar, A. Valinevicius, V. Markevicius, D. Navikas, M. Zilys, Quantitative Analysis of Parameters Dependence of PVDF Films Polarization, 2022 26th International Conference Electronics, IEEE, 2022, pp. 1-6.
[312] A. Thakur, S. Dam, S. Hussain, Probing the effect of CdS loading on crystallinity and morphology of free standing thin films of CdS/PVDF, Materials Today: Proceedings 46 (2021) 6156-6160.
[313] S. Ippili, V. Jella, J.-H. Eom, J. Kim, S. Hong, J.-S. Choi, V.-D. Tran, N. Van Hieu, Y.-J. Kim, H.-J. Kim, An eco-friendly flexible piezoelectric energy harvester that delivers high output performance is based on lead-free MASnI3 films and MASnI3-PVDF composite films, Nano Energy 57 (2019) 911-923.
[314] B.K. Panigrahi, D. Sitikantha, A. Bhuyan, H. Panda, K. Mohanta, Dielectric and ferroelectric properties of PVDF thin film for biomechanical energy harvesting, Materials Today: Proceedings 41 (2021) 335-339.

[315] A. Abdelaziem, A.M. Mohamed, Y.M. Yousry, R. Borayek, A.S. Razeen, N. Zhang, S. Chen, L. Zhang, K. Lin, Z. Liu, Effect of poling on the dielectric properties of synthesized β-poly (vinylidene fluoride) foam, Journal of Applied Physics 133(12) (2023).
[316] G.H. Tabhane, S.M. Giripunje, Robust flower-like ZnO assembled β-PVDF/BT hybrid nanocomposite: Excellent energy harvester, Polymer Testing 88 (2020) 106564.
[317] B. Athira, A. George, K. Vaishna Priya, U. Hareesh, E.B. Gowd, K.P. Surendran, A. Chandran, High-performance flexible piezoelectric nanogenerator based on electrospun PVDF-BaTiO3 nanofibers for self-powered vibration sensing applications, ACS Applied Materials & Interfaces 14(39) (2022) 44239-44250.
[318] B. Hermenegildo, R. Meira, A. Díez, D. Correia, S. Ribeiro, J. Serra, C. Ribeiro, L. Pérez-Álvarez, J.L. Vilas-Vilela, S. Lanceros-Méndez, Ionic liquid modified electroactive polymer-based microenvironments for tissue engineering, Polymer 246 (2022) 124731.
[319] A. Mahdavi Varposhti, M. Yousefzadeh, E. Kowsari, M. Latifi, Enhancement of β-phase crystalline structure and piezoelectric properties of flexible PVDF/ionic liquid surfactant composite nanofibers for potential application in sensing and self-powering, Macromolecular Materials and Engineering 305(3) (2020) 1900796.
[320] M. Zeyrek Ongun, S. Oguzlar, E.C. Doluel, U. Kartal, M. Yurddaskal, Enhancement of piezoelectric energy-harvesting capacity of electrospun β-PVDF nanogenerators by adding GO and rGO, Journal of Materials Science: Materials in Electronics 31 (2020) 1960-1968.
[321] W. Deng, T. Yang, L. Jin, C. Yan, H. Huang, X. Chu, Z. Wang, D. Xiong, G. Tian, Y. Gao, Cowpea-structured PVDF/ZnO nanofibers based flexible self-powered piezoelectric bending motion sensor towards remote control of gestures, Nano Energy 55 (2019) 516-525.
[322] R.S. Sabry, A.D. Hussein, PVDF: ZnO/BaTiO3 as high out-put piezoelectric nanogenerator, Polymer Testing 79 (2019) 106001.
[323] R. Dey, R. Bhunia, S. Hussain, B.R. Chakraborty, R. Bhar, A.K. Pal, Flexible and free-standing films containing cobalt-doped nanocrystalline zinc oxide dispersed in polyvinylidene fluoride matrix: synthesis and characterization, Polymer Bulletin 75 (2018) 307-325.
[324] J.H. Eun, S.M. Sung, M.S. Kim, B.K. Choi, J.S. Lee, Effect of MWCNT content on the mechanical and piezoelectric properties of PVDF nanofibers, Materials & Design 206 (2021) 109785.
[325] S. Sharafkhani, M. Kokabi, Ultrathin-shell PVDF/CNT nanocomposite aligned hollow fibers as a sensor/actuator single element, Composites Science and Technology 200 (2020) 108425.
[326] A. Kaeopisan, H. Wattanasarn, Piezoelectric PVDF/CNT Flexible Applied on Motorcycle, Integrated Ferroelectrics 214(1) (2021) 166-172.
[327] Z. Jin, D. Lei, Y. Wang, L. Wu, N. Hu, Influences of poling temperature and elongation ratio on PVDF-HFP piezoelectric films, Nanotechnology Reviews 10(1) (2021) 1009-1017.
[328] E. Nilsson, A. Lund, C. Jonasson, C. Johansson, B. Hagström, Poling and characterization of piezoelectric polymer fibers for use in textile sensors, Sensors and Actuators A: Physical 201 (2013) 477-486.
[329] H.J. Lee, J.S. Won, S.C. Lim, S.G. Lee, Preparation and characterization of the PVDF/LDPE thermoplastic composite having piezoelectric property, Polymer Bulletin 73 (2016) 2639-2647.
[330] A.S. Elmezayyen, J. Zheng, C. Xu, Simply preparation of self-poled PVDF/nanoceria nanocomposite through one-step formation approach, Polymer Bulletin 78 (2021) 5547-5566.
[331] R. Tao, J. Shi, M. Rafiee, A. Akbarzadeh, D. Therriault, Fused filament fabrication of PVDF films for piezoelectric sensing and energy harvesting applications, Materials Advances 3(12) (2022) 4851-4860.

[332] D. Zhang, X. Zhang, X. Li, H. Wang, X. Sang, G. Zhu, Y. Yeung, Enhanced piezoelectric performance of PVDF/BiCl3/ZnO nanofiber-based piezoelectric nanogenerator, European Polymer Journal 166 (2022) 110956.
[333] Z. Liu, M. Cai, X. Zhang, X. Yu, S. Wang, X. Wan, Z.L. Wang, L. Li, Cell-Traction-Triggered On-Demand Electrical Stimulation for Neuron-Like Differentiation, Advanced Materials 33(51) (2021) 2106317.
[334] Y. Guo, J. Xu, W. Wu, S. Liu, J. Zhao, E. Pawlikowska, M. Szafran, F. Gao, Ultralight graphene aerogel/PVDF composites for flexible piezoelectric nanogenerators, Composites Communications 22 (2020) 100542.
[335] J.-X. Chen, J.-W. Li, C.-C. Cheng, C.-W. Chiu, Piezoelectric property enhancement of PZT/Poly (vinylidenefluoride-co-trifluoroethylene) hybrid films for flexible piezoelectric energy harvesters, ACS omega 7(1) (2021) 793-803.
[336] F. Gheorghiu, R. Stanculescu, L. Curecheriu, E. Brunengo, P. Stagnaro, V. Tiron, P. Postolache, M.T. Buscaglia, L. Mitoseriu, PVDF–ferrite composites with dual magneto-piezoelectric response for flexible electronics applications: synthesis and functional properties, Journal of Materials Science 55(9) (2020) 3926-3939.
[337] A. Sasmal, S. Sen, P.S. Devi, Synthesis and characterization of SmFeO3 and its effect on the electrical and energy storage properties of PVDF, Materials Research Bulletin 130 (2020) 110941.
[338] S. Bairagi, S.W. Ali, A unique piezoelectric nanogenerator composed of melt-spun PVDF/KNN nanorod-based nanocomposite fibre, European Polymer Journal 116 (2019) 554-561.
[339] B. Zazoum, Investigation on Dielectric Permittivity of PVDF/BaTiO3 Nanocomposites Materials by Response Surface Methodology, ECS Journal of Solid State Science and Technology 11(7) (2022) 073010.
[340] C. Shao, Y. Zhao, L. Qu, Recent advances in highly integrated energy conversion and storage system, SusMat 2(2) (2022) 142-160.
[341] J. Lv, J. Chen, P.S. Lee, Sustainable wearable energy storage devices self-charged by human-body bioenergy, SusMat 1(2) (2021) 285-302.
[342] M. Wu, Y. Wang, S. Gao, R. Wang, C. Ma, Z. Tang, N. Bao, W. Wu, F. Fan, W. Wu, Solution-synthesized chiral piezoelectric selenium nanowires for wearable self-powered human-integrated monitoring, Nano energy 56 (2019) 693-699.
[343] J. Wang, H.Y. Man, C. Meng, P. Liu, S. Li, H.S. Kwok, Y. Zi, A fully self-powered, natural-light-enabled fiber-optic vibration sensing solution, SusMat 1(4) (2021) 593-602.
[344] H. Jiang, L. Song, Z.-X. Huang, M. Liu, Y. Zhao, S. Zhang, J. Guo, Y. Li, Q. Wang, J.-P. Qu, A novel concept of hierarchical porous structural design on enhancing output performance of piezoelectric nanogenerator, Nano Energy 104 (2022) 107921.
[345] M.C. Sekhar, E. Veena, N.S. Kumar, K.C.B. Naidu, A. Mallikarjuna, D.B. Basha, A review on piezoelectric materials and their applications, Crystal Research and Technology 58(2) (2023) 2200130.
[346] C. Chen, X. Wang, Y. Wang, D. Yang, F. Yao, W. Zhang, B. Wang, G.A. Sewvandi, D. Yang, D. Hu, Additive manufacturing of piezoelectric materials, Advanced Functional Materials 30(52) (2020) 2005141.
[347] X. Wang, Y. Huan, S. Ji, Y. Zhu, T. Wei, Z. Cheng, Ultra-high piezoelectric performance by rational tuning of heterovalent-ion doping in lead-free piezoelectric ceramics, Nano Energy 101 (2022) 107580.
[348] H. Kim, S. Yun, K. Kim, W. Kim, J. Ryu, H.G. Nam, S.M. Han, S. Jeon, S. Hong, Breaking the elastic limit of piezoelectric ceramics using nanostructures: A case study using ZnO, Nano Energy 78 (2020) 105259.

[349] J. Huang, M. Yao, X. Yao, A novel approach to improving the electromechanical properties of PZT-based piezoelectric ceramics via a grain coating modification strategy, Ceramics International 47(11) (2021) 16294-16302.
[350] T. Wittinanon, R. Rianyoi, A. Chaipanich, Effect of polyvinylidene fluoride on the fracture microstructure characteristics and piezoelectric and mechanical properties of 0-3 barium zirconate titanate ceramic-cement composites, Journal of the European Ceramic Society 40(14) (2020) 4886-4893.
[351] Y. Wu, Y. Ma, H. Zheng, S. Ramakrishna, Piezoelectric materials for flexible and wearable electronics: A review, Materials & Design 211 (2021) 110164.
[352] C. Zhang, Y. Li, W. Kang, X. Liu, Q. Wang, Current advances and future perspectives of additive manufacturing for functional polymeric materials and devices, SusMat 1(1) (2021) 127-147.
[353] R. Dallaev, T. Pisarenko, D. Sobola, F. Orudzhev, S. Ramazanov, T. Trčka, Brief review of PVDF properties and applications potential, Polymers 14(22) (2022) 4793.
[354] L. Lu, W. Ding, J. Liu, B. Yang, Flexible PVDF based piezoelectric nanogenerators, Nano Energy 78 (2020) 105251.
[355] M. Smith, S. Kar-Narayan, Piezoelectric polymers: theory, challenges and opportunities, Int. Mater. Rev. 67(1) (2022) 65-88.
[356] P. Eltouby, I. Shyha, C. Li, J. Khaliq, Factors affecting the piezoelectric performance of ceramic-polymer composites: A comprehensive review, Ceramics International 47(13) (2021) 17813-17825.
[357] S. Im, S.Y. Cho, J.-H. Cho, G.-T. Hwang, A.I. Kingon, S.D. Bu, W. Jo, S.-H. Kim, C.K. Jeong, Study on relaxor polymer interface matrix for piezoelectric nanocomposite generators, Applied Surface Science 613 (2023) 156031.
[358] A. Megdich, M. Habibi, L. Laperrière, A review on 3D printed piezoelectric energy harvesters: materials, 3D printing techniques, and applications, Materials Today Communications 35 (2023) 105541.
[359] A. De Neef, C. Samuel, H. Amorín, G. Stoclet, R. Jiménez, P. Dubois, J. Soulestin, J.-M. Raquez, Beta phase crystallization and ferro-and piezoelectric performances of melt-processed Poly (vinylidene difluoride) Blends with Poly (methyl methacrylate) copolymers containing ionizable moieties, ACS Applied Polymer Materials 2(9) (2020) 3766-3780.
[360] A.M. Chandran, S. Varun, P.K.S. Mural, Development of self-poled PVDF/MWNT flexible nanocomposites with a boosted electroactive β-phase, New Journal of Chemistry 44(34) (2020) 14578-14591.
[361] M. Yan, J. Zhong, S. Liu, Z. Xiao, X. Yuan, D. Zhai, K. Zhou, Z. Li, D. Zhang, C. Bowen, Flexible pillar-base structured piezocomposite with aligned porosity for piezoelectric energy harvesting, Nano Energy 88 (2021) 106278.
[362] M.M. Abolhasani, M. Naebe, M. Hassanpour Amiri, K. Shirvanimoghaddam, S. Anwar, J.J. Michels, K. Asadi, Hierarchically structured porous piezoelectric polymer nanofibers for energy harvesting, Advanced Science 7(13) (2020) 2000517.
[363] S. Song, Y. Han, Y. Li, Q. Wang, 3D printed piezoelectric porous structure with enhanced output performance and stress-electricity response for road energy harvesting, Additive Manufacturing 72 (2023) 103625.
[364] H. Pei, J. Jing, Y. Chen, J. Guo, N. Chen, 3D printing of PVDF-based piezoelectric nanogenerator from programmable metamaterial design: Promising strategy for flexible electronic skin, Nano Energy 109 (2023) 108303.
[365] R.W. Lewis, A.C. Dent, R. Stevens, C.R. Bowen, Microstructural modelling of the polarization and properties of porous ferroelectrics, Smart materials and structures 20(8) (2011) 085002.

[366] X. Yuan, X. Gao, J. Yang, X. Shen, Z. Li, S. You, Z. Wang, S. Dong, The large piezoelectricity and high power density of a 3D-printed multilayer copolymer in a rugby ball-structured mechanical energy harvester, Energy & Environmental Science 13(1) (2020) 152-161.
[367] Z. Abdelhamid, H. Mohamed, S. Kelouwani, The use of machine learning in process–structure–property modeling for material extrusion additive manufacturing: a state-of-the-art review, Journal of the Brazilian Society of Mechanical Sciences and Engineering 46(2) (2024) 70.
[368] A. Ziadia, M. Habibi, S. Kelouwani, Machine learning study of the effect of process parameters on tensile strength of FFF PLA and PLA-CF, Eng 4(4) (2023) 2741-2763.
[369] L. Koroglu, E. Ayas, N. Ay, 3D printing of polyvinylidene fluoride based piezoelectric nanocomposites: an overview, Macromolecular Materials and Engineering 306(10) (2021) 2100277.
[370] H. Zhang, F. Ke, J. Shao, C. Wang, H. Wang, Y. Chen, One-step fabrication of highly sensitive pressure sensor by all FDM printing, Composites Science and Technology 226 (2022) 109531.
[371] M. Safaei, H.A. Sodano, S.R. Anton, A review of energy harvesting using piezoelectric materials: state-of-the-art a decade later (2008–2018), Smart materials and structures 28(11) (2019) 113001.
[372] T. Li, P.S. Lee, Piezoelectric energy harvesting technology: from materials, structures, to applications, Small Structures 3(3) (2022) 2100128.
[373] A. Aabid, B. Parveez, M.A. Raheman, Y.E. Ibrahim, A. Anjum, M. Hrairi, N. Parveen, J. Mohammed Zayan, A review of piezoelectric material-based structural control and health monitoring techniques for engineering structures: Challenges and opportunities, Actuators, MDPI, 2021, p. 101.
[374] J. Yin, N. Liu, P. Jia, Z. Ren, Q. Zhang, W. Lu, Q. Yao, M. Deng, Y. Gao, MXene-enhanced environmentally stable organohydrogel ionic diode toward harvesting ultralow-frequency mechanical energy and moisture energy, SusMat 3(6) (2023) 859-876.
[375] R. Li, S. Zhang, H. Chen, Y. Huang, B. Wang, X. Wu, Q. Jiang, S. Zhao, F. Wang, Y. Zhao, Multicolored structural coloration of carbon nanotube fibers, SusMat 3(1) (2023) 102-110.
[376] T.E. Hooper, J.I. Roscow, A. Mathieson, H. Khanbareh, A.J. Goetzee-Barral, A.J. Bell, High voltage coefficient piezoelectric materials and their applications, J. Eur. Ceram. Soc. 41(13) (2021) 6115-6129.
[377] Q. Guo, F. Li, F. Xia, P. Wang, X. Gao, H. Hao, H. Liu, H. Sun, S. Zhang, Piezoelectric ceramics with high piezoelectricity and broad temperature usage range, Journal of Materiomics 7(4) (2021) 683-692.
[378] B. Xun, A. Song, J. Yu, Y. Yin, J.-F. Li, B.-P. Zhang, Lead-free BiFeO3-BaTiO3 ceramics with high Curie temperature: fine compositional tuning across the phase boundary for high piezoelectric charge and strain coefficients, ACS Applied Materials & Interfaces 13(3) (2021) 4192-4202.
[379] J.-Y. Lee, H. Lee, H.-S. Kim, J. Jang, S.-H. Kim, J.-H. Ryu, J.-H. Jang, S.-L. Hwang, H. Ahn, D. Ha, Improving the efficiency of PZT-based piezoelectric energy harvesting by mixing MWCNTs under solar radiation, Materials Today Sustainability 24 (2023) 100481.
[380] P.J. Liu, K. Wang, L. Li, R. Zhang, Z.P.G. Xu, Lead-free piezoelectric materials for musculoskeletal tissue engineering, Materials Today Sustainability (2023) 100393.
[381] T. Rodrigues-Marinho, N. Perinka, P. Costa, S. Lanceros-Mendez, Printable lightweight polymer-based energy harvesting systems: materials, processes, and applications, Materials Today Sustainability 21 (2023) 100292.

[382] X. Lv, Y. Liu, J. Yu, Z. Li, B. Ding, Smart fibers for self-powered electronic skins, Advanced Fiber Materials 5(2) (2023) 401-428.
[383] S. Mishra, S. Mohanty, A. Ramadoss, Functionality of flexible pressure sensors in cardiovascular health monitoring: a review, Acs Sensors 7(9) (2022) 2495-2520.
[384] M. Pusty, P.M. Shirage, Insights and perspectives on graphene-PVDF based nanocomposite materials for harvesting mechanical energy, Journal of Alloys and Compounds 904 (2022) 164060.
[385] A. Kurakula, S.A. Graham, P. Manchi, M.V. Paranjape, J.S. Yu, Enhanced energy harvesting ability of bismuth sodium titanate/polyvinylidene fluoride composite film-based piezoelectric nanogenerators for mechanical energy scavenging and safety-walker applications, Materials Today Sustainability 25 (2024) 100616.
[386] J. Ma, U. Azhar, C. Zong, Y. Zhang, A. Xu, C. Zhai, L. Zhang, S. Zhang, Core-shell structured PVDF@ BT nanoparticles for dielectric materials: A novel composite to prove the dependence of dielectric properties on ferroelectric shell, Materials & Design 164 (2019) 107556.
[387] N. Bhaskar, M.C. Kachappilly, V. Bhushan, H.J. Pandya, B. Basu, Electrical field stimulated modulation of cell fate of pre-osteoblasts on PVDF/BT/MWCNT based electroactive biomaterials, Journal of Biomedical Materials Research Part A 111(3) (2023) 340-353.
[388] A. Megdich, M. Habibi, L. Laperrière, Modeling and optimization of piezoelectric and dielectric properties of poled PVDF/BT nanocomposites, Polymer Bulletin (2024) 1-21.
[389] Z. Li, Z. Liu, H. Sun, C. Gao, Superstructured assembly of nanocarbons: fullerenes, nanotubes, and graphene, Chemical reviews 115(15) (2015) 7046-7117.
[390] N. Nurazzi, F. Sabaruddin, M. Harussani, S. Kamarudin, M. Rayung, M. Asyraf, H. Aisyah, M. Norrrahim, R. Ilyas, N. Abdullah, Mechanical performance and applications of cnts reinforced polymer composites—A review, Nanomaterials 11(9) (2021) 2186.
[391] A.C. Hurtado, P. Peralta, R. Ruiz, M.M. Alamdari, E. Atroshchenko, Shape optimization of piezoelectric energy harvesters of variable thickness, Journal of Sound and Vibration 517 (2022) 116503.
[392] C. Wang, G. Yu, H. Cao, S. Wang, Y. Li, Structure simulation optimization and test verification of piezoelectric energy harvester device for road, Sensors and Actuators A: Physical 315 (2020) 112322.
[393] H. Yang, Y. Wei, W. Zhang, Y. Ai, Z. Ye, L. Wang, Development of piezoelectric energy harvester system through optimizing multiple structural parameters, Sensors 21(8) (2021) 2876.
[394] J. Seong, B.-U. Bak, D. Lee, J. Jin, J. Kim, Tribo-piezoelectric synergistic BaTiO3/PDMS micropyramidal structure for high-performance energy harvester and high-sensitivity tactile sensing, Nano Energy 122 (2024) 109264.
[395] X. Du, P. Li, Z. Li, X. Liu, W. Wang, Q. Feng, L. Du, H. Yu, J. Wang, X. Xie, Multi-Pillar Piezoelectric Stack Harvests Ocean Wave Energy with Oscillating Float Buoy, Energy (2024) 131347.
[396] S.M. AlTowireb, S. Goumri-Said, Core-Shell structures for the enhancement of energy harvesting in piezoelectric Nanogenerators: A review, Sustainable Energy Technologies and Assessments 55 (2023) 102982.
[397] E. Mancuso, L. Shah, S. Jindal, C. Serenelli, Z.M. Tsikriteas, H. Khanbareh, A. Tirella, Additively manufactured BaTiO3 composite scaffolds: A novel strategy for load bearing bone tissue engineering applications, Materials Science and Engineering: C 126 (2021) 112192.
[398] J. Li, F. Yang, Y. Long, Y. Dong, Y. Wang, X. Wang, Bulk ferroelectric metamaterial with enhanced piezoelectric and biomimetic mechanical properties from additive manufacturing, ACS nano 15(9) (2021) 14903-14914.

[399] W. Zhou, D. Du, Q. Cui, C. Lu, Y. Wang, Q. He, Recent research progress in piezoelectric vibration energy harvesting technology, Energies 15(3) (2022) 947.
[400] X. Zhou, K. Parida, J. Chen, J. Xiong, Z. Zhou, F. Jiang, Y. Xin, S. Magdassi, P.S. Lee, 3D Printed Auxetic Structure-Assisted Piezoelectric Energy Harvesting and Sensing, Advanced Energy Materials 13(34) (2023) 2301159.
[401] K. Chen, S. Fang, Q. Gao, D. Zou, J. Cao, W.-H. Liao, Enhancing power output of piezoelectric energy harvesting by gradient auxetic structures, Applied Physics Letters 120(10) (2022).
[402] S. Vyavahare, S. Teraiya, S. Kumar, FDM manufactured auxetic structures: An investigation of mechanical properties using machine learning techniques, International Journal of Solids and Structures 265 (2023) 112126.
[403] R. Patel, C. Desai, S. Kushwah, M. Mangrola, A review article on FDM process parameters in 3D printing for composite materials, Materials Today: Proceedings 60 (2022) 2162-2166.
[404] A. Megdich, M. Habibi, L. Laperrière, A review on 4D printing: Material structures, stimuli and additive manufacturing techniques, Materials Letters 337 (2023) 133977.
[405] H. Kim, S. Kim, K. Xue, J. Seok, Modeling and performance analysis of electromagnetic energy harvester based on torsional galloping phenomenon, Mechanical Systems and Signal Processing 195 (2023) 110287.
[406] T.I. Toluwaloju, C.K. Thein, D. Halim, J. Yang, Dynamic responses of the 2DOF electromagnetic vibration energy harvester through different electrical coil connections, Mechanical Systems and Signal Processing 184 (2023) 109709.
[407] H. Zhao, H. Ouyang, A vibro-impact triboelectric energy harvester with a magnetic bistable mechanism and grating-patterned films for dual power enhancement, Mechanical Systems and Signal Processing 178 (2022) 109318.
[408] Z. Liu, C. Zhao, G. Hu, Y. Yang, A multi-degree-of-freedom triboelectric energy harvester for dual-frequency vibration energy harvesting, Mechanical Systems and Signal Processing 188 (2023) 109951.
[409] S. Li, Z. Feng, X. He, Y. Ye, J. Li, An in-plane omnidirectional flutter piezoelectric wind energy harvester, Mechanical Systems and Signal Processing 200 (2023) 110637.
[410] Z. Zhang, Y. Gu, S. Wang, J. Wang, S. Li, F. Meng, J. Kan, Dynamic modeling and experimental validation of a low frequency piezoelectric vibration energy harvester via secondary excitation of pressured fluid, Mechanical Systems and Signal Processing 191 (2023) 110170.
[411] G. Sui, X. Shan, C. Hou, H. Tian, J. Hu, T. Xie, An underwater piezoelectric energy harvester based on magnetic coupling adaptable to low-speed water flow, Mechanical Systems and Signal Processing 184 (2023) 109729.
[412] X. Wang, Q. Du, Y. Zhang, F. Li, T. Wang, G. Fu, C. Lu, Dynamic characteristics of axial load bi-stable energy harvester with piezoelectric polyvinylidene fluoride film, Mechanical Systems and Signal Processing 188 (2023) 110065.
[413] A. Jamshiddoust, M. Avarzamani, A. Farrokhabadi, Experimental investigation of damages in the bimorph piezoelectric energy harvester with multilayer composite substrate, Mechanical Systems and Signal Processing 195 (2023) 110307.
[414] B. Zhao, J. Wang, G. Hu, A. Colombi, W.-H. Liao, J. Liang, Time-sharing Orbit Jump and Energy Harvesting in Nonlinear Piezoelectric Energy Harvesters Using a Synchronous Switch Circuit, arXiv preprint arXiv:2305.06016 (2023).
[415] S. Panda, H. Shin, S. Hajra, Y. Oh, W. Oh, J. Lee, P. Rajaitha, B.K. Panigrahi, J. Shukla, A.K. Sahu, Ferroelectric composite-based piezoelectric energy harvester for self-powered detection of obstructive sleep, Journal of Materiomics (2023).

[416] Y. Zhao, L.-C. An, K. Li, Y.-J. Gong, T.-M. Guo, F.-F. Gao, Y. Lei, Q. Li, W. Li, X.-H. Bu, A new piezoelectric hybrid metal thiocyanide for energy harvesting and human motion sensing, Science China Materials (2023) 1-7.
[417] Z. Wang, K. Maruyama, F. Narita, A novel manufacturing method and structural design of functionally graded piezoelectric composites for energy-harvesting, Materials & Design 214 (2022) 110371.
[418] M. Bonnin, F.L. Traversa, F. Bonani, An impedance matching solution to increase the harvested power and efficiency of nonlinear piezoelectric energy harvesters, Energies 15(8) (2022) 2764.
[419] L. Yang, T. Wei, N. Chen, High-Efficiency Energy Management Circuit Combining Synchronized Switch Harvesting on Inductor Rectifier and Impedance Matching for Impact-Type Piezoelectric Energy Harvester, Energy Technology 10(11) (2022) 2200434.
[420] J. Han, T. Maeda, H. Itakura, D. Kitazawa, Experimental study on the wave energy harvesting performance of a small suspension catamaran exploiting the maximum power point tracking approach, Ocean Engineering 243 (2022) 110176.
[421] R. Hua, S. Marin-Quiros, H.K. Mohan, Y. Wang, Maximum power point tracking for a multi-layered piezoelectric heel charger with a levered mechanism toward impact-based energy harvesting, Review of Scientific Instruments 93(9) (2022).
[422] M. Lallart, High gain, load-tolerant self-powered series–parallel synchronized switching technique for piezoelectric energy harvesting, IEEE Transactions on Power Electronics 37(7) (2022) 8649-8658.
[423] B. Zhang, H. Liu, B. Hu, S. Zhou, Analysis and optimization of self-powered parallel synchronized switch harvesting on inductor circuit for piezoelectric energy harvesting, Smart Materials and Structures 31(9) (2022) 095040.
[424] D. Li, C. Wang, X. Cui, D. Chen, C. Fei, Y. Yang, Recent progress and development of interface integrated circuits for piezoelectric energy harvesting, Nano Energy 94 (2022) 106938.
[425] M. Mousavi, S. Ziaei-Rad, A.H. Karimi, Piezoelectric-based energy harvesting from bridge vibrations subjected to moving successive vehicles by functionally graded cantilever beams–Theoretical and experimental investigations, Mechanical Systems and Signal Processing 188 (2023) 110015.
[426] C. Zhao, G. Hu, Y. Yang, A cantilever-type vibro-impact triboelectric energy harvester for wind energy harvesting, Mechanical Systems and Signal Processing 177 (2022) 109185.
[427] M. Yao, P. Liu, L. Ma, H. Wang, W. Zhang, Experimental study on broadband bistable energy harvester with L-shaped piezoelectric cantilever beam, Acta Mechanica Sinica 36 (2020) 557-577.
[428] D. Liu, M. Al-Haik, M. Zakaria, M.R. Hajj, Piezoelectric energy harvesting using L-shaped structures, Journal of Intelligent Material Systems and Structures 29(6) (2018) 1206-1215.
[429] X. Nie, T. Tan, Z. Yan, Z. Yan, M.R. Hajj, Broadband and high-efficient L-shaped piezoelectric energy harvester based on internal resonance, International Journal of Mechanical Sciences 159 (2019) 287-305.
[430] X. Nie, S. Pei, T. Tan, Z. Yan, Z. Yan, Nonlinear 1: 2 internal resonance response of L-shaped piezoelectric energy harvester under the influence of electrical damping, International Journal of Mechanical Sciences 225 (2022) 107365.
[431] H. Li, H. Sun, B. Song, D. Zhang, X. Shang, D. Liu, Nonlinear dynamic response of an L-shaped beam-mass piezoelectric energy harvester, Journal of Sound and Vibration 499 (2021) 116004.

[432] S.A. Kouritem, H.A. El-Gamal, K.T. Mohamed, Effect of major factors on broadband natural frequency energy harvesting for rectangular and L-shaped cantilever harvesters, Microsystem Technologies 29(5) (2023) 729-743.
[433] S. Shi, W. Geng, K. Bi, Y. Shi, F. Li, J. He, X. Chou, High sensitivity MEMS accelerometer using PZT-based four L-shaped beam structure, IEEE Sensors Journal 22(8) (2022) 7627-7636.
[434] Y. Zheng, S. Sun, Global optimization of excitation directions for scavenging energy based on a cross-jointed L-shape multidirectional piezoelectric energy harvester, Sensors and Actuators A: Physical 342 (2022) 113651.
[435] H. Miao, X. Chen, H. Cai, F. Li, Comparative face-shear piezoelectric properties of soft and hard PZT ceramics, Journal of Applied Physics 118(21) (2015).
[436] H. Li, D. Liu, J. Wang, X. Shang, M.R. Hajj, Broadband bimorph piezoelectric energy harvesting by exploiting bending-torsion of L-shaped structure, Energy Conversion and Management 206 (2020) 112503.
[437] X. Li, D. Upadrashta, K. Yu, Y. Yang, Analytical modeling and validation of multi-mode piezoelectric energy harvester, Mechanical Systems and Signal Processing 124 (2019) 613-631.
[438] S. Rakici, J. Kim, A stabilized non-ordinary peridynamic model for linear piezoelectricity, Applied Mathematical Modelling (2023).
[439] S.-H. Jo, B.D. Youn, An improved analytical model that considers lateral effects of a phononic crystal with a piezoelectric defect for elastic wave energy harvesting, International Journal of Mechanical Sciences 205 (2021) 106593.
[440] J. Jia, X. Shan, D. Upadrashta, T. Xie, Y. Yang, R. Song, An asymmetric bending-torsional piezoelectric energy harvester at low wind speed, Energy 198 (2020) 117287.
[441] Y. Cao, D. Cao, G. He, X. Ge, Y. Hao, Vibration analysis and distributed piezoelectric energy harvester design for the L-shaped beam, European Journal of Mechanics-A/Solids 87 (2021) 104214.
[442] S. Osinaga, S. Machado, M. Febbo, An analytical model of the electromechanical coupling for a piezoelectric stepped buckled beam for energy harvesting applications, Mechanical Systems and Signal Processing 179 (2022) 109355.
[443] A. Homayouni-Amlashi, A. Mohand-Ousaid, M. Rakotondrabe, Analytical modelling and optimization of a piezoelectric cantilever energy harvester with in-span attachment, Micromachines 11(6) (2020) 591.
[444] Y. Chen, Z. Yang, Z. Chen, K. Li, L. Wang, S. Zhou, Theoretical and experimental investigations of multibifurcated piezoelectric energy harvesters with coupled bending and torsional vibrations, Acta Mechanica Sinica 38(5) (2022) 521434.
[445] A. Zolfagharian, A. Kaynak, M. Bodaghi, A.Z. Kouzani, S. Gharaie, S. Nahavandi, Control-based 4D printing: Adaptive 4D-printed systems, Applied Sciences 10(9) (2020) 3020.
[446] Y. Liu, F. Zhang, J. Leng, T.-W. Chou, Microstructural design of 4D printed angle-ply laminated strips with tunable shape memory properties, Materials Letters 285 (2021) 129197.
[447] H. Pandey, S.S. Mohol, R. Kandi, 4D printing of tracheal scaffold using shape-memory polymer composite, Materials Letters 329 (2022) 133238.
[448] J. Huang, J. Fan, L. Cao, C. Xu, Y. Chen, A novel strategy to construct co-continuous PLA/NBR thermoplastic vulcanizates: Metal-ligand coordination-induced dynamic vulcanization, balanced stiffness-toughness and shape memory effect, Chemical Engineering Journal 385 (2020) 123828.
[449] A. Gupta, S. Hasanov, I. Fidan, Processing and characterization of 3d-printed polymer matrix composites reinforced with discontinuous fibers, (2019).
[450] D. Mohan, T.Z. Khai, M.S. Sajab, H. Kaco, Well-dispersed cellulose-graphene in 4D printing biopolymer, Materials Letters 303 (2021) 130522.

[451] A. Zolfagharian, A. Kaynak, S.Y. Khoo, A. Kouzani, Pattern-driven 4D printing, Sensors and Actuators A: Physical 274 (2018) 231-243.
[452] T.T. Nguyen, J. Kim, 4D-printing—Fused deposition modeling printing and PolyJet printing with shape memory polymers composite, Fibers and Polymers 21 (2020) 2364-2372.
[453] K. Zhang, A. Geissler, M. Standhardt, S. Mehlhase, M. Gallei, L. Chen, C. Marie Thiele, Moisture-responsive films of cellulose stearoyl esters showing reversible shape transitions, Scientific reports 5(1) (2015) 1-13.
[454] L. Ren, B. Li, Q. Liu, L. Ren, Z. Song, X. Zhou, P. Gao, 4D printing dual stimuli-responsive bilayer structure toward multiple shape-shifting, Frontiers in Materials 8 (2021) 655160.
[455] C.-Y. Wu, J.-R. Chen, C.-K. Su, 4D-printed pH sensing claw, Analytica Chimica Acta 1204 (2022) 339733.
[456] M. Quanjin, M. Rejab, M. Idris, N.M. Kumar, M. Abdullah, G.R. Reddy, Recent 3D and 4D intelligent printing technologies: A comparative review and future perspective, Procedia Computer Science 167 (2020) 1210-1219.
[457] H. Chu, W. Yang, L. Sun, S. Cai, R. Yang, W. Liang, H. Yu, L. Liu, 4D printing: a review on recent progresses, Micromachines 11(9) (2020) 796.
[458] D.G. Tamay, T. Dursun Usal, A.S. Alagoz, D. Yucel, N. Hasirci, V. Hasirci, 3D and 4D printing of polymers for tissue engineering applications, Frontiers in bioengineering and biotechnology 7 (2019) 164.
[459] M. Rafiee, R.D. Farahani, D. Therriault, Multi-material 3D and 4D printing: a survey, Advanced Science 7(12) (2020) 1902307.
[460] X. Wang, Y. He, Y. Liu, J. Leng, Advances in shape memory polymers: Remote actuation, multi-stimuli control, 4D printing and prospective applications, Materials Science and Engineering: R: Reports 151 (2022) 100702.
[461] A. Subash, B. Kandasubramanian, 4D printing of shape memory polymers, European Polymer Journal 134 (2020) 109771.
[462] J. Zhang, Z. Yin, L. Ren, Q. Liu, L. Ren, X. Yang, X. Zhou, Advances in 4D printed shape memory polymers: from 3D printing, smart excitation, and response to applications, Advanced Materials Technologies 7(9) (2022) 2101568.
[463] W. Zhao, C. Yue, L. Liu, Y. Liu, J. Leng, Research progress of shape memory polymer and 4D printing in biomedical application, Advanced Healthcare Materials 12(16) (2023) 2201975.
[464] Y. Chen, C. Chen, H.U. Rehman, X. Zheng, H. Li, H. Liu, M.S. Hedenqvist, Shape-memory polymeric artificial muscles: Mechanisms, applications and challenges, Molecules 25(18) (2020) 4246.
[465] M. Herath, J. Epaarachchi, Shape memory polymer composites and their smart structural applications, Composite Materials, Elsevier2021, pp. 581-610.
[466] L. Luo, F. Zhang, L. Wang, Y. Liu, J. Leng, Recent Advances in Shape Memory Polymers: Multifunctional Materials, Multiscale Structures, and Applications, Advanced Functional Materials 34(14) (2024) 2312036.
[467] S. Rodinò, C. Maletta, Design Considerations and Applications of Shape Memory Alloy-Based Actuation in Morphing Structures: A Systematic Review, Progress in Engineering Science (2024) 100021.
[468] G. Scalet, Two-way and multiple-way shape memory polymers for soft robotics: An overview, Actuators, MDPI, 2020, p. 10.
[469] C. Lin, J. Lv, Y. Li, F. Zhang, J. Li, Y. Liu, L. Liu, J. Leng, 4D-printed biodegradable and remotely controllable shape memory occlusion devices, Advanced Functional Materials 29(51) (2019) 1906569.

[470] Y. Wang, H. Cui, Y. Wang, C. Xu, T.J. Esworthy, S.Y. Hann, M. Boehm, Y.-L. Shen, D. Mei, L.G. Zhang, 4D printed cardiac construct with aligned myofibers and adjustable curvature for myocardial regeneration, ACS applied materials & interfaces 13(11) (2021) 12746-12758.
[471] J.G. Choi, G.M. Spinks, S.J. Kim, Mode shifting shape memory polymer and hydrogel composite fiber actuators for soft robots, Sensors and Actuators A: Physical 342 (2022) 113619.
[472] K. Bouguermouh, M. Habibi, L. Laperrière, Z. Li, Y. Abdin, 4D-printed PLA-PETG polymer blends: comprehensive analysis of thermal, mechanical, and shape memory performances, Journal of Materials Science (2024) 1-18.
[473] B. Karima, M. Habibi, L. Laperrière, 4D printing of fiber-reinforced auxetic structures: the building blocks: a review, Smart Material Structures 33(6) (2024) 063001.
[474] R. Purwar, R. Sachan, Thermoresponsive shape memory polymers for smart textiles, Advances in functional and protective textiles, Elsevier2020, pp. 37-62.
[475] M. Wang, F. Yang, Y.J. Zhang, Tunable Thermo-Responsive Shape Memory Materials Enabled by Poly (E-Caprolactone)-Poly (2-Vinyl) Ethylene Glycol Copolymers Via Facile Thiol-Ene Photo-Crosslink, Available at SSRN 4956901.
[476] X. Yang, X. He, L. Wang, C. Zhao, D. Xiang, H. Li, J. Lai, G. Yan, Z. Li, L. Sun, Durable semi-interpenetrating polymer network containing dynamic boroxine bonds for multi-shape manipulated deformation, Chemical Engineering Journal 491 (2024) 151905.
[477] W. Liu, D. Kong, W. Zhao, J. Leng, Multi-stimulus responsive shape memory polyurea incorporating stress-mismatching structure for soft actuators and reversible deployable structures, Composite Structures 334 (2024) 117966.
[478] A. ISLAM, J. HASAN, K.R. HOSSAIN, Intelligent materials in 3D printing: A journey from additive manufacturing to 4D printing, Journal of Advanced Manufacturing Science and Technology 4(4) (2024).
[479] Y.-F. Shih, W.-C. Hou, C.-W. Chang, C.-H. Wu, R.-J. Jeng, Y.-H. Chen, Carbon nanotube/microcapsule/polyurethane nanocomposites for multistimuli responsive shape memory polymers.
[480] A. Concellón, P. Mainik, C. Vazquez-Martel, C. Álvarez-Solana, E. Blasco, 4D Printing of Liquid Crystal Emulsions for Smart Structures with Multiple Functionalities, Angewandte Chemie e202421162.
[481] J. zhang, Q. Zhang, W. Pan, M. Jiao, Y. Chen, H. Pei, X. Li, Y. Qi, J. Zhao, Ethylene vinyl acetate/copper sulphide with near-infrared light active shape memory behavior, Journal of Elastomers & Plastics (2024) 00952443241297450.
[482] S. Nandha, D. Rajan, U. Shivakumar, Nanocellulose Incorporated Liquid Crystal Elastomers as Soft Actuators, ACS Applied Polymer Materials 6(20) (2024) 12842-12853.
[483] Z. Liu, Y. Li, S. Ma, C. Liu, Y. Zhang, X. Lu, Z. Lin, Y. Liang, Near-infrared light-driven programmable shape memory polymer for self-shaping 3D printing methods, Virtual and Physical Prototyping 19(1) (2024) e2422384.
[484] N. Phetnoi, L. Amornkitbamrung, K. Charoensuk, C. Sapcharoenkun, C. Jubsilp, S. Ekgasit, S. Rimdusit, Fast magnetic-responsive shape memory composites from bio-based benzoxazine/polyglycerol polyglycidyl ether copolymers highly filled with iron oxide nanoparticles, Composites Part A: Applied Science and Manufacturing 186 (2024) 108398.
[485] J. Liu, S. Wang, S. Huang, K. Zhang, Z. Chen, C. Huang, Y. Zhang, S. Du, T. Xu, Magnetic and radio frequency dual-responsive shape-programmable robots for adaptive aneurysm embolization, Cell Reports Physical Science 5(9) (2024).
[486] A. Ahangari, H. Doostmohammadi, M. Baniassadi, M. Bodaghi, M. Baghani, Development and 4D printing of magneto-responsive PMMA/TPU/Fe3O4 nanocomposites

with superior shape memory and toughness properties, European Polymer Journal 220 (2024) 113495.
[487] K. Ruenpanya, P. Mora, P. Karagiannidis, K. Bunyanuwat, S. Rimdusit, Magnetic-responsive triple shape memory polymer from bio-based benzoxazine/urethane polymer alloys with iron oxide nanoparticles, Advanced Industrial and Engineering Polymer Research (2024).
[488] P. Kumar, P. Suryavanshi, S.K. Dwivedy, S. Banerjee, Stimuli-responsive materials for 4D Printing: Mechanical, Manufacturing, and Biomedical Applications, Journal of Molecular Liquids (2024) 125553.
[489] L. Zhang, X. Huang, T. Cole, H. Lu, J. Hang, W. Li, S.-Y. Tang, C. Boyer, T.P. Davis, R. Qiao, 3D-printed liquid metal polymer composites as NIR-responsive 4D printing soft robot, Nature Communications 14(1) (2023) 7815.
[490] H. Liu, F. Wang, W. Wu, X. Dong, L. Sang, 4D printing of mechanically robust PLA/TPU/Fe3O4 magneto-responsive shape memory polymers for smart structures, Composites Part B: Engineering 248 (2023) 110382.
[491] X. Dong, F. Zhang, L. Wang, Y. Liu, J. Leng, 4D printing of electroactive shape-changing composite structures and their programmable behaviors, Composites Part A: Applied Science and Manufacturing 157 (2022) 106925.
[492] K. Dong, M. Panahi-Sarmad, Z. Cui, X. Huang, X. Xiao, Electro-induced shape memory effect of 4D printed auxetic composite using PLA/TPU/CNT filament embedded synergistically with continuous carbon fiber: A theoretical & experimental analysis, Composites Part B: Engineering 220 (2021) 108994.
[493] A.D.B. Ferreira, P.R. Nóvoa, A.T. Marques, Multifunctional Material Systems: A state-of-the-art review, Composite Structures 151 (2016) 3-35.
[494] W. Zhao, L. Liu, J. Leng, Y. Liu, Thermo-mechanical behavior prediction of particulate reinforced shape memory polymer composite, Composites Part B: Engineering 179 (2019) 107455.
[495] K.K. Westbrook, P.H. Kao, F. Castro, Y. Ding, H.J. Qi, A 3D finite deformation constitutive model for amorphous shape memory polymers: a multi-branch modeling approach for nonequilibrium relaxation processes, Mechanics of Materials 43(12) (2011) 853-869.
[496] W. Zhao, L. Liu, X. Lan, J. Leng, Y. Liu, Thermomechanical constitutive models of shape memory polymers and their composites, Applied Mechanics Reviews 75(2) (2023) 020802.
[497] S.H. Ladakhan, R.B. Sreesha, S.M. Adinarayanappa, 4D printing of polylactic acid (PLA)/PLA-thermoplastic polyurethane (TPU)-based metastructure: examining the mechanical, thermal, and shape memory properties, Smart Materials and Structures 33(10) (2024) 105037.
[498] B. Goo, C.-H. Hong, K. Park, 4D printing using anisotropic thermal deformation of 3D-printed thermoplastic parts, Materials & Design 188 (2020) 108485.
[499] C. Shuai, W. Xu, H. He, F. Yang, J. Liu, P. Feng, Layered co-continuous structure in bone scaffold fabricated by laser additive manufacturing for enhancing electro-responsive shape memory properties, Journal of Materials Research and Technology 30 (2024) 61-69.
[500] C. Zeng, L. Liu, W. Bian, Y. Liu, J. Leng, 4D printed electro-induced continuous carbon fiber reinforced shape memory polymer composites with excellent bending resistance, Composites Part B: Engineering 194 (2020) 108034.
[501] A. Megdich, M. Habibi, L. Laperrière, Z. Li, Y. Abdin, Advanced 3D-printed PVDF/BT piezoelectric energy harvester with a bio-inspired 3D structure for a self-powered smart mouse, Nano Energy (2024) 109876.
[502] A. Megdich, M. Habibi, L. Laperrière, Z. Li, Y. Abdin, Enhanced piezoelectric performance of PVDF/MWCNTs energy harvester through a 3D-printed multimodal auxetic structure for smart security systems, Materials Today Sustainability 27 (2024) 100847.

[503] R. Krishna, M. Manjaiah, C. Mohan, Developments in additive manufacturing, Additive manufacturing, Elsevier2021, pp. 37-62.
[504] T.D. Ngo, A. Kashani, G. Imbalzano, K.T. Nguyen, D. Hui, Additive manufacturing (3D printing): A review of materials, methods, applications and challenges, Composites Part B: Engineering 143 (2018) 172-196.
[505] S.-M. Chang, S. Hur, J. Park, D.-G. Lee, J. Shin, H.S. Kim, S.E. Song, J.M. Baik, M. Kim, H.-C. Song, Optimization of piezoelectric polymer composites and 3D printing parameters for flexible tactile sensors, Additive Manufacturing 67 (2023) 103470.
[506] A. Ahmadpour, A.K. Yetisen, S. Tasoglu, Piezoelectric metamaterial blood pressure sensor, ACS Applied Electronic Materials 5(6) (2023) 3280-3290.
[507] S. Gao, A.K. Gain, L. Zhang, A metamaterial for wearable piezoelectric energy harvester, Smart Materials and Structures 30(1) (2020) 015026.
[508] A. Meshkinzar, A. M. Al-Jumaily, Cylindrical piezoelectric PZT transducers for sensing and actuation, Sensors 23(6) (2023) 3042.
[509] G. Song, Z. Liu, F. Zhang, F. Liu, Y. Gu, Z. Liu, Y. Li, High-throughput synthesis and electrical properties of BNT–BT–KNN lead-free piezoelectric ceramics, Journal of Materials Chemistry C 8(11) (2020) 3655-3662.
[510] X. Du, Z. Zhou, Z. Zhang, L. Yao, Q. Zhang, H. Yang, Porous, multi-layered piezoelectric composites based on highly oriented PZT/PVDF electrospinning fibers for high-performance piezoelectric nanogenerators, Journal of Advanced Ceramics 11 (2022) 331-344.
[511] N. Chamankar, R. Khajavi, A.A. Yousefi, A. Rashidi, F. Golestanifard, A flexible piezoelectric pressure sensor based on PVDF nanocomposite fibers doped with PZT particles for energy harvesting applications, Ceramics International 46(12) (2020) 19669-19681.
[512] P. Bhatele, S. Mali, A. Mali, M. Chrungoo, A. Mali, R. Makode, Energy Generation Via Footsteps Using Piezoelectric Sensor, International Research Journal of Engineering and Technology (2022) 9-12.
[513] M. Logeshwaran, J.J.J. Sheela, A.P. Priya, A High-Efficiency Power Generator by Footsteps Using Piezoelectric Effect, 2022 Second International Conference on Artificial Intelligence and Smart Energy (ICAIS), IEEE, 2022, pp. 1547-1553.
[514] H.D. Mayekol Mayck, A.M.R. Fath El-Bab, E. Murimi, P. Moukala Mpele, A human heartbeat frequencies based 2-DOF piezoelectric energy harvester for pacemaker application, Energy Harvesting and Systems 8(1) (2021) 1-11.
[515] Y. Luo, Y. Xiao, J. Liu, Y. Wu, Z. Zhao, Design and application of a flexible nano cardiac sound sensor based on P (VDF-TrFE)/KNN/GR composite piezoelectric film for heart disease diagnosis, Nanotechnology 35(7) (2023) 075502.
[516] D. Al-Yafeai, T. Darabseh, A.-H. I. Mourad, A state-of-the-art review of car suspension-based piezoelectric energy harvesting systems, Energies 13(9) (2020) 2336.
[517] A. Ali, S. Ali, H. Shaukat, E. Khalid, L. Behram, H. Rani, W.A. Altabey, S.A. Kouritem, M. Noori, Advancements in piezoelectric wind energy harvesting: A review, Results in Engineering (2024) 101777.
[518] S.D. Mahapatra, P.C. Mohapatra, A.I. Aria, G. Christie, Y.K. Mishra, S. Hofmann, V.K. Thakur, Piezoelectric materials for energy harvesting and sensing applications: roadmap for future smart materials, Advanced Science 8(17) (2021) 2100864.
[519] N.M. Nor, H.H. Hamzah, K.A. Razak, Recent advancement in sustainable energy harvesting using piezoelectric materials, Sustainable Materials for Next Generation Energy Devices, Elsevier2021, pp. 221-248.
[520] I. Akbar, M. El Hadrouz, M. El Mansori, D. Lagoudas, Toward enabling manufacturing paradigm of 4D printing of shape memory materials: Open literature review, European Polymer Journal 168 (2022) 111106.

[521] G. Liu, X. Zhang, X. Lu, Y. Zhao, Z. Zhou, J. Xu, J. Yin, T. Tang, P. Wang, S. Yi, 4D additive–subtractive manufacturing of shape memory ceramics, Advanced Materials 35(39) (2023) 2302108.
[522] S. Chen, J. Li, H. Shi, X. Chen, G. Liu, S. Meng, J. Lu, Lightweight and geometrically complex ceramics derived from 4D printed shape memory precursor with reconfigurability and programmability for sensing and actuation applications, Chemical Engineering Journal 455 (2023) 140655.
[523] X. Huang, M. Panahi-Sarmad, K. Dong, R. Li, T. Chen, X. Xiao, Tracing evolutions in electro-activated shape memory polymer composites with 4D printing strategies: a systematic review, Composites Part A: Applied Science and Manufacturing 147 (2021) 106444.
[524] M.A. Kouka, F. Abbassi, M. Habibi, F. Chabert, A. Zghal, C. Garnier, 4D printing of shape memory polymers, blends, and composites and their advanced applications: a comprehensive literature review, Advanced Engineering Materials 25(4) (2023) 2200650.
[525] M. Ramezani, Z. Mohd Ripin, 4D printing in biomedical engineering: Advancements, challenges, and future directions, Journal of functional biomaterials 14(7) (2023) 347.
[526] K. McLellan, Y.-C. Sun, H.E. Naguib, A review of 4D printing: Materials, structures, and designs towards the printing of biomedical wearable devices, Bioprinting 27 (2022) e00217.
[527] S.Y. Hann, H. Cui, M. Nowicki, L.G. Zhang, 4D printing soft robotics for biomedical applications, Additive Manufacturing 36 (2020) 101567.
[528] M.Y. Khalid, Z.U. Arif, W. Ahmed, R. Umer, A. Zolfagharian, M. Bodaghi, 4D printing: Technological developments in robotics applications, Sensors and Actuators A: Physical 343 (2022) 113670.
[529] S. Gopinath, N.N. Adarsh, P. Radhakrishnan Nair, S. Mathew, Recent trends in thermo-responsive elastomeric shape memory polymer nanocomposites, Polymer Composites 44(8) (2023) 4433-4458.
[530] A. Andreu, P.-C. Su, J.-H. Kim, C.S. Ng, S. Kim, I. Kim, J. Lee, J. Noh, A.S. Subramanian, Y.-J. Yoon, 4D printing materials for vat photopolymerization, Additive Manufacturing 44 (2021) 102024.
[531] H. Wang, J. Zhao, Z. Luo, Z. Li, Recent research developments of 4D printing technology for magnetically controlled smart materials: a review, Magnetochemistry 9(8) (2023) 204.
[532] F. Momeni, X. Liu, J. Ni, A review of 4D printing, Materials & design 122 (2017) 42-79.
[533] X. Yuan, Z. Mai, Z. Li, Z. Yu, P. Ci, S. Dong, A 3D-printing approach toward flexible piezoelectronics with function diversity, Materials Today (2023).
[534] S. Bodkhe, P. Ermanni, Challenges in 3D printing of piezoelectric materials, Multifunctional Materials 2(2) (2019) 022001.
[535] J. Fan, L. Zhang, S. Wei, Z. Zhang, S.-K. Choi, B. Song, Y. Shi, A review of additive manufacturing of metamaterials and developing trends, Materials Today 50 (2021) 303-328.
[536] I.J. Solomon, P. Sevvel, J. Gunasekaran, A review on the various processing parameters in FDM, Materials Today: Proceedings 37 (2021) 509-514.
[537] A. Dey, N. Yodo, A systematic survey of FDM process parameter optimization and their influence on part characteristics, Journal of Manufacturing and Materials Processing 3(3) (2019) 64.
[538] A. Kafle, E. Luis, R. Silwal, H.M. Pan, P.L. Shrestha, A.K. Bastola, 3D/4D printing of polymers: fused deposition modelling (FDM), selective laser sintering (SLS), and stereolithography (SLA), Polymers 13(18) (2021) 3101.
[539] J. Huang, Q. Qin, J. Wang, A review of stereolithography: Processes and systems, Processes 8(9) (2020) 1138.

[540] M. Mukhtarkhanov, A. Perveen, D. Talamona, Application of stereolithography based 3D printing technology in investment casting, Micromachines 11(10) (2020) 946.
[541] Z. Zhao, X. Tian, X. Song, Engineering materials with light: recent progress in digital light processing based 3D printing, Journal of Materials Chemistry C 8(40) (2020) 13896-13917.
[542] J. Zhang, Q. Hu, S. Wang, J. Tao, M. Gou, Digital light processing based three-dimensional printing for medical applications, International journal of bioprinting 6(1) (2020).
[543] M. Saadi, A. Maguire, N.T. Pottackal, M.S.H. Thakur, M.M. Ikram, A.J. Hart, P.M. Ajayan, M.M. Rahman, Direct ink writing: a 3D printing technology for diverse materials, Advanced Materials 34(28) (2022) 2108855.
[544] R.Y. Tay, Y. Song, D.R. Yao, W. Gao, Direct-ink-writing 3D-printed bioelectronics, Materials Today (2023).
[545] S. Tagliaferri, A. Panagiotopoulos, C. Mattevi, Direct ink writing of energy materials, Materials Advances 2(2) (2021) 540-563.
[546] N.W. Solís Pinargote, A. Smirnov, N. Peretyagin, A. Seleznev, P. Peretyagin, Direct ink writing technology (3d printing) of graphene-based ceramic nanocomposites: A review, Nanomaterials 10(7) (2020) 1300.
[547] M.K. Kim, I.H. Lee, H.-C. Kim, Effect of fabrication parameters on surface roughness of FDM parts, International Journal of Precision Engineering and Manufacturing 19 (2018) 137-142.
[548] V. Shanmugam, O. Das, K. Babu, U. Marimuthu, A. Veerasimman, D.J. Johnson, R.E. Neisiany, M.S. Hedenqvist, S. Ramakrishna, F. Berto, Fatigue behaviour of FDM-3D printed polymers, polymeric composites and architected cellular materials, International Journal of Fatigue 143 (2021) 106007.
[549] A.M. Arefin, N.R. Khatri, N. Kulkarni, P.F. Egan, Polymer 3D printing review: Materials, process, and design strategies for medical applications, Polymers 13(9) (2021) 1499.
[550] F. Jelínek, P. Breedveld, Design for additive manufacture of fine medical instrumentation—DragonFlex case study, Journal of Mechanical Design 137(11) (2015) 111416.
[551] E.M. Maines, M.K. Porwal, C.J. Ellison, T.M. Reineke, Sustainable advances in SLA/DLP 3D printing materials and processes, Green Chemistry 23(18) (2021) 6863-6897.
[552] M. Pagac, J. Hajnys, Q.-P. Ma, L. Jancar, J. Jansa, P. Stefek, J. Mesicek, A review of vat photopolymerization technology: materials, applications, challenges, and future trends of 3D printing, Polymers 13(4) (2021) 598.
[553] J. Borrello, P. Nasser, J.C. Iatridis, K.D. Costa, 3D printing a mechanically-tunable acrylate resin on a commercial DLP-SLA printer, Additive manufacturing 23 (2018) 374-380.
[554] Z. Chen, Z. Li, J. Li, C. Liu, C. Lao, Y. Fu, C. Liu, Y. Li, P. Wang, Y. He, 3D printing of ceramics: A review, Journal of the European Ceramic Society 39(4) (2019) 661-687.
[555] S.P. Stier, H. Böse, Ablative Laser Structuring for Stretchable Multilayer and Multi-Material Electronics and Sensor Systems, Proceedings, MDPI, 2020, p. 21.
[556] J. Gopinathan, I. Noh, Recent trends in bioinks for 3D printing, Biomaterials research 22(1) (2018) 11.
[557] Y.L. Yap, S.L. Sing, W.Y. Yeong, A review of 3D printing processes and materials for soft robotics, Rapid Prototyping Journal 26(8) (2020) 1345-1361.
[558] T. Sathies, P. Senthil, M. Anoop, A review on advancements in applications of fused deposition modelling process, Rapid Prototyping Journal 26(4) (2020) 669-687.
[559] S.C. Daminabo, S. Goel, S.A. Grammatikos, H.Y. Nezhad, V.K. Thakur, Fused deposition modeling-based additive manufacturing (3D printing): techniques for polymer material systems, Materials today chemistry 16 (2020) 100248.

[560] A.J. Sheoran, H. Kumar, Fused Deposition modeling process parameters optimization and effect on mechanical properties and part quality: Review and reflection on present research, Materials Today: Proceedings 21 (2020) 1659-1672.
[561] R.B. Kristiawan, F. Imaduddin, D. Ariawan, Ubaidillah, Z. Arifin, A review on the fused deposition modeling (FDM) 3D printing: Filament processing, materials, and printing parameters, Open Engineering 11(1) (2021) 639-649.
[562] M. Lalegani Dezaki, M.K.A. Mohd Ariffin, S. Hatami, An overview of fused deposition modelling (FDM): Research, development and process optimisation, Rapid Prototyping Journal 27(3) (2021) 562-582.
[563] Y. Du, R. Wang, M. Zeng, S. Xu, M. Saeidi-Javash, W. Wu, Y. Zhang, Hybrid printing of wearable piezoelectric sensors, Nano Energy 90 (2021) 106522.
[564] H. Pei, Y. Chen, Q. Lv, Z. Peng, X. Wang, N. Chen, H. Zhang, A novel microwave assisted multi-material 3D printing strategy to architect lamellar piezoelectric generators for intelligent sensing, Composites Part B: Engineering 280 (2024) 111529.
[565] M.Q. Zafar, H. Zhao, 4D printing: future insight in additive manufacturing, Metals and Materials International 26 (2020) 564-585.
[566] J. Carrell, G. Gruss, E. Gomez, Four-dimensional printing using fused-deposition modeling: a review, Rapid Prototyping Journal 26(5) (2020) 855-869.
[567] M. Bodaghi, R. Noroozi, A. Zolfagharian, M. Fotouhi, S. Norouzi, 4D printing self-morphing structures, Materials 12(8) (2019) 1353.
[568] P. Fu, H. Li, J. Gong, Z. Fan, A.T. Smith, K. Shen, T.O. Khalfalla, H. Huang, X. Qian, J.R. McCutcheon, 4D printing of polymers: Techniques, materials, and prospects, Progress in Polymer Science 126 (2022) 101506.
[569] M. Bodaghi, A. Serjouei, A. Zolfagharian, M. Fotouhi, H. Rahman, D. Durand, Reversible energy absorbing meta-sandwiches by FDM 4D printing, International Journal of Mechanical Sciences 173 (2020) 105451.
[570] S.-J. Ahn, H. Lee, K.-J. Cho, 3D printing with a 3D printed digital material filament for programming functional gradients, Nature Communications 15(1) (2024) 3605.
[571] C.-Y. Cheng, H. Xie, Z.-y. Xu, L. Li, M.-N. Jiang, L. Tang, K.-K. Yang, Y.-Z. Wang, 4D printing of shape memory aliphatic copolyester via UV-assisted FDM strategy for medical protective devices, Chemical Engineering Journal 396 (2020) 125242.
[572] M. Barletta, A. Gisario, M. Mehrpouya, 4D printing of shape memory polylactic acid (PLA) components: Investigating the role of the operational parameters in fused deposition modelling (FDM), Journal of Manufacturing Processes 61 (2021) 473-480.
[573] M. Hosseinzadeh, M. Ghoreishi, K. Narooei, 4D printing of shape memory polylactic acid beams: an experimental investigation into FDM additive manufacturing process parameters, mathematical modeling, and optimization, Journal of Manufacturing Processes 85 (2023) 774-782.
[574] F. Wang, F. Luo, Y. Huang, X. Cao, C. Yuan, 4D printing via multispeed fused deposition modeling, Advanced Materials Technologies 8(2) (2023) 2201383.
[575] R. Noroozi, M. Bodaghi, H. Jafari, A. Zolfagharian, M. Fotouhi, Shape-adaptive metastructures with variable bandgap regions by 4D printing, Polymers 12(3) (2020) 519.
[576] T. van Manen, S. Janbaz, K.M. Jansen, A.A. Zadpoor, 4D printing of reconfigurable metamaterials and devices, Communications Materials 2(1) (2021) 56.
[577] S.K. Melly, L. Liu, Y. Liu, J. Leng, On 4D printing as a revolutionary fabrication technique for smart structures, Smart Materials and Structures 29(8) (2020) 083001.
[578] H.A. Alshahrani, Review of 4D printing materials and reinforced composites: Behaviors, applications and challenges, Journal of Science: Advanced Materials and Devices 6(2) (2021) 167-185.

[579] J. Saroia, Y. Wang, Q. Wei, M. Lei, X. Li, Y. Guo, K. Zhang, A review on 3D printed matrix polymer composites: its potential and future challenges, The international journal of advanced manufacturing technology 106 (2020) 1695-1721.
[580] K. Mohammad-Jafari, S.M. Naghib, 3D Printing of Microfluidic-assisted Liposomes Production for Drug Delivery and Nanobiomedicine: A Review, Current Medicinal Chemistry (2024).
[581] D. Sun, Y. Lu, T. Karaki, Review of the applications of 3D printing technology in the field of piezoelectric ceramics, Resources Chemicals and Materials 2(2) (2023) 128-142.
[582] W. Wang, J. Sun, B. Guo, X. Chen, K.P. Ananth, J. Bai, Fabrication of piezoelectric nano-ceramics via stereolithography of low viscous and non-aqueous suspensions, Journal of the European Ceramic Society 40(3) (2020) 682-688.
[583] K. Zheng, D. Ding, Y. Quan, J. Zhuang, C. Fei, J. Zhao, L. Wang, T. Zhao, Z. Wang, M. Liu, 3D printing orientation controlled PMN-PT piezoelectric ceramics, Journal of the European Ceramic Society 43(6) (2023) 2408-2416.
[584] H. Lu, H. Cui, G. Lu, L. Jiang, R. Hensleigh, Y. Zeng, A. Rayes, M.K. Panduranga, M. Acharya, Z. Wang, 3D Printing and processing of miniaturized transducers with near-pristine piezoelectric ceramics for localized cavitation, Nature communications 14(1) (2023) 2418.
[585] L. He, X. Wang, F. Fei, L. Chen, X. Song, Selectively doped piezoelectric ceramics with tunable piezoelectricity via suspension-enclosing projection stereolithography, Additive manufacturing 48 (2021) 102407.
[586] A. Sotov, A. Kantyukov, A. Popovich, V. Sufiiarov, LCD-SLA 3D printing of BaTiO3 piezoelectric ceramics, Ceramics International 47(21) (2021) 30358-30366.
[587] D. Yao, H. Cui, R. Hensleigh, P. Smith, S. Alford, D. Bernero, S. Bush, K. Mann, H.F. Wu, M. Chin-Nieh, Achieving the upper bound of piezoelectric response in tunable, wearable 3D printed nanocomposites, Advanced Functional Materials 29(42) (2019) 1903866.
[588] T. Brossier, M. Habib, B.T. Benkhaled, G. Volpi, V. Lapinte, S. Blanquer, 4D printing of hydrogels based on poly (oxazoline) and poly (acrylamide) copolymers by stereolithography, Materials Advances (2024).
[589] S. Miao, H. Cui, M. Nowicki, S.-j. Lee, J. Almeida, X. Zhou, W. Zhu, X. Yao, F. Masood, M.W. Plesniak, Photolithographic-stereolithographic-tandem fabrication of 4D smart scaffolds for improved stem cell cardiomyogenic differentiation, Biofabrication 10(3) (2018) 035007.
[590] Y.Y.C. Choong, S. Maleksaeedi, H. Eng, J. Wei, P.-C. Su, 4D printing of high performance shape memory polymer using stereolithography, Materials & Design 126 (2017) 219-225.
[591] A.S. Mathews, S. Abraham, S.K. Kumaran, J. Fan, C. Montemagno, Bio nano ink for 4D printing membrane proteins, RSC advances 7(66) (2017) 41429-41434.
[592] R. Yu, X. Yang, Y. Zhang, X. Zhao, X. Wu, T. Zhao, Y. Zhao, W. Huang, Three-dimensional printing of shape memory composites with epoxy-acrylate hybrid photopolymer, ACS Applied Materials & Interfaces 9(2) (2017) 1820-1829.
[593] N. Inverardi, S. Pandini, F. Bignotti, G. Scalet, S. Marconi, F. Auricchio, Sequential motion of 4D printed photopolymers with broad glass transition, Macromolecular Materials and Engineering 305(1) (2020) 1900370.
[594] J. Chowdhury, P.V. Anirudh, C. Karunakaran, V. Rajmohan, A.T. Mathew, K. Koziol, W.F. Alsanie, C. Kannan, A.S. Balan, V.K. Thakur, 4D printing of smart polymer nanocomposites: Integrating graphene and acrylate based shape memory polymers, Polymers 13(21) (2021) 3660.
[595] Q. Ge, B. Jian, H. Li, Shaping soft materials via digital light processing-based 3D printing: A review, Forces in Mechanics 6 (2022) 100074.

[596] M. Yang, K. Kowsari, N.O. Myrie, D. Espinosa-Hoyos, A. Jagielska, S. Kim, N.X. Fang, K.J. Van Vliet, Additive manufacturing of high aspect-ratio structures with self-focusing photopolymerization, Light: Advanced Manufacturing 3(3) (2022) 542-571.
[597] C.-L. Liu, Q. Du, J.-M. Wu, G. Zhang, Y.-S. Shi, Novel 3D printed PZT-based piezoceramics for piezoelectric energy harvesting via digital light processing, Chemical Engineering Journal 492 (2024) 152004.
[598] Q. He, Y. Zeng, L. Jiang, Z. Wang, G. Lu, H. Kang, P. Li, B. Bethers, S. Feng, L. Sun, Growing recyclable and healable piezoelectric composites in 3D printed bioinspired structure for protective wearable sensor, Nature Communications 14(1) (2023) 6477.
[599] J. Shi, K. Ju, H. Chen, A. Mirabolghasemi, S. Akhtar, A. Sasmito, A. Akbarzadeh, 3D Printed Architected Shell-based Ferroelectric Metamaterials with Programmable Piezoelectric and Pyroelectric properties, Nano Energy (2024) 109385.
[600] L. Yue, S. Macrae Montgomery, X. Sun, L. Yu, Y. Song, T. Nomura, M. Tanaka, H. Jerry Qi, Single-vat single-cure grayscale digital light processing 3D printing of materials with large property difference and high stretchability, Nature communications 14(1) (2023) 1251.
[601] N. Paunović, D. Meyer, A. Krivitsky, A.R. Studart, Y. Bao, J.-C. Leroux, 4D printing of biodegradable elastomers with tailorable thermal response at physiological temperature, Journal of Controlled Release 361 (2023) 417-426.
[602] A. Cosola, M. Sangermano, D. Terenziani, R. Conti, M. Messori, H. Grützmacher, C.F. Pirri, A. Chiappone, DLP 3D–printing of shape memory polymers stabilized by thermoreversible hydrogen bonding interactions, Applied Materials Today 23 (2021) 101060.
[603] Y. He, R. Yu, X. Li, M. Zhang, Y. Zhang, X. Yang, X. Zhao, W. Huang, Digital light processing 4D printing of transparent, strong, highly conductive hydrogels, ACS Applied Materials & Interfaces 13(30) (2021) 36286-36294.
[604] A.K. Miri, D. Nieto, L. Iglesias, H. Goodarzi Hosseinabadi, S. Maharjan, G.U. Ruiz-Esparza, P. Khoshakhlagh, A. Manbachi, M.R. Dokmeci, S. Chen, Microfluidics-enabled multimaterial maskless stereolithographic bioprinting, Advanced Materials 30(27) (2018) 1800242.
[605] Q.T. Che, J.W. Seo, K. Charoensri, M.H. Nguyen, H.J. Park, H. Bae, 4D-printed microneedles from dual-sensitive chitosan for non-transdermal drug delivery, International Journal of Biological Macromolecules 261 (2024) 129638.
[606] X. Wan, L. Luo, Y. Liu, J. Leng, Direct ink writing based 4D printing of materials and their applications, Advanced Science 7(16) (2020) 2001000.
[607] K.R. Ryan, M.P. Down, C.E. Banks, Future of additive manufacturing: Overview of 4D and 3D printed smart and advanced materials and their applications, Chemical Engineering Journal 403 (2021) 126162.
[608] B. Wang, M. Gao, X. Fu, M. Geng, Y. Liu, N. Cheng, J. Li, L. Li, Z. Zhang, Y. Song, 3D printing deep-trap hierarchical architecture-based non-contact sensor for multi-direction motion monitoring, Nano Energy 107 (2023) 108135.
[609] F. Chen, Z. An, Y. Chen, Y. Li, X. Liu, N. Chen, Y. Ru, D. Gao, Multi-material 3D printing of piezoelectric and triboelectric integrated nanogenerators with voxel structure, Chemical Engineering Journal 471 (2023) 144770.
[610] R. Tao, F. Granier, D. Therriault, Multi-material freeform 3D printing of flexible piezoelectric composite sensors using a supporting fluid, Additive Manufacturing 60 (2022) 103243.
[611] S.S. Hossain, S. Jang, S. Park, C.-J. Bae, Understanding ink design and printing dynamics of extrusion-based 3D printing: Defect-free dense piezoelectric ceramics, Journal of Manufacturing Processes 92 (2023) 1-11.

[612] Y. Zhou, G. Wei, J. Yuan, X. Sang, J.-T. Miao, R. Liu, UV-assisted direct ink writing 4D printing of benzoxazine/epoxy thermosets, Chemical Engineering Journal 477 (2023) 147221.
[613] A. Sun, S. Ma, X. Shi, C. Chu, J. Guo, H. Jing, G. Xu, Y. Cheng, 4D printing of temperature-responsive composites with programmable thermochromic deformation bifunctional, Sensors and Actuators A: Physical (2024) 115138.
[614] Y. Li, F. Zhang, Y. Liu, J. Leng, 4D printed shape memory bismaleimide resin with high storage modulus and low shrinkage rate via second-stage curing, Chemical Engineering Journal 491 (2024) 152196.
[615] E. Liao, Y. Zhang, Y. Su, C. Zhang, C. Geng, C. Li, X. Liu, Y. Liu, A. Lu, Active mixing of two-component viscoelastic silicone ink at molecular level for spatiotemporally controlled 3D/4D printing of cellular silicones, Polymer 302 (2024) 127053.
[616] L. Ren, Y. He, L. Ren, Z. Wang, X. Zhou, Q. Wu, K. Wang, B. Li, Q. Liu, Multi-parameter-encoded 4D printing of liquid crystal elastomers for programmable shape morphing behaviors, Additive Manufacturing 61 (2023) 103376.
[617] P. Bhatnagar, S.H. Zaferani, N. Rafiefard, B. Baraeinejad, A.R. Vazifeh, R. Mohammadpour, R. Ghomashchi, H. Dillersberger, D. Tham, D. Vashaee, Advancing personalized healthcare and entertainment: Progress in energy harvesting materials and techniques of self-powered wearable devices, Progress in Materials Science (2023) 101184.
[618] H. Zhou, Y. Zhang, Y. Qiu, H. Wu, W. Qin, Y. Liao, Q. Yu, H. Cheng, Stretchable piezoelectric energy harvesters and self-powered sensors for wearable and implantable devices, Biosensors and Bioelectronics 168 (2020) 112569.
[619] L. Sun, L. He, G. Yu, X. Zheng, H. Wang, D. Yu, J. Lin, Recent developments in wearable piezoelectric energy harvesters, Review of Scientific Instruments 95(4) (2024).
[620] Y. Huang, S. Chen, Y. Li, Q. Lin, Y. Wu, Q. Shi, Flexible piezoelectric sensor based on PAN/MXene/PDA@ ZnO composite film for human health and motion detection with fast response and highly sensitive, Chemical Engineering Journal 488 (2024) 150997.
[621] C. Dagdeviren, Y. Su, P. Joe, R. Yona, Y. Liu, Y.-S. Kim, Y. Huang, A.R. Damadoran, J. Xia, L.W. Martin, Conformable amplified lead zirconate titanate sensors with enhanced piezoelectric response for cutaneous pressure monitoring, Nature communications 5(1) (2014) 4496.
[622] M. Fahad, A. Waqar, B. Kim, Effective-performance of inorganic and organic (barium zirconium titanate/polyvinylidene fluoride) piezoelectric composite for energy harvesting and self-powered smart IoT-based electronics, Journal of Alloys and Compounds (2024) 174033.
[623] G. Shi, X. Liang, Y. Xia, S. Jia, X. Hu, M. Yuan, H. Xia, B. Wang, A novel dual piezoelectric-electromagnetic energy harvester employing up-conversion technology for the capture of ultra-low-frequency human motion, Applied Energy 368 (2024) 123479.
[624] B. Wang, Z. Long, Y. Hong, Q. Pan, W. Lin, Z. Yang, Woodpecker-mimic two-layer band energy harvester with a piezoelectric array for powering wrist-worn wearables, Nano Energy 89 (2021) 106385.
[625] S. Asano, S. Nishimura, Y. Ikeda, T. Morita, H. Hosaka, Energy harvester for safety shoes using parallel piezoelectric links, Sensors and actuators a: physical 309 (2020) 112000.
[626] A. Mahapatra, R. Ajimsha, M. Ittoop, A. Sharma, S. Karmakar, A. Shaikh, P.R. Sankar, P. Misra, Flexible ZnO: PVDF based free standing piezoelectric nanogenerator for vibrational energy harvesting and wearable shoe insole pedometer sensor, Journal of Alloys and Compounds 960 (2023) 170898.
[627] Z. Yin, S. Gao, L. Jin, S. Guo, Q. Wu, Z. Li, A shoe-mounted frequency up-converted piezoelectric energy harvester, Sensors and Actuators A: Physical 318 (2021) 112530.

[628] Y.K. Fuh, B.S. Wang, C.-Y. Tsai, Self-powered pressure sensor with fully encapsulated 3D printed wavy substrate and highly-aligned piezoelectric fibers array, Scientific Reports 7(1) (2017) 6759.
[629] A.C. Turkmen, C. Celik, Energy harvesting with the piezoelectric material integrated shoe, Energy 150 (2018) 556-564.
[630] C. Su, X. Huang, L. Zhang, Y. Zhang, Z. Yu, C. Chen, Y. Ye, S. Guo, Robust superhydrophobic wearable piezoelectric nanogenerators for self-powered body motion sensors, Nano Energy 107 (2023) 108095.
[631] R. Tao, J. Shi, F. Granier, M. Moeini, A. Akbarzadeh, D. Therriault, Multi-material fused filament fabrication of flexible 3D piezoelectric nanocomposite lattices for pressure sensing and energy harvesting applications, Applied Materials Today 29 (2022) 101596.
[632] S.Y. Jeong, W.S. Hwang, J.Y. Cho, J.C. Jeong, J.H. Ahn, K.B. Kim, S. Do Hong, G.J. Song, D.H. Jeon, T.H. Sung, Piezoelectric device operating as sensor and harvester to drive switching circuit in LED shoes, Energy 177 (2019) 87-93.
[633] S. Vyas, S. Saxena, Piezoelectric power generation using vibrations from human heart, Materials Today: Proceedings (2023).
[634] J. An, H. Park, Y.H. Jung, S. Min, D.H. Kim, D.J. Joe, S.-G. Lee, D.Y. Hyeon, Y. Je, H.-S. Seo, In vivo flexible energy harvesting on porcine heart via highly-piezoelectric PIN–PMN–PT single crystal, Nano Energy 121 (2024) 109227.
[635] B. Lu, Y. Chen, D. Ou, H. Chen, L. Diao, W. Zhang, J. Zheng, W. Ma, L. Sun, X. Feng, Ultra-flexible piezoelectric devices integrated with heart to harvest the biomechanical energy, Scientific reports 5(1) (2015) 16065.
[636] Y. Zhang, L. Zhou, C. Liu, X. Gao, Z. Zhou, S. Duan, Q. Deng, L. Song, H. Jiang, L. Yu, Self-powered pacemaker based on all-in-one flexible piezoelectric nanogenerator, Nano Energy 99 (2022) 107420.
[637] G. Ji, J. Huber, Recent progress in acoustic metamaterials and active piezoelectric acoustic metamaterials-a review, Applied Materials Today 26 (2022) 101260.
[638] Y.H. Jung, S.K. Hong, H.S. Wang, J.H. Han, T.X. Pham, H. Park, J. Kim, S. Kang, C.D. Yoo, K.J. Lee, Flexible piezoelectric acoustic sensors and machine learning for speech processing, Advanced Materials 32(35) (2020) 1904020.
[639] P. Shivashankar, S. Gopalakrishnan, Review on the use of piezoelectric materials for active vibration, noise, and flow control, Smart materials and structures 29(5) (2020) 053001.
[640] Z. Zhao, J. Zhu, W. Chen, Size-dependent vibrations and waves in piezoelectric nanostructures: a literature review, International Journal of Smart and Nano Materials 13(3) (2022) 391-431.
[641] C. Lu, X. Jiang, L. Li, H. Zhou, A. Yang, M. Xin, G. Fu, X. Wang, Wind energy harvester using piezoelectric materials, Review of Scientific Instruments 93(3) (2022).
[642] W. Sun, K. Zhong, Y. Liu, H. Xiao, D. Zhao, Z. Yan, T. Tan, Enhanced metamaterial vibration for high-performance acoustic piezoelectric energy harvesting, Composites Communications 35 (2022) 101342.
[643] T. Weimann, A. Molter, L. Fernandez, M. He, Structural vibration control based on the effect of acoustic black holes and piezoelectric actuators, Finite Elements in Analysis and Design 224 (2023) 103992.
[644] C.S. Schimidt, L.P.R. de Oliveira, C.D.M. Junior, Vibro-acoustic performance of graded piezoelectric metamaterial plates, Composite Structures 327 (2024) 117656.
[645] M. Jin, B. Liang, J. Yang, J. Yang, J.-c. Cheng, Ultrathin planar metasurface-based acoustic energy harvester with deep subwavelength thickness and mechanical rigidity, Scientific reports 9(1) (2019) 11152.

[646] R. Gomasa, V. Talakokula, S.K.R. Jyosyula, T. Bansal, A review on health monitoring of concrete structures using embedded piezoelectric sensor, Construction and Building Materials 405 (2023) 133179.
[647] S. Du, J. Zhou, F. Li, Dynamic deformation monitoring of cantilever beams using piezoelectric sensors: Theory and experiment, Measurement (2024) 114305.
[648] C. Wu, Q. Xiao, D. Zhu, Piezoelectric ceramic sensor-based structural health monitoring of diagonally braced H-shaped steel structures, Scientific Reports 13(1) (2023) 14964.
[649] M. Iqbal, F.U. Khan, Hybrid vibration and wind energy harvesting using combined piezoelectric and electromagnetic conversion for bridge health monitoring applications, Energy conversion and management 172 (2018) 611-618.
[650] Y.J. Lee, Y. Qi, G. Zhou, K.B. Lua, Vortex-induced vibration wind energy harvesting by piezoelectric MEMS device in formation, Scientific reports 9(1) (2019) 20404.
[651] M. Iqbal, F. Khan, Hybrid acoustic, vibration, and wind energy harvester using piezoelectric transduction for self-powered wireless sensor node applications, Energy Conversion and Management 277 (2023) 116635.
[652] D. Maurya, S. Khaleghian, R. Sriramdas, P. Kumar, R.A. Kishore, M.G. Kang, V. Kumar, H.-C. Song, S.-Y. Lee, Y. Yan, 3D printed graphene-based self-powered strain sensors for smart tires in autonomous vehicles, Nature communications 11(1) (2020) 5392.
[653] K.K. Meena, I. Arief, A.K. Ghosh, H. Liebscher, S. Hait, J. Nagel, G. Heinrich, A. Fery, A. Das, 3D-printed stretchable hybrid piezoelectric-triboelectric nanogenerator for smart tire: Onboard real-time tread wear monitoring system, Nano Energy 115 (2023) 108707.
[654] C.-X. Xing, Q.-B. Zhang, Z.-H. Wang, J.-X. Guo, M.-L. Li, D.-H. Yu, Y.-D. Wang, Q. Zhou, W. Tang, Z. Li, Soft-metal bonding-enabled recyclable and anti-interference flexible multilayer piezoelectric sensor for tractor tire strain monitoring, Nano Energy 127 (2024) 109704.
[655] J. Wang, Y. Cao, H. Xiang, Z. Zhang, J. Liang, X. Li, D. Ding, T. Li, L. Tang, A piezoelectric smart backing ring for high-performance power generation subject to train induced steel-spring fulcrum forces, Energy Conversion and Management 257 (2022) 115442.
[656] P. Bharanitharan, R. Anbalagan, T. Mani, V. Arumugam, Electric Bikes as Exercise Equipment: A Technical Study on Design and Energy Recovery for Home and Fitness Center Use, SAE Technical Paper, 2023.
[657] C. Jettanasen, P. Songsukthawan, A. Ngaopitakkul, Development of micro-mobility based on piezoelectric energy harvesting for smart city applications, Sustainability 12(7) (2020) 2933.
[658] X. Dai, H. Wang, H. Wu, Y. Pan, D. Luo, A. Ahmed, Z. Zhang, A hybrid energy harvesting system for self-powered applications in shared bicycles, Sustainable Energy Technologies and Assessments 51 (2022) 101891.
[659] M.C. Arellano-Sánchez, J. Reyes-Reyes, M. Ponce-Silva, V. Olivares-Peregrino, C. Astorga-Zaragoza, Static technologies associated with pedaling energy harvesting through rotary transducers, a review, Applied Energy 263 (2020) 114607.
[660] M. Shelke, S. Sole, S. Bhatlawande, Automatic Piezoelectric Bicycle Headlight, 2023 14th International Conference on Computing Communication and Networking Technologies (ICCCNT), IEEE, 2023, pp. 1-5.
[661] C. Jettanasen, P. Songsukthawan, A. Ngaopitakkul, Conversion of mechanical energy to electrical energy using piezoelectric materials for bicycle lane lighting systems, Applied Sciences 12(14) (2022) 7237.
[662] P. Chen, Y. Yang, Design, dynamics modeling, and experiments of a vibration energy harvester on bicycle, IEEE/ASME Transactions on Mechatronics 28(5) (2023) 2670-2678.
[663] J. Patdiya, B. Kandasubramanian, Progress in 4D printing of stimuli responsive materials, Polymer-Plastics Technology and Materials 60(17) (2021) 1845-1883.

[664] F. Doberenz, K. Zeng, C. Willems, K. Zhang, T. Groth, Thermoresponsive polymers and their biomedical application in tissue engineering–a review, Journal of Materials Chemistry B 8(4) (2020) 607-628.
[665] S. Pardeshi, F. Damiri, M. Zehravi, R. Joshi, H. Kapare, M.K. Prajapati, N. Munot, M. Berrada, P.S. Giram, S. Rojekar, Functional thermoresponsive hydrogel molecule to material design for biomedical applications, Polymers 14(15) (2022) 3126.
[666] M. Li, Z. Chen, Thermo-responsive polymers for thermal regulation in electrochemical energy devices, Journal of Polymer Science 59(20) (2021) 2230-2245.
[667] Z. Wei, L. Yu, S. Lu, Y. Zhao, Reversibly thermo-responsive materials applied in lithium batteries, Energy Storage Materials (2023) 102901.
[668] C. Ni, D. Chen, Y. Yin, X. Wen, X. Chen, C. Yang, G. Chen, Z. Sun, J. Wen, Y. Jiao, Shape memory polymer with programmable recovery onset, Nature 622(7984) (2023) 748-753.
[669] L. Yue, X. Sun, L. Yu, M. Li, S.M. Montgomery, Y. Song, T. Nomura, M. Tanaka, H.J. Qi, Cold-programmed shape-morphing structures based on grayscale digital light processing 4D printing, Nature Communications 14(1) (2023) 5519.
[670] K. Li, J. Zhao, A. Zhussupbekova, C.E. Shuck, L. Hughes, Y. Dong, S. Barwich, S. Vaesen, I.V. Shvets, M. Möbius, 4D printing of MXene hydrogels for high-efficiency pseudocapacitive energy storage, Nature Communications 13(1) (2022) 6884.
[671] B. Liu, H. Li, F. Meng, Z. Xu, L. Hao, Y. Yao, H. Zhu, C. Wang, J. Wu, S. Bian, 4D printed hydrogel scaffold with swelling-stiffening properties and programmable deformation for minimally invasive implantation, Nature Communications 15(1) (2024) 1587.
[672] J. Liu, Y.-S. Huang, Y. Liu, D. Zhang, K. Koynov, H.-J. Butt, S. Wu, Reconfiguring hydrogel assemblies using a photocontrolled metallopolymer adhesive for multiple customized functions, Nature Chemistry (2024) 1-10.
[673] Y. Zheng, C. Li, Photothermally-driven oxazine hydrogel actuators at the water-air interface, Giant 16 (2023) 100192.
[674] K. Qian, Y. Shao, Z. Yang, S. Jiang, A multi-element encrypted and decrypted photoresponsive liquid crystal polymer network through the cooperation of cyanostilbene and spiropyran, Chemical Engineering Journal (2024) 152713.
[675] W. Yang, Z. Wang, X. Wang, Y. Chen, Z. Ge, H. Yu, Bio-inspired propeller robot with controllable pitch driven by magnetic and optical coupling field, Sensors and Actuators B: Chemical 382 (2023) 133509.
[676] M.-J. Wang, B. Li, Y.-L. Wei, S.-N. Zhao, S.-Q. Zang, The guest CH3CN molecule triggers solid-state photochromism in a Cu2I2-based MOF for advanced time-dependent encryption and inkless erasable printing, Chinese Chemical Letters 35(3) (2024) 108491.
[677] E. Yarali, M. Baniasadi, A. Zolfagharian, M. Chavoshi, F. Arefi, M. Hossain, A. Bastola, M. Ansari, A. Foyouzat, A. Dabbagh, Magneto-/electro-responsive polymers toward manufacturing, characterization, and biomedical/soft robotic applications, Applied Materials Today 26 (2022) 101306.
[678] Y. Wang, H. Ye, J. He, Q. Ge, Y. Xiong, Electrothermally controlled origami fabricated by 4D printing of continuous fiber-reinforced composites, Nature Communications 15(1) (2024) 2322.
[679] A. Fallah, S. Asif, G. Gokcer, B. Koc, 4D printing of continuous fiber-reinforced electroactive smart composites by coaxial additive manufacturing, Composite Structures 316 (2023) 117034.
[680] D. Chen, Q. Liu, P. Geng, S. Tang, J. Zhang, S. Wen, Y. Zhou, C. Yan, Z. Han, Y. Shi, A 4D printing strategy and integrated design for programmable electroactive shape-color double-responsive bionic functions, Composites Science and Technology 208 (2021) 108746.

[681] X. Zhou, N. Zhang, S. Kandalai, H. Li, F. Hossain, S. Zhang, J. Zhu, J. Zhang, J. Cui, Q. Zheng, Dynamic and wearable electro-responsive hydrogel with robust mechanical properties for drug release, ACS Applied Materials & Interfaces 15(13) (2023) 17113-17122.
[682] E. Yarali, M.J. Mirzaali, A. Ghalayaniesfahani, A. Accardo, P.J. Diaz-Payno, A.A. Zadpoor, 4D printing for Biomedical Applications, Advanced Materials (2024) 2402301.
[683] R. Sajjad, S.T. Chauhdary, M.T. Anwar, A. Zahid, A.A. Khosa, M. Imran, M.H. Sajjad, A Review of 4D Printing-Technologies, Shape Shifting, Smart Materials, and Biomedical Applications, Advanced Industrial and Engineering Polymer Research (2023).
[684] L. Wang, Y. Chang, S. Wu, R.R. Zhao, W. Chen, Physics-aware differentiable design of magnetically actuated kirigami for shape morphing, Nature Communications 14(1) (2023) 8516.
[685] H. Shinoda, S. Azukizawa, K. Maeda, F. Tsumori, Bio-mimic motion of 3D-printed gel structures dispersed with magnetic particles, Journal of The Electrochemical Society 166(9) (2019) B3235-B3239.
[686] Y. Kim, H. Yuk, R. Zhao, S.A. Chester, X. Zhao, Printing ferromagnetic domains for untethered fast-transforming soft materials, Nature 558(7709) (2018) 274-279.
[687] P. Cataldi, M. Liu, M. Bissett, I.A. Kinloch, A review on printing of responsive smart and 4D structures using 2D materials, Advanced Materials Technologies 7(11) (2022) 2200025.
[688] A. Zaszczyńska, A. Gradys, P. Sajkiewicz, Progress in the applications of smart piezoelectric materials for medical devices, Polymers 12(11) (2020) 2754.
[689] M. Qu, X. Chen, D. Yang, D. Li, K. Zhu, X. Guo, J. Xie, Monitoring of physiological sounds with wearable device based on piezoelectric MEMS acoustic sensor, Journal of Micromechanics and Microengineering 32(1) (2021) 014001.
[690] S. Min, D.H. Kim, D.J. Joe, B.W. Kim, Y.H. Jung, J.H. Lee, B.Y. Lee, I. Doh, J. An, Y.N. Youn, Clinical validation of a wearable piezoelectric blood-pressure sensor for continuous health monitoring, Advanced Materials 35(26) (2023) 2301627.
[691] S. Mohith, A.R. Upadhya, K.P. Navin, S. Kulkarni, M. Rao, Recent trends in piezoelectric actuators for precision motion and their applications: A review, Smart Materials and Structures 30(1) (2020) 013002.
[692] X. Gao, J. Yang, J. Wu, X. Xin, Z. Li, X. Yuan, X. Shen, S. Dong, Piezoelectric actuators and motors: materials, designs, and applications, Advanced Materials Technologies 5(1) (2020) 1900716.
[693] S.K. Melly, L. Liu, Y. Liu, J. Leng, Active composites based on shape memory polymers: overview, fabrication methods, applications, and future prospects, Journal of Materials Science 55 (2020) 10975-11051.
[694] W. Zheng, Y. Shi, L. Zhao, S. Jia, L. Li, C.L. Gan, D. Zhang, Q. Guo, Realizing reversible phase transformation of shape memory ceramics constrained in aluminum, Nature Communications 14(1) (2023) 7103.
[695] M.A. Ansari, P. Somdee, Piezoelectric polymeric foams as flexible energy harvesters: a review, Advanced Energy and Sustainability Research 3(9) (2022) 2200063.
[696] Z. Zhao, Y. Dai, S. Dou, J. Liang, Flexible nanogenerators for wearable electronic applications based on piezoelectric materials, Materials Today Energy 20 (2021) 100690.
[697] K.K.R. Bannuru, A.R.P. Mathai, P.V. y Alvarado, H.Y. Low, Freestanding 3D piezoelectric PVDF sensors via electroprinting, Materials Today: Proceedings 70 (2022) 447-453.
[698] X. Yuan, X. Gao, X. Shen, J. Yang, Z. Li, S. Dong, A 3D-printed, alternatively tilt-polarized PVDF-TrFE polymer with enhanced piezoelectric effect for self-powered sensor application, Nano Energy 85 (2021) 105985.

[699] M. Xie, M. Zhu, Z. Yang, S. Okada, S. Kawamura, Flexible self-powered multifunctional sensor for stiffness-tunable soft robotic gripper by multimaterial 3D printing, Nano Energy 79 (2021) 105438.
[700] C. Zhao, J. Xu, J. Tao, C. Xiao, X. Jin, W. Wang, X. Liu, J. Chen, Z. Zhu, Multi-scale alignment in highly piezoelectric polyacrylonitrile nanofibers separator for advanced self-charging supercapacitor, Nano Energy 116 (2023) 108812.
[701] C. Ge, E. Cretu, A polymeric piezoelectric MEMS accelerometer with high sensitivity, low noise density, and an innovative manufacturing approach, Microsystems & Nanoengineering 9(1) (2023) 151.
[702] L.J. Tan, W. Zhu, K. Zhou, Recent progress on polymer materials for additive manufacturing, Advanced Functional Materials 30(43) (2020) 2003062.
[703] F. Alam, J. Ubaid, H. Butt, N. El-Atab, Swift 4D printing of thermoresponsive shape-memory polymers using vat photopolymerization, NPG Asia Materials 15(1) (2023) 65.
[704] W. Zhang, H. Wang, H. Wang, J.Y.E. Chan, H. Liu, B. Zhang, Y.-F. Zhang, K. Agarwal, X. Yang, A.S. Ranganath, Structural multi-colour invisible inks with submicron 4D printing of shape memory polymers, Nature Communications 12(1) (2021) 112.
[705] M. Hippler, E. Blasco, J. Qu, M. Tanaka, C. Barner-Kowollik, M. Wegener, M. Bastmeyer, Controlling the shape of 3D microstructures by temperature and light, Nature communications 10(1) (2019) 232.
[706] H. Yang, N. D'Ambrosio, P. Liu, D. Pasini, L. Ma, Shape memory mechanical metamaterials, Materials Today 66 (2023) 36-49.
[707] Q. Ge, A.H. Sakhaei, H. Lee, C.K. Dunn, N.X. Fang, M.L. Dunn, Multimaterial 4D printing with tailorable shape memory polymers, Scientific reports 6(1) (2016) 31110.
[708] K.-H. Lee, J. Jeon, W. Cho, S.-W. Kim, H. Moon, J.J. Wie, S.-Y. Lee, Light-triggered autonomous shape-reconfigurable and locomotive rechargeable power sources, Materials Today 55 (2022) 56-65.
[709] B. Li, C. Zhang, F. Peng, W. Wang, B.D. Vogt, K. Tan, 4D printed shape memory metamaterial for vibration bandgap switching and active elastic-wave guiding, Journal of Materials Chemistry C 9(4) (2021) 1164-1173.
[710] M. Staszczak, M. Nabavian Kalat, K.M. Golasiński, L. Urbański, K. Takeda, R. Matsui, E.A. Pieczyska, Characterization of polyurethane shape memory polymer and determination of shape fixity and shape recovery in subsequent thermomechanical cycles, Polymers 14(21) (2022) 4775.
[711] B. Zhang, H. Li, J. Cheng, H. Ye, A.H. Sakhaei, C. Yuan, P. Rao, Y.F. Zhang, Z. Chen, R. Wang, Mechanically robust and UV-curable shape-memory polymers for digital light processing based 4D printing, Advanced Materials 33(27) (2021) 2101298.
[712] Y.Y.C. Choong, S. Maleksaeedi, H. Eng, S. Yu, J. Wei, P.-C. Su, High speed 4D printing of shape memory polymers with nanosilica, Applied Materials Today 18 (2020) 100515.
[713] X. Wan, Y. He, Y. Liu, J. Leng, 4D printing of multiple shape memory polymer and nanocomposites with biocompatible, programmable and selectively actuated properties, Additive Manufacturing 53 (2022) 102689.
[714] M. Han, Y. Yang, L. Li, Energy consumption modeling of 4D printing thermal-responsive polymers with integrated compositional design for material, Additive Manufacturing 34 (2020) 101223.
[715] T. Zhao, R. Yu, X. Li, B. Cheng, Y. Zhang, X. Yang, X. Zhao, Y. Zhao, W. Huang, 4D printing of shape memory polyurethane via stereolithography, European Polymer Journal 101 (2018) 120-126.
[716] E. Sachyani Keneth, R. Lieberman, M. Rednor, G. Scalet, F. Auricchio, S. Magdassi, Multi-material 3D printed shape memory polymer with tunable melting and glass transition temperature activated by heat or light, Polymers 12(3) (2020) 710.

[717] K. Wang, Y.-G. Jia, X. Zhu, Biocompound-based multiple shape memory polymers reinforced by photo-cross-linking, ACS Biomaterials Science & Engineering 1(9) (2015) 855-863.
[718] H. Wu, P. Chen, C. Yan, C. Cai, Y. Shi, Four-dimensional printing of a novel acrylate-based shape memory polymer using digital light processing, Materials & Design 171 (2019) 107704.
[719] Z. Zhao, F. Peng, K.A. Cavicchi, M. Cakmak, R. Weiss, B.D. Vogt, Three-dimensional printed shape memory objects based on an olefin ionomer of zinc-neutralized poly (ethylene-co-methacrylic acid), ACS applied materials & interfaces 9(32) (2017) 27239-27249.
[720] X.L. Wu, S.F. Kang, X.J. Xu, F. Xiao, X.L. Ge, Effect of the crosslinking density and programming temperature on the shape fixity and shape recovery in epoxy–anhydride shape-memory polymers, Journal of Applied Polymer Science 131(15) (2014).
[721] M. Dadkhah, J.-M. Tulliani, A. Saboori, L. Iuliano, Additive manufacturing of ceramics: Advances, challenges, and outlook, Journal of the European Ceramic Society (2023).
[722] C.L. Cramer, E. Ionescu, M. Graczyk-Zajac, A.T. Nelson, Y. Katoh, J.J. Haslam, L. Wondraczek, T.G. Aguirre, S. LeBlanc, H. Wang, Additive manufacturing of ceramic materials for energy applications: Road map and opportunities, Journal of the European Ceramic Society 42(7) (2022) 3049-3088.
[723] Y. Lakhdar, C. Tuck, J. Binner, A. Terry, R. Goodridge, Additive manufacturing of advanced ceramic materials, Progress in Materials Science 116 (2021) 100736.
[724] Y. Huang, L. Zhang, R. Jing, M. Tang, D. Alikin, V. Shur, X. Wei, L. Jin, Lead zirconate titanate-based ceramics with high piezoelectricity and broad usage temperature range, Chemical Engineering Journal 477 (2023) 147192.
[725] L. Song, S. Glinsek, E. Defay, Toward low-temperature processing of lead zirconate titanate thin films: Advances, strategies, and applications, Applied Physics Reviews 8(4) (2021).
[726] Y. Yan, L.D. Geng, H. Liu, H. Leng, X. Li, Y.U. Wang, S. Priya, Near-ideal electromechanical coupling in textured piezoelectric ceramics, Nature communications 13(1) (2022) 3565.
[727] Z. Jiang, R.J. Dickinson, T.L. Hall, J.J. Choi, A PZT–PVDF stacked transducer for short-pulse ultrasound therapy and monitoring, IEEE Transactions on Ultrasonics, Ferroelectrics, and Frequency Control 68(6) (2021) 2164-2171.
[728] J. Li, L. He, J. Cai, Y. Hu, J. Wen, J. Ma, N. Wan, A walking type piezoelectric actuator based on the parasitic motion of obliquely assembled PZT stacks, Smart Materials and Structures 30(8) (2021) 085030.
[729] S. Yan, C. Sun, Q. Cui, M. He, R. Wang, J. Hao, X. Chu, Dielectric, piezoelectric and dc bias characteristics of Bi-doped PZT multilayer ceramic actuator, Materials Chemistry and Physics 255 (2020) 123605.
[730] M. Sawane, M. Prasad, MEMS piezoelectric sensor for self-powered devices: A review, Materials Science in Semiconductor Processing 158 (2023) 107324.
[731] H.H. Pan, J.-C. Guan, Stress and strain behavior monitoring of concrete through electromechanical impedance using piezoelectric cement sensor and PZT sensor, Construction and Building Materials 324 (2022) 126685.
[732] A. Aabid, M.A. Raheman, Y.E. Ibrahim, A. Anjum, M. Hrairi, B. Parveez, N. Parveen, J. Mohammed Zayan, A systematic review of piezoelectric materials and energy harvesters for industrial applications, Sensors 21(12) (2021) 4145.
[733] J. Li, X. Liu, G. Zhao, Z. Liu, Y. Cai, S. Wang, C. Shen, B. Hu, X. Wang, Piezoelectric materials and techniques for environmental pollution remediation, Science of The Total Environment 869 (2023) 161767.

[734] R. Damamme, L. Seveyrat, A. Borta-Boyon, V.-C. Nguyen, M.-Q. Le, P.-J. Cottinet, 3D printing of doped barium-titanate using robocasting-Toward new generation lead-free piezoceramic transducers, Journal of the European Ceramic Society 43(8) (2023) 3297-3306.
[735] K. Chen, Y. Wang, C. Wu, Y. Du, H. Tang, S. Zheng, Z. Zhou, H. Zheng, G. Wu, ln vitro assessment of immunomodulatory and osteogenic properties in 3D-printed hydroxyapatite/barium titanate piezoelectric ceramic scaffolds, Ceramics International 50(6) (2024) 8751-8759.
[736] Z. Jiang, L. Cheng, Y. Zeng, Z. Zhang, Y. Zhao, P. Dong, J. Chen, 3D printing of porous scaffolds BaTiO3 piezoelectric ceramics and regulation of their mechanical and electrical properties, Ceram. Int. 48(5) (2022) 6477-6487.
[737] Y. Hong, S. Liu, X. Yang, W. Hong, Y. Shan, B. Wang, Z. Zhang, X. Yan, W. Lin, X. Li, A bioinspired surface tension-driven route toward programmed cellular ceramics, Nature Communications 15(1) (2024) 5030.
[738] C.-L. Liu, Q. Du, H. Zhou, S. Chen, J.-M. Wu, G. Zhang, Y.-S. Shi, 3D printing of lead zirconate titanate piezoelectric ceramics via digital light processing (DLP), Ceramics International 49(17) (2023) 28492-28499.
[739] Z. Li, J. Li, H. Luo, X. Yuan, X. Wang, H. Xiong, D. Zhang, Direct ink writing of 3D piezoelectric ceramics with complex unsupported structures, Journal of the European Ceramic Society 42(9) (2022) 3841-3847.
[740] W. Zheng, L. Li, L. Zhao, Q. Guo, Design of Shape Memory Ceramics: Principles, Strategies and Perspectives, JOM (2024) 1-18.
[741] P. Zhao, K. Hu, Q. Wang, Z. Lu, Programmable ceramic 4D printing via multi-material vat photopolymerization, Additive Manufacturing (2024) 104235.
[742] R. Wang, C. Yuan, J. Cheng, X. He, H. Ye, B. Jian, H. Li, J. Bai, Q. Ge, Direct 4D printing of ceramics driven by hydrogel dehydration, Nature Communications 15(1) (2024) 758.
[743] D. Kong, A. Guo, H. Wu, X. Li, J. Wu, Y. Hu, P. Qu, S. Wang, S. Guo, Four-Dimensional Printing of Polymer-Derived Ceramics with High-resolution, Reconfigurability, and Shape Memory Effects, Additive Manufacturing (2024) 104050.
[744] F. Wang, C. Liu, H. Yang, H. Wang, H. Zhang, X. Zeng, C. Wang, W. Zhang, W. Lv, P. Zhu, 4D printing of ceramic structures, Additive Manufacturing 63 (2023) 103411.
[745] L. Wan, Z. Mao, H. Liu, Y. Xie, F. Lyu, Z. Cao, Y. He, J. Yin, X. Han, W.Y.K. Chan, Direct 4D printing of gradient structure of ceramics, Chemical Engineering Journal 465 (2023) 142804.
[746] F. Mokhtari, B. Azimi, M. Salehi, S. Hashemikia, S. Danti, Recent advances of polymer-based piezoelectric composites for biomedical applications, Journal of the Mechanical Behavior of Biomedical Materials 122 (2021) 104669.
[747] N.A. Shepelin, P.C. Sherrell, E.N. Skountzos, E. Goudeli, J. Zhang, V.C. Lussini, B. Imtiaz, K.A.S. Usman, G.W. Dicinoski, J.G. Shapter, Interfacial piezoelectric polarization locking in printable Ti3C2T x MXene-fluoropolymer composites, Nature communications 12(1) (2021) 3171.
[748] Z. Wang, X. Yuan, J. Yang, Y. Huan, X. Gao, Z. Li, H. Wang, S. Dong, 3D-printed flexible, Ag-coated PNN-PZT ceramic-polymer grid-composite for electromechanical energy conversion, Nano Energy 73 (2020) 104737.
[749] S.M.A.Z. Shawon, Z.D. Carballo, V.S. Vega, C. Lin, M.S. Rafaqut, A.X. Sun, J.J. Li, M.J. Uddin, Surface modified hybrid ZnSnO3 nanocubes for enhanced piezoelectric power generation and wireless sensory application, Nano Energy 92 (2022) 106653.
[750] Z. Hanani, I. Izanzar, M.b. Amjoud, D. Mezzane, M. Lahcini, H. Uršič, U. Prah, I. Saadoune, M. El Marssi, I.A. Luk'yanchuk, Lead-free nanocomposite piezoelectric nanogenerator film for biomechanical energy harvesting, Nano Energy 81 (2021) 105661.

[751] J. Villafuerte, X. Zhang, E. Sarigiannidou, F. Donatini, O. Chaix-Pluchery, L. Rapenne, M.-Q. Le, L. Petit, J. Pernot, V. Consonni, Boosting the piezoelectric coefficients of flexible dynamic strain sensors made of chemically-deposited ZnO nanowires using compensatory Sb doping, Nano Energy 114 (2023) 108599.
[752] S. Kang, S.H. Kim, H.B. Lee, S. Mhin, J.H. Ryu, Y.W. Kim, J.L. Jones, Y. Son, N.K. Lee, K. Lee, High-power energy harvesting and imperceptible pulse sensing through peapod-inspired hierarchically designed piezoelectric nanofibers, Nano Energy 99 (2022) 107386.
[753] P. Cheng, Y. Peng, S. Li, Y. Rao, A. Le Duigou, K. Wang, S. Ahzi, 3D printed continuous fiber reinforced composite lightweight structures: A review and outlook, Composites Part B: Engineering 250 (2023) 110450.
[754] Q. Wang, X. Tian, D. Zhang, Y. Zhou, W. Yan, D. Li, Programmable spatial deformation by controllable off-center freestanding 4D printing of continuous fiber reinforced liquid crystal elastomer composites, Nature Communications 14(1) (2023) 3869.
[755] B.F. Winhard, P. Haida, A. Plunkett, J. Katz, B. Domènech, V. Abetz, K.P. Furlan, G.A. Schneider, 4D-printing of smart, nacre-inspired, organic-ceramic composites, Additive manufacturing 77 (2023) 103776.
[756] C. Zeng, L. Liu, W. Bian, J. Leng, Y. Liu, Compression behavior and energy absorption of 3D printed continuous fiber reinforced composite honeycomb structures with shape memory effects, Additive Manufacturing 38 (2021) 101842.
[757] T. Gu, H. Bi, H. Sun, J. Tang, Z. Ren, X. Zhou, M. Xu, Design and development of 4D-printed cellulose nanofibers reinforced shape memory polymer composites: Application for self-deforming plant bionic soft grippers, Additive Manufacturing 70 (2023) 103544.
[758] G. Sossou, F. Demoly, H. Belkebir, H.J. Qi, S. Gomes, G. Montavon, Design for 4D printing: A voxel-based modeling and simulation of smart materials, Materials & Design 175 (2019) 107798.
[759] H. Cui, R. Hensleigh, D. Yao, D. Maurya, P. Kumar, M.G. Kang, S. Priya, X. Zheng, Three-dimensional printing of piezoelectric materials with designed anisotropy and directional response, Nature materials 18(3) (2019) 234-241.
[760] R. Sharma, R. Singh, A. Batish, Study on barium titanate and graphene reinforced PVDF matrix for 4D applications, Journal of Thermoplastic Composite Materials 34(9) (2021) 1234-1253.
[761] S. Bodkhe, P. Ermanni, 3D printing of multifunctional materials for sensing and actuation: Merging piezoelectricity with shape memory, European Polymer Journal 132 (2020) 109738.
[762] S. Bodkhe, T. Frei, P. Ermanni, 4D printing of multifunctional materials, Proceedings of the 2019 International Conference on Composite Materials, RMIT University, 2019, p. 152.
[763] D. Grinberg, S. Siddique, M.Q. Le, R. Liang, J.F. Capsal, P.J. Cottinet, 4D Printing based piezoelectric composite for medical applications, Journal of Polymer Science Part B: Polymer Physics 57(2) (2019) 109-115.
[764] H.B. Lee, Y.W. Kim, J. Yoon, N.K. Lee, S.-H. Park, 3D customized and flexible tactile sensor using a piezoelectric nanofiber mat and sandwich-molded elastomer sheets, Smart Materials and Structures 26(4) (2017) 045032.
[765] K. Liu, Q. Zhang, C. Zhou, Y. Shi, C. Sun, H. Sun, C. Yin, J. Hu, S. Zhou, Y. Zhang, 4D printing of lead zirconate titanate piezoelectric composites transducer based on direct ink writing, Frontiers in Materials 8 (2021) 659441.
[766] L. Persano, A. Camposeo, F. Matino, R. Wang, T. Natarajan, Q. Li, M. Pan, Y. Su, S. Kar-Narayan, F. Auricchio, Advanced materials for energy harvesting and soft robotics: Emerging frontiers to enhance piezoelectric performance and functionality, Advanced Materials 36(45) (2024) 2405363.

[767] M. Han, H. Wang, Y. Yang, C. Liang, W. Bai, Z. Yan, H. Li, Y. Xue, X. Wang, B. Akar, Three-dimensional piezoelectric polymer microsystems for vibrational energy harvesting, robotic interfaces and biomedical implants, Nature Electronics 2(1) (2019) 26-35.
[768] A. Ali, H. Shaukat, S. Bibi, W.A. Altabey, M. Noori, S.A. Kouritem, Recent progress in energy harvesting systems for wearable technology, Energy Strategy Reviews 49 (2023) 101124.
[769] S.V. Fernandez, F. Cai, S. Chen, E. Suh, J. Tiepelt, R. McIntosh, C. Marcus, D. Acosta, D. Mejorado, C. Dagdeviren, On-body piezoelectric energy harvesters through innovative designs and conformable structures, ACS Biomaterials Science & Engineering 9(5) (2021) 2070-2086.
[770] R. Hesham, A. Soltan, A. Madian, Energy harvesting schemes for wearable devices, AEU-International Journal of Electronics and Communications 138 (2021) 153888.
[771] A.I. Sadaf, R.U. Ahmed, H. Ahmed, Cantilever configurations in vibration-based piezoelectric energy harvesting: A comprehensive review on beam shapes and multi-beam formations, Smart Materials and Structures (2024).
[772] Q. Xu, A. Gao, Y. Li, Y. Jin, Design and optimization of piezoelectric cantilever beam vibration energy harvester, Micromachines 13(5) (2022) 675.
[773] X. He, D. Li, H. Zhou, X. Hui, X. Mu, Theoretical and experimental studies on MEMS variable cross-section cantilever beam based piezoelectric vibration energy harvester, Micromachines 12(7) (2021) 772.
[774] J.-X. Wang, W.-B. Su, J.-C. Li, C.-M. Wang, A rotational piezoelectric energy harvester based on trapezoid beam: Simulation and experiment, Renewable Energy 184 (2022) 619-626.
[775] J. Song, G. Sun, X. Zeng, X. Li, Q. Bai, X. Zheng, Piezoelectric energy harvester with double cantilever beam undergoing coupled bending-torsion vibrations by width-splitting method, Scientific Reports 12(1) (2022) 583.
[776] M.S. Salem, S. Ahmed, A. Shaker, M.T. Alshammari, K.A. Al-Dhlan, A. Alanazi, A. Saeed, M. Abouelatta, Bandwidth broadening of piezoelectric energy harvesters using arrays of a proposed piezoelectric cantilever structure, Micromachines 12(8) (2021) 973.
[777] J. Wang, Z. Xue, C. Cai, D. Wang, A novel piezoelectric energy harvester with different circular arc spiral cantilever beam, IEEE Sensors Journal 22(11) (2022) 11016-11022.
[778] K. Chen, Q. Gao, S. Fang, D. Zou, Z. Yang, W.-H. Liao, An auxetic nonlinear piezoelectric energy harvester for enhancing efficiency and bandwidth, Applied Energy 298 (2021) 117274.
[779] L. He, H. Kurita, F. Narita, Multimode auxetic piezoelectric energy harvester for low-frequency vibration, Smart Materials and Structures 33(3) (2024) 035020.
[780] I.E. Piyarathna, A.M. Thabet, M. Ucgul, C. Lemckert, Y.Y. Lim, Z.S. Tang, Linear segmented arc-shaped piezoelectric branch beam energy harvester for ultra-low frequency vibrations, Sensors 23(11) (2023) 5257.
[781] Z. Wang, T. Li, Y. Du, Z. Yan, T. Tan, Nonlinear broadband piezoelectric vibration energy harvesting enhanced by inter-well modulation, Energy Conversion and Management 246 (2021) 114661.
[782] R. Dauksevicius, R. Gaidys, V. Ostasevicius, R. Lockhart, A.V. Quintero, N. De Rooij, D. Briand, Nonlinear piezoelectric vibration energy harvester with frequency-tuned impacting resonators for improving broadband performance at low frequencies, Smart Materials and Structures 28(2) (2019) 025025.
[783] S. Nabavi, L. Zhang, Nonlinear multi-mode wideband piezoelectric MEMS vibration energy harvester, IEEE Sensors Journal 19(13) (2019) 4837-4848.
[784] C. Wang, S.-K. Lai, Z.-C. Wang, J.-M. Wang, W. Yang, Y.-Q. Ni, A low-frequency, broadband and tri-hybrid energy harvester with septuple-stable nonlinearity-enhanced

mechanical frequency up-conversion mechanism for powering portable electronics, Nano Energy 64 (2019) 103943.
[785] Z. Xu, X. Shan, D. Chen, T. Xie, A novel tunable multi-frequency hybrid vibration energy harvester using piezoelectric and electromagnetic conversion mechanisms, Applied Sciences 6(1) (2015) 10.
[786] A. Megdich, M. Habibi, L. Laperriere, Electromechanical modelling of l-shaped bending-torsion piezoelectric energy harvesting systems, Applied Mathematical Modelling 138 (2025) 115755.
[787] B. Tiwari, T. Babu, R. Choudhary, Piezoelectric lead zirconate titanate as an energy material: A review study, Materials Today: Proceedings 43 (2021) 407-412.
[788] L. Hou, Y. Huan, M. Zheng, Y. Liu, C. Wang, X. Wang, C. Li, Z. Wang, T. Wei, 3D vertically aligned microchannel structure to enhance piezoelectric energy harvesting performance of PZT/PVDF&CNTs piezoelectric composites, Journal of Materiomics 10(5) (2024) 1063-1070.
[789] V. Ogbonna, A. Popoola, O. Popoola, Piezoelectric ceramic materials on transducer technology for energy harvesting: A review, Frontiers in Energy Research 10 (2022) 1051081.
[790] J. Wang, X. Qin, Z. Liu, G. Ding, G. Cai, Experimental study on fatigue degradation of piezoelectric energy harvesters under equivalent traffic load conditions, International Journal of Fatigue 150 (2021) 106320.
[791] T. Satyanarayana, Y. Nikhitha, C.N. Kumar, K.J.N. Sai, V. Lohitha, Optimization of bimorph cantilever based piezoelectric energy harvester for high efficiency, Materials Today: Proceedings 80 (2023) 2883-2887.
[792] M. Rashmi, K.T. Sairam, A. Suresh, Energy harvesting through piezoelectric technology, Materials Today: Proceedings (2023).
[793] R. Wang, E. Tang, G. Yang, Y. Han, C. Chen, Dynamic fracture behavior of piezoelectric ceramics under impact: force-electric response and electrical breakdown, Journal of The European Ceramic Society 41(16) (2021) 139-150.
[794] R. Lay, G.S. Deijs, J. Malmström, The intrinsic piezoelectric properties of materials–a review with a focus on biological materials, RSC advances 11(49) (2021) 30657-30673.
[795] M. Abbasipour, R. Khajavi, A.H. Akbarzadeh, A comprehensive review on piezoelectric polymeric and ceramic nanogenerators, Advanced Engineering Materials 24(6) (2022) 2101312.
[796] I. Mendoza, D. Drury, A. Matejunas, J. Ivy, S. Koumlis, P. Jewell, G. Brennecka, L. Lamberson, Quasi-static and dynamic fracture behavior of lead zirconate titanate: a study of poling and loading rate, Engineering Fracture Mechanics 247 (2021) 107669.

ANNEXE 1

Supporting Information

Modeling and optimization of piezoelectric and dielectric properties of poled PVDF/BT nanocomposites

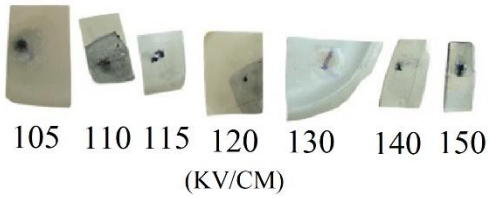

Figure S1: defected specimens due to applying an electric field greater than 100 KV /cm.

Table S1: Experimental data obtained from the BBD runs.

Inputs					Output								
Exp. No.	T (°C)	t (min)	V (KV/cm)	BT (%)	D33 (pC/N)			Permittivity			F(β) (%)		
					E1	E2	Moy	E1	E2	Moy	E1	E2	Moy
1	50	60	65	30	4	5	4.5	20.073	20.162	20.117	82.429	82.347	82.388
2	50	120	65	30	7	6	6.5	18.596	18.457	18.526	86.033	86.113	86.073
3	150	60	65	30	17	17	17	23.195	23.324	23.259	89.283	89.445	89.364
4	150	120	65	30	13	14	13.5	19.983	20.063	20.023	91.708	91.718	91.713
5	100	90	30	20	5	4	4.5	16.346	16.683	16.514	79.671	79.771	79.721
6	100	90	30	40	6	5	5.5	20.221	20.727	20.474	77.187	77.209	77.198
7	100	90	100	20	16	16	16	20.643	20.469	20.556	94.543	94.523	94.533
8	100	90	100	40	18	19	18.5	24.484	24.384	24.434	92.53	92.538	92.534
9	100	90	65	30	20	21	20.5	21.5	21.411	21.455	91.722	91.733	91.727
10	50	90	65	20	6	6	6	17.842	18.08	17.961	79.307	79.315	79.311
11	50	90	65	40	8	8	8	20.98	21.232	21.106	77.347	77.34	77.343
12	150	90	65	20	11	12	11.5	21.455	21.649	21.552	89.659	89.582	89.621
13	150	90	65	40	10	11	10.5	23.73	23.909	23.819	88.344	88.256	88.3

14	100	60	30	30	7	8	7.5	18.467	18.581	18.524	84.548	84.495	84.521
15	100	60	100	30	21	22	21.5	23.121	23.195	23.158	93.148	93.151	93.149
16	100	120	30	30	8	9	8.5	18.551	18.457	18.504	81.024	81.106	81.065
17	100	120	100	30	16	17	16.5	19.478	19.552	19.515	91.248	92.248	91.748
18	100	90	65	30	21	20	20.5	20.692	20.816	20.754	89.774	89.974	89.874
19	50	90	30	30	4	5	4.5	20.4	20.469	20.434	79.038	79.195	79.116
20	50	90	100	30	15	16	15.5	23.591	23.661	23.626	93.359	93.69	93.525
21	150	90	30	30	9	9	9	18.001	18.08	18.041	91.818	91.057	91.438
22	150	90	100	30	24	24	24	24.622	24.712	24.667	94.318	94.518	94.418
23	100	60	65	20	9	10	9.5	18.08	18.318	18.199	80.181	80.108	80.144
24	100	60	65	40	8	8	8	20.519	20.42	20.469	87.927	88.326	88.127
25	100	120	65	20	5	6	5.5	18.457	18.269	18.363	77.23	77.53	77.38
26	100	120	65	40	6	7	6.5	20.306	20.221	20.263	89.234	89.396	89.315
27	100	90	65	30	20	21	20.5	23.948	23.79	23.869	84.711	84.911	84.811

Table S2: S/N ratios of the output results.

Exp. No.	SN ratio of d33 coefficient	SN ratio of the permittivity	SN ratio of F(β)
1	19.064	38.317	26.071
2	16.258	38.697	25.356
3	21.584	39.023	27.332
4	22.607	39.249	26.031
5	13.064	38.247	25.201
6	19.807	37.752	25.261
7	24.082	39.512	27.613
8	25.343	39.326	26.222
9	21.235	39.621	26.595
10	15.563	37.987	26.167
11	18.062	37.768	26.488
12	21.214	39.048	27.416
13	20.424	38.919	27.539
14	17.501	38.539	25.355
15	26.649	39.384	27.294
16	18.588	38.177	25.345
17	24.35	39.252	25.807
18	26.235	39.073	26.342
19	13.064	37.965	26.207
20	23.807	39.419	27.468
21	19.085	39.222	25.125
22	27.604	39.501	27.842

23	19.554	38.077	25.201
24	18.062	38.902	25.337
25	14.807	37.773	25.279
26	16.258	39.018	25.38
27	26.235	38.569	27.557

Table S3: Comparison between predicted values and experimental values.

Exp. No.	D33 (pC/N)			Permittivity			F(β) (%)		
	Predicted value	Target Value	Error (%)	Predicted value	Target Value	Error (%)	Predicted value	Target Value	Error (%)
1	4.954	4.5	10.088	19.93	20.117	0.93	77.809	82.388	5.558
2	7.275	6.5	11.923	21.758	18.526	17.446	89.689	86.073	4.201
3	19.07	17	10.854	20.86	23.259	10.314	95.705	89.364	7.096
4	12.727	13.5	5.725	22.718	20.023	13.46	94.807	91.713	3.374
5	4.501	4.5	0.022	16.701	16.514	1.132	77.308	79.721	3.027
6	5.405	5.5	1.727	19.601	20.474	4.264	78.559	77.198	1.763
7	11.905	16	25.593	22.636	20.556	10.119	86.894	94.533	8.081
8	18.396	18.5	0.562	24.085	24.434	1.428	93.686	92.534	1.245
9	21.293	20.5	3.868	21.56	21.455	0.489	90.162	91.727	1.706
10	4.228	6	29.533	18.27	17.961	1.72	79.324	79.311	0.016
11	7.478	8	6.525	21.679	21.106	2.715	78.574	77.343	1.592
12	12.493	11.5	8.634	22.166	21.552	2.849	89.513	89.621	0.121
13	11.321	10.5	7.819	22.834	23.819	4.135	95.65	88.3	8.324
14	6.537	7.5	12.84	19.783	18.524	6.797	85.661	84.521	1.349
15	22.177	21.5	3.148	21.961	23.158	5.169	94.811	93.149	1.784
16	7.406	8.5	12.87	18.128	18.504	2.032	81.695	81.065	0.777
17	15.077	16.5	8.624	19.502	19.515	0.067	91.606	91.748	0.155
18	21.293	20.5	3.868	21.56	20.754	3.884	90.162	89.874	0.32
19	4.637	4.5	3.044	19.008	20.434	6.979	77.9	79.116	1.537
20	14.85	15.5	4.193	23.424	23.626	0.855	92.311	93.525	1.298
21	12.806	12	6.716	17.828	18.041	1.181	93.261	91.438	1.994
22	24.186	24	0.775	24.918	24.667	1.018	95.67	94.418	1.326
23	8.151	9.5	14.2	17.488	18.199	3.907	82.553	80.144	3.006
24	6.583	8	17.712	20.918	20.469	2.194	88.031	88.127	0.109
25	4.509	5.5	18.018	18.478	18.363	0.626	78.251	77.38	1.126
26	6.616	6.5	1.784	21.355	20.263	5.389	88.031	89.315	1.438
27	21.293	20.5	3.868	21.56	23.869	9.674	90.162	84.811	6.309

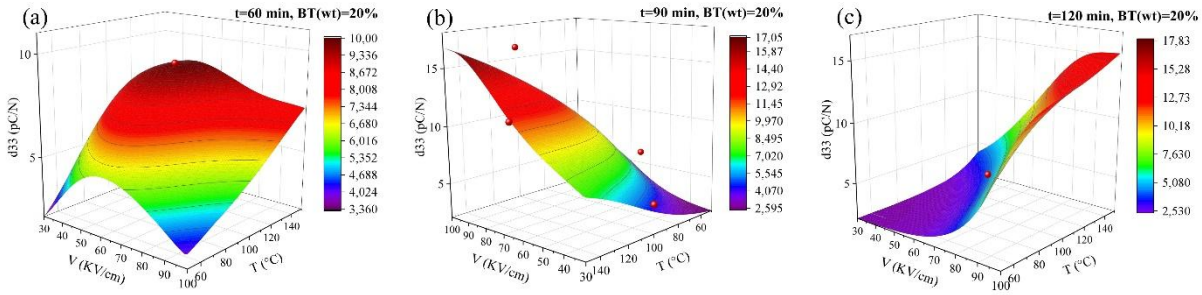

Figure S2: Response surface plot of d33 coefficient for BT=20 wt% according to ANN.

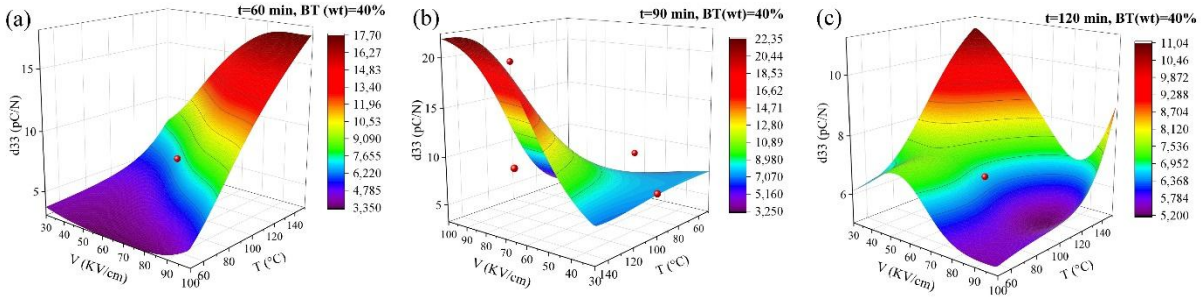

Figure S3: Response surface plot of d33 coefficient for BT=40 wt% according to ANN.

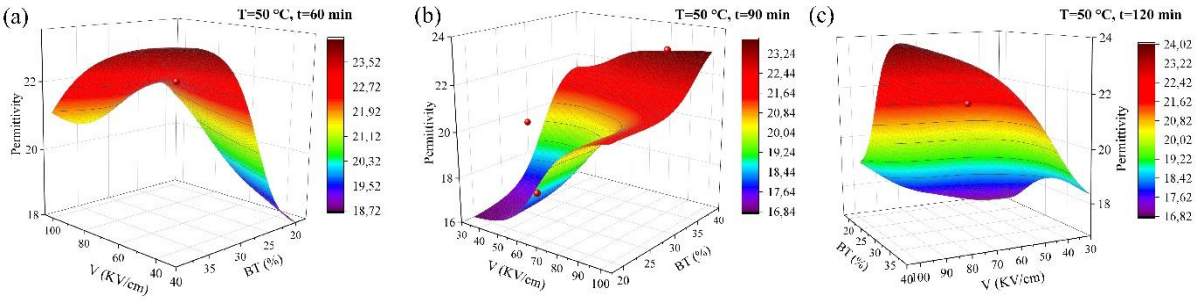

Figure S4: Response surface plot of permittivity for T=50°C according to ANN.

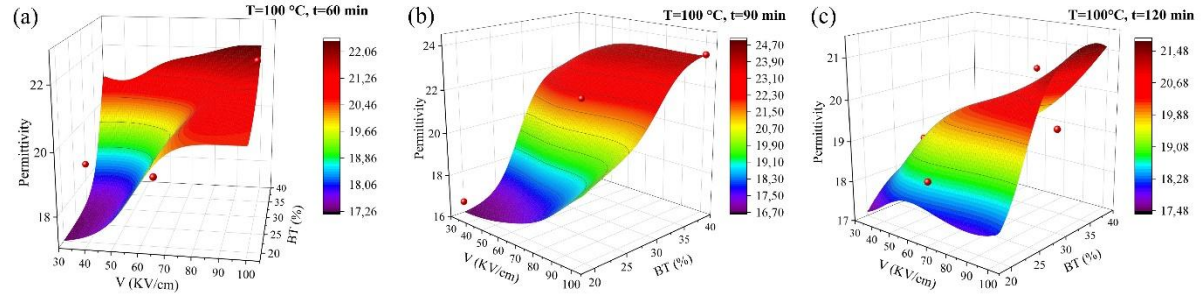

Figure S5: Response surface plot of permittivity for T=100°C according to ANN.

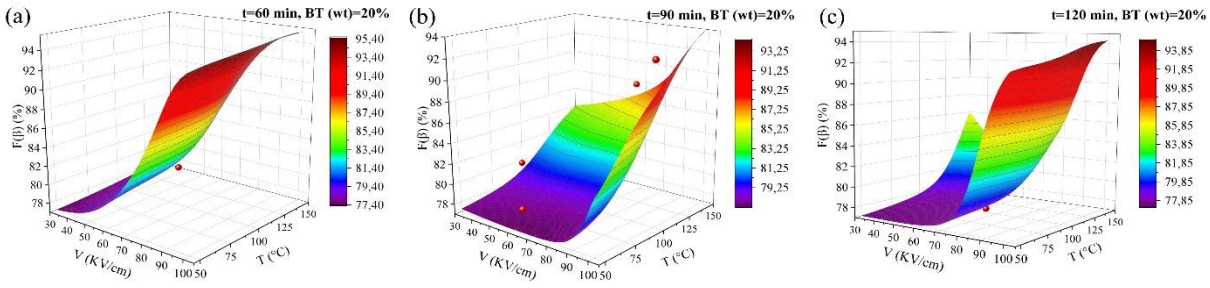

Figure S6: Response surface plot of F(β) for BT=20 wt% according to ANN.

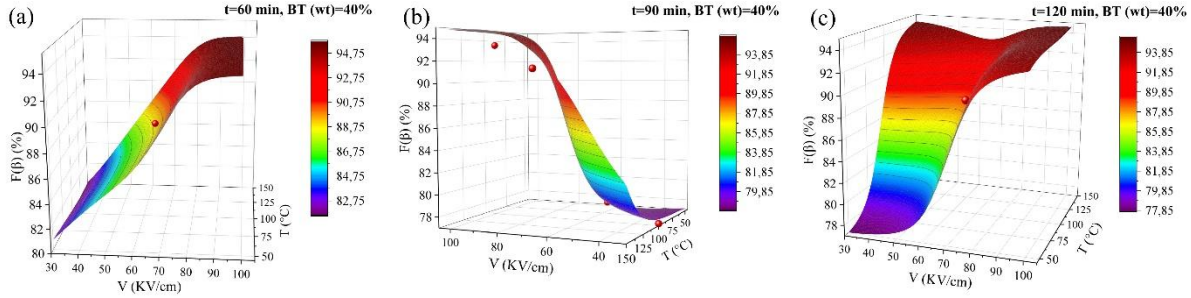

Figure S7**:** Response surface plot of F(β) for BT=40 wt% according to ANN.

ANNEXE 2

Supporting Information

Advanced 3D-printed PVDF/BT piezoelectric energy harvester with a bio-inspired 3D structure for a self-powered smart mouse

Poling parameters:

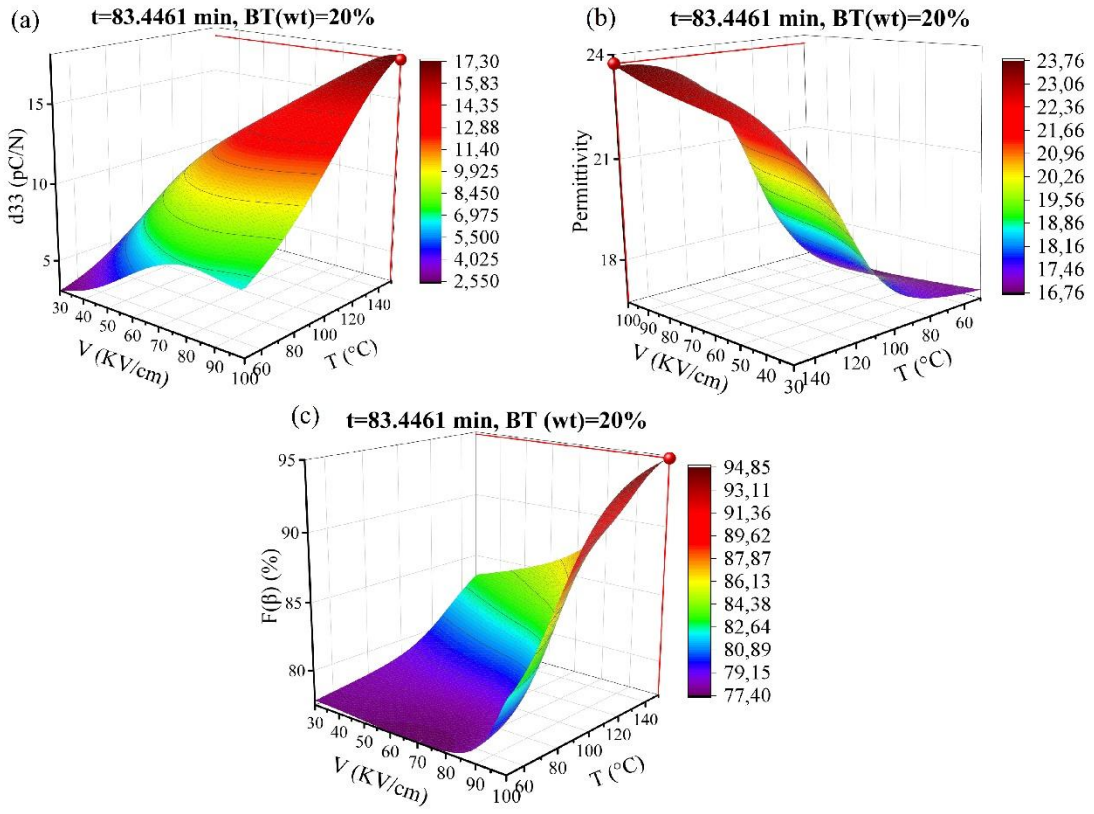

Figure S1: Optimal poling parameters for BT-20 sample.

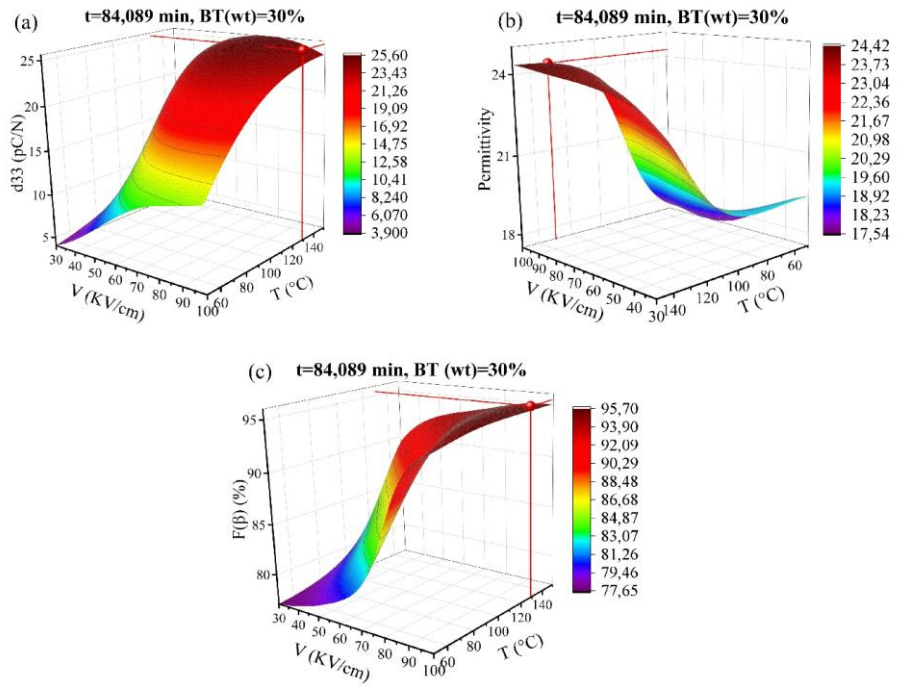

.

Figure S2: Optimal poling parameters for BT-30 sample.

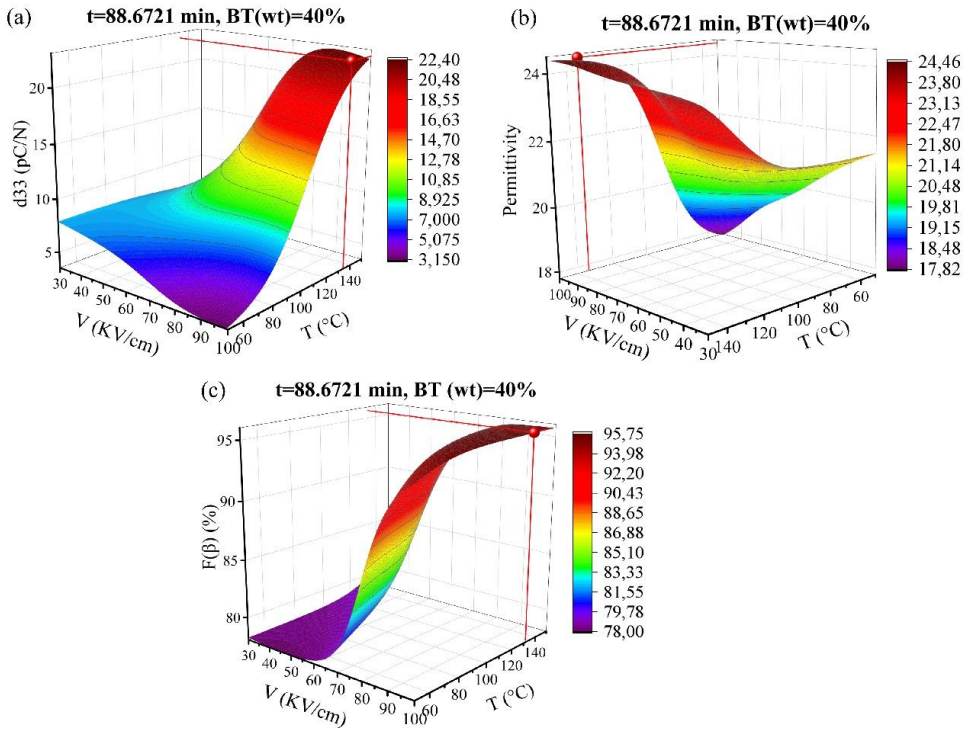

Figure S3: Optimal poling parameters for BT-40 sample.

Tensile test:

After selecting BT -30 as the nanocomposite with the best piezoelectric and dielectric properties. Finite element simulations were performed using COMSOL software to optimize the structure of the final PEH. Since the PEH is subjected to compressive forces in the z-direction, the elastic modulus E33 of the BT -30 nanocomposite is required. The dimensions of the tensile specimen were chosen according to ASTM D638 type IV as shown in Figure S16a. The 3D structure of the specimen was designed using Solidworks software (Figure S16b). As shown in Figure S16c to measure the E33 of the specimen, the infill angle was set to 90°. Then, the specimen was printed using an FDM 3D printer (Figure S16d) and tested using Universal Testing Machine (Figure S16e). Figure S16f shows the 3D-printed specimen.

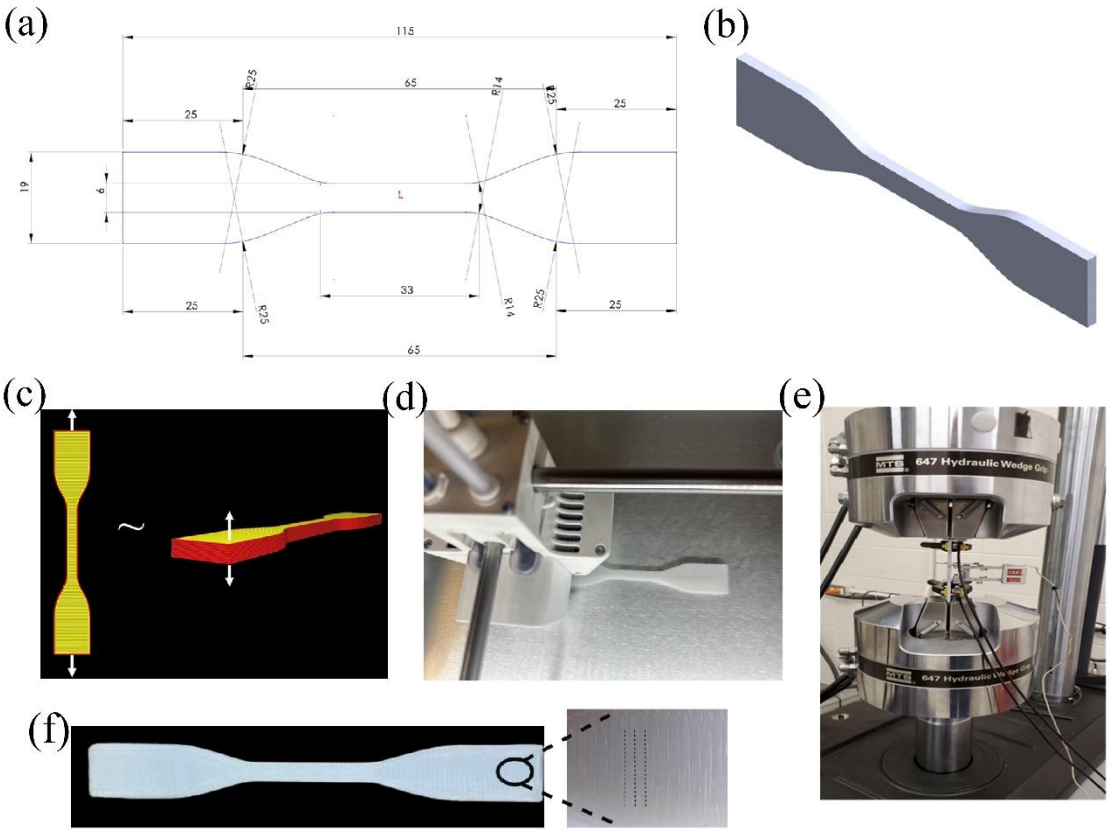

Figure S4: (a) dimensions of the specimen according to ASTM D638 type IV, (b) 3D structure of the specimen, (c) reason for choosing the infill angle θ=90°, (d) 3D printing of the specimen, (e) tensile test setup, (f) 3D printed specimen for tensile test.

The tensile test results of the BT -30 sample were compared with the tensile test results of a pure PVDF sample printed under the same conditions. As predicted, the addition of BT to PVDF significantly increased its elastic modulus due to the high stiffness of the BT particles, as shown in Figure S17. When BT particles are dispersed in PVDF, they can act as a reinforcing agent, adding stiffness and strength to the composite. However, this resulted in a decrease in tensile strength and tensile elongation of the material. Our results are in good agreement with previous works [797, 798]. The tensile test results are listed in Table S9.

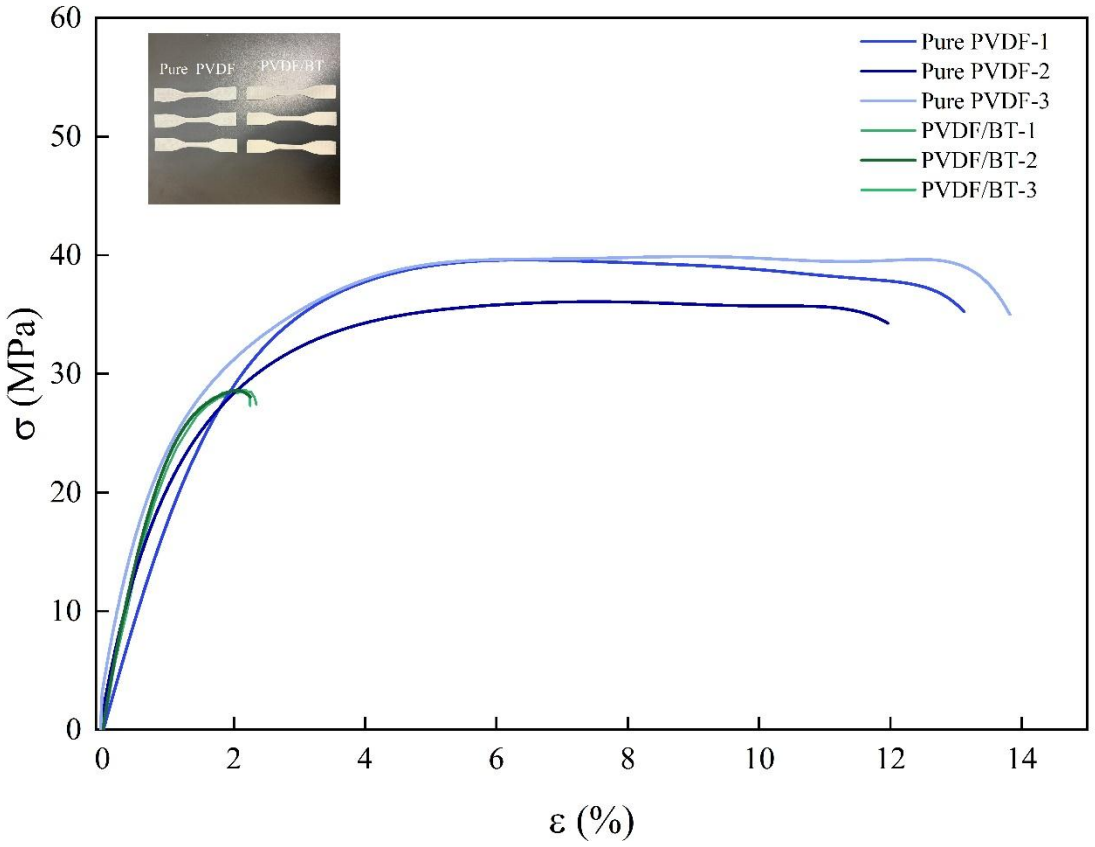

Figure S5: Stress–strain curve at the strain rate of 3 mm/min for 3D printed pure PVDF and BT-30 samples.

Table S1: Tensile test results for 3D printed pure PVDF and BT-30 samples.

	Pure PVDF	**BT-30**
Tensile Strength (Mpa)	38,7186667	27,8353333
Young's modulus (MPa)	2258,11833	2844,216
Tensile Elongation (%Strain)	12,9913333	2,41333333

Numerical simulations:

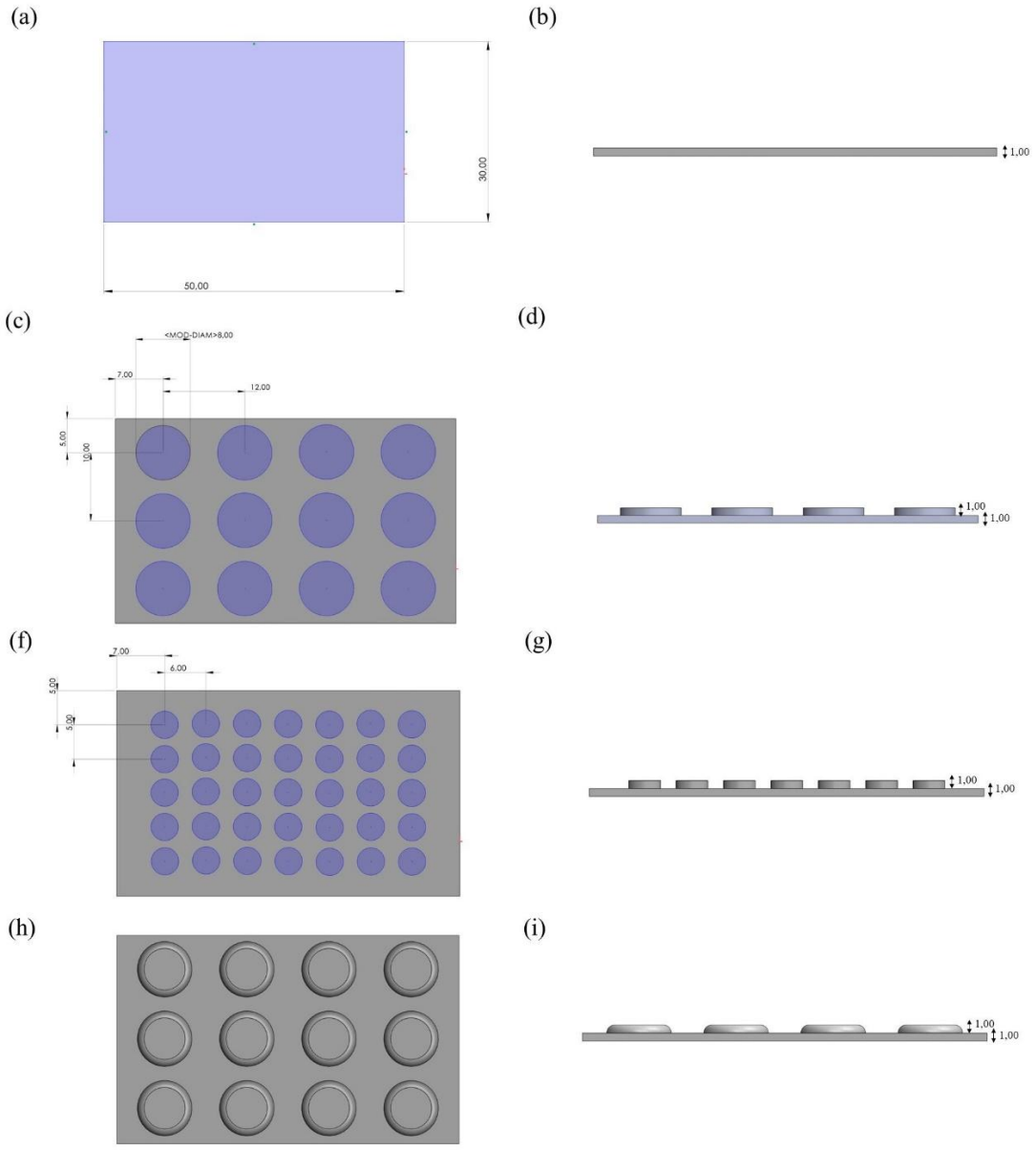

Figure S6: PEHs dimensions.

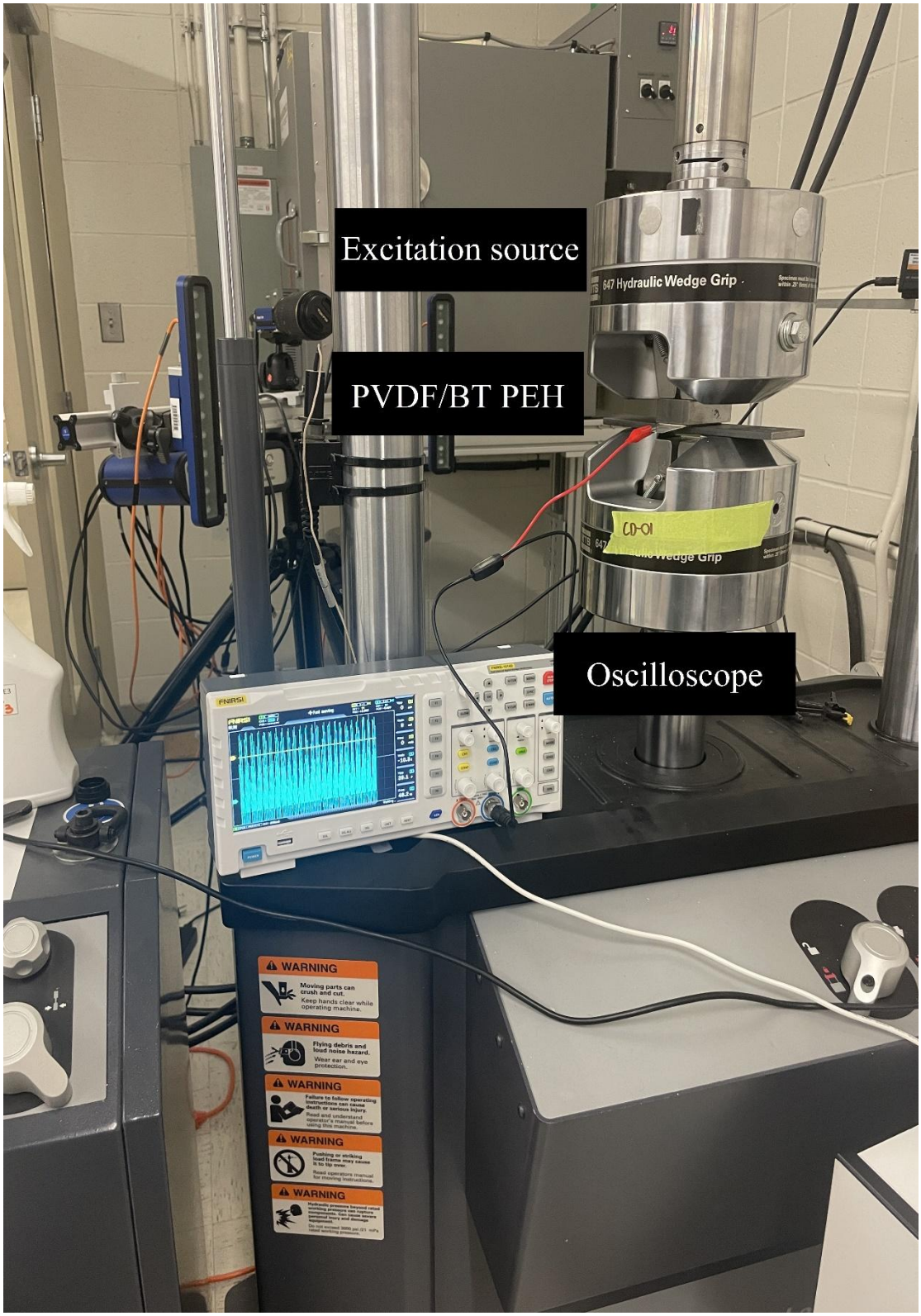

Figure S7: Photo of the piezoelectric testing system.

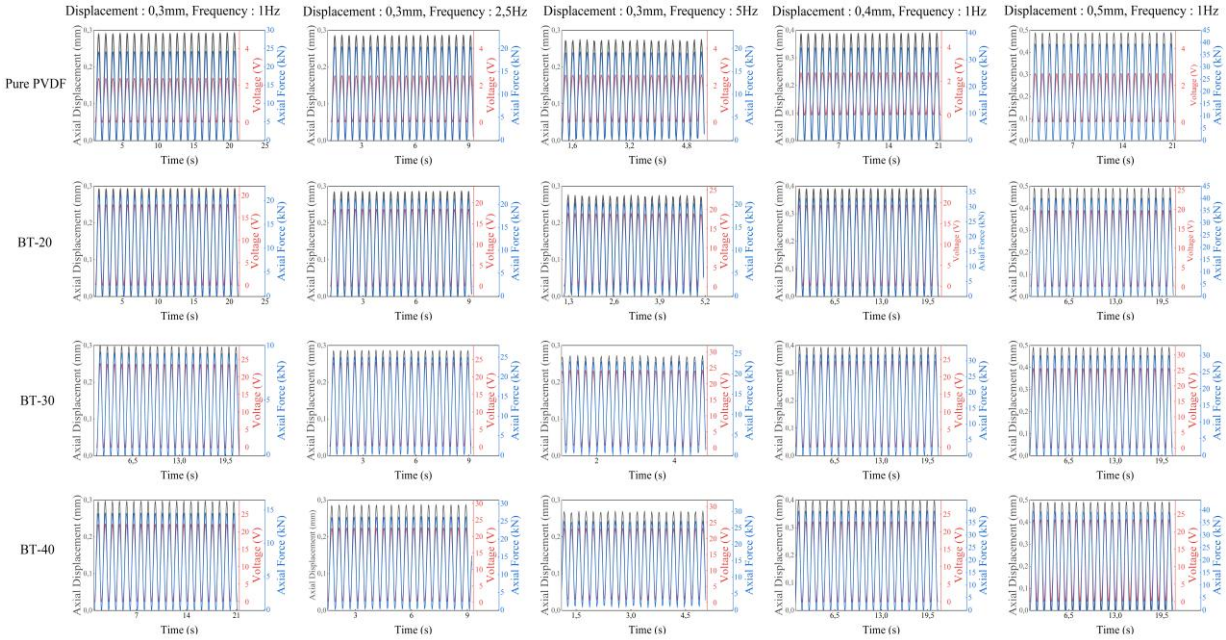

Figure S8: Axial displacement and (b) frequency dependence of the open-circuit voltage signals and the axial force of each composition.

The mechanism of the piezoelectric nanogenerator shown in Figure S22 is based solely on the alignment of the dipoles under mechanical stress. When pressing the mouse button, piezoelectric charges are induced, creating a potential difference between the electrodes. External charges move to cancel the potential, resulting in a positive signal. Upon release the button, the accumulated charges reverse, causing the potential to disappear and producing a negative signal.

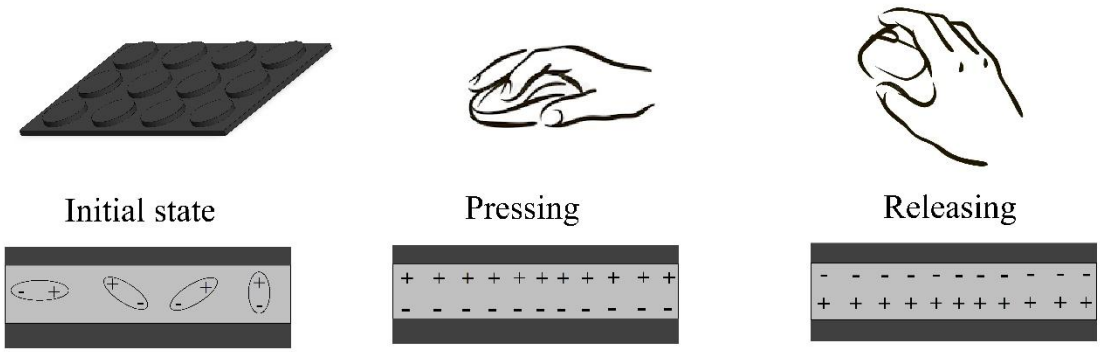

Figure S9: Working mechanism of the device.

Table S2: Comparison of the piezoelectric performance obtained in this work and other reported works.

Material	Open circuit voltage (V)	Short circuit current (nA)	Ref
PVDF/CNT	9.8		[1]
PVDF/MWCNT	1.4		[2]
PVDF/GPn	16.97	274	[3]
PVDF/BT@PDA/Ag	10	142	[4]
PVDF/BaTiO3/carbon	5.7	79.8	[5]
PVDF/BTO@PDA	9.3	86	[6]
PVDF/BT/CNT	19.3	415	[7]
PVDF/TPPC/BT	11.5	220	[8]
PVDF/BT	10.9	126.9	[9]
PVDF/BT	4		[10]
PVDF	0.289		[11]
PVDF/BT	20.9	250	[12]
PVDF/WO3	2.1		[13]
PVDF/PVA	10.7	166.42	[14]
PVDF/BT	8.22	3360	[15]
PVDF/BNT	19	1200	[16]
PVDF/BT	30.9	3788	This work

References

[1] S. Sharafkhani, M. Kokabi, Ultrathin-shell PVDF/CNT nanocomposite aligned hollow fibers as a sensor/actuator single element, Compos. Sci. Technol. 200 (2020) 108425.

[2] J.H. Eun, S.M. Sung, M.S. Kim, B.K. Choi, J.S. Lee, Effect of MWCNT content on the mechanical and piezoelectric properties of PVDF nanofibers, Mater. Des. 206 (2021) 109785.

[3] S. Song, Y. Li, Q. Wang, C. Zhang, Boosting piezoelectric performance with a new selective laser sintering 3D printable PVDF/graphene nanocomposite, Compos. Part A Appl. Sci. Manuf. 147 (2021) 106452.

[4] C. Shuai, G. Liu, Y. Yang, F. Qi, S. Peng, W. Yang, C. He, G. Wang, G. Qian, A strawberry-like Ag-decorated barium titanate enhances piezoelectric and antibacterial activities of polymer scaffold, Nano Energy 74 (2020) 104825.

[5] F. Qi, Z. Zeng, J. Yao, W. Cai, Z. Zhao, S. Peng, C. Shuai, Constructing core-shell structured BaTiO3@ carbon boosts piezoelectric activity and cell response of polymer scaffolds, Mater. Sci. Eng. C 126 (2021) 112129.

[6] Y. Yang, H. Pan, G. Xie, Y. Jiang, C. Chen, Y. Su, Y. Wang, H. Tai, Flexible piezoelectric pressure sensor based on polydopamine-modified BaTiO3/PVDF composite film for human motion monitoring, Sens. Actuator A Phys. 301 (2020) 111789.

[7] C. Yang, S. Song, F. Chen, N. Chen, Fabrication of PVDF/BaTiO3/CNT piezoelectric energy harvesters with bionic balsa wood structures through 3D printing and supercritical carbon dioxide foaming, ACS Appl. Mater. Interfaces 13(35) (2021) 41723-41734.

[8] H. Pei, S. Shi, Y. Chen, Y. Xiong, Q. Lv, Combining solid-state shear milling and FFF 3D-printing strategy to fabricate high-performance biomimetic wearable fish-scale PVDF-based piezoelectric energy harvesters, ACS Appl. Mater. Interfaces 14(13) (2022) 15346-15359.

[9] X. Liu, Y. Shang, J. Liu, Z. Shao, C. Zhang, 3D printing-enabled in-situ orientation of BaTi2O5 nanorods in β-PVDF for high-efficiency piezoelectric energy harvesters, ACS Appl. Mater. Interfaces 14(11) (2022) 13361-13368.

[10] S. Bodkhe, G. Turcot, F.P. Gosselin, D. Therriault, One-step solvent evaporation-assisted 3D printing of piezoelectric PVDF nanocomposite structures, ACS Appl. Mater. Interfaces 9(24) (2017) 20833-20842.

[11] N.A. Shepelin, V.C. Lussini, P.J. Fox, G.W. Dicinoski, A.M. Glushenkov, J.G. Shapter, A.V. Ellis, 3D printing of poly (vinylidene fluoride-trifluoroethylene): a poling-free technique to manufacture flexible and transparent piezoelectric generators, MRS Commun. 9(1) (2019) 159-164.

[12] C. Yang, F. Chen, J. Sun, N. Chen, Boosted mechanical piezoelectric energy harvesting of polyvinylidene fluoride/barium titanate composite porous foam based on three-dimensional printing and foaming technology, ACS omega 6(45) (2021) 30769-30778.

[13] N. Arul, M. Suresh, M. Satthiyaraju, N.K. Babu, Flexible electrospun PVDF/WO3 nanocomposite fibers for piezoelectric energy harvesting applications, Polym. Compos. 45(1) (2024) 360-372.

[14] Y. Yu, X. Zhao, H. Ge, L. Ye, A self-powered piezoelectric Poly (vinyl alcohol)/Polyvinylidene fluoride fiber membrane with alternating multilayer porous structure for energy harvesting and wearable sensors, Compos Sci Technol . 247 (2024) 110429.

[15] M. Kumar, N.D. Kulkarni, P. Kumari, Piezoelectric performance enhancement of electrospun functionally graded PVDF/BaTiO3 based flexible nanogenerators, Mater. Res. Bull. (2024) 112739.

[16] A. Kurakula, S.A. Graham, P. Manchi, M.V. Paranjape, J.S. Yu, Enhanced energy harvesting ability of bismuth sodium titanate/polyvinylidene fluoride composite film-based piezoelectric nanogenerators for mechanical energy scavenging and safety-walker applications, Mater. Today Sustainability 25 (2024) 100616.

ANNEXE 3

Supporting Information

Enhanced piezoelectric performance of PVDF/MWCNTs energy harvester through a 3D-printed multimodal auxetic structure for smart security systems

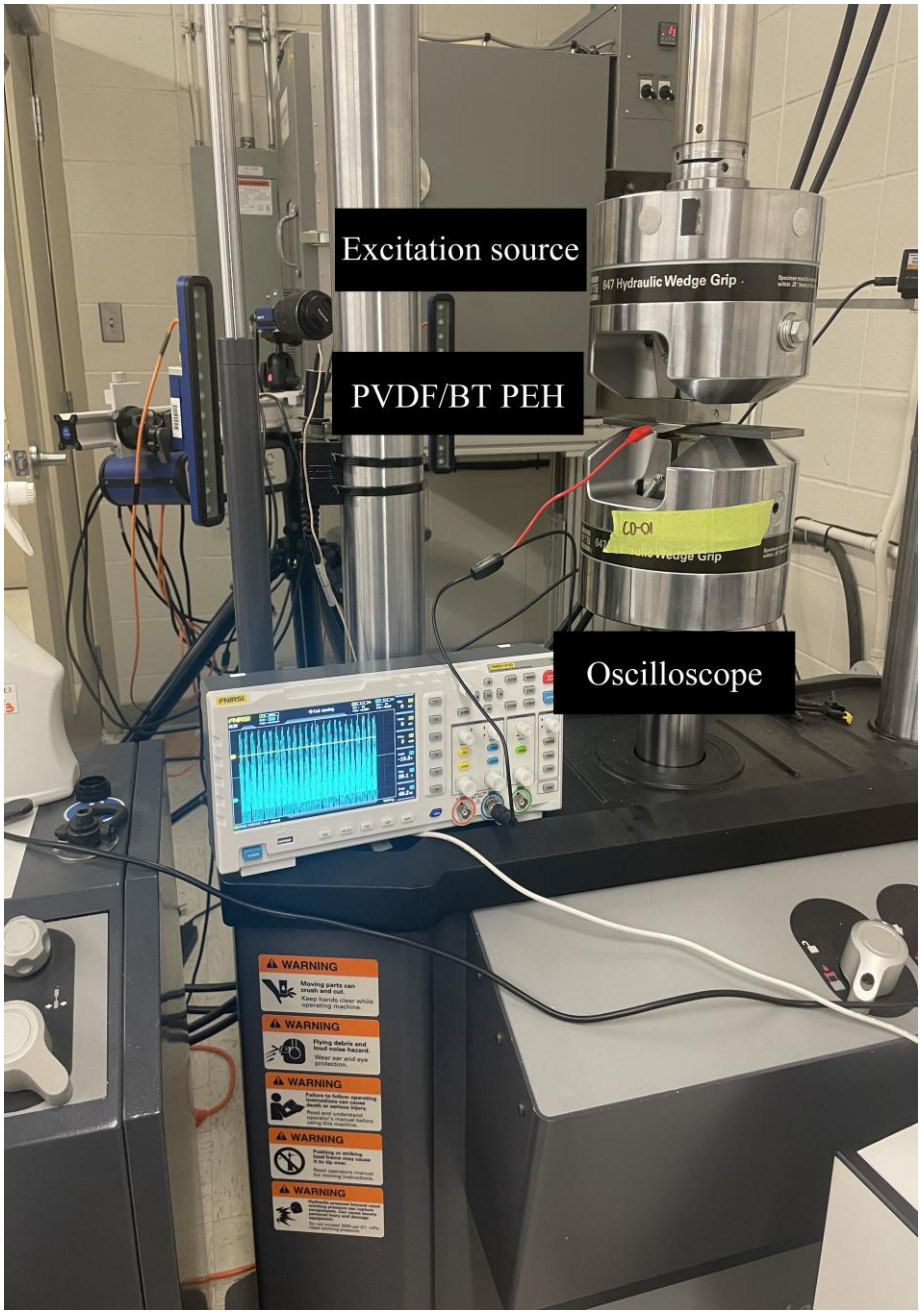

Figure S1: Photo of the piezoelectric testing system.

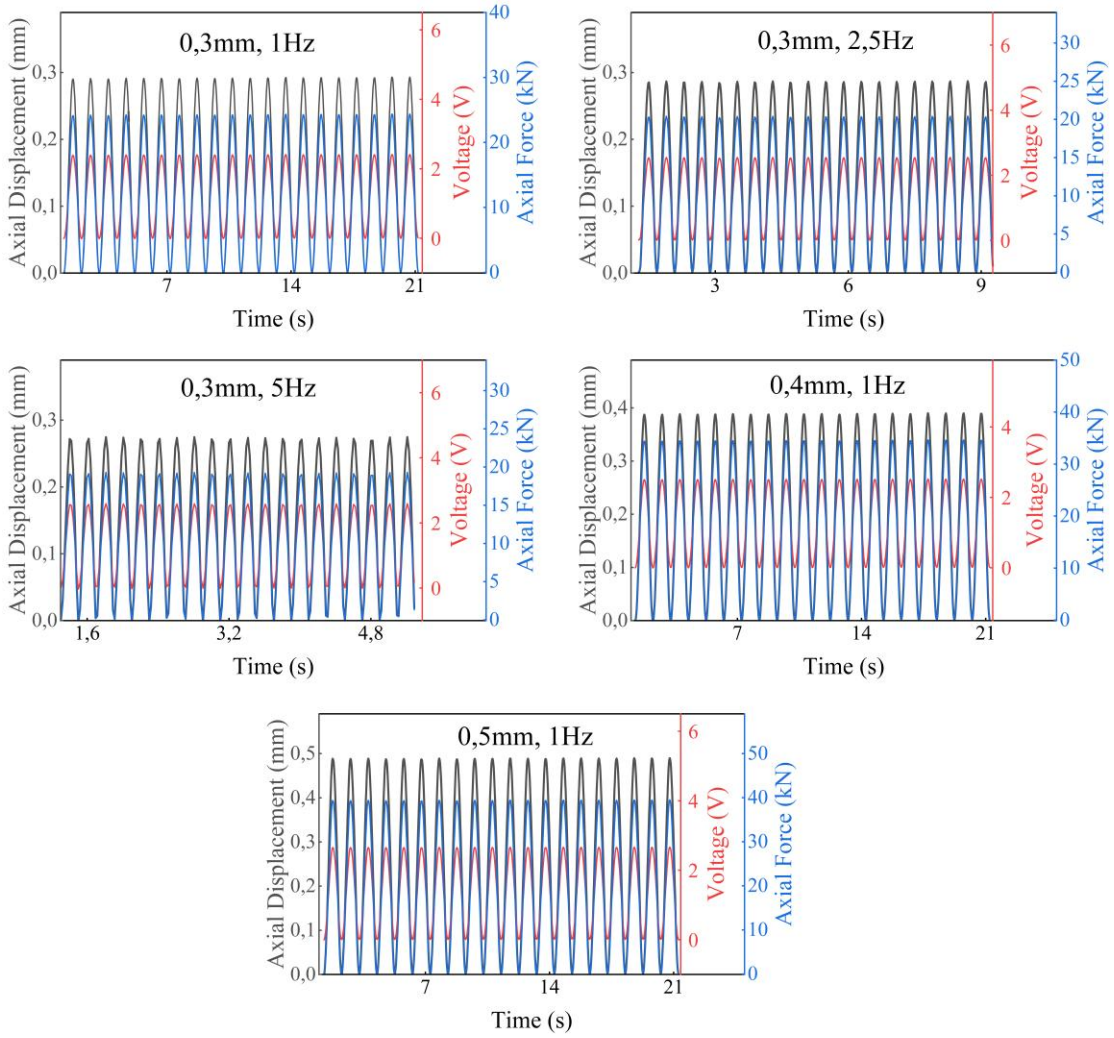

Figure S2: Axial displacement and frequency dependence of the open-circuit voltage signals and the axial force of the pure PVDF sample.

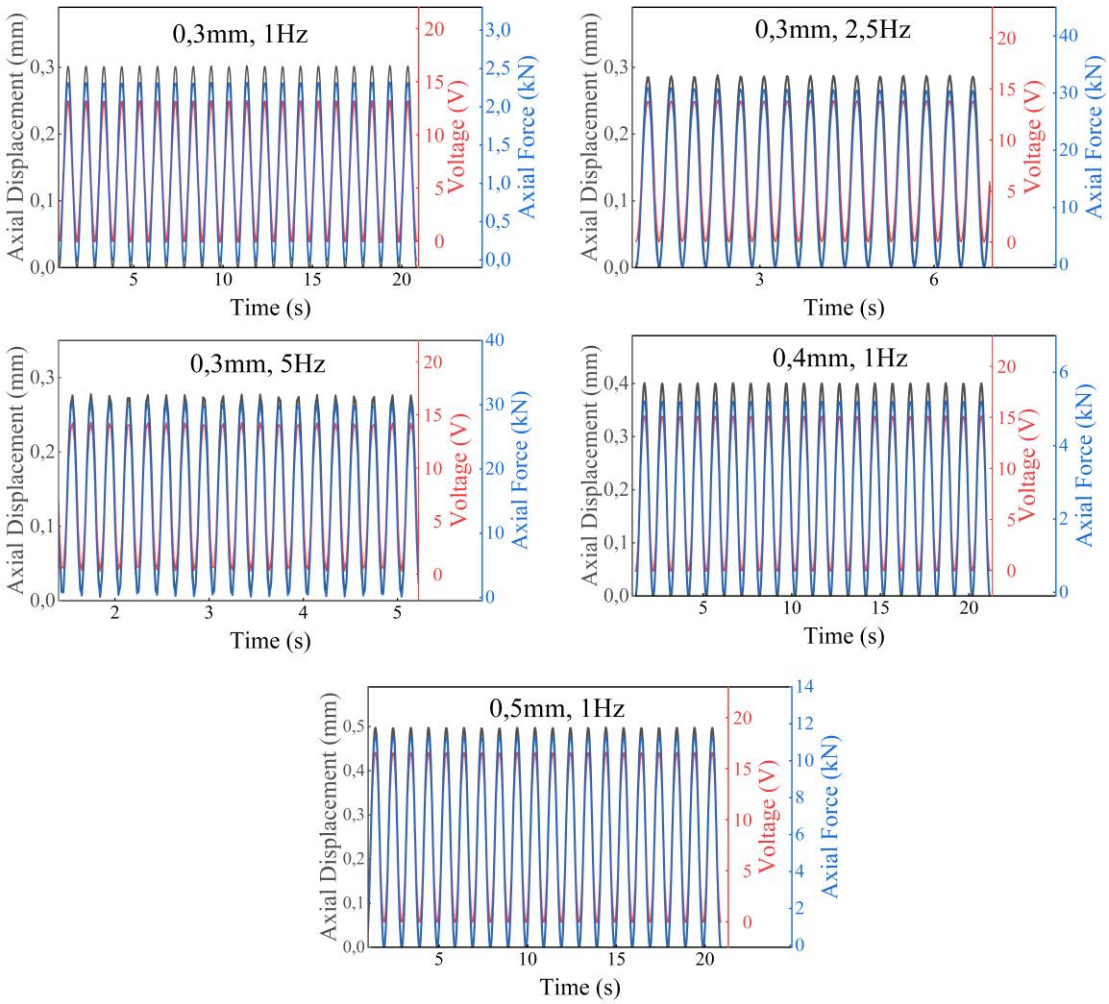

Figure S3: Axial displacement and frequency dependence of the open-circuit voltage signals and the axial force of the C-0.3 sample.

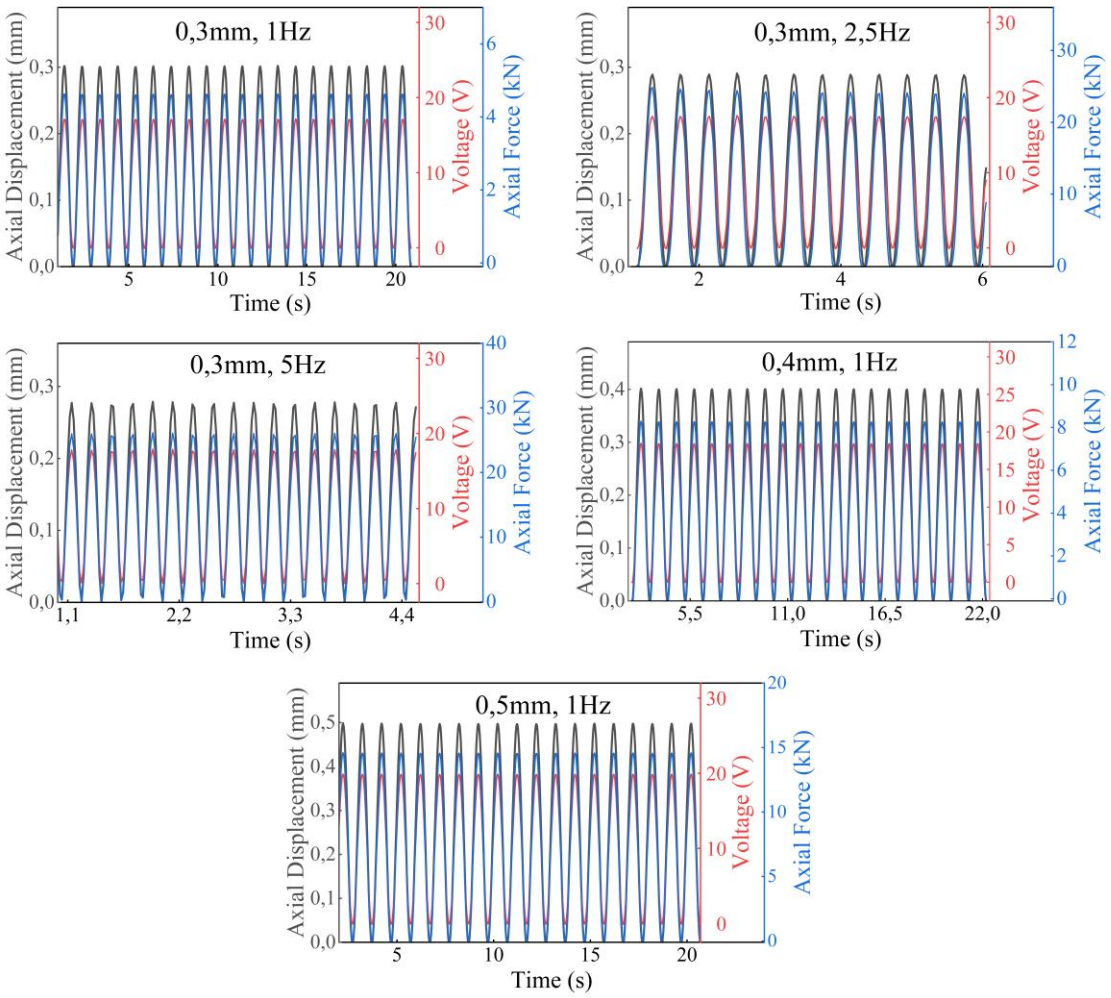

Figure S4: Axial displacement and frequency dependence of the open-circuit voltage signals and the axial force of the C-0.5 sample.

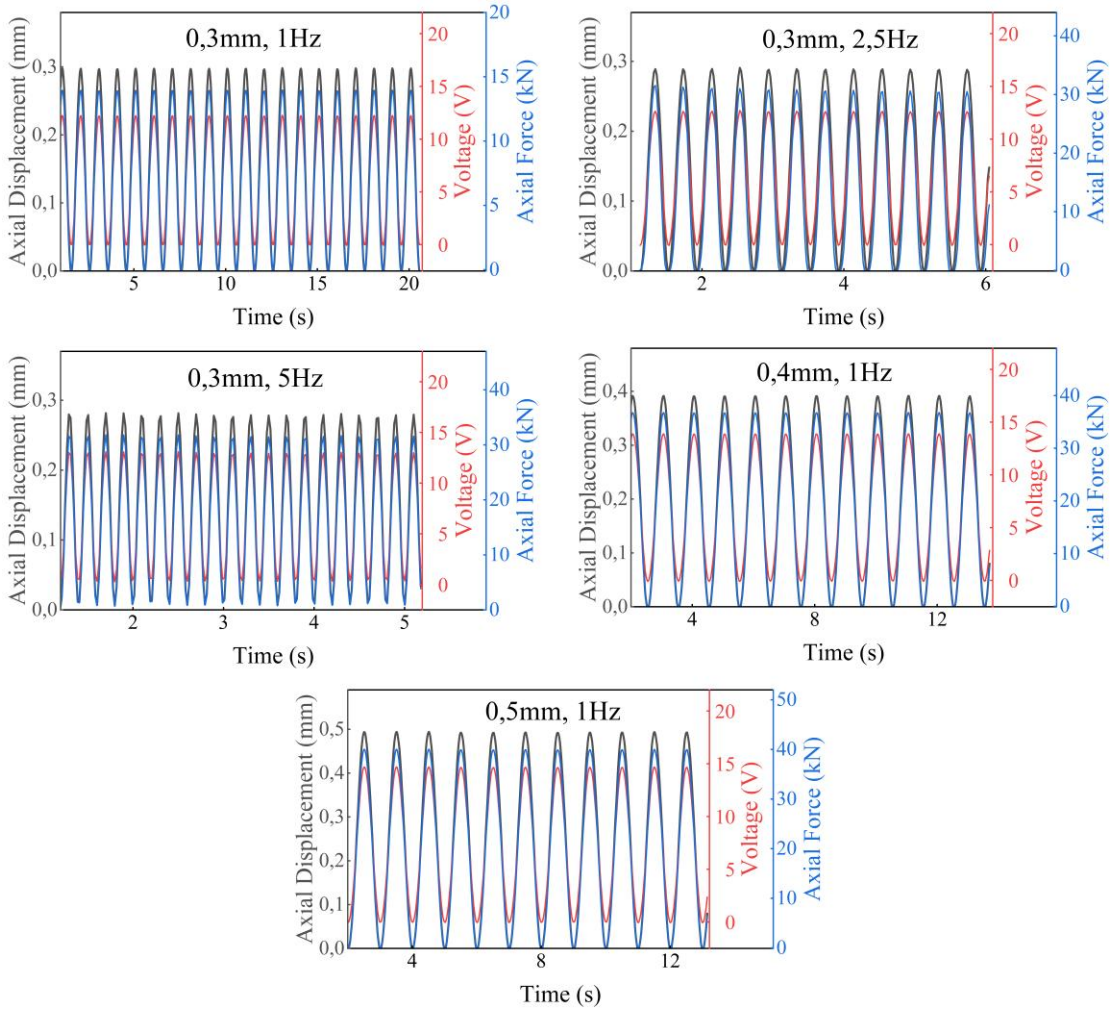

Figure S5: Axial displacement and frequency dependence of the open-circuit voltage signals and the axial force of the C-0.7 sample.

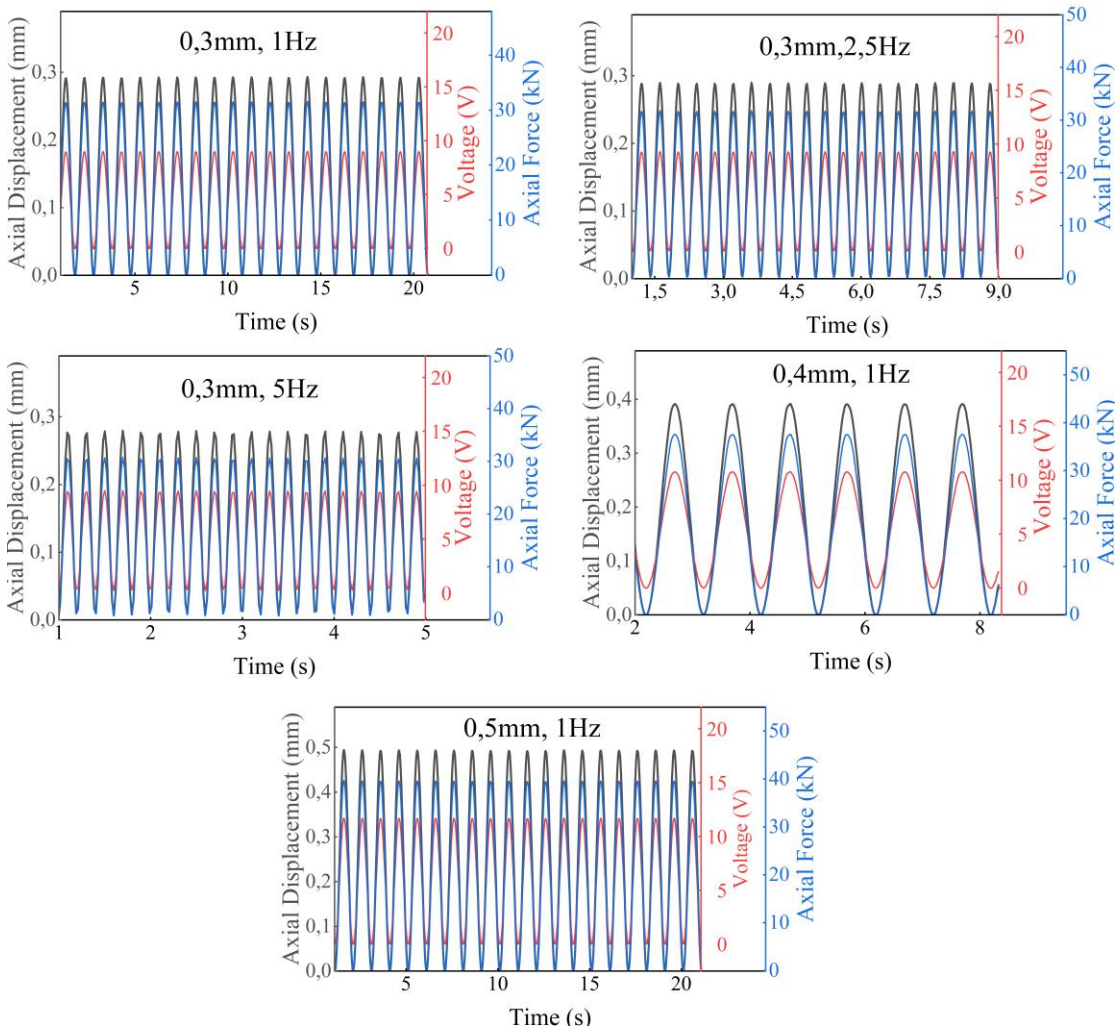

Figure S6: Axial displacement and frequency dependence of the open-circuit voltage signals and the axial force of the C-1 sample.

Considering the complicated auxetic structure, which is characterized by its high intricate details, and considering the significant warping observed in the nanocomposite PVDF/MWCNTs during 3D printing due to internal stresses resulting from the different thermal contraction behavior of the PVDF and the MWCNTs components, we implemented a multi-material 3D printing approach. A Polyvinyl alcohol (PVA) material was incorporated into the voids within the structure. PVA was chosen due to its high solubility in water, which prevents the PVDF/MWCNTs nanocomposite from dissolving simultaneously. The dissolution process lasted about 3 hours at a temperature of 70°C and high stirring speed and finally resulted in the desired final structure. The whole fabrication process is outlined in Figure S9a, while Figure S9b shows a photo of the multi-material structure during and after printing.

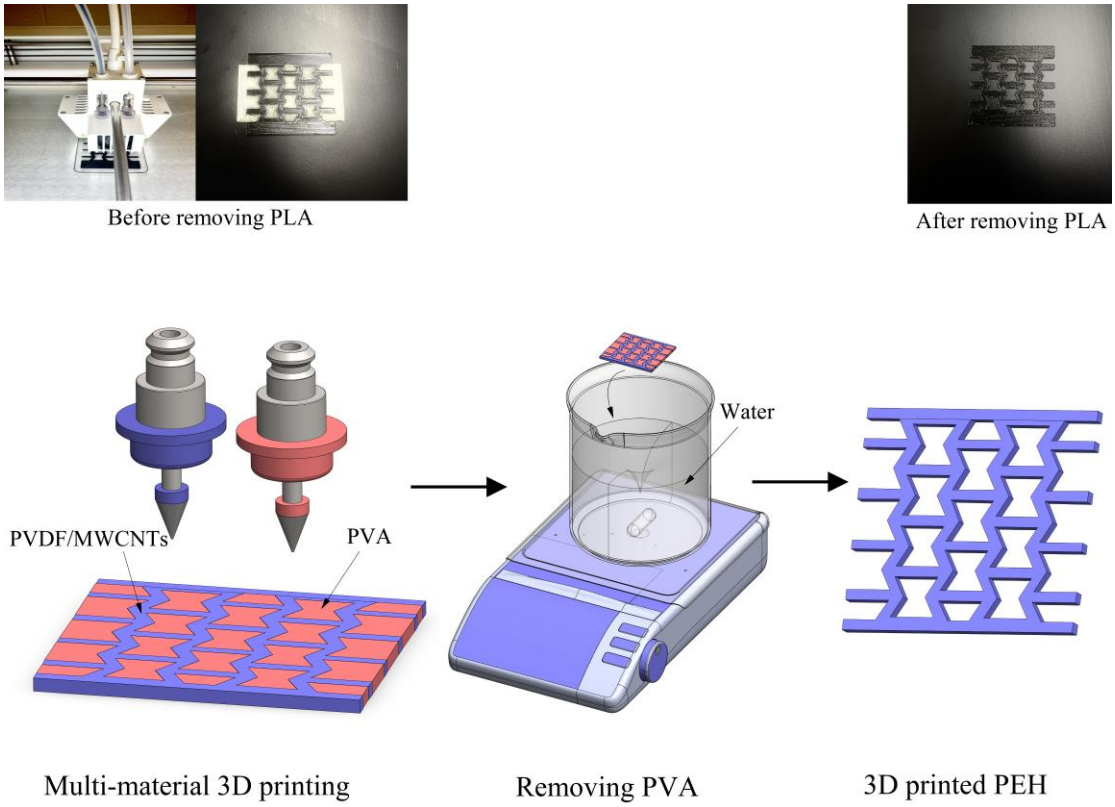

Figure S7: (a) Fabrication process of the PVDF-based auxetic structure with 0.5 wt% of MWCNT.

Figure S8: Photo showing the high flexibility of the 3D printed auxetic structure with 0.5 wt% of MWCNT.

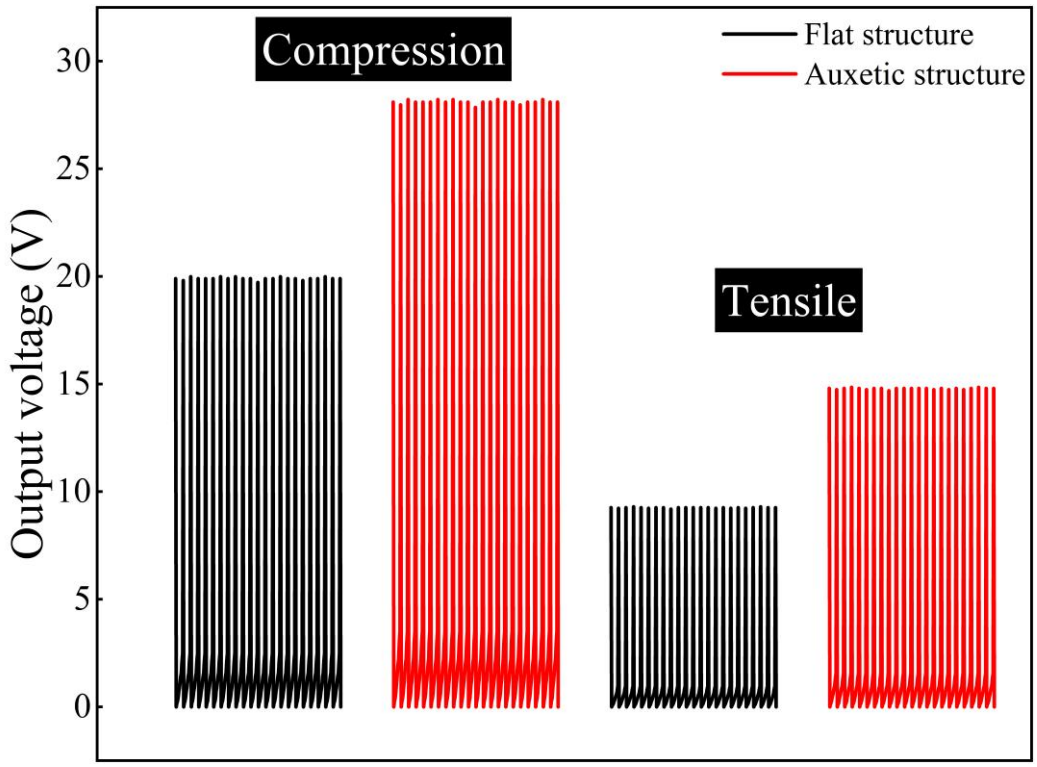

Figure S9: Comparison of the conventional flat structure and the auxetic structure piezoelectric performances during compression and tensile tests.

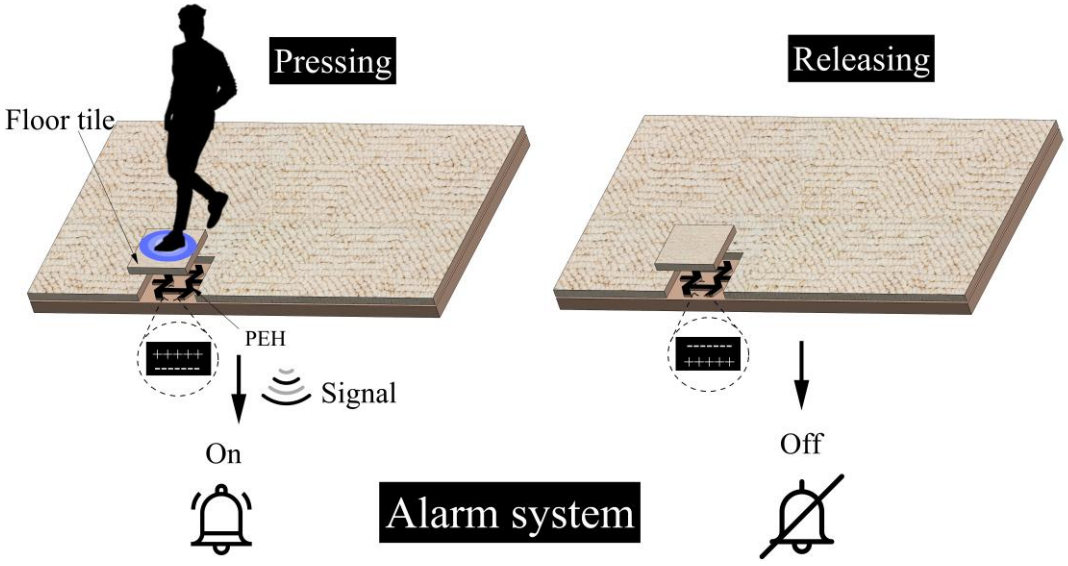

Figure S10: Working mechanism of the system.

The mechanism of the piezoelectric nanogenerator shown in Figure S10 is based solely on the alignment of the dipoles under mechanical stress. When pressing the mouse button, piezoelectric charges are induced, creating a potential difference between the electrodes. External charges move to cancel the potential, resulting in a positive signal. Upon release the button, the accumulated charges reverse, causing the potential to disappear and producing a negative signal.

Numerical simulations:

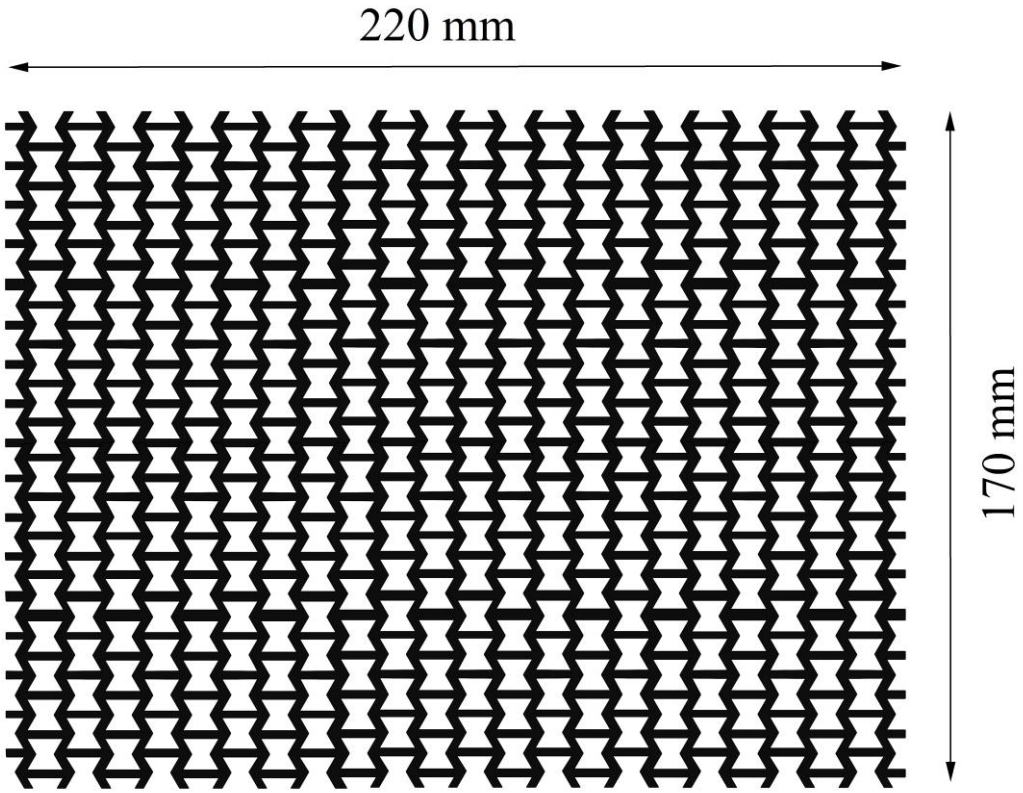

Figure S11: Dimensions of the auxetic structure used in the numerical simulation of the PEH's application.

Table S3: Comparison of the piezoelectric performances obtained in this work and other reported works.

Material	Open circuit voltage (V)	Short circuit current (nA)	Ref
PVDF/CNT	9.8		[1]
PVDF/MWCNT	1.4		[2]

PVDF/GPn	16.97	274	[3]
PVDF/BT@PDA/Ag	10	142	[4]
PVDF/BaTiO3/carbon	5.7	79.8	[5]
PVDF/BTO@PDA	9.3	86	[6]
PVDF/BT/CNT	19.3	415	[7]
PVDF/TPPC/BT	11.5	220	[8]
PVDF/BT	10.9	126.9	[9]
PVDF/BT	4		[10]
PVDF	0.289		[11]
PVDF/BT	20.9	250	[12]
PVDF/WO3	2.1		[13]
PVDF/PVA	10.7	166.42	[14]
PVDF/BT	8.22	3360	[15]
PVDF/BNT	19	1200	[16]
PVDF/MWCNT	28.2	2580	This work

References

[1] S. Sharafkhani, M. Kokabi, Ultrathin-shell PVDF/CNT nanocomposite aligned hollow fibers as a sensor/actuator single element, Composites Science and Technology 200 (2020) 108425.

[2] J.H. Eun, S.M. Sung, M.S. Kim, B.K. Choi, J.S. Lee, Effect of MWCNT content on the mechanical and piezoelectric properties of PVDF nanofibers, Materials & Design 206 (2021) 109785.

[3] S. Song, Y. Li, Q. Wang, C. Zhang, Boosting piezoelectric performance with a new selective laser sintering 3D printable PVDF/graphene nanocomposite, Composites Part A: Applied Science and Manufacturing 147 (2021) 106452.

[4] C. Shuai, G. Liu, Y. Yang, F. Qi, S. Peng, W. Yang, C. He, G. Wang, G. Qian, A strawberry-like Ag-decorated barium titanate enhances piezoelectric and antibacterial activities of polymer scaffold, Nano Energy 74 (2020) 104825.

[5] F. Qi, Z. Zeng, J. Yao, W. Cai, Z. Zhao, S. Peng, C. Shuai, Constructing core-shell structured BaTiO3@ carbon boosts piezoelectric activity and cell response of polymer scaffolds, Materials Science and Engineering: C 126 (2021) 112129.

[6] Y. Yang, H. Pan, G. Xie, Y. Jiang, C. Chen, Y. Su, Y. Wang, H. Tai, Flexible piezoelectric pressure sensor based on polydopamine-modified BaTiO3/PVDF composite film for human motion monitoring, Sensors and Actuators A: Physical 301 (2020) 111789.

[7] C. Yang, S. Song, F. Chen, N. Chen, Fabrication of PVDF/BaTiO3/CNT piezoelectric energy harvesters with bionic balsa wood structures through 3D printing and supercritical carbon dioxide foaming, ACS Applied Materials & Interfaces 13(35) (2021) 41723-41734.

[8] H. Pei, S. Shi, Y. Chen, Y. Xiong, Q. Lv, Combining solid-state shear milling and FFF 3D-printing strategy to fabricate high-performance biomimetic wearable fish-scale PVDF-based piezoelectric energy harvesters, ACS Applied Materials & Interfaces 14(13) (2022) 15346-15359.

[9] X. Liu, Y. Shang, J. Liu, Z. Shao, C. Zhang, 3D printing-enabled in-situ orientation of BaTi2O5 nanorods in β-PVDF for high-efficiency piezoelectric energy harvesters, ACS Applied Materials & Interfaces 14(11) (2022) 13361-13368.

[10] S. Bodkhe, G. Turcot, F.P. Gosselin, D. Therriault, One-step solvent evaporation-assisted 3D printing of piezoelectric PVDF nanocomposite structures, ACS applied materials & interfaces 9(24) (2017) 20833-20842.

[11] N.A. Shepelin, V.C. Lussini, P.J. Fox, G.W. Dicinoski, A.M. Glushenkov, J.G. Shapter, A.V. Ellis, 3D printing of poly (vinylidene fluoride-trifluoroethylene): a poling-free technique to manufacture flexible and transparent piezoelectric generators, MRS Communications 9(1) (2019) 159-164.

[12] C. Yang, F. Chen, J. Sun, N. Chen, Boosted mechanical piezoelectric energy harvesting of polyvinylidene fluoride/barium titanate composite porous foam based on three-dimensional printing and foaming technology, ACS omega 6(45) (2021) 30769-30778.

[13] N. Arul, M. Suresh, M. Satthiyaraju, N.K. Babu, Flexible electrospun PVDF/WO3 nanocomposite fibers for piezoelectric energy harvesting applications, Polymer Composites 45(1) (2024) 360-372.

[14] Y. Yu, X. Zhao, H. Ge, L. Ye, A self-powered piezoelectric Poly (vinyl alcohol)/Polyvinylidene fluoride fiber membrane with alternating multilayer porous structure for energy harvesting and wearable sensors, Composites Science and Technology 247 (2024) 110429.

[15] M. Kumar, N.D. Kulkarni, P. Kumari, Piezoelectric performance enhancement of electrospun functionally graded PVDF/BaTiO3 based flexible nanogenerators, Materials Research Bulletin (2024) 112739.

[16] A. Kurakula, S.A. Graham, P. Manchi, M.V. Paranjape, J.S. Yu, Enhanced energy harvesting ability of bismuth sodium titanate/polyvinylidene fluoride composite film-based piezoelectric nanogenerators for mechanical energy scavenging and safety-walker applications, Materials Today Sustainability 25 (2024) 100616.

ANNEXE 4

Supporting Information

Advanced Nanocomposites for 4D Printing: High-Performance Electroactive Shape Memory Polymers for Smart Applications

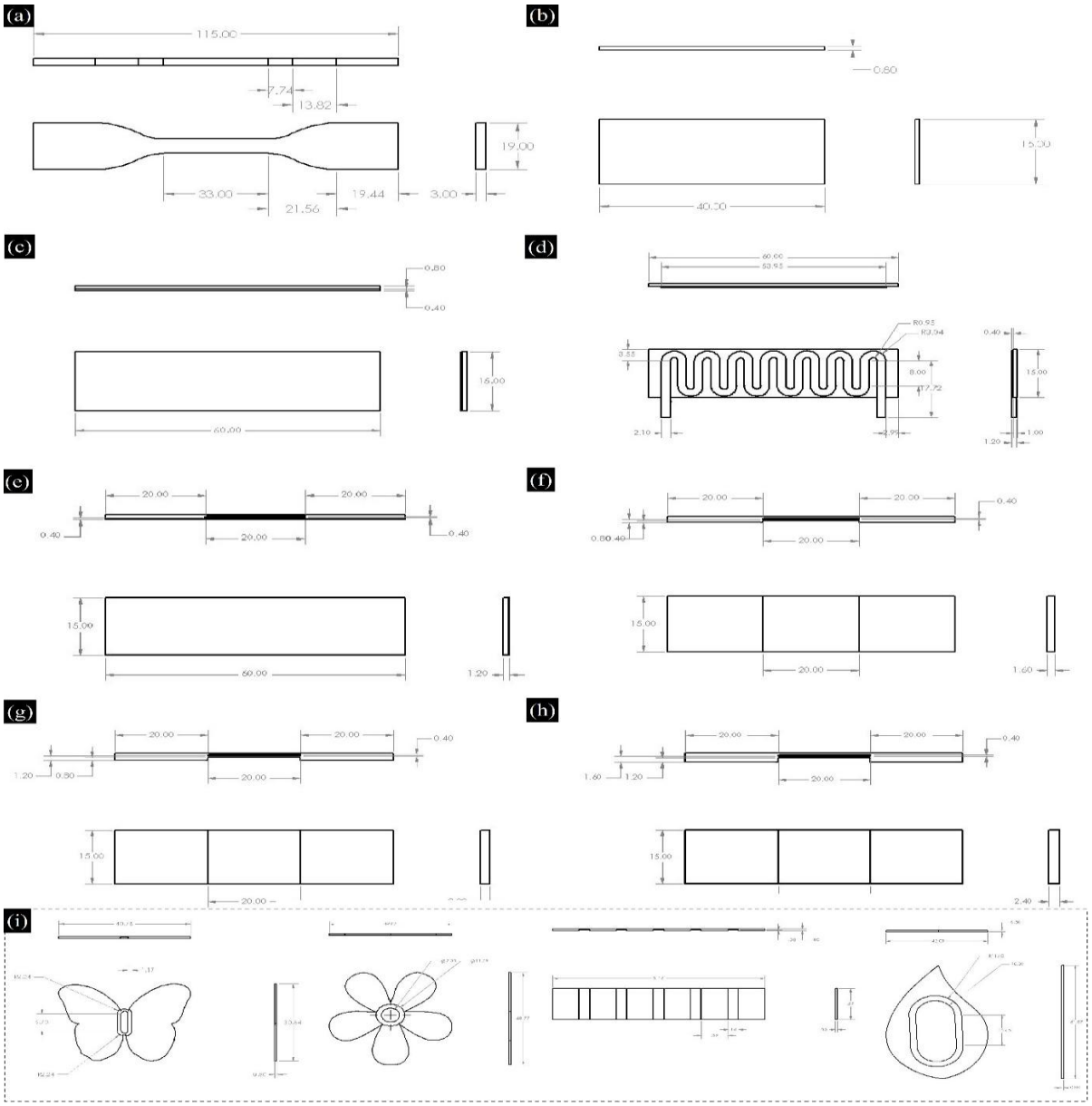

Figure S1: dimensions of (a) tensile specimens according to ASTM D638 type IV standards (b) 3D-printed PLA/MWCNTs samples for electrothermal conversion evaluation, (c) Bio-inspired origami structures for both numerical simulations and experimental validations; Electrorespensive SMP samples with (d) 3 layers, (e) 4 layers, (f) 5 layers, and (g) 6 layers; (h) Structure S2, and (i) structure S3.

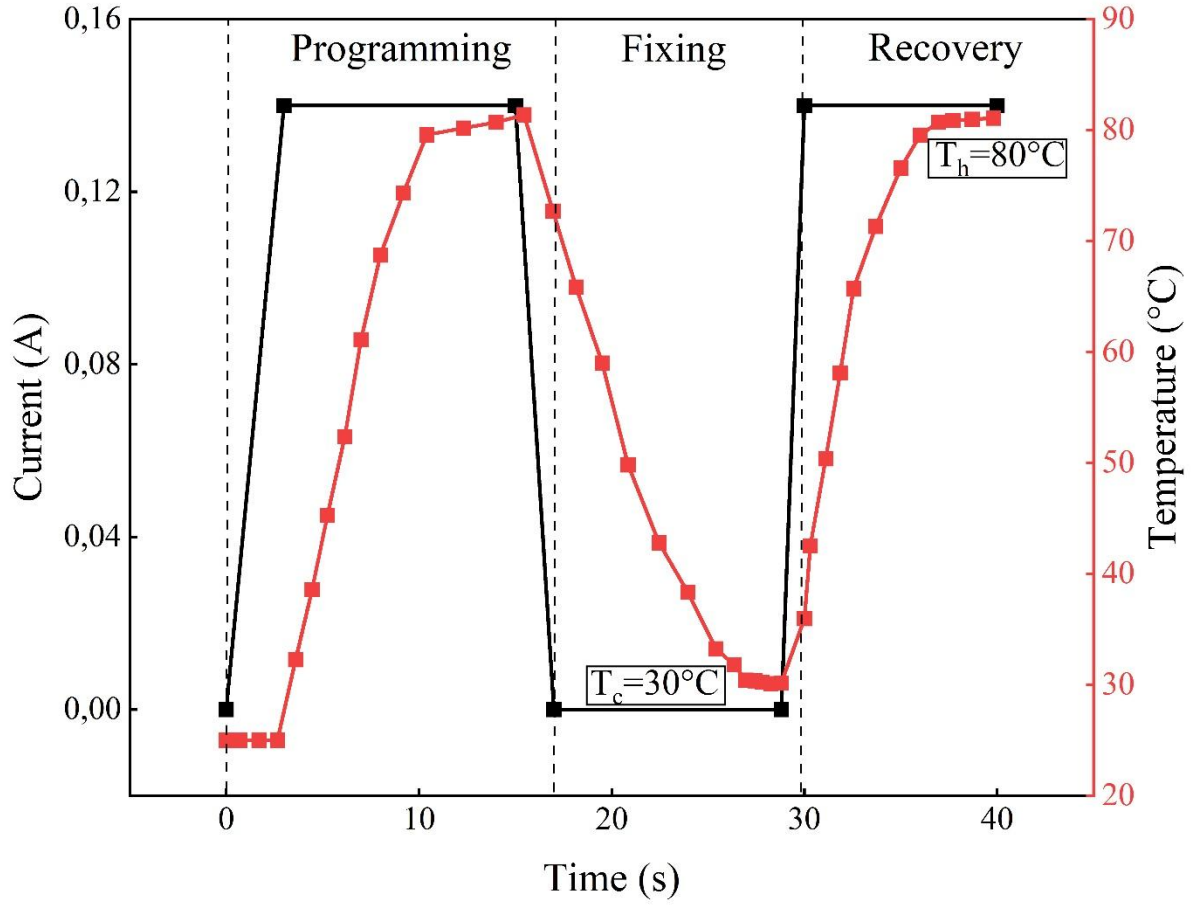

Figure S2: Electrothermal behavior of electroresponsive shape memory polymer during shape memory cycle.

Figure S2 illustrates the thermal and electrical behavior of an electroresponsive shape memory polymer (SMP) during a complete shape memory cycle, which consists of three different phases: programming, fixing, and recovery. In the programming phase, an electric current of 0.14 A is applied, which raises the temperature from 30°C to 80°C and allows the SMP to be deformed into a new shape. During the fixing phase, the current is reduced to zero and the temperature gradually drops back to 30°C, solidifying the material in its programmed shape. In the final recovery phase, the current is reapplied, and the temperature is increased again to 80°C, causing the material to return to its original shape due to the shape memory effect.

Finite element model

Considering the rate of heat generation per unit time and volume within the electrothermal joint, the generalized differential equation governing the temperature distribution is expressed as follows:

$$\rho c \frac{\partial T}{\partial t} = \dot{\Phi}_{JH}(t) + k\nabla^2 T - \dot{\Phi}_{\mathrm{CONV}}$$

The left-hand term represents the increase in internal energy during the transient state, where ρ and c denote the density and the specific heat capacity of the composite, respectively.

$\dot{\Phi}_{JH}(t)$ refers to the Joule heat generated per unit time and per unit volume in the joint and is given by the following expression:

$$\dot{\Phi}_{JH}(t) = \frac{I^2 \rho_0}{S^2}\left(1 + \alpha_F (T(t) - T_0)\right)$$

Here, S represents the cross-sectional area of the joint. The second term on the right side of the equation deals with the standard heat conduction within the hinges and stiff panels, where k is the thermal conductivity of the nanocomposite material. $\dot{\Phi}_{\mathrm{CONV}}$ accounts for natural convection, which is included in the heat transfer analysis to accurately capture the thermal response of the electrothermal joint. The heat loss by convection per unit time and unit volume is expressed as follows:

$$\dot{\Phi}_{\mathrm{CONV}} = \frac{hA}{V}(T_{\mathbf{s}} - T_{\mathbf{a}}),$$

Here, h is the convection coefficient, A and V represent the convection surface area and volume, respectively. T_s denotes the temperature of the convection surface, and T_a is the air temperature in proximity to the convection surfaces.

By applying Boltzmann's superposition principle, the total stress σ as a function of time t is expressed as follows:

$$\sigma(t) = \left(E_{\mathrm{eq.}\,P} + E_{\mathrm{eq.}\,A}\right)e(t) + \sum_{i=1}^{n} E_i \int_0^t \frac{\partial e(s)}{\partial s} \exp\left[-\int_s^t \frac{dt'}{\tau_i(T)}\right] ds,$$

where ε represents the total strain, $E_{eq.P}$ and $E_{eq.A}$ denote the elastic moduli of the equilibrium branches corresponding to the polymer matrix and additive, respectively. Additionally, E_i and $\tau_i(T)$ refer to the elastic modulus and the temperature-dependent relaxation time in the ith nonequilibrium branch, respectively.

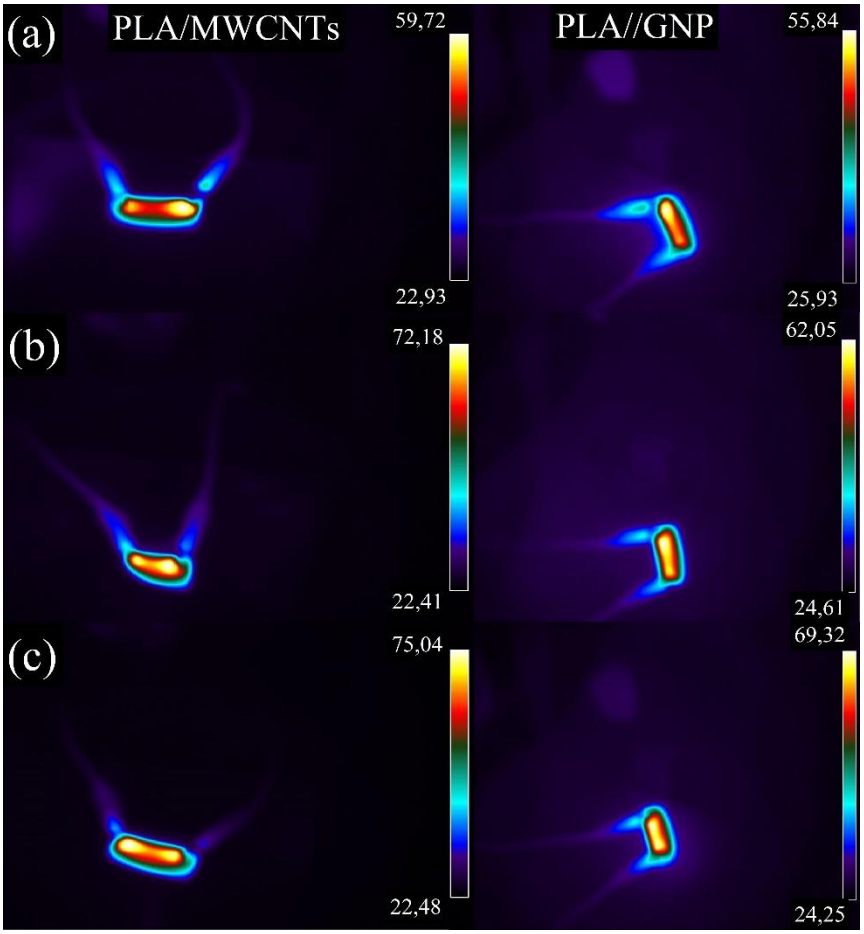

Figure S3: Thermal images of PLA/MWCNTs and PLA/GNP nanocomposites after 10 seconds application of 0.1A electric current at different mass fractions: (a) 5%, (b) 7.5% and (c) 10%

Figure S3 shows a comparison of thermal images between two types of composite materials: PLA/MWCNTs (left column) and PLA/GNP (right column) under similar conditions (I=0.1A, V=10V, t=10s) with three different proportions (5%, 7.5% and 10%). The thermal images illustrate the temperature distribution in each material. The PLA/MWCNTs samples consistently exhibit higher maximum temperatures than the PLA/GNP samples. For example, when the mass fraction of fillers is 10%, the PLA/MWCNTs sample reaches a maximum temperature of about 75.04°C, while the PLA/GNP sample reaches about 69.32°C. This indicates that the PLA/MWCNTs nanocomposite has a higher thermal conductivity, allowing it to heat up more efficiently under the same conditions. The consistent temperature differences demonstrate that the integration of multi-walled carbon nanotubes (MWCNTs) into the PLA matrix leads to more effective heat generation compared to graphene nanoplatelets (GNPs). These results emphasize the superior thermal response of PLA/MWCNTs nanocomposites.

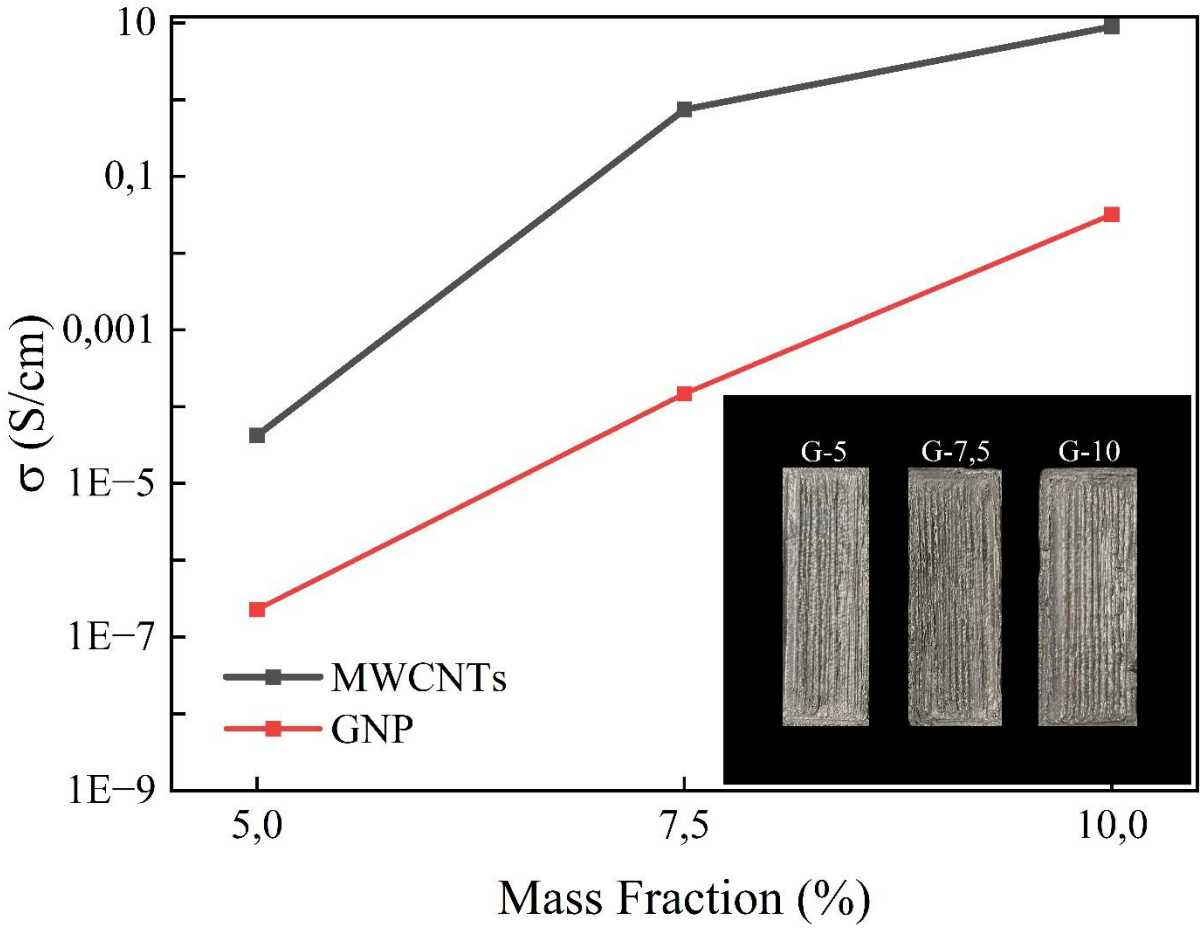

Figure S4: Electrical Conductivity of PLA/MWCNT and PLA/GNP Composites as a Function of Mass Fractions.

Figure S4 shows the relationship between the electrical conductivity and the mass fraction of PLA/MWCNTs and PLA/GNP illustrating their effectiveness in converting electricity into heat. As the mass fraction of MWCNTs and GNPs increases, the electrical conductivity of the composites increases significantly, which improves their ability to convert electrical energy into thermal energy. MWCNTs have a much higher conductivity compared to GNPs at the same mass fraction, making them more effective for applications requiring efficient heat generation from electricity. This is in good agreement with the results in Figure S3.

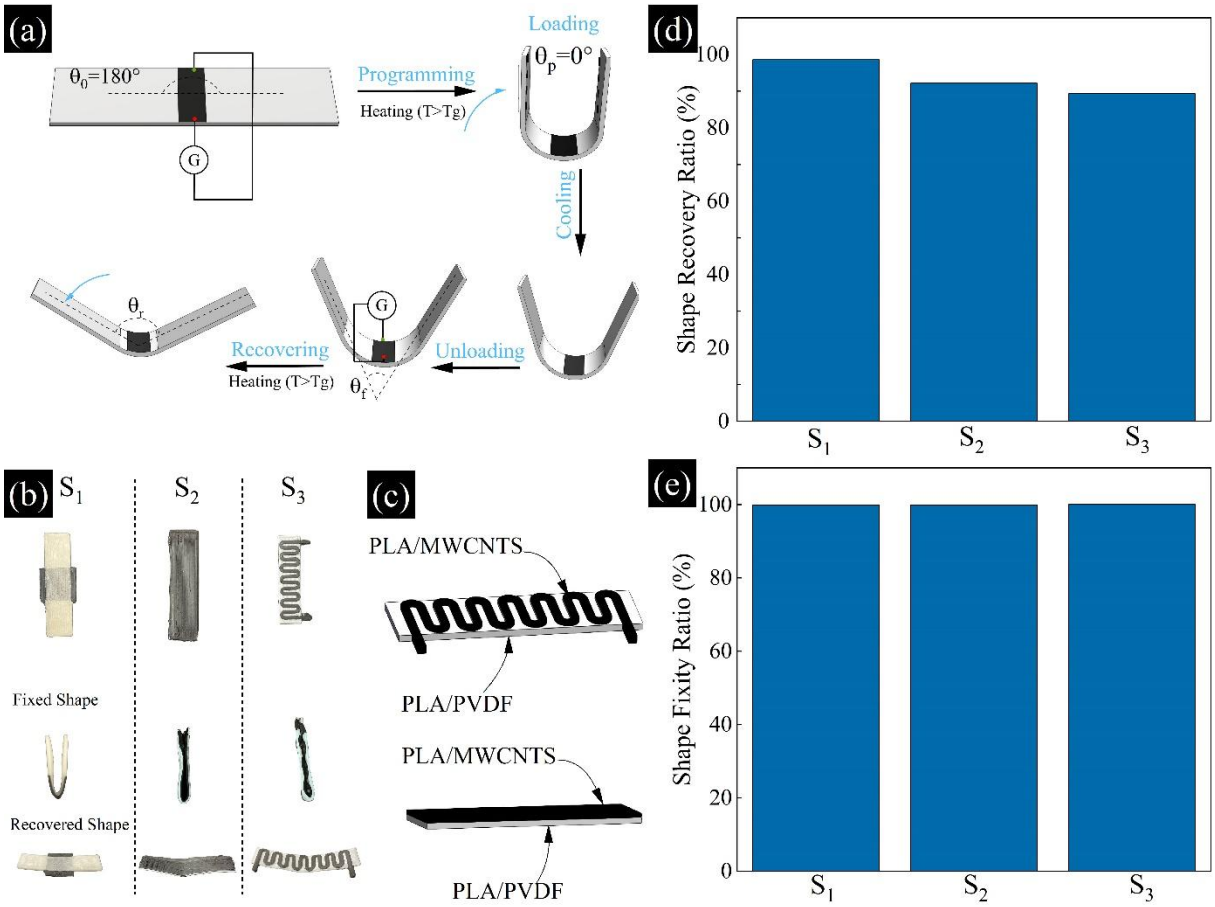

Figure S5: Figure 4: (a) Shape memory cycle: programming, cooling and recovery, (b) Visual appearance of the 3D-printed electrosensitive SMP structures in the initial, fixed and recovered states, (c) Schematic representation of PLA/MWCNTs nanocomposite integration in PLA/PVDF for structures S2 and S3, (d) shape recovery ratio (SRR) and (e) shape fixation ratio (SFR) for the three proposed structures.

To improve heat generation and shape memory performance, three different structures were proposed, tested, and compared. Figure S5 (a) shows the programming and recovery cycle applied to each structure. It illustrates how the samples are heated above the glass transition temperature (T>Tg) for programming, cooled to fix their shape and reheated for recovery. Figure S5 (b) shows photographs of the three structures (S1, S2 and S3) showing their original, fixed and recovered shapes. Figure S5 (c) shows a schematic representation of the structural configurations of S2 and S3, illustrating the integration of the PLA/MWCNTs nanocomposite into the PLA/PVDF samples to enable electrothermal activation. Figures S5 (d) and (e) show bar charts representing the shape recovery ratio (SRR) and shape fixity ratio (SFR) for each sample. The results indicate that although all three structures have high SFR values close to 100%, the SRR of S1 (98.56%) is significantly higher than that of S2 (92.13%) and S3 (89.27%). This difference is due to the design of S1, in which the PLA/MWCNTs nanocomposite is concentrated exclusively in the joint, enabling faster and more efficient heating than in S2 and S3,

where the PLA/MWCNTs nanocomposites are distributed throughout the entire structure, as detailed in Figure S5 (c).

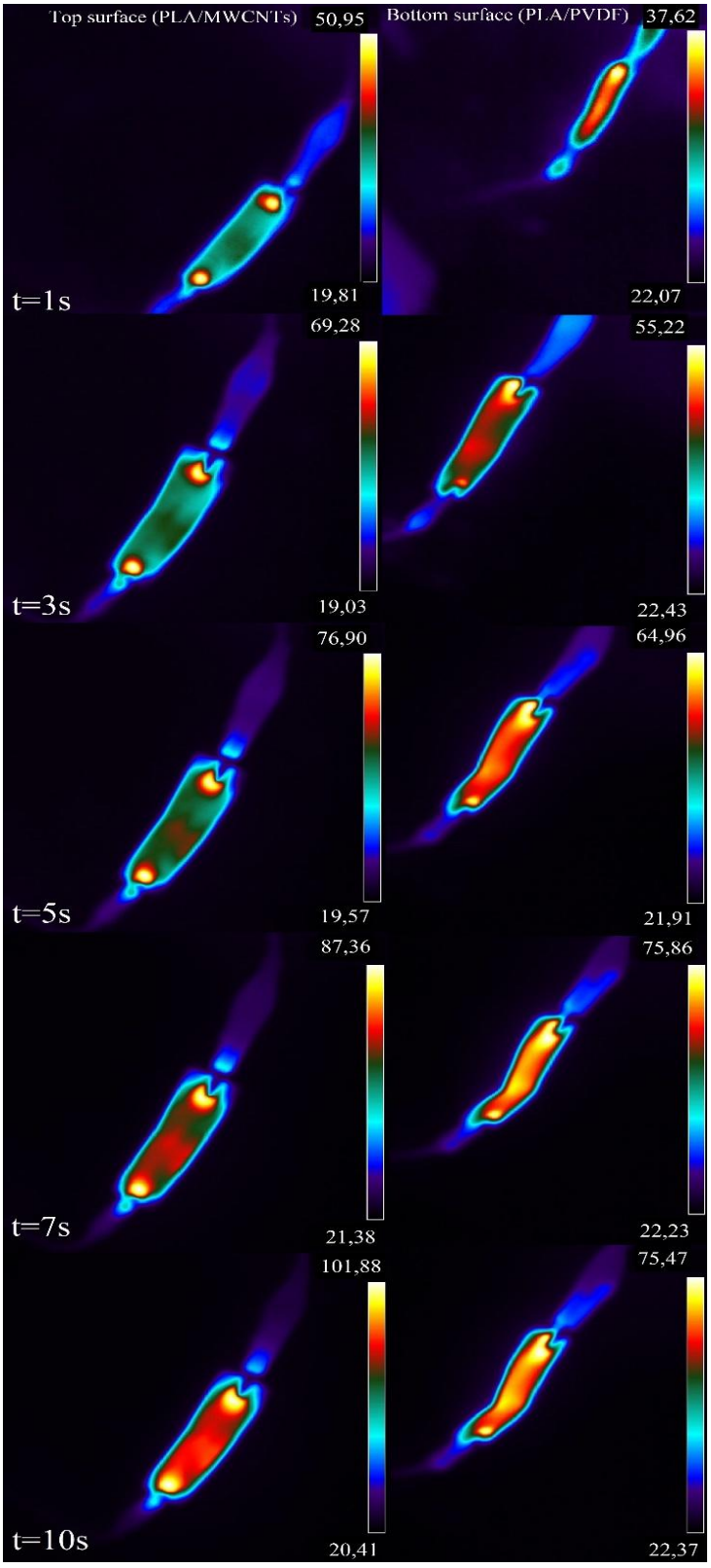

Figure S6: Thermal imaging of S2 shows temperature differences between PLA/MWCNTs regions (top surface) and PLA/PVDF regions (bottom surface) for 10 seconds electrical heating under A=0.14A.

Figure S6 shows thermal images of S2 taken during heating at different time intervals (1s, 3s, 5s, 7s and 10s). The images consistently show that the top surface comprising the PLA/MWCNTs layer reaches significantly higher temperatures, peaking at around 101.88°C, compared to the bottom PLA/PVDF layers which only reach around 75.47°C. This uneven heating suggests that the different thermal response could have a negative impact on the shape recovery process, resulting in a lower shape recovery ratio (SRR).

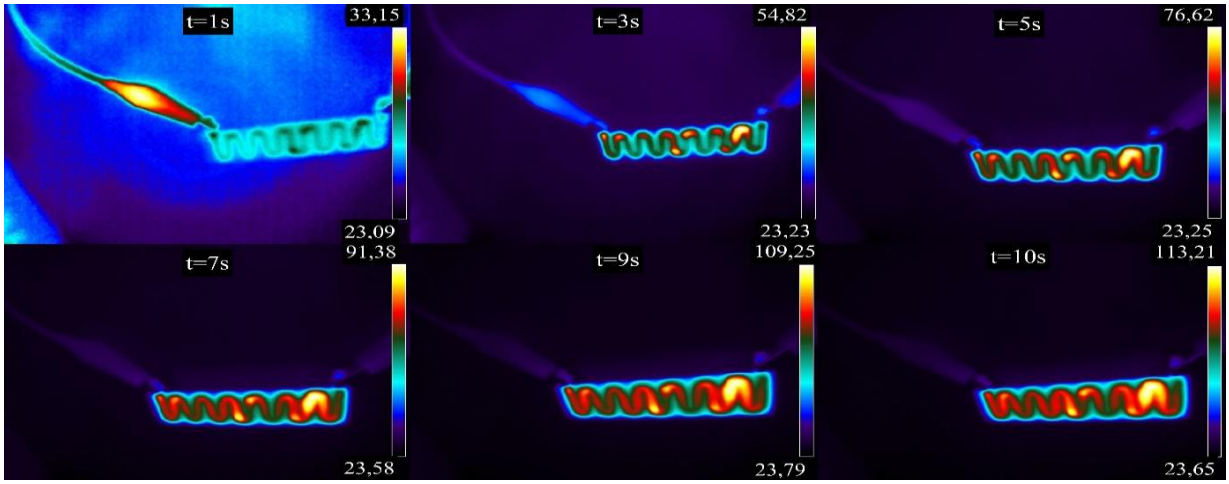

Figure S7: Thermal imaging of S3 shows temperature differences between PLA/MWCNTs regions and PLA/PVDF regions for 10 seconds electrical heating under A=0.14A.

Figure S7 shows thermal images of S3 taken at different time intervals (1s, 3s, 5s, 7s, 9s and 10s) during heating. The PLA/MWCNTs zigzag component heats up rapidly, reaching a temperature of 113.21°C within 10 seconds, while the surrounding PLA/PVDF regions remain significantly cooler. This discrepancy indicates poor heat transfer from the PLA/MWCNTs to the PLA/PVDF regions. The high temperatures reached by the PLA/MWCNTs could lead to thermal damage or degradation of the material over time, while the PLA/PVDF regions do not reach sufficient temperatures to effectively activate a thermal response. As a result, this uneven heating could compromise the overall structural integrity of the material and limit its effectiveness in shape recovery process.

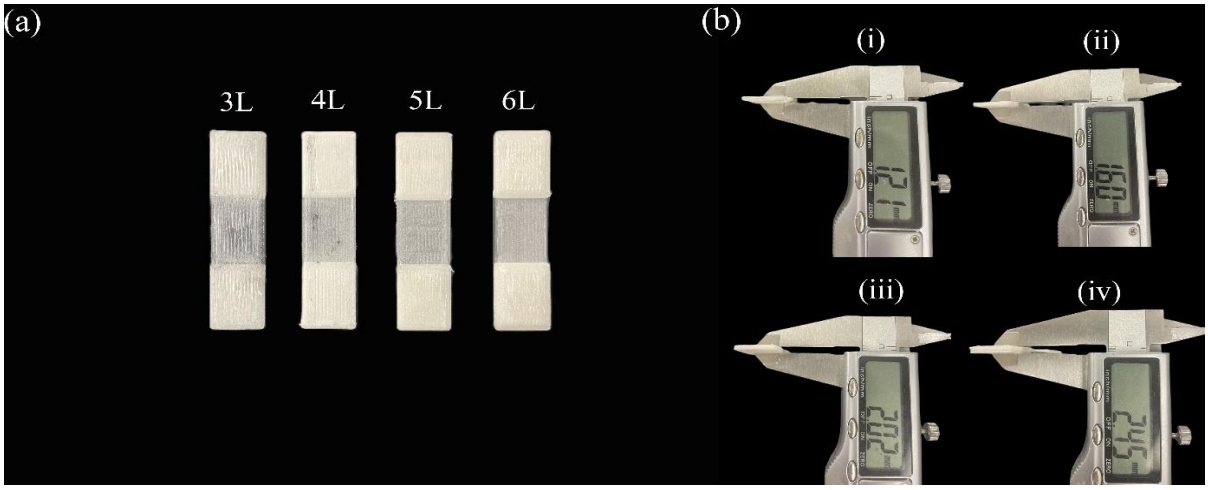

Figure S8: photographs, and (b) caliper measurements of the four-3D printed P5F5 samples with different layers number.

Figures S8 and S9 provides an analysis of shape memory behavior in samples with varying layer counts, denoted as 3L, 4L, 5L, and 6L. Figure S8 (a) shows photographs of the four different samples, visually displaying the structural differences based on the number of layers. Figure S8 (b) presents caliper measurements, confirming consistent dimensions across samples, which ensures uniformity for comparative analysis.

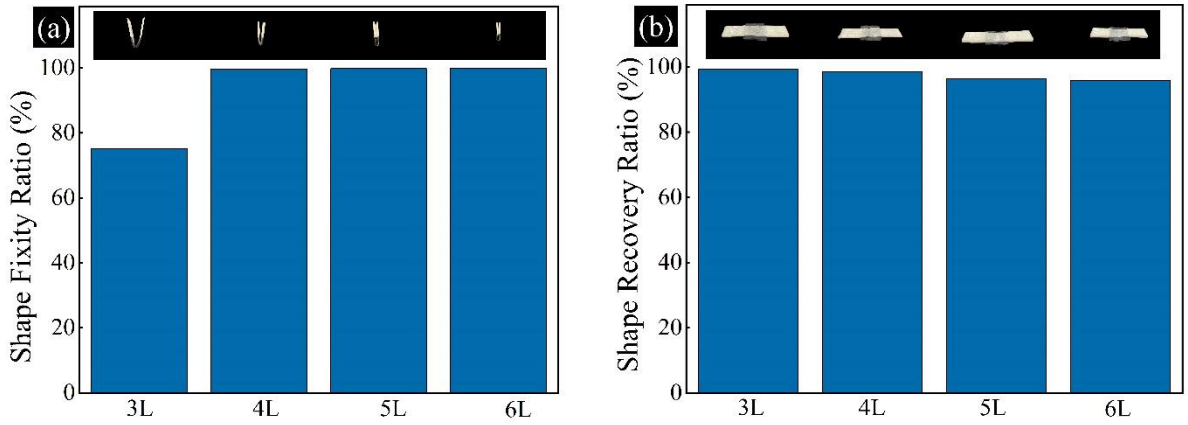

Figure S9: (a) Shape Recovery Ratio (SRR) and (b) Shape Fixity Ratio (SFR) of the four 3D printed P5F5 samples with different layers number.

The bar charts in Figures S9 (a) and (b) show the Shape Recovery Ratio (SRR) and Shape Fixity Ratio (SFR), respectively. All samples exhibit high SRR, close to 100%, indicating excellent shape memory capabilities. However, the SFR shows variation, with the 3L sample demonstrating a lower fixity ratio compared to the others, suggesting that increasing the number of layers improves the ability of the material to retain its deformed shape. These results

highlight the influence of layer count on both the shape recovery and fixity properties, suggesting that more layered structures enhance the material's overall shape memory performance.

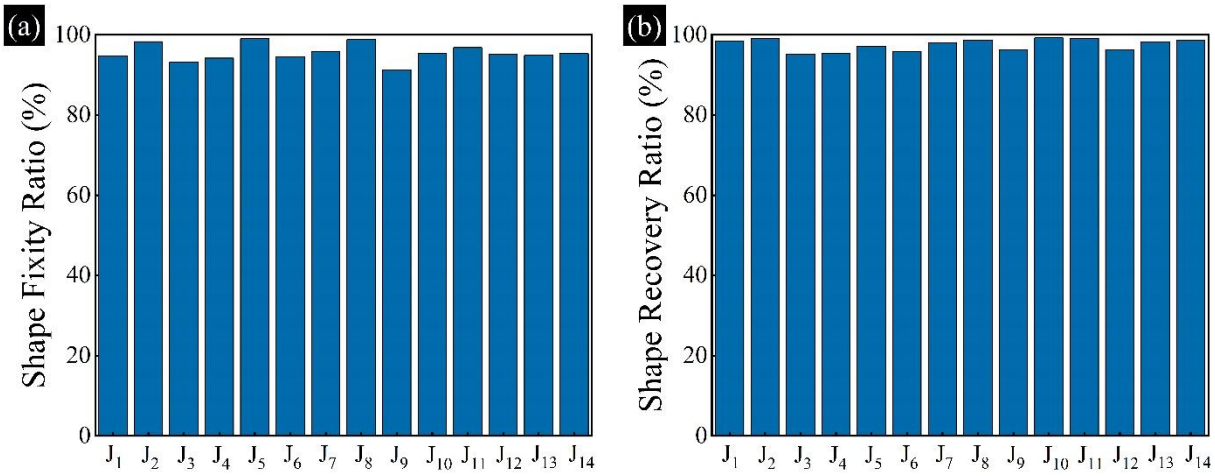

Figure S10: (a) Shape Recovery Ratio (SRR) and (b) Shape Fixity Ratio (SFR) of each joint of the 4D-printed origami robotic hand.

ANNEXE 5

Supporting Information

4D-Printed Multi-Responsive Shape Memory Composite for Enhanced Piezoelectric Energy Harvesting: Adaptive Design and Analytical Modeling

- **L-shaped structure**

Constitutive equations

Assuming an Euler-Bernoulli beam model and Hooke's law, the mechanical strain for both main and auxiliary beams and the stress tensor for the copper layer of the two beams can be written as follows

$$\varepsilon_{\mathrm{i}} = \begin{pmatrix} -yv_{\mathrm{i}}''(x,t) & 0 & 0 \\ 0 & 0 & 0 \\ 0 & 0 & 0 \end{pmatrix},\ \sigma_c = \begin{pmatrix} -E_c yv''(x,t) & 0 & 0 \\ 0 & 0 & 0 \\ 0 & 0 & 0 \end{pmatrix},\ y \in [y_0, y_1] \qquad (\mathbf{S1})$$

For electromechanical coupling effect of piezoelectric material, we assumed linear constitutive equations for the unbounded piezoelectric continuum

$$\sigma_p = E_p{:}\,\varepsilon^p\text{-}e^p.E^p \qquad (\mathbf{S2})$$

$$D^p = e^p{:}\,\varepsilon^p + \epsilon^{\varepsilon^p} \cdot E^p \quad (\mathbf{S3})$$

where D^p denotes the electric displacement matrix, ϵ^{ε^p} denotes the permittivity matrix at constant strain, E^p denotes the electric field matrix, ε^p denotes the strain matrix of piezoelectric layer, σ_p denotes the stress matrix, E_p denotes the elastic stiffness constant matrix, symbol "." and ":" denote dot product and double contraction-point multiplication respectively, e^p denotes the piezoelectric constant matrix at constant stress, which is given by

$$e^p = d^p{:}\,E_p, \quad (\mathbf{S4})$$

Considering only the coefficient e_{31}, the mechanical stress σ_{pi} and the electric displacement D^{pi} of each piezoelectric layer i, can be written as follows:

$$\sigma_{pi} = \begin{pmatrix} -E_{pi} yv_i''(x,t) - e_{31}^{pi} E_3^{pi} & 0 & 0 \\ 0 & 0 & 0 \\ 0 & 0 & 0 \end{pmatrix},\ y \in [y_1, y_2] \quad (\mathbf{S5})$$

$$D^{pi} = \begin{pmatrix} 0 \\ 0 \\ e_{31}^{pi} \cdot \varepsilon_{11}^{pi} + \epsilon_{33}^{\varepsilon^{pi}} \cdot E_3^{pi} \end{pmatrix} \quad \text{(S6)}$$

Hamilton's principle

In this section, Hamilton's principle is applied to formulate a distributed-parameter model for the harvesters and derive the governing equations of motion and the corresponding boundary conditions. The demonstration focuses specifically on the first configuration (a cantilever beam), which consists of a main beam, an auxiliary beam and an SMP section considered as a rigid mass block positioned between the two beams. However, the governing equations of motion and boundary conditions are developed for the four configurations.

Kinetic energy

We used the the extended Hamilton's principle, defined by

$$\int_{t_1}^{t_2} \delta(\mathcal{L} + W_{nc})dt = 0 \qquad \text{(S7)}$$

where $\mathcal{L}$ is the Lagrangian of the system, W_{nc} is the work of the nonconservative forces and δ is the variation which describes infinitesimal changes in the virtual sense. The variation obeys the rules of differential calculus. The lagrangian is defined by:

$$L = T - U, \qquad \text{(S8)}$$

where T and V are respectively the kinetic energy and the potential energy of the system.

The kinetic energy of the main and auxiliary beams can be written respectively as follows

$$T_1 = \int_0^{L_1} \frac{1}{2}\rho A(\dot{v}_1(x,t) + \dot{Y}(t))^2 dx, \quad T_2 = \int_0^{L_2} \frac{1}{2}\rho A\left(\dot{v}_2(x,t)\right)^2 dx + \frac{1}{2}\rho A L_2\left(\dot{v}_1(L_1,t)\right)^2 \qquad \text{(S9)}$$

Where the terms ρ, and A are respectively the density, and the cross section of the composite beams. And the term ρA is given by

$$\rho A = \sum_{i=1}^{2} \int_{-\frac{h_i}{2}}^{\frac{h_i}{2}} \int_{-\frac{b}{2}}^{\frac{b}{2}} \rho_i dz dy \qquad \text{(S10)}$$

with the terms h_i is the thickness of the ist layer.

The SMP component here is considered as a rigid mass block, thus its kinetic energy can be written as follows:

$$T_{m1} = \frac{1}{2}M_1\left(\dot{v}_1(L_1,t)\right)^2 + \frac{1}{2}J_{m1}\left(\dot{v}'_1(L_1,t)\right)^2 + M_1\frac{L_{\mathrm{m}}}{4}\left(\dot{v}_1(L_1,t)\right)\left(\dot{v}'_1(L_1,t)\right),$$

$$T_{m2} = \frac{1}{2} M_2 \left(\dot{v}_1(L_1,t)\right)^2 + \left(\frac{L_\mathrm{m}}{2} + \frac{h_\mathrm{m}}{2}\right)\left(\dot{v}_1(L_1,t)\right)\left(\dot{v}'_1(L_1,t)\right)$$

(S**11**)

Where J_m is the mass moment of inertia.

The variation of the kinetic energy is obtained by applying the differential to Equation (S9) and (S11).

$$\begin{gathered}\int_{t1}^{t2} \delta T dt = -\int_{t1}^{t2} \int_0^{L1} \rho A\left[\ddot{v}_1(x,t) + \ddot{Y}(t)\right]\delta v_1(x,t)dx + \int_0^{L2} \rho A[\ddot{v}_2(x,t)] \\ \delta v_2(x,t)dx + \rho A L_2\left(\ddot{v}_1(L_1,t)\right)\delta v_1(L_1,t) + M_1\left(\ddot{v}_1(L_1,t)\right)\delta v_1(L_1,t) + M_1 \tfrac{L_\mathrm{m}}{4}\left(\ddot{v}_1(L_1,t)\right)\delta v'_1(L_1,t) \\ +M_1 \tfrac{L_\mathrm{m}}{4}\left(\ddot{v}'_1(L_1,t)\right)\delta v_1(L_1,t) + J_{m1}\left(\ddot{v}'_1(L_1,t)\right)\delta v'_1(L_1,t) + +M_2\left(\ddot{v}_1(L_1,t)\right)\delta v_1(L_1,t) + \\ M_2\left(\tfrac{L_\mathrm{m}}{2} + \tfrac{h_\mathrm{m}}{2}\right)\left(\ddot{v}'_1(L_1,t)\right)\delta v_1(L_1,t)\end{gathered} \quad (\mathbf{S12})$$

Potential energy

The potential energy of the main and auxiliary beam U_1 and U_2,can be expressed respectively as follows:

$$U_1 = \tfrac{1}{2}\int_v \sigma_{p1}{:}\,\varepsilon + \sigma_{c1}{:}\,\varepsilon dV,\; U_2 = \tfrac{1}{2}\int_v \sigma_{p2}{:}\,\varepsilon + \sigma_{c2}{:}\,\varepsilon dV \quad (\mathbf{S13})$$

Replacing the strain and stress matrix with their expressions, and assuming that the electric field across the piezoelectric layers is

$$E_3^{pi} = -\tfrac{V_i(t)}{h_{pi}}\left[H(x) - H\left(x - L_j\right)\right], i \in \{1,2\} \quad (\mathbf{S14})$$

where $V_1(\mathrm{t})$ and $V_2(\mathrm{t})$ are the respective output voltages from the main and auxiliary beams. Equation (S13) becomes

$$U_1 = \tfrac{1}{2}\int_0^{L_1} EI_1 v_1''^2(x,t) + \Theta_1 V_1(t)[H(x) - H(x - L_1)]v_1''(x,t)dx \quad (\mathbf{S15})$$

and

$$U_2 = \tfrac{1}{2}\int_0^{L_2} EI_2 v_2''^2(x,t) + \Theta_2 V_2(t)[H(x) - H(x - L_2)]v_2''(x,t)dx \quad (\mathbf{S16})$$

where H (.) designates the Heaviside function, which is added for mathematical reasons. The bending stiffness EI_i of the composite cross section of the i-th beam are given by

$$EI_1 = \tfrac{1}{3}E_{p1}b(y_2^3 - y_1^3) + \tfrac{1}{3}E_{c1}b(y_1^3 - y_0^3) \quad (\mathbf{S17})$$

$$EI_2 = \frac{1}{3}E_{p2}b(y_2^3 - y_1^3) + \frac{1}{3}E_{c2}b(y_1^3 - y_0^3) \quad \text{(S18)}$$

and the piezoelectric coupling term Θ_i for parallel connection is expressed as

$$\begin{aligned}\Theta_1 &= -\frac{1}{2}b\left[e_{31}^{p1}(y_1 + y_2)\right] \\ \Theta_2 &= -\frac{1}{2}b\left[e_{31}^{p2}(y_1 + y_2)\right]\end{aligned} \quad \text{(S19)}$$

The variation of the potential energy of the system is

$$\begin{aligned}\int_{t1}^{t2} \delta U dt = \int_{t1}^{t2} \int_0^{L1} M_{b1}''(x,t)\delta v_1(x,t)dx - \\ [M_{b1}'(x,t)\delta v_1(x,t)]_0^{L1} + [M_{b1}(x,t)\delta v_1'(x,t)]_0^{L1} + \int_0^{L2} M_{b2}''(x,t)\delta v_2(x,t)dx - \\ [M_{b2}'(x,t)\delta v_2(x,t)]_0^{L_2} + [M_{b2}(x,t)\delta v_2'(x,t)]_0^{L_2} dt\end{aligned} \quad \text{(S20)}$$

where $M_{b1}, and\ M_{b2}$ are respectively the bending moment of the main beam and the auxiliary beam.

$$\begin{aligned}M_{b1}(x,t) &= EI_1 v_1''(x,t) + \Theta_1 V_1(t)[H(x) - H(x - L_1)] \\ M_{b2}(x,t) &= EI_2 v_2''(x,t) + \Theta_2 V_2(t)[H(x) - H(x - L_2)]\end{aligned} \quad \text{(S21)}$$

Variation of the non-conservative forces

The auxiliary beam stimulates the main beam's bending in x = L_1 by applying a bending moment opposite to its internal bending moment ($M_{b2}(0,t)$). As a result, the variation of the non-conservative forces for this harvester can be written as follows:

$$\int_{t1}^{t2} \delta W_{nc} dt = \int_{t1}^{t2} -M_{b2}(0,t)\delta v'_1(L_1,t)dt \quad \text{(S22)}$$

Equations of motion and boundary conditions

From (S7), (S8), (S12), (S20) and (S22), we can deduce the equations of motions:

$$\rho A\ddot{v}_1(x,t) + EI_1 v_1''''(x,t) + \Theta_1 V_1(t)[H''(x) - H''(x - L_1)] = -\rho A\ddot{Y}(t) \quad \text{(S23)}$$

$$\rho A[\ddot{v}_2(x,t)] + EI_2 v_2''''(x,t) + \Theta_2 V_2(t)[H''(x) - H''(x - L_2)] = 0, \quad \text{(S24)}$$

and the associated boundary conditions

$$
\begin{gathered}
v_1(0,t)=0 \\
v_1'(0,t)=0 \\
EI_1 v_1''(L_1,t)=-J_{m1}\left(\ddot{v}'_1(L_1,t)\right)-M_1\frac{L_\mathrm{m}}{4}\left(\ddot{v}_1(L_1,t)\right)+EI_2 v_2''(0,t) \\
EI_1 v_1'''(L_1,t)=(\mathrm{M}+\rho AL_2)\left(\ddot{v}_1(L_1,t)\right)+M_1\frac{L_\mathrm{m}}{4}\ddot{v}'_1(L_1,t)+M_2\left(\frac{L_\mathrm{m}}{2}+\frac{h_\mathrm{m}}{2}\right)\ddot{v}'_1(L_1,t) \\
v_2(0,t)=0 \\
v_2'(0,t)=0 \\
EI_2 v_2''(L_2,t)=0 \\
EI_{gz} v_2'''(L_2,t)=0
\end{gathered}
\qquad (\mathbf{S25})
$$

where $J_{m1}=\frac{1}{12}M_{\mathrm{m1}}\left(h_\mathrm{m}^2+\frac{{L_\mathrm{m}}^2}{4}\right)+M_1(\frac{L_\mathrm{m}}{4})^2$,

Electrical equations

The electric current I is given by applying Gauss's and Kirchhoff's laws,

$$
I_i=\frac{\mathrm{d}}{\mathrm{d}t}\int_A D_3^{pi}\,\mathrm{d}A, i\in\{1,2\} \qquad (\mathbf{S26})
$$

Using the expression of the electric displacement (Equation (S6)), the electric currents generated by piezoelectric layers of the harvester in parallel connection can be written as follows

$$
\begin{gathered}
-\left(h_{cp1}e_{31}\right)b\int_0^{L_1}\dot{v}_1''\mathrm{d}x-\left(\frac{\epsilon_{33}^{sp1}}{h_{p1}}\right)bL_1\dot{V}_1(t)=\frac{V_1(t)}{R_1} \\
-\left(h_{cp2}e_{31}\right)b\int_0^{L_2}\dot{v}_2''\mathrm{d}x-\left(\frac{\epsilon_{33}^{sp2}}{h_{p2}}\right)bL_2\dot{V}_2(t)=\frac{V_2(t)}{R_2}
\end{gathered}
\qquad (\mathbf{S27})
$$

where h_{cpi} ($\mathrm{i}\in\{1,2\}$) are given by

$$
h_{cp1}=\frac{h_{s1}+h_{p1}}{2}, h_{cp2}=\frac{h_{s2}+h_{p2}}{2} \qquad (\mathbf{S28})
$$

Equation (S27) can be written as

$$
\begin{gathered}
C_{p1}\dot{V}_1(t)+\frac{V_1(t)}{R_1}=bk_1\left(\dot{v}'_1(L_1,t)-\dot{v}'_1(0,t)\right) \\
C_{p2}\dot{V}_2(t)+\frac{V_2(t)}{R_2}=bk_2\left(\dot{v}'_2(L_2,t)-\dot{v}'_2(0,t)\right)
\end{gathered}
\qquad (\mathbf{S29})
$$

where

$$
\begin{gathered}
C_{p1}=\left(\frac{\epsilon_{33}^{sp1}}{h_{p1}}\right)bL_1 \\
C_{p2}=\left(\frac{\epsilon_{33}^{sp2}}{h_{p2}}\right)bL_2
\end{gathered}
\qquad (\mathbf{S30})
$$

are respectively the internal capacitances of the piezoelectric layers of the main and auxiliary composite beams, and $k_1, and\ k_2$ indicate constants related to material properties and beam geometries, which are represented by

$$\begin{matrix} k_1 = -h_{cp1}e_{31}^{p1} \\ k_2 = -h_{cp2}e_{31}^{p2} \end{matrix} \quad \text{(S31)}$$

Structural natural frequencies and mode shapes

To calculate the natural frequencies and corresponding mode shapes, the deflections $v_i(\mathrm{x},\mathrm{t})$ of the two composite beams are represented by separable functions of time and space.

$$\begin{matrix} v_1(x,t) = \phi_1(x)exp\ (i\omega t) \\ v_2(x,t) = \phi_2(x)exp\ (i\omega t) \end{matrix} \quad \text{(S32)}$$

where $\phi_1(x), and\ \phi_2(x)$ are respectively the eigenfunctions of the bending of the main and auxiliary beams.

The eigenvalue problem that results is written as follows:

$$\phi_1''''(x) - \frac{\rho A\omega^2}{EI_1}\phi_1(x) = 0 \quad \text{(S33)}$$

$$\phi_2''''(x) - \frac{\rho A\omega^2}{EI_2}\phi_2(x) = 0 \quad \text{(S34)}$$

and the associated boundary conditions are:

$$\begin{matrix} \phi_1(0) = 0 \\ \phi_1'(0) = 0 \\ EI_1\phi_1''(L_1) = -J_{m1}\omega^2\phi_1'(L_1) - M_1\frac{L_\mathrm{m}}{4}\omega^2\phi_1(L_1) \\ +EI_2\phi_2''(0) \\ EI_1\phi_1'''(L_1) = (\mathrm{M} + \rho AL_2)\omega^2\phi_1(L_1) + M_1\frac{L_\mathrm{m}}{4}\omega^2\phi'_1(L_1) + M_2\left(\frac{L_\mathrm{m}}{2} + \frac{h_\mathrm{m}}{2}\right)\omega^2\phi'_1(L_1) \\ \phi_2(0) = 0 \\ \phi_2'(0) = 0 \\ EI_2\phi_2''(L_2) = 0 \\ EI_2\phi_2'''(L_2) = 0 \end{matrix} \quad \text{(S35)}$$

The general solutions of Equations (S33) and (S34) are given by

$$\begin{matrix} \phi_1(x) = A_1cos\ (\beta_1 x) + B_1sin\ (\beta_1 x) + C_1cosh\ (\beta_1 x) + D_1sinh\ (\beta_1 x) \\ \phi_2(x) = A_2cos\ (\beta_2 x) + B_2sin\ (\beta_2 x) + C_2cosh\ (\beta_2 x) + D_2sinh\ (\beta_2 x) \end{matrix} \quad \text{(S36)}$$

where A_i, B_i, C_i and D_i are the modal coefficients of the eigenfunctions. And β_i are the frequency number, which are obtained as

$$\beta_1 = \sqrt[4]{\frac{\rho A\omega^2}{EI_1}}, \beta_2 = \sqrt[4]{\frac{\rho A\omega^2}{EI_2}} \quad \text{(S37)}$$

Reduced-order model and analytical solution

In this section, we use the Galerkin procedure and the Euler-Lagrange method to discretize the ROM for the considered configurations, based on exploiting the systems' natural frequencies and corresponding mode shapes in bending movements. Then the dynamic responses, and the electric voltage outputs are presented in terms of closed-form formulas.

Reduced order model

Using the Galerkin, we can define the deflections $v_i(x,t)$ of the two composite beams as an absolutely and uniformly convergent series of the eigenfunctions

$$\begin{matrix} v_1(x,t) = \sum_{r=1}^{\infty} \phi_{1r}(x)\eta_r(t) \\ v_2(x,t) = \sum_{r=1}^{\infty} \phi_{2r}(x)\eta_r(t) \end{matrix} \quad \text{(S38)}$$

where $\phi_{1r}(\mathrm{x}), and\ \phi_{2r}(\mathrm{x})$ are the eigenfunctions of respectively the bending of the main beam, and the bending of the auxiliary beam, and $\eta_r(\mathrm{t})$ are the modal coordinates of the displacements $v_1\ and\ v_2$ in the orthogonal base formed by the the eigenfunction for the r-th mode. The aim of this subsection is to create a reduced-order model of the structure using the Euler Lagrange approach, so, we limit ourselves to the first two structural mode shapes to discretize the system. This choice is linked to the application of applied excitation frequencies, which are generally lower than the third structural natural frequency. The Euler-Lagrange approach is defined as follows:

$$\frac{d}{dt}\frac{\partial \mathcal{L}}{\partial \dot{\eta}_s} - \frac{\partial \mathcal{L}}{\partial \eta_s} = 0 \quad \text{(S39)}$$

where $\mathcal{L}$ is Lagrangian of the system which is introduced in Equation 2.40. Using the expressions of kinetic energy and potential energy developed in the previous chapter, the Lagrangian can be written as follows:

$$\begin{aligned} L = \frac{1}{2}\int_0^{L_1} \rho A\left(\dot{v}_1(x,t) + \dot{Y}(t)\right)^2 - EI_1 v_1''^2(x,t) - \Theta_1 V_1(t) v_1''(x,t)dx + \frac{1}{2}\int_0^{L_2} \rho A\left(\dot{v}_2(x,t)\right)^2 - \\ EI_2 v_2''^2(x,t) - \Theta_2 V_2(t) v_2''(x,t)dx + \frac{1}{2}\rho A L_2\left(\dot{v}_1(L_1,t)\right)^2 + \frac{1}{2}M_1\left(\dot{v}_1(L_1,t)\right)^2 + \frac{1}{2}J_{m1}\left(\dot{v}'_1(L_1,t)\right)^2 + \\ M_1\frac{L_\mathrm{m}}{4}\left(\dot{v}_1(L_1,t)\right)\left(\dot{v}'_1(L_1,t)\right) \\ + \frac{1}{2}M_2\left(\dot{v}_1(L_1,t)\right)^2 + M_2\left(\frac{L_\mathrm{m}}{2} + \frac{h_\mathrm{m}}{2}\right)\left(\dot{v}_1(L_1,t)\right)\left(\dot{v}'_1(L_1,t)\right) \end{aligned} \quad \text{(S40)}$$

Substituting Equation (S38) into Equation (S40), we obtain

$$
\begin{aligned}
L = {} & \frac{1}{2}\int_0^{L_1} \rho A\left(\sum_{r=1}^{2} \phi_{1r}(x)\dot{\eta}_r(t) + \dot{Y}(t)\right)^2 - EI_1 \sum_{r=1}^{2} \phi_{1r}''^2(x)\eta_r^2(t) - \\
& \Theta_1 V_1(t) \sum_{r=1}^{2} \phi_{1r}''(x)\eta_r(t) + \frac{1}{2}\int_0^{L_2} \rho A \sum_{r=1}^{2} (\phi_{2r}(x)\dot{\eta}_r(t))^2 - EI_2 \sum_{r=1}^{2} \phi_{2r}''^2(x)\eta_r^2(t) \\
& -\Theta_2 V_2(t) \sum_{r=1}^{2} \phi_{2r}''(x)\eta_r(t)dx + \frac{1}{2}M_1 \sum_{r=1}^{2} \phi_{1r}^2(L_1)\dot{\eta}_r^2(t) + \frac{1}{2}J_{m1} \sum_{r=1}^{2} \phi_{1r}'^2(L_1)\dot{\eta}_r^2(t) \\
& + M_1 \frac{L_{\mathrm{m}}}{4}\left(\sum_{r=1}^{2} \phi_{1r}^2(L_1)\dot{\eta}_r^2(t)\right)\left(\sum_{r=1}^{2} \phi_{1r}'^2(L_1)\dot{\eta}_r^2(t)\right) + \frac{1}{2}M_2 \sum_{r=1}^{2} \phi_{1r}^2(L_1)\dot{\eta}_r^2(t) \\
& + M_2\left(\frac{L_{\mathrm{m}}}{2} + \frac{h_{\mathrm{m}}}{2}\right)\left(\sum_{r=1}^{2} \phi_{1r}^2(L_1)\dot{\eta}_r^2(t)\right)\left(\sum_{r=1}^{2} \phi_{1r}'^2(L_1)\dot{\eta}_r^2(t)\right)
\end{aligned}
\tag{S41}
$$

Using the orthogonality conditions for the L-shaped bimorph beam-mass structure with torsional and bending mode

$$
\begin{gathered}
EI_1 \int_0^{L_1} \phi_{1r}''(x)\phi_{1s}''(x)dx + EI_2 \int_0^{L_2} \phi_{2r}''(x)\phi_{2s}''(x)dx = \omega_r^2 \delta_{rs} \\
\int_0^{L_1} (\rho A)\phi_{1r}\phi_{1s}\,\mathrm{d}x + \int_0^{L_2} (\rho A)\phi_{2r}\phi_{2s}\mathrm{d}x + (\rho A)L_2\phi_{1r}(L_1)\phi_{1s}(L_1) + M_1\phi_{1r}(L_1)\phi_{1s}(L_1) \\
+J_{\mathrm{m1}}\phi_{1r}'(L_1)\phi_{1s}'(L_1) + M_1\frac{L_{\mathrm{m}}}{4}\left(\phi_{1r}'(L_1)\phi_{1s}(L_1) + \phi_{1r}(L_1)\phi_{1s}'(L_1)\right) + M_2\phi_{1r}(L_1)\phi_{1s}(L_1) \\
+M_2\left(\frac{L_{\mathrm{m}}}{2} + \frac{h_{\mathrm{m}}}{2}\right)\left(\phi_{1r}'(L_1)\phi_{1s}(L_1) + \phi_{1r}(L_1)\phi_{1s}'(L_1)\right) = \delta_{rs}
\end{gathered}
\tag{S42}
$$

we obtain the forced equation of motion in modal coordinates

$$
\ddot{\eta}_r(t) + 2\xi_r\omega_r\dot{\eta}_r(t) + \omega_r^2\eta_r(t) + \chi_{1r}V_1(t) + \chi_{2r}V_2(t) = f_r(t), r \in \{1,2\} \tag{S43}
$$

where ξ_r is the modal damping ratio of the r-th bending vibration mode, χ_{ir} are the modal electromechanical coupling terms, which are given by

$$
\begin{aligned}
\chi_{1r} &= \Theta_1(\phi_{1r}'(L_1) - \phi_{1r}'(0)) \\
\chi_{2r} &= \Theta_2(\phi_{2r}'(L_i) - \phi_{2r}'(0))
\end{aligned}
\tag{S44}
$$

and $f_r(\mathrm{t})$ is the modal force given by

$$
f_r(t) = -\int_0^{L_1} \rho A\phi_{1r}(x)dx\ddot{Y}(t) \tag{S45}
$$

Substituting equation (S38) into equation (S29), the governing circuit equations are written as

$$
\begin{aligned}
C_{p1}\dot{V}_1(t) + \frac{V_1(t)}{R_1} &= \sum_{r=1}^{2} K_{1r}\,\dot{\eta}_r(t) \\
C_{p2}\dot{V}_2(t) + \frac{V_2(t)}{R_2} &= \sum_{r=1}^{2} K_{2r}\dot{\eta}_r(t)
\end{aligned}
\tag{S46}
$$

where K_{1r} and K_{3r} are the r-th modal coupling terms of the piezoelectric layers of the main beam, and K_{2r} is the r-th modal coupling term of the piezoelectric layers of the auxiliary beam

$$
K_{ir} = k_i b(\phi_{ir}'(L_i) - \phi_{ir}'(0)), i \in \{1,2\}. \tag{S47}
$$

Analytical solution

We note that $Y(t) = \Im[Y_0 e^{j\Omega t}]$, where $\Im$ stands for the imaginary part. Consequently, we seek the solutions of Equations (S43), and (S46) in the form

$$\begin{matrix} \eta_r(t) = \Im[H_r e^{j\Omega t}], r \in \{1,2\} \\ V_i(t) = \Im[U_i e^{j\Omega t}], i \in \{1,2\} \end{matrix} \quad (\mathbf{S48})$$

Substituting Equation (S48) into Equation (S43),

$$H_r = \frac{f_{r0} - \chi_i U_1 - \chi_2 U_2}{\omega_r^2 - \omega^2 + 2\xi\omega_r\omega j} \quad (\mathbf{S49})$$

where f_{r0} is the complex amplitude of the modal force function $f_r(t)$

$$f_{r0}(t) = -\int_0^{L_1} \rho A \phi_{1r}(x) dx \ddot{Y}_0 \quad (\mathbf{S50})$$

Considering Equation (S46), we obtain the following equation system

$$\begin{cases} U_1 Z_1 = Z_3 - Z_2 U_2 \\ U_2 Z_5 = Z_6 - Z_4 U_1 \end{cases} \quad (\mathbf{S51})$$

Finally, the steady state voltage outputs are given by

$$\begin{matrix} U_1 = \frac{Z_3 Z_5 - Z_2 Z_6}{Z_1 Z_5 - Z_2 Z_4} \\ U_2 = \frac{Z_1 Z_6 - Z_3 Z_4}{Z_1 Z_5 - Z_2 Z_4} \end{matrix}, \quad (\mathbf{52})$$

where

$$\begin{matrix} Z_1 = jC_{p1}\Omega + \frac{1}{R_1} + \sum_{r=1}^{2} \frac{\Omega j}{\omega_r^2 - \Omega^2 + 2j\xi_r\omega_r\Omega} (K_{1r})\chi'_{1r} \\ Z_2 = \sum_{r=1}^{2} \frac{\Omega j}{\omega_r^2 - \Omega^2 + 2j\xi_r\omega_r\Omega} (K_{1r})\chi_{2r} \\ Z_3 = \sum_{r=1}^{2} \frac{\Omega j}{\omega_r^2 - \Omega^2 + 2j\xi_r\omega_r\Omega} (K_{1r}) f_{r0} \\ Z_4 = \sum_{r=1}^{2} \frac{\Omega j}{\omega_r^2 - \Omega^2 + 2j\xi_r\omega_r\Omega} K_{2r}\chi'_{1r} \\ Z_5 = jC_{p2}\Omega + \frac{1}{R_2} + \sum_{r=1}^{2} \frac{\Omega j}{\omega_r^2 - \Omega^2 + 2j\xi_r\omega_r\Omega} K_{2r}\chi_{2r} \\ Z_6 = \sum_{r=1}^{2} \frac{\Omega j}{\omega_r^2 - \Omega^2 + 2j\xi_r\omega_r\Omega} K_{2r} f_{r0} \end{matrix} \quad (\mathbf{S53})$$

- **V-shaped structure**

Constitutive equations

Assuming an Euler-Bernoulli beam model and Hooke's law, the mechanical strain for both main and auxiliary beams and the stress tensor for the copper layer of the two beams can be written as follows

$$\varepsilon_{\mathrm{i}} = \begin{pmatrix} -yv_{\mathrm{i}}''(x,t) & 0 & 0 \\ 0 & 0 & 0 \\ 0 & 0 & 0 \end{pmatrix},\ \sigma_c = \begin{pmatrix} -E_c yv''(x,t) & 0 & 0 \\ 0 & 0 & 0 \\ 0 & 0 & 0 \end{pmatrix}, y \in [y_0, y_1] \quad \text{(S54)}$$

For electromechanical coupling effect of piezoelectric material, we assumed linear constitutive equations for the unbounded piezoelectric continuum

$$\sigma_p = E_p : \varepsilon^p - e^p . E^p \quad \text{(S55)}$$

$$D^p = e^p : \varepsilon^p + \epsilon^{\varepsilon^p} \cdot E^p \quad \text{(S56)}$$

where D^p denotes the electric displacement matrix, ϵ^{ε^p} denotes the permittivity matrix at constant strain, E^p denotes the electric field matrix, ε^p denotes the strain matrix of piezoelectric layer, σ_p denotes the stress matrix, E_p denotes the elastic stiffness constant matrix, symbol "." and ":" denote dot product and double contraction-point multiplication respectively, e^p denotes the piezoelectric constant matrix at constant stress, which is given by

$$e^p = d^p : E_p, \quad \text{(S57)}$$

Considering only the coefficient e_{31}, the mechanical stress σ_{pi} and the electric displacement D^{pi} of each piezoelectric layer i, can be written as follows:

$$\sigma_{pi} = \begin{pmatrix} -E_{pi} yv_i''(x,t) - e_{31}^{pi} E_3^{pi} & 0 & 0 \\ 0 & 0 & 0 \\ 0 & 0 & 0 \end{pmatrix},\ y \in [y_1, y_2] \quad \text{(S58)}$$

$$D^{pi} = \begin{pmatrix} 0 \\ 0 \\ e_{31}^{pi} \cdot \varepsilon_{11}^{pi} + \epsilon_{33}^{\varepsilon^{pi}} \cdot E_3^{pi} \end{pmatrix} \quad \text{(S59)}$$

In the following subsections, the analytical solutions of the electromechanical coupling equations of the harvesters with bending modes are deduced.

Hamilton's principle

In this section, Hamilton's principle is applied to formulate a distributed-parameter model for the harvesters and derive the governing equations of motion and the corresponding boundary conditions. The demonstration focuses specifically on the first configuration (a cantilever beam), which consists of a main beam, an auxiliary beam and an SMP section considered as a rigid mass block positioned between the two beams. However, the governing equations of motion and boundary conditions are developed for the four configurations.

Kinetic energy

We used the the extended Hamilton's principle, defined by

$$\int_{t_1}^{t_2} \delta(\mathcal{L} + W_{nc})dt = 0 \qquad \text{(S60)}$$

where $\mathcal{L}$ is the Lagrangian of the system, W_{nc} is the work of the nonconservative forces and δ is the variation which describes infinitesimal changes in the virtual sense. The variation obeys the rules of differential calculus. The lagrangian is defined by:

$$L = T - U, \qquad \text{(S61)}$$

where T and V are respectively the kinetic energy and the potential energy of the system.

The kinetic energy of the main and auxiliary beams can be written respectively as follows

$$T_1 = \int_0^{L_1} \frac{1}{2}\rho A(\dot{v}_1(x,t) + \dot{Y}(t))^2 dx, \quad T_2 = \int_0^{L_2} \frac{1}{2}\rho A\left(\dot{v}_2(x,t)\right)^2 dx + \frac{1}{2}\rho A L_2\left(\dot{v}_1(L_1,t)\right)^2 \qquad \text{(S62)}$$

Where the terms ρ, and A are respectively the density, and the cross section of the composite beams. And the term ρA is given by

$$\rho A = \sum_{i=1}^{2} \int_{-\frac{h_i}{2}}^{\frac{h_i}{2}} \int_{-\frac{b}{2}}^{\frac{b}{2}} \rho_i dz dy \qquad \text{(S63)}$$

with the terms h_i is the thickness of the ist layer.

The SMP component here is considered as a rigid mass block, thus its kinetic energy can be written as follows:

$$T_{m1} = \frac{1}{2}M_1\left(\dot{v}_1(L_1,t)\right)^2 + \frac{1}{2}J_{m1}\left(\dot{v}'_1(L_1,t)\right)^2 + M_1\frac{L_\mathrm{m}}{4}\left(\dot{v}_1(L_1,t)\right)\left(\dot{v}'_1(L_1,t)\right),$$

$$T_{m2} = \frac{1}{2}M_2\left(\dot{v}_1(L_1,t)\right)^2 + M_2\left(\frac{L_\mathrm{m}}{4}cos\,(\alpha) + \frac{h_\mathrm{m}}{2}\right)\left(\dot{v}_1(L_1,t)\right)\left(\dot{v}'_1(L_1,t)\right)$$

(S64)

Where J_m is the mass moment of inertia.

The variation of the kinetic energy is obtained by applying the differential to Equation (S62) and (S64).

$$\begin{gathered}\int_{t1}^{t2} \delta T dt = -\int_{t1}^{t2}\int_0^{L1} \rho A\left[\ddot{v}_1(x,t) + \ddot{Y}(t)\right]\delta v_1(x,t)dx + \int_0^{L2} \rho A[\ddot{v}_2(x,t)] \\ \delta v_2(x,t)dx + \rho A L_2\left(\ddot{v}_1(L_1,t)\right)\delta v_1(L_1,t) + M_1\left(\ddot{v}_1(L_1,t)\right)\delta v_1(L_1,t) + M_1\tfrac{L_\mathrm{m}}{4}\left(\ddot{v}_1(L_1,t)\right)\delta v'_1(L_1,t) \\ +M_1\tfrac{L_\mathrm{m}}{4}\left(\ddot{v}'_1(L_1,t)\right)\delta v_1(L_1,t) + J_{m1}\left(\ddot{v}'_1(L_1,t)\right)\delta v'_1(L_1,t) + +M_2\left(\ddot{v}_1(L_1,t)\right)\delta v_1(L_1,t) + \\ M_2\left(\tfrac{L_\mathrm{m}}{4}cos\,(\alpha) + \tfrac{h_\mathrm{m}}{2}\right)\left(\ddot{v}'_1(L_1,t)\right)\delta v_1(L_1,t)\end{gathered} \qquad \text{(S65)}$$

Potential energy

The potential energy of the main and auxiliary beam U_1 and U_2,can be expressed respectively as follows:

$$U_1 = \frac{1}{2}\int_v \sigma_{p1}:\varepsilon + \sigma_{c1}:\varepsilon dV,\ U_2 = \frac{1}{2}\int_v \sigma_{p2}:\varepsilon + \sigma_{c2}:\varepsilon dV \quad (\mathbf{S66})$$

Replacing the strain and stress matrix with their expressions, and assuming that the electric field across the piezoelectric layers is

$$E_3^{pi} = -\frac{V_i(t)}{h_{pi}}\big[H(x) - H\big(x - L_j\big)\big], i \in \{1,2\} \quad (\mathbf{S67})$$

where $V_1(\mathrm{t})$ and $V_2(\mathrm{t})$ are the respective output voltages from the main and auxiliary beams. Equation (S66) becomes

$$U_1 = \frac{1}{2}\int_0^{L_1} EI_1 v_1''^2(x,t) + \Theta_1 V_1(t)[H(x) - H(x - L_1)]v_1''(x,t)dx \quad (\mathbf{S68})$$

and

$$U_2 = \frac{1}{2}\int_0^{L_2} EI_2 v_2''^2(x,t) + \Theta_2 V_2(t)[H(x) - H(x - L_2)]v_2''(x,t)dx \quad (\mathbf{S69})$$

where H (.) designates the Heaviside function, which is added for mathematical reasons. The bending stiffness EI_i of the composite cross section of the i-th beam are given by

$$EI_1 = \frac{1}{3}E_{p1}b(y_2^3 - y_1^3) + \frac{1}{3}E_{c1}b(y_1^3 - y_0^3) \quad (\mathbf{S70})$$

$$EI_2 = \frac{1}{3}E_{p2}b(y_2^3 - y_1^3) + \frac{1}{3}E_{c2}b(y_1^3 - y_0^3) \quad (\mathbf{S71})$$

and the piezoelectric coupling term Θ_i for parallel connection is expressed as

$$\begin{aligned}\Theta_1 &= -\frac{1}{2}b\big[e_{31}^{p1}(y_1 + y_2)\big]\\ \Theta_2 &= -\frac{1}{2}b\big[e_{31}^{p2}(y_1 + y_2)\big]\end{aligned} \quad (\mathbf{S72})$$

The variation of the potential energy of the system is

$$\begin{aligned}\int_{t1}^{t2} \delta U dt = \int_{t1}^{t2}\int_0^{L1} M_{b1}''(x,t)\delta v_1(x,t)dx - \\ [M_{b1}'(x,t)\delta v_1(x,t)]_0^{L1} + [M_{b1}(x,t)\delta v_1'(x,t)]_0^{L1} + \int_0^{L2} M_{b2}''(x,t)\delta v_2(x,t)dx - \\ [M_{b2}'(x,t)\delta v_2(x,t)]_0^{L_2} + [M_{b2}(x,t)\delta v_2'(x,t)]_0^{L_2}dt\end{aligned} \quad (\mathbf{S73})$$

where $M_{b1}, and\ M_{b2}$ are respectively the bending moment of the main beam and the auxiliary beam.

$$\begin{aligned}M_{b1}(x,t) &= EI_1 v_1''(x,t) + \Theta_1 V_1(t)[H(x) - H(x - L_1)]\\ M_{b2}(x,t) &= EI_2 v_2''(x,t) + \Theta_2 V_2(t)[H(x) - H(x - L_2)]\end{aligned} \quad (\mathbf{S74})$$

Variation of the non-conservative forces

The auxiliary beam stimulates the main beam's bending in x = L_1 by applying a bending moment opposite to its internal bending moment ($M_{b2}(0,t)$). As a result, the variation of the non-conservative forces for this harvester can be written as follows:

$$\int_{t1}^{t2} \delta W_{nc} dt = \int_{t1}^{t2} -M_{b2}(0,t)\delta v'_1(L_1,t)dt \quad \text{(S75)}$$

Equations of motion and boundary conditions

From (S60), (S61), (S65), (S73) and (S75), we can deduce the equations of motions:

$$\rho A\ddot{v}_1(x,t) + EI_1 v_1''''(x,t) + \Theta_1 V_1(t)[H''(x) - H''(x-L_1)] = -\rho A\ddot{Y}(t) \quad \text{(S76)}$$

$$\rho A[\ddot{v}_2(x,t)] + EI_2 v_2''''(x,t) + \Theta_2 V_2(t)[H''(x) - H''(x-L_2)] = 0, \quad \text{(S77)}$$

and the associated boundary conditions

$$\begin{gathered} v_1(0,t) = 0 \\ v_1'(0,t) = 0 \\ EI_1 v_1''(L_1,t) = -J_{m1}\left(\ddot{v}'_1(L_1,t)\right) - M_1\frac{L_\mathrm{m}}{4}\left(\ddot{v}_1(L_1,t)\right) + EI_2 v_2''(0,t) \\ EI_1 v_1'''(L_1,t) = (\mathrm{M} + \rho AL_2)\left(\ddot{v}_1(L_1,t)\right) + M_1\frac{L_\mathrm{m}}{4}\ddot{v}'_1(L_1,t) + M_2\left(\frac{L_\mathrm{m}}{4}\cos(\alpha) + \frac{h_\mathrm{m}}{2}\right)\ddot{v}'_1(L_1,t) \\ v_2(0,t) = 0 \\ v_2'(0,t) = 0 \\ EI_2 v_2''(L_2,t) = 0 \\ EI_{gz} v_2'''(L_2,t) = 0 \end{gathered} \quad \text{(S78)}$$

where $J_{m1} = \frac{1}{12}M_{\mathrm{m}1}\left(h_\mathrm{m}^2 + \frac{L_\mathrm{m}^2}{4}\right) + M_1(\frac{L_\mathrm{m}}{4})^2$,

Electrical equations

The electric current I is given by applying Gauss's and Kirchhoff's laws,

$$I_i = \frac{\mathrm{d}}{\mathrm{d}t}\int_A D_3^{pi}\,\mathrm{d}A, i \in \{1,2\} \quad \text{(S79)}$$

Using the expression of the electric displacement (Equation (6)), the electric currents generated by piezoelectric layers of the harvester in parallel connection can be written as follows

$$\begin{gathered} -\left(h_{cp1}e_{31}\right)b\int_0^{L_1}\dot{v}_1''\mathrm{d}x - \left(\frac{\epsilon_{33}^{sp1}}{h_{p1}}\right)bL_1\dot{V}_1(t) = \frac{V_1(t)}{R_1} \\ -\left(h_{cp2}e_{31}\right)b\int_0^{L_2}\dot{v}_2''\mathrm{d}x - \left(\frac{\epsilon_{33}^{sp2}}{h_{p2}}\right)bL_2\dot{V}_2(t) = \frac{V_2(t)}{R_2} \end{gathered} \quad \text{(S80)}$$

where h_{cpi} (i ∈ {1,2}) are given by

$$h_{cp1} = \frac{h_{s1}+h_{p1}}{2}, h_{cp2} = \frac{h_{s2}+h_{p2}}{2} \quad \text{(S81)}$$

Equation (S80) can be written as

$$\begin{aligned} C_{p1}\dot{V}_1(t) + \frac{V_1(t)}{R_1} &= bk_1\left(\dot{v}_1'(L_1,t) - \dot{v}_1'(0,t)\right) \\ C_{p2}\dot{V}_2(t) + \frac{V_2(t)}{R_2} &= bk_2\left(\dot{v}_2'(L_2,t) - \dot{v}_2'(0,t)\right) \end{aligned} \quad \text{(S82)}$$

where

$$\begin{aligned} C_{p1} &= \left(\frac{\epsilon_{33}^{sp1}}{h_{p1}}\right) bL_1 \\ C_{p2} &= \left(\frac{\epsilon_{33}^{sp2}}{h_{p2}}\right) bL_2 \end{aligned} \quad \text{(S83)}$$

are respectively the internal capacitances of the piezoelectric layers of the main and auxiliary composite beams, and $k_1, and\ k_2$ indicate constants related to material properties and beam geometries, which are represented by

$$\begin{aligned} k_1 &= -h_{cp1}e_{31}^{p1} \\ k_2 &= -h_{cp2}e_{31}^{p2} \end{aligned} \quad \text{(S84)}$$

Structural natural frequencies and mode shapes

To calculate the natural frequencies and corresponding mode shapes, the deflections $v_i(\mathrm{x},\mathrm{t})$ of the two composite beams are represented by separable functions of time and space.

$$\begin{aligned} v_1(x,t) &= \phi_1(x)exp\ (i\omega t) \\ v_2(x,t) &= \phi_2(x)exp\ (i\omega t) \end{aligned} \quad \text{(S85)}$$

where $\phi_1(x), and\ \phi_2(x)$ are respectively the eigenfunctions of the bending of the main and auxiliary beams.

The eigenvalue problem that results is written as follows:

$$\phi_1''''(x) - \frac{\rho A\omega^2}{EI_1}\phi_1(x) = 0 \quad \text{(S86)}$$

$$\phi_2''''(x) - \frac{\rho A\omega^2}{EI_2}\phi_2(x) = 0 \quad \text{(S87)}$$

and the associated boundary conditions are:

$$
\begin{gathered}
\phi_1(0) = 0 \\
\phi_1'(0) = 0 \\
EI_1\phi_1''(L_1) = -J_{m1}\omega^2\phi_1'(L_1) - M_1\frac{L_\mathrm{m}}{4}\omega^2\phi_1(L_1) \\
+EI_2\phi_2''(0) \\
EI_1\phi_1'''(L_1) = (\mathrm{M} + \rho AL_2)\omega^2\phi_1(L_1) + M_1\frac{L_\mathrm{m}}{4}\omega^2\phi'_1(L_1) + M_2(\frac{L_\mathrm{m}}{4}cos\ (\alpha) + \frac{h_\mathrm{m}}{2})\omega^2\phi'_1(L_1) \\
\phi_2(0) = 0 \\
\phi_2'(0) = 0 \\
EI_2\phi_2''(L_2) = 0 \\
EI_2\phi_2'''(L_2) = 0
\end{gathered}
\qquad (\mathbf{S88})
$$

The general solutions of Equations (S86) and (S87) are given by

$$
\begin{gathered}
\phi_1(x) = A_1cos\ (\beta_1 x) + B_1sin\ (\beta_1 x) + C_1cosh\ (\beta_1 x) + D_1sinh\ (\beta_1 x) \\
\phi_2(x) = A_2cos\ (\beta_2 x) + B_2sin\ (\beta_2 x) + C_2cosh\ (\beta_2 x) + D_2sinh\ (\beta_2 x)
\end{gathered}
\qquad (\mathbf{S89})
$$

where A_i, B_i, C_i and D_i are the modal coefficients of the eigenfunctions. And β_i are the frequency number, which are obtained as

$$
\beta_1 = \sqrt[4]{\frac{\rho A\omega^2}{EI_1}}, \beta_2 = \sqrt[4]{\frac{\rho A\omega^2}{EI_2}} \qquad (\mathbf{S90})
$$

Reduced-order model and analytical solution

In this section, we use the Galerkin procedure and the Euler-Lagrange method to discretize the ROM for the considered configurations, based on exploiting the systems' natural frequencies and corresponding mode shapes in bending movements. Then the dynamic responses, and the electric voltage outputs are presented in terms of closed-form formulas.

Reduced order model

Using the Galerkin, we can define the deflections $v_i(x,t)$ of the two composite beams as an absolutely and uniformly convergent series of the eigenfunctions

$$
\begin{gathered}
v_1(x,t) = \sum_{r=1}^{\infty}\ \phi_{1r}(x)\eta_r(t) \\
v_2(x,t) = \sum_{r=1}^{\infty}\ \phi_{2r}(x)\eta_r(t)
\end{gathered}
\qquad (\mathbf{S91})
$$

where $\phi_{1r}(\mathrm{x}), and\ \phi_{2r}(\mathrm{x})$ are the eigenfunctions of respectively the bending of the main beam, and the bending of the auxiliary beam, and $\eta_r(\mathrm{t})$ are the modal coordinates of the displacements $v_1\ and\ v_2$ in the orthogonal base formed by the the eigenfunction for the r-th mode. The aim of this subsection is to create a reduced-order model of the structure using the Euler Lagrange approach, so, we limit ourselves to the first two structural mode shapes to discretize the system. This choice is linked to the application of applied excitation frequencies, which are generally lower than the third structural natural frequency. The Euler-Lagrange approach is defined as follows:

$$\frac{d}{dt}\frac{\partial \mathcal{L}}{\partial \dot{\eta}_s} - \frac{\partial \mathcal{L}}{\partial \eta_s} = 0 \quad \text{(S92)}$$

where $\mathcal{L}$ is Lagrangian of the system which is introduced in Equation 2.40. Using the expressions of kinetic energy and potential energy developed in the previous chapter, the Lagrangian can be written as follows:

$$\begin{aligned} L = {} & \tfrac{1}{2}\int_0^{L_1} \rho A\big(\dot{v}_1(x,t) + \dot{Y}(t)\big)^2 - EI_1 v_1''^2(x,t) - \Theta_1 V_1(t) v_1''(x,t)dx + \tfrac{1}{2}\int_0^{L_2} \rho A\big(\dot{v}_2(x,t)\big)^2 - \\ & EI_2 v_2''^2(x,t) - \Theta_2 V_2(t) v_2''(x,t)dx + \tfrac{1}{2}\rho A L_2\big(\dot{v}_1(L_1,t)\big)^2 + \tfrac{1}{2}M_1\big(\dot{v}_1(L_1,t)\big)^2 + \tfrac{1}{2}J_{m1}\left(\dot{v}'_1(L_1,t)\right)^2 \\ & + M_1\tfrac{L_\mathrm{m}}{4}\big(\dot{v}_1(L_1,t)\big)\left(\dot{v}'_1(L_1,t)\right) + \tfrac{1}{2}M_2\big(\dot{v}_1(L_1,t)\big)^2 + M_2\big(\tfrac{L_\mathrm{m}}{4}cos\,(\alpha) + \tfrac{h_\mathrm{m}}{2}\big)\big(\dot{v}_1(L_1,t)\big)\left(\dot{v}'_1(L_1,t)\right) \end{aligned} \quad \text{(S93)}$$

Substituting Equation (S91) into Equation (S93), we obtain

$$\begin{aligned} L = {} & \tfrac{1}{2}\int_0^{L_1} \rho A\big(\textstyle\sum_{r=1}^{2} \phi_{1r}(x)\dot{\eta}_r(t) + \dot{Y}(t)\big)^2 - EI_1 \textstyle\sum_{r=1}^{2} \phi_{1r}''^2(x)\eta_r^2(t) - \\ & \Theta_1 V_1(t) \textstyle\sum_{r=1}^{2} \phi_{1r}''(x)\eta_r(t) + \tfrac{1}{2}\int_0^{L_2} \rho A \textstyle\sum_{r=1}^{2} (\phi_{2r}(x)\dot{\eta}_r(t))^2 - EI_2 \textstyle\sum_{r=1}^{2} \phi_{2r}''^2(x)\eta_r^2(t) \\ & -\Theta_2 V_2(t) \textstyle\sum_{r=1}^{2} \phi_{2r}''(x)\eta_r(t)dx + \tfrac{1}{2}M_1 \textstyle\sum_{r=1}^{2} \phi_{1r}^2(L_1)\dot{\eta}_r^2(t) + \tfrac{1}{2}J_{m1} \textstyle\sum_{r=1}^{2} \phi_{1r}'^2(L_1)\dot{\eta}_r^2(t) \\ & + M_1\tfrac{L_\mathrm{m}}{4}\big(\textstyle\sum_{r=1}^{2} \phi_{1r}^2(L_1)\dot{\eta}_r^2(t)\big)\big(\textstyle\sum_{r=1}^{2} \phi_{1r}'^2(L_1)\dot{\eta}_r^2(t)\big) + \tfrac{1}{2}M_2 \textstyle\sum_{r=1}^{2} \phi_{1r}^2(L_1)\dot{\eta}_r^2(t) \\ & + M_2\big(\tfrac{L_\mathrm{m}}{4}cos\,(\alpha) + \tfrac{h_\mathrm{m}}{2}\big)\big(\textstyle\sum_{r=1}^{2} \phi_{1r}^2(L_1)\dot{\eta}_r^2(t)\big)\big(\textstyle\sum_{r=1}^{2} \phi_{1r}'^2(L_1)\dot{\eta}_r^2(t)\big) \end{aligned} \quad \text{(S94)}$$

Using the orthogonality conditions for the L-shaped bimorph beam-mass structure with torsional and bending mode

$$\begin{gathered} EI_1\int_0^{L_1} \phi_{1r}''(x)\phi_{1s}''(x)dx + EI_2\int_0^{L_2} \phi_{2r}''(x)\phi_{2s}''(x)dx = \omega_r^2\delta_{rs} \\ \int_0^{L_1} (\rho A)\phi_{1r}\phi_{1s}\,\mathrm{d}x + \int_0^{L_2} (\rho A)\phi_{2r}\phi_{2s}\mathrm{d}x + (\rho A)L_2\phi_{1r}(L_1)\phi_{1s}(L_1) + M_1\phi_{1r}(L_1)\phi_{1s}(L_1) \\ + J_{\mathrm{m}1}\phi'_{1r}(L_1)\phi'_{1s}(L_1) + M_1\tfrac{L_\mathrm{m}}{4}\big(\phi'_{1r}(L_1)\phi_{1s}(L_1) + \phi_{1r}(L_1)\phi'_{1s}(L_1)\big) + M_2\phi_{1r}(L_1)\phi_{1s}(L_1) \\ + M_2\big(\tfrac{L_\mathrm{m}}{4}cos\,(\alpha) + \tfrac{h_\mathrm{m}}{2}\big)\big(\phi'_{1r}(L_1)\phi_{1s}(L_1) + \phi_{1r}(L_1)\phi'_{1s}(L_1)\big) = \delta_{rs} \end{gathered} \quad \text{(S95)}$$

we obtain the forced equation of motion in modal coordinates

$$\ddot{\eta}_r(t) + 2\xi_r\omega_r\dot{\eta}_r(t) + \omega_r^2\eta_r(t) + \chi_{1r}V_1(t) + \chi_{2r}V_2(t) = f_r(t), r \in \{1,2\} \quad \text{(S96)}$$

where ξ_r is the modal damping ratio of the r-th bending vibration mode, χ_{ir} are the modal electromechanical coupling terms, which are given by

$$\begin{aligned} \chi_{1r} &= \Theta_1(\phi'_{1r}(L_1) - \phi'_{1r}(0)) \\ \chi_{2r} &= \Theta_2(\phi'_{2r}(L_i) - \phi'_{2r}(0)) \end{aligned} \quad \text{(S97)}$$

and $f_r(\mathrm{t})$ is the modal force given by

$$f_r(t) = -\int_0^{L_1} \rho A\phi_{1r}(x)dx\ddot{Y}(t) \quad \text{(S98)}$$

Substituting equation (S91) into equation (S82), the governing circuit equations are written as

$$\begin{matrix} C_{p1}\dot{V}_1(t) + \frac{V_1(t)}{R_1} = \sum_{r=1}^{2} K_{1r}\,\dot{\eta}_r(t) \\ C_{p2}\dot{V}_2(t) + \frac{V_2(t)}{R_2} = \sum_{r=1}^{2} K_{2r}\dot{\eta}_r(t) \end{matrix} \quad \text{(S99)}$$

where K_{1r} and K_{3r} are the r-th modal coupling terms of the piezoelectric layers of the main beam, and K_{2r} is the r-th modal coupling term of the piezoelectric layers of the auxiliary beam

$$K_{ir} = k_i b(\phi'_{ir}(L_i) - \phi'_{ir}(0)), i \in \{1,2\}. \quad \text{(S100)}$$

Analytical solution

We note that $Y(t) = \Im[Y_0 e^{j\Omega t}]$, where $\Im$ stands for the imaginary part. Consequently, we seek the solutions of Equations (47), and (50) in the form

$$\begin{matrix} \eta_r(t) = \Im[H_r e^{j\Omega t}], r \in \{1,2\} \\ V_i(t) = \Im[U_i e^{j\Omega t}], i \in \{1,2\} \end{matrix} \quad \text{(S101)}$$

Substituting Equation (S101) into Equation (S96),

$$H_r = \frac{f_{r0} - \chi_i U_1 - \chi_2 U_2}{\omega_r^2 - \omega^2 + 2\xi\omega_r\omega j} \quad \text{(S102)}$$

where f_{r0} is the complex amplitude of the modal force function $f_r(t)$

$$f_{r0}(t) = -\int_0^{L_1} \rho A \phi_{1r}(x) dx \ddot{Y}_0 \quad \text{(S103)}$$

Considering Equation (S99), we obtain the following equation system

$$\begin{cases} U_1 Z_1 = Z_3 - Z_2 U_2 \\ U_2 Z_5 = Z_6 - Z_4 U_1 \end{cases} \quad \text{(S104)}$$

Finally, the steady state voltage outputs are given by

$$\begin{matrix} U_1 = \frac{Z_3 Z_5 - Z_2 Z_6}{Z_1 Z_5 - Z_2 Z_4} \\ U_2 = \frac{Z_1 Z_6 - Z_3 Z_4}{Z_1 Z_5 - Z_2 Z_4} \end{matrix}, \quad \text{(S105)}$$

where

$$
\begin{aligned}
Z_1 &= jC_{p1}\Omega + \frac{1}{R_1} + \sum_{r=1}^{2} \frac{\Omega j}{\omega_r^2 - \Omega^2 + 2j\xi_r\omega_r\Omega}(K_{1r})\chi'_{1r} \\
Z_2 &= \sum_{r=1}^{2} \frac{\Omega j}{\omega_r^2 - \Omega^2 + 2j\xi_r\omega_r\Omega}(K_{1r})\chi_{2r} \\
Z_3 &= \sum_{r=1}^{2} \frac{\Omega j}{\omega_r^2 - \Omega^2 + 2j\xi_r\omega_r\Omega}(K_{1r})f_{r0} \\
Z_4 &= \sum_{r=1}^{2} \frac{\Omega j}{\omega_r^2 - \Omega^2 + 2j\xi_r\omega_r\Omega}K_{2r}\chi'_{1r} \\
Z_5 &= jC_{p2}\Omega + \frac{1}{R_2} + \sum_{r=1}^{2} \frac{\Omega j}{\omega_r^2 - \Omega^2 + 2j\xi_r\omega_r\Omega}K_{2r}\chi_{2r} \\
Z_6 &= \sum_{r=1}^{2} \frac{\Omega j}{\omega_r^2 - \Omega^2 + 2j\xi_r\omega_r\Omega}K_{2r}f_{r0}
\end{aligned}
\qquad \text{(S106)}
$$

- **U-shaped structure**

Constitutive equations

Assuming an Euler-Bernoulli beam model and Hooke's law, the mechanical strain for both main and auxiliary beams and the stress tensor for the copper layer of the two beams can be written as follows

$$
\varepsilon_{\mathrm{i}} = \begin{pmatrix} -yv_{\mathrm{i}}''(x,t) & 0 & 0 \\ 0 & 0 & 0 \\ 0 & 0 & 0 \end{pmatrix},\ \sigma_c = \begin{pmatrix} -E_c yv''(x,t) & 0 & 0 \\ 0 & 0 & 0 \\ 0 & 0 & 0 \end{pmatrix}, y \in [y_0, y_1] \qquad \textbf{(S107)}
$$

For electromechanical coupling effect of piezoelectric material, we assumed linear constitutive equations for the unbounded piezoelectric continuum

$$
\sigma_p = E_p : \varepsilon^p \text{-} e^p . E^p \qquad \text{(S108)}
$$

$$
D^p = e^p : \varepsilon^p + \epsilon^{\varepsilon^p} \cdot E^p \quad \text{(S109)}
$$

where D^p denotes the electric displacement matrix, ϵ^{ε^p} denotes the permittivity matrix at constant strain, E^p denotes the electric field matrix, ε^p denotes the strain matrix of piezoelectric layer, σ_p denotes the stress matrix, E_p denotes the elastic stiffness constant matrix, symbol "." and ":" denote dot product and double contraction-point multiplication respectively, e^p denotes the piezoelectric constant matrix at constant stress, which is given by

$$
e^p = d^p : E_p, \quad \text{(S110)}
$$

Considering only the coefficient e_{31}, the mechanical stress σ_{pi} and the electric displacement D^{pi} of each piezoelectric layer i, can be written as follows:

$$
\sigma_{pi} = \begin{pmatrix} -E_{pi} yv_i''(x,t) - e_{31}^{pi} E_3^{pi} & 0 & 0 \\ 0 & 0 & 0 \\ 0 & 0 & 0 \end{pmatrix},\ y \in [y_1, y_2] \quad \text{(S111)}
$$

$$D^{pi} = \begin{pmatrix} 0 \\ 0 \\ e_{31}^{pi} \cdot \varepsilon_{11}^{pi} + \epsilon_{33}^{\varepsilon^{pi}} \cdot E_3^{pi} \end{pmatrix} \quad \text{(S112)}$$

In the following subsections, the analytical solutions of the electromechanical coupling equations of the harvesters with bending modes are deduced.

Hamilton's principle

In this section, Hamilton's principle is applied to formulate a distributed-parameter model for the harvesters and derive the governing equations of motion and the corresponding boundary conditions. The demonstration focuses specifically on the first configuration (a cantilever beam), which consists of a main beam, an auxiliary beam and an SMP section considered as a rigid mass block positioned between the two beams. However, the governing equations of motion and boundary conditions are developed for the four configurations.

Kinetic energy

We used the the extended Hamilton's principle, defined by

$$\int_{t_1}^{t_2} \delta(\mathcal{L} + W_{nc})dt = 0 \qquad \text{(S113)}$$

where $\mathcal{L}$ is the Lagrangian of the system, W_{nc} is the work of the nonconservative forces and δ is the variation which describes infinitesimal changes in the virtual sense. The variation obeys the rules of differential calculus. The lagrangian is defined by:

$$L = T - U, \qquad \text{(S114)}$$

where T and V are respectively the kinetic energy and the potential energy of the system.

The kinetic energy of the main and auxiliary beams can be written respectively as follows

$$T_1 = \int_0^{L_1} \frac{1}{2}\rho A(\dot{v}_1(x,t) + \dot{Y}(t))^2 dx, \quad T_2 = \int_0^{L_2} \frac{1}{2}\rho A\left(\dot{v}_2(x,t) + \dot{v}_1(L_1,t)\right)^2 dx \qquad \text{(S115)}$$

Where the terms ρ, and A are respectively the density, and the cross section of the composite beams. And the term ρA is given by

$$\rho A = \sum_{i=1}^{2} \int_{-\frac{h_i}{2}}^{\frac{h_i}{2}} \int_{-\frac{b}{2}}^{\frac{b}{2}} \rho_i dz dy \qquad \text{(S134)}$$

with the terms h_i is the thickness of the ist layer.

The SMP component here is considered as a rigid mass block, thus its kinetic energy can be written as follows:

$$T_{m1} = \frac{1}{2}M_1\left(\dot{v}_1(L_1,t)\right)^2 + \frac{1}{2}J_{m1}\left(\dot{v'}_1(L_1,t)\right)^2 + M_1\frac{L_c}{8}\left(\dot{v}_1(L_1,t)\right)\left(\dot{v'}_1(L_1,t)\right),$$

$$T_{m2} = \frac{1}{2}M_2\left(\dot{v}_1(L_1,t)\right)^2 + M_2\left(\frac{L_m}{4}+\frac{h_m}{2}\right)\left(\dot{v}_1(L_1,t)\right)\left(\dot{v'}_1(L_1,t)\right)$$

$$T_{m3} = \frac{1}{2}M_3\left(\dot{v}_1(L_1,t)\right)^2 + M_3\frac{L_m}{8}\left(\dot{v}_1(L_1,t)\right)\left(\dot{v'}_1(L_1,t)\right)$$

(S**117**)

Where J_m is the mass moment of inertia.

The variation of the kinetic energy is obtained by applying the differential to Equation (S115) and (S117).

$$\begin{gathered}\int_{t1}^{t2}\delta T dt = -\int_{t1}^{t2}\int_0^{L1}\rho A\left[\ddot{v}_1(x,t)+\ddot{Y}(t)\right]\delta v_1(x,t)dx + \int_0^{L2}\rho A[\ddot{v}_2(x,t)+\ddot{v}_1(L_1,t)]\\ \delta v_2(x,t)dx + M_1\left(\ddot{v}_1(L_1,t)\right)\delta v_1(L_1,t) + M_1\tfrac{L_m}{4}\left(\ddot{v}_1(L_1,t)\right)\delta v'_1(L_1,t)\\ +M_1\tfrac{L_m}{8}\left(\ddot{v'}_1(L_1,t)\right)\delta v_1(L_1,t) + J_{m1}\left(\ddot{v'}_1(L_1,t)\right)\delta v'_1(L_1,t) + M_2\left(\ddot{v}_1(L_1,t)\right)\delta v_1(L_1,t) +\\ M_2\left(\tfrac{L_m}{4}+\tfrac{h_m}{2}\right)\left(\ddot{v'}_1(L_1,t)\right)\delta v_1(L_1,t) + M_3\left(\ddot{v}_1(L_1,t)\right)\delta v_1(L_1,t) + M_3\tfrac{L_m}{8}\left(\ddot{v'}_1(L_1,t)\right)\delta v_1(L_1,t)\end{gathered} \quad (\text{S}\mathbf{118})$$

Potential energy

The potential energy of the main and auxiliary beam U_1 and U_2,can be expressed respectively as follows:

$$U_1 = \tfrac{1}{2}\int_v \sigma_{p1}:\varepsilon + \sigma_{c1}:\varepsilon dV,\ U_2 = \tfrac{1}{2}\int_v \sigma_{p2}:\varepsilon + \sigma_{c2}:\varepsilon dV \quad (\text{S}\mathbf{119})$$

Replacing the strain and stress matrix with their expressions, and assuming that the electric field across the piezoelectric layers is

$$E_3^{pi} = -\tfrac{V_i(t)}{h_{pi}}\left[H(x) - H\left(x-L_j\right)\right], i \in \{1,2\} \quad (\text{S}\mathbf{120})$$

where $V_1(\mathrm{t})$ and $V_2(\mathrm{t})$ are the respective output voltages from the main and auxiliary beams. Equation (S119) becomes

$$U_1 = \tfrac{1}{2}\int_0^{L_1} EI_1 v_1''^2(x,t) + \Theta_1 V_1(t)[H(x) - H(x-L_1)]v_1''(x,t)dx \quad (\text{S}\mathbf{121})$$

and

$$U_2 = \tfrac{1}{2}\int_0^{L_2} EI_2 v_2''^2(x,t) + \Theta_2 V_2(t)[H(x) - H(x-L_2)]v_2''(x,t)dx \quad (\text{S}\mathbf{122})$$

where H (.) designates the Heaviside function, which is added for mathematical reasons. The bending stiffness EI_i of the composite cross section of the i-th beam are given by

$$EI_1 = \frac{1}{3}E_{p1}b(y_2^3 - y_1^3) + \frac{1}{3}E_{c1}b(y_1^3 - y_0^3) \quad \text{(S123)}$$

$$EI_2 = \frac{1}{3}E_{p2}b(y_2^3 - y_1^3) + \frac{1}{3}E_{c2}b(y_1^3 - y_0^3) \quad \text{(S124)}$$

and the piezoelectric coupling term Θ_i for parallel connection is expressed as

$$\begin{aligned}\Theta_1 &= -\frac{1}{2}b\left[e_{31}^{p1}(y_1 + y_2)\right] \\ \Theta_2 &= -\frac{1}{2}b\left[e_{31}^{p2}(y_1 + y_2)\right]\end{aligned} \quad \text{(S125)}$$

The variation of the potential energy of the system is

$$\begin{aligned}\int_{t1}^{t2} \delta U dt = \int_{t1}^{t2} \int_0^{L1} M_{b1}''(x,t)\delta v_1(x,t)dx - \\ [M_{b1}'(x,t)\delta v_1(x,t)]_0^{L1} + [M_{b1}(x,t)\delta v_1'(x,t)]_0^{L1} + \int_0^{L2} M_{b2}''(x,t)\delta v_2(x,t)dx - \\ [M_{b2}'(x,t)\delta v_2(x,t)]_0^{L_2} + [M_{b2}(x,t)\delta v_2'(x,t)]_0^{L_2} dt\end{aligned} \quad \text{(S126)}$$

where $M_{b1}, and\ M_{b2}$ are respectively the bending moment of the main beam and the auxiliary beam.

$$\begin{aligned}M_{b1}(x,t) &= EI_1 v_1''(x,t) + \Theta_1 V_1(t)[H(x) - H(x - L_1)] \\ M_{b2}(x,t) &= EI_2 v_2''(x,t) + \Theta_2 V_2(t)[H(x) - H(x - L_2)]\end{aligned} \quad \text{(S127)}$$

Variation of the non-conservative forces

The auxiliary beam stimulates the main beam's bending in x = L_1 by applying a shear force opposing to its internal shear force ($T_{y2}(0,t)$) in x=0. and a bending moment opposite to its internal bending moment ($M_{b2}(0,t)$). As a result, the variation of the non-conservative forces for this harvester can be written as follows:

$$\int_{t1}^{t2} \delta W_{nc} dt = \int_{t1}^{t2} -M_{b2}(0,t)\delta v'_1(L_1,t) - T_{y2}(0,t)\delta v_1(L_1,t)dt \quad \text{(S128)}$$

Equations of motion and boundary conditions

From (113), (114), (118), (126) and (128), we can deduce the equations of motions:

$$\rho A\ddot{v}_1(x,t) + EI_1 v_1''''(x,t) + \Theta_1 V_1(t)[H''(x) - H''(x - L_1)] = -\rho A\ddot{Y}(t) \quad \text{(S129)}$$

$$\rho A[\ddot{v}_2(x,t)] + EI_2 v_2''''(x,t) + \Theta_2 V_2(t)[H''(x) - H''(x - L_2)] = 0, \quad \text{(S130)}$$

$$
\begin{gathered}
v_1(0,t)=0 \\
v_1'(0,t)=0 \\
EI_1 v_1''(L_1,t)=-J_{m1}\left(\ddot{v}'_1(L_1,t)\right)-M_1\frac{L_\mathrm{c}}{8}\left(\ddot{v}_1(L_1,t)\right)+EI_2 v_2''(0,t) \\
EI_1 v_1'''(L_1,t)=M\left(\ddot{v}_1(L_1,t)\right)+M_1\frac{L_\mathrm{c}}{8}\ddot{v}'_1(L_1,t)+M_2\left(\frac{L_\mathrm{m}}{4}+\frac{h_\mathrm{m}}{2}\right)\ddot{v}'_1(L_1,t)+M_3\frac{L_\mathrm{m}}{8}\ddot{v}'_1(L_1,t)++EI_2 v_2'''(0,t) \\
v_2(0,t)=0 \\
v_2'(0,t)=0 \\
EI_2 v_2''(L_2,t)=0 \\
EI_{gz} v_2'''(L_2,t)=0
\end{gathered}
$$

(S**131**)

Where $J_{m1}=\frac{1}{12}M_1\left(h_\mathrm{m}^2+\frac{{L_\mathrm{m}}^2}{16}\right)+M_1(\frac{L_\mathrm{m}}{8})^2$

Electrical equations

The electric current I is given by applying Gauss's and Kirchhoff's laws,

$$I_i=\frac{\mathrm{d}}{\mathrm{d}t}\int_A D_3^{pi}\,\mathrm{d}A, i\in\{1,2\} \qquad \text{(S132)}$$

Using the expression of the electric displacement (Equation (6)), the electric currents generated by piezoelectric layers of the harvester in parallel connection can be written as follows

$$
\begin{gathered}
-\left(h_{cp1}e_{31}\right)b\int_0^{L_1}\dot{v}_1''\mathrm{d}x-\left(\frac{\epsilon_{33}^{sp1}}{h_{p1}}\right)bL_1\dot{V}_1(t)=\frac{V_1(t)}{R_1} \\
-\left(h_{cp2}e_{31}\right)b\int_0^{L_2}\dot{v}_2''\mathrm{d}x-\left(\frac{\epsilon_{33}^{sp2}}{h_{p2}}\right)bL_2\dot{V}_2(t)=\frac{V_2(t)}{R_2}
\end{gathered}
\qquad \text{(S134)}
$$

where h_{cpi} (i $\in\{1,2\}$) are given by

$$h_{cp1}=\frac{h_{s1}+h_{p1}}{2}, h_{cp2}=\frac{h_{s2}+h_{p2}}{2} \qquad \text{(S135)}$$

Equation (S133) can be written as

$$
\begin{gathered}
C_{p1}\dot{V}_1(t)+\frac{V_1(t)}{R_1}=bk_1\left(\dot{v}_1'(L_1,t)-\dot{v}_1'(0,t)\right) \\
C_{p2}\dot{V}_2(t)+\frac{V_2(t)}{R_2}=bk_2\left(\dot{v}_2'(L_2,t)-\dot{v}_2'(0,t)\right)
\end{gathered}
\qquad \text{(S136)}
$$

where

$$C_{p1} = \left(\frac{\epsilon_{33}^{sp1}}{h_{p1}}\right) bL_1$$
$$C_{p2} = \left(\frac{\epsilon_{33}^{sp2}}{h_{p2}}\right) bL_2 \quad \text{(S137)}$$

are respectively the internal capacitances of the piezoelectric layers of the main and auxiliary composite beams, and $k_1, and\ k_2$ indicate constants related to material properties and beam geometries, which are represented by

$$k_1 = -h_{cp1} e_{31}^{p1}$$
$$k_2 = -h_{cp2} e_{31}^{p2} \quad \text{(S138)}$$

Structural natural frequencies and mode shapes

To calculate the natural frequencies and corresponding mode shapes, the deflections $v_i(\mathrm{x},\mathrm{t})$ of the two composite beams are represented by separable functions of time and space.

$$v_1(x,t) = \phi_1(x) exp\ (i\omega t)$$
$$v_2(x,t) = \phi_2(x) exp\ (i\omega t) \quad \text{(S139)}$$

where $\phi_1(x), and\ \phi_2(x)$ are respectively the eigenfunctions of the bending of the main and auxiliary beams.

The eigenvalue problem that results is written as follows:

$$\phi_1''''(x) - \frac{\rho A\omega^2}{EI_1}\phi_1(x) = 0 \quad \text{(S140)}$$

$$\phi_2''''(x) - \frac{\rho A\omega^2}{EI_2}\phi_2(x) = 0 \quad \text{(S241)}$$

and the associated boundary conditions are:

$$\phi_1(0) = 0$$
$$\phi_1'(0) = 0$$
$$EI_1\phi_1''(L_1) = -J_{m1}\omega^2\phi_1'(L_1) - M_1\frac{L_c}{8}\omega^2\phi_1(L_1) + EI_2\phi_2''(0)$$
$$EI_1\phi_1'''(L_1) = M\omega^2\phi_1(L_1) + M_1\frac{L_c}{8}\omega^2\phi_1'(L_1) + M_2\left(\frac{L_m}{4} + \frac{h_m}{2}\right)\omega^2\phi_1'(L_1) + M_3\frac{L_m}{8}\omega^2\phi_1'(L_1) + EI_2\phi_2'''(0)$$
$$\phi_2(0) = 0$$
$$\phi_2'(0) = 0$$
$$EI_2\phi_2''(L_2) = 0$$
$$EI_2\phi_2'''(L_2) = 0$$
(S142)

The general solutions of Equations (S139), and (S140) are given by

$$\phi_1(x) = A_1 cos\ (\beta_1 x) + B_1 sin\ (\beta_1 x) + C_1 cosh\ (\beta_1 x) + D_1 sinh\ (\beta_1 x)$$
$$\phi_2(x) = A_2 cos\ (\beta_2 x) + B_2 sin\ (\beta_2 x) + C_2 cosh\ (\beta_2 x) + D_2 sinh\ (\beta_2 x) \quad \text{(S143)}$$

where A_i, B_i, C_i and D_i are the modal coefficients of the eigenfunctions. And β_i are the frequency number, which are obtained as

$$\beta_1 = \sqrt[4]{\frac{\rho A \omega^2}{EI_1}}, \beta_2 = \sqrt[4]{\frac{\rho A \omega^2}{EI_2}} \quad \text{(S144)}$$

Reduced-order model and analytical solution

In this section, we use the Galerkin procedure and the Euler-Lagrange method to discretize the ROM for the considered configurations, based on exploiting the systems' natural frequencies and corresponding mode shapes in bending movements. Then the dynamic responses, and the electric voltage outputs are presented in terms of closed-form formulas.

Reduced order model

Using the Galerkin, we can define the deflections $v_i(x,t)$ of the two composite beams as an absolutely and uniformly convergent series of the eigenfunctions

$$\begin{matrix} v_1(x,t) = \sum_{r=1}^{\infty} \phi_{1r}(x)\eta_r(t) \\ v_2(x,t) = \sum_{r=1}^{\infty} \phi_{2r}(x)\eta_r(t) \end{matrix} \quad \text{(S145)}$$

where $\phi_{1r}(\mathrm{x}), and\ \phi_{2r}(\mathrm{x})$ are the eigenfunctions of respectively the bending of the main beam, and the bending of the auxiliary beam, and $\eta_r(\mathrm{t})$ are the modal coordinates of the displacements $v_1\ and\ v_2$ in the orthogonal base formed by the the eigenfunction for the r-th mode. The aim of this subsection is to create a reduced-order model of the structure using the Euler Lagrange approach, so, we limit ourselves to the first two structural mode shapes to discretize the system. This choice is linked to the application of applied excitation frequencies, which are generally lower than the third structural natural frequency. The Euler-Lagrange approach is defined as follows:

$$\frac{d}{dt}\frac{\partial \mathcal{L}}{\partial \dot{\eta}_s} - \frac{\partial \mathcal{L}}{\partial \eta_s} = 0 \quad \text{(S146)}$$

Using the expressions of kinetic energy and potential energy developed in the previous chapter, the Lagrangian can be written as follows:

$$\begin{aligned} L = {} & \frac{1}{2}\int_0^{L_1} \rho A\left(\dot{v}_1(x,t) + \dot{Y}(t)\right)^2 - EI_1 v_1''^2(x,t) - \Theta_1 V_1(t) v_1''(x,t)dx + \frac{1}{2}\int_0^{L_2} \rho A(\dot{v}_2(x,t) + \dot{v}_1(L_2,t))^2 - \\ & EI_2 v_2''^2(x,t) - \Theta_2 V_2(t) v_2''(x,t)dx + \frac{1}{2}M_1\left(\dot{v}_1(L_1,t)\right)^2 + \frac{1}{2}J_{m1}\left(\dot{v}'_1(L_1,t)\right)^2 + M_1\frac{L_\mathrm{m}}{8}\left(\dot{v}_1(L_1,t)\right)\left(\dot{v}'_1(L_1,t)\right) \\ & + \frac{1}{2}M_2\left(\dot{v}_1(L_1,t)\right)^2 + M_2\left(\frac{L_\mathrm{m}}{4} + \frac{h_\mathrm{m}}{2}\right)\left(\dot{v}_1(L_1,t)\right)\left(\dot{v}'_1(L_1,t)\right) + \frac{1}{2}M_3\left(\dot{v}_1(L_1,t)\right)^2 + M_3\frac{L_\mathrm{m}}{8}\left(\dot{v}_1(L_1,t)\right)\left(\dot{v}'_1(L_1,t)\right) \end{aligned}$$

(S147)

Substituting Equation (S144) into Equation (S146), we obtain

$$L = \frac{1}{2}\int_0^{L_1} \rho A\left(\sum_{r=1}^{2} \phi_{1r}(x)\dot{\eta}_r(t) + \dot{Y}(t)\right)^2 - EI_1 \sum_{r=1}^{2} \phi_{1r}''^2(x)\eta_r^2(t) -$$
$$\Theta_1 V_1(t) \sum_{r=1}^{2} \phi_{1r}''(x)\eta_r(t) + \frac{1}{2}\int_0^{L_2} \rho A \sum_{r=1}^{2} (\phi_{2r}(x)\dot{\eta}_r(t) + \phi_{1r}(L_1)\dot{\eta}_r(t))^2 - EI_2 \sum_{r=1}^{2} \phi_{2r}''^2(x)\eta_r^2(t)$$
$$-\Theta_2 V_2(t) \sum_{r=1}^{2} \phi_{2r}''(x)\eta_r(t)dx + \frac{1}{2}M_1 \sum_{r=1}^{2} \phi_{1r}^2(L_1)\dot{\eta}_r^2(t) + \frac{1}{2}J_{m1} \sum_{r=1}^{2} \phi_{1r}'^2(L_1)\dot{\eta}_r^2(t)$$
$$+M_1 \frac{L_m}{8}\left(\sum_{r=1}^{2} \phi_{1r}^2(L_1)\dot{\eta}_r^2(t)\right)\left(\sum_{r=1}^{2} \phi_{1r}'^2(L_1)\dot{\eta}_r^2(t)\right) + \frac{1}{2}M_2 \sum_{r=1}^{2} \phi_{1r}^2(L_1)\dot{\eta}_r^2(t) + \frac{1}{2}M_3 \sum_{r=1}^{2} \phi_{1r}^2(L_1)\dot{\eta}_r^2(t)$$
$$+M_2\left(\frac{L_m}{4} + \frac{h_m}{2}\right)\left(\sum_{r=1}^{2} \phi_{1r}^2(L_1)\dot{\eta}_r^2(t)\right)\left(\sum_{r=1}^{2} \phi_{1r}'^2(L_1)\dot{\eta}_r^2(t)\right) + M_3 \frac{L_m}{8}\left(\sum_{r=1}^{2} \phi_{1r}^2(L_1)\dot{\eta}_r^2(t)\right)\left(\sum_{r=1}^{2} \phi_{1r}'^2(L_1)\dot{\eta}_r^2(t)\right)$$

(S**148**)

Using the orthogonality conditions for the L-shaped bimorph beam-mass structure with torsional and bending mode

$$EI_1 \int_0^{L_1} \phi_{1r}''(x)\phi_{1s}''(x)dx + EI_2 \int_0^{L_2} \phi_{2r}''(x)\phi_{2s}''(x)dx = \omega_r^2 \delta_{rs}$$
$$\int_0^{L_1} (\rho A)\phi_{1r}\phi_{1s}\,dx + \int_0^{L_2} (\rho A)(\phi_{2r}\phi_{2s} + \phi_{2r}\phi_{1s}(L_1) + \phi_{1r}(L_1)\phi_{1s}(L_1))dx + M_1\phi_{1r}(L_1)\phi_{1s}(L_1)$$
$$+J_{m1}\phi_{1r}'(L_1)\phi_{1s}'(L_1) + M_1 \frac{L_m}{8}\left(\phi_{1r}'(L_1)\phi_{1s}(L_1) + \phi_{1r}(L_1)\phi_{1s}'(L_1)\right) + M_2\phi_{1r}(L_1)\phi_{1s}(L_1)$$
$$+M_2\left(\frac{L_m}{4} + \frac{h_m}{2}\right)\left(\phi_{1r}'(L_1)\phi_{1s}(L_1) + \phi_{1r}(L_1)\phi_{1s}'(L_1)\right) + M_3\phi_{1r}(L_1)\phi_{1s}(L_1) + M_3 \frac{L_m}{8}\left(\phi_{1r}'(L_1)\phi_{1s}(L_1) + \phi_{1r}(L_1)\phi_{1s}'(L_1)\right) = \delta_{rs}$$

(S**149**)

we obtain the forced equation of motion in modal coordinates

$$\ddot{\eta}_r(t) + 2\xi_r\omega_r\dot{\eta}_r(t) + \omega_r^2\eta_r(t) + \chi_{1r}V_1(t) + \chi_{2r}V_2(t) = f_r(t), r \in \{1,2\} \quad (\mathbf{S150})$$

where ξ_r is the modal damping ratio of the r-th bending vibration mode, χ_{ir} are the modal electromechanical coupling terms, which are given by

$$\chi_{1r} = \Theta_1(\phi_{1r}'(L_1) - \phi_{1r}'(0))$$
$$\chi_{2r} = \Theta_2(\phi_{2r}'(L_i) - \phi_{2r}'(0)) \quad (\mathbf{S151})$$

and $f_r(\mathrm{t})$ is the modal force given by

$$f_r(t) = -\int_0^{L_1} \rho A\phi_{1r}(x)dx\ddot{Y}(t) \quad (\mathbf{S152})$$

Substituting equation (S144) into equation (S135), the governing circuit equations are written as

$$C_{p1}\dot{V}_1(t) + \frac{V_1(t)}{R_1} = \sum_{r=1}^{2} K_{1r}\,\dot{\eta}_r(t)$$
$$C_{p2}\dot{V}_2(t) + \frac{V_2(t)}{R_2} = \sum_{r=1}^{2} K_{2r}\dot{\eta}_r(t) \quad (\mathbf{S153})$$

where K_{1r} and K_{3r} are the r-th modal coupling terms of the piezoelectric layers of the main beam, and K_{2r} is the r-th modal coupling term of the piezoelectric layers of the auxiliary beam

$$K_{ir} = k_i b(\phi_{ir}'(L_i) - \phi_{ir}'(0)), i \in \{1,2\}. \quad (\mathbf{S154})$$

Analytical solution

We note that $Y(t) = \Im[Y_0 e^{j\Omega t}]$, where $\Im$ stands for the imaginary part. Consequently, we seek the solutions of Equations (149), and (152) in the form

$$\begin{matrix} \eta_r(t) = \Im[H_r e^{j\Omega t}], r \in \{1,2\} \\ V_i(t) = \Im[U_i e^{j\Omega t}], i \in \{1,2\} \end{matrix} \quad \text{(S155)}$$

Substituting Equation (S154) into Equation (S149),

$$H_r = \frac{f_{r0} - \chi_i U_1 - \chi_2 U_2}{\omega_r^2 - \omega^2 + 2\xi\omega_r\omega j} \quad \text{(S156)}$$

where f_{r0} is the complex amplitude of the modal force function $f_r(t)$

$$f_{r0}(t) = -\int_0^{L_1} \rho A \phi_{1r}(x) dx \ddot{Y}_0 \quad \text{(S157)}$$

Considering Equation (S152), we obtain the following equation system

$$\begin{cases} U_1 Z_1 = Z_3 - Z_2 U_2 \\ U_2 Z_5 = Z_6 - Z_4 U_1 \end{cases} \quad \text{(S168)}$$

Finally, the steady state voltage outputs are given by

$$\begin{matrix} U_1 = \frac{Z_3 Z_5 - Z_2 Z_6}{Z_1 Z_5 - Z_2 Z_4} \\ U_2 = \frac{Z_1 Z_6 - Z_3 Z_4}{Z_1 Z_5 - Z_2 Z_4} \end{matrix}, \quad \text{(S159)}$$

where

$$\begin{matrix} Z_1 = jC_{p1}\Omega + \frac{1}{R_1} + \sum_{r=1}^{2} \frac{\Omega j}{\omega_r^2 - \Omega^2 + 2j\xi_r\omega_r\Omega}(K_{1r})\chi'_{1r} \\ Z_2 = \sum_{r=1}^{2} \frac{\Omega j}{\omega_r^2 - \Omega^2 + 2j\xi_r\omega_r\Omega}(K_{1r})\chi_{2r} \\ Z_3 = \sum_{r=1}^{2} \frac{\Omega j}{\omega_r^2 - \Omega^2 + 2j\xi_r\omega_r\Omega}(K_{1r})f_{r0} \\ Z_4 = \sum_{r=1}^{2} \frac{\Omega j}{\omega_r^2 - \Omega^2 + 2j\xi_r\omega_r\Omega} K_{2r}\chi'_{1r} \\ Z_5 = jC_{p2}\Omega + \frac{1}{R_2} + \sum_{r=1}^{2} \frac{\Omega j}{\omega_r^2 - \Omega^2 + 2j\xi_r\omega_r\Omega} K_{2r}\chi_{2r} \\ Z_6 = \sum_{r=1}^{2} \frac{\Omega j}{\omega_r^2 - \Omega^2 + 2j\xi_r\omega_r\Omega} K_{2r} f_{r0} \end{matrix} \quad \text{(S160)}$$

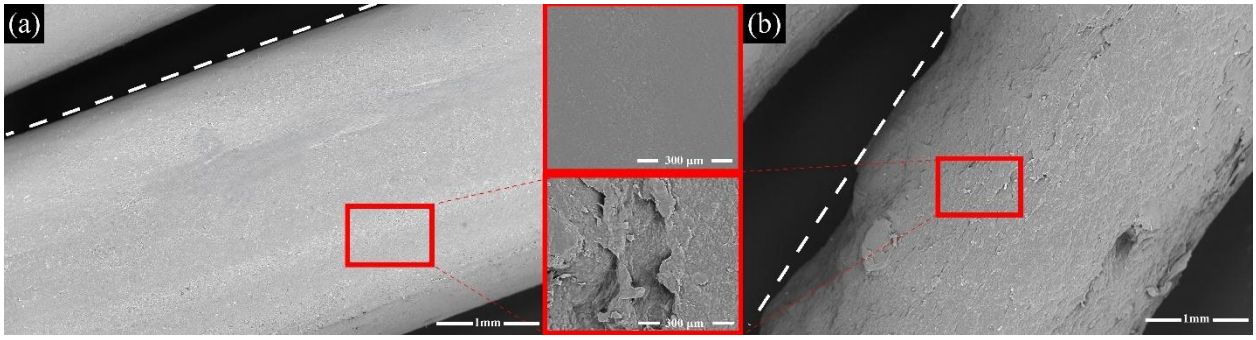

Figure S1: SEM image of the extruded filament surface of (a) C-7.5, and (b) C-10.

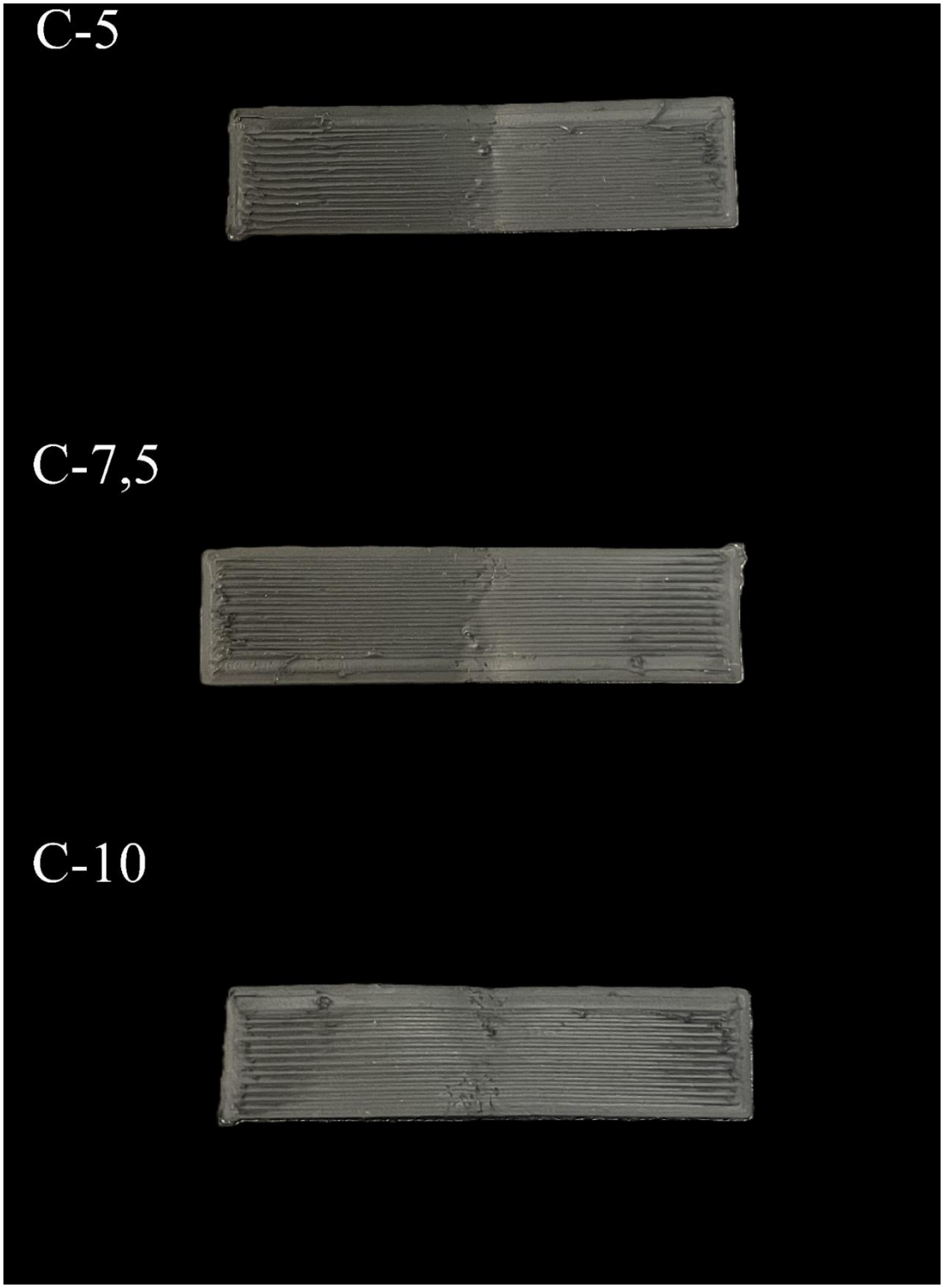

Figure S2: Recovered state of C-5, C-7.5, and C-10 under an electric stimulus.

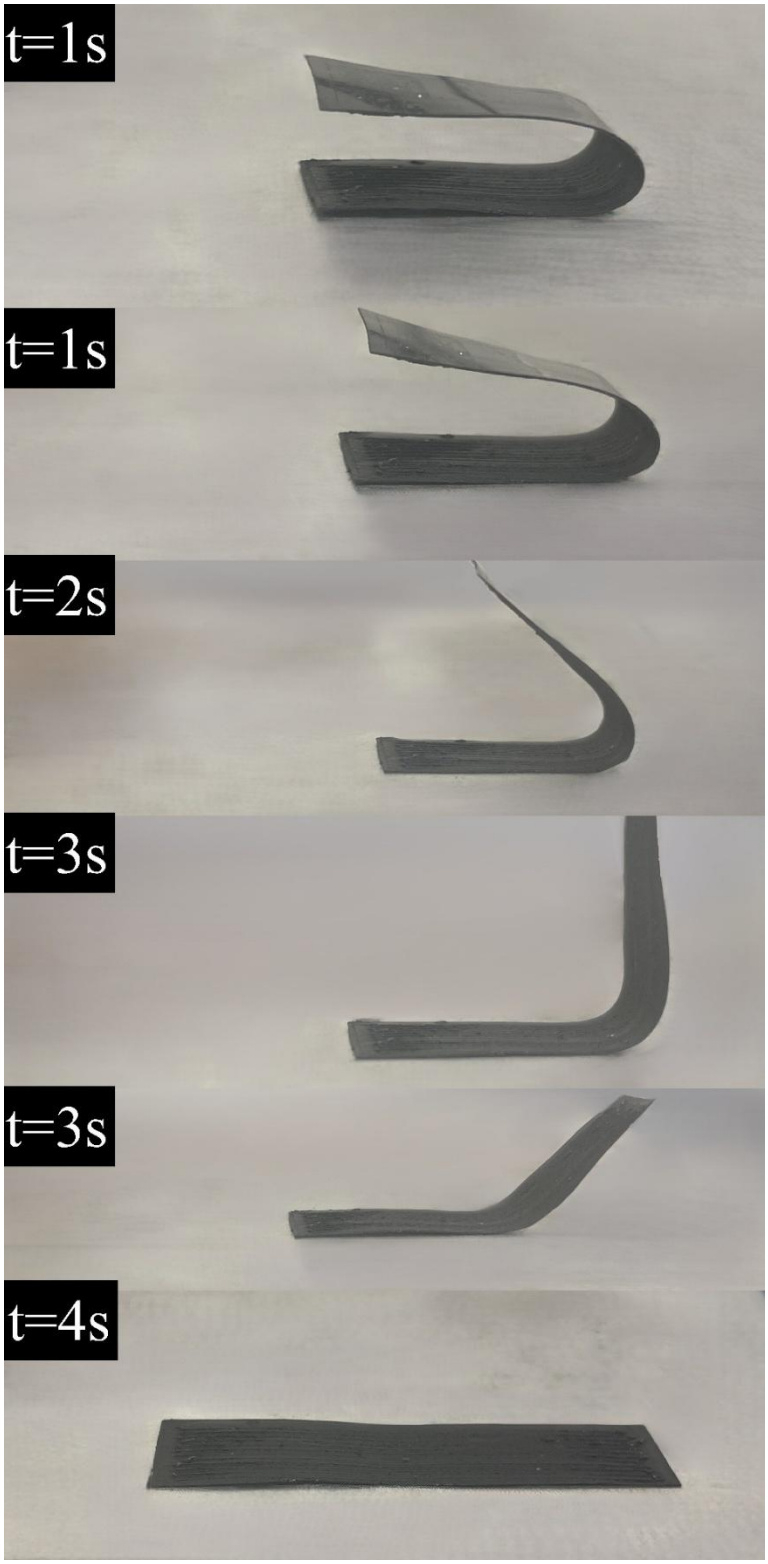

Figure S3: Recovery cycle of C-7.5 under applied heat stimulus.

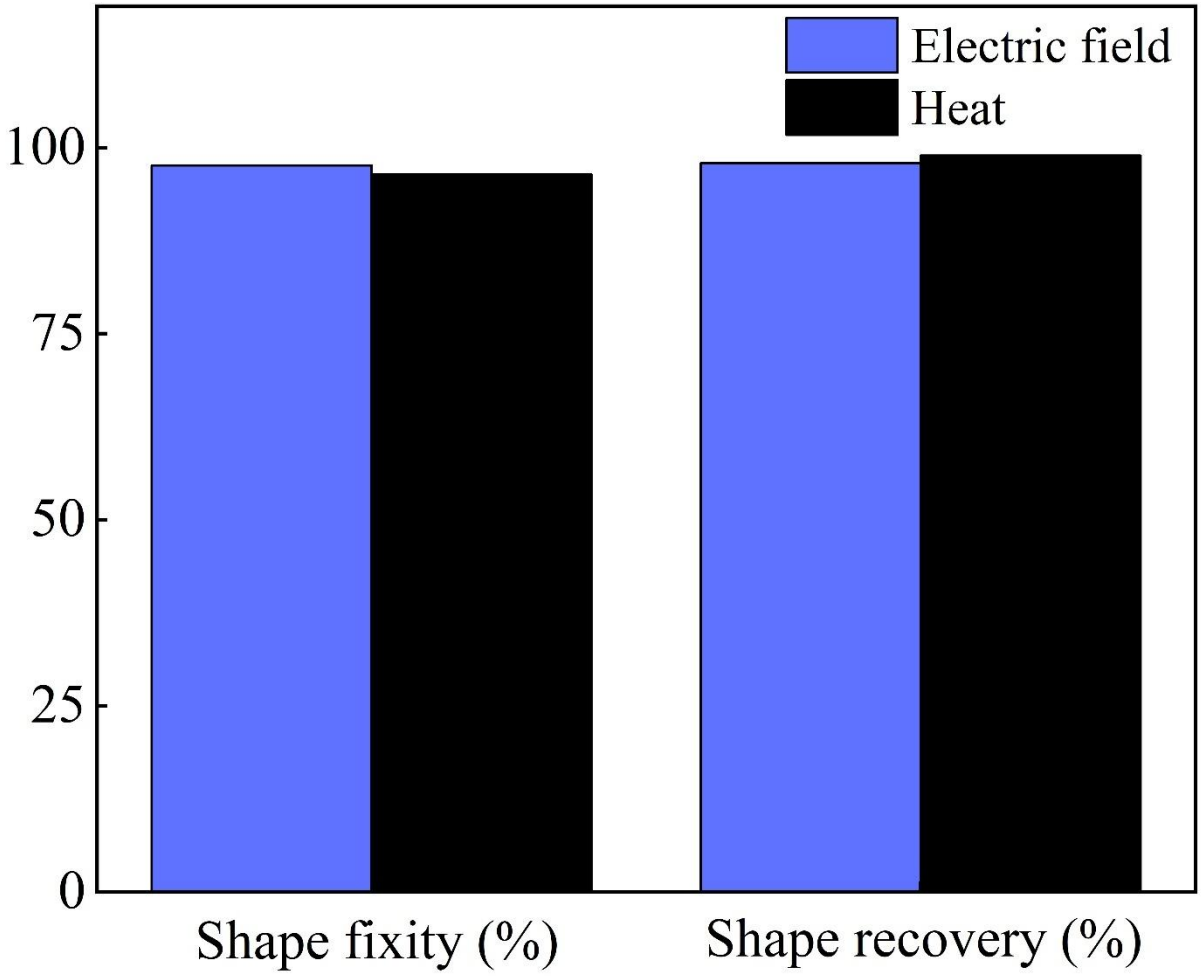

Figure S4: Comparison of shape fixity and shape recovery ratio of C-7.5 under two different stimuli.

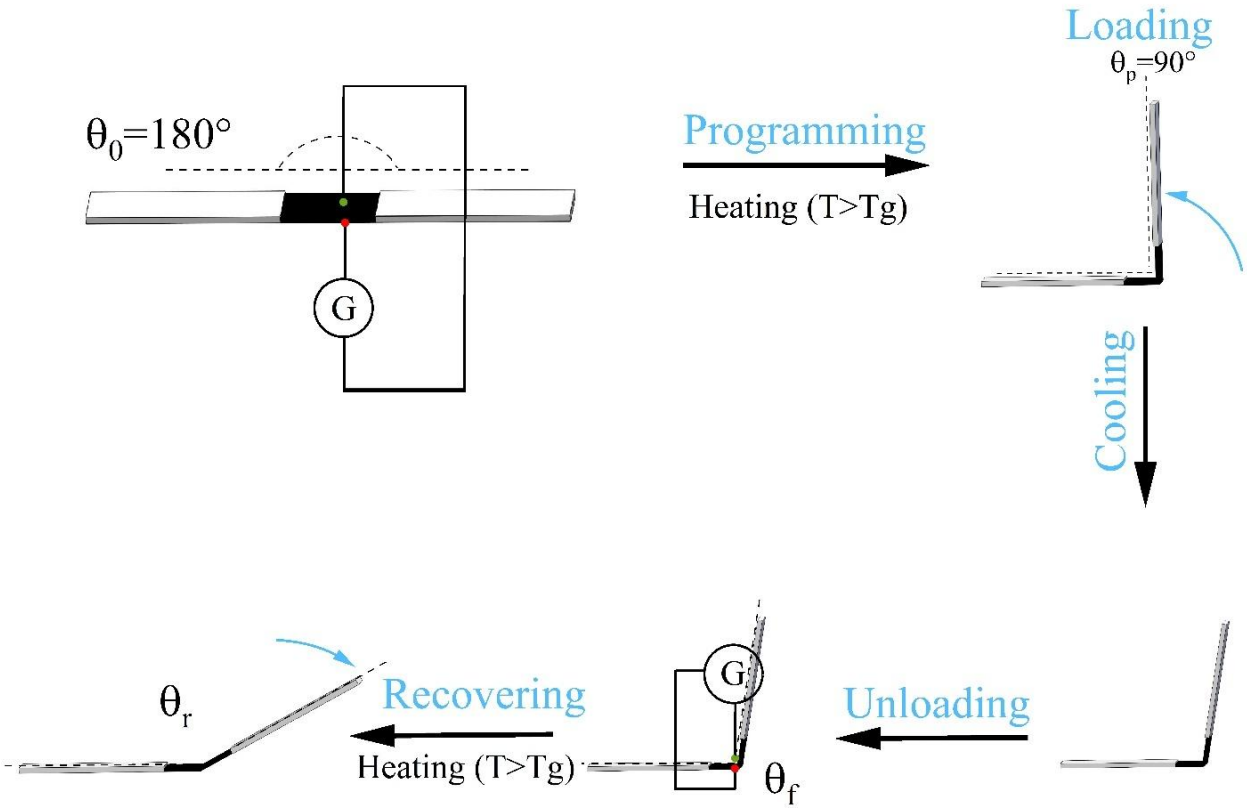

Figure S5: Shape memory cycle of a MSMC-PEH: Programming, cooling, and recovery

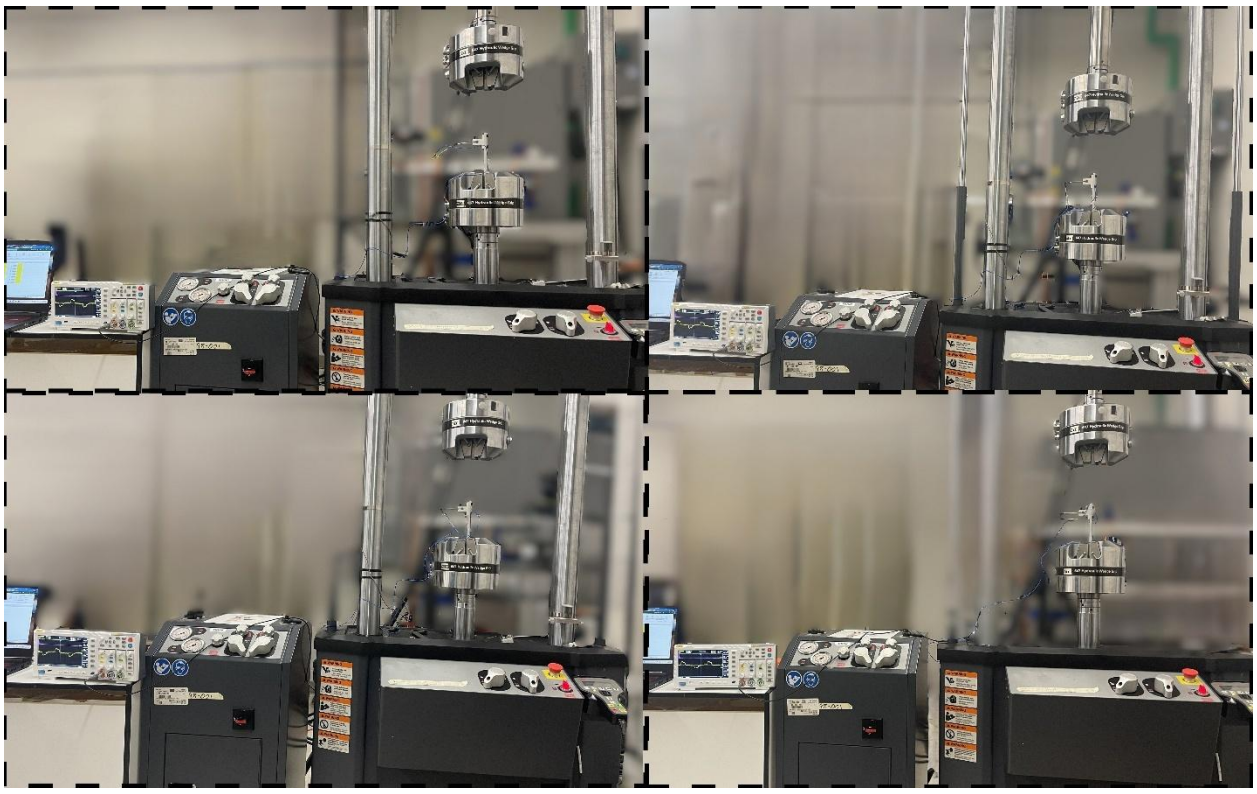

Figure S6: Experimental setup used to test the piezoelectric performance of each configuration